Application of High T/High P Rock Mechanics to the Problem of Extraction of Granitic Magma from its Protolith

Thesis

UNRESTRICTED

Application of high T / high P rock mechanics to the problem of extraction of granitic magma from its protolith

A thesis submitted for the Degree of Doctor of Philosophy

Ditta Hildegard Katharina Neumann

BSc (Honours), University of Liverpool 1989

Department of Earth Sciences
The Open University
Walton Hall
Milton Keynes, MK7 6AA
United Kingdom

December 1994

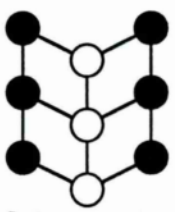

Date of submission : 1st December 1994

Date of award : 24th February 1995

ProQuest LLC.
789 East Eisenhower Parkway
P.O. Box 1346
Ann Arbor, MI 48106 – 1346

To Ernie

Abstract

The mechanical deformation behaviour of a partially molten granitic protolith is investigated. Implications towards a mechanism for extraction of low melt percentages (<<30 %) are mathematically explored.

For this purpose a series of experiments on Westerly granite (with no added water) are presented in which samples were heated to temperatures between 800 and 1200 °C, at a confining pressure of 250 MPa. Samples were uniaxially deformed to study the effects of constant strain-rate ($4 * 10^{-4}$ to $2 * 10^{-7}$ s^{-1}), creep and stress relaxation tests on the mechanical behaviour. The volumetric percentage of melt (Φ) in samples ranged from 3 % at 800 °C to 77 % at 1200 °C at heating times between 2.5 and 170 hours. However, none of the samples attained chemical equilibrium, due to the short duration of tests. An equilibrium melt percentage was also not reached. Over this temperature interval the supported strength decreased from 500 MPa to less than 1 MPa (at a constant strain rate of $8 * 10^{-5}$ s^{-1}) monotonically. No step-like drop in strength, corresponding to a *rheological critical melt percentage* (van der Molen & Paterson 1979) was observed. A preliminary flow law for the partially molten rock was obtained to allow extrapolation to lower strain-rates. The viscosity of the melt was estimated at 950 and 1000 °C from distances it could be made to permeate into porous sand under a known pressure gradient. Melt distribution in static tests indicated a very low wetting angle (< 5°) which results in high melt contiguity even at low melt percentages along grain boundaries.

Under all conditions, the solid phases deformed by brittle fracture only. Samples with $3 \leq \Phi \leq 10$ % failed by forming a macroscopic, cataclastic fault zone and associated axial cracks with voids in-filled by melt. Samples with $10 \leq \Phi \leq 45$ % deformed by pervasive cataclastic flow. Melt was extruded into low pressure regions such as axial cracks in the piston shadows and between sample and jacket. These microstructures are interpreted to occur due to *shear enhanced compaction* of melt filled voids by analogy with uniaxial compaction of porous sands. In samples with $\Phi >$ 45 % grains were carried about passively in the flowing liquid.

A simple mathematical model is erected to describe a two stage process of extracting low volume percentage, granitic melt from its partially molten protolith with the aid of non-hydrostatic stress. *Shear-enhanced compaction* drives melt from the protolith into a series of interconnected melt-filled veins, whereupon porous flow through the high-permeability vein network allows rapid drainage of melt to higher crustal levels. Modeling suggests that melt extraction, with $\Phi <$ 10 % and a melt viscosity of 10^{11} Pas, is possible within geologically realistic time periods (10 Ma).

Acknowledgements

There are such a large number of people that have helped over the last five and a bit years, that it is difficult where to start. These can be roughly spatially divided into three groups: People working or associated with the Open University at Milton Keynes, Duror of Appin and at the Victoria University of Manchester.

Firstly I must thank my two supervisors, Steve Blake and Chris Hawkesworth for inviting me to take up an Open University funded PhD studentship, investigating *crustal melting processes*. Especial thanks to Steve for thorough and patiently reading through yet another version of chapters and appendices in the last couple of months. Thanks are due to Kay Chambers who spent many hours making beautifully polished thin sections and Pete Webb who carried out XRD whole rock analyses on Westerly granite samples.

Even though none of the field work was included in the final work I still spent several months in sunny Scotland. I had the pleasure to find the Scots to be some of the most warm hearted people I've ever met.I had the great fortune to be accommodated and to become friends with the community of Duror of Appin and Cuil Bay, especially Ian and Francis Munro and the madhouse of Kim and Elspeth Malcolm, including their menagerie of cats, dogs, ducks, chicken, sheep, and not to forget Pugwash, the Vietnamese pot-bellied pig. Many happy memories of waiting out yet another rain storm and evenings spent talking. My parents not only invited me to stay with them at the glorious house of Clachan Geala, but also turned out to be extremely keen field assistants. Not everyone has a mother who specially flys in for a week just to sit on a bleak hill top and take notes.

After an extremely unfruitful first field season I had the great fortune of listening to a talk by John Clemens at the Open University which led me to contact the Geology Department of the Victoria University of Manchester to try and re-direct my research aims. John Clemens introduced me to Ernie Rutter who kindly agreed to allow me to perform a couple of deformation experiments on my field rocks. Little did he know that I was to stay for three years. During this time I had the great pleasure of working together with a genius. I certainly received more than my fair share of encouragement and help from him. I wish to thank both him and Rob Holloway, as well as the rest of the B63 crew for their support and friendship over this time. I also had the privilege to spend much time on the Secondary electron microscope at the University of Manchester, and received much help from Tim Hopkins, Dave Plant and Steve Caldwell. Both John

Clemens and Gary Stevens gave invaluable help in analysing and interpreting the multitude of EDS analyses. Experimental assistance was also provided by Gray Stevens, Kathy Davis and Dave Hamilton. During this time I was very kindly accommodated by Tom Houghton in Liverpool and Sue Maher in Manchester (the best landlady in town). Sue also gave invaluable advice on photographic issues, helped out just before talks when the sky was just about to fall on my head, and printed most of the photos.

My long suffering husband Phil gave strong moral support over the last five years, but also gave up dreams about a holiday to New Zealand to spend 16 days coped up in England helping me during the final editing stages (what a mug!).

Lastly, a thought to my wonderful mechanical companion François. Having met him during fieldwork as the field car supplied by me by the Open University, this trusty Renault 4 now has a very proud German owner.

Figure Ac.01: Françoise surveying Cuil Bay and Loch Linnhe from the Chaotic Zone on Ballachulish Mountain in Glen Duror.

My brother Jasper very kindly spent several weeks brooding over the problem of cracks and holes to finally come up with the beautiful program CRACKS. It was very regrettable that the original cracks the program was to analyze were unsuitable.

Table of contents

Chapter 5: Stress-strain and stress relaxation data

Chapter 6: Melt viscosity and activation enthalpy

Chapter 7: Deformation microstructures

Chapter 8: Mathematical modeling of melt extraction

Appendix 6: Chemical analyses of minerals and melt

Appendix 7: !ROCKDEF

Appendix 8: !ROCKDEF program

Appendix 9: Modeling of melt extraction rates

Appendix 10: Stress-strain and stress relaxation mechanical data

Table of figures

Chapter 2: Westerly granite - Rock for deformation experiments

Chapter 3: Westerly granite melt: Physical properties and melting kinetics

Chapter 4: Geochemistry

Chapter 5: Stress-strain and stress relaxation data

Chapter 6: Melt viscosity and activation enthalpy

Chapter 7: Deformation microstructures

Chapter 8: Mathematical modeling of melt extraction

Appendix 1 "Paterson" Gas Rig

Appendix 2: Data processing of gas rig output

Appendix 4: Measurement of micro-crack density and orientation

Appendix 5: Thermogravimetry

Appendix 7: !ROCKDEF

Chapter 1

Introduction

1.1 Aims and Introduction

This thesis sets out to find a mechanical solution to the problem of extracting a granitic melt occupying a small volume fraction (<< 0.30) from a partially molten source rock. It has long been the belief of geochemists (e.g. White & Chappell 1977) that certain granitoid melts represent minimum melts of igneous and metasedimentary source rock, that can be extracted from their source rock. For example Sawyer (1991) suggested that the segregated migmatites he investigated displayed rare earth element distributions in restite and leucosomes indicative of between 0.12 and 0.36 partial melting of the host metabasites. This stands in contrast to the results of rock mechanics experiments (e.g. Arzi 1978; van der Molen & Paterson 1979) which suggests that a *rheological critical melt fraction* exists, at about 0.30 - 0.35 melt, below which melt extraction is very unlikely.

In recent years considerable progress has been made in the theory of melt extraction from a residual matrix of solid grains, particularly when driven by the density difference between the melt and the residuum (e.g. Turcotte & Schubert 1982; McKenzie 1984, 1985; Sleep 1988). Application of these ideas to the partial melting of peridotites has been very successful. However, granitic melt extraction by this method was deemed impossible on geologically realistic time scales due to the high viscosity of acidic melts (e.g. Wickham 1987).

Experimental studies on basic systems (Cooper & Kohlstedt 1984; Cooper 1990) have demonstrated the role of differential stress in aiding melt extraction. The presence of differential stresses in lower crustal rocks has been widely recognized to accompany migmatization in the form of e.g. foliation, folds, shear zones, boudinage etc. indicative of large scale flow. However, the attainment of metamorphic microstructural equilibrium, after most of the deformation has been accomplished, means that the evidence of deformation mechanisms operative during the migmatic episode have generally been removed. Several attempts have been made to devise microstructural criteria diagnostic of "magmatic flow" (McLellan 1984; Ashworth & McLellan 1985; Nicolas et al. 1988; Quick et al. 1992; Rutter et al. 1993).

Clemens & Mawer (1992) argued that a rapid collection of melts into an interconnected dyke system was necessary to extract granitic melts, and several authors have noted the common association of granites with shear zones and have argued that deformation may play a central role in the mechanics of accumulating granitic melts (e.g. Wickham 1987; Hutton et al. 1990; Hutton & Ingram 1992; Davidson et al. 1992; Hippert 1994). It has been argued that melt is transported in dykes (Clemens & Mawer 1992) and emplaced at higher crustal levels where the dykes balloon to form plutons and batholiths (Fowler 1994).

Experiments on granitic melt extraction must study systems that are as simple as possible. As the minimum melt extracted from metabasites, metasediments and granites will always be of granitic composition (White & Chappell 1977; MacRae & Nesbitt 1980) it is realistic to use a 'granite' (sensu lato) as the starting material for partial melting experiments. The advantage in choosing a granite over a metabasite is that much lower temperatures are needed to induce partial melting (depending on fluid activity). Metasediments, especially metapelites, have much lower melting temperatures than granite but tend to have a strong preferential mineral fabric (schistosity), as well as containing a large number of different phases. In granite the major phases are very limited (usually to quartz, feldspars and mica) and they tend to show a good uniform fabric. Also the grain size is usually large enough to allow easy recognition of different phases. This makes a 'granite' an ideal experimental rock.

Few experimental studies on the deformation of partially molten granitic material have been carried out. In the seminal study of van der Molen and Paterson (1979) known amounts of water were added to control the amount of melt generated at the single test temperature (800 °C) and confining pressure (300 MPa) used. They demonstrated how the strength of the rock was dramatically decreased as the amount of melt increased, largely owing to the reduction of the effective confining pressure through the pressure exerted by the melt, coupled with the progressive breakdown of the contiguity of the matrix of solid grains. Similar results were obtained in the studies of Arzi (1978), Auer et al. (1981), Paquet and Francois (1980) and Paquet et al. (1981). In such studies the deformation of the matrix was by cataclasis. Dell'Angelo et al. (1987) and Dell'Angelo and Tullis (1988) studied the flow of partially molten granitic rocks under conditions favouring intracrystalline plastic flow of the solid matrix (900 °C and 1500 MPa confining pressure), again with added water. They also showed that fine-grained, sintered granitic aggregates could flow by melt-aided diffusive mass transfer. These observations differ significantly from the structures predicted by McKenzie (1984), who envisaged that the grains would be plastically deformed, so reducing the porosity of the rock, and expelling the melt without causing large scale grain damage.

In this thesis a series of experiments on Westerly granite are presented in which specimens were heated to temperatures between 800 and 1200 °C with no added water. The amount of melt was therefore primarily controlled by the temperature as all water available to the melt came from the breakdown of phyllosilicate minerals. The experiments were aimed at determining the mechanical behaviour of the combined melt plus crystalline matrix of grains and the rheology of the melt alone. Microstructural and microchemical studies were performed to determine deformation mechanisms, the amount of melting and its distribution, plus compositional variations in the melt and the way they relate to adjacent minerals. Finally an attempt was made to apply these results to a simple model for natural syntectonic extraction and accumulation of granitic melts.

1.2 Methodology

A first approach to study the mechanical behaviour of partially molten rocks, including deformation behaviour and melt extraction was fieldwork on the metamorphic aureole surrounding the Ballachulish Igneous Complex, Scotland. Diorite intruded at mid crustal levels caused partial melting in the pelitic country rocks (Ballachulish Slate, Appin Transition Series and Leven Schist). The aureole shows no evidence of overprint by either metamorphism or deformation after the partial melting event and it is therefore well suited to the study of primary partial melt structures. However, several aspects of the Ballachulish partial melt structures (e.g. metamorphic reactions leading to partial melting, melt dihedral angles, melt geochemistry, deformation associated with emplacement of the igneous complex, and melt structures associated with partial melting) had been investigated in earlier studies (e.g. Bailey & Maufe 1960; Pattison 1985; Weiss 1986; Linklater 1990; Platten 1990). Detailed structural mapping of melt morphologies in partially molten pelitic lithologies was undertaken. These included orientation measurements of interconnected vein systems at Coire Chaorann, and widespread boudinage, exfoliation and viscous flow structures in the Chaotic Zone. However, without independent constraints on the stress field operating during partial melting and the absence of microstructural deformation evidence (due to extensive re-crystallization) it was impossible to constrain mechanical behaviour. Melt in the aureole is restricted to the zone of partial melting; no melt extraction beyond the realm of partial melting was observed. It was therefore impossible to study melt extraction in this setting.

From questions posed through fieldwork on Leven Schist, Appin Transition Series and Ballachulish Slate (melt distribution in the partially molten host rock) it was clear that it

was necessary to have a better understanding of the mechanical behaviour of the combined melt plus crystalline matrix and the rheology of melt alone, in order to understand the deformation mechanisms of rocks containing a low melt fraction. Professor E. H. Rutter (Experimental Rock Deformation Lab, Manchester) very kindly invited the author to perform several rock deformation experiments on the Ballachulish lithologies that show partial melting structures in the aureole of the granite. Care was taken to collect specimens for rock deformation experiments outside the realm of influence of the Ballachulish Igneous Complex. On returning to the laboratory cores were drilled from the samples. However, due to a very strong foliation in the metasediments, the cores were too friable to handle and commonly disintegrated into stacks of disks when drilled orthogonal to cleavage. Also the grain size of mica (in excess of 2 mm) was deemed too large to give a homogeneous and representative sample in cores of 6.3 mm diameter and 10 mm height. Tests on Leven Schist and Ballachulish Slate were consequently abandoned. However, it was still felt that experimental investigation into microstructures and deformation behaviour of partially molten metapelites was worth pursuing.

A replacement for the rocks collected at Ballachulish was found in a homogeneous purple North Wales Slate. This rock type was of a fine grain size and of homogeneous composition, containing a pervasive slaty cleavage. Cores were easily obtained and were less friable. The confining pressure was chosen to be 250 MPa, as this is thought to be similar to the confining pressure of country rocks during the intrusion of the Ballachulish Igneous Complex (Weiss 1991). Over a period of 11 months (in 1991) 21 deformation tests (at 250 MPa confining pressure and temperatures between 550 and 700 °C) were carried out using "Nimonic" deformation machines (see Covey-Crump (1993) for further machine descriptions). The solidus was found to be near 650 °C. The relatively small sample size (6 mm diameter and 10 mm length) prohibited measurement of the strength of partially molten samples above background noise (about 3 MPa differential load). Also the small grain size provided many nucleation sites, causing the melt to recrystallize during quenching such that glass could not be clearly observed optically and under the (secondary) electron microscope. Experiments were discontinued and a new test material had to be found.

A more simple rock was required in which the evolving melt could easily be observed and analysed, even at low melt fractions. As the minimum melt of a metasediment, as well as metabasites and igneous rocks is granitic (see section 1.1 above) it seemed reasonable to choose an igneous rock as a substitute. A rock superbly suited to study the rheological behaviour of partial melt and the microstructural interaction of melt and solid matrix during deformation was found in the fine grained monzogranite

Westerly granite from Rhode Island, USA. This rock has been extensively used by others in rock mechanics experiments to determine natural rock behaviours due to its fine, isotropic grain size (960 μm average diameter of grains occupying more than 97 % of the rock volume) and homogeneous composition (e.g. Brace et al. 1968; Scholz & Kranz 1974; Zoback & Byerlee 1975; Wu & Thomsen 1975; Hadley 1976; Janach 1977; Kranz et al. 1982; Carter et al. 1981; Wong 1982; Wong et al. 1989; Hall & Bodnar 1989).

Experiments on Westerly granite were carried out in an internally heated "Paterson" gas rig in which cylindrical rock samples of ~20 mm length and 10 mm diameter were heated to temperatures between 800 and 1200 °C at a constant confining pressures of 250 MPa. Constant strain rate tests were carried out with the load applied by compressive movement of a piston at strain rates between $4 * 10^{-4}$ to $2 * 10^{-7}$ s^{-1}. During the experiments stress and axial displacement were recorded. Melt stress relaxation behaviour was recorded at maximum strain and at several points during the deformation history. Deformation was followed by rapid quenching of the sample at 100 °C per minute. Thin sections of the deformed samples were studied using optical and electron microscopes. From microstructural observations an extraction model for melt constituting a small volume fraction of the protolith (below 0.15) is proposed.

Ideally it would have been desirable to test this extraction mechanism using field observations. However, the exposure and microstructures observed were unsuitable for this purpose. The extensive re-crystallization in the partially molten rocks in the Ballachulish aureole prohibited comparison to microstructures observed in quenched samples of Westerly granite that were deformed in the laboratory. Extraction of melt into veins outside the zone affected by partial melting could not be observed in the field, hence prohibiting comparison of meso-structures in the field with this part of the melt extraction model. It also proved impossible to either construct a model describing deformation of the Ballachulish aureole during the partial melting interval, or significantly improve on meso-structural descriptions above those described by Harte et al. (1992). It was therefore felt that an inclusion of data collected during fieldwork on the Ballachulish aureole did not add towards the conclusion reached in the following chapters. Therefore, descriptions of partial melting structures observed in the Ballachulish aureole have not been included in this work.

1.3 Layout

In the following six chapters the results from experimental deformation of WESTERLY GRANITE are described. This is followed by a chapter on mathematical modeling of

partial melt extraction from a host rock deformed during the melting interval. In detail the chapters comprise:

In **Chapter 2** the characteristics of untreated Westerly granite are described to set a bench mark against which to judge microstructural and geochemical changes induced by elevated temperatures and applied hydrostatic and differential stress.

Chapter 3 describes the effects of temperature and test time on melt fraction and crystal dissolution. The effect of crystallization on melt fraction is discussed. The melt habit in undeformed samples is described.

Chapter 4 encompasses geochemical analysis of the test runs, including analysis of the compositional variations within the major phases with increasing temperature and analysis of the phases generated as a by-product of melting. The melt phase is analysed with respect to spatial variation and the influence of adjacent phases on melt composition is investigated. Conclusions are drawn about the attainment of chemical equilibrium between the residual solid phases and melt in the experiments.

In **Chapter 5** the results of stress-strain measurements recorded during deformation and stress relaxation are discussed and analysed. These give information on the strength and bulk rheology of partially molten charges.

Chapter 6 describes experiments designed to measure the viscosity and activation enthalpy for viscous flow of melt. These results are compared to the bulk rheology and discussed in the light of the results of van der Molen & Paterson (1979).

Chapter 7 deals with the development of microstructures over the temperature interval studied. Analogies are drawn between the deformation microstructures observed in a porous sandstone compacted under differential stress (Rutter & Hadizadeh 1992) and those observed in the partially molten Westerly Granite. The stress conditions under which shear enhanced compaction is expected to operate are explored.

Chapter 8 comprises mathematical modelling of melt extraction by *shear enhanced compaction*, as observed in samples deformed at intermediate temperatures, in association with gravity driven extraction of melt from an interconnected framework of veins. This is compared to the gravity-settling model proposed by McKenzie (1984). Mathematical modelling is extended from Westerly granite to granitoid magmas in general to allow the calculation of melt extraction rates of granitic melts at different melt fractions, melt viscosities and water contents, at variable strain rates and applied differential stresses.

Chapter 9 summarises the preceding chapters and draws general conclusions concerning the extraction of low melt fraction, granitic melts of high viscosity from their source. The transposition of microstructures observed in experiments to structures that can be observed in a natural setting is discussed, evaluating several partially molten rock scenarios.

The appendices describe the experimental equipment and procedures and the computer programs used in data processing. They are as follows:

Appendix 1. The "Paterson" gas rig is described briefly, including a detailed description of the ways different parameters were measured.This is followed by a description of sample preparation and procedures taking place during uniaxial compression testing. Finally post-testing sample treatment is described.

Appendix 2. The steps taken during data processing to determine the true stress and strain supported by the sample are described.

Appendix 3. The secondary electron microscope used is briefly described and the limitations of image processing and geochemical analysis are discussed.

Appendix 4. The routines used in crack density and crack orientation measurements are explored in this appendix.

Appendix 5. Thermogravimetry as a method for determining the water content of samples is described and the results for Westerly granite are presented.

Appendix 6. Chemical analyses of crystals and melt are listed, followed by a listing of analyses from the powder sample (WG1).

Appendix 7. The data processing routines that allow on line and post-test data processing are described, that form part of the program !ROCKDEF.

Appendix 8. Listing of the data processing package !ROCKDEF written by Professor E.H. Rutter.

Appendix 9. In this program the formulas used for constructing diagrams plotting extraction rates of melt from partially molten Westerly granite and granitoid protoliths are described, associated with a listing of the resultant spreadsheets.

Appendix 10. Listing of the processed mechanical data from deformed samples (WG2 to WG30).

1.4 Degree of cooperation with co-workers

Although the author was supervised by Professor Hawkesworth and Dr Blake at the Open University, all experimental rock deformation was carried out in the Experimental Rock Deformation Laboratory at the Geology Department of the Victoria University of Manchester under the guidance of Professor E. H. Rutter. The author has worked in close cooperation with Professor E. H. Rutter effectively in the role of a research assistant over a time period of three and a half years. As the "Paterson" gas rig (on which all deformation experiments on Westerly granite were performed) was installed and commissioned during the time the author spent at Manchester the controlling and data processing software had to be written in parallel with running samples on this and other projects. This software was written by Professor E. H. Rutter (**Appendix 5**) due to the developmental nature of the work on this machine during this period. As there was not complete user control during the duration of the author's stay, the "Paterson" gas rig was operated solely by Professor E. H. Rutter. As with every research machine, problems were anticipated and encountered during experiments. To complement the experimental rock deformation, the author carried out some data processing and all geochemical, microstructural, melt fraction and fieldwork analysis, while Professor E.H. Rutter carried out viscosity calculations presented in **Chapter 6** and modeling carried out in **Chapter 8**. The latter chapter is an extract from a jointly written paper (Rutter & Neumann 1995) and was included as the work presented in it builds on results from the deformation experiments.

1.5 Abbreviations used in diagrams

Several abbreviations are commonly used on photographic plates, in order to allow distinction between different phases. These are listed in **Table 1.01**.

Abbreviation	Phase
am	Amphibole
ap	Apatite
bio	Biotite
ca	Calcite
ch	Chlorite
cpx	Clinopyroxene
ep	Epidote
gar	Garnet
hae	Haematite
ilm	Ilmenite
K-fsp	Potassium feldspar
melt	Melt
mu	Muscovite

ol	Olivine
plag	Plagioclase
opx	Orthopyroxene
qtz	Quartz
ru	Rutile
sph	Sphene
spi	Spinel
wol	Wollastonite
z	Zircon

Table 1.01: List of mineral and melt abbreviations used on photographic plates.

1.6 Symbols used in mathematical equations

The symbols used throughout the following chapters and appendices are listed in **Table 1.02**. Roman symbols are listed first, followed by Greek symbols in the first columns. The next columns explains what the symbols represent, followed by a column listing the appropriate SI units. In the right hand column the equation, table, figure, chapter and appendix are listed, in which the symbol is first used. Letters represent:

A Appendix
C Chapter
E Equation
F Figure
T Table

Symbol	Variable	Unit	Equ.
A	Increase in hydrostatic pressure due to applied deviatoric stress	Pa	E7.01
a	Effective radius of annulus. **2a** = spacing between veins	m	E8.10
B	Pore fluid coefficient	dimensionless	E7.01
b	Width of melt channels (veins)	m	E8.06
C_b	Compressibility of pore-free solid	Pa^{-1}	E6.05
C_f	Compressibility of melt	Pa^{-1}	E6.05
C_r	Compressibility of rock (pores+ solid)	Pa^{-1}	E6.05
D	Exponential scaling factor	dimensionless	E5.02
c	Specific heat	$kJ\ kg^{-1}\ K^{-1}$	E8.23
d	Increment of increase	dimensionless	E5.01
E	Young's modulus	Pa	EA2.01
e	Factor **e**, base of natural log = 2.71828	dimensionless	E5.02
erfc	Complimentary error function	dimensionless	E6.02
F	Melt fraction in fault zone	vol fraction	T3.01
f	Exponential scaling factor	dimensionless	E3.01

g	Acceleration due to gravity (= 9.81)	$m\ s^{-2}$	E8.02
H	Activation enthalpy for viscous flow of partially molten rock	$J\ mol^{-1}$	E5.02
h	Thickness of partially molten layer	m	E8.04
h_m	Thickness of melt layer extracted from layer **h**	m	E8.04
I	Arbitrary point in circle	dimensionless	EA4.01
i	Exponential scaling factor	dimensionless	E8.20
J	Production of melt = vein emptying (melt fraction per second)	s^{-1}	E8.09
j	Radius of circle	pixel	EA4.01
k	Permeability	m^2	E6.02
L_o	Original specimen length	mm	EA2.01
L_t	Specimen length after time **t**	mm	EA2.01
ln	Logarithm to the base **e** (natural log)		
log	Logarithm to the base 10		
M	Melt fraction, after neo-crystallization	vol fraction	T3.01
m	Slope of force/displacement line and machine complience	dimensionless	FA3.02
N	Number of melt channels per metre	dimensionless	E8.07
n	Empirical constant = slope of stress-relaxation curves	dimensionless	E5.01
O	Mid-point of square	dimensionless	EA4.01
P	Pressure	Pa	E7.01
P(r)	Local fluid pressure at radius **r**	Pa	E8.10
P(x,t)	Pressure variation with distance (**x**) and time (**t**)	Pa	E6.02
P_{conf}	Confining = hydrostatic pressure	Pa	T6.01
P_o	Pressure in source	Pa	E6.02
P_v	Melt pressure in veins	Pa	E8.10
Q	Activation enthalpy for viscous flow of melt	$J\ mol^{-1}$	E6.07
q	Melt fraction extracted into an adjacent layer of quartzite	vol fraction	T3.01
R	Gas constant = 8.31441	$J\ mol^{-1}\ K^{-1}$	E5.03
r	Radius between 0 and a, point at which **P = P(r)** etc.	m	E8.10
RMSE	Root mean square error	dimensionless	C3.05
S	Machine stiffness	$kN\ mm^{-1}$	EA2.06
s_a	Complience of alumina specimen (=1/stiffness)	$mm\ kN^{-1}$	EA2.02
s_m	Machine complience	$mm\ kN^{-1}$	EA2.02
s_s	Specimen complience	$mm\ kN^{-1}$	EA2.02
s_t	Total complience	$mm\ kN^{-1}$	EA2.02
T	Temperature	K	E5.03
$T_{@def}$	Temperature at which sample was deformed	°C	T6.01
T_b	Temperature of country rock	K	E8.22
T_c	Temperature in Celsius	°C	E3.01

T_Δ	Temperature at distance **x** from heat source	°C	E8.22
T_{max}	Maximum temperature the sample was heated to	°C	E3.01
T_o	Temperature of heat source	K	T8.22
t	Time	s	E6.06
t_h	Time to compact layer of thickness **h**	s	E8.04
$t_{to\ def}$	Time sample remained at temperature prior to deformation	h	T5.01
t_{total}	Total time remained at temperature (>21°C), prior to quenching	h	T5.01
U	Mean velocity in melt channels	$m\ s^{-1}$	E8.06
u	Dummy variable in complimentary error function	dimensionless	E6.04
V	Volume	mm^3	E3.04
v	Direction of σ_1	dimensionless	C8.2.3
w_o	Upward velocity of fluid relative to matrix	$m\ s^{-1}$	E8.02
x	Transport distance	m	E6.02
y	Distance	m	E8.22
z	Grain size diameter	m	E6.03
∇^2	Laplace's operator	m^{-2}	E8.09
α_{av}	Average spacing between pixels	pixel	A4.3
α_{max}	Maximum spacing between pixels	pixel	A4.3
β	Fluid storage capacity of the solid	Pa^{-1}	E6.02
δ_c	Compaction length	m	E8.01
ε	Strain	%	
$\dot{\varepsilon}$	Strain rate	s^{-1}	E5.01
ε_{max}	Maximum strain	%	T5.01
ε_u	Strain at Ultimate strength of sample	%	C5.2.1
ε_y	Strain at yield point	%	C5.2.1
Φ	Melt percentage	vol %	C9.3
ϕ	Melt fraction (= Melt percentage/100), porosity in quartzite	dimensionless	E3.01
γ	Coefficient of thermal conduction	$W\ m^{-1}\ K^{-1}$	E8.23
η	Fluid viscosity	Pa s	E6.01
φ	Crack orientation	°	A4.3
κ	Thermal diffusivity	mm^2	E8.22
λ	Angle of macroscopic fault with respect to σ_1	°	F5.17
Θ	Cross section area of specimen	mm^2	EA2.01
ρ	Density	$kg\ m^{-3}$	E8.23
$\Delta\rho$	Melt/matrix density difference	$kg\ m^{-3}$	E8.02
σ	Stress	Pa	E5.01
$\bar{\sigma}$	Hydrostatic stress	Pa	C7.7.2
σ'	Octahedral shear stress	Pa	C7.7.2

σ_1	Maximum principal stress	Pa	E6.01
σ_2	Intermediate principal stress (assumed to equal σ_3)	Pa	C8.2.3
σ_3	Minimum principal stress	Pa	E6.01
σ_a	Average stress from remotely applied σ_1	Pa	E8.12
σ_{max}	Maximum stress = Ultimate strength of rock	Pa	T5.01
σ_{xx}	Normal stress	Pa	F8.09
σ_{xy}	Resolved shear stress	Pa	F8.09
σ_y	Stress at yield strength	Pa	C5.2.1
τ_o	Compaction time	s	E8.03
ψ	Water content	wt %	E8.16
μ	Effective viscosity of solid matrix	Pa s	E8.01
π	Factor π = 3.14159	dimensionless	E6.06

Table 1.02: Symbols used in chapters and appendixes to describe mathematical variables.

Chapter 2

Westerly granite: Rock for deformation experiments

2.1 Introduction

All experimental rock deformation tests were carried out on cylinders cored from a single block of Westerly granite (see **Appendix 1** for sample preparation). In order to understand and interpret changes to the starting material due to heating and uniaxial, compressional, deformation it is necessary to understand the starting material in some detail. Therefore the initial chemical composition, petrography mineral compositions and microstructural fabric of the Westerly granite block used was examined.

The bulk chemistry served as a point of comparison for the composition of melts developed during the high temperature experiments and the documentation of original phase relationships and compositions allowed the melting process to be explored in **Chapter 4**. The microstructural fabrics were described to check for any preferred orientation that might effect the deformation and were later compared to microstructures developed during deformation experiments to allow a discussion of deformation mechanisms (**Chapter 7**).

The polished thin section of Westerly granite that was used in all textural and chemical analysis of minerals in the starting material was arbitrary given the name WG0 to ease comparison with samples heated to temperatures between 800 and 1200 °C that were given names between WG1 and WG30.

2.2 Whole rock geochemistry

Major and trace element concentrations for bulk Westerly granite were analysed by XRF at the Open University (**Table 2.01**).

Oxide (wt %)		Trace elements (ppm)		CIPW norm (wt %)	
SiO_2	68.72	Rb	186	Q	22.20
TiO_2	0.05	Sr	462	C	0.57
Al_2O_3	15.43	Y	9.8	or	27.13
Fe_2O_3	2.68	Zr	308	ab	35.29

MnO	0.03	Nb	12.9	an	8.28
MgO	0.75	Ba	1868	hy	1.87
CaO	1.83	Pb	29	mt	0.60
Na_2O	4.17	Th	26	hm	1.59
K_2O	4.59	U	2	il	0.96
P_2O_5	0.14	Sc	3	ap	0.32
LOI	0.61	V	35	Total	98.81
Total	99.46	Cr	15		
		Co	3		
		Ni	7		
		Cu	9		
		Zn	84		
		Ga	23		

Table 2.01: Whole-rock analysis of Westerly granite. Analyses by P. Webb, Open University.

When plotted on a total alkali-silica plot, Westerly granite (with this composition) lies on the rhyolite-dacite boundary in the classification scheme of Cox et al. (1979).

2.3 Petrography

Westerly granite is a fine grained monzogranite (**Figure 2.01**). It is dominated by feldspar and quartz, leaving a small volume to be occupied by mica (biotite, chlorite and muscovite) and accessory phases (apatite, calcite, epidote, ilmenite, haematite, rutile, sphene and zircon). The granite has an even grain size distribution with no obvious phenocryst development. The grains form a tight interlocking fabric with many 60 ° grain boundary triple junctions indicating textural equilibrium.

Modal compositions were estimated using the image processing facility linked to the *Secondary electron microscope*, at the Geology Department of the Victoria University of Manchester (see **Appendix 3** for machine description). The areal proportions of phases in 51 images (at a magnification of * 110) were estimated, assuming that the areal percentage can be taken to equal the volume percentage (Underwood 1970). The errors on the modal percentages were estimated from the results of a study of the error in melt percent determination (**Chapter 3.2.1**). The modal percentages of the major phases are recorded in **Table 2.02** and compared to those determined by Wong et al. (1989) on a different sample of Westerly granite.

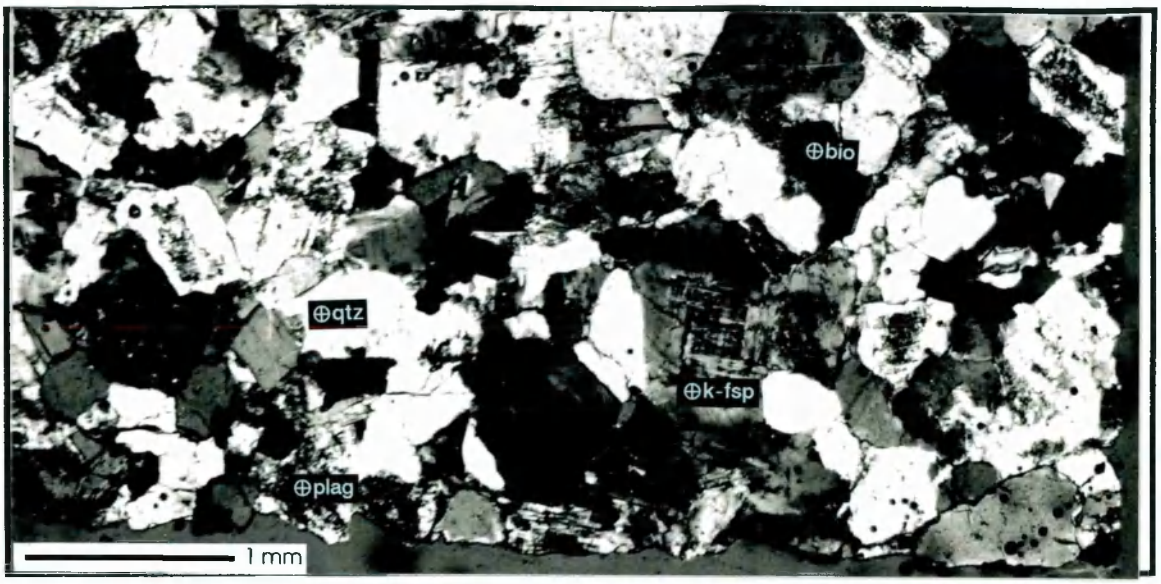

Figure 2.01: Optical photograph of Westerly granite (WG0) taken at half polars.

Phase	This study	Wong et al. (1989)
Plagioclase	38.0 (± 5.7)	31.4
Quartz	29.2 (± 4.6)	27.5
Microcline	26.2 (± 4.0)	35.4
Mica + accessories	6.5 (± 1.4)	5.7
Biotite	3.8	
Muscovite	1.4	
Chlorite	0.8	
Accessories	0.6	

Table 2.02: Modal composition of Westerly granite (volume %) estimated using image processing associated with the Secondary Electron Microscope at the Geology Department of the Victoria University of Manchester with deviatoric error in brackets. Hydrous phases (Biotite, muscovite,chlorite) and accessories were further differentialted using a point counter with 1000 points counted. The right hand column lists modal proportions of Westerly granite as measured by Wong et al. (1989) using optical microscopy point counting.

The main difference between the volumetric percentages estimated in this study and by Wong et al. (1989) is the microcline to plagioclase ratio. The ratio recorded in this study is consistent with the CIPW norm percentages determined from whole rock analysis (though CIPW norm calculations will overestimate orthoclase, as all K_2O in mica is recast as orthoclase) (**Table 2.01**). Differences between the two analyses can be related to a combination of different compositions due to heterogeneities of the monzogranite on a pluton scale, and difficulty in distinguishing between feldspars optically, due to lack of twinninng.

The grain size of the starting material was estimated by tracing the outlines of minerals from a thin section photo collage. The tracing was then scanned and processed using the program !GRAINS (Evans 1995) to estimate average grain diameter; an average of 300 μm was determined. However, this estimate of average grain size includes both major and accessory phases the latter being significantly smaller. As less than 2 % of the rock by volume is composed of a large number of accessory phases with a very small grain size, a grain size cut-off of 200 μm was used to determine the average diameter of the major phases. It was felt that this result, 960 μm, reflected the average grain size of phases that control the deformation behaviour. This latter estimate compares well with an average diameter of 750 μm, determined by Wong et al. (1989).

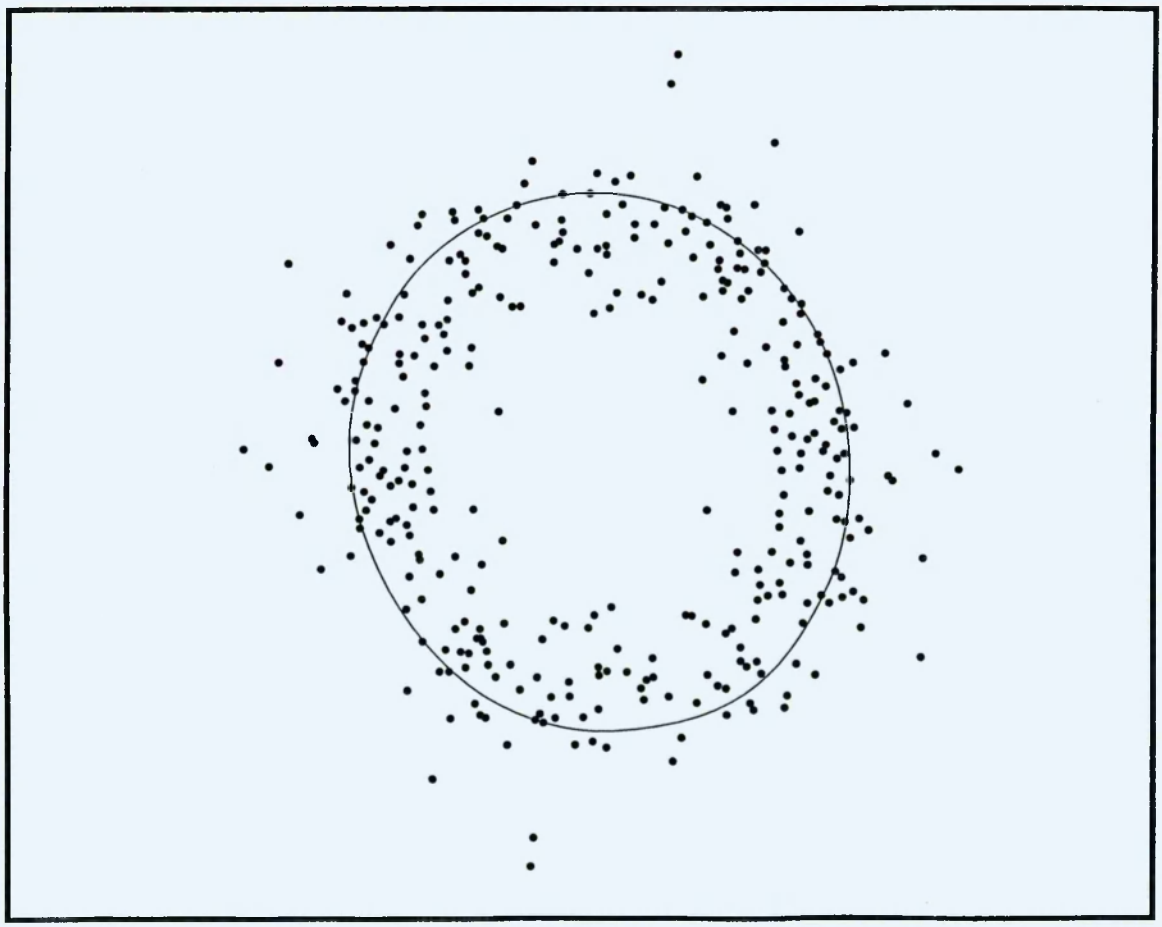

Figure 2.02: A Fry plot of grain centre points from a thin section of Westerly granite. The results indicate a slight mineral elongation of 5 %. 342 grain centre points were used to construct the plot. Semi-major = 1.03, semi-minor = 0.94.

The program !GRAINS (Evans 1995) was further used to estimate the degree to which undeformed Westerly granite has a shape fabric. This was accomplished by comparing the distance between the mid-point of each grain with those surrounding it and plotting data on a Fry plot (**Figure 2.02**). A slight shape fabric with mineral elongation of

Epidote: The radioactive epidote allanite is found as light brown needles in quartz and as a product of sericitization of plagioclase.

Haematite: This oxide is found as large (up to 100 μm diameter) euhedral crystals in the vicinity of biotite where it reflects very strongly in back-scattered electron images.

Ilmenite: Ilmenite occurs as a euhedral accessory phase in the Westerly granite starting material. It occurs commonly in the vicinity of biotite but also forms part of the sericitization of plagioclase.

Muscovite: Forms alteration rims around biotite and it is the major component in feldspar sericitization, even though it forms 1.4 vol % of the rock. Under the optical microscope small flecks and, in some areas, small booklets can be observed.

Rutile: Titanium oxide is found as small (below 10 μm diameter) inclusions in biotites and quartz crystals.

Sphene: Titanite can be found adjacent to biotites. It forms euhedral crystals up to 20 μm in length and it was found as a large inclusion in plagioclase feldspar.

Spinel (magnetite): A small percentage (<< 1 % by volume) of spinel is found in the vicinity of biotite.

Zircon: This phase is found as very well rounded crystals included in biotites.

2.5 Crack characteristics of Westerly granite in sample WG0

The starting material shows a randomly orientated network of cracks with a low crack density (9 mm/mm^2) when compared to crack densities in deformed samples (**Figure 7.09**). Cracks are concentrated on grain boundaries (**Figure 2.07**). In the fan-fold **Figure 2.07** a collage of backscattered SE images is shown in conjunction with a tracing of phase boundaries and cracks, visible as black lines on the collage. Holes are shaded black. Some of the minerals have been labeled on the phase boundary map.

Crack density in quartz crystals is low. They have curvilinear shapes and commonly split the crystal, with few crack terminations in the centre of quartz crystals. In feldspars the highest crack density is concentrated in sites of sericitization towards the centre of the plagioclase crystals. Often the cracks associated with sericitization do not extend to the grain boundary. Biotite has little to no cracks in the untreated material except occasional cleavage parallel cracks. Accessory phases were too small to study at the

presented magnification of * 85, though in general only few curvilinear cracks are found in most, with the exception of chlorite and muscovite that developed cracks parallel to cleavage.

Crack orientation in WG0 is plotted against a randomly chosen orientation in **Figure 2.06**. Except for a strong preferred orientation in a horizontal and vertical orientation (with respect to scanning direction (**Appendix 4**))an insignificant preferred orientation was observed. The preferred orientation indicated is thought to relate to the shape of pixels (square), rather than an actual alignment in the starting material (compare to **Figure 2.07**) and is thus an artifact of the grain orientation analysis program CRACKS by J. L. Neumann (pers. comm. 1994, **Appendix 4**). Therefore all other crack orientation measurements have been normalized with respect to WG0 (**Figure 7.10**).

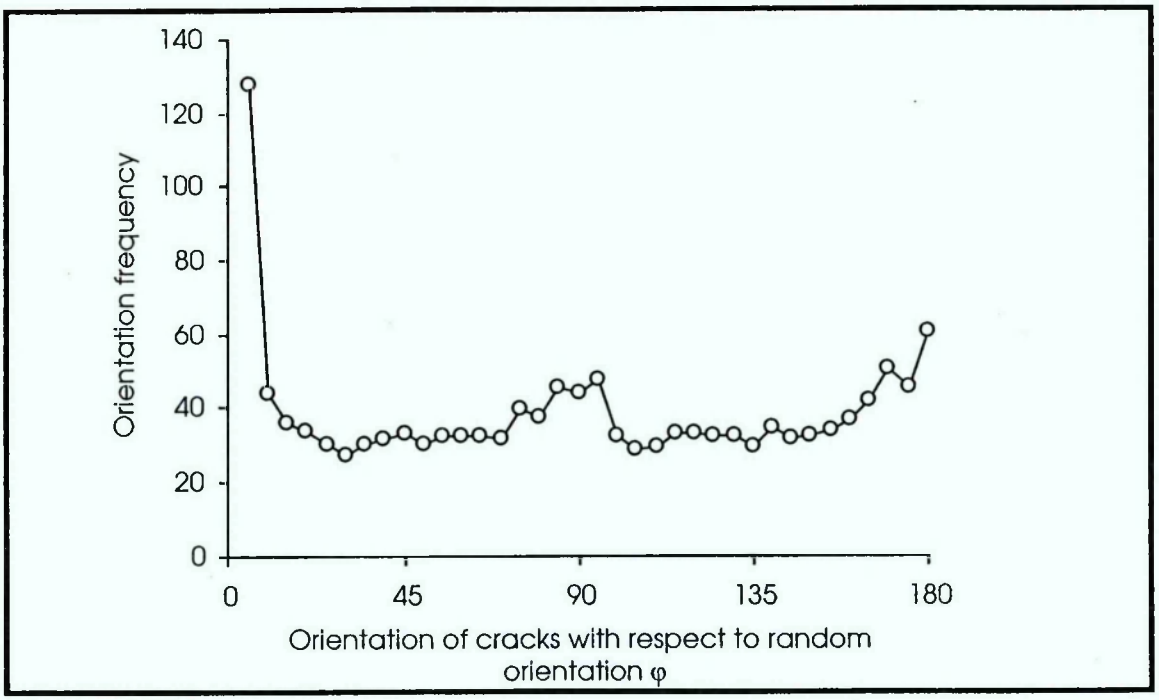

Figure 2.06: Crack orientation characteristics of WG0. Peaks at zero, 90 and 180 ° are thought to be artifacts of the program CRACKS by J. L. Neumann (pers. comm. 1994) (**Appendix 4**).

no more than 5 % was observed. However, this fabric is very small and might be an artifact of a small sample size, 342 grains. These measurements confirm the generally isotropic nature of Westerly granite.

2.4 Mineral compositions

The chemical composition and microstructural habits of the major phases (feldspars, quartz, and biotite) are initially evaluated. This is followed by a description of accessory phases, totalling less than 2 % of the rock. A detailed description of geochemical variation of phases is given in **Chapter 4**, with representative chemical analysis listed in **Appendix 6**.

2.4.1 K-feldspar

K-feldspar occurs in its low temperature structural form microcline. It varies compositionally between $Or_{(96.9-89.6)}Ab_{(10.4-3.1)}An_{(0.7-0.0)}$(**Figure 2.3, b**, **Appendix 6** for geochemical analysis).

The microcline crystals are anhedral with many acutely angled corners (**Figure 2.03, a**). Overall the crystals are commonly roughly equant to rectangular. The cross-hatched twinning pattern is well developed towards the centre of the crystals but is generally absent towards the rims. In some examples only small remnant areas of cross-hatching persist. Areas of cross-hatching are commonly associated with sericite alteration. Microcline crystals are occasionally intergrown with albite to form microperthite. The orientation of perthite veins is commonly oblique to cleavage in the K-feldspar host.

2.4.2 Plagioclase

Plagioclase appears highly sericitized in WG0 but where fresh it has a composition of $Or_{(1.5-0)}Ab_{(99.0-80.4)}An_{(20.1-1.0)}$ (**Figure 2.03, b**). Sericitized feldspars show inclusions of calcite, epidote and most commonly muscovite. However, minerals associated with feldspar alteration rarely replace as much as 3 % of the volume of plagioclases.

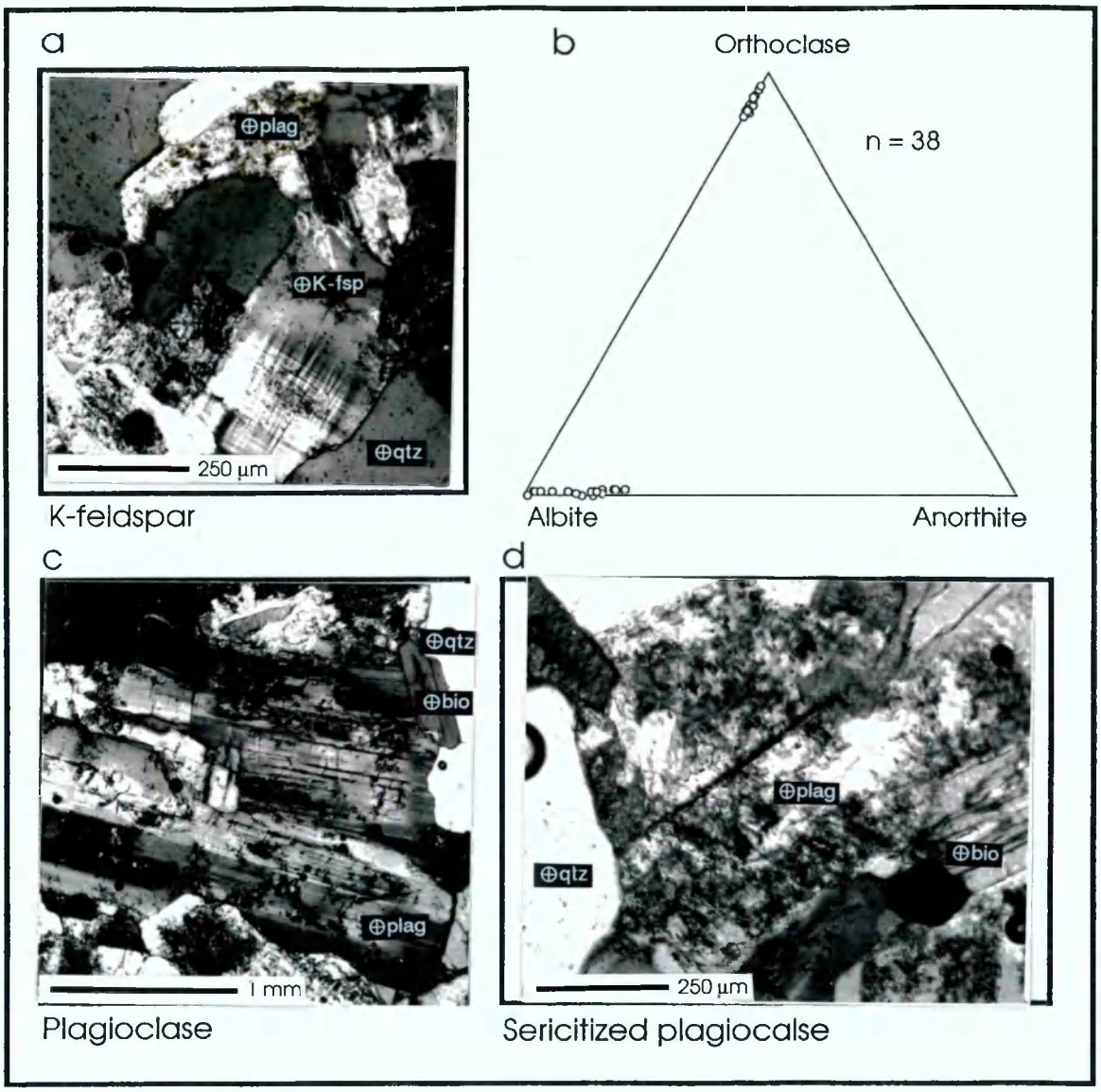

Figure 2.03: K-feldspar and plagioclase chemistry and petrology in WG0.

Plagioclase forms anhedral but generally rectangular crystals with well rounded corners (**Figure 2.03, c**). It has less of an interstitial character than K-feldspar and commonly shows a high degree of alteration concentrated in the centre of the crystals (**Figure 2.03, d**). Antiperthite is occasionally observed where K-feldspar forms amorphous blebs within a plagioclase crystal. Cleavage is generally poorly developed with sub-planar cracks cutting the crystals oblique to cleavage. Large numbers of small scale cracks are associated with the alteration products in the centre of the feldspar crystals that interlink to form an intricate network (**Figure 2.06**).

2.3.3 Quartz

Quartz generally shows an equant anhedral shape with rounded corners but often scalloped crystal edges (**Figure 2.04, a**). Quartz-feldspar intergrowths can be observed. Unstrained quartz crystals often contain fluid inclusion trails and rutile needles, which can make up to 1 % of the volume of the quartz crystal. Quartz grains with well developed strain-mottled extinction occur locally (**Figure 2.04, b**). They show more sub-rounded shapes than unstrained quartz crystals and are free from fluid inclusion trails and rutile needles (**Figure 6.01, b**). Quartz crystals show a low density of curvilinear cracks (**Figure 2.06**).

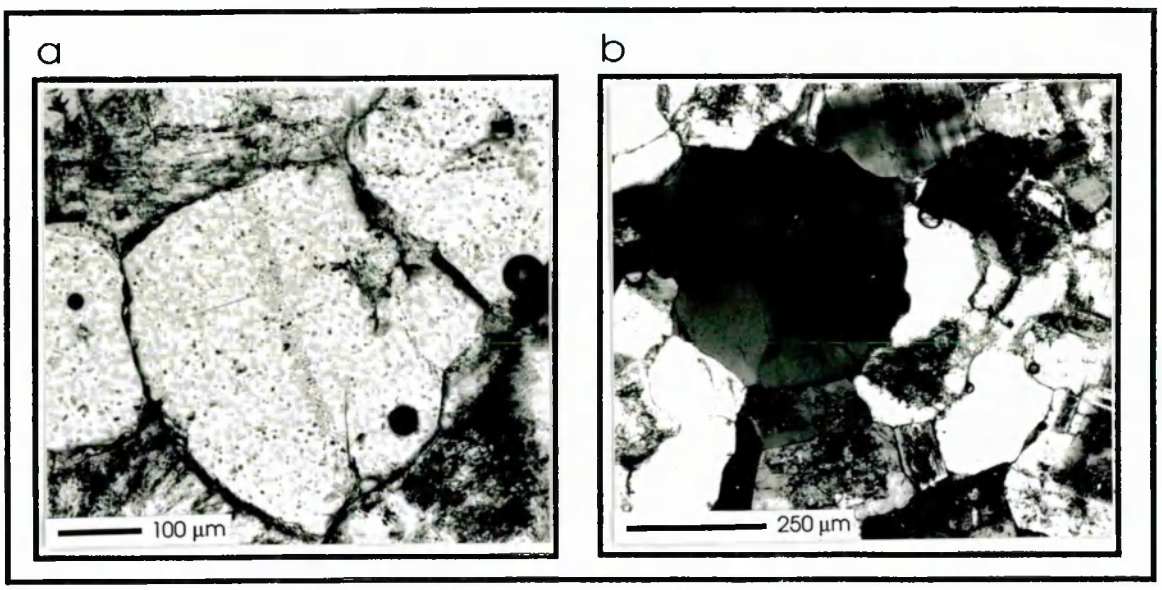

Figure 2.04: Optical micrographs of quartz in WG0. **a.)** Quartz crystal containing fluid inclusion trails; **b.)** strained quartz.

2.4.4 Biotite

Biotite forms the next major constituent of Westerly granite, accounting for 3.8 vol % and commonly has a grain size of about 500 µm. It is associated with accessory apatite, calcite, ilmenite, haematite and allanite and shows little chemical variation (**Figure 2.05, b**).

Biotite forms well developed rectangular books without deformation structures (**Figure 2.05, a**). Fractures in biotite develop parallel and orthogonal to cleavage. Partial alteration to chlorite takes place parallel to cleavage and alterations of whole biotite crystals are seen occasionally. Chlorite fibres show radiating and parallel alignment,

though parallel fibres usually develop oblique to the biotite cleavage they are replacing (**Figure 2.05, a**). Occasional muscovite overgrowths are observed.

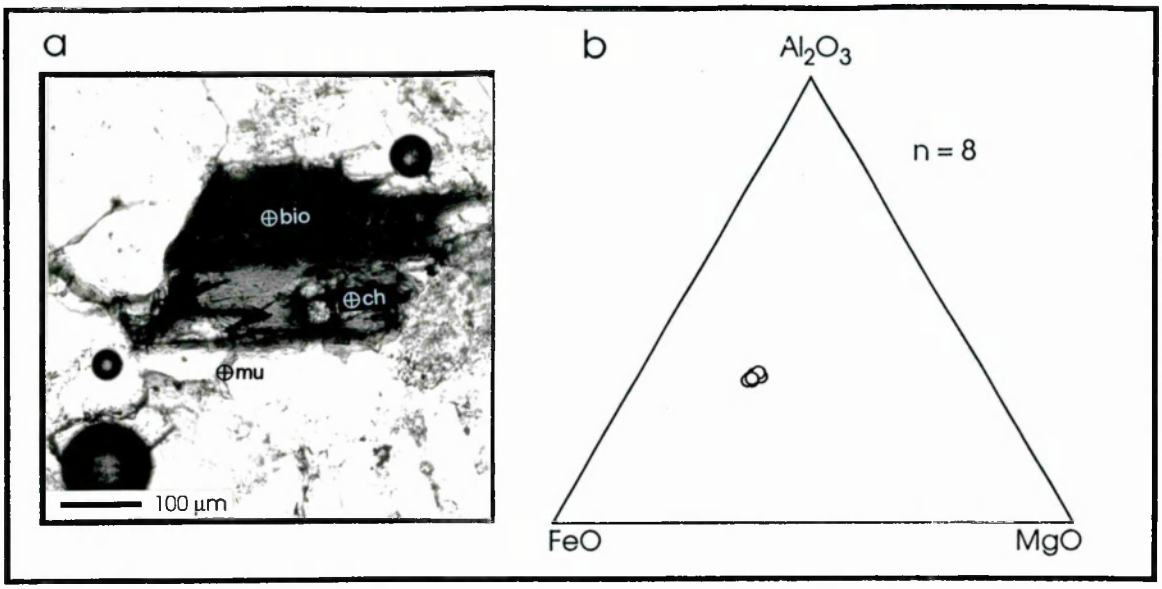

Figure 2.05: Biotite chemistry and petrology in WG0. The biotite has been partially replaced by chlorite and shows muscovite overgrowth.

2.4.5 Accessory phases

Several accessory phases were found, usually associated with sericite in feldspars or clustering around biotite crystals. Combined they contribute less than 2 % of the rock by volume. They are listed in alphabetical order:

Apatite: Apatite is found as euhedral lath-shaped inclusions in biotite, parallel to the mica cleavage, where it forms grains with diameters reaching 200 µm. Locally euhedral apatite crystals occur adjacent to biotites (**Figure 4.04**). Apatite is also one of the phases associated with feldspar sericitization.

Calcite: Small traces of calcite, well below 0.2 % of the total rock, are found as part of the sericitization in plagioclase feldspars. It also occurs as laths parallel to and incorporated in biotite crystals, possibly as a biotite alteration product. It occasionally forms biotite pseudomorphs.

Chlorite: Is commonly found to replace biotite (see section 2.3.4 above). However, chlorite replacement is rare (forming 0.8 vol % of the rock).

Figure 2.07: Collage of backscattered SEM images of the starting material (WG0) with grain boundary and crack maps. Black shaded areas on both SEM pictures and tracings are either the edge of the thin section or holes within the section.

WG 0 1.0 mm
SEM Backscattered Image

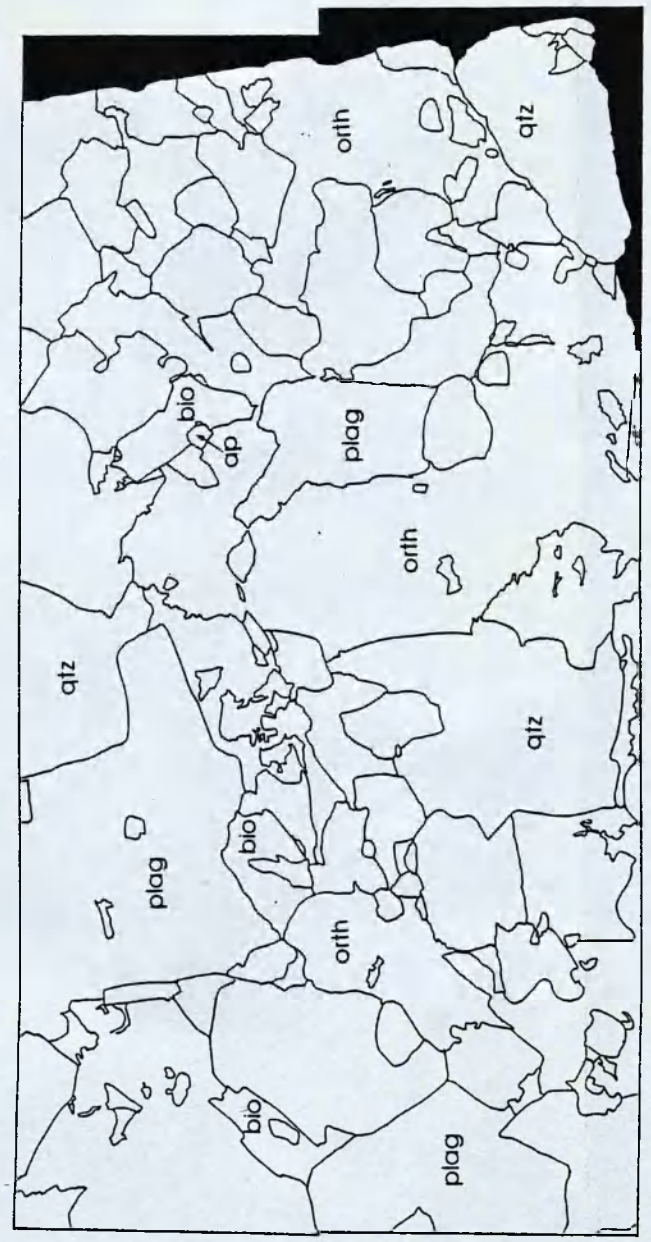

Outline of grain boundaries

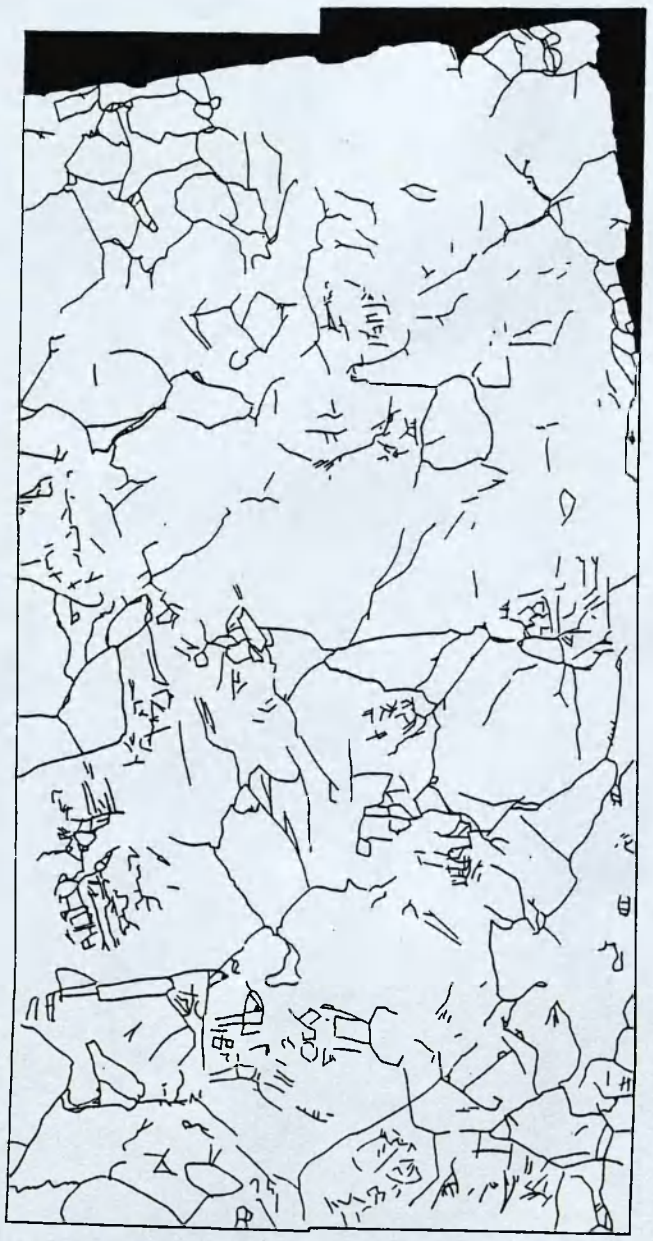

Cracks

This page has intentionally been left blank

Chapter 3

Westerly granite melt: Physical properties and melting kinetics

3.1 Introduction

In the experiments described in this study, Westerly granite samples were heated to between 800 and 1200 °C (**Table 3.01**), the elevated temperatures causing partial melting. The rapid quenching which terminated the experiments (**Appendix 1**) caused the melt to form a glass, thus allowing melt fraction, melt distribution and melt morphology to be described. The compositional variations of the melt are described in **Chapter 4.3**.

Melting kinetics were explored by documenting the variation of melt fraction with temperature and the time samples were held at high temperature. The temperature effect was further explored in three experiments (WG18, WG21 and WG22), in which the samples were heated to 1100 - 1200 °C prior to deformation at 850 - 900 °C. These experiments were designed to measure melt viscosity (**Chapter 6**) but extensive neo-crystallization occurred after dropping the temperature. Finally the effect of melt extraction was documented. In four experiments (WG23, WG24, WG25 and WG27), also conducted to measure melt viscosity (**Chapter 6**), melt flowed into a crushed quartzite low pressure reservoir above the specimen. This appeared to lower the amount of melt generated.

Melt water content is another critical parameter that can effect the melt fraction. The experiments in this study were conducted under essentially vapour absent conditions, the samples having been oven dried prior to use (**Appendix 1**). However, small quantities of water were generated by the melting of hydrous phases such as mica and chlorite. To allow comparison of the results of this study with those of other workers and to facilitate the extrapolation of the experimental results to a real geological environment (**Chapter 8**), an attempt was made to measure the quantity of water available in the Westerly granite to be incorporated in the melt.

Sample	Peculiarities	T_{max}(°C)	P (MPa)	def. type	t @T (h)	melt fraction
WG1	powder	900	250	static	129.0	0.27
WG2		800	250	dynamic	2.4	0.05
WG3		900	250	dynamic	2.5	0.07
WG4		1000	250	dynamic	2.5	0.20
WG5		950	250	dynamic	3.0	0.14
WG6		850	250	dynamic	2.5	0.04
WG7		800	250	dynamic	4.0	0.03
WG8		800	250	dynamic	96.0	0.30
WG9		900	250	dynamic	46.5	0.12
WG10		900	250	dynamic	96.0	0.13
WG11		1000	250	dynamic	71.0	0.27
WG12		1050	250	dynamic	4.0	0.34
WG13		1100	250	dynamic	4.0	0.48
WG14		1000	250	static	52.0	0.28
WG15		900	250	static	56.0	0.12
WG16		900	250	dynamic	17.5	0.14
WG17		900	250	dynamic	52.5	0.18
WG18	T ⇓ 1100°C⇒	900	250	dynamic	25.0	M 0.47 / 0.25
WG19		900	0	static	10.0	0.77
WG20		900	250	dynamic	171.0	0.17
WG21	T ⇓ 1200°C⇒	850	250	dynamic	47.75	M 0.63 / 0.16
WG22	T ⇓ 1100°C⇒	900	250	static	27.5	M 0.60 / 0.38
WG23	melt extraction	1000	250	dynamic	3.25	.1/q.01/ F.25
WG24	melt extraction	1000	250	static	3.25	0.9/q 0.1
WG25	melt extraction	940	250	static	3.5	0.6 / q 0.0
WG26		1000	250	dynamic	124.75	0.44
WG27	melt extraction	950	250	dynamic	8.5	0.8 / q 0.002
WG28		900	250	dynamic	51.0	0.16
WG29		1000	250	dynamic	44.75	0.26
WG30		1000	250	dynamic	168.0	0.31

Table 3.01: List of Samples and their temperature, confining pressure, deformation histories (dynamic = suffered deformation), time sample spent at temperature (hours), and average melt volume fraction, determined by BSEM method (Section 3.3.1). M = melt fraction determined from glass and neo-crystals; q = melt extracted into crushed quartzite, recalculated to volume fraction of the Westerly granite sample (Section 3.3.4); F = melt fraction in fault zone. The heating sequence is complicated in samples WG18, WG21 and WG22. These were initially heated to 1100 and 1200 °C respectively, but held at a lower temperature prior to quenching.

3.2 Melt fraction determination

Melt fraction was estimated using two different methods:

1. Computer aided image processing of back scattered electron images,(**Appendix 3**) (**Figure 3.01, b**).
2. Area fraction of melt traced on photo collages of optical thin section photos (**Figure 3.01, a**).

In both methods, the area fraction of glass in the sample is estimated; it is assumed that this is equal to the volume melt fraction in the sample immediately prior to quenching

(Underwood 1970). The methodology of each procedure is first explained, followed by a comparison between the two methods of melt fraction determination.

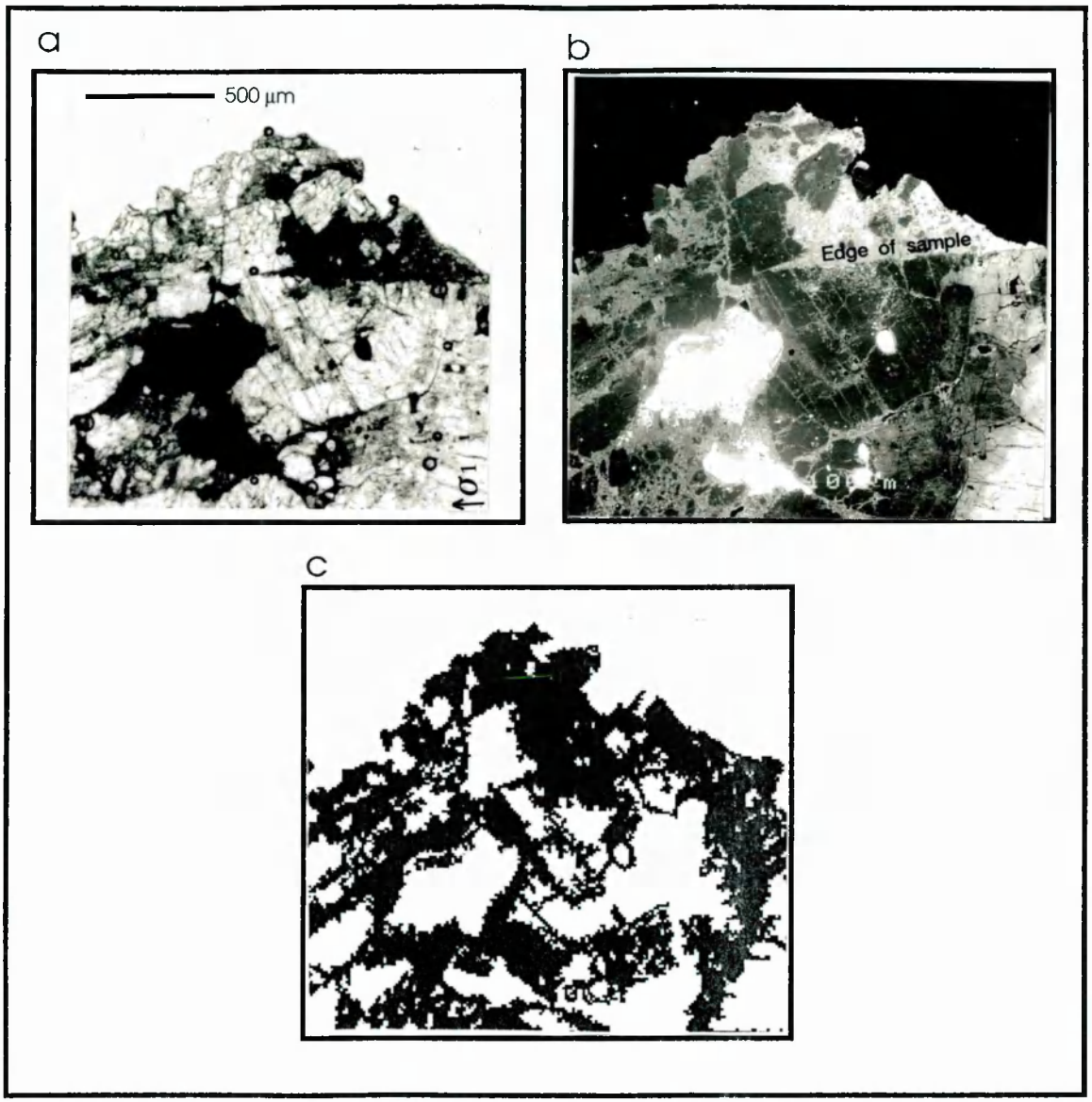

Figure 3.01: Melt distribution in a partially molten sample (WG12). All three images are of the same location and magnification on the thin section. **a.**) Optical micrograph (half crossed polars), isotropic glass identifies melt location. It is difficult to distinguish between melt and holes in the thin section; **b.**) SEM back scattered image, the grey scale displaying contrasts in atomic number. The melt has a shading of grey between those for plagioclase and K-feldspar. It is easily distinguished from hole. **c.**) Tracing of area occupied by melt (shaded), using both optical and SEM pictures. The indicated edge of the sample in **b.)** markes the original sample edge prior to deformation. Some melt plus fragments protrude beyond this edge due to melt movement (compare with **Chapter 7.3.2**).

3.2.1 Back scattered electron microscopy (BSEM) image processing

In this method, melt fraction was determined by analysing a back scattered electron image showing atomic number contrasts (**Figure 3.01**), thus enabling the distinction between different phases (**Appendix 3**). First the brightness and contrast of the image was adjusted to best differentiate glass from crystalline phases, a feel for the melt distribution having been gained from optical microscopy and EDS spot analysis under the SEM (**Chapter 4**). These images were then imported into an image processing package where the continuous grey scale image was split into 8 colour bands corresponding to 1/8 of the grey scale respectively. The band closest to the glass grey scale value was selected and the cutoffs were adjusted so that, as far as was possible, no crystalline phases fell within the band and all the glass was highlighted (See **Appendix 3**). This was difficult as most melt has a grey scale value between that of plagioclase and K-feldspar and a transitional change between feldspars and melt was commonly seen (**Figure 3.12**). This results in an inherent error in the measuring method which is evaluated below. Commonly the melt was heterogeneously distributed in the samples, so an attempt was made to cover as much of the sample as possible within a reasonable time. To this end over 60 melt estimates of melt fraction were made for each sample from evenly spaced images at a magnification of * 110, covering approximately 80 % of the sample area. The volume melt fraction was taken as the average of these measurements.

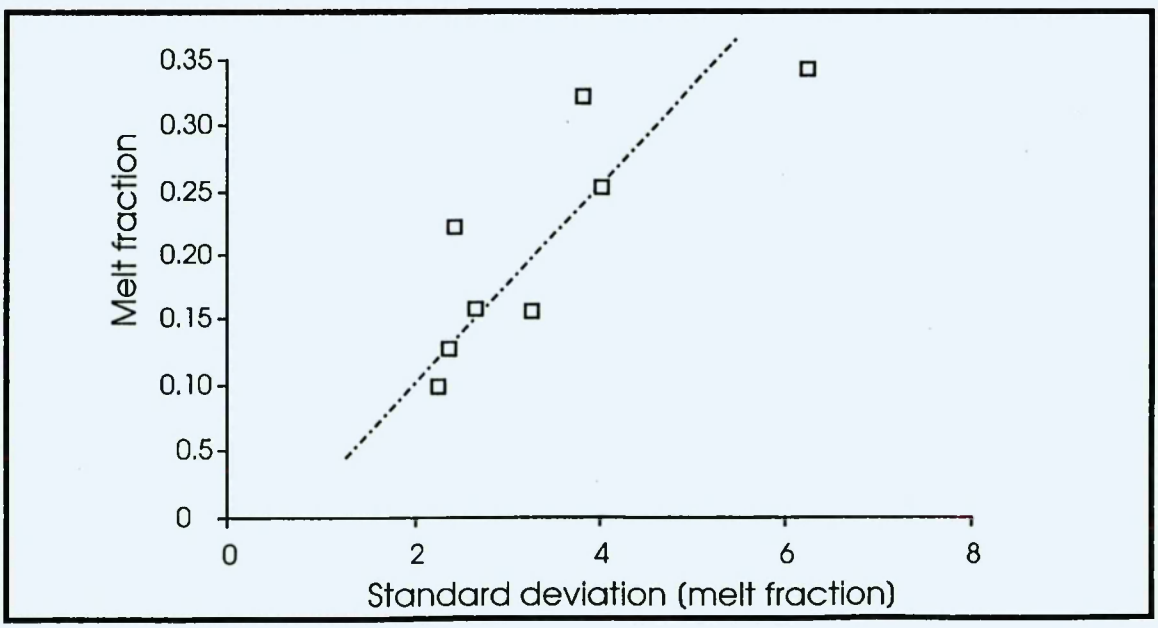

Figure 3.02: Standard deviation of melt fraction measurements using the BSEM image processing facility. On one sample, WG17, eight localities were chosen which had contrasting melt fraction. At each of these localities, six estimates of melt fraction were made from images

with varying contrast and brightness. The standard deviation of melt fraction at each locality was calculated and plotted against the average of the six measurements.

In order to evaluate the inherent error in this melt fraction determination method, eight image locations were selected in WG17 with contrasting glass content. At each locality six estimates of melt fraction were made from images with different contrast and brightness settings, the grey scale band cut-offs for melt being independently set for each image. The standard deviation of the six melt fraction estimates was calculated and plotted against average melt fraction for the locality (**Figure 3.02**). This defined a linear increase in standard deviation with melt fraction which was extrapolated to higher and lower melt fractions. The inherent error was estimated as plus or minus one standard deviation. A complete melt estimation run was repeated for one sample, WG14. The difference between the two readings, 0.28 and 0.29, is well within the predicted measurement error of ± 4.5%.

3.2.2 Optical melt fraction determination method

In the optical method, the volume melt fractions were determined from the area fraction of glass identified on photo collages taken on an optical microscope at magnifications of * 4 and * 10 (**Figure 3.01**). Each collage covered less than one quarter of a thin section and only one collage was created per thin section due to the length of time required to process each sample. Under crossed polars, glass is isotropic and indistinguishable from holes and cracks in the thin section. However, with half crossed polars, the melt can be identified as a uniformly grey phase that stands slightly proud of the epoxy glue used for fixing the specimen to the glass slide. The outlines of melt dominated areas were transferred onto tracing paper and the area melt fraction was estimated using a subroutine in the !GRAINS program (Evans 1995).

3.2.3 Comparison between different measurement techniques

The optical method was felt to be inferior to the SEM method for three reasons. (1) As a result of the much higher magnifications used, the BSEM method gives a better estimate of melt fraction in areas where significant quantities of small crystalline phases were generated during the melting process (**Figure 3.04, c**) or where the melt is intimately associated with the remnants of a primary phase. (2) Due to the automation possible in the BSEM method it was possible to cover a much greater area of the specimen in a shorter time than was possible for the optical method. The

heterogeneous distribution of the melt makes this an important factor. (3) The automation of the BSEM also reduces the subjectivity in defining the area of melt.

Melt fractions were estimated by both methods for samples WG3, WG8, WG16, WG18, WG19, WG22, and WG24 and the values obtained were compared (**Figure 3.03**). There was good agreement in the melt fractions obtained by both methods except for samples WG22 and WG18. These two samples were both from temperature stepping experiments which resulted in the growth of a significant proportion of neo-crystals. There was not sufficient resolution in the optical method to differentiate the glass from the neo-crystals for these two samples.

In the light of the above considerations, it was felt that the BSEM method provided an efficient, reproducible and accurate method for the determination of melt fraction. It was this method that was used for determining the melt fractions recorded in **Table 3.01**.

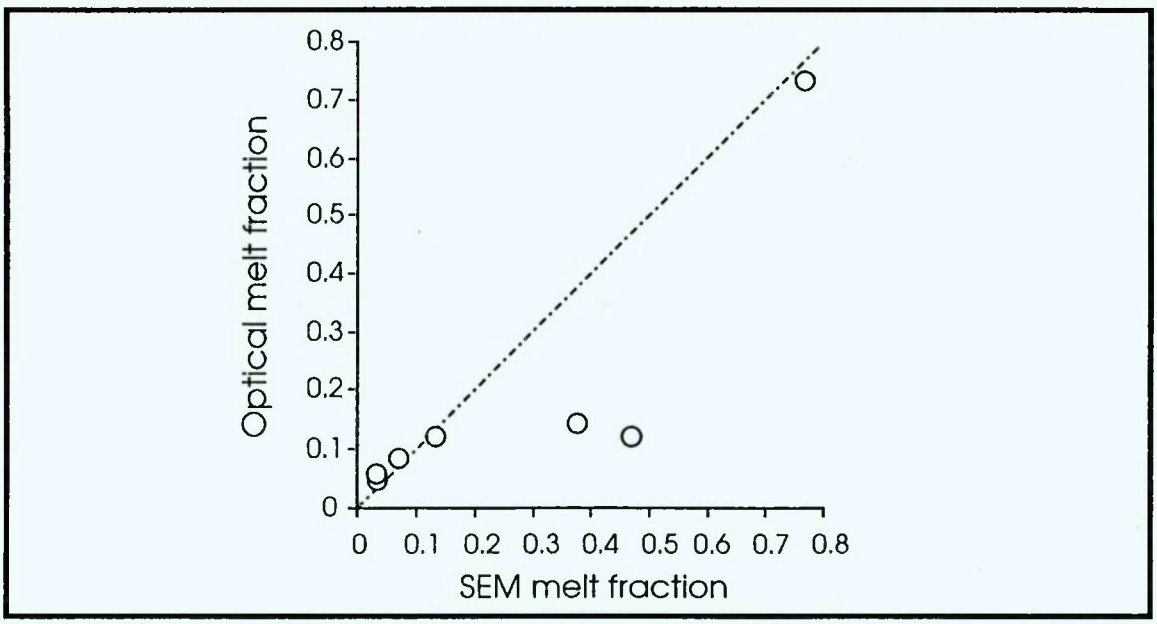

Figure 3.03: Plot of melt fraction estimated using optical micrograph collages against those obtained from image processing of BSEM images for samples WG3, WG8, WG16, WG18, WG19, WG22 and WG24.

3.3 Melt habit and distribution

3.3.1 Melt habit in hydrostatic samples

In order to understand the melting process, it is important to describe the habit of glass and quenched melt, in samples heated under hydrostatic stress conditions; the discussion is completed in conjunction with the geochemical data in **Chapter 4**. The glass habit in hydrostatic samples also serves as an important point of reference when describing the micro-structures and deformation mechanisms in samples deformed in a differential stress regime (**Chapter 6**). In the following section, the glass habit in samples WG14, WG15, WG24, WG25 and WG29 is described. These were all heated under hydrostatic conditions, the details of temperature, heating time and melt fraction being summarised in **Table 3.01**.

In the lowest melt fraction samples , WG24 and WG25 (0.06 and 0.08 melt volume fraction), glass occurs as films along quartz/quartz boundaries and, less commonly, on quartz/feldspar boundaries. Melt wetting of quartz grains was thorough enough to fill cracks cutting through this mineral (**Figure 3.04, a**). No glass films were observed on feldspar/feldspar boundaries, in these samples, but commonly there was evidence for partial melting in the sericitized cores of plagioclase crystals. Biotite crystals were all surrounded by thin glass films and melt was seen to have penetrated cleavage parallel cracks. Glass in the vicinity of biotite commonly shows brown iron staining. The grain boundaries of the primary phases are rounded when compared to the starting material. However, the melt-grain boundaries do not have a consistent radius of curvature and there are occasional sharp angular corners remaining on the primary phases.

With increasing melt fraction the grain boundary wetting becomes more pervasive and larger melt pools develop at the sites of primary biotites, K-feldspar and quartz. In WG15, 0.12 melt by volume, feldspar/feldspar contacts were wetted by melt films (**Figure 3.04, b**) and in WG14, 0.28 melt by volume, even the isolated melt pockets in the sericitized cores of plagioclase crystals are connected via melt filled cracks to the surrounding melt network (**Figure 3.04, c**). In WG14, the presence of secondary mineral phases in the melt can be clearly observed (**Figure 3.04, c**); these are discussed in **Chapter 4.2.4**.

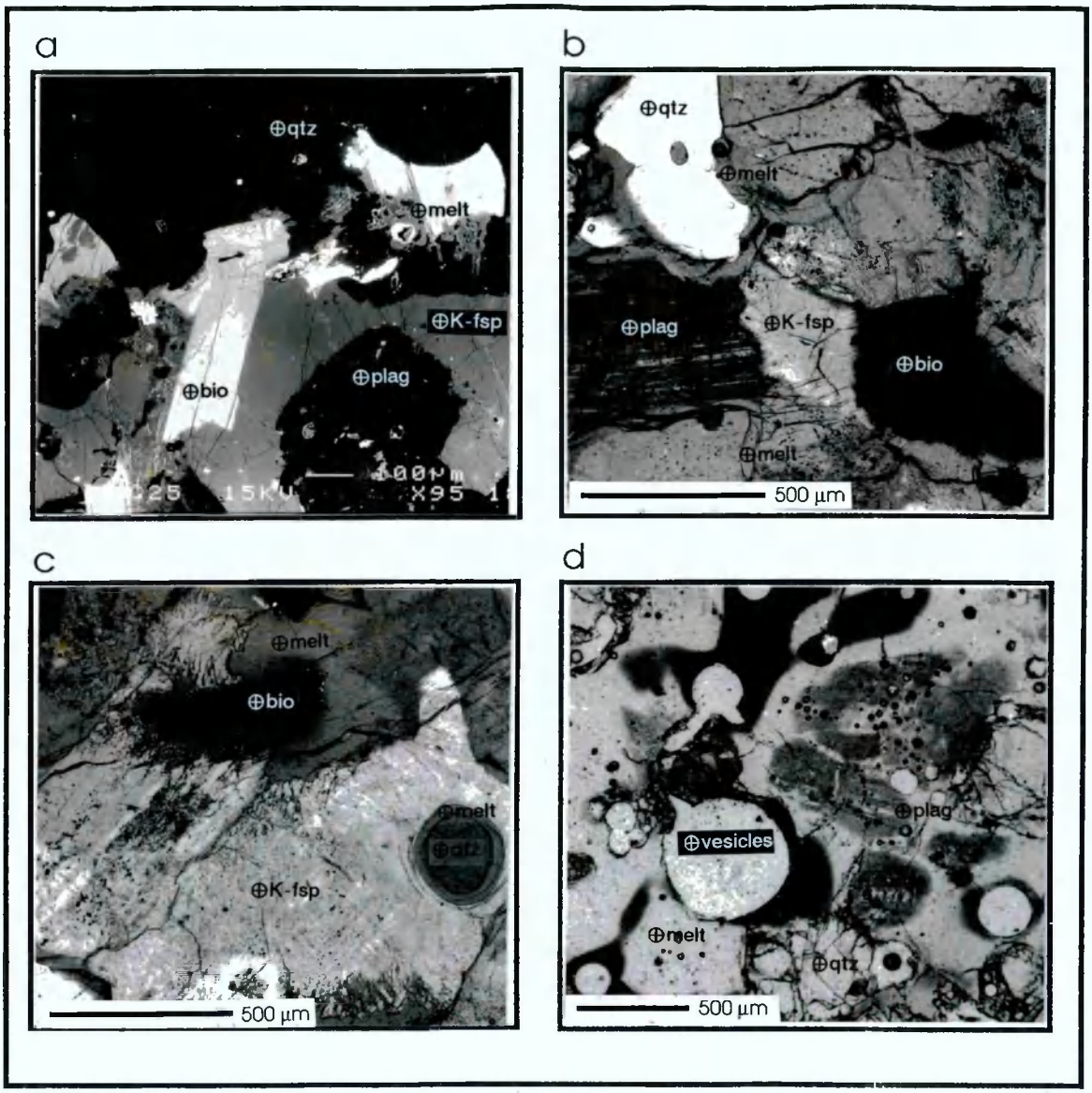

Figure 3.04: Melt habit in hydrostatic tests **a.)** WG25, 0.06 melt, **b.)** WG15, 0.117 melt, **c.)** WG14, 0.281 melt and **d.)** WG19, 0.768 melt.

If the textures described above are assumed to represent textual equilibrium, the ubiquitously observed grain boundary wetting would imply very low melt wetting angles. This is in marked contrast to the equilibrium wetting angles of 50 - 60 °C predicted and observed by Jurewicz and Watson (1984, 1985) for granitic systems. In the present experiments, although grain edges, particularly quartz, are rounded relative to the starting material, there are sufficient sharp grain corners and breaks in the radius of curvature of grain melt boundaries to suggest that the samples have not reached textural equilibrium (Bulau et al. 1979). However, similar grain coating melt films were reported by Laporte (1994) experiments were carried out under dis-equilibrium conditions due to short run times. Laporte measured dihedral angles of between 12 to

Figure 3.05: Collage of back scattered SEM images of WG19 from which boundaries between different phases and cracks were traced. Black shading emphasises the large number of vesicles in the sample. WG19 was heated at room pressure to 1200 °C and contains 0.768 melt.

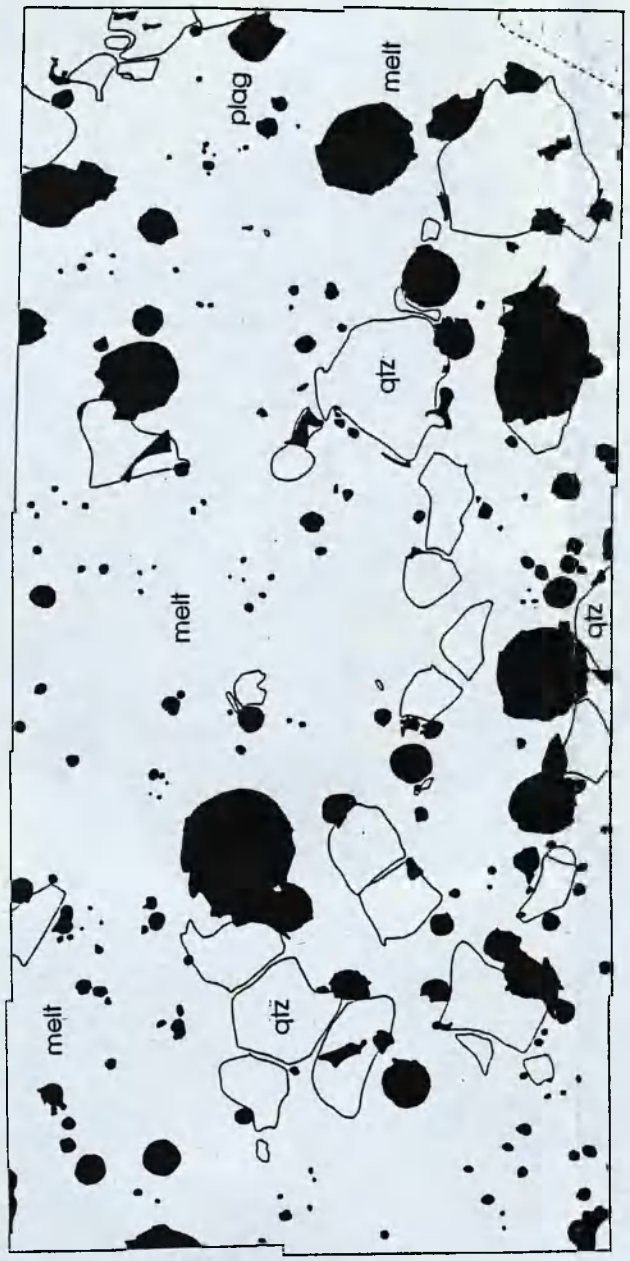

Outline of grain boundaries

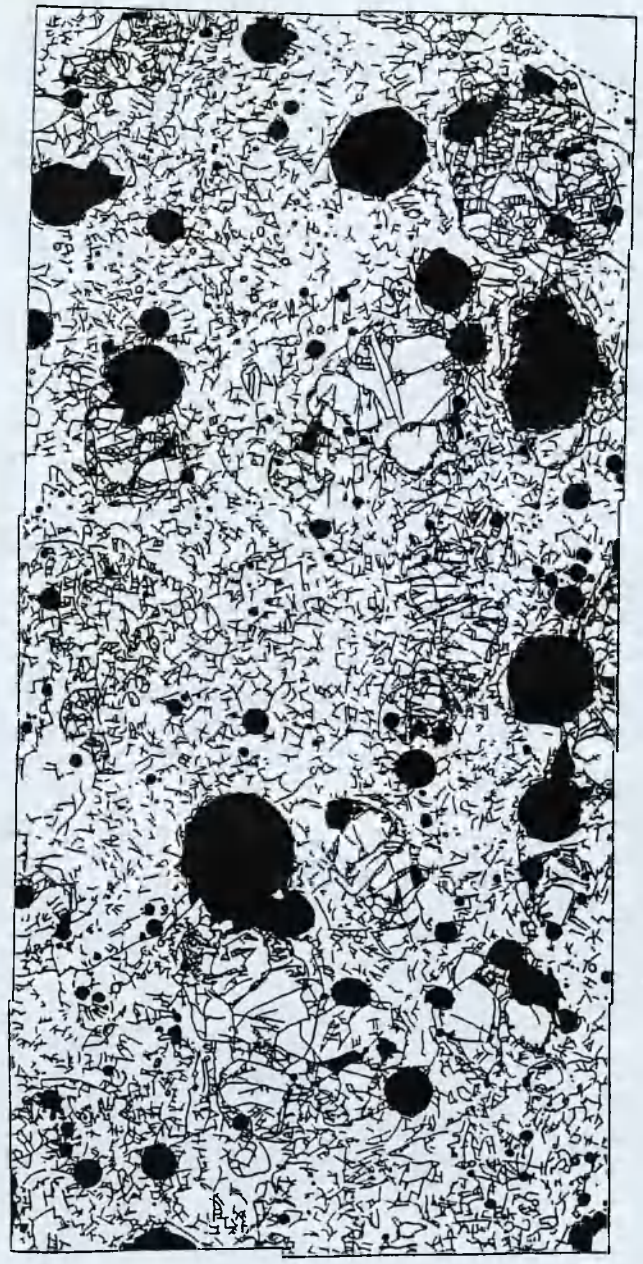

Cracks

This page has intentionally been left blank

16 ° at quartz triple junctions. For melt wetting angle of less than 60°, the melt forms a continuously interconnected network along grain edges allowing melt mobilization (von Bargen & Waff 1986). The low wetting angles of melt developed in the experiments of this study indicate that it should therefore be possible to mobilize melt even at low melt fractions.

Test WG19 was heated to the highest temperature of 1200 °C at room pressure. In contrast to the tests described above, there was a significant development of vesicles (0.2084 by volume, **Figure 3.04, d**). Larger vesicles are commonly surrounded by intensely iron stained glass. The only primary crystal phases remaining in this sample are well rounded quartz crystals. Crypto-crystalline feldspar needles form shadowy ghosts marking the former sites of primary feldspar crystals.

The vesicles observed in WG19 were caused by the release of volatiles on melting of (primarily) micas under atmospheric pressure. This suggestion is supported by the intense iron oxide staining rimming the vesicles. Smaller vesicles may have developed during the melting of sericite, a mixture of muscovite, carbonate and feldspar. The presence of angular quartz crystals in WG19 could be due to spalling of angular fragments from quartz grains during the melting interval (**Figure 3.05**). This could be due to differential stress induced by melt expansion in the melt-filled cracks in the quartz crystals or due to the rapid heating or quenching of the sample. Vesiculation is suppressed in samples heated under confining pressure. Instead volatiles are dissolved into the melt phase.

3.3.2. Melt distribution in deformed samples

Melt is not homogeneously distributed in deformed samples. In most samples with macroscopic fault development, the fault zone was found to have a higher melt fraction than the rest of the sample. For instance in specimen WG23, the fault zone contains 0.25 melt by volume whereas the sample contains only a 0.10 melt fraction (**Figure 3.06**). Melt was also collected between the jacket and the specimen (bulge of material in **Figure 3.01**). Melt concentration are also found in low pressure regions associated with the pressure shadows produced by the pistons, filling open axial fractures.

In all these instances melt is concentrated into dilatant zones., with pore fluid pressure lower than that in the surrounding sample. This pressure gradient between dilatant zones and the remaining sample drove melt towards low pressure regions, as is

graphically illustrated by the melt extraction experiments WG23, WG25, WG26, and WG27 where melt moved into the low pressure crushed quartzite reservoirs placed adjacent to the Westerly granite samples (**Chapter 6, Figure 3.11**)

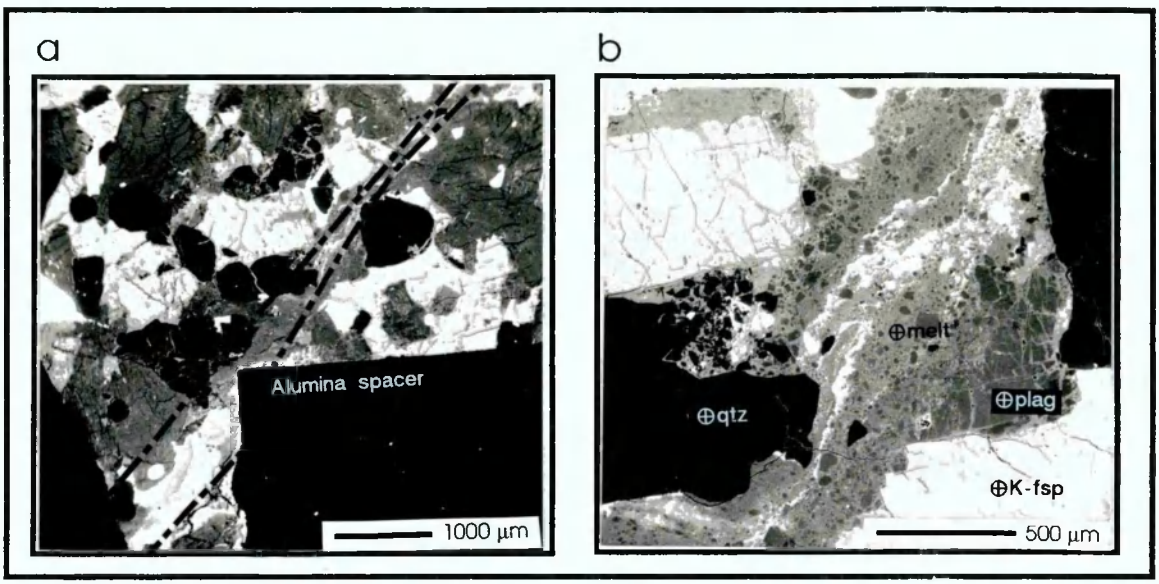

Figure 3.06: Melt concentration along the fault zone in sample WG23. While the bulk rock contained as little as 0.103 melt, the fault zone contains as much as 0.247melt. **a.)** BSEM image of fault zone with cataclastic fault material plus melt protruding adjacent to the alumina spacer at the end of the sample (spacer has been removed and is now marked by square indent at the bottom of the section). **b.)** detail of fault zone.

3.4 Melting kinetics

The most significant control on the melt fraction achieved in the experiments was expected to be temperature. A plot of melt fraction against the maximum temperature for all experiments (**Figure 3.07**), using the data recorded in **Table 3.01**, does indeed show an increase in the maximum melt fractions achieved with temperature but it also shows a considerable scatter of melt fraction determinations across the temperature range, especially at low melt fractions. The factors which could explain this data scatter are explored before an attempt is made to determine a temperature / melt fraction relationship.

The melt fraction data are differentiated on **Figure 3.07** in the following manner:

1. *Normal tests* were heated to a particular temperature and then quenched after a period of time that may have involved deformation.

2. In the *Temperature step tests* the sample temperature was reduced during the tests. On **Figure 3.07** the remnant glass fraction is plotted (see section 3.4.2. below).
3. The *Powder test* was an experiment conducted on powdered Westerly granite at 250 MPa.
4. *Melt extraction tests* were similar to normal tests but melt was extracted into a low pressure crushed quartzite reservoir (**Chapter 6**)

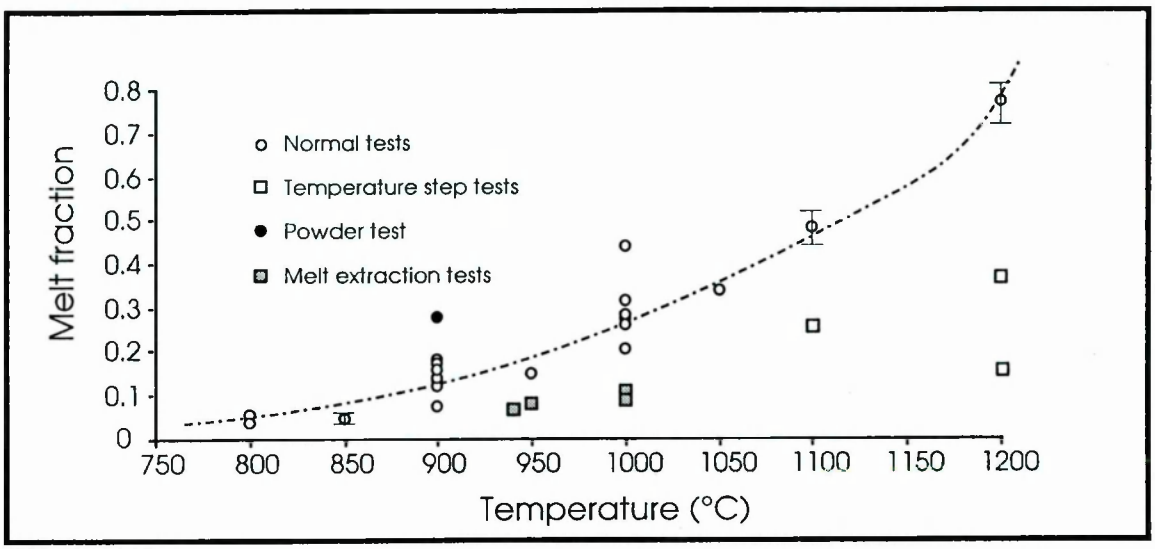

Figure 3.07: Plot of melt fraction versus maximum temperature. See text for explanation of sample differentiation. Error bars give RMSE ranges on melt fraction uncertainties.

3.4.1 Melt fractions in *normal* samples, the effect of temperature and time

Normal tests, identified as open circles in **Figure 3.07** show a general increase in melt fraction with time. While there is an initial gradual rise between 800 and 950 °C, melt fractions increase more rapidly at temperatures in excess of 950 °C, with complete melting expected close to 1300 °C. However, large deviation from the best fit line can be observed, especially at 900 and 1000 °C. This can be due to either heterogeneities of the starting material, or due to the effect of time the sample spent at temperature.

The relationship between heating time and melt fraction is illustrated by the spread of melt fraction recorded at 900 and 1000 °C (**Figure 3.08**). A poorly defined general increase in melt fraction with heating time is recorded for both of these temperatures. Extrapolation of this trend at 900 °C implies that at least several weeks would be required to achieve the melt fraction seen in the *powder* sample (WG1) in solid

Westerly granite cylinders. The broad spread of melt fraction measurements around the general trend could result from material variation. The gradual increase in melt fraction over a long period of time recorded in these vapour absent experiments is in marked contrast to observations by Piwinskii and Martin (1970). They found that in a granite-water system a heating time as low as 3 hours was sufficient to develop a constant amount of melting.

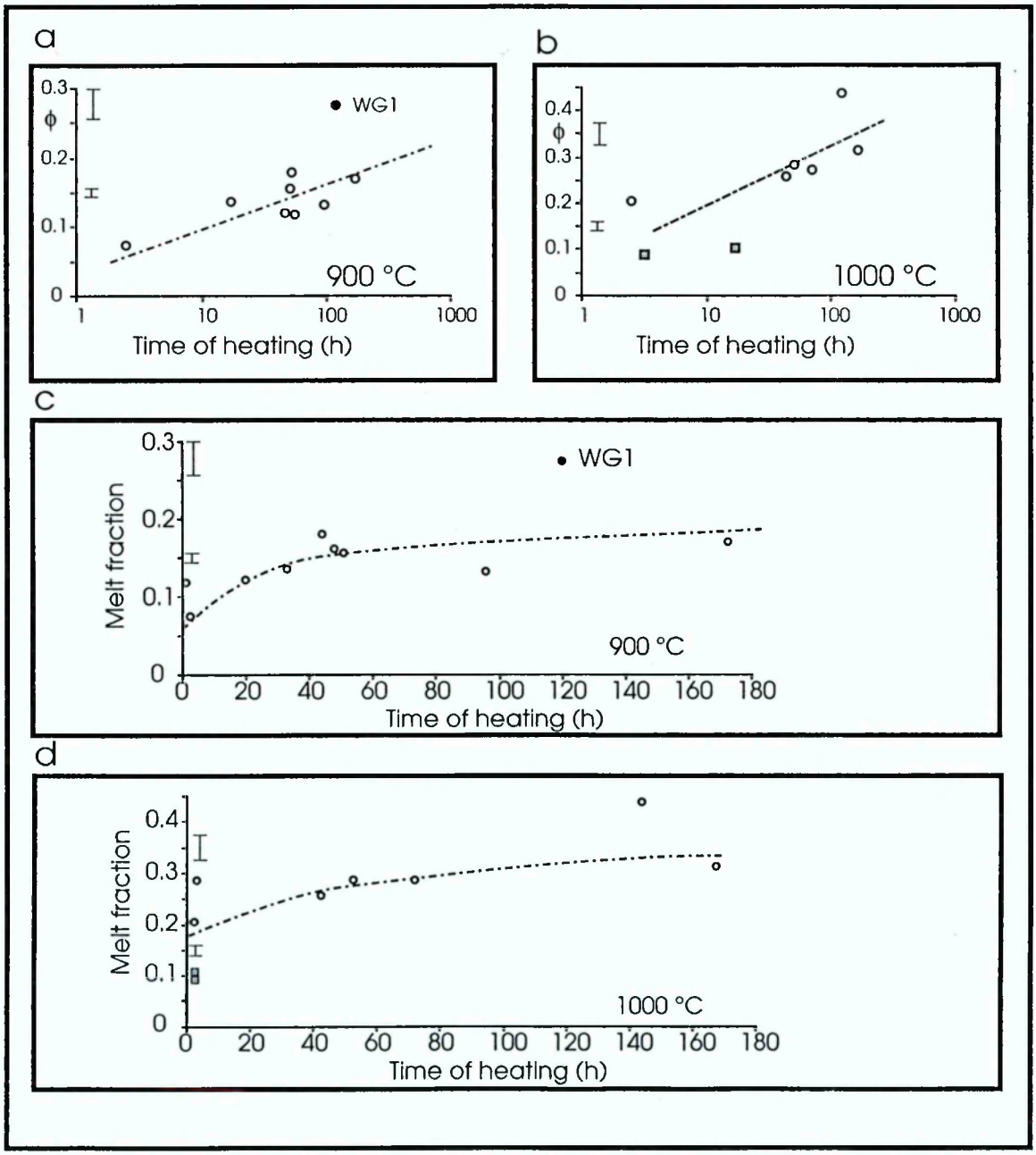

Figure 3.08: Melt fraction increase against time the sample spent at temperature. Symbols as in figure 3.7. Dashed line marks trend of increase. **a.)** samples heated to 900 °C with log time scale, **b.)** samples heated to 1000 °C with log time scale, **c.)** repeat of a.) with linear time scale, **d.)** repeat of b.) with linear time scale.

3.4.2 Melt fraction reduction due to neo-crystallization of melt

Three tests were initially heated to elevated temperatures (1100 and 1200 °C) prior to a temperature drop to between 900 and 850 °C where the samples remained for several hours before quenching. This caused neo-crystallization of the melt phase reducing the glass fraction present in the sample (**Figure 3.09**). The melt fraction present at the maximum temperature was estimated by adding together the volume fraction of neo-crystals and glass.

Sample	T_{max}	total	t @⇓T	neo-cryst (frac.)	glass fraction	ϕ melt @ max T
WG18	1100	25.0	21.5	0.216 (0.460)	0.254 (0.54)	0.470 (1)
WG21	1200	47.7	30.7	0.465 (0.744)	0.160 (0.256)	0.625 (1)
WG22	1200	27.5	25.3	0.216 (0.364)	0.377 (0.636)	0.593 (1)

Table 3.02: Reduction of melt fraction in rock samples due to partial crystallization of the melt phase. The maximum temperature, the total heating time, the time spent at or below 900 °C, the fraction of newly crystallized phases , the fraction of glass remaining in the sample and an estimation of the melt fraction at the maximum temperature are listed. In brackets are fractions of neo-crystals and glass are recast as a fraction of the melt at maximum temperature.

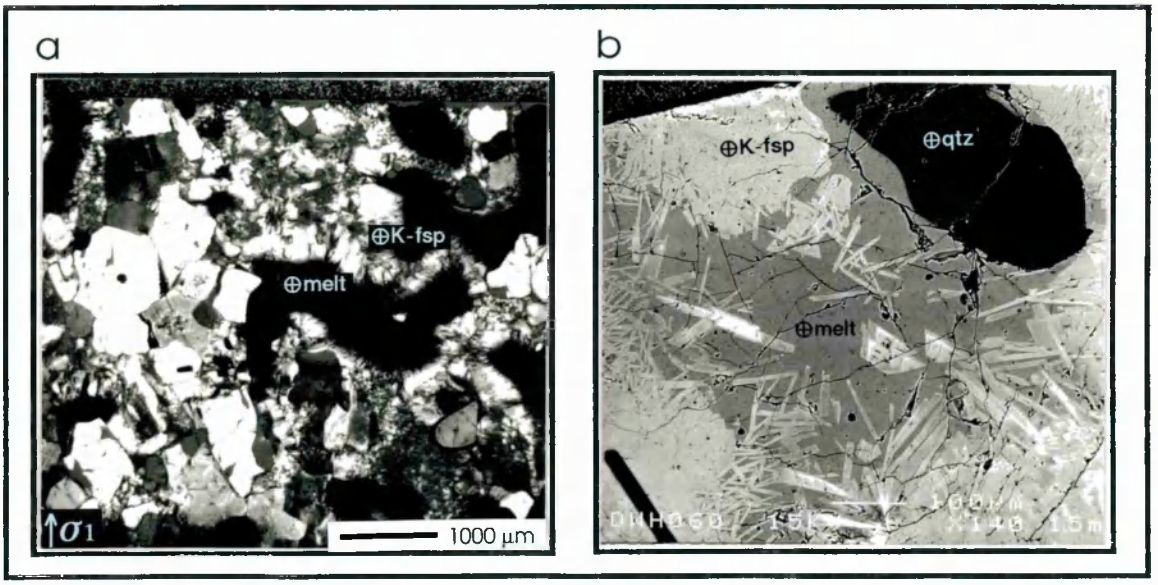

Figure 3.09: Illustration of neo-crystals and remnant glass in WG21. It is estimated that in this sample the melt fraction at the maximum temperature (1200 °C), 0.625, was reduced to 0.160 on cooling to 850 °C. **a.)** Optical thin section photo of sample with newly formed acicular feldspars showing a light grey colour against the black backdrop of melt. **b.)** BSEM image of the same section. Light grey feldspar crystals grow in the darker grey melt. Compositional zoning in the feldspars is indicated by bands of different grey shading.

In sample WG21, the neo-crystals appear to account for up to a fraction of 0.75 of the original melt fraction and grew in 47 hours. This rapid neo-crystallization is in contrast to

observations by Piwinskii and Martin (1970), who suggested that between 7 and 18 days are required to completely neo-crystallize a wet granitic melt.

3.4.3 Powder melt fraction

In one test (WG1) Westerly granite was crushed to reduce the grain size of 960 μm in the starting material to below 20 μm. The sample was then heated to 900 °C at 250 MPa for 129 hours. The small grain size and the long duration of heating were chosen to allow phases to equilibrate, hence attempting to generate an equilibrium melt fraction measurement at this temperature. A melt fraction of 0.168 was measured, significantly in excess of melt fractions measured in other tests at the same temperature, however, geochemical evidence suggests that even in this sample chemical equilibrium was not achieved (**Chapter 4.3.3**). This indicates the possibility that with considerably longer experiments, higher melt fractions could have been achieved in the majority of experiments, including the powder sample WG1.

3.4.4 Decrease in melt fraction during melt extraction

An attempt to determine melt viscosity (**Chapter 6.3**) involved four specimens, where a 4 mm thick layer of crushed quartzite of 200 μm average diameter was added beneath the specimen. Samples showed melt penetration from the granite into the adjacent quartzite (**Figure 3.08**), with the exception of WG25. Calculating area fraction of pores on BSEM images, the crushed quartzite was found to have an average porosity of 6% (assuming area fraction equalling volume fraction (Underwood 1970)). Measuring the average penetration distance of the melt into the quartzite allowed the volume of melt contained in the quartzite to be estimated. This was normalized as a fraction of the Westerly granite sample volume, calculated from the measured length of the specimen and the initial specimen diameter of 9.4 mm.

Sample	T (°C)	Specimen L	Penet. in qtz	ϕ melt gran	norm. ϕ melt qtz	Total
WG23	1000	16.4 mm	3.1 mm	0.103	0.014	0.117
WG24	1000	14.7 mm	1.8 mm	0. 88	0.011	0.099
WG25	940	15.9 mm	0	0.060	0.0	0.060
WG27	950	15.4 mm	0.88 mm	0.076	0.004	0.080

Table 3.03: Melt fraction reduction in partially molten granite due to extraction into adjacent porous quartzite. Extracted melt fractions are recalculated to equal volume fraction as if contained in the granite.

The total melt fractions in these tests fall significantly short of the average melt fraction of other tests performed at 1000°C (shaded squares in **Figure 3.04** and **3.06**) which is between 0.20 and 0.28 melt. The shortfall in final melt fraction may be due to extraction of melt inhibiting further melt production in the "restite".

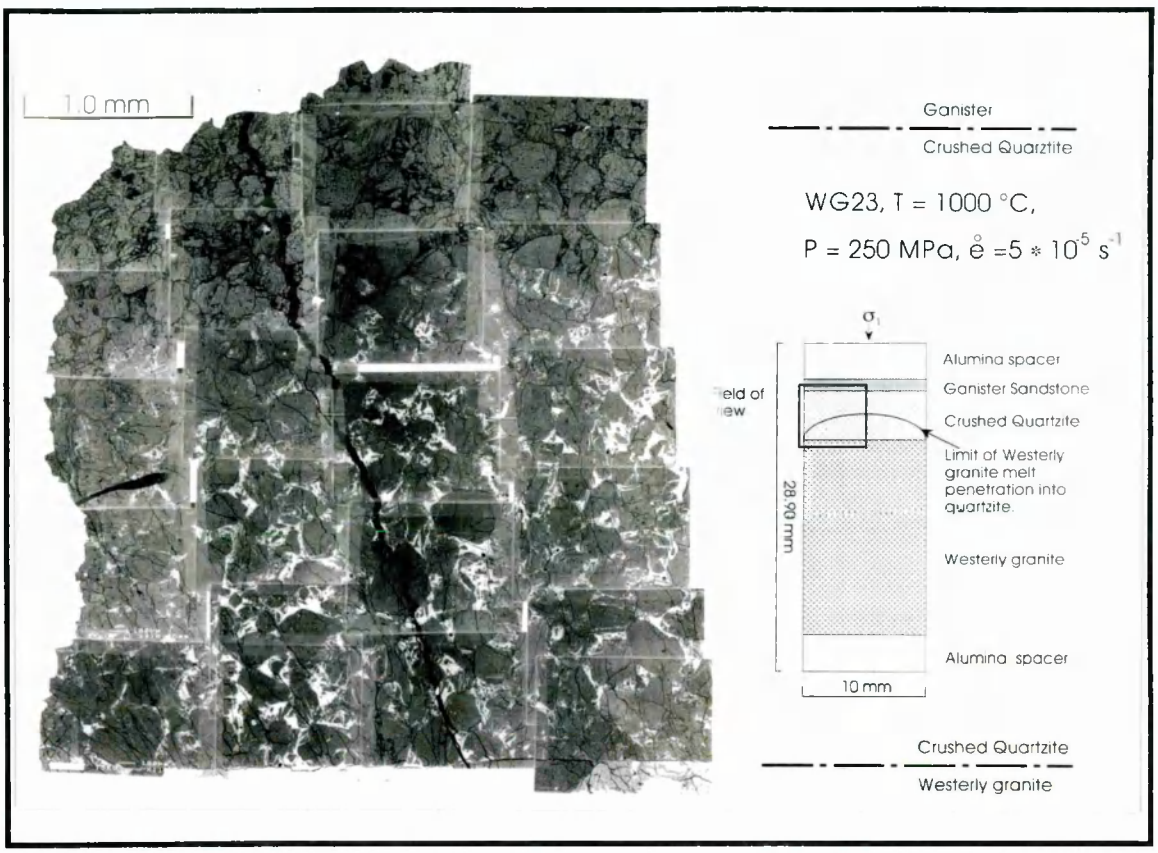

Figure 3.10: Set up of melt extraction test and BSEM collage of quartzite layer (black = holes, dark grey = quartz crystals) into which light grey melt has partially penetrated.

3.5 Determination of a melt fraction temperature relationship

In order to define the temperature dependence of melt fraction, only *normal tests*, as defined in **Chapter 3.3.1**, in which the total heating time was 10 hours or less were considered (see **Table 3.01**). This was done to exclude the effects of heating time, melt extraction and neo-crystallization. The selected data define a clear exponential increase in melt fraction with temperature (**Figure 3.04**). Plotting log melt fraction vs temperature, a good linear fit (RMSE = 0.9) was obtained for temperatures between 800

and 1050 °C (**Figure 3.05**), giving a relationship of melt fraction (ϕ) and temperature in degree Celsius (T_C):

$$\log \phi \propto \frac{0.00875}{2.303} * T_C \qquad \text{E3.01}$$

This can be re-written as

$$\log \phi = \log f + \frac{0.00875}{2.303} * T_C \qquad \text{E3.02}$$

solving for the exponential constant (f) a formula expressing the exponential relationship between melt fraction and temperature can be expressed as:

$$\phi = 3.77 * 10^{-5} \exp (0.00875 * T_C) \qquad \text{E 3.03}$$

This exponential relationship is only valid up to 1050 °C. The slower increase in melt % with temperature above 1050 °C is indicated by the dashed line on **Figure 3.11, b.**

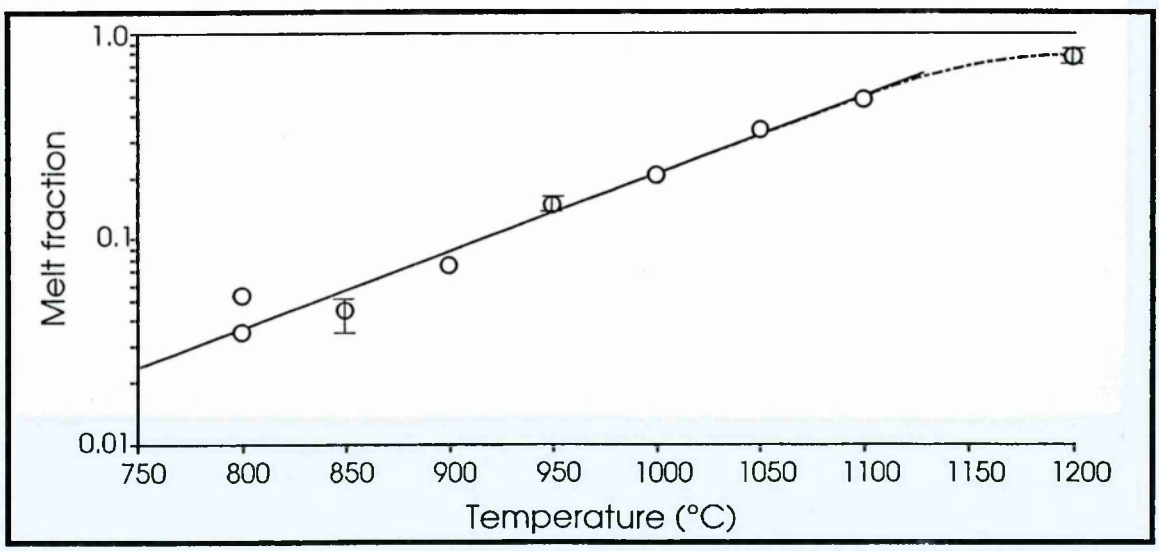

Figure 3.11: Plot of temperature against log melt fraction , see text for selection of data; Solid line shows linear fit for data below 1050 °C, while the dashed line depicts the general trend towards a slower increase in melt fraction at temperatures in excess of 1050 °C.

3.6 Water content of Westerly granite samples

Although the experiments on Westerly granite were conducted on oven dried samples, small amounts of water are available to be incorporated in the melt phase. This water is present in the crystalline structure of chlorite and mica and in quartz fluid inclusions. Three approaches were taken to the estimation of water content.

First an estimation of the volatile content of the granite was obtained by thermogravimetry (**Appendix 5**) and from the loss on ignition quantity obtained from whole rock XRF analysis (**Table 2.01**). Thermogravimetry measures the weight loss of a crushed sample heated up to 1100 °C, while the LOI is the proportion of emission lost in whole rock analysis, thought to equal the volatile content.

Secondly an attempt was made to calculate the water content (ψ) available from the percentage of mica (biotite, muscovite and chlorite) observed in the Westerly granite starting material (**Table 2.02**). In this method all the mica in the rock (6.0 vol %, **Table 2.02**) was assumed to be 3.8 % biotite (containing an average water content of 4 wt %), 1.4 % muscovite (containing 4.54 wt % H_2O) and 0.8 % chlorite (with 11.8 wt % H_2O) (averages after Deer et al 1966). For this calculation it was assumed that volume percent and weight percent could be interchanged. By making this approximation it is assumed that the density of the three sheet silicates is about the same as the density of the experimental charge.

A third attempt used the volume of vesicles in WG19 (heated to 1200 °C at room pressure. In this sample 20.84 % of the area of the thin section were occupied by vesicles. This can be taken to equal the volume fraction of vesicles (Underwood 1970). Using Boyle's law

$$\frac{P_1 * V_1}{T_1} = \frac{P_2 * V_2}{T_2} \qquad \text{E3.04}$$

a volume for 1 mole of water ($V_1 = 1.11 * 10^8$ mm^3) at 1200 °C and 0.1 MPa can be calculated, assuming that the volume of vapourized water at 25 °C and 0.1 MPa occupies $22.4 * 10^6$ mm ^{3}. However, the volume of the rock cylinder (9.4 mm diameter and 20 mm length) is only 590 mm^3, of which 20.84 % is occupied by vesicles. The vesicles therefore contain 118.6 mm^3, which contain $5.49 * 10^{-6}$ mol water. Assuming a density of granite of 2.65 kg m^{-3} and of water = 1 kg m^{-3} the weight of water is $\psi = 2.07 * 10^{-4}$ % in the starting material.

Method	LOI	Thermogravimetry	% of mica	vesicles
% water	0.61	0.64 (± 0.01)	0.25	0.000207

Table 3.04: Weight percentage water available in Westerly granite to be incorporated in the melt phase. Methods are **1.** Loss on ignition (XRF whole rock data **Table 2.1**), **2.** Thermogravimetry (**Appendix 9**) **3.** calculating the water extractable from mica, recast as weight percentage of bulk rock, and **4.** Vesicle volume in WG19 (1200 °C, 0.1 MPa).

The thermogravimetry and loss on ignition results place an upper limit on water available. This is because volatiles are also released by the decomposition of calcite (CO_2), present in the feldspar alteration material,. Confidence in this upper limit is increased by the close agreement between the thermogravimetry and LOI results.

The mica calculation provides a minimum estimate. This is because it is difficult to account for all the mica in fine grained sericite and the method does not account for water in quartz fluid inclusions, which would be released at temperatures in excess of 800 °C (Roedder 1984).

The water content, estimated from the volume of vesicles in WG19, is thought to be unrealistically low, as it is probable that not all water will exsolve from the melt. Also vesicle volume could be smaller than expected, as true adiabatic expansion might not have taken place due to the short duration of the test and large viscosity of the melt surrounding the vesicles, as well as vesicle shrinkage on cooling.

Confirmation of the water percentage available for the melt can be obtained by comparing the temperature melt fraction relationship defined by the experiments for this study with the theoretical melt fractions derived from partial melting of a general pelite with variable water content (Clemens & Vielzeuf 1987). In **Figure 3.12** results presented by Clemens and Vielzeuf (1987), calculated at 1000 MPa and 500 MPa, have been extrapolated to 250 MPa and the short duration *normal test* Westerly granite data (see **Chapter 3.4.1**) and the *powder test* WG1 have been plotted. The extrapolation is most accurate at low water content and low melt fractions where there is least difference between the Clemens & Vielzeuf models at 1000 and 500 MPa. The comparison suggests that the Westerly granite *normal test* data are consistent with a water percentage of about 0.15% whereas the *powder test* is consistent with a water percentage of 0.3%. It is possible that either more water was released in the longer duration powder test, increasing the melt fraction, or that the short duration tests underestimate the melt water content as they did not reach an equilibrium melt fraction. A water content of $\psi = 0.3$ wt % in the starting material is also inferred when comparing melt viscosity data with empirical data by Shaw (1965) (**Figure 8.06**).

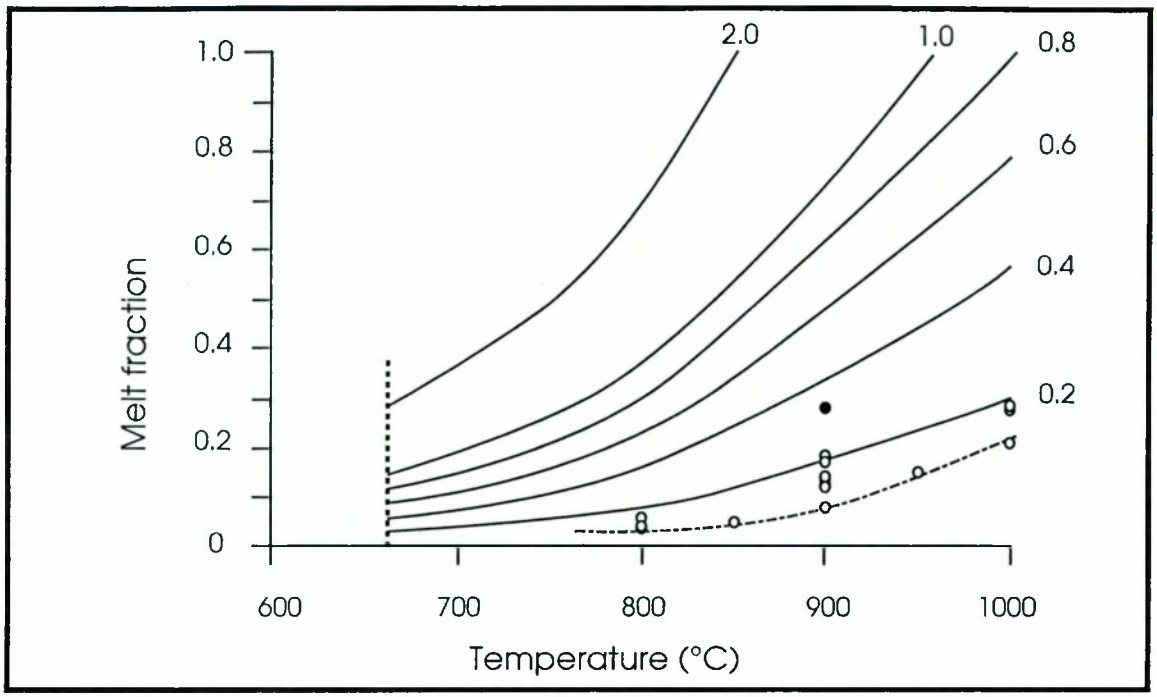

Figure 3.12: Melt generation in a general pelite with variable water content extrapolated to 250 MPa (after Clemens & Vielzeuf 1987). Open circles represent Westerly granite short duration test data and closed circle represents WG1, *the powder test*. Dashed line is the best fit short duration melt fraction temperature relationship (Section 3.4.5).

3.7 Conclusion

With the onset of melting static tests showed the development of very low melt wetting angles, with melt films surrounding quartz and mica crystals (**Chapter 3.3.1**). This indicated an immediate contiguity of the melt phase from the onset of melting. Melt was not homogeneously distributed throughout deformed samples, but was concentrated in low pressure regions such as adjacent to pistons and in dilatant cataclastic fault zones cutting the specimen (**Chapter 3.3.2**).

Complete melting of muscovite and chlorite took place at temperatures below 800 °C, while biotite and K-feldspar disappears in tests above 1050 °C, and plagioclase above 1200 °C. Vesiculation of melt heated to 1200 °C at room pressures (WG19) is concentrated at sites of former hydrous phases (**Chapter 3.3.1**).

Melt fraction was found to be dependent on heating time and temperature and was also reduced in melt extraction experiments (**Chapter 3.4**). An exponential melt fraction temperature relationship was defined for the short duration tests over the temperature

range 800-1050 °C (**E3.03**). In none of the experiments was an equilibrium melt fraction attained.

The water content of Westerly granite charges available to be incorporated in the melt is estimated to lie at or above $\psi = 0.3$ with an upper limit at 0.6 weight % (**Chapter 3.6**). An attempt to estimate the water content of a vesiculated melt generated at atmospheric pressure produced a value of 0.0002 %. This is thought to be an underestimate.

Chapter 4

Geochemistry

4.1 Introduction

In this chapter the chemical compositions of crystalline phases and melt are explored. The change in composition of minerals in the starting material with increasing melt fraction and minerals formed during the melting interval are documented. The chemical variation of melt at different temperatures, and thus different melt fractions, is discussed and the major influences on melt compositions are evaluated. Although a detailed account / assessment of the chemical processes occurring during partial melting is beyond the scope of this thesis, some general conclusions are drawn regarding the major influences on melt and mineral compositions.

The sample WG1 is described, in which a powdered rock sample was heated to 900 °C for 129 h in an attempt to determine the equilibrium melt composition of melt at this temperature. Finally the minerals produced during crystallization in samples WG18 and WG21 (**Chapter 3.3.5**) are described and compared to compositions of the same minerals in the starting material.

The chemical compositions of minerals and melt were determined by energy-dispersive x-ray spectroscopy on the Manchester scanning electron microscope (**Appendix 5, 10**). Samples for chemical analyses were chosen to cover the temperature spread between 800 and 1100 °C, spaced at 100 °C intervals (**Table 4.01**). Between 53 and 125 spot analyses were taken per sample, and representative data are listed in **Appendix 6**.

Sample	T_{max}(°C)	P (MPa)	t (h) @ T	melt fraction
WG2	800	250	2.4	0.053
WG8	800	250	96.0	0.035
WG3	900	250	2.5	0.073
WG11	1000	250	71.0	0.271
WG12	1050	250	4.0	0.335
WG13	1100	250	4.0	0.477

Table 4.01: Experimental test temperatures, confining pressures, duration of heating and melt fractions of samples used in chemical evaluation.

4.2 Mineral compositions in experimental charges.

The crystalline phases can be split into those occurring in the starting material (**chapter 2**) that are involved in the melting process, and phases occurring only in samples heated to 800 °C and above.

Sample Temperature	WG0 21	WG2&WG8 800		WG3 900	WG11 1000	WG12 1050	WG13 1100
amphibole	•	•				•	
apatite	•		•	•	•		
biotite	•	•	•	•	•	•	
calcite	•						
chlorite	•						
epidote	•						
garnet		•		•			
haematite	•		•	•			
ilmenite	•	•		•	•	•	
K-feldspar	•	•	•	•	•	•	
muscovite	•	•					
olivine					•	•	•
plagioclase	•	•	•	•	•	•	•
pyroxene			•	•	•	•	•
quartz	•	•	•	•	•	•	•
rutile	•						
sphene	•		•				
spinel	•		•	•	•	•	•
wollastonite			•	•		•	
zircon	•						

Table 4.02: List of crystalline phases found in the starting material and in samples heated to between 800 and 1100 °C.

Table 4.02 lists the occurrence of phases in samples heated to different temperatures. As WG2 and WG8 were both heated to 800 °C, analyses from these two samples are grouped together in the following discussion. Representative analyses of all crystalline phases are displayed in **Appendix 6**. In this section the chemical compositions of the major constituents of the starting material (feldspars, quartz and biotite) are explored first. This is followed by an investigation of accessory phases that together form less than 1 % of the volume of the rock. These are listed alphabetically.

4.2.1 Feldspar

Both K-feldspar and plagioclase occur in the starting material. Compositional ranges of both feldspars at different temperatures are listed in **Table 4.03**.

T (°C)	K-feldspar	Plagioclase
21	$Or_{(96.9-89.6)}Ab_{(10.4-3.1)}An_{(0.7-0)}$	$Or_{(1.5-0)}Ab_{(99.0-80.4)}An_{(20.1-1.0)}$
800	$Or_{(94.8-40.6)}Ab_{(51.4-5.1)}An_{(4.6-0)}$	$Or_{(10.8-0)}Ab_{(98.1-65.4)}An_{(26.0-1.3)}$

900	$Or_{(94.9-49.1)}Ab_{(40.3-4.5)}An_{(7.6-0)}$	$Or_{(19.5-0)}Ab_{(91.2-61.4)}An_{(19.6-3.9)}$
1000	$Or_{(89.9-57.6)}Ab_{(40.3-9.0)}An_{(2.1-0)}$	$Or_{(12.3-1.2)}Ab_{(84-68.1)}An_{(19.6-14.6)}$
1050	$Or_{(89.5-40)}Ab_{(47.5-10.5)}An_{(14.3-0)}$	$Or_{(7-0.8)}Ab_{(87.6-13)}An_{(82.2-11.0)}$
1100	not present in sample	$Or_{(28.3-0.9)}Ab_{(81.7-47)}An_{(27-17.2)}$

Table 4.03: Chemical variation of feldspars with increasing temperature

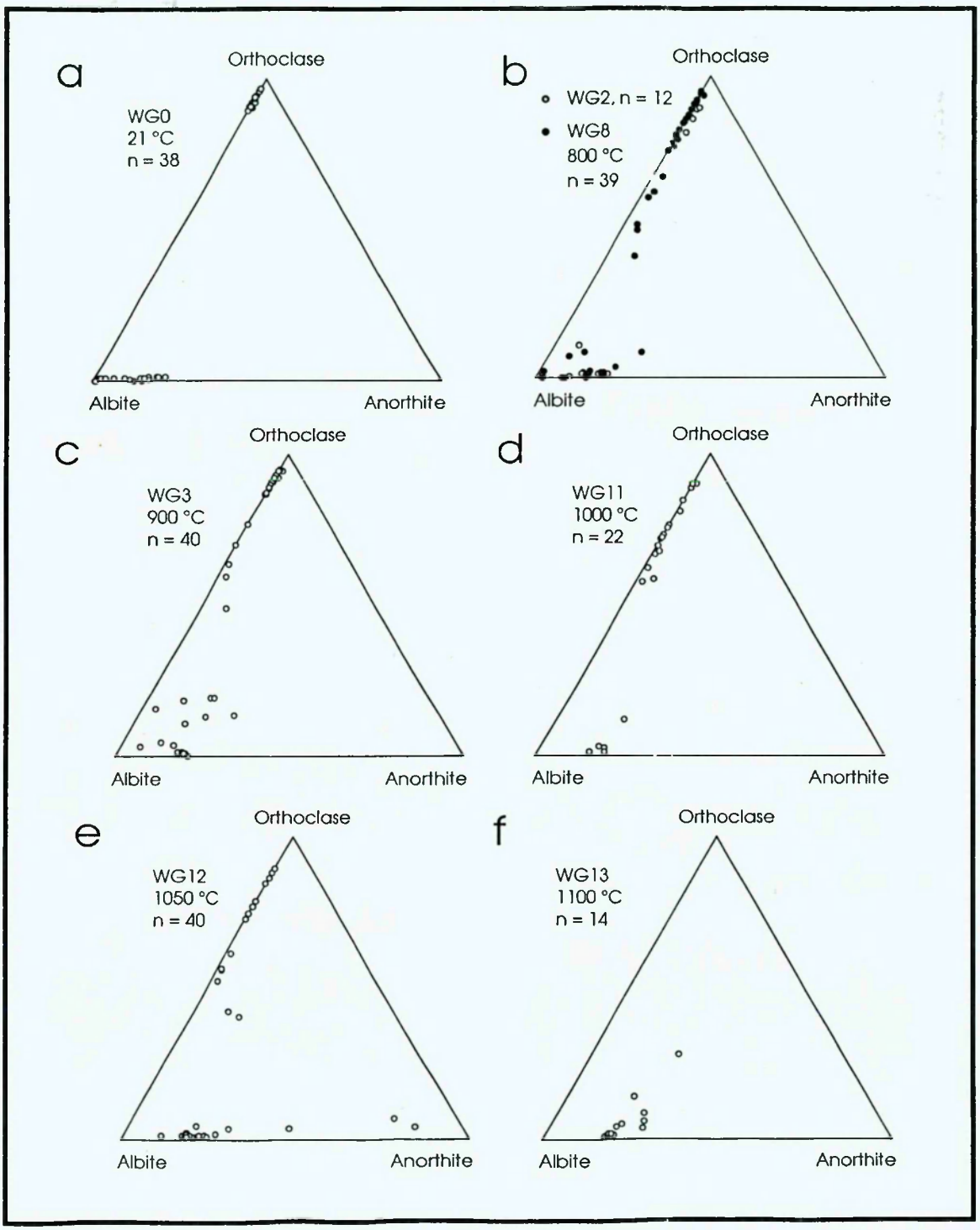

Figure 4.01: Triangular plots of feldspar composition with respect to orthoclase, albite and anorthite content. **a.)** WG0; **b.)** WG2 and WG8; **c.)** WG3; **d.)** WG11; **e.)** WG12 and **f.)** WG13.

In the starting material potassium feldspar occurs in its low temperature polymorph microcline with an average composition of $Or_{(92.7)}$ $Ab_{(6.8)}$ $An_{(0.3)}$.

With increasing temperature K-feldspar compositions show an increase in sodia, such that the increase in albite content increases from below 10.4 % to over 47 % (**Figure 4.01, Table 4.03**). This increase in sodium is also often associated with an additional component of calcium. At 1050 °C only remnants of K-feldspars remain, while in sample WG13, heated to 1100 °C, all crystalline K-feldspar has disappeared. Melting of K-feldspars takes place from the edge of the crystal towards its core and along cracks (**Figure 4.02**).

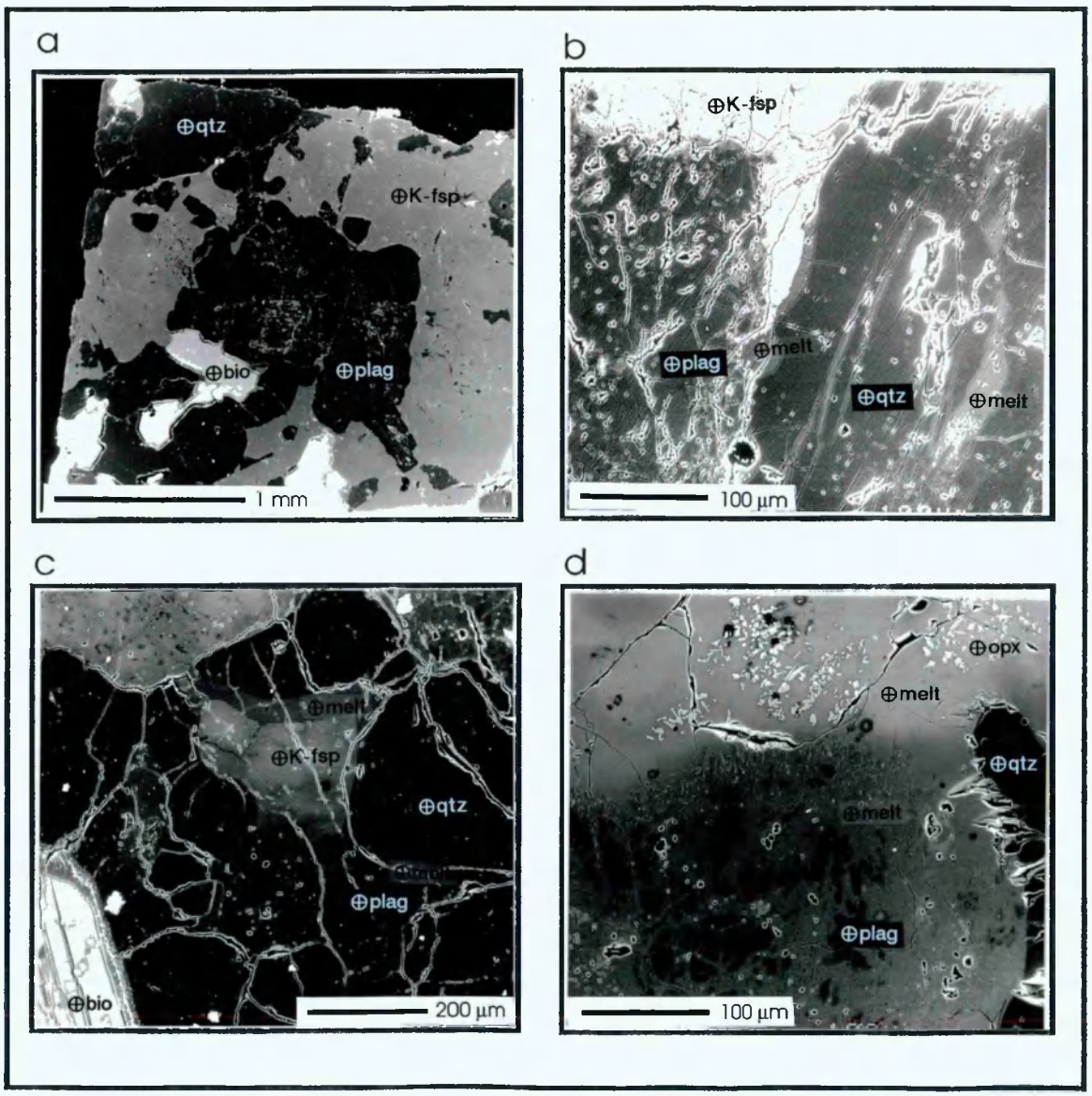

Figure 4.02: BSEM images of feldspars in the starting material and at elevated temperatures. **a.)** WG0; **b.)** WG8, Melting along quartz-K-feldspar and quartz-plagioclase boundaries; **c.)** WG11. Large melt pools where plagioclase and orthoclase have melted. **d.)** WG13. Remnants of plagioclase are visible with light grey shaded areas in the melt indicating former sites of orthoclase crystals.

On backscattered SEM images a gradual transition from the grey value (indicative of average atomic weight ratio) of K-feldspars to that of melt are observed (**Figure 4.02, c**). At 1100 °C (**Figure 4.02, d**) positions of melted K-feldspars are visible in backscattered images as light, diffuse, rectangular areas, indicating that the K-feldspar components had not diffused completely into the surrounding melt. With increasing temperature the plagioclase turns more anorthitic, often associated with the introduction of some potassium into the mineral structure (**Figure 4.01**). Plagioclases with strong ternary character (all three cations present in significant quantities) are found at temperatures of 800 and 900 °C (**Figure 4.01**). With further increase in temperature plagioclases show more anorthitic character, that is particularly pronounced at 1050 °C. At 1100 °C plagioclases plotting at the most anorthitic end of plagioclases in the starting material and more anorthitic plagioclases with strong ternary character remain. Complete melting of plagioclases takes place just above 1200 °C, as only small ghost-like remnants of plagioclase crystals were observed in sample WG19 (heated to 1200 °C at room pressure) (**Figure 3.04, d**). Melting takes place around sericite inclusions and from crystal edges and cracks (**Figure 4.02,b & c**). As in K-feldspar the transition between grey values of melt and plagioclase is transitional in backscattered SEM images (**Figure 4.02**).

4.2.2 Quartz

Quartz was rarely analysed and, as expected, only small compositional variation was observed. This was manifested by oxide traces of alumina (up to 1.4 wt %), iron oxide (1.5 wt %) and magnesia (0.9 wt %) (for representative analyses see **Appendix 6**). However, the occurrence of trace elements may be due to edge contamination, as all anomalous readings were taken very close to the crystal boundaries (less than 10 μm). It occasionally contains epidote (allanite) and rutile needles. Quartz is the only primary mineral that survives heating to 1200 °C, though it clearly contributes to the partial melting process. SEM back-scattered images (**Figure 4.02, c, d**) show that partial melting results in the loss of the original angular crystal shape of quartz. The crystals become rounded and melt penetrates along cracks. Contacts between quartz and melt are always sharp in BSE images, rather than gradational as in the case of feldspars.

4.2.3 Biotite

Biotite forms the fourth major constituent of Westerly granite. It is commonly altered to chlorite and shows muscovite rims in the starting material; it is commonly associated with accessory phases such as apatite, calcite, ilmenite and haematite, zircon and allanite. The starting material (WG0) shows a narrow compositional spread of biotite compositions (**Figure 4.03**). Recalculating mineral formula and plotting biotite compositions on the phlogopite-biotite compositional field (after Deer, Howie & Zussman 1966) all biotite analyses falls into the biotite field, plotting half way between annite and siderophyllite and half way between phlogopite and annite (**Figure 4.03 c, d**).

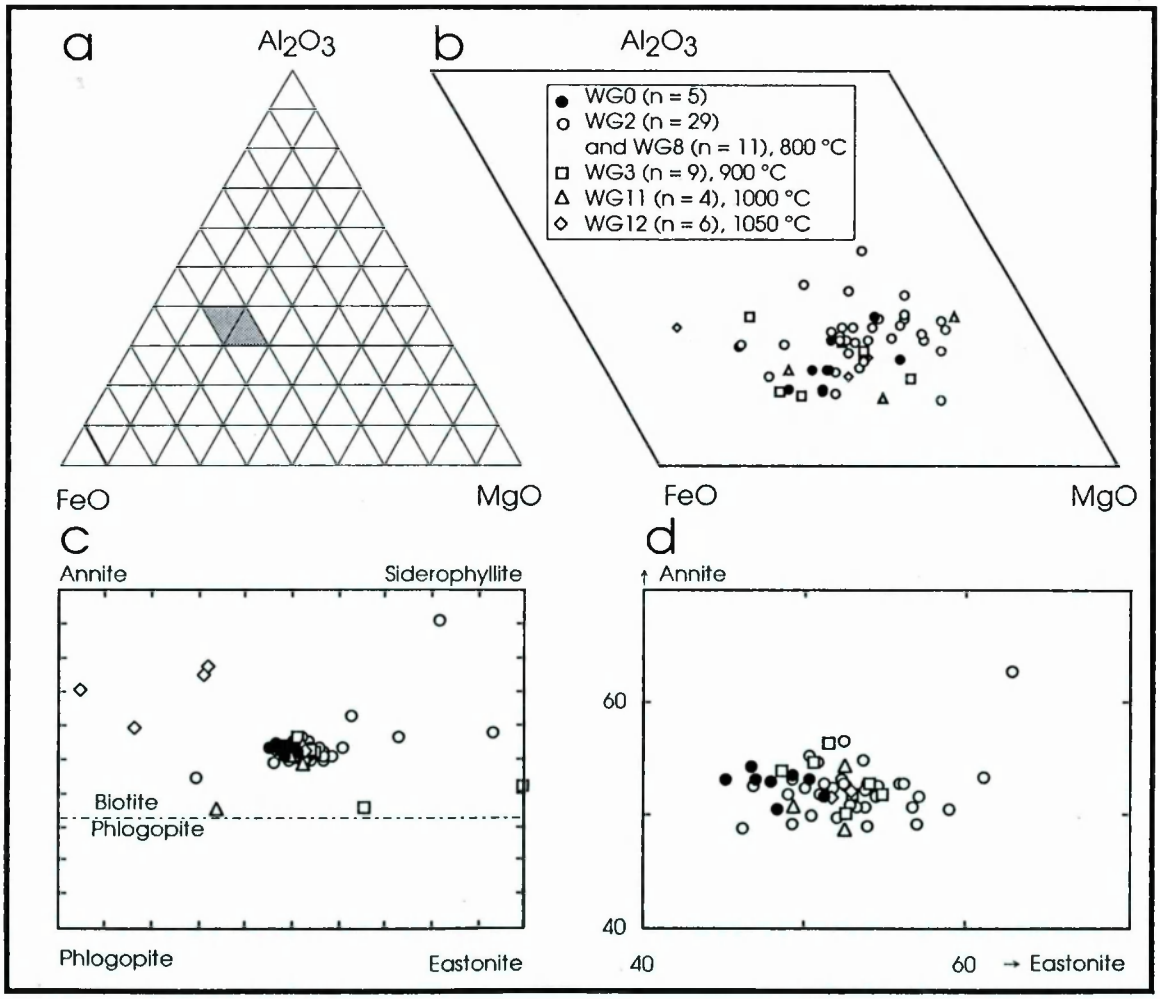

Figure 4.03: Triangular plots of biotite compositions with respect to proportion of aluminium, iron and magnesium oxide. The grey shaded area in **a.)** indicates the enlargement of the parallelogram **b.)**. The biotite-phlogopite compositional field is plotted (after Deer, Howie & Zussman 1966, p. 212) in **c.)** with an enlargement of the area containing the highest concentration of analyses in **d.)**.

Figure 4.04: BSEM images of biotite in the starting material and at elevated temperatures. Identified phases are labeled. **a.)** WG0, biotite showing muscovite intergrowth parallel to cleavage; **b.)** WG8, Melting parallel to cleavage; **c.)** WG3, melting parallel to cleavage and on biotite grain boundary; **d.)** enlargement of c.) to show secondary phases resulting from biotite

melting; **e.)** WG11 and **f.)** WG12. Most of the biotite has melted, with only small remnants remaining.

Despite large compositional spread most biotite analyses for each temperature (800 to 1050 °C) plot near the composition of biotites in the starting material. There is a slight shift towards siderophyllite enrichment with increasing temperatures, suggesting biotites with higher crystallization and melting temperatures (Deer et al. 1966). There was a very slight increase in the phlogopite/annite ratio with increasing temperature.

At 800 °C, breakdown of biotite takes place along cleavage planes (**Figure 4.04, b**). This results in the production of melt and secondary minerals (pyroxenes, amphibole , olivine, sphene and spinel) that grow in layers parallel to the original biotite cleavage. In sample WG3 (900 °C) biotites have melted sufficiently to allow mobilisation of the biotite-dominated melt (**Figure 4.04 c, d, e**). In the highest temperature run where biotite was observed (WG12, 1050 °C), only ragged remnants of biotite remained (**Figure 4.04, f**). In sample WG13, 1100 °C, all biotite had been consumed, with pyroxene, spinel, garnet and olivine and other accessory phases marking the sites of former biotites (**Figure 4.02, d**).

4.2.4 Accessory minerals

While accessory minerals in the starting material are apatite, chlorite, epidote, ilmenite, hematite and muscovite (**Chapter 2.4.5**), the accessory phases formed as a product of melting include pyroxenes, garnet, olivine, amphiboles, sphene and spinel (**Table 4.02**).

Amphibole: Amphibole was found in the starting material (WG0), as well as in samples WG2 (heated to 800 °C) and WG12 (heated to 1050 °C). As these samples represent test run across almost the entire temperature interval, with only seven positively identified analyses (listed in **Appendix 6**), it is likely that amphibole may have been present at intermediate temperatures, but was not found due to its extremely low volume (<<1 %) in samples. While amphiboles in WG0 and WG2 have silica contents averaging 33.1 % this value rises to 49.2 % in WG12. Increases in iron, magnesium, sodium, and potassium were offset by a loss in calcium. Still, all amphiboles can be classified as belonging to the hornblende group. In WG0 amphibole occurred as a 50 μm euhedral crystal, whereas the hornblende found in WG2 forms a dendritic inclusion parallel to cleavage in biotite. In the case of WG12 amphibole crystals are very small needles (below 2 μm width) in melted areas of plagioclase feldspar. This indicates that

the amphibole in WG2 was likely to be primary, whereas the needles in WG12 might have formed as a by-product of one of the melting reactions. Amphibole might be retrograde epidote.

Apatite: This mineral was found in the starting material, as well as at 800 °C (WG8), 900 °C (WG3) and 1000 °C (WG11). There is little variation between crystals in the same sample and with increasing temperature with CaO forming between 53.1 and 55.7 % and P_2O_5 between 40.8 and 43.7 %). Minor traces (0 to 1 %) of silica, Al_2O_3, FeO, Na_2O and K_2O were found. Apatite in WG0, WG8, WG3 and WG11 are euhedral crystals, with sizes ranging between 50 and 100 μm. In WG3 the apatite crystals were found as inclusions in biotite, whereas in WG13 they form hexagonal crystals surrounded by melt. It is thought that apatites play little to no role in partial melting, at least up to 1100 °C.

Calcite: This phase only occurred in WG0 where small traces of silica, Al_2O_3, and FeO were found, each contributing less that 1 % to the total analysis (**Appendix 6** for analyses). It forms small, < 10 μm diameter, crystals and forms part of the host of crystals associated with plagioclase sericitization. It is found as inclusions in both quartz and plagioclase.

Chlorite: This alteration product of biotite was only found in WG0. Mineral analyses showed that all chlorites belong to the iron-rich end-member brunsvigite (**Appendix 6** for analyses) with magnesia forming between 13.0 and 14.2 %.. Silica contents vary between 25.4 and 26.0 %, aluminium oxide forms between 17.6 and 18.7 % and iron oxide between 25.7 and 27.6 %. The crystals also contain traces of manganese.

Epidote: As for chlorite, this mineral was only found in the starting material. Mineral appearance (brown staining, see **chapter 2**) and low totals (**Appendix 6**) indicate that all epidote crystals that were analysed are allanite, containing significant thorium, yttrium and rare earth elements (Deer et al. 1966).

Garnet: This mineral was found in samples WG2 (800 °C) and WG3 (900 °C), where it forms as inclusions in plagioclase and in areas of molten biotites, never achieving diameters above 10 μm. Compositionally they fall near the grossular end member with between 25.8 to 45.8 % SiO_2, 18.8 to 35.8 % Al_2O_3 and 17.3 to 28 % CaO. Minor components of iron, titanium, sodium and potassium oxides were found, never exceeding 1.2 %.

Haematite: Haematite was found both in the starting material, WG8 heated to 800 °C, and WG3 heated to 900 °C. Some of the samples contain traces of silica, alumina, titania and sodia though never more than one element in each analysis and never

exceeding more than 0.4 %. It occurs as 10 to 50 μm diameter well rounded crystals, or as small inclusions in biotite.

Ilmenite: This phase was found in the starting material, as well as in samples heated between 800 and 1100 °C, with the exception of 1050 °C (WG12). Ilmenites across the temperature range contain between 44.7 and 58.19 % TiO_2 and 49.2 to 58.8 % total iron as FeO, with the exception of two analyses at 800 °C that are enriched in iron to 68 and 76 % (**Appendix 6**). Some samples are also enriched in MnO up to 9.8 %.

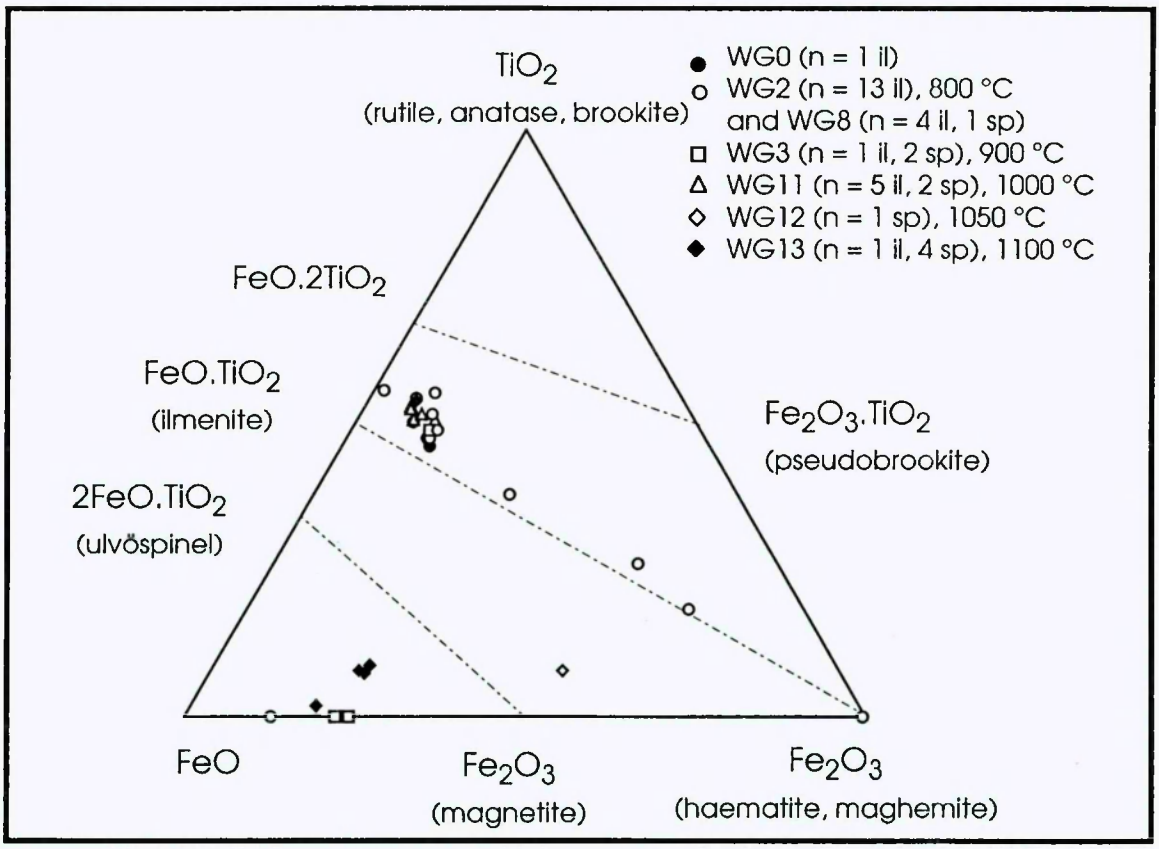

Figure 4.05: Fe-Ti analyses plotted on triangular compositional diagrams of the combined spinel and ilmenite data with titanium oxide plotted against FeO and Fe_2O_3 (after Deer, Howie & Zussman 1966). Major compositional solid solutions series are included. Phases are plotted on mol per cent basis.

On **Figure 4.05** ilmenite compositions show a general slight enrichment in titanium with respect to the solid solution line between ilmenite and haematite. Analyses at 800 °C show solid solution of ilmenite towards haematite, which is also present in these samples. Higher temperature analyses cluster around the composition of ilmenite in WG0. Crystals appear at all temperatures in two different forms. In the first it appears as well rounded crystals, often up to 200 μm in diameter, while the latter form is as small anhedral crystals (<20 μm diameter) that appear in the vicinity of melting biotites, often enclosed by biotites.

Muscovite: This white mica was found as overgrowths on biotites in WG0. However, no muscovite was observed at elevated temperatures. Compositionally this phase appears to be strongly heterogeneous. While silica varies from 29.8 to 47.3 %, aluminium oxide shows a spread from 7.3 to 28.6 % and iron oxides show a spread of 3.8-9.1 %. Additionally a host of other oxides are found. While individual oxides are not present in every muscovite analysis, they can attain up to 11.4 wt %. (TiO_2 0-1.2 %, MgO 0-2.7 %, CaO 0-10.1 %, K_2O 0-11.4%, Na_2O 0-0.4 %). The only oxides that were not detected were those of manganese and phosphorus. The large scale of isomorphous replacements at both octahedral sites in the muscovite crystal lattice can account for the compositional variations observed (Deer, Howie & Zussman 1966).

Olivine: This mineral was found in samples heated to between 1000 and 1100 °C. Whereas all olivine analyses at 1050 and 1100 °C have an average olivine compositions of Fa = 32.9, Fo = 67.1% with little compositional spread those at 1000 °C are somewhat richer in iron ($Fa_{51.5}Fo_{48.5}$). Small traces of alumina,, manganesia, calcia and sodia can be found, though never exceeding 1 %. At 1000 °C olivine forms euhedral crystals adjacent to melting biotites, attaining 20 μm diameter. With increasing temperature, olivine crystals increase in size and are still always associated with sites of biotite breakdown. At 1100 °C olivine can be seen to form skeletal crystals attaining diameters of 100 μm (**Figure 4.11, c**).

Pyroxene: Both ortho- and clinopyroxene were found in samples between 800 and 1100 °C. Clinopyroxenes are found at temperatures between 800 and 1000 °C, while orthopyroxenes occur over the whole temperature range (**Figure 4.06**).

Clinopyroxenes plot near the boundary between augite and ferroaugite. Traces of titanium, manganese, sodium and potassium oxide are found in mineral analyses, though never exceeding 1.7 % (full analyses in **Appendix 6**). Clinopyroxene have amorphous crystal shapes of less than 10 μm diameter, forming at sites of biotite breakdown (**Figure 4.04, e**). In contrast, orthopyroxene forms euhedral, orthorhombic crystals up to 20 μm length and 5 μm width. These always occur in reaction rims between quartz and extensively melted areas (**Figure 4.11, b**), or in melt films between biotite and quartz as in the case of WG11 (**Figure 4.04, e**). Compositions of orthopyroxenes fall in the hypersthene (WG13) to ferrohypersthene fields, and range just into the pigeonite field. Pure enstatite (100%) is also found in samples WG3 and WG13 (at 900 and 1100 °C respectively) and forms at sites of biotite breakdown, often in close association with olivine. Again traces of all other oxides are found in orthopyroxene analyses.

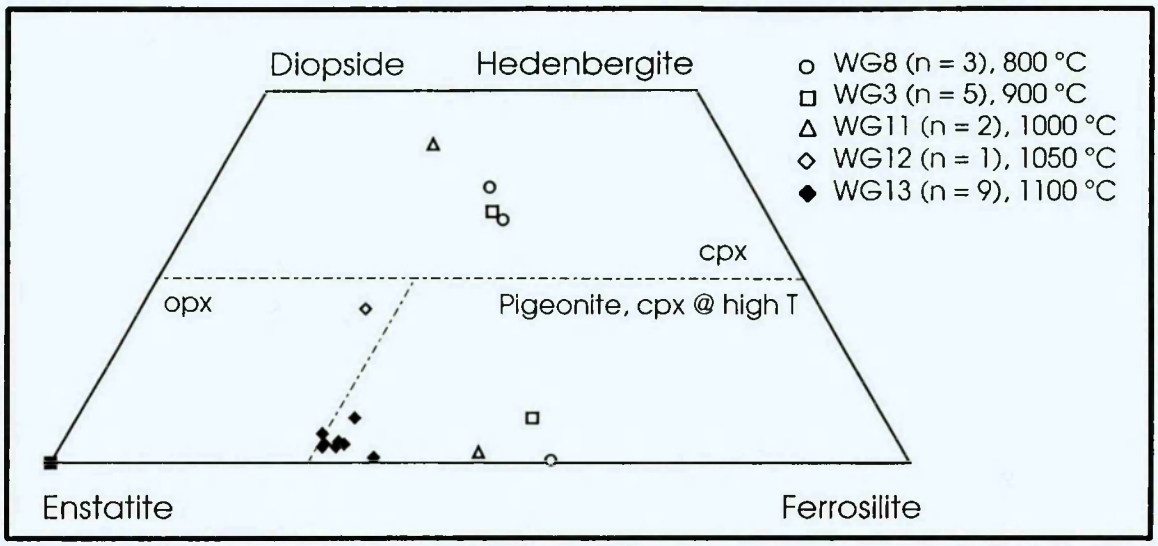

Figure 4.06: Pyroxene quadrilateral showing end member compositions of pyroxene solid solution series (after Deer, Howie & Zussman 1966). Horizontal dot-dashed line marks transition between ortho- and clinopyroxene, the inclined line the transition at 30 % ferrosilite the transition into the pigeonite/hypersthene field that has minerals with monoclinic symmetry at high temperatures (Deer, Howie & Zussman 1966).

Rutile: This mineral was found in the starting material, as well as in samples WG2 and WG3, heated to 800 and 900 °C respectively. Samples show small percentages of silica, iron, magnesium and potassium oxides, though never forming more than 5 % of the total weight of analyses. As in the starting material, rutile is generally included in biotites where it forms amorphous crystals, rarely attaining sizes above 5 μm, with the exception of WG3, where a 30 μm rutile crystal was found, with anhedral crystal shapes.

Sphene: Sphene was found in the starting material and WG8, heated to 800 °C. Only one analysis in each sample could be identified as sphene. Compositionally substitutions of alumina (up to 6.1 %) and iron oxide(2.4 %) could be observed. In both thin sections this phase forms euhedral crystals of 100 μm length.

Spinel: Spinel crystals were found at all temperatures. Compositional trends are displayed in **Figure 4.05**. While most spinel compositions are close to that of magnetite analyses display significant amounts of aluminium and magnesium oxide percentages (**Figure 4.05**) (for analyses see **Appendix 6**). No end-member magnetite compositions were found. Instead iron re-allocation shows mineral phases tending further towards FeO. In the starting material spinel falls in the Hercynite compositional field with contributions of alumina (47.7%), iron oxide(44.3 %) and manganese oxide (6.4%). This composition is not reflected at elevated temperatures. The manganese oxide content falls to below 1%, in all samples from 800 to 1100 °C, associated with a rise in silica (0.3-4.4%), magnesia (5-8.4%), calcia (0-1.2%) and potassia (0-0.5 %). (The manganese oxide content will decrease as garnet crystallizes). However, the most marked increase is in

titania, that rises from 0.6 to 12.6 % at temperatures between 1000 and 1100 °C, indicating a change in composition towards titaniferrous magnetite. Spinel crystals are generally associated with biotites. In the starting material and at temperatures up to 900 °C spinel crystals rarely attain diameters above 20 μm. At higher temperatures (1000 to 1100 °C) spinels form needles of up to 10 μm length that turn more dendritic with increasing temperature. At 1100 °C spinel is found at sites of former biotites (**Figure 4.04, c**).

Wollastonite: Wollastonite is found at temperatures between 800 and 1050 °C (WG8, WG3, WG12). Traces of titanium, aluminium, iron, manganese and magnesium oxides were found, though never exceeding 1 % (**Appendix 6** for mineral analyses). Recalculating mineral analyses in terms of wollastonite - enstatite - ferrosilite content only the lowest temperature sample shows pure end-member compositions, while up to 1.2 % contributions from both pyroxene end members can be found between 900 and 1050 °C (**Appendix 6**). This phase is generally found in the vicinity of partially molten biotites, where wollastonite dendritic needles rarely attain sizes above 5 μm.

Zircon: This phase was only found in the starting material. Here it is enclosed in biotites, often associated with a pleochroic halo. Oxides of aluminium, iron, calcium and sodium never exceed 1.5% (**Appendix 6**). Crystal sizes rarely attain 10 μm diameter with euhedral shapes.

4.3. Melt compositions

As described in the previous section and **Chapter 3**, melting of phases takes place from the grain boundary towards its centre, thus forming an interconnected network of melt. In addition isolated melting takes place in the core of feldspar crystals in areas of sericitization (compare to **Section 5.2.1**).

In this section the compositional variations of the melt phase at various temperatures in the test samples are discussed. This is followed by an investigation of how adjacent mineral phases influence melt compositions by plotting melt compositions. Next, the change in composition with distance to primary crystalline phases is explored. Finally melt compositions in the powder sample (WG1) is analysed in which an attempt was made to establish the equilibrium melt composition at 900 °C by heating a crushed sample (with grain size around 10 μm) for 129 hours.

Melt was identified in back-scattered electron images (**Chapter 3.2**). Using a focussed electron beam of 1 μm diameter, spot analyses of melt compositions were carried out. Counting times were set to 25 seconds to reduce the loss of low atomic weight atoms

such as sodium, as light atoms are easily displaced in a phase without a crystal structure by prolonged exposure to an electron beam. Points for melt analysis were chosen so as to explore the variability of melt with respect to distance to different phases. Distinction between feldspar and melt analysis were made by the present of magnesium and iron in the chemical analysis and the maintenance of feldspar stoichiometry at oxide totals between the set limits (**Appendix 4**). The bias in data collection due to subjective selection of sites is compensated for by the large number of analyses carried out.

4.3.1 Compositional variation of the melt phase

Harker plots

The variation of oxides in the melt phase was first explored by plotting all other oxides against SiO_2 in weight percentage in **Figure 4.07**. Each plot contains the melt analyses of all samples listed in **Table 4.01**, as well as mineral phases occurring in the starting material that contain the elements analysed in the plot.

The only minerals in the starting material that contain appreciable amounts of titanium are biotite, sphene and rutile. Plotting titania against silica (**Figure 4.07, a**), melt analyses show up generally less than 3 wt % titanium, if any. There is a small increase in the amount of titania in some melt analyses with lower than average silica content (60.5 %) at temperatures between 800 and 1100 °C. Also analyses with higher than average silica content sharply reduce their titanium content to approach zero.

Alumina concentrations vary between zero and 70 % (**Figure 4.07, b**). The largest proportion of analyses from samples between 800 and 900 °C, cluster around silica/aluminium ratios of feldspars. Other analyses define one trend at below average silica (60.5 %) and constant aluminium content (≈ 20 %) towards compositions of mica, and another trend towards an increase in aluminium with decreasing silica content, tending towards spinel compositions.

Few melt analyses contain manganese (**Figure 4.07, c**). Analyses containing manganese show a weak increase in manganese with deceasing silica content, trending towards spinel compositions.

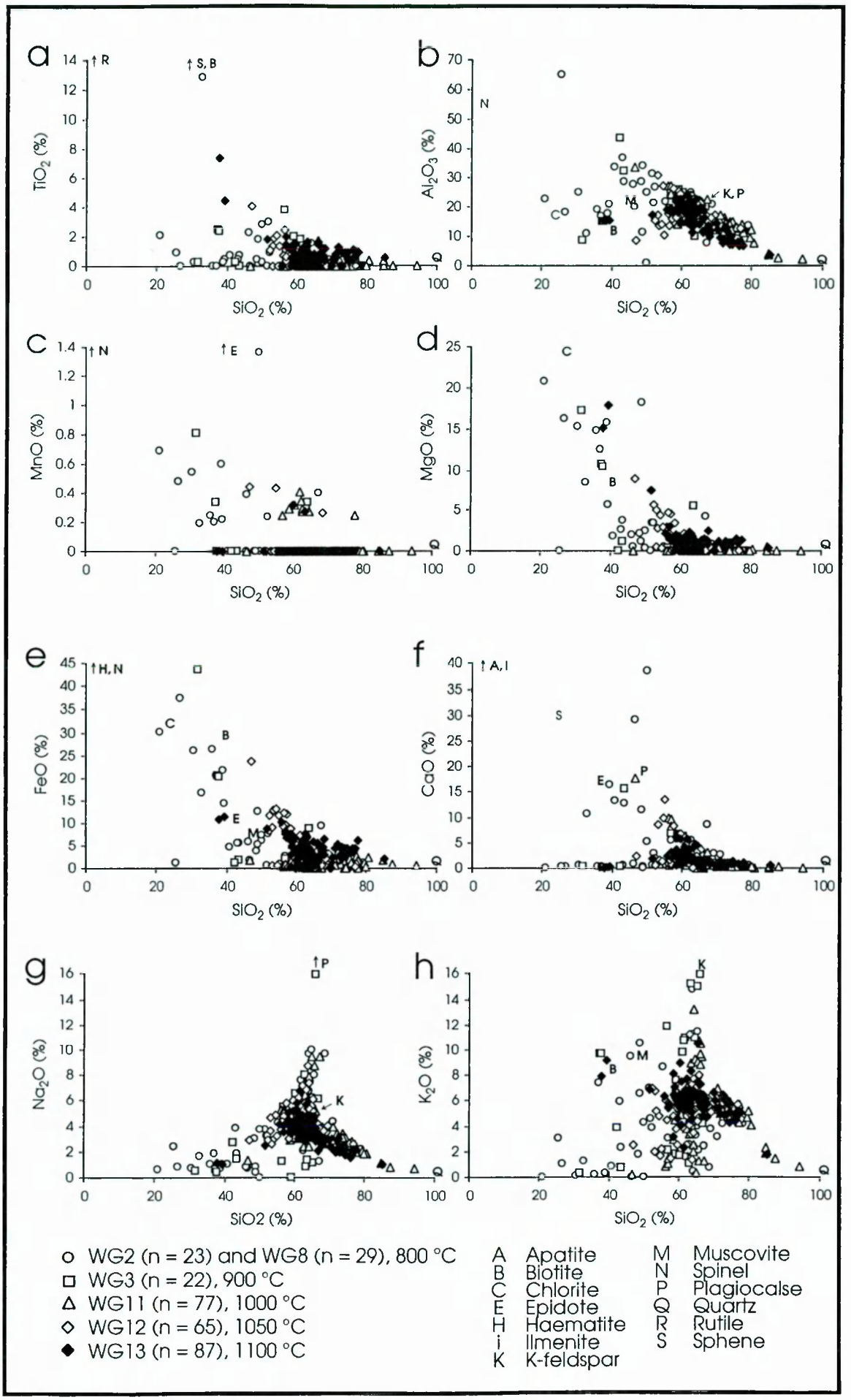
a
b
c
d
e
f
g
h
TiO2 (%)
Al2O3 (%)
MnO (%)
MgO (%)
FeO (%)
CaO (%)
Na2O (%)
K2O (%)
SiO2 (%)
SiO2 (%)
SiO2 (%)
SiO2 (%)
SiO2 (%)
SiO2 (%)
SiO2 (%)
SiO2 (%)
R
S, B
N
K, P
N
E
C
H, N
A, I
P
K
WG2 (n = 23) and WG8 (n = 29), 800 °C
WG3 (n = 22), 900 °C
WG11 (n = 77), 1000 °C
WG12 (n = 65), 1050 °C
WG13 (n = 87), 1100 °C
A Apatite
B Biotite
C Chlorite
E Epidote
H Haematite
i Ilmenite
K K-feldspar
M Muscovite
N Spinel
P Plagiocalse
Q Quartz
R Rutile
S Sphene

Figure 4.07: Harker plots of melt compositions. Letters on each plot indicate the composition of mineral phases contained in the starting material. A vertical arrow next to the letter representing a mineral indicates that these phases contain higher percentages of the oxide in question than displayed in the plot, such as rutile with 100 % TiO_2 in **a.)**. An inclined arrow, such as that next to K and P in **b.)** points to a true location of these two phases at the centre of melt analyses accumulation where it was impossible to locate the indicative mineral letter, without obscuring other data.

The same increase in oxide found in the previous examples with decreasing silica content is observed when plotting magnesium and iron oxide against silica (**Figure 4.07, d, e**). The general trends fall along the line on which the two magnesium containing phases in the starting material fall (chlorite and biotite). The 800 °C melts show the greatest spread in composition.

In the calcium Harker plot (**Figure 4.07, f**) melt analyses either show no appreciable calcium content, or show a tightly clustered trend towards plagioclase. Few show appreciable increases in calcium, these are dominated by the lowest temperature samples (800 °C) , trending towards epidote, sphene, ilmenite and apatite.

A more clearly defined relationship between the compositions of melt and different phases contained in the starting material is shown when plotting sodia against silica (**Figure 4.07, g**). While the majority of data cluster around the sodium/silica ratio of K-feldspar there are clear trends towards increased sodium/silica ratio of plagioclase and decreased sodia/silica ratio of quartz. A weak trend of decreasing sodium content with decreasing silica content can also be observed.

The Harker plot of potassium against silica (**Figure 4.07, h**) shows similar trends to sodium Harker plot (**Figure 4.07, g**) with compositions trending towards quartz and K-feldspar from the maximum density of analyses at around 7 % K_2O, 65 % SiO_2. Some melt analyses also trend towards the compositions of biotite and muscovite or show a decrease in potassium with decreasing silica towards the baseline.

In conclusion, the Harker plots show that melt compositions show no tight clustering of compositions, with limited increase in clustering toward a point of equilibrium composition with increasing temperature. Compositional trends can be explained by increased contributions of different minerals in the starting material to the melt. Melt compositions are also controlled by varying diffusional rates of elements and have not been homogenized.

Total alkalis versus silica plot

In order to further investigate melt compositions the analyses at different temperatures are plotted on a diagram of $Na_2O + K_2O$ versus SiO_2 (**Figure 4.08**).

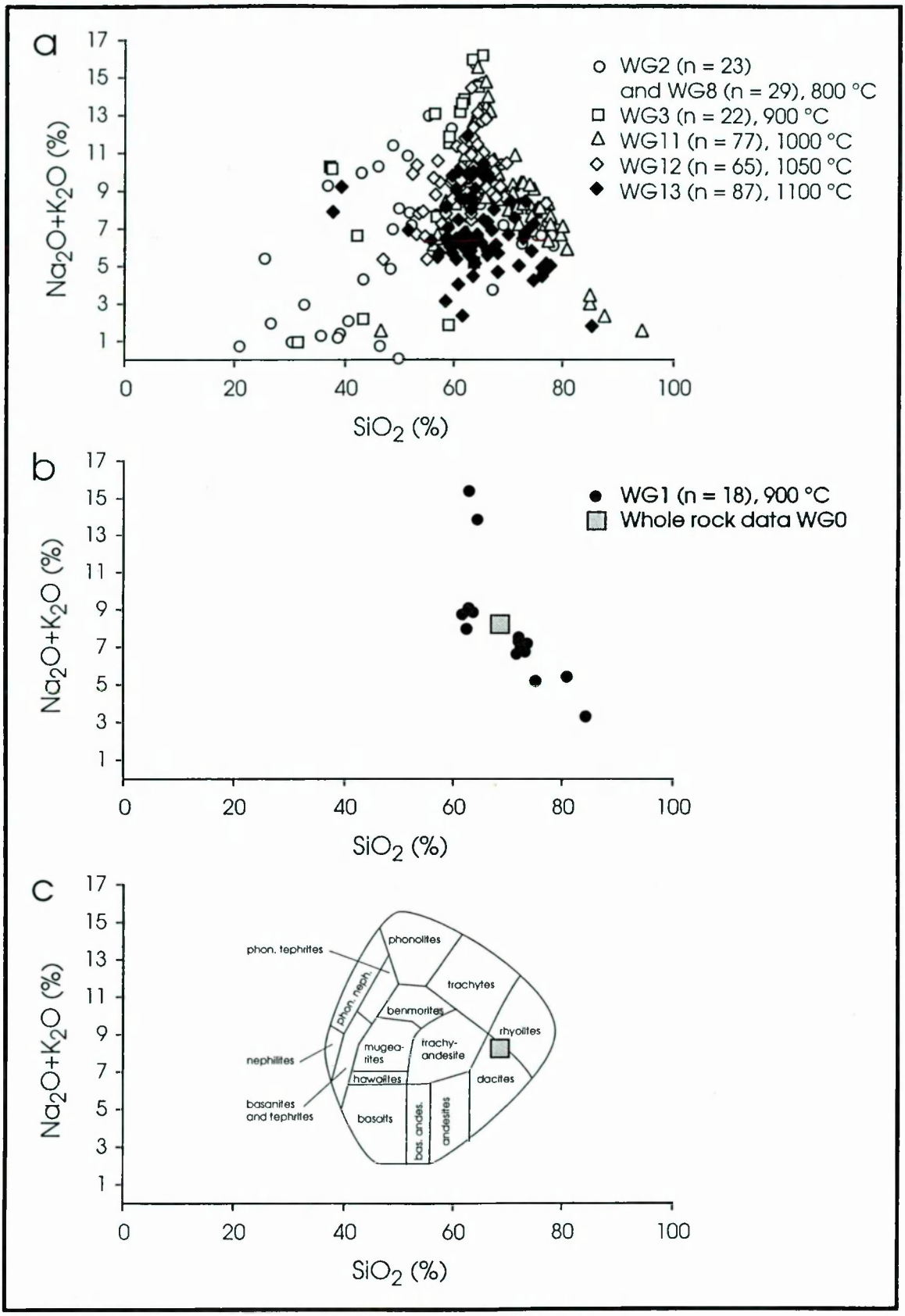

Figure 4.08: Total alkalis versus silica plot. **a.)** melt analyses at temperatures between 800 and 1100 °C; **b.)** melt analyses of powder experiment WG1, heated to 900 °C for 126 hours (filled circles) and Westerly granite whole rock data, results are discussed in **Chapter 4.3.3** (see Table 2.1 for analyses); **c.)** Compositional fields of common volcanic rocks (after Cox, Bell & Pankhurst 1979) with square indicating composition of Westerly granite.

Figure 4.08, a clearly indicates that no equilibrium composition was reached in any of the compositional charges heated to between 800 and 1100 °C. While there is a tighter cluster of analyses at the highest temperature (1100 °C) there is still a significant spread in composition. The compositional spread of the analysed melts is greater than that of volcanic rocks (**Figure 4.08, c**). Analyses show the greatest density towards more silica rich, acidic, compositions, which centres near or at the whole rock composition of Westerly granite (**Chapter 2**) at the boundary between rhyolites and dacites. This plot emphasises the degree of disequilibrium of melt at all temperatures.

Mineral-specific triangular plots of melt compositions

An attempt was also made to evaluate the influence of main constituents of Westerly granite, namely quartz, feldspars and mica, on melt compositions. In order to study compositional variation of the melt, compositions were plotted on a triangular plot using SiO_2, $CaO + Na_2O + K_2O$ and $MgO + FeO$ at the apexes to represent the three mineral groups respectively (**Figure 4.09**). The positions of feldspar end-members and biotite are also plotted for reference, as well as the composition of melt resulting from 10 % biotite breakdown to orthopyroxene plus melt (grey oval).

Melt compositions at 800 °C (**Figure 4.09, a**) fall on or near the feldspar base-line with some samples trending towards quartz. Some melts contain components from biotite, though no pure biotite melts were observed. This trend is also found in all higher temperatures, as well as an apparent increase in biotite and quartz influence on melt compositions.

Oxide percentages of melt were re-calculated in terms of norm composition, in order to further evaluate the influence of major crystalline phases on melt compositions. As melt compositions across the temperature range showed little compositional trends with increasing temperature it was felt that one sample could be chosen for analysis. The melt analyses data from WG11 (1000 °C) were chosen (**Figure 4.10**) as a large number of analyses were carried out on this sample and it contains all the main mineral phases.

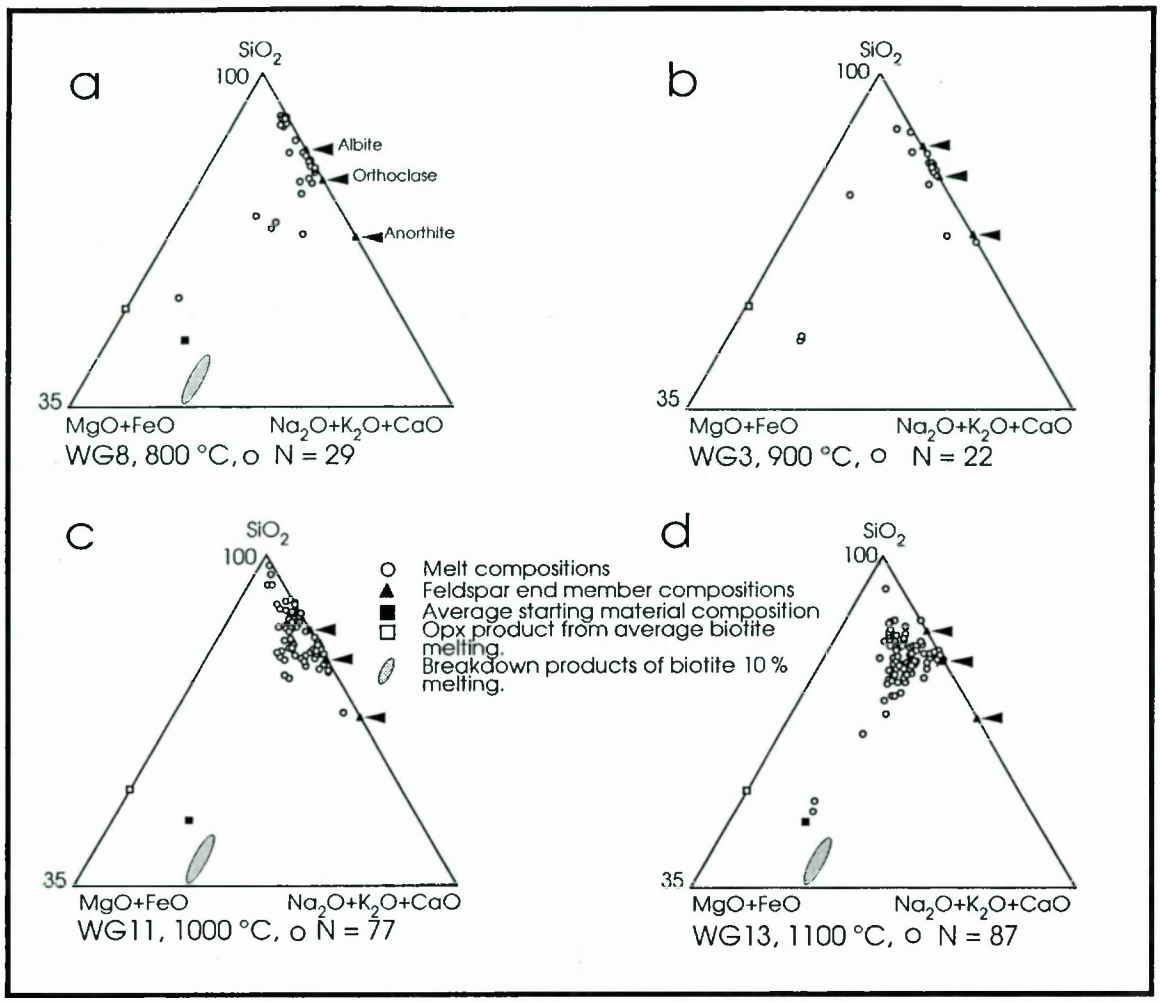

Figure 4.09: Oxide triangular plots of melt compositions determined by EDS spot analysis. Apexes were chosen to represent the three major phases. Quartz = SiO_2; biotite = MgO+FeO; feldspars = Na_2O+K_2O+CaO. Positions of feldspar end members fall along the base-line between SiO_2 and $Na_2O + K_2O + CaO$ and are highlighted by arrows, while biotite compositions are plotted as filled squares with open crossed squares representing biotite end-member compositions and the filled square marking the average biotite composition in the starting material. Open square marks position of orthopyroxene, which is the by-product of 10 % melting of biotite (grey oval).**a.)** 800 °C; **b.)** 900 °C; **c.)** 1000 °C; **d.)** 1100 °C.

Melt compositions on **Figure 4.10, a** either scatter near the feldspar base-line or show a tight mixing trend between average feldspar and quartz. **Figure 4.10, b** confirms the small influence of biotite on melt composition. Melt compositions near the average feldspars show the strongest influence by biotite. Melt compositions projected onto the feldspar plane (**Figure 4.10, c**) fall halfway between orthoclase and albite or are found to plot in the area of high temperature ternary feldspars.

Figure 4.10 (on following page): CIPW normative compositions of melts in sample WG11, 1100 °C, 27.2 % melt, n = 77. Black triangles and circles mark compositions of feldspars in the same sample, n = 21. **a.)** Quartz, albite and orthoclase diagram, indicating mixing trends between quartz and feldspar compositions. **b.)** Corundum, albite and orthoclase triplot, indicating mixing trends between biotite and feldspars, as muscovite and biotite are the only corundum normative minerals in the starting material. **c.)** Orthoclase, albite and anorthite triplot. Melt compositions are superimposed onto the standard feldspar compositional triangle.

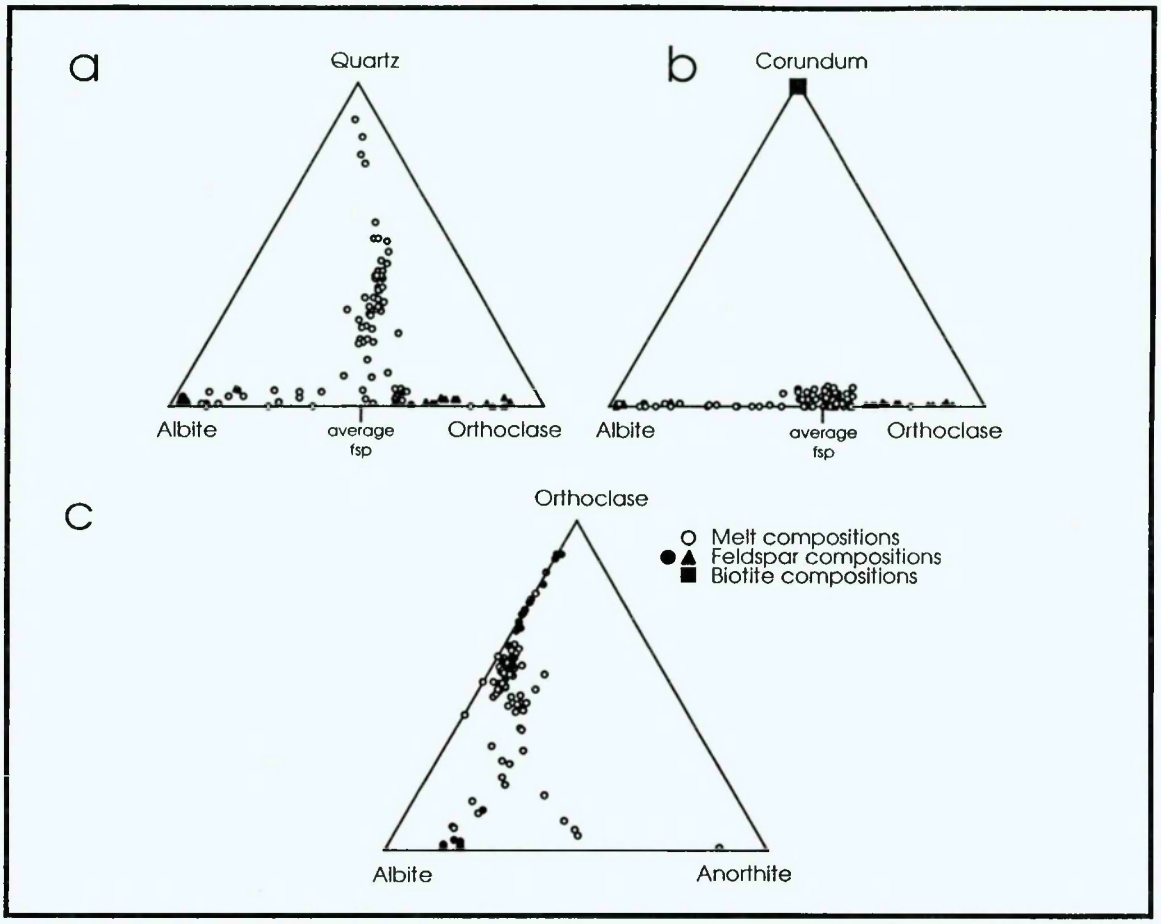

4.3.2 Spatial variation of melt composition with respect to adjacent phases

In this section the spatial variation in melt composition with distance to crystalline phases will be explored. For this purpose three BSEM images were chosen in which melt analyses were found to be sufficient in number to explore this problem. One image of WG11 and two from WG13 were chosen (**Figure 4.11**) and compositions plotted on mineral specific triplots adjacent to the BSEM photo, on which the points of analyses have been marked.

In **Figure 4.11, a** the composition of melt (e.g. **Table 4.04**) surrounded by K-feldspar, plagioclase and quartz is explored. Melt compositions (number 119, 128 and 125) fall on the feldspar baseline though are generally enriched in quartz relative to adjacent feldspars.

Melt analyses 119, 125 and 128 show compositions between quartz and feldspars (Figure 4.11, a), that agree with the location of these analyses between quartz, plagioclase and K-feldspar. In contrast to these, the analysis 124 shows a decrease in silica associated with an increase in alumina, calcia and sodia.

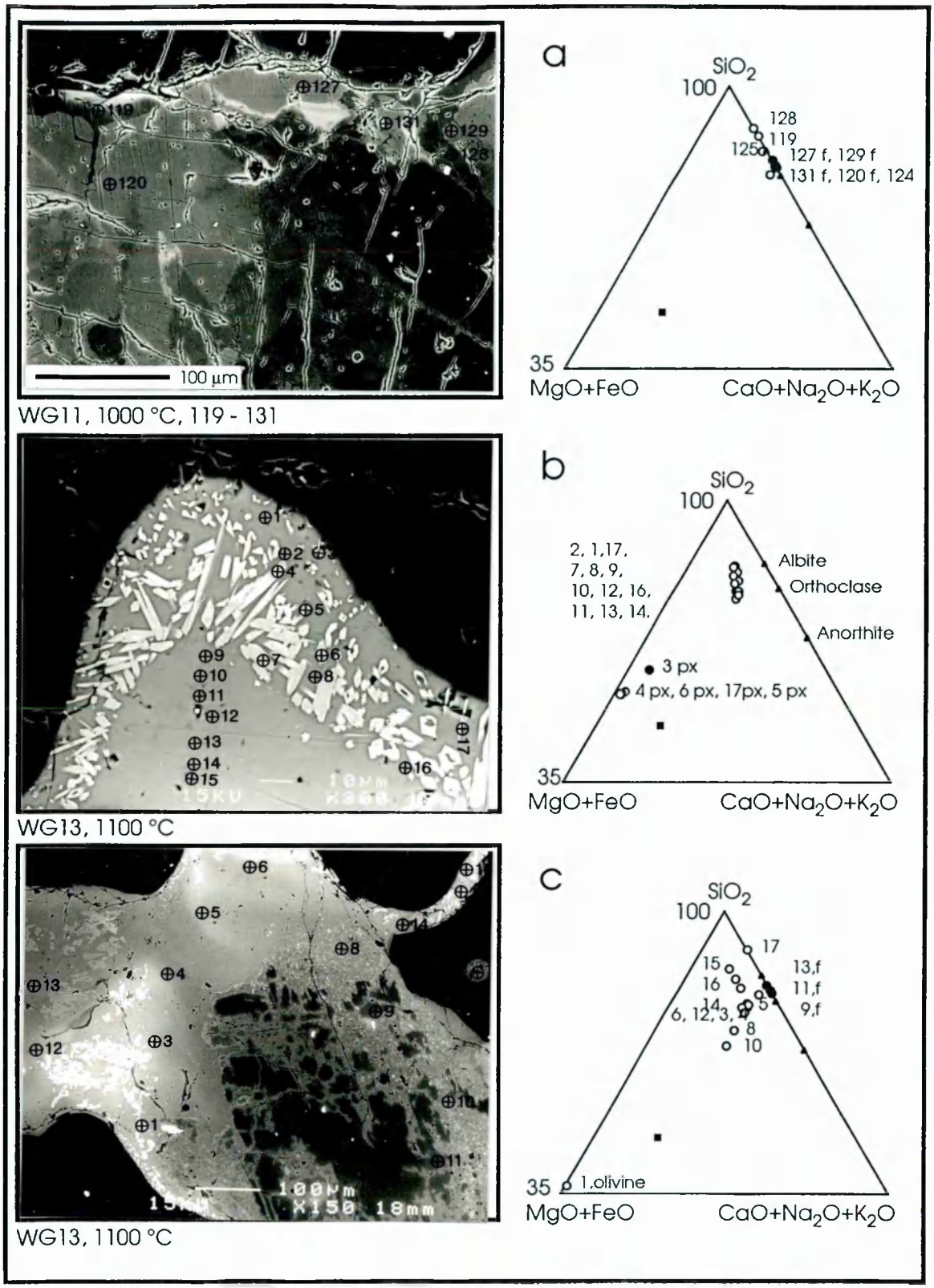

Figure 4.11: Spatial variation of melt and crystal compositions. Images on the left are BSEM images, where numbers mark sites of chemical analysis that are then displayed to the right of the photo on a triangular plot as open (melt) and closed (mineral) circles. Numbers on the plot correspond with those on the adjacent photo, ordered with decreasing SiO_2 content. Letters identify the mineral type (**f** = feldspar; **px** = pyroxene). Triangles mark feldspar end-member compositions and the filled square average biotite composition in WG0. Numbers which appear only on the BSEM image relate to analysis where no phase could be positively identified, or totals fell below 96 %.

	Min	SiO2	TiO2	Al2O3	FeO	MnO	MgO	CaO	Na2O	K2O	Total
119	XX	73.74	0	14.29	0	0	0	0.43	3.12	6.19	97.77
124	XX	64.3	0	21.76	0	0	0	3.08	7.77	2.54	99.45
125	XX	70.93	0	17.35	0.56	0	0.29	0.86	3.95	6.98	100.9
128	XX	74.21	0	12.16	0	0	0	0.27	2.18	5.51	94.34
120	FP	65.32	0	18.64	0	0	0	0.19	3.57	11.2	98.92
127	FP	66.05	0.3	19.16	0	0	0	0.27	3.45	11.58	100.8
129	FP	65.95	0.4	18.85	0	0	0	0	2.69	12.59	100.5
131	FP	65.81	0	18.92	0	0	0	0.43	4.51	9.79	99.46

Table 4.04: Compositions of melt and K-feldspar in sample WG11 with sampling localities indicated in **Figure 4.11, a**. *XX* indicates melt compositions, while *FP* identifies feldspar analyses.

Analysis 125 is the only melt composition hinting at some accessory phase influence with traces of iron and magnesium and increased alumina. Generally, melt analyses reflect the composition of partially melting crystals surrounding it.

In **Figure 4.11, b** the top half of the image is dominated by a quartz crystal, with melt and pyroxene crystals beneath. In this image the change in melt composition with distance from this quartz crystal in WG13 was explored, with analyses listed in **Table 4.05.**

Num.	Min	SiO2	TiO2	Al2O3	FeO	MnO	MgO	CaO	Na2O	K2O	Total
1	XX	73.68	0.92	7.51	4.29	0	0.96	0.95	2.15	4.9	95.35
17	XX	73.11	0.88	8.61	4.55	0	1.11	1.02	1.93	4.88	96.10
2	XX	74.64	0.92	8.37	4.50	0	1.04	1.02	2.20	5.06	97.75
7	XX	71.24	0.83	9.66	4.41	0	1.08	1.27	2.22	5.38	96.11
8	XX	67.06	0.93	11.69	4.72	0	1.42	1.43	2.11	4.84	94.23
12	XX	63.15	0.97	13.18	5.49	0	1.66	1.99	2.79	5.23	94.46
16	XX	63.03	1.34	13.17	5.47	0	1.70	2.09	3.08	5.65	95.53
15	XX	62.11	1.26	14.37	5.87	0	1.96	2.19	3.02	5.51	96.29
3	PX	58.42	0.27	2.38	16.38	0.31	17.54	2.42	0.73	0.97	99.41
4	PX	54.81	0	0.66	18.66	0.50	23.35	1.87	0	0	99.85
5	PX	53.40	0.35	0.52	19.53	0.47	22.46	1.06	0	0.15	97.93
6	PX	54.62	0.34	0.61	20.05	0.62	22.95	1.38	0	0	100.57
17	PX	54.29	0	0.73	19.31	0.46	23.57	1.27	0	0	99.63

Table 4.05: Compositions of melt and orthopyroxene in sample WG13 with sampling localities indicated in **Figure 4.11, b**. *XX* indicates melt compositions, while *PX* identifies pyroxene analyses. Melt analyses are sorted according to increasing distance from quartz crystal.

A steady decrease in silica content with distance from the quartz crystal was observed. Melt compositions show an increase in titanium, aluminium, iron, magnesium, calcium, sodium and potassium oxide closest to the contact with quartz whose fraction continues to increase with distance to the quartz crystal. The decrease in silica away from the partially molten crystal bears witness to slow diffusion of silica from the dissolving quartz crystal. The compositional trend of melt compositions with distance is not towards the composition of biotite in the starting material (**Figure 4.11, b**), but towards a possible mixed source influenced by both mica and feldspars. Light minerals that mantle the quartz contact are orthopyroxenes, formed as a reaction product of the melting process. The position of this pyroxene mantle indicates that the average

melt composition, away from the quartz crystals needs to be enriched in silica to allow the formation of pyroxenes.

Figure 4.11, c shows melt surrounding quartz and plagioclase remnants. The former site of a now completely melted biotite is indicated by the abundance of accessory phases, including olivine, clinopyroxene and apatite, in the bottom left hand corner of the picture. Oxide concentrations of analyses are listed in **Table 4.06**.

	Min	SiO2	TiO2	Al2O3	FeO	MnO	MgO	CaO	Na2O	K2O	Total
10.2	XX	64.11	0	19.16	3.72	0	1.23	1.2	4.35	6.72	100.49
10.3	XX	60.86	0	20.59	4.55	0	1.5	1.43	4.53	6.41	99.87
10.4	XX	59.98	0.47	19.98	3.84	0	1.21	1.46	4.38	6.31	97.63
10.5	XX	65.25	0	20.19	1.70	0	0.42	1.17	4.71	7.49	100.92
10.6	XX	61.67	0.47	18.73	3.54	0	1.14	1.51	4.28	6.56	97.9
10.7	XX	62.26	0.85	16.84	4.46	0	1.44	1.62	3.81	6.31	97.58
10.8	XX	58.44	0.56	19.04	7.66	0	1.81	0.50	4.18	8.09	100.27
10.10	XX	55.77	0	19.17	10.14	0	2.04	2.33	4.16	6.37	99.97
10.12	XX	61.21	0.94	18.40	4.57	0	1.38	1.35	4.99	6.21	99.04
10.14	XX	67.79	0.57	13.79	3.33	0	1.12	0.98	2.94	6.15	96.67
10.15	XX	76.54	0.56	7.03	3.76	0	1.13	0.41	1.76	4.66	95.84
10.16	XX	73.40	0.61	9.98	3.88	0	0.95	0.76	2.54	5.75	98.47
10.11	OL	37.90	0	0.50	31.09	0.34	33.86	0	0.57	0	104.26
10.9	FP	62.92	0	24.30	0	0	0	5.83	8.25	0.68	101.97
10.13	FP	64.87	0	23.01	0	0	0	3.94	9.10	0.30	101.21
10.14	FP	65.73	0.53	18.92	0	0	0	0.39	4.16	10.13	99.86

Table 4.06: Compositions of melt and minerals in sample WG13 with sampling localities indicated in **Figure 4.11, c**. *XX* indicates melt compositions, while *Ol* identifies olivine analyses and *FP* plagioclase analyses.

Two compositional trends can be suggested from the triplot associated with **Figure 4.11, c**. The first is marked by an increase in both silica and mafic components and, while the second trend is characterised by an decrease in silica, associated with an increase in iron and magnesium oxide. Analyses associated with the first trend are taken in the melt channel between two quartz crystals towards the top right hand corner of the image. The increase in silica can be explained by the proximity to partially molten quartz, while the increase in mafic content possibly relates to biotite that melted outside the image view. However, in this case one would have expected an elevated iron and magnesium contents in analyses 2, 3 and 12 that are adjacent to the large accumulation of accessory crystals that are thought to represent a former site of biotite. However, most of the accessory phases are found to be olivine, that would have quickly reduced the amount of both iron and magnesium in the surrounding melt on crystallization. Analyses associated with the second trend are located close to a partially molten plagioclase crystal. If melt surrounding this plagioclase crystal represents a mixture of predominantly biotite and feldspar components, then the lack of accessory crystallization might explain the elevated iron and magnesium content in points 8 and 10. The melt analyses in this image thus suggest that melt compositions are

controlled by a combination of partially melting minerals and crystallizing phases in close proximity to the spot analysed.

4.3.3 Powder experiment WG1 - attempt at producing an equilibrium melt composition.

As the melts in the previously examined samples have been demonstrated not to have homogeneous compositions at different temperatures, an attempt was made to determine an equilibrium chemical composition at 900 °C. For this purpose a sample of Westerly granite was crushed to a grain size equal to and below 20 µm by agate milling. The sample was then statically heated at 900 °C and 250 MPa for 129 hours. After quenching, a thin section was produced from the sample, followed by treatment identical to that for the other samples discussed in this chapter (polishing, carbon coating & EDS spot analysis).

Figure 4.12 shows the textures and melt compositions of this sample. Despite grain size reduction (from 960 µm in the starting material to 20 µm in WG1) there is still large chemical variation between different melt analyses when projecting analysis on a SiO_2 versus $CaO + Na_2O + K_2O$ and $MgO + FeO$ triangular plot.

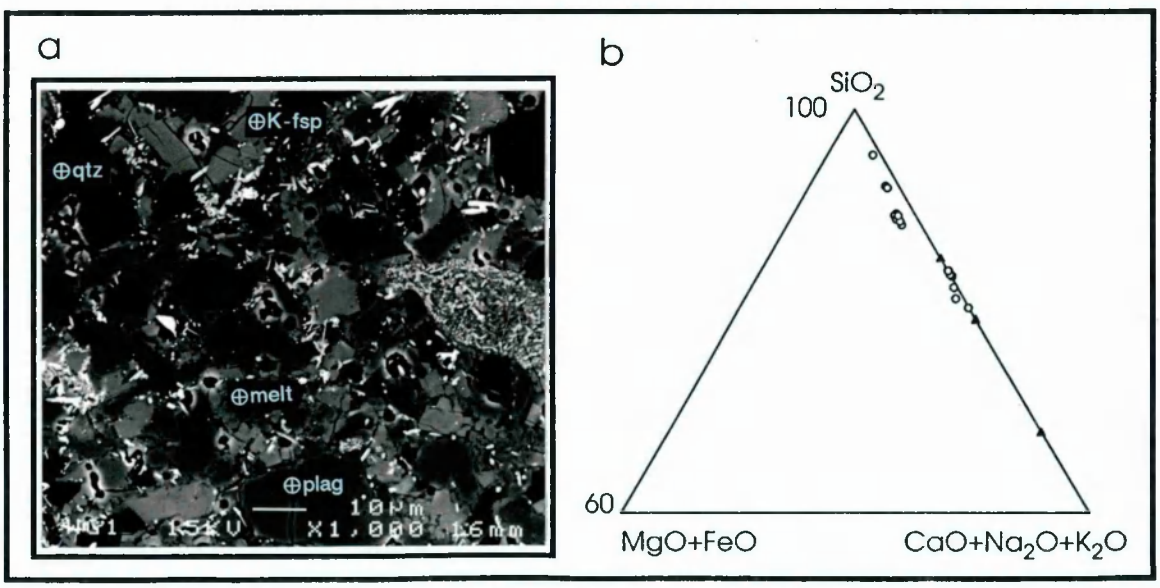

Figure 4.12: Microstructures and chemical analyses of melt of sample WG1 that was powdered, then heated to 900 °C for 129 hours in an attempt to produce a sample with equilibrium melt percentage and composition. **a.)** Texture of sample WG1; **b.)** mineral specific triplot of melt compositions with n = 15 (open circles). Closed triangles show the positions of feldspar end members.

While some melt compositions fall between those of the feldspar end members others show a preferential enrichment in both silica and magnesium plus iron (**Appendix 6**). The compositional trends of melt in sample WG1 are further explored in **Figure 4.08, b** in which total alkalis are plotted against silica. Again, compositions do not converge on a single point. However, more basic melt analyses in samples WG3 heated to the same temperature of 900 °C were not observed with most compositions falling into the rhyolite and dacite fields of volcanic rock nomenclature. Compositional variation indicates that 129 hours was insufficient to allow an equilibrium melt to be attained, both compositionally, and volumetrically (compare to **Chapter 3**), despite the fine grain size.

4.4 Interpretation of mineral and melt compositions in terms of partial melting processes

In all experimental charges heated to and above 800 °C melting of crystalline phases occurs. An increase in temperature not only results in a gain in melt fraction, but also changes the composition of some of the remnant primary phases, most notably in feldspars. Also, several crystalline phases are formed as by-products of melting reactions. As melting took place under disequilibrium conditions it was deemed impossible to draw up actual melting reactions. However, some general reaction paths can be hinted at, as individual melt compositions strongly reflect the compositions of minerals they are closest to. Following a discussion on compositional changes of remnant feldspars with increasing temperature the interrelationship between primary and secondary phases with respect to broad melting reactions is evaluated.

4.4.1 Interpretation of chemical variation of feldspars with increasing melt fraction

Over the melting interval the volume fraction of feldspars decreases and the composition of the remnant feldspar crystals changes. With increasing temperature and melt fraction the potassium content of K-feldspars and the sodium content of plagioclases are reduced (**Figure 4.01**). These changes are accompanied by an increased ternary character of the feldspars and can possibly be attributed to several factors that can work in isolation or conjunction:

1. In general, melting takes place from the edge of a crystal towards its centre except where the system is melting along grain-transecting cracks or at sites of plagioclase sericitization. If feldspar crystals are systematically zoned (for instance more albitic cores

for K-feldspars), then marginal melting of feldspar crystals will tend to reduce the compositional distribution.

2. Feldspars with different compositions have different melting temperatures, as the liquidus and solidus are inclined between the feldspar end-members. This will lead to preferential melting of feldspars with the lower solidus and liquidus. An inclined solidus between albite and anorthite (**Figure 4.13, a**) has been reported by Deer, Howie and Zussman (1966). This results in a preferential melting of plagioclases with a higher sodium content, leaving remnants of plagioclases with the most anorthitic character at the highest temperatures (1100 °C). This trend was observed in plagioclases, where only plagioclases with the highest anorthite content (of plagioclases in the starting material) are preserved at 1100 °C.

However, this method does not explain the preferential disappearance of potassium rich orthoclase, as the solidus is wing-shaped with an increase towards both orthoclase and albite with a minimum at around $Ab_{75}Or_{25}$ (Deer, Howie & Zussman 1966).

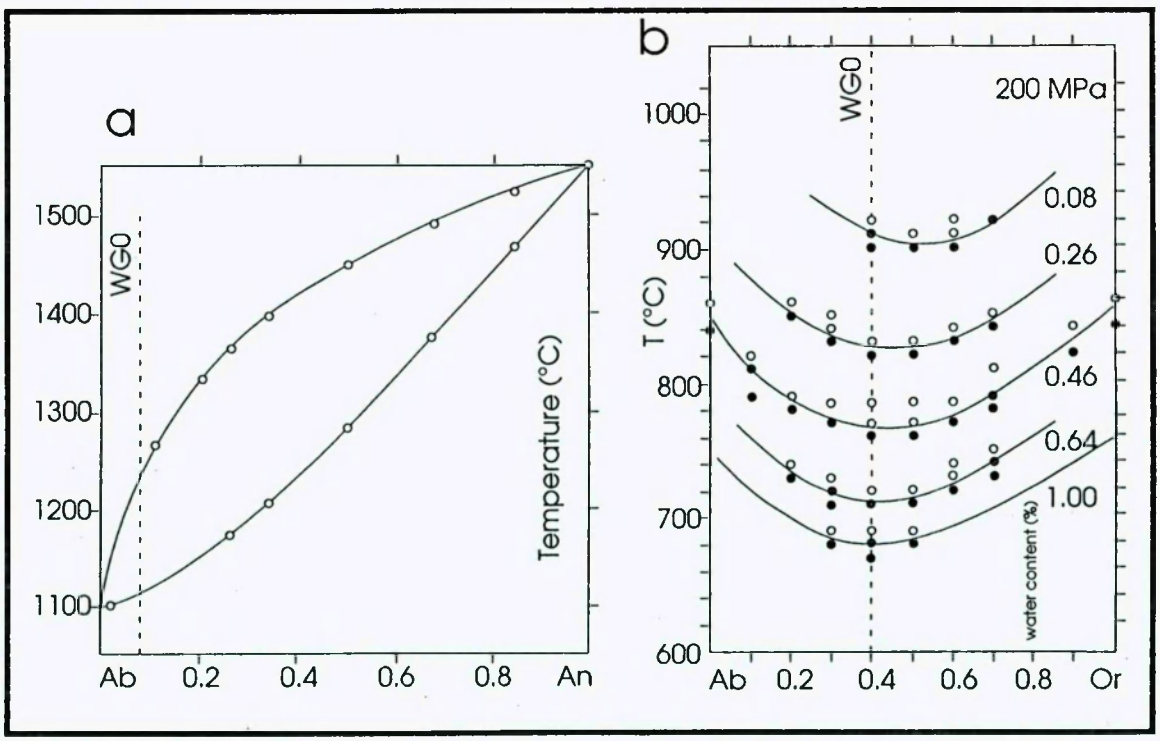

Figure 4.13: Change of remnant feldspar compositions on partial melting. Vertical dotted lines mark compositions of feldspars in starting material. **a.)** Change of plagioclase minerals on melting. Top curved line is the liquidus, the lower line is the solidus. With increasing melt fraction the remnant plagioclases are more anorthitic (after Deer, Howie & Zussman 1966); **b.)** Solidus between alkali feldspar end members. Curved lines mark solidii of coexisting vapour with different water contents (after Ebadi & Johannes 1991). Note that Ebadi and Johannes (1991) used a system with varying X_{CO2} fluid, rather than fluid absent.

3. As plagioclase, K-feldspar and quartz are the major constituents of the starting material (38, 29% and 29 % by volume respectively, **Table 2.2**), plagioclase / K-feldspar / quartz triple junctions are relatively common. The melting reaction is therefore expected to involve all three phases. Ebadi and Johannes (1991) (**Figure 4.13, b**) demonstrated that in such a system, the minimum temperature on the solidus will always occur with roughly equal molar proportions of albite and orthoclase, whatever the water content. Assuming that most melting occurs in the vicinity of the triple junctions described above, it is expected that approximately equal volumes of albite and orthoclase end members will be consumed during melting.

The average cation contents of feldspars in the starting material is K-feldspar = $Or_{93}Ab_{07}$ and plagioclase = $Ab_{90.3}An_{9.7}$. As there is 1.3 times more albite than orthoclase present in the starting material, there is an excess of the albite end member over the orthoclase end member. If melting continues to consume approximately equal proportions of both end-member feldspars, as suggested above, this would explain the survival of primary plagioclase crystals at higher temperatures than K-feldspar.

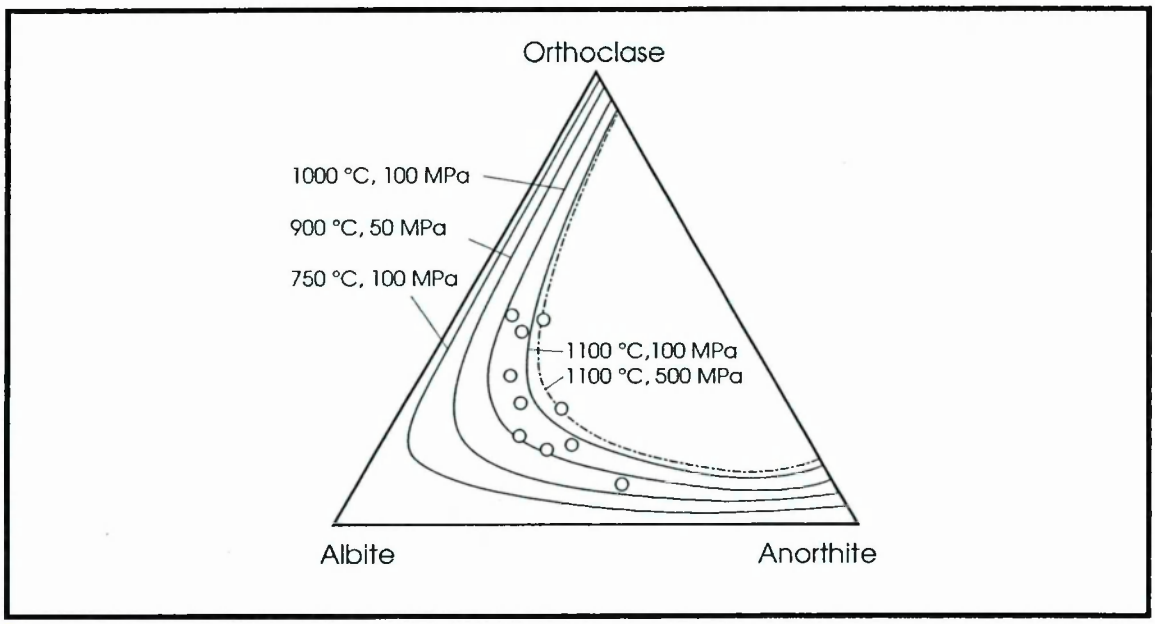

Figure 4.14: Feldspar compositional isotherms for ternary feldspars. Circles represent the compositions of some strongly ternary natural feldspars. After Deer, Howie & Zussman (1992), page 394.

4. The increase in ternary character of feldspars with increasing temperature can be explained by the increased freedom for cation substitution with increasing temperature (**Figure 4.14**) (Deer, Howie & Zussman 1992, p. 392). The proximity of feldspars belonging to the two solid-solution series and presence of melt containing all three cations might

allow some cation exchange to take place near crystal boundaries affected by partial melting.

Another explanation is that these readings do not refer to crystalline phases but come from melt compositions which have permeated into the dissolving feldspar crystals that maintain feldspar stoichiometry within the set limits (± 4 % of ideal stoichiometry, compare to **Appendix 4**).

4.4.2 Accessory phases - reactants and products to melting reactions

Accessory phase relationships are listed in **Table 4.07**. This table lists accessory minerals that are spatially linked to the *independent* minerals to the left of the table. The middle column lists accessory minerals found incorporates in the *independent* minerals in the starting material, while the right hand column lists accessory phases not found in the starting material, that are found at sites of partially or completely molten *independent* minerals at temperatures between 800 and 1100 °C. It seems likely that a combination of *independent* plus accessories are likely to be involved in a melting reaction which produces melt plus reaction products. However, while there are likely to be influences on the melt formed by other adjacent grains (e.g. it is impossible to obtain pyroxenes by merely reacting quartz with small amounts of epidote) the reaction products also change with temperature. The most obvious change in reaction product with temperature is the transition between garnet and olivine as products of biotite melting at temperatures around 950 °C. All other reaction products change with temperature are less marked and both products can be found in samples heated to temperatures spanning several hundred degrees Celsius, such as the change between spinel and ilmenite where there is an increase in volume ratio of spinel /ilmenite with increasing temperature, with ilmenite not found in samples above 1050 °C.

One aspect also illustrated by the variety and composition of crystalline reaction products is the disequilibrium conditions under which melting took place. It is highly unlikely that the olivine crystals detected have formed in a silica saturated system (Deer, Howie & Zussman 1966), as olivine of intermediate composition are unstable in this kind of setting. Sites where biotite melting took place are generally characterized by several accessory phases usually associated with more basic melts.

Independent	Alteration / Inclusion	Reaction product
Amphibole Apatite		
Biotite	Amphibole Apatite Chlorite Haematite Muscovite Rutile Spinel Zircon	Garnet Ilmenite Olivine Pyroxene Spinel Wollastonite
Haematite Ilmenite K-feldspar		
Plagioclase	Epidote Calcite Muscovite	Garnet
Quartz	Epidote	Pyroxene
Sphene Spinel		

Table 4.07: Inclusions and crystalline reaction products associated with independent crystalline phases found in the starting material WG0. Alteration products are minerals in the starting material that formed by the sub-solidus breakdown of the host, such as chlorite replacing biotite, whereas reaction products are crystalline by-products of a melting reaction, associated with or surrounding the site of the host.

4.4.2 Summary of compositional trends of melt

From the outset, Harker plots revealed the role of crystalline phases in influencing melt compositions. Compositional trends can in all cases (**Figure 4.7, 4.8**) be attributed to variable contributions from major and accessory phases. With increasing temperature the compositional spread decreases, but in no case was the melt composition reduced to a homogeneous composition. This disequilibrium in melt compositions is also confirmed when melt analyses of all temperatures are projected onto a total acid versus silica plot. Melt compositions fall in all field of volcanic rock types (after Cox, Bell & Pankhurst 1979). Spread of analyses decreases with increasing temperature, clustering near the projected point of Westerly granite whole rock data that falls on the boundary between the rhyolite and dacite compositional fields. Projection of analyses onto triangular plots with apexes chosen to represent the three major phase groups (SiO_2 = quartz; $CaO + Na_2O + K_2O$ = feldspars and $FeO + MgO$ = mica) showed melt compositions dominated by feldspar and quartz with only minor influence by mafic oxides. An overall melting reaction of Bt + Qtz + Plag +K-fsp = Melt + Gar / Opx / Spinel. In no case did melt phases reflect compositions expected from pure biotite breakdown (biotite $\rightarrow$ melt + orthopyroxene). Spatial melt analyses variation proved that melt compositions are strongly influenced by the crystals surrounding that are contributing to

the melt formation, as well as crystalline phases forming as a by-product of the melting reaction. Only localized equilibria are attained at best, with limited melt movement being insufficient to effect chemical homogenization of the melt. Grain size reduction in WG1 to 20 μm was insufficient to reduce diffusion distances to a degree where an equilibrium melt composition could be established in the time span at which the sample was kept at temperature (129 hours at 900 °C and 250 MPa). Data from WG1 agrees with the trends for melt compositions in other analysed samples between 800 and 1100 °C.

4.5 Melt re-crystallization products

Three samples were initially heated to between 1100 and 1200 °C, followed by a temperature drop to between 850 and 1027 °C where the samples were held for several hours prior to quenching (**Table 3.3, Chapter 3.3.5**). This process led to partial neo-crystallization of the melt phase. The lower temperature test WG18 (heated to 1100 °C, prior to deformation between 900 and 1027 °C), shows crystallization of both feldspars and biotite (**Figure 4.15**), while the higher temperature samples WG21 and WG22 only displayed extensive feldspar crystallization. The compositions of biotite neo-crysts in WG18 are first compared to compositions of biotite in the starting material, followed by an investigation of feldspar compositions in sample WG21.

4.5.1 Biotite neo-crystallization in WG18

Biotite crystals with an average diameter of around 20 μm were found to have crystallized in the melt of WG18 in close association with olivine, sphene and apatite, as well as feldspars (which were not analyzed) (**Figure 4.15**). Analyses of biotites in the starting material and neo-biotites in WG18 are displayed in **Table 4.08**.

Compared to biotites in the starting material (WG0) the newly crystallized biotites in WG18 are enriched in calcia and sodia but reduced in potassia content. The neo-crysts have somewhat higher annite/siderophyllite and phlogopite/annite ratios than in the starting material (**Figure 4.15, b**). This indicates that the biotite crystals in WG18 may have formed at lower temperatures than those in the starting material (Deer, Howie & Zussman 1966). This compositional shift of WG18 with respect to WG0 contrasts sharply with the development of biotite compositions in the samples analysed previously (**Figure 4.3**) where biotite compositions remained close to that in the starting material with a slight decrease in annite/siderophyllite ratio. The larger spread in compositions is

also confirmed in the aluminium versus iron and magnesium triangular plot (compare **Figure 4.3** with **Figure 4.15**).

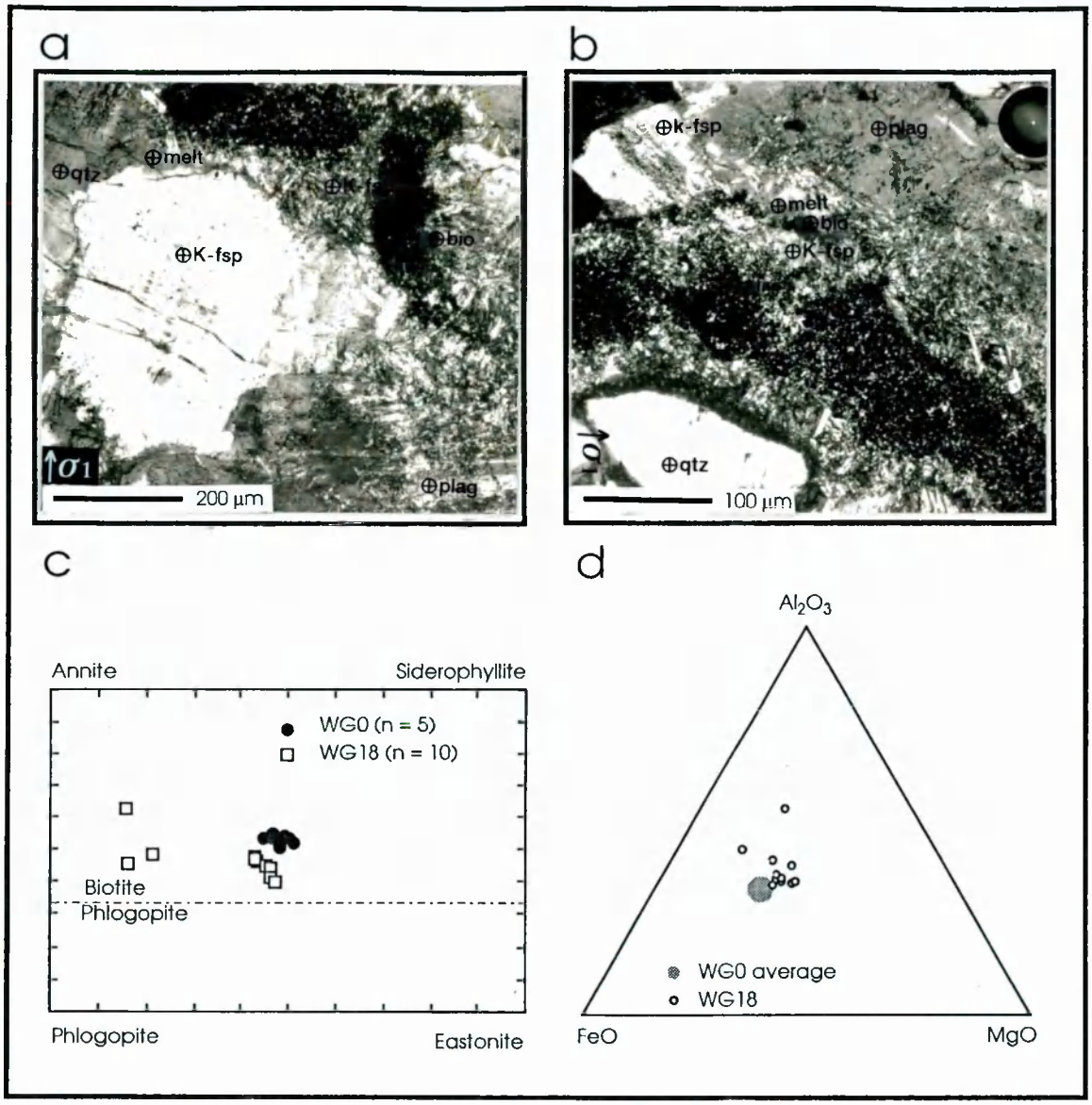

Figure 4.15: Neo-crystallization of biotite and feldspars in WG18, due to sample being kept at temperatures between 900 and 1027 °C after initial heating to 1100 °C. **a.), b.)** optical thin section photos of WG18, where **b)** gives an enlargement on **a.). c.)** plot of biotite analyses from WG0 (filled circles) and WG18 (open squares) on phlogopite-biotite compositional field. Plot after Deer, Howie & Zussman (1966). **d.)** composition of neo-biotite crystals (open circles) with respect to aluminium, iron and magnesium. The large shaded circle represents average biotite in WG0.

	Min	SiO2	TiO2	Al2O3	FeO	MnO	MgO	CaO	Na_2O	K_2O	Total
WG0											
25	BI	38.4	2.33	15.1	20.1	0	11.1	0	0.39	9.57	97
26	BI	37.2	2.49	14.8	20.7	0	10.1	0	0	9.78	95
40	BI	38	2.68	14.6	20.3	0.33	10.1	0.19	0.42	9.71	96.3
41	BI	37.2	2.83	14.5	20.7	0.36	10.3	0	0.51	9.84	96.3
45	BI	37.2	2.98	14.9	20.1	0.3	10	0	0.38	9.67	95.6
46	BI	37	2.94	14.4	20.9	0.23	9.89	0	0.7	9.82	95.9
50	BI	37.8	3.2	15.2	19.6	0	10.3	0.13	0.39	9.48	96.1
72	BI	37.3	2.27	14.7	20.4	0.33	10.2	0	0	9.86	95
average		37.5	2.72	14.8	20.4	0.19	10.2	0.04	0.35	9.72	91.5
		40.96	2.97	16.17	22.9	0.21	11.1	0.04	0.38	10.6	100.0
WG18											
10	BI	46.4	1.86	14.5	7.79	0	5.28	4.47	2.89	5.98	91.8
11	BI	50	0.31	15.6	15.8	0.43	5.44	2.7	4.36	2.74	97.7
13	BI	35.7	1.02	13.5	15.3	0	10.1	0.58	0.94	7.75	84.9
14	BI	37.1	4.78	14.3	16.2	0	11.4	0.38	1.09	8.53	93.8
17	BI	35.2	2.78	13.7	14.8	0	10.5	1.1	1.11	8.14	88
18	BI	35.7	5.27	13.5	16.8	0	10.5	0	0.99	8.3	91.2
19	BI	39.4	5.58	15.3	13.9	0	11.2	0.53	1.89	7.96	95.7
21	BI	39.1	2.2	14.1	15.3	0	12.7	1.56	1.24	8.72	96
22	BI	37.1	5.82	14.5	14.9	0	13	0	1.07	8.34	94.7
23	BI	37.1	6.26	14	15.2	0	9.9	0.42	1.03	7.75	91.7
24	BI	45.8	2.79	14.8	14.1	0	8.62	0.29	1.96	7.71	96
average		39.9	3.51	14.3	14.5	0.04	9.88	1.09	1.69	7.45	92.9
		43.0	3.75	15.4	15.6	0.04	10.6	1.17	1.82	8.02	100.0

Table 4.08: Analyses of biotites in WG0 and neo-crystallized biotite in WG18.

4.5.2 Feldspar neo-crystallization in WG21

In contrast to WG18, the neo-crystallization in samples initially heated to 1200 °C (WG21 and WG22) was restricted to feldspars (**Figure 3.9**). In **Figure 4.13** the compositions of neo-feldspars and adjacent melt have been plotted, with analyses listed in **Table 4.09**.

There is little compositional variation between newly crystallized feldspars and the melt surrounding (**Figure 4.13**). A decrease in silica is associated with a slight rise in calcia, sodia and potassia in the neo-crystallized feldspars (**Table 4.09**). However, the most marked difference between neo-crystallized feldspars and melt is the ten fold increase in titania and lack of iron oxide in the feldspars. The small compositional variation in major oxides (silica, alumina, calcia, sodia and potassia) between feldspars and melt is confirmed by the low contrast between the two phases on BSEM images (**Figure 3.9**). Feldspar compositional zoning is indicated by the striped appearance of feldspars (**Figure 3.9, b**). The composition of K-feldspars crystallized (**Figure 4.16, a**) contain roughly equal proportions of sodium and potassium.

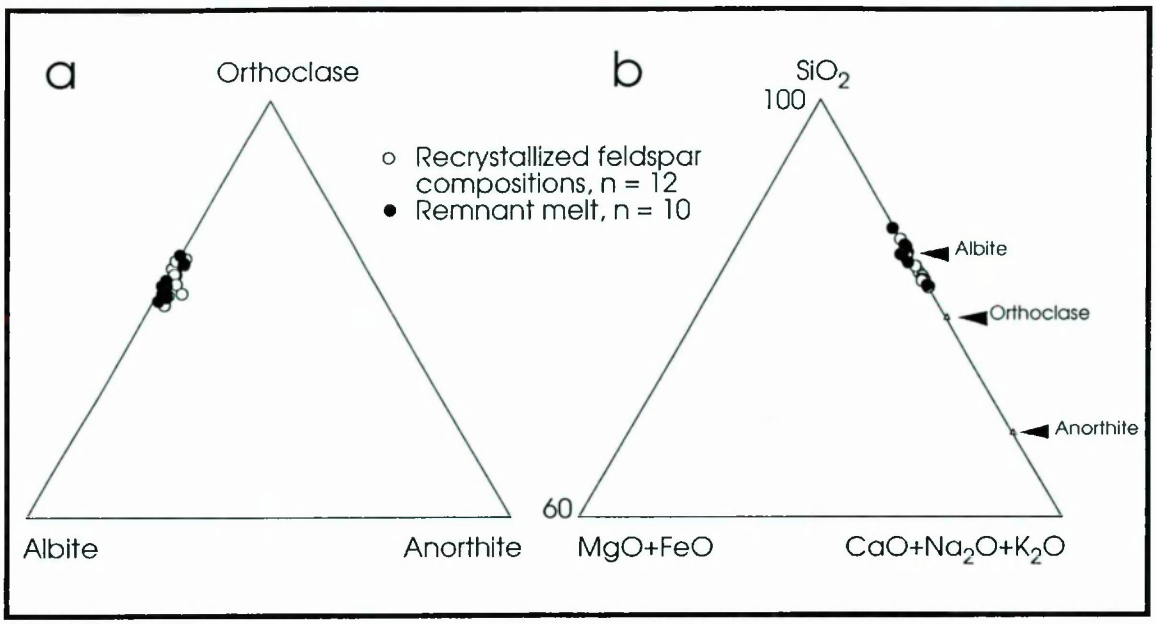

Figure 4.16: Compositional variation of neo-crystallized feldspars and remaining melt in WG21. Neo-feldspars are given an open circle symbol, while analyses of melt surrounding the feldspars are given a filled circle symbol. **a.)** compositions of melt and neo-feldspars are projected onto the feldspar plane; **b.)** compositions of melt and crystals with respect to major phases present in the starting material.

	Min	SiO_2	TiO_2	Al_2O3	FeO	MnO	MgO	CaO	Na_2O	K_2O	Total
4	XX	65.4	0	16	0	0	0	0.12	3.5	6.93	92
8	XX	62.8	0	16.3	0	0	0	0	3.5	7.16	89.8
9	XX	64.7	0	16.8	0	0	0	0.21	2.51	6.19	90.4
11	XX	64.9	0	16.1	0.58	0	0	0.2	3.66	6.74	92.2
12	XX	63.1	0.47	17.5	0	0	0	0	3.72	9.73	94.5
13	XX	63.3	0	16.9	0.31	0	0	0.32	3.78	6.84	91.5
15	XX	63.1	0	16.8	0.28	0	0	0.29	3.72	6.78	91
16	XX	64.7	0	16.3	0	0	0	0	3.64	6.97	91.6
18	XX	63.1	0	16.9	0.29	0	0	0.18	3.72	6.94	91.1
22	XX	63.3	0	16.7	0.33	0	0	0.16	4.07	6.93	91.4
average		63.8	0.05	16.6	0.18	0	0	0.15	3.58	7.12	91.5
		69.7	0.05	18.1	0.20	0	0	0.16	3.91	7.78	100.0
1	FP	62.5	1.08	17.5	0	0	0	0	3.71	8.49	93.3
2	FP	63.1	0.63	17.6	0	0	0	0	3.84	9.37	94.5
3	FP	62.6	0.86	17.8	0	0	0	0.3	3.51	9.23	94.2
5	FP	63	0	17	0	0	0	0.36	4	7.45	91.8
6	FP	63.7	0	17.9	0	0	0	0.29	4.19	9.39	95.5
7	FP	59.6	1.1	18	0	0	0	0.82	4.02	8.05	91.5
10	FP	63.6	0	14.8	0	0	0	0.15	3.4	6.2	88.2
14	FP	63.4	0.41	17.7	0	0	0	0.18	4.03	8.83	94.6
17	FP	63.5	0.48	17.9	0	0	0	0.28	3.86	9.64	95.6
19	FP	63.4	0.67	17.9	0	0	0	0.39	4.41	8	94.8
20	FP	63.6	0.27	18.2	0	0	0	0.47	4.61	7.87	95.1
24	FP	63.6	0.64	18.1	0	0	0	0.22	4.48	8.39	95.5
average		63.0	0.51	17.5	0	0	0	0.29	4.01	8.41	93.8
		67.2	0.54	18.7	0	0	0	0.31	4.27	9.00	100.0

Table 4.09: Compositions of neo-crystallized feldspars and surrounding melt in WG21. *XX* identifies melt analyses, while *FP* relates to feldspar analyses.

4.5.3 Interpretation of neo-crystallization

Neo-crystallization of the melt phase in samples WG18 and WG21 took place under disequilibrium conditions. Crystallization was rapid, as indicated by zoning in feldspars in WG21 and the small size of biotites in WG18. Biotite compositions also suggest lower crystallization temperatures than those at which biotites in the starting material crystallized. Neo-feldspars in WG21 with roughly equal proportions of sodium and potassium cations correspond with the minimum in the K-feldspar solidus curve displayed in **Figure 4.13, b**.

4.6 Summary and Conclusion

At temperatures 800 °C and higher melting of Westerly granite took place in the experimental charges studied. Partial melting not only results in the production of melt but leads to chemical changes in the remnant crystalline phases and the creation of accessory phases that form crystalline by-products of melting reactions.

K-feldspars increase their albite content with increasing temperature until complete melting commences at temperatures above 1050 °C (**Chapter 4.2.1**), associated with an increase in anorthitic character in plagioclase that are still found in the highest temperature run analysed at 1100 °C. These compositional trends can be explained by several different processes working in isolation or conjunction. **1.)**A differences in chemical compositions between rims and cores of minerals will result in a gradational change of composition as the rims become molten. **2.)** An inclined solidus between feldspar end-members will result in preferential dissolution of feldspars with compositions closer to the end-member with the lower melting temperature (**Chapter 4.4.1**). **3.)** An overall increase in ternary character of feldspar compositions with increasing temperature can be explained by an increase in freedom for feldspar compositions at elevated temperatures (Deer, Howie & Zussman 1966). **4.)** The preferential dissolution of K-feldspar can be explained if the melting reaction involves both feldspar groups, whereupon the minimum in the solidus falls at a point where sub-equal proportions of orthoclase and albite are present. As K-feldspars fill a smaller volume fraction of the starting material when compared to plagioclase, K-feldspar volume is reduced more rapidly (**Chapter 4.4.1**).

Quartz crystals show no compositional change, but belts of pyroxene crystals mantle quartz contacts to melt at temperatures in excess of 1000 °C (**Chapter 4.2.2**).

With increasing temperature the siderophyllite to annite ratio of biotite rises until complete melting commences at temperatures in excess of 1050 °C (**Chapter 4.2.3**).

Melting takes place parallel to cleavage and is associated with the production of several different accessory phases (garnet, ilmenite, olivine, pyroxene, spinel and wollastonite). Transitions between crystalline by-products with temperature can be observed. There is a sharp transition from garnet to olivine between 900 and 1000 °C (**Chapter 4.2.4**) and a gradational transition towards orthopyroxene from clinopyroxene over the temperature interval of 800 to 1050 °C (**Chapter 4.2.4**).

Melt compositions generally reflect the compositions of partially melting crystalline phases and minerals forming as a by-product of the melting reaction (**Chapter 4.3.2**). The majority of melt analysis cluster around the composition of whole rock Westerly granite (**Chapter 4.3.1**). However, melt compositions show a large compositional spread in oxide content in all samples heated to between 800 and 1100 °C. In no case, including the powder test WG1, were melts in chemical equilibrium produced.

Neo-crystallization of melt in samples WG18 and WG21 (**Chapter 4.5**) resulted in biotite and feldspar nucleation. Biotite and feldspars crystallized in the lower temperature sample WG18 (initially heated to 1100 °C), with biotite compositions indicating a lower temperature of nucleation than those found in the starting material. Only K- feldspars crystallized in WG21 (heated to 1200 °C). Compositions of both melt and feldspars in WG21 plot near the solidus minimum between orthoclase and albite compositions (in the quartz-orthoclase-albite system (Ebadi & Johannes 1991) (**Figure 4.13, b**). Rapid crystallization is suggested by zoning of feldspars on WG21 and small crystal sizes of biotites in WG18.

In conclusion, partial melting of the rock took place under disequilibrium conditions in all tests (including WG1) and generated a large number of different accessory phases as crystalline melting by-products. Only local melt - mineral equilibria were attained at best, and limited melt movement and chemical diffusion were insufficient to affect homogenization during the time interval where the rock was partially molten.

Chapter 5

Stress-strain and stress relaxation data

5.1 Introduction

In this chapter the mechanical output from stress-strain and stress relaxation tests are presented and discussed, along with information on the macroscopic deformation behaviour of the samples.

Cylindrical samples of Westerly granite (20 mm length and 9.5 mm diameter) were deformed in the PATERSON gas rig (see **Appendix 1** for test procedures and machine descriptions and **Appendix 2** for data processing) at temperatures between 800 and 1100 °C and a constant confining pressure of 250 MPa. Applied strain rates ranged between $2 * 10^{-7}$ s^{-1} to $3 * 10^{-4}$ s^{-1}, with maximum strains varying between 8.4 and 57.4 %. Experiments lasted between 2.5 and 171 hours. The deformation histories of deformed samples are listed in **Table 5.01** (compare also to **Appendix 10** for detailed mechanical data for individual tests).

Stress and strain on the sample were recorded during constant uniaxial compression. This was followed by a stress relaxation cycle where the specimen was allowed to relax at approximately constant strain with stress and strain rate measured and calculated. Finally the samples were quenched at a rate of 100 °C per minute to preserve microstructures induced during uniaxial compression (these are described in **Chapter 7**).

The general trends in stress-strain tests with varying strain rate, temperature and melt fraction are studied. The influences of temperature and melt fraction on the maximum supported stress by the samples are discussed in **Chapter 5.2**. Stress relaxation curves are studied to evaluate their dependence on strain and melt fraction (**Chapter 5.3**). This is followed by a discussion of the inter-relationship between stress-strain and stress relaxation data for samples deformed under similar conditions (temperature and strain rate). The assumption that stress relaxation data can be used to evaluate slow strain rate stress-strain behaviour is tested and conclusions are drawn towards deformation characteristics in the three dimensional field of stress - strain - strain rate, at different melt fractions (**Chapter 5.4**). The evolution of macroscopic deformation behaviour with temperature are discussed in **Chapter 5.5** (for microstructures see **Chapter 7**).

	T (°C)	σ_{max} (MPa)	ε_{max} (%)	$\dot{\varepsilon}$ (%)	ss/sr Nº	t to def (h)	t total (h)	melt ϕ (fract)	fault (°)
WG2	800	487.15	9.41	8E-05	1	2	2.4	0.053	44
WG3	900	196.95	14.07	8E-05	1	2	2.5	0.073	35, 37
WG4	1000	36.79	12.25	8E-05	1	2	2.5	0.203	78, 81
WG5	950	105.17	13.77	8E-05	1	2	3	0.144	90, 49
WG6	850	518.86	8.44	8E-05	1	2	2.5	0.044	45, 47
WG7	800	372.63	8.82	8E-05	1	2	4	0.033	37, 41
WG8	800	343.4	14.3	8E-05	1	90	96	0.035	37, 40, 44
WG9	900	63.63	16.62	8E-05	1	46	46.5	0.120	39, 42
WG10	900	153.58	15.26	8E-05	1	94	96	0.131	52
WG11	1000	58.13	13.23	8E-05	1	69.5	71	0.271	53
WG12	1050	20.75	32.63	8E-05	1	2.5	4	0.335	none
WG13	1100	2.81	30.13	8E-05	1	2.5	4	0.477	none
WG16	900	181.68	22.6	8E-05	3	3.5	17.5	0.135	42, 63
WG17	900	119.94	17.36	2E-6	1	0	52.4	0.179	90, 90, 90
WG18	1100	0.48		8E-04	1	3.25			
	1027	4.61		1E-05	2	3.5			
	946	82.83		2E-04	1	4.5			
	896	176.04		1E-04	1	5.5			
	946	104.09	24.51	8E-04	1	24.5	25	M .25/.47	46, 51
WG20	900	102.78		2E-07	1	0.75			
	900	139.19	13.36	8E-05	1	166	171	0.168	none
WG21	1200⇓900	30	creep	2E-07	1	18.0			
	850	30	creep	6E-08	1	20.0			
	900	30	creep	2E-07	1	23.5			
	953	30	creep	5E-06	1	42.0	47.75	M .16/.62	62
WG23	1000	194.22	24.52	8E-05	1	2	3.25	0.103	50
WG26	1000	14.08		2E-07	1				
	1000	26.28		9E-06	1				
	1000	14.08	14.77	4E-04	1	26.5	124.75	0.435	none
WG27	950	243.42	24.95	1E-04	1	4	8.5	0.076	45
WG28	900	114.98	*42.14	*4E-05	5	2	51	0.155	37
WG29	1000	41.42	*45.57	*6E-05	5	3	44.75	0.257	none
WG30	1000	12.98		*2E-07		1			
	1000	39.46	*57.40	*3E-04	2	166.5	168	0.313	38

Table 5.01: Test histories of deformed samples. ss/sr Nº lists the number of stress-strain-stress relaxation cycles the sample underwent under the foregoing conditions. The macroscopic fault angle with respect to σ_1 is listed in the right hand column. The starred (*) samples WG28 to WG30 suffered a 50 °C temperature profile across the sample, hence only half the specimen was deformed in each case, thus explaining the very high strains (ε_{max}). WG21 was deformed at constant stress creep conditions at 30 MPa. Results from stress-strain data of WG21 are described in **Chapter 6.2.2.** See **Table 3.01** for static test histories.

5.2 Stress-strain behaviour

The influence of strain rate, strain, temperature, melt fraction and strain history on the stress-strain behaviour of samples are explored in this section.

5.2.1 General shapes of stress-strain curves

With increasing applied strain the stress supported by the sample rises in an approximately linear fashion until the *yield point* is encountered (at ε_Y and σ_Y in **Figure 5.01**). With further increase in stress the deformation behaviour departs from linear elastic, with a slowing increase in stress with strain until a maximum stress value has been attained and the stress-strain curve turned horizontal (at ε_U and σ_{max} in **Figure 5.01**). This point is called the *ultimate strength* at which the sample changes in behaviour from strain hardening to strain weakening. This is usually associated with the localization of a macroscopic fault in low temperature samples (compare with section on macroscopic behaviour, **Chapter 5.5**).

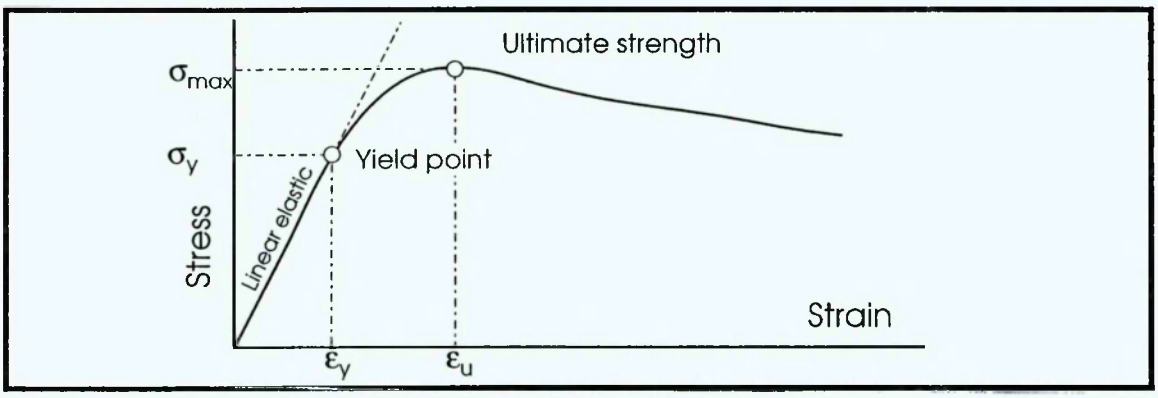

Figure 5.01: Basic shape of stress-strain curves on which the position of the yield point and the ultimate strength of the sample have been highlighted.

Prior to reaching the yield point the sample is elastically deformed. Beyond this point the sample will deform plastically with increasing stress. Whereas active deformation and localization of fractures happen in the rising part of the stress-strain curve, the deformation of the sample is characterized by sliding along pre-existing dislocations in the strain weakening part of the curve, after the ultimate strength of the rock has been exceeded.

5.2.2 Samples deformed at near identical conditions - the effect of material heterogeneities on sample behaviour

This section considers a suite of fifteen isothermal experiments in which samples were deformed at a strain rate of $8 * 10^{-5}$ s^{-1} at temperatures between 800 and 1100 °C (**Table 5.01**). At temperatures of 800, 900 and 1000 °C several samples were deformed at the same strain rate and temperature, thus at near identical conditions. These give

information on the reproducibility of tests and allow an error bar to be established, which reflects the material variability (for errors due to experimental and measuring uncertainties see **Appendix 2**).

Of the three samples deformed at 800 °C (WG2, WG7, WG8) (**Figure 5.02, a**), the strongest (WG2) showed a steep increase in stress with increasing strain until σ_{max} was attained. The stress then dropped rapidly with increasing strain. WG7 displays medium strength at low strains with stress dropping slowly with increasing strain. The weakest test at low strains (WG8) had no pronounced peak stress, but displayed a very smooth and gradual increase in stress with increasing strain that finally flattened out to constant stress with increasing strain. The ultimate strength of samples varied not only in value of σ_{max}, but also with strain ε_U at which σ_{max} was attained. Ultimate strength deviates by 79.7 MPa. An average stress curve of WG2 and WG7 was added to **Figure 5.02, a** (dot-dashed line), while the vertical range bar gives an indication of variability in peak stress. The horizontal range bar gives the deviation in strain at which the ultimate strength was attained.

Four tests were deformed at 900 °C (WG3, WG9, WG10, WG16) (**Figure 5.02, b**). Of these, three can be seen to fall roughly in the same error margin as tests deformed at 800 °C (WG3, WG10, WG16). However, sample WG9 is significantly weaker than the others. This marked deviation is thought to be a result of a slow jacket leak, increasing pore pressure in the specimen and thus decreasing the yield strength (confirmed by microstructural evidence; compare with **Chapter 7.2**). Data from WG9 was not used when calculating the average deformation characteristics at these temperature and strain rate conditions.

At 1000 °C two samples were deformed at the same strain rate (**Figure 5.02, c**). The sample WG11 displays a σ_{max} 63 % higher that σ_{max} for WG4. However, with increasing strain the strength of WG11 drops rapidly, while the strength of WG4 steadily rises with increasing strain, resulting in similar supported stress at 12 % strain.

Variation in the stress-strain behaviour of samples deformed under near identical conditions can be summarized as follows: The ultimate strength of samples varied by ± 30 %. Also shapes of stress strain curves differ. Samples (WG2, WG7 (**Figure 5.02, a**); WG3, WG10 (**Figure 5.02, b**) and WG11 (**Figure 5.02, c**)) showed a dramatic decrease in supported stress, once the ultimate strength of the sample had been exceeded (as sketched in **Figure 5.01**).

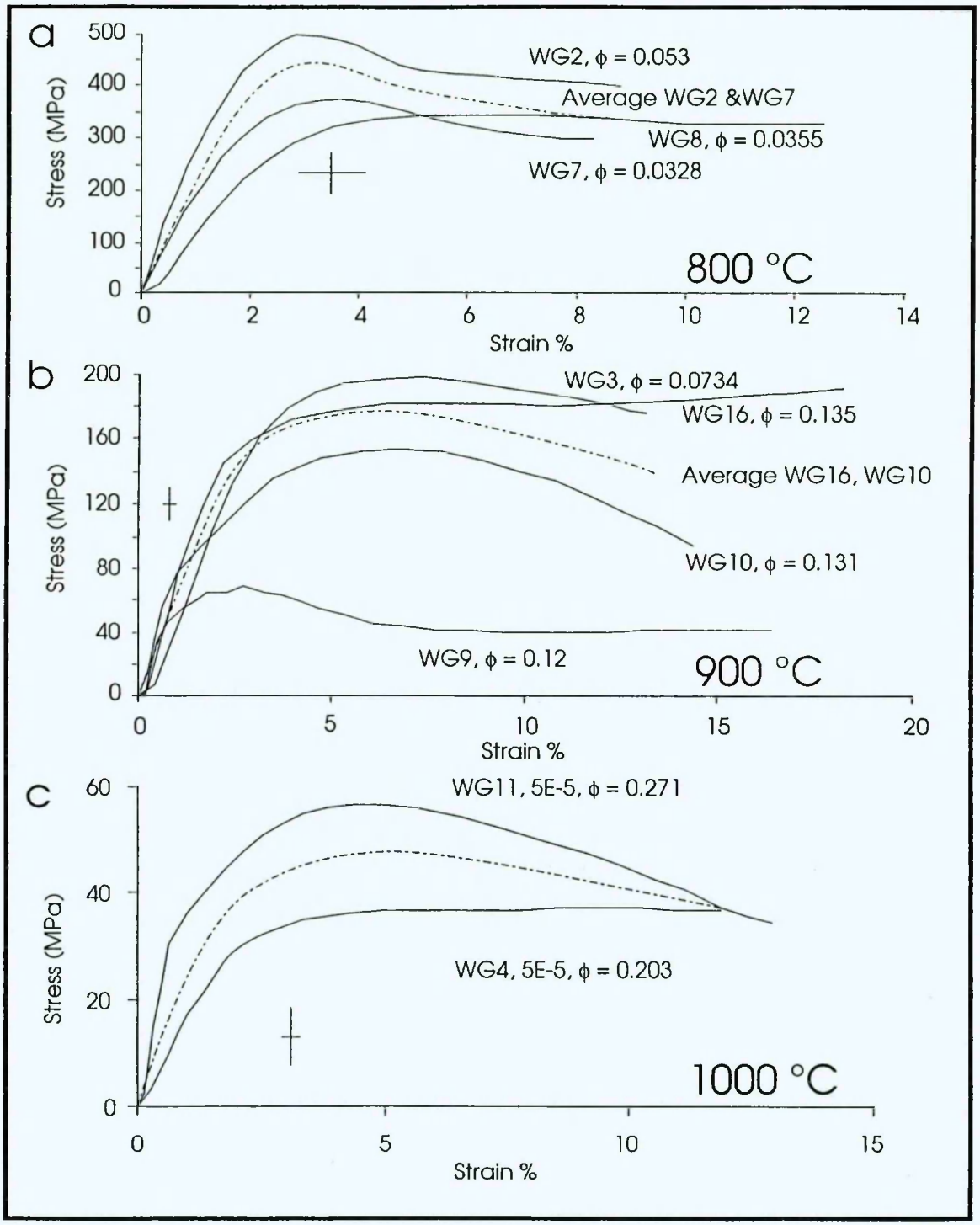

Figure 5.02: Stress-strain curves for samples deformed at a constant strain rate of $5*10^{-5}$ under isothermal conditions. **a.)** 800 °C; **b.)** 900 °C; **c.)** 1000 °C. Range bars give deviation of ultimate strength of different samples from idealized stress-strain curve (dot-dashed line).

In contrast, samples WG8 (**Figure 5.02,a**), WG16 (**Figure 5.02, b**) and WG4 (**Figure 5.02, c**) showed more diffuse yield behaviour and more shallow increase of stress with increasing strain.

As indicated by the stress strain data assembled in **Figure 5.02**, samples deformed under near identical conditions can have different stress-strain curve shapes. This is most likely related to the different evolution of microstructures, related to heterogeneous material of samples, due to the large grain size of 0.96 mm, compared with a small sample size of a cylinder of 9.4 mm diameter and 20 to 21 mm length.

5.2.3 Effect of temperature on stress-strain behaviour

In **Figure 5.03** the average stress-strain curves derived in **Figure 5.02** are plotted in conjunction with results from experiments at 850 °C (WG6) , 950 °C (WG5), 1050 °C (WG12) and 1100 °C (WG13).

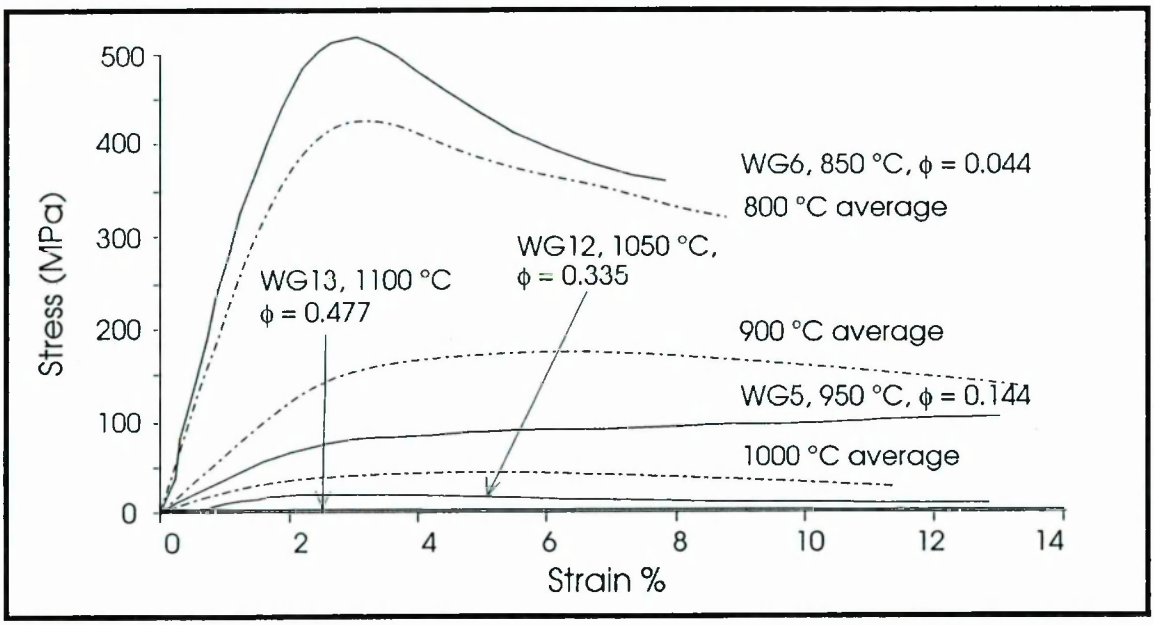

Figure 5.03: Stress strain curves of isothermal samples deformed at a constant strain rate of $8 * 10^{-5}$ s^{-1} at various temperatures. Solid lines mark single experiments; dashed lines mark averages of several experiments determined in **Figure 5.02**. Maximum strain readings from WG12 (5.86 MPa at 32.5 % strain) and WG13 (1.31 MPa at 30.13 %) were not included to ease comparison between the different stress-strain curves.

With increasing temperature a dramatic drop in maximum supported stress can be observed. While samples deformed at 800 to 850 °C supported as much as σ_{max} = 518.86 MPa, the sample deformed at 1100 °C (WG13) supported only σ_{max} = 2.81 MPa. Associated with this decrease in supported stress is a change in the shape of the stress-strain curves. At low temperatures (800 to 850 °C) a steep increase in strength with increasing strain can be observed, until the yield point is reached. With further strain the samples strength drops sharply.

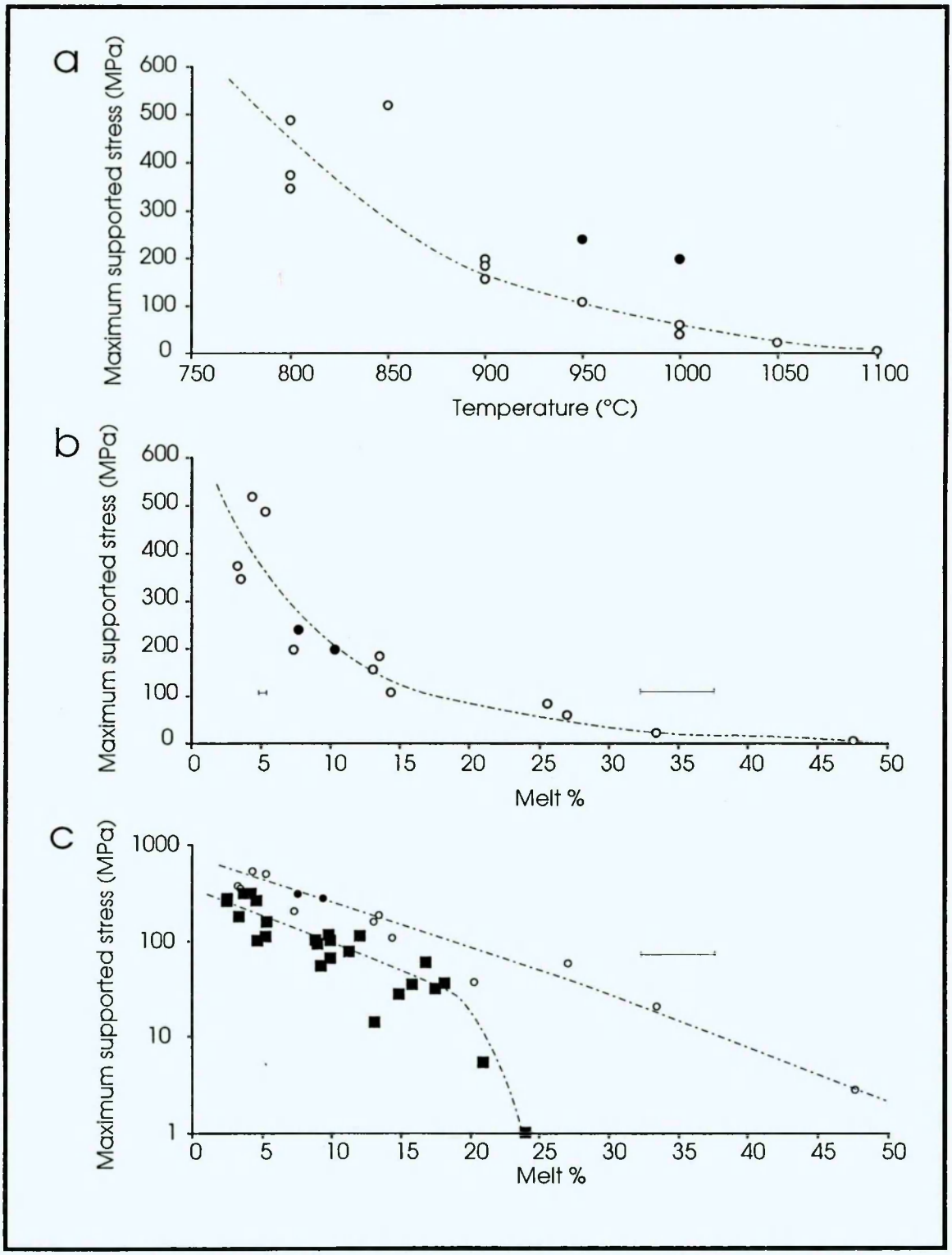

Figure 5.04: Control of temperature and melt fraction on the maximum supported stress of samples deformed at a constant strain rate of $5 * 10^{-5}$ s^{-1} and temperature. Open circles mark samples WG2 to WG13 (excluding WG9) and WG16, while the filled circles highlight samples WG23 and WG27, where part of the melt was extracted into adjoining quartzite, reducing the overall melt fraction. Range bars on **b.)** give standard deviatoric error on melt fraction (after **Figure 3.2**); **c.)** Log maximum supported stress versus melt fraction with open and filled circles as above. Filled squares are data by van der Molen & Paterson (1979) where Delegate aplite was heated to 800 °C at 200 MPa with different melt fractions produced by the addition of water (0 - 2 wt %) to produce a variety of melt fractions. The result plotting on the x-axis refers to van der Molen and Paterson's (1979) powder specimen (compare to **Chapter 6.4**).

In contrast, higher temperature samples (900 to 1100 °C) show a much more gradual initial increase of stress with strain. These samples have more diffuse yield behaviour, with a less pronounced decrease in supported stress with increasing strain beyond the ultimate sample strength. An increase in strain at which the ultimate strength of the sample was exceeded with increasing temperature was not observed.

The maximum stress supported by samples deformed at the same strain rate is plotted against temperature in **Figure 5.04, a**. The steep decline in maximum stress with increasing temperature is easily seen. However, there is quite large deviation of supported stress of samples from the general trend (drawn as a dashed line), especially WG6, heated to 850 °C and the two filled circles that mark sample WG27 and WG23 at 950 and 1000 °C respectively. The strength of the samples decreases most markedly at temperatures between 800 and 900 °C. However, there is insufficient data to say whether this decrease is smooth (as indicated by the dashed line) or step like.

5.2.4 Change of maximum stress supported with melt fraction

The increase in sample temperature is also closely linked to a general increase in melt fraction (**Chapter 3.3**). As there is no linear relationship between melt fraction and temperature, the relationship between maximum supported stress and melt fraction needs to be explored (**Figure 5.04, b**). For isothermal samples a smooth drop of maximum stress over the melt fraction interval can be seen. The steepest decrease in specimen strength occurs at melt fractions between 0 and 0.10 by volume. With increasing melt fraction the strength decreases smoothly over the melting interval of (ϕ = 0.10 to 0.477), until it approaches the flow strength of melt at ϕ = 1 melt. A *critical melt fraction* (van der Molen & Paterson 1979) at approximately ϕ = 0.30 melt, at which a sudden drop in strength of the rock, associated with a step from sample behaviour controlled by matrix to melt dominated behaviour, was not observed (**Figure 5.04, c**). This aspect in studied further in **Chapter 6.4** where the effect of melt viscosity on σ_{max} is assessed.

5.2.5 Effect of strain rate on sample behaviour.

Further tests were performed at strain rates between $1 * 10^{-3}$ s^{-1} and $2 * 10^{-7}$ s^{-1} in order to study the effect of strain rate on deformation behaviour. An upper limit to strain rates is set primarily by the maximum data-logging rate of the machine (1 per second) and

the maximum differential stress that can be applied without causing permanent plastic deformation of the rig. Thus, a practical maximum speed corresponds to about 20 % shortening in about 1 minute. On the other hand very slow strain rates will cause partially molten rocks to have strengths close to the detection limit of the machine (~1 MPa) (compare also to **Appendix 2**).

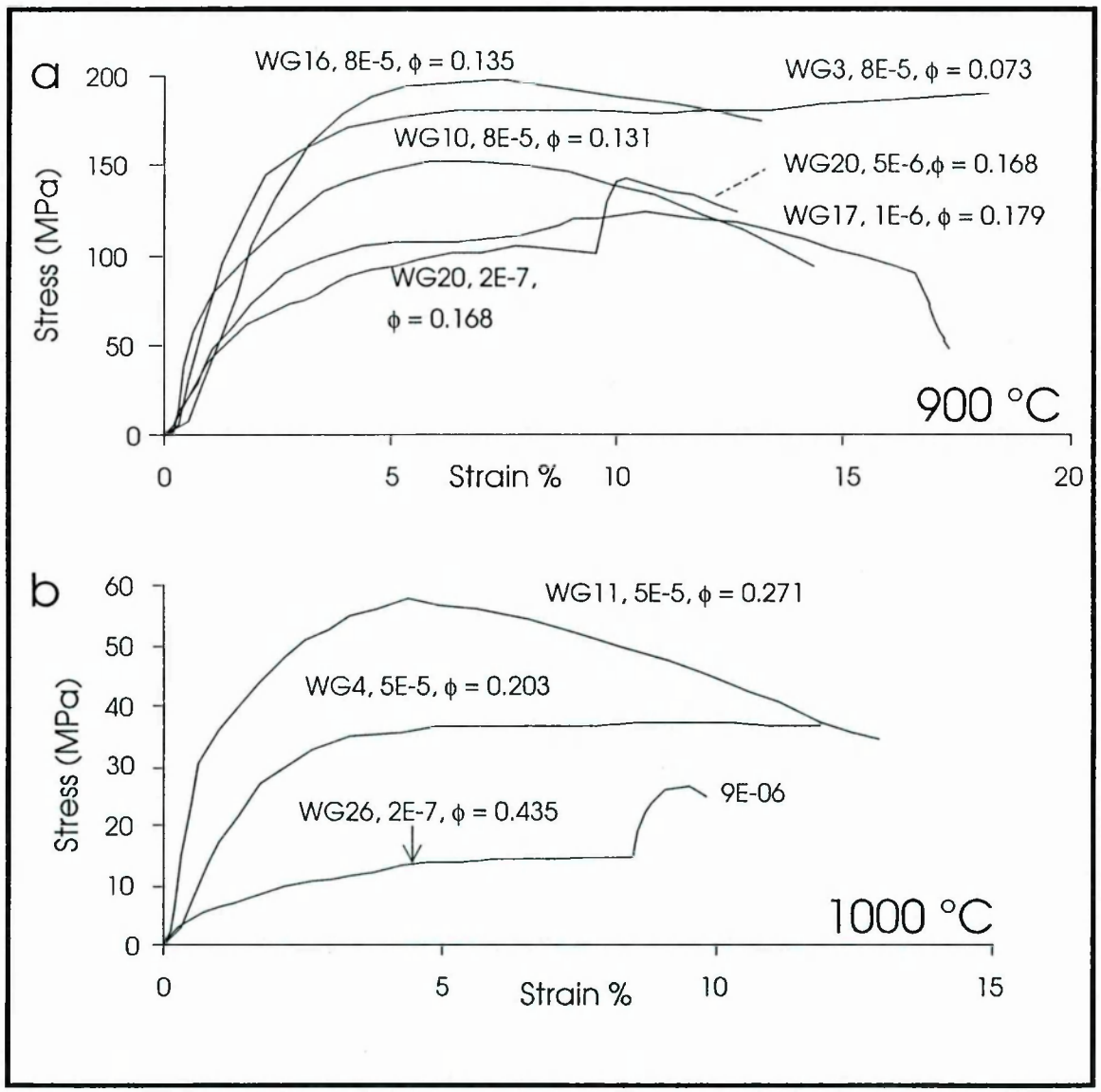

Figure 5.05: Stress-strain curve dependency on strain rates **a.)** 900 °C; **b.)** 1000 °C.

In **Figure 5.05, a** all isothermal tests deformed at 900 °C at strain rates of $8 * 10^{-5}$ s^{-1} or slower (with the exception of WG9) are displayed on a stress-strain plot. As the strain rate is reduced there is a decrease in σ_{max}. The step in the WG20 stress strain curve is due to strain rate stepping from $1 * 10^{-7}$ to $5 * 10^{-6}$ s^{-1} during the test run. Additional complications arise in comparing tests deformed at different strain rates at the same

temperature, as a lower strain rate required much longer test runs which resulted in higher melt fractions (**Chapter 3**).

The decrease in supported stress with decreasing strain rate can also be observed at 1000 °C (**Figure 5.5, b**). The stress-strain curve of WG26, deformed at $2 * 10^{-7}$ s^{-1} rises smoothly over the strain interval, until the strain rate was stepped up.

5.2.6 Effect of strain history on stress-strain deformation behaviour.

Besides tests consisting of a single loading event followed by a single stress relaxation, several tests involved a more complex deformation history. These tested whether stress relaxation events influenced stress-strain behaviour over a long strain interval. Two types of isothermal strain history tests were conducted:

- Constant strain rate test punctuated by several stress relaxation events (WG28, WG29).
- Multiple stress-strain – stress relaxation events with stress-strain tests performed at various strain rates (WG20, WG26).

Two multiple loading events at a constant strain rate of $8 * 10^{-5}$ s^{-1}, separated by stress relaxation events were performed at 900 and 1000 °C (WG28 and WG29 respectively). Both samples experienced a 50 °C temperature profile length-wise across the sample, leading to deformation entirely confined to one half of the specimen cylinder. To allow for this heterogenelty, strain rates were therefore recalculated (**Appendix 2 , Appendix 10**) assuming that all compressive movement was accommodated by the hotter half of the sample, thus doubling the strain and halving the strain rate imposed on this half of the samples. However, as only relative stress-strain values are used in assessing the effect of multiple loading events on stress-strain curve shapes, the data from these two samples can be used in **Figure 5.06**.

At 900 °C (**Figure 5.06, a**) sample WG28 suffered five separate loading events. At the beginning of each loading event the supported stress increased sharply until the yield surface was met. At the inflection of the stress-strain curve (from near vertical to near horizontal) permanent deformation of the specimen proceeds . The parts of the curves representing the post-yield behaviour were joined (by a dot-dashed line) to give the complete stress-strain curve of the specimen (**Figure 5.02, a**). This curve is similar in shape to the surface obtained for samples deformed at the same strain rate, but involving only one deformation cycle (**Figure 5.02, b**). However, the maximum stress measured in WG28 was 25 % less than σ_{max} in the other tests. This related to the short

effective length for samples WG28 owing to the described temperature profile. A similar trend can be observed in WG29 (**Figure 5.06, b**). Again a single stress-strain curve can be drawn that joins flattened parts of the different loading events. The ultimate strength of the sample was not reached in the second and third loading event, explaining the divergence of maximum stress of the sample from the fit (dot-dashed line) in the strain interval of 5 to 16 %. In difference to WG28, there is a better match of ultimate strength between samples deformed with a single deformation cycle (**Figure 5.02, c**) and WG29 (**Figure 5.06**).

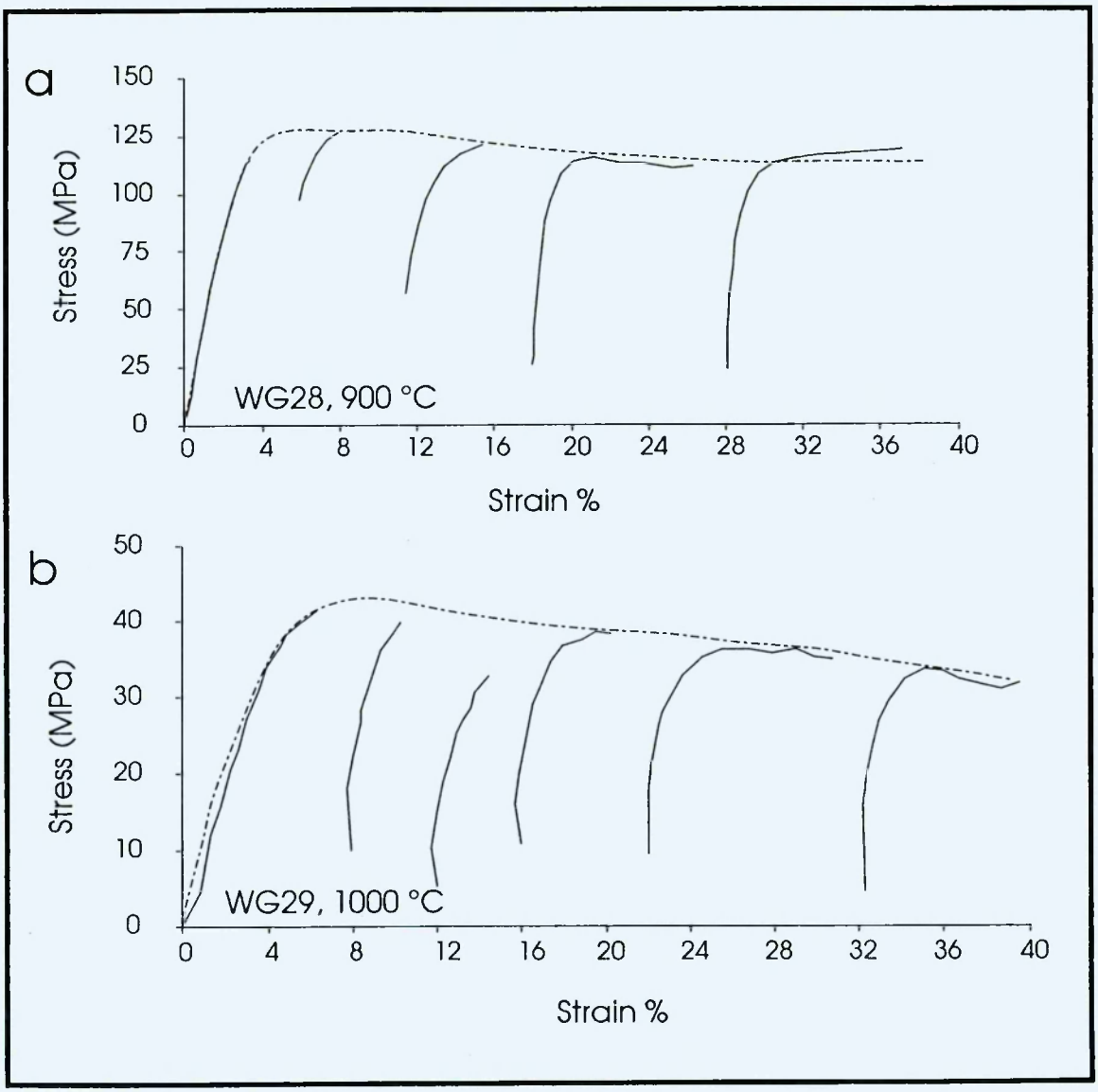

Figure 5.06: Multiple loading of samples at constant strain rate. **a.)** WG28, 900 °C; **b.)** WG29, 1000 °C. Solid line marks stress-strain history of the sample. Steep sections mark loading of samples after a stress-relaxation event; permanent deformation occurred where the stress-strain curve flattens. Dot-dashed lines mark fit to flattenend parts of multiple loading events.

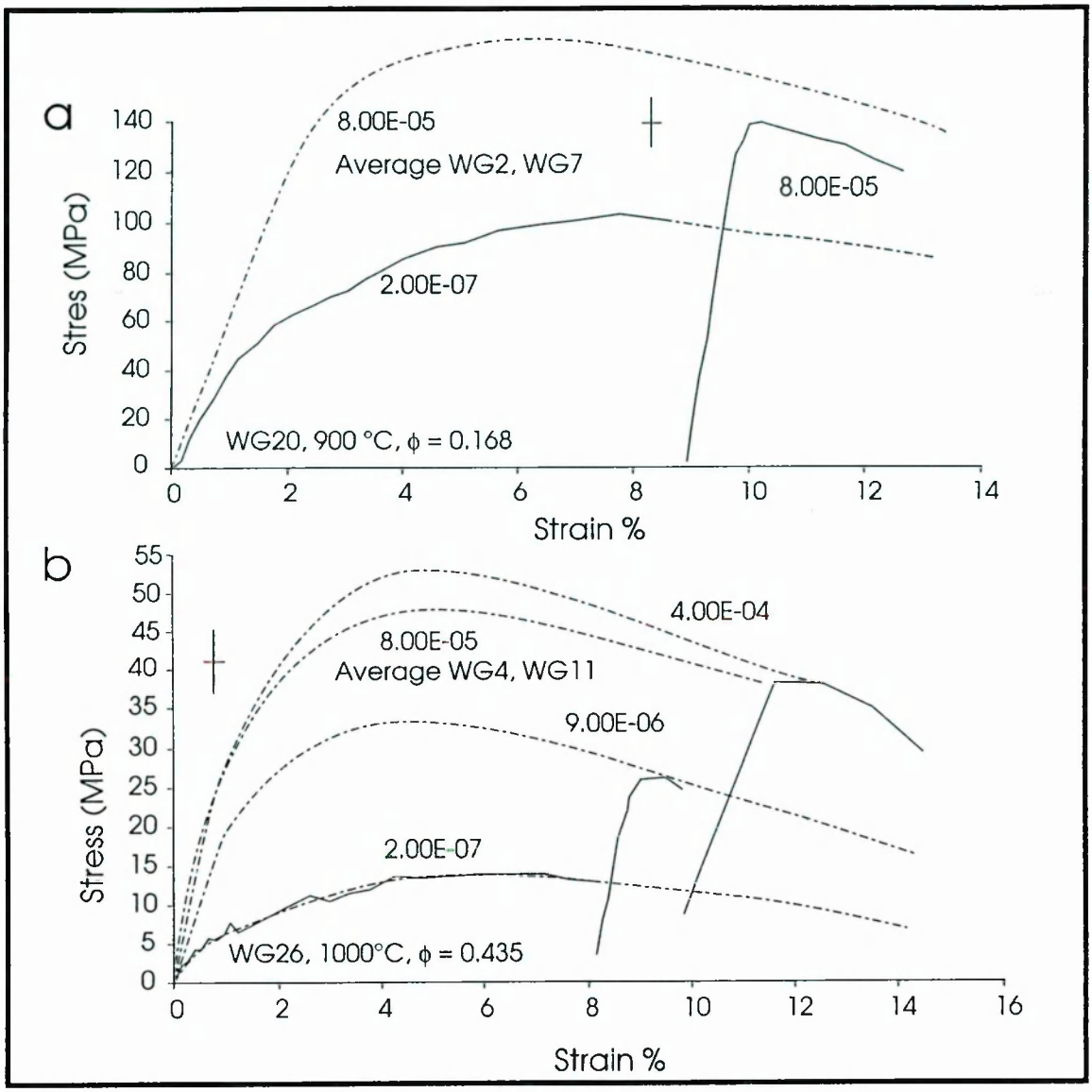

Figure 5.07: Multiple loading of samples at different strain rates. **a.)** WG20, loaded at 900 °C at strain rates of $2 * 10^{-7}$ s^{-1} and $5 * 10^{-5}$ s^{-1}. Dot-dashed line is the average stress-strain curve of WG2 and WG7 from **Figure 5.02, b, b.)** WG26 deformed at 1000 °C at strain rates of $2 * 10^{-7}$ s^{-1}, $9 * 10^{-6}$ s^{-1}, and $4 * 10^{-4}$ s^{-1}. Dot-dashed line is the average stress-strain curve of WG4 and WG11 from **Figure 5.02, c**. Range bars in **a.)** and **b.)** give variation of ultimate strength of samples that made up average curves (after **Figure 5.02**).

In nine tests strain rate stepping was carried out, of which two are displayed in **Figure 5.07**. Strain rate stepping was accomplished either by altering the strain rate during on-going deformation, or by separating different strain rate tests by stress relaxation events. In all tests strain rates were increased with strain and time. In WG20 (**Figure 5.07, a**) the two compressional events were separated by a stress relaxation event. Loading of this sample after the stress relaxation event produced a steep rise of the stress-strain curve, followed by permanent deformation associated with a flattening of the stress-strain curve. At the faster strain rate the sample supported a higher stress. Superimposed on

Figure 5.07, a is the average stress-strain curve of samples WG2 and WG7 (from **Figure 5.02, b**) which were deformed at the same temperature and strain rate as the second loading event of WG20. The two curves show a fit within the indicated range bar marking the difference in ultimate strength.

Sample WG26 (**Figure 5.07, b**) suffered three loading events at increasing strain rates, separated by stress relaxation events. As for WG20 (**Figure 5.07, a**) stress-strain curves can be drawn as dot-dashed lines for specimen behaviour at low strains for the higher strain rate curves. The average curve of WG4 and WG11 is also included, which allowed modelling of the low strain equivalents of the faster strain rate deformation segments. The fitted curve for the fastest strain rate segment of $4 * 10^{-4}$ s^{-1} falls within the range error of ultimate strength belonging to the average curve of WG4 and WG11.

Both types of multiple stress-strain- stress relaxation cycles demonstrate that the strain history of the sample does not influence the shape of stress-strain curves at higher strains.

5.3 Stress relaxation tests

At certain stages during uniaxial deformation the compressive deformation of the specimen was stopped and the specimen was allowed to relax at constant strain as described in **Appendix 1**. Stress and strain were recorded (**Appendix 10**). During stress relaxation, elastic deformation of the sample (accumulated during differential compression of the sample) was dissipated through plastic strain within the specimen. As the sample was no longer dynamically deformed during stress relaxation the strain rate decreased from the strain rate at which the sample was deformed during the stress-strain test and approached zero at infinite time. Therefore, stress relaxation data are displayed as logarithmic plots of stress versus strain rate. Stress relaxation tests were terminated after a strain rate of between $10^{-5.7}$ s^{-1} and $10^{-8.5}$ s^{-1}, as a further decrease in magnitude of strain rate could only be achieved by a further increase in magnitude of time. Several aspects of stress relaxation were studied:

- Stress relaxation tests on samples at the same temperature and with approximately the same melt fraction provide information on the variability in the starting material and repeatability of experiments.
- Effect of temperature on stress relaxation behaviour.
- Effect of melt fraction on stress relaxation behaviour.
- Effect of progressively increasing strain on stress relaxation behaviour.

- Effect of initial strain rate on the subsequent stress relaxation behaviour.

5.3.1 Effect of starting material variability on stress relaxation behaviour

As already described in **Chapter 5.2**, several suites of tests were performed at identical temperatures, pressures, and strain rates with roughly similar melt fractions that were terminated by a single stress relaxation cycle.

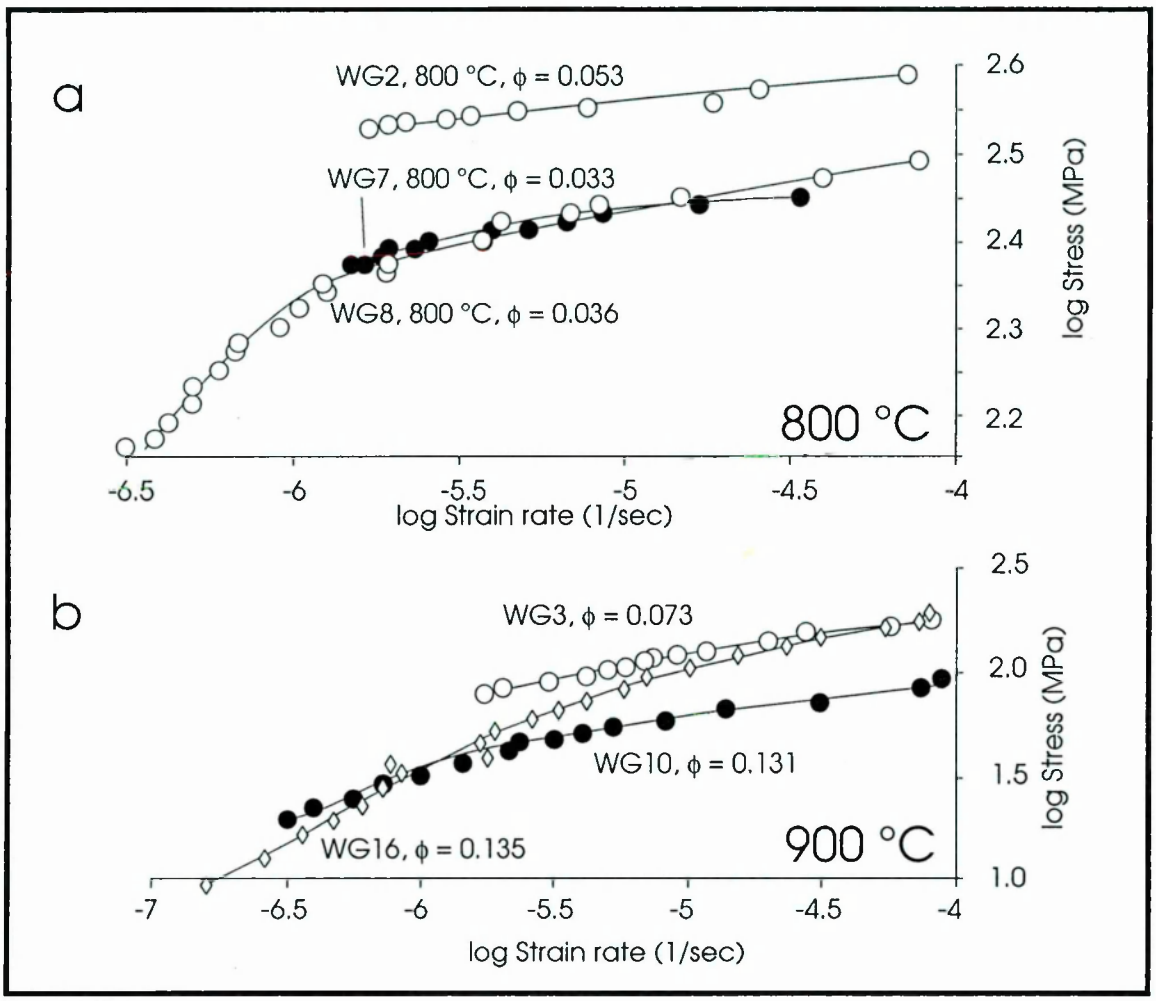

Figure 5.08: Stress relaxation curves of samples deformed under near identical conditions at 800 and 900 °C.

Stress relaxation curves in **Figure 5.08** show some intrinsic variability in magnitude of stress with strain rate. This effect is most clearly seen at low temperatures (**Figure 5.08, a**). At 800 °C little to no stress relaxation occurred in samples WG2 and WG7 at strain rates above $2 * 10^{-6}$ s^{-1}. With decreasing strain rate sample WG8 relaxed at strain rates below $2 * 10^{-6}$ s^{-1} at a constant gradient. While WG7 and WG8 showed very similar

stress relaxation behaviour, sample WG2 supported a larger stress. This difference in behaviour has to be attributed to mineralogical and structural heterogeneities of the starting material.

With increasing temperature samples relaxed more readily. At 900 °C there is less variation in supported stress at the same strain rate (**Figure 5.08, b**) than there was at 800 °C (**Figure 5.08, a**). Despite WG16 relaxing faster than WG3 and WG10, an overall constant stress relaxation gradient was maintained.

5.3.2 Effect of temperature on stress relaxation

On Figure 5.09 representative stress relaxation curves of samples deformed at different temperatures are displayed. A drop in supported stress was seen with increasing temperature and melt fraction. While little to no stress relaxation takes place at fast strain rates (above 2 * 10-6 s-1) in tests heated to 800 and 850 °C, samples heated above 900 °C show stress relaxation over the strain rate interval 10-4 to 10-7 s-1.

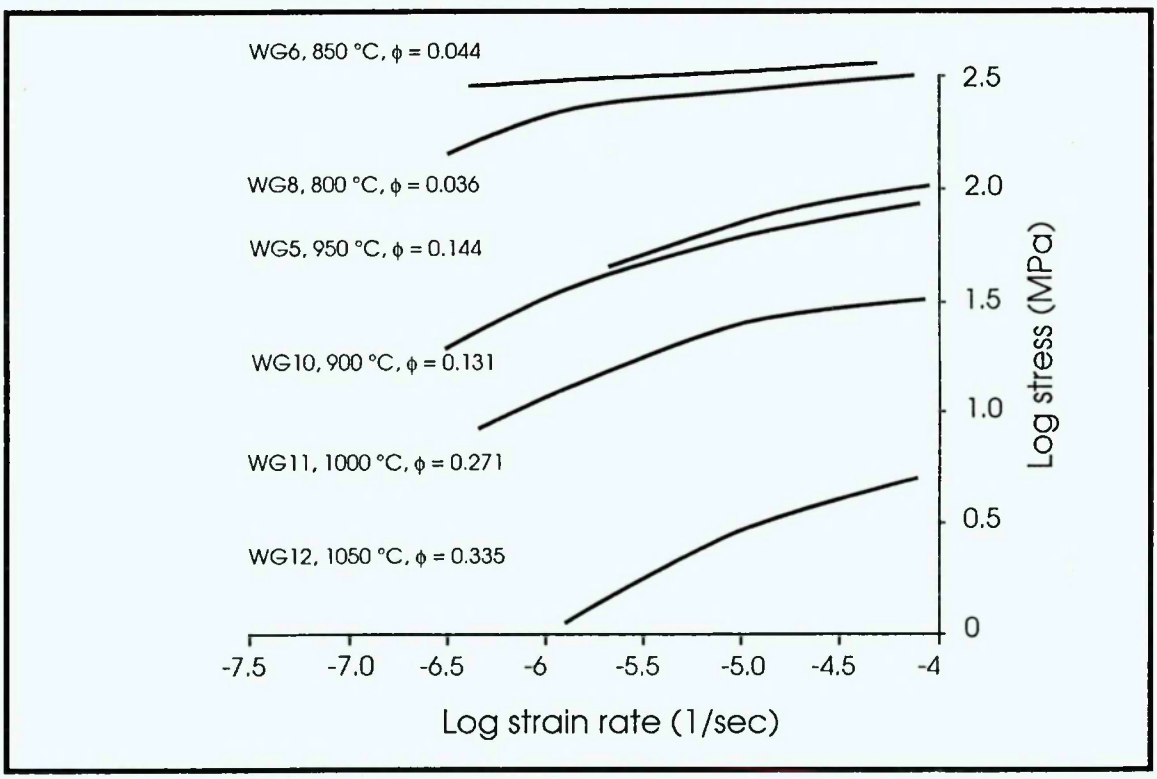

Figure 5.09: Stress relaxation curves at temperatures between 800 and 1050 °C. For spread of stress relaxation data on individual curves compare with **Figure 5.08** and **Figure 5.10**.

Over the temperature interval 900 to 1050 °C and in the strain rate range of 10^{-5} to 10^{-7} s^{-1} a constant slope of all stress relaxation curves was observed. This constant slope suggested that the material relaxed at a constant gradient over the temperature interval. A slope not equal to one indicates that the material has a non-Newtonian rheology over the studied temperature/strain rate interval.

5.3.3 Effect of melt fraction on stress relaxation

Two samples (WG18, WG21) were heated to high temperatures (1100 and 1200 °C respectively), in order to produce a high melt fraction, followed by deformation and stress relaxation at lower temperatures , assuming that the melt fraction established at higher temperatures are maintained (compare to **Chapter 3.3.5**). As deformation and stress relaxation events on these two samples took place at 850, 900, 950 and 1000 °C, it is possible to compare the stress relaxation curves of these two samples with those of other samples deformed at the same temperature, but with comparatively lower melt fractions. Comparison is complicated by neo-crystallization of biotite and feldspars in the melt phase of these samples (**Chapter 3.4.1, Chapter 6.2.1**). In samples WG23 and WG27 the overall melt fraction was reduced by extrusion of some of the melt into an adjacent layer of quartzite. Melt fractions of all samples are listed in **Table 3.01**.

In **Figure 5.10, a** the stress relaxation behaviour of WG18 with ϕ = 0.254 glass (but glass plus neo-crysts in the melt phase equal 0.47) is plotted as a dashed line next to the results from other experiments deformed at 900 °C but from samples containing an average melt fraction of 0.073 to 0.179 (average ϕ = 0.136). Sample WG18 shows the same stress relaxation behaviour as the other runs in supporting a similar stress and relaxing at the same rate as the other samples. This indicates that in the case of WG18 the glass fraction does not influence the maximum supported stress at 900 °C. The dot-dashed line on **Figure 5.10, a** links the terminations of differential deformation at different strain rates and demonstrates that a slope of stress supported at different strain rates is more shallow in stress-strain experiments than during stress relaxation.

In contrast to WG18 at 900 °C WG27 and WG21 show different stress relaxation behaviour at 950 °C (**Figure 5.10, b**). While sample WG18 showed similar supported stress to WG5 (WG18 ϕ = 0.254, WG5 ϕ = 0.144) with similar slopes of stress relaxation curves, sample WG27, containing less than half the volume of melt than WG5 (with ϕ = 7.6) supported a much higher stress than samples WG5 and WG18, though stress relaxation took place at the same slope as found in the two former samples.

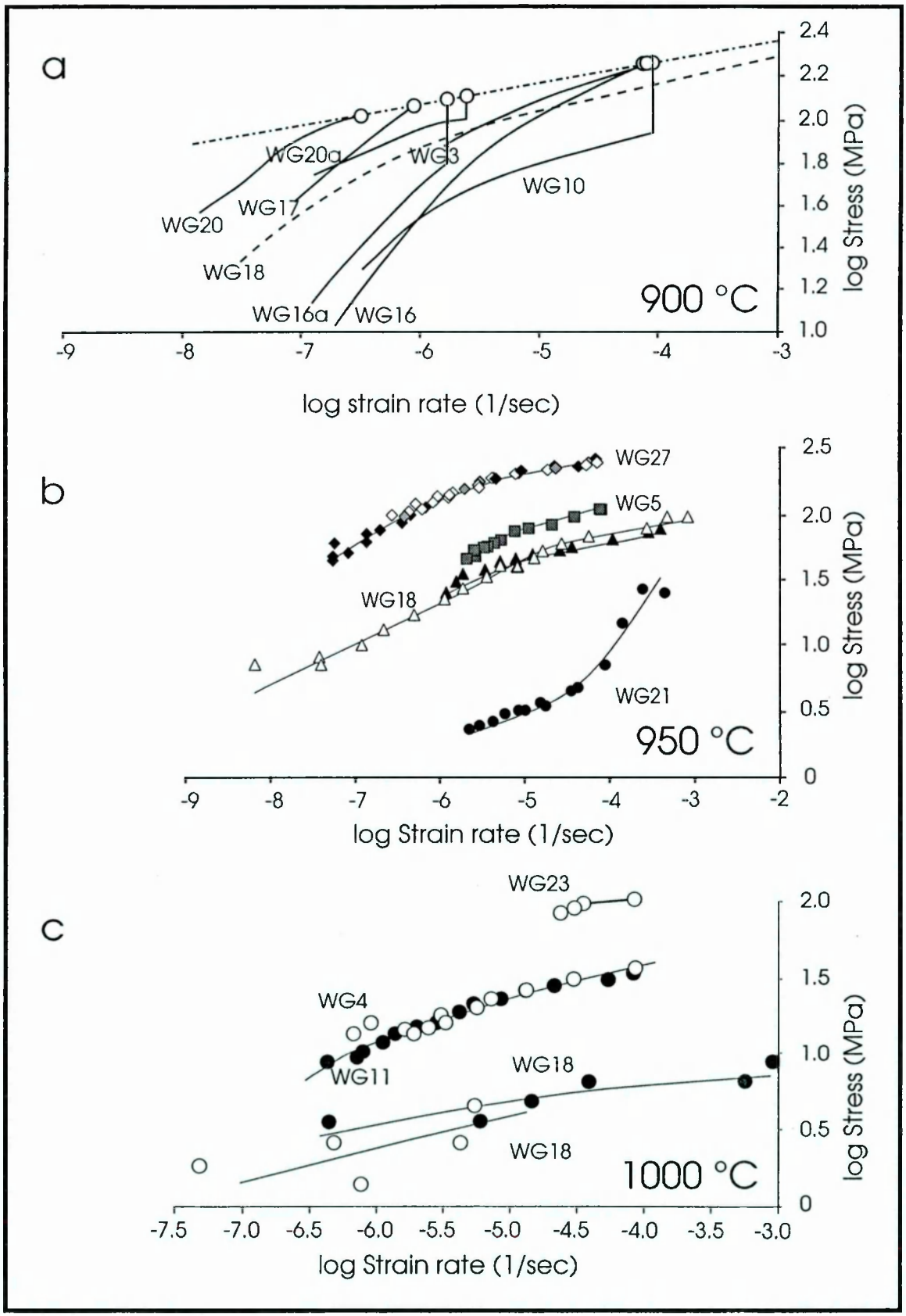

Figure 5.10: Effect of melt fraction on stress relaxation. **a.)**Solid lines mark stress relaxation curves of samples heated to a maximum temperature of 900 °C,while the dashed line indicates the stress relaxation curve for WG18 (ϕ = 0.256 - 0.47), initially heated to 1100 °C, prior to deformation at 900 °C (ϕ = 0.073 - 0.179), and hence containing a higher melt fraction than other samples. The dot-

dashed line joins the termination of stress-strain curves, indicating stress relaxation of samples under differential compression. **b.)** Stress relaxation at 950 °C. WG27 (ϕ = 0.076) had a lower melt fraction than WG5 (ϕ = 0.144), while WG18 (ϕ = 0.256 - 0.47) and WG21 (ϕ = 0.16 - 0.625) have increased melt fractions. Filled and open triangles mark different stress relaxation events on WG18. **c.)** Stress relaxation at 1000 °C. WG23 (ϕ = 0.103) has a lower melt fraction than WG4 (ϕ = 0.203) and WG11 (ϕ = 0.271), while WG18 (ϕ = 0.256 - 0.47) had a higher melt fraction. Again two separate stress relaxation events for WG18 are marked.

In contrast sample WG21 (that was initially heated to 1200 °C) showed much more pronounced strain weakening up to strain rates of $5 * 10^{-4}$ s^{-1}, followed by a flattening of stress relaxation curve trending at the same slope as WG18 and WG5. This sudden increase in strength with decreasing strain rate (below $5 * 10^{-4}$ s^{-1}) might relate to the onset of neo-crystallization in WG21.

At 1000 °C (**Figure 5.10, c**) the effect of reduced (WG23) and increased melt fraction (WG18) on supported stress is similar to that observed in WG21 and WG27 at 950 °C. The general gradient of stress relaxation is maintained in all samples at 1000 °C. WG23 (ϕ = 0.103 melt) supports a larger stress than WG4 (ϕ = 0.203) and WG11 (ϕ = 0.272). In contrast to lower temperature sets (**Figure 5.10, a** and **b**) sample WG18 supports a much lower stress than WG4 and WG11. This may be due to crystallization of the melt phase not having taken place at this temperature in WG18, in which case the sample would have contained a melt fraction up to twice that of WG4 and WG 11 (ϕ = 0.47).

5.3.4 Effect of strain on stress relaxation behaviour

The effect of strain on stress relaxation was studied in three samples undergoing multiple stress-strain - stress relaxation cycles (**Figure 5.11**).

In sample WG26 the stress relaxation curves shift with increasing strain (**Figure 5.11, a**). This sample became progressively weaker with increasing strain, though the slope of the stress relaxation curve was maintained. The dot-dashed line links the starting points of stress relaxation events, as WG26 suffered strain rate stepping in the stress-strain part of the deformation cycles. This dot-dashed line also points to some strain weakening with decreasing strain rate and increasing strain. In the other two tests multiple loading at constant strain rates and stress relaxation cycles were applied. The stress relaxation curves lie closer together and have the same slope (**Figure 5.11, b** and **c**), indicating less strain weakening. Especially in sample WG29 (**Figure 5.11, b**) the stress relaxation curves from different stress relaxation events superimpose on each other. A slight shift towards a smaller supported stress with increasing strain can be seen in WG30 (**Figure 5.11, c**). In summary, there was insufficient and ambiguous evidence to suggest that strain influences the slope of stress relaxation curves.

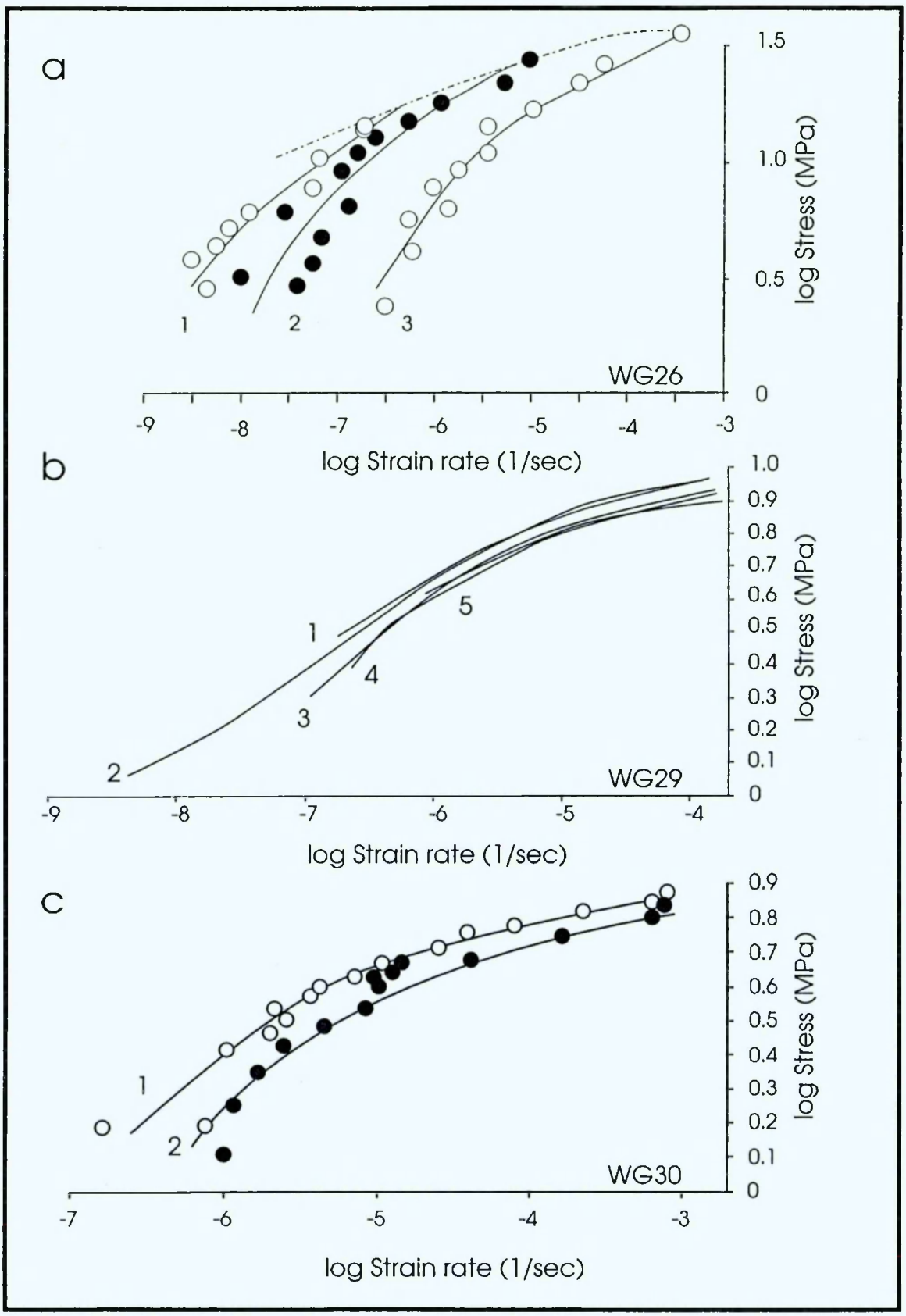

Figure 5.11: Effect of strain on stress relaxations at 1000 °C. Three samples **(a.)** WG26, **b.)** WG29 and **c.)** WG30 suffered multiple loading and stress relaxation cycles. Numbers adjacent to stress relaxation curves relate to the position of consecutive stress relaxation cycles in the stress-strain history of the sample. Circles indicate spread of data, while the dotted line in **a.)** links the beginning of stress relaxation cycles. **a.)** Stress relaxation cycles of WG26 at strain between 8.11 -

8.29 (1), 8.83 - 10.17 (2) and 13.3 - 14.77 % (3) respectively. **b.)** stress relaxation cycles of WG29 at strains between 9.91 - 11.32 % (1), 20.03 - 21.20 % (2), 30.42 - 31.66 % (3), 39.28 - 40.40 % (4) and 44.46 - 45.57 % (5) respectively. Note, that reprocessing only assumed half the specimen length (**Table 5.01**). **c.)** stress relaxation cycles of WG30 at strain between 48.63 - 49.73 % (1) and 56.52 - 57.40 % (2) strain respectively. Note, that reprocessing only assumed half the specimen length (**Table 5.01**) (**Appendix 10**).

5.4 Stress, strain, strain rate interrelationship

Assuming that there is no change in the slope of stress relaxation curves with increasing strain (**Chapter 5.3.4**), the stress relaxation data can be used to predict the shapes of stress-strain curves at higher strains (in the case of strain rate stepping), and, more importantly at lower strain rates than can be achieved in the laboratory. This allows the deformation behaviour of partially molten Westerly granite at geologically realistic strain rates (below 10^{-13} s^{-1}) and stresses (below 1 MPa, the detection limit of the deformation rig) to be predicted.

In **Figure 5.12, a** stress relaxation data are used to predict the shape of stress-strain curves at elevated strains. The vertical parts of the solid stress-strain curve (**Figure 5.12, a**) describe stress relaxation events. Stress relaxation curves of WG26 are displayed in **Figure 5.12, b**. Circles in **Figure 5.12, a** mark the stress values at identical strain rates to those at which the samples were deformed at, extracted from the stress relaxation data. These points are linked to the horizontal, differential deformation part of the stress-strain curves using a dot-dashed line. A good agreement between stress-strain curves predicted from stress relaxation data and stress-strain experiments can be observed.

Thus stress relaxation data can be used to predict the shapes of stress strain curves at far lower strain rates than experimentally possible (down to strain rates of $10^{-8.5}$ s^{-1}). This allows the construction of a stress envelope at various temperatures in differential stress - strain rate - strain space (**Figure 5.13**). A marked decrease in strength with increasing strain and decreasing strain rate can be observed, leading to supportable stress at strains above 15 % and below a strain rate of $2 * 10^{-7}$ s^{-1} below 1 MPa, even at 900 °C. With increasing strain rate and decreasing strain the strength of the sample rises rapidly.

At geological strain rates (below 10^{-13} s^{-1}) a sample containing a melt fraction below ϕ = 0.10 will give little resistance to deformation over the whole temperature interval studied (800 to 1050 °C). The difference in supported strength with varying strain rate is more marked at lower temperatures.

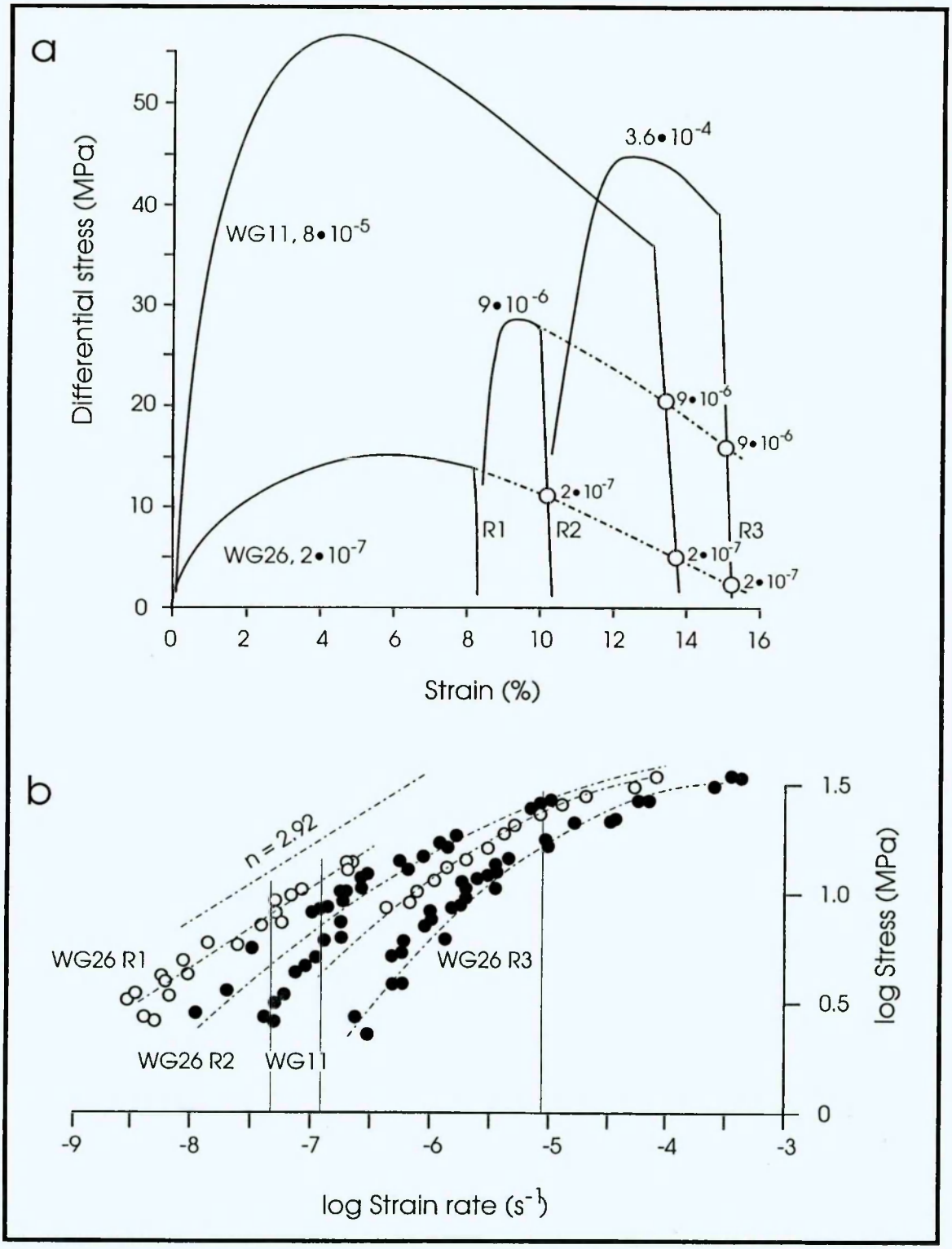

Figure 5.12: Prediction of stress-strain curves from stress relaxation data. **a.)** Plot of stress strain curves of WG11 and WG26 (1000 °C). While only one stress-strain - stress relaxation cycle was carried out on WG11, sample WG26 suffered three cycles, with consecutive stress-strain events at higher strain rates, separated by stress relaxation events. Stress relaxations are identified by near vertical drops and increases of stress. Open circles mark positions of lower strain rates of other stress-strain events, extracted from stress strain data, with dash-dotted lines linking these circles with relevant stress-strain curves. **b.)** Stress-relaxation curves of WG26, used to predict shapes of stress-strain curves in the plot above. Open and closed circles indicate spread of data.

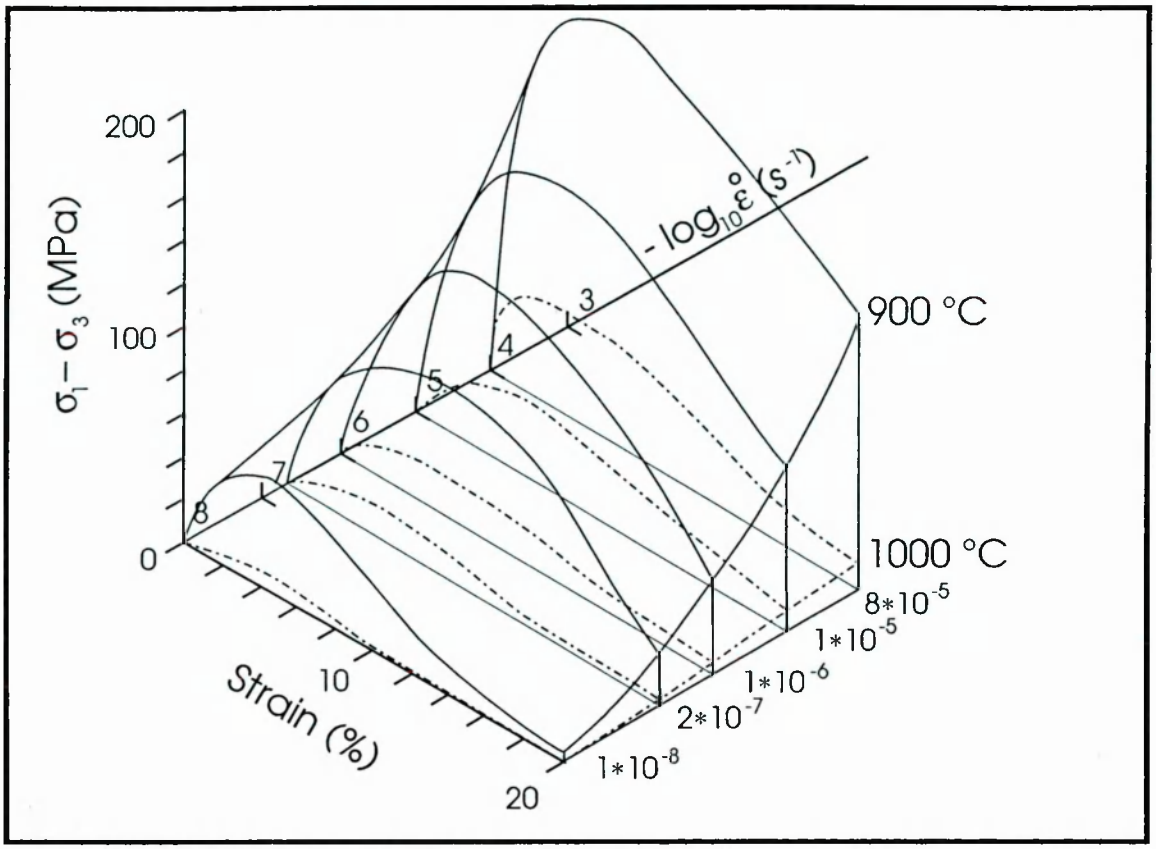

Figure 5.13: Shape of stress envelopes at 900 (solid line) and 1000 °C (dot-dashed line) in differential stress - strain - strain rate space.

5.5 Flow law for partially molten Westerly granite using stress relaxation data

So far it has been noted that stress relaxation curves tend towards a common gradient at slower strain rates, with little to no effect of temperature (**Chapter 5.3.2**) or strain (**Chapter 5.3.4**). This indicates that in stress relaxation deformation is dominated by the deformation behaviour of melt, as there is no change in slope over the melting interval indicative of a change in deformation behaviour from crystal dominated to melt dominated deformation behaviour. As stress-relaxations fall on the expected extrapolations of stress-strain curves (**Figure 5.12**) the behaviour of the partially molten rock must be controlled by the behaviour of the melt, rather than the plastic deformation rate of the matrix of solid grains, even at low melt fractions in the area where a common gradient on stress relaxation curves could be observed (below a strain rate of 10^{-6} s^{-1} at temperatures of 800 to 850 °C and at all studied strain rates below 10^{-3} s^{-1} at temperatures above 850 °C).

By determining the slope of stress relaxation lines (*n value*) that applies to stress relaxation data and fitting polynomial regressions to stress relaxation curves at

individual temperatures, it is possible to formulate a flow law for the deformation behaviour of Westerly granite over the temperature interval of 800 to 1050 °C. Equally spaced points are chosen on individual temperature lines, with the regression repeated for other temperatures, giving equal weighting to all temperatures.

Defining *n* as the inverse slope of the linear fit to the stress relaxation curves at slower strain rates, the slopes of the stress relaxation curves (*n value*) (**Figure 5.12**) of linear fits to the lower strain rate portion of the stress can be expressed using the formula:

$$n = \frac{d\log \dot{\varepsilon}}{d\log \sigma} \qquad \text{E5.01}$$

$$n = 2.92$$

with d marking an increment of increase. The n-value is associated with a root mean squared error (RMSE) for the first order fit of ± 0.266. The RMSE is the standard deviatoric error of stress relaxation data to the linear fit, with strain rate dependent on stress and temperature. The *n value* is the same for all temperatures, as data from all temperatures was used to define the slope, with equal weighting given to each temperature.

The flow law, associated with this stress relaxation behaviour can be given as:

$$\dot{\varepsilon} = D\, e^{-H/RT}\, \sigma^n \qquad \text{E5.02}$$

with D is an exponential scaling factor, H being the activation enthalpy and n being the stress exponent equal to the slope of the curve. This formula can be rewritten as:

$$\log \dot{\varepsilon} = \log D - \frac{H}{RT} + n * \log \sigma \qquad \text{E5.03}$$

The factor H/R is the spacing between the temperature lines. Hence the activation enthalpy can be calculated, for multiple regression, as $H = 510061 \pm 1000$ J mol^{-1}.

The flow law for partially molten Westerly granite can thus be expressed as:

$$\dot{\varepsilon} = 10^{-5.832} \exp \frac{-510061}{RT} \sigma^{2.92} \qquad \text{E5.04}$$

with temperature (T) in Kelvin and stress (σ) in Pascals. Though this formula is only an approximation of the deformation behaviour of partially molten granite under the experimental conditions described above, it is used in melt extraction modeling in **Chapter 8.**

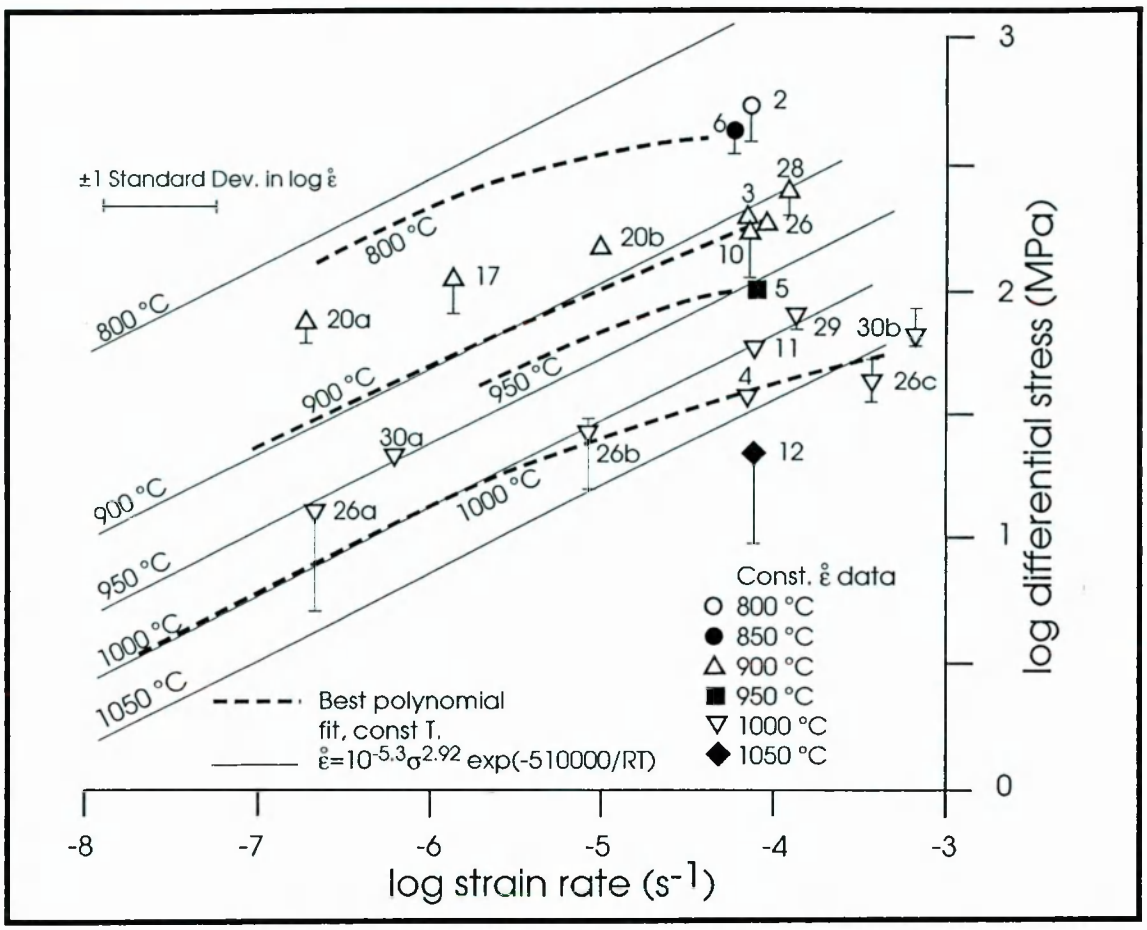

Figure 5.14: First order linear fits to lower strain rate stress relaxation data of samples WG2 to WG13, excluding WG9, giving an n value of 2.92, associated with a root mean square error (RMSE) of ±0.266. Black filled symbols give the point of onset of stress relaxation in selected samples between 900 and 1050 °C.

In order to test the influence of strain on the *n value* of stress relaxation, the slope of the first order fits (**Figure 5.14**) on straight segments of stress relaxation curves was plotted against strain (**Figure 5.15**). Results from multiple regression are plotted as a solid horizontal line between 5 to 20 % strain, with the large white box indicating the RMSE. Tests in which several stress-relaxation events took place are plotted as open and closed symbols, with consecutive stress relaxation events linked by a dot dashed line. Despite a large spread of strains, mainly due to half effective lengths of samples WG28, WG29 and WG30 (**Table 5.01**), no significant increase in *n* values with increasing strain was noted, despite some strain influence on samples such as WG18 and WG26.

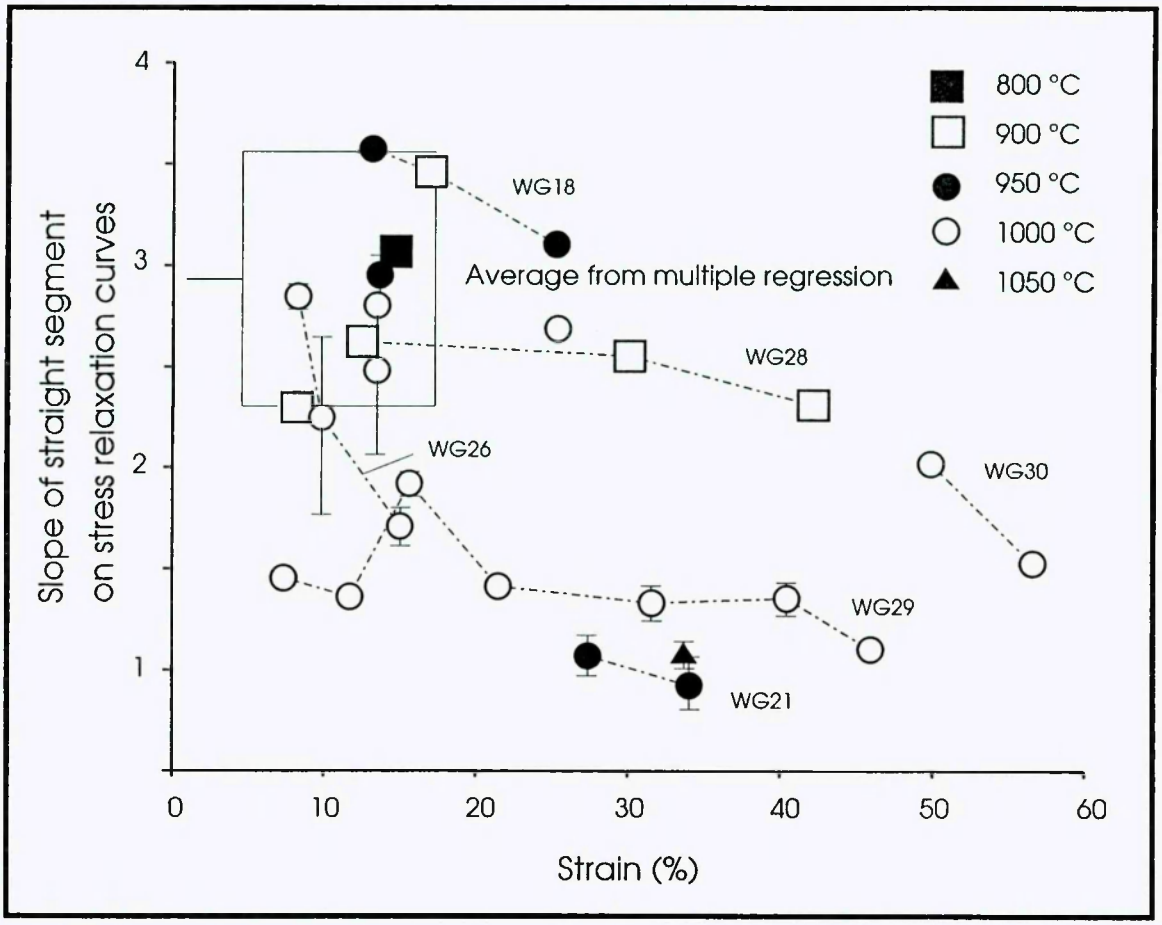

Figure 5.15: Plot of the slope of first order fits of stress-relaxation data versus fraction strain. The white box marks the result from multiple regression data (**Figure 5.12**), while dot-dashed lines link consecutive stress relaxation events of a single sample. Error ranges mark root mean square error ranges for regression on single readings. Points without error ranges have RMSE's less than the diameter of the chosen symbol.

5.6 Morphology of deformed samples

The macroscopic shapes of deformed samples and the location of ridges and faults visible on the iron jacket surrounding each sample are shown in **Figure 5.16**. Conclusions are drawn towards deformation processes at different temperatures. For this purpose the remnants of samples after thin section making (**Appendix 1**) were analysed and their outlines traced (**Figure 5.16**).

Samples deformed at temperatures between 800 and 900 °C developed a single fault plane or conjugate set of faults cutting the specimen obliquely. Between 950 and 1050 °C fault surfaces were less well developed, associated with barrelling of samples giving a more "lumpy" exterior shape and buckling the iron jacket. Thickening of the specimen took place where the fault intersected the sides of the specimen. WG13, deformed at

1100 °C, shows a smooth sample outline with thickening of the specimen at the piston ends, resulting in a dog-bone shaped specimen.

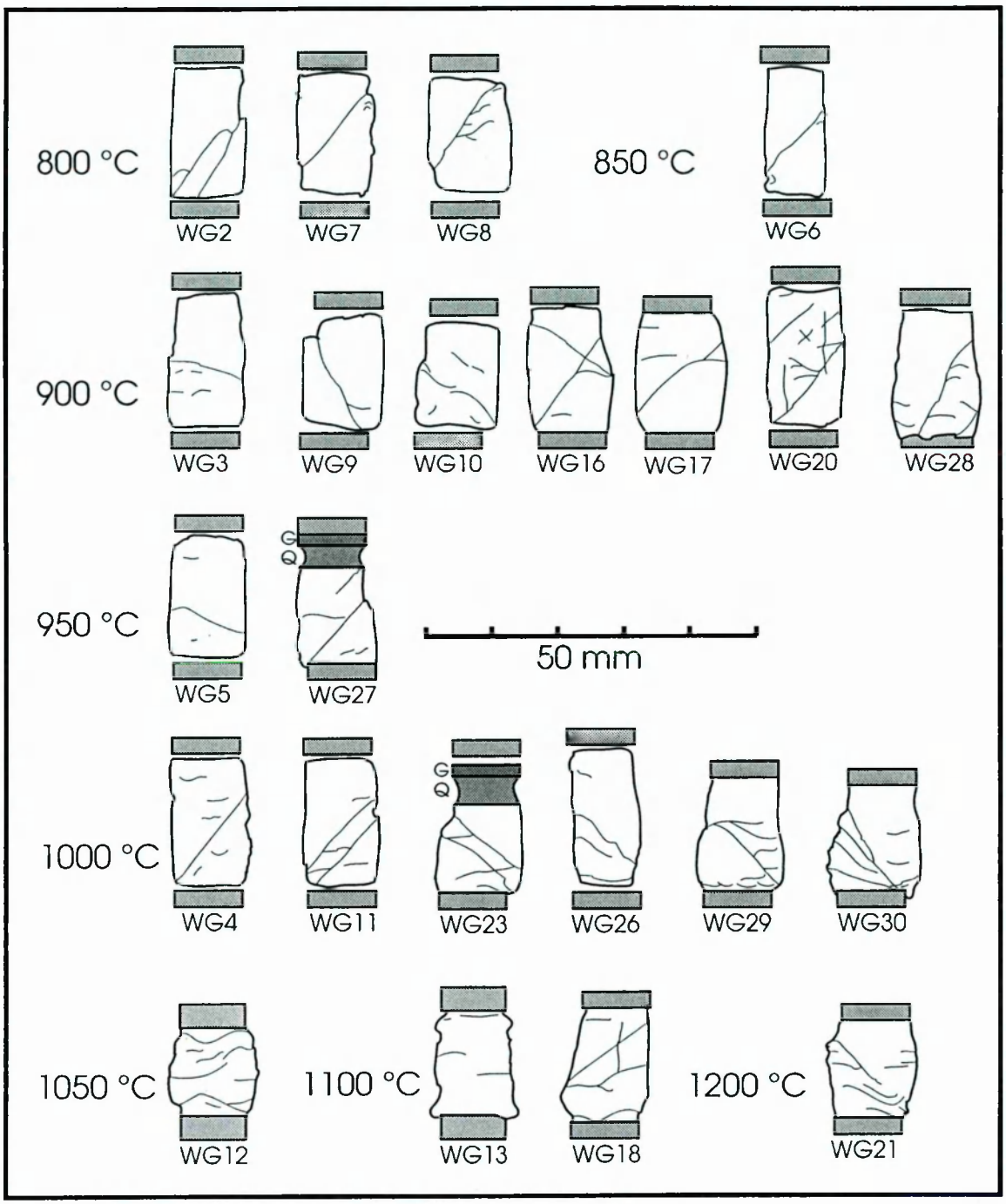

Figure 5.16: Outlines of specimens after thin section making (compare also to **Appendix 1**), at natural scale. Samples were cut longitudinally, at a right angle to any macroscopic faulting, where present. The extraction of one to four thin sections, close to the specimen axis leads to apparent varying thickness of samples. Lines within sample confines detail ridges of fault lines or humps of the iron jacket, mantling the sample. Light grey shaded blocks indicate the location of alumina spacers. Where the spacers are still attached to the specimen analysed the grey squares are drawn adjoining the sample, otherwise a gap is left. Darker shaded areas in WG27 and WG23 show location of crushed quartzite (Q) and Outhibridge Ganister Sandstone (G) (compare also to **Figure 3.10**).

Exceptions from this classification are samples WG27 and WG23, that developed a well defined fault trace, more characteristic of samples deformed at lower temperatures, and samples WG18 and WG21 that faulted despite initial heating to temperatures in excess of 1050 °C. Temperature profiles of 50 °C across samples WG28, WG29 and WG30 resulted in heterogeneous deformation, leading to bulging in the lower half of the samples (where the sample temperature was hotter) and straight sided sections in the colder, upper half.

As suggested by **Figure 5.04**, the deformation behaviour of the samples was controlled more by melt fraction than temperature. A lowering of melt fraction by extraction into adjacent quartzite (WG27, WG23) and neo-crystallization of the melt phase (WG18, WG21) took place in all abnormally shaped samples (**Table 5.1**), suggesting that macroscopic behaviour was primarily controlled by melt fraction. Excluding low melt fraction samples the remaining samples can be divided between those that deform brittilely (below 1050 °C) and those that deform ductilely (above 1050 °C).

The brittle section can further be subdivided into those showing a strong localization of the fault zone and those with more pervasive deformation. This marks the transition between brittle and more ductile deformation behaviour and occurs between 900 and 1000 °C.

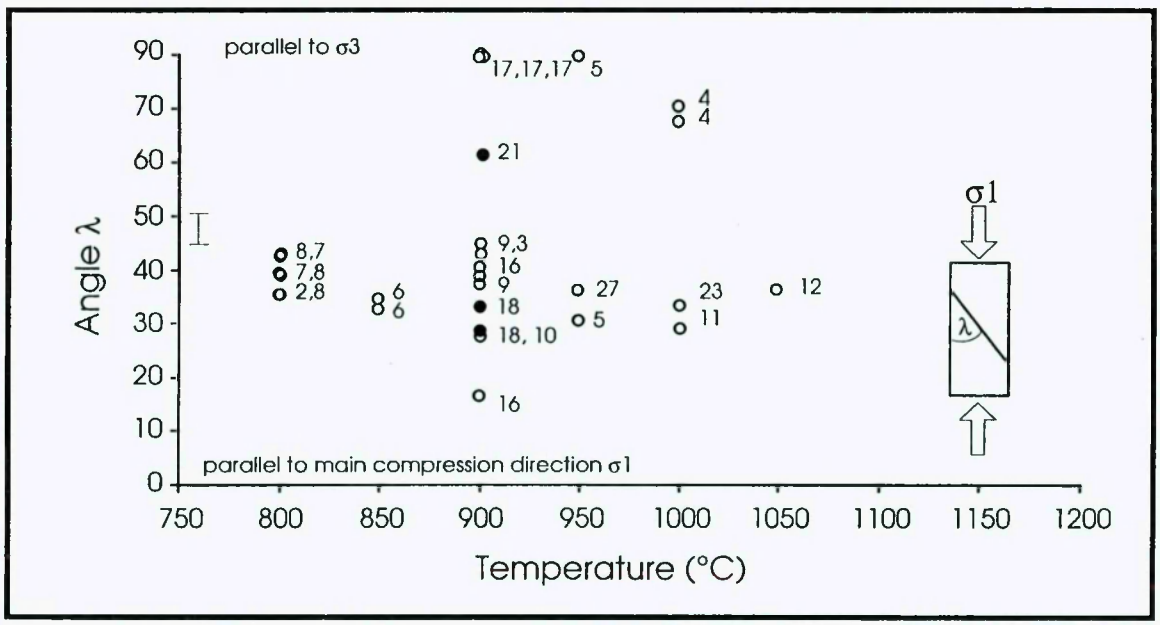

Figure 5.17: Angle of macroscopic faults in deformed samples. $\lambda = 0°$ is parallel to the differential compression direction σ_1, while $\lambda = 90$ °C is at right angles to this orientation and parallel to σ_3. λ is associated with a measuring error of ± 3 °, due to the barreling of samples. Numbers adjacent to

open circles refer to sample number (WG). Filled circles mark fault angles developed in WG18 and WG21 that were initially heated to 1100 and 1200 °C, but deformed at lower temperatures.

Fault angles measured with respect to σ_1 at temperatures between 800 and 850 °C show quite a tight spread between 37 to 47 ° with an average of $\lambda = 42$ ° (**Figure 5.17**). A much wider spread of fault angles is found between 900 and 1050 °C. Here a spread from σ_1 parallel cracks to bulges parallel to σ_3 can be found, with diffuse bulges dominating at the higher temperature end of this zone (compare also to **Figure 5.16**). Deviation from the average 42 ° with increasing temperature and melt fraction must be related to a change in the microscopic deformation behaviour (possibly due to an increase in melt fraction) and will be explored further in **Chapter 7**. No fault zones were observed in samples deformed at temperatures in excess of 1050 °C.

5.7 Summary and conclusion

Differentially deformed samples of partially molten Westerly granite show an initial approximately linear increase in stress with increasing strain until the yield point is encountered, followed by a more gradual rise in stress until the ultimate strength of the sample has been reached (**Chapter 5.2.1**). While some samples show strain softening with a further increase in strain, other samples (deformed at the same temperature and strain rate conditions) display more diffuse yield behaviour without strain weakening at higher strains, thus indicating different evolutions of microstructures. This difference in stress-strain behaviour can be attributed to a difference in phase distribution and composition of phases in the starting material due to large crystal diameters (~ 0.96 mm) and small sample sizes (10 mm diameter and 20 mm height).

With increasing temperature a steep decline in supported stress from 800 °C (520 MPa) to 1100 °C (3 MPa) can be observed (**Chapter 5.2.2**), associated with a more diffuse yield behaviour. The ultimate strength of samples was reached at similar strains (ε_U average = 4 %) over the temperature interval. However, the fit of decrease in stress with increasing temperature is less satisfactory than the fit with increasing melt fraction (**Chapter 5.2.4**). A linear fit of log stress versus melt fraction between $\phi = 0.03$ and 0.477 confirms the absence of a *critical melt fraction* (van der Molen & Paterson 1979) at $\phi = 0.30$. The steepest decline in strength occurs in the melt interval between $\phi = 0.03$ and 0.10 and agrees with data by van der Molen and Paterson (1979). Stress supported throughout the stress-strain experiment is proportional to the applied strain rate (**Chapter 5.2.5**). This relationship is unaltered by the deformation history of the sample (**Chapter 5.2.6**).

Stress relaxation tests show little stress relaxation of samples between 800 and 850 °C at strain rates faster than $1 * 10^{-6.5}$ s^{-1}. Below this strain rate and at temperatures in excess of 850 °C stress relaxation occurs at a common slope (**Chapter 5.3.1, 5.3.2**). Sample heterogeneity has little influence on the supported stress (**Chapter 5.3.2**). The supported stress is closely linked to the melt fraction. An increase in melt fraction is associated with a decrease in supported stress and vice versa. There is insufficient evidence to support the notion that an increase in strain results in a decrease in supported stress (**Chapter 5.3.4**). While strain softening is evident in some samples (e.g. WG26 in **Figure 5.11, a**), no strain softening is observed in others (e.g. WG29 in **Figure 5.11, b**). There is no increase in slope of stress relaxation curves with increasing temperature and melt fraction, indicating that there is no change from matrix dominated to melt dominated deformation behaviour over the temperature (800 to 1050 °C) and melt fraction (3.5 to 33.5 %) interval. Instead samples are presumed to be dominated by melt deformation behaviour, even at low melt fractions (ϕ = 0.03) in stress relaxation experiments. Stress relaxation data was used to predict the shape of stress-strain curves at 900 and 1000 °C in stress - strain - strain rate space at strain rates below those accessible in stress-strain experiments. Using a combination of stress-strain and stress relaxation data indicates that a sample deformed at geologically realistic strain rates ($1 * 10^{-13}$ s^{-1}) at the temperature interval of 800 to 1050 °C will pose little resistance to deformation (<< 1 MPa).

Using multiple regression on stress relaxation data it is possible to establish a flow law for partially molten Westerly granite deformed under the presented experimental conditions (**Chapter 5.5**). The slope of stress relaxation curves (*n-value*) of 2.92 equals the stress exponent in the flow law and the spacing of temperature lines in **Figure 5.14** allow an activation enthalpy of H = 510061 J mol^{-1} to be calculated. Thus the flow law can be written as $\dot{\varepsilon} = 10^{-5.832} e^{(-510061/RT)} \sigma^{2.92}$ (E5.04) with R being the gas constant in J mol^{-1} K^{-1} and T the sample temperature in Kelvin.

The morphology of deformed samples (**Chapter 5.6**) suggests that three different macroscopic deformation behaviours operate over the temperature interval:

1. 800 - 900 °C: Samples with localized brittle fault
2. 900 - 1050 °C: Samples with more pervasive brittle deformation
3. > 1050 °C: Ductilely deforming samples

Samples with reduced melt fractions indicate that deformation behaviour is strongly influenced by melt fraction, rather than temperature (compare also to **Chapter 7**). The change in fault angles from λ = 42 ° (± 3 °) at 800 to 900 °C to a much larger spread between 900 and 1050 °C from axial cracking (parallel to σ_1) to specimen bulges parallel to σ_3 confirm a change in deformation mechanism.

Chapter 6

Melt viscosity and activation enthalpy

6.1 Introduction

In order to understand the deformation behaviour of partially molten WESTERLY GRANITE it is necessary to understand the properties of the melt phase. Melt viscosity, which varies significantly with both water content and temperature, will control the strain rate when the deformation is accommodated by melt flow.

There are severe difficulties when trying to measure the viscosity of a melt derived from a partially molten rock. In the high pressure / temperature apparatus used in the present study it is not possible to extract the small quantities of melt generated to allow direct measurement of viscosity by conventional methods, such as monitoring the speed of falling spheres. Instead an effort was made to determine the melt viscosity indirectly, making observations within the confines of the experimental setup.

Two approaches were taken to attempt to estimate the properties of melt alone. In the first, samples were initially heated to 1100 or 1200 °C in order to fuse most of the rock volume. The temperature was then lowered rapidly to between 850 and 1000 °C, whereupon the sample was deformed. Melt viscosity was estimated using stress relaxation or constant stress creep data for what was ideally a cylindrical sample of viscous liquid. In the second approach, melt was allowed to penetrate into the pores of an adjacent layer of quartz sand. The depth of penetration at different temperatures was used to calculate melt viscosity and its temperature sensitivity. In this chapter both approaches are described and results are discussed in detail.

6.2 Apparent viscosity measurement by stress relaxation, creep or constant strain rate deformation

Two samples were initially heated to 1100 (WG18) and 1200 °C (WG21) in order to fuse most of the rock volume ($T_{initial}$) (**Table 6.1**). The temperature was then lowered rapidly to the range of 850 to 1000 °C, where the samples were deformed (T_{def}).

Sample	WG18				WG21			
$T_{initial}$ (°C)	1100				1200	const. stress creep		
$P_{confining}$ (MPa)	250				250			
T @ def (°C)	1027	946	896	946	900	850	900	953
t before def (h)	3.5	4.5	5.5	24.5	18.0	20.0	23.5	42.0
σ_{max} (MPa)	4.61	82.83	176	104.1	30.0	30.0	30.0	30.0
strain rate (s^{-1})	1E-5	2E-4	1E-4	8E-4	2E-07	6E-06	2E-07	5E-06
ε_{max} (%)				24.51				32.66
t total (h)				25				47.75
glass ϕ + ncryst				0.47				0.625
glass ϕ				0.256				0.160

Table 6.01: Deformation history and melt fractions of temperature stepping experiments WG18 and WG21.

Assuming that the mechanical behaviour of the rock is melt controlled in samples containing in excess of $\phi = 0.45$ melt (this is well in excess of the melt fraction of $\phi = 0.35$ above which it is to be expected that solid phases no longer form an interconnected structural framework) it should be possible to measure viscosity and activation enthalpy values close to those of pure melt. It was impossible to measure the strength directly of samples deformed at temperatures as high as 1100 and 1200 °C, because the jacket strength exceeds that of the sample at these temperatures (**Appendix 3**). The samples were deformed at temperatures between 850 and 1000 °C (**Table 6.01**), therefore the increase in apparent viscosity with decreasing temperature allowed meaningful stress-strain and stress relaxation measurements to be recorded.

Apparent viscosity (of melt plus crystals) was measured indirectly at temperatures of 900 and 1000 °C. The apparent viscosity (η) of the sample can be calculated as (Nadai 1930; Griggs 1936):

$$\eta = \frac{(\sigma_1 - \sigma_3)}{3\,\dot{\varepsilon}} \qquad \text{E 6.01}$$

where $(\sigma_1 - \sigma_3)$ is the differential stress applied and $\dot{\varepsilon}$ is the axial strain rate. The $(^1/_3)$ factor takes into account the axisymmetric deformation geometry, as the viscosity is defined as shear stress divided by shear strain rate.

Two contrasting deformation regimes were applied to attempt to measure apparent melt viscosity. In the first sample (WG18) a constant strain rate testing routine was used

and stress relaxation data were recorded at various temperatures. The second sample (WG21) was deformed under a constant stress creep regime, with the resultant strain rates used to calculate apparent viscosity.

6.2.1 Viscosity estimate using temperature stepping associated with stress relaxation

For the test WG18 a rock sample was initially heated to 1100 °C for 4 hours producing ϕ = 0.47 melt, followed by a step-wise lowering of temperature to 896 °C (**Table 6.01**).

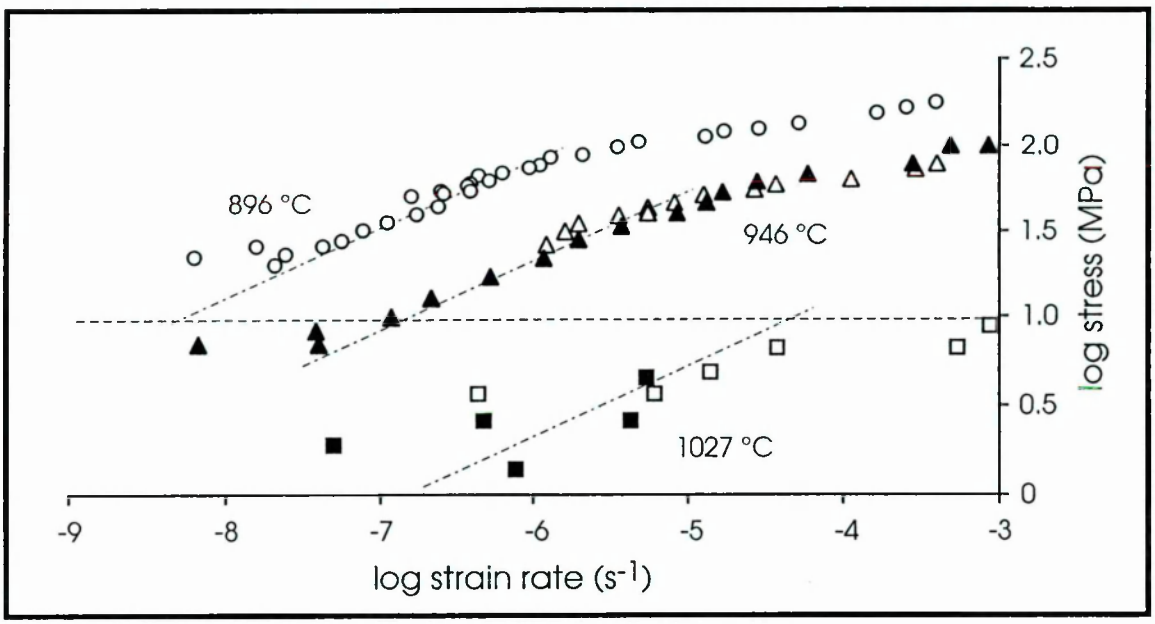

Figure 6.01: Stress relaxation curves of WG18 at 1027 to 896 °C. The dashed line indicates level of stress (10 MPa) at which strain rate was read off to calculate bulk viscosity. Dot-dashed lines lines mark general trends of different stress relaxation events.

As the slope of the stress relaxation (**Figure 6.01**) curves does not equal unity, the bulk rheology is non-Newtonian. The apparent viscosity decreases with increasing stress. It is therefore necessary to state at what stress value the viscosities were calculated. The stress relaxation paths were plotted (**Figure 6.01**) and strain rates read off at a common differential stress value of 10 MPa. The stress of 10 MPa was chosen as it is significantly above the stress supported by the iron sample jacket over the temperature interval (**Appendix 2**) and is accessible at more than one temperature. Apparent viscosity estimates using WG18 stress relaxation data at various temperatures are given in **Table 6.02**:

Temperature (°C)	Viscosity @ 10 MPa for WG18
896	$1.6 * 10^{14}$ Pascal seconds
946	$4.2 * 10^{13}$ Pascal seconds
1027	$1.6 * 10^{12}$ Pascal seconds

Table 6.02: Apparent sample viscosities at $(\sigma 1 - \sigma 3) = 10$ MPa as a function of temperature, calculated from stress relaxation data of WG18.

6.2.2 Viscosity measurement using temperature stepping associated with constant creep stress deformation

In contrast to WG18, the sample WG21 was deformed under constant stress creep conditions (**Figure 6.02**). A constant stress of 30 MPa was applied at temperatures of 846, 900, and 953 °C, after the sample had been cooled from 1200 °C, and the increase of strain with time was recorded.

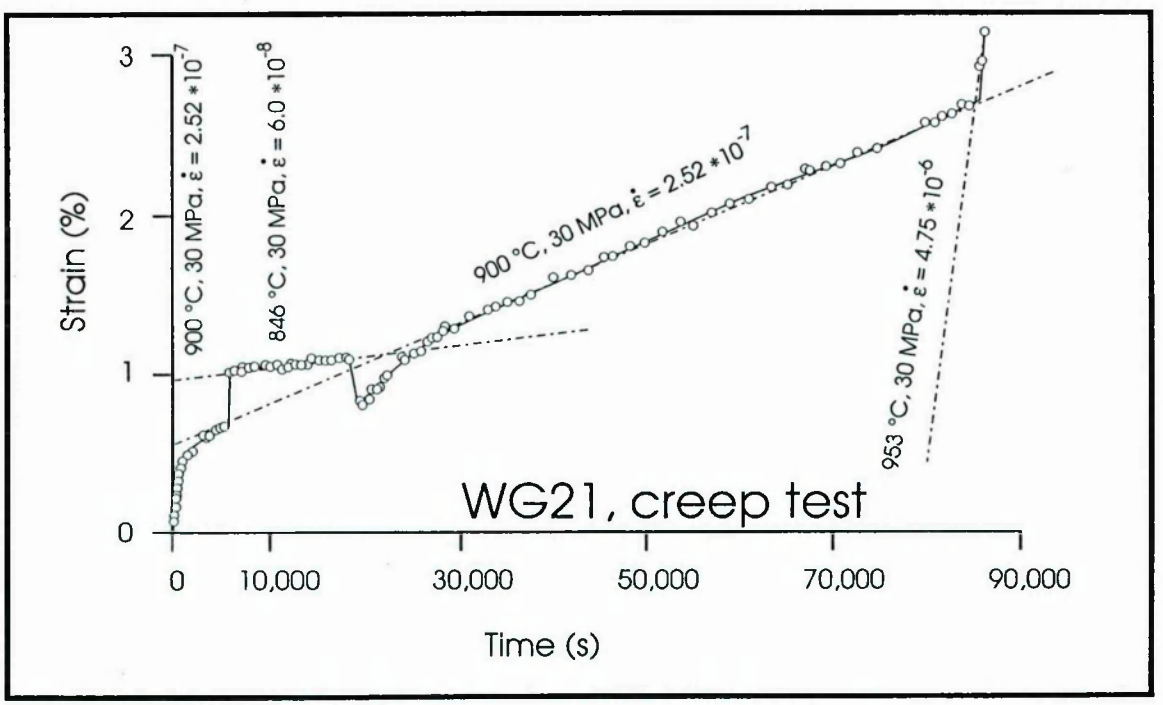

Figure 6.02: Strain - time plot of WG21 deformed under constant creep conditions at 846, 900 and 953 °C, after initial heating to 1200 °C. A change in temperature is associated with a change in the strain rate. Open circles mark a selection of individual data points, while the dot-dashed lines are first order fits to strain-time data. Calculated strain rates are listed.

Using the constant stress value plus measured strain rates it is possible to calculate the viscosity of this sample, using equation **E6.01**:

Temperature (°C)	Viscosity @ 30 MPa for WG21
953	$2.1 * 10^{12}$ Pascal seconds
900	$4.0 * 10^{13}$ Pascal seconds
846	$1.6 * 10^{14}$ Pascal seconds

Table 6.03: Apparent sample viscosities of WG21 deformed at constant creep conditions at ($\sigma 1$ - $\sigma 3$) = 30 MPa.

6.2.3 Discussion

While apparent viscosities of WG18 and WG21 are quite close to the viscosities predicted by Shaw (1965) at high temperatures (1100 and 950 °C respectively) apparent viscosities are significantly increased at lower temperatures (**Figure 6.03**). The most pronounced change in viscosity is between 1000 and 1100 °C in WG18 and between 950 and 900 °C in WG21.

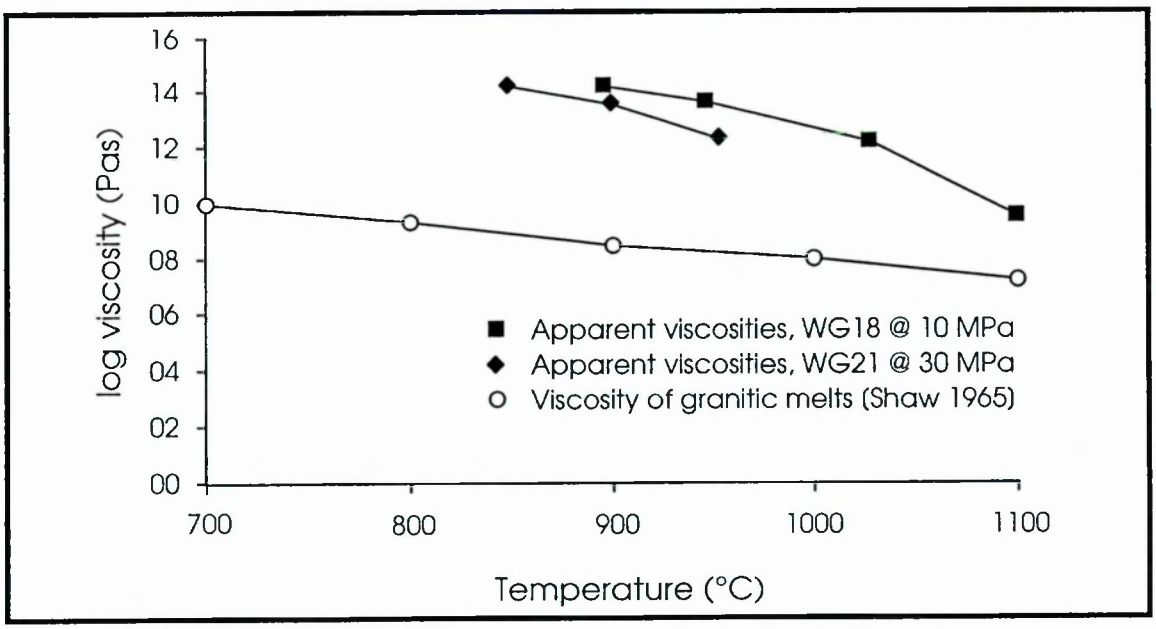

Figure 6.03: Change in apparent viscosity with temperature in WG18 and WG21 with viscosity of granitic melts by Shaw (1965) plotted as reference.

On thin section examination, much of the melt phase in both samples was found to have crystallized (**Table 3.01**, **Table 3.03**, **Table 6.01**, and **Figure 3.08**, **Figure 4.15**). As a result of neo-crystallization the glass fraction in both samples was reduced, from ϕ = 0.470 to 0.256 in WG18 and ϕ = 0.625 to 0.16 in WG 21. The hoped for high melt fractions during deformation were not realised. It is suggested that the steepest portion of the viscosity temperature trend for WG18 in **Figure 6.3** marks the onset of neo-crystallization.

The lowest viscosity difference between Shaw's (1965) empirical data and those calculated from deformation data of WG18 and WG21 were recorded at the start of deformation tests, possible before crystallization of the melt phase occurred (compare also to **Chapter 5.3.3**).

6.3 Melt viscosity and viscosity activation enthalpy calculations from melt permeation experiments

In a second approach to measure melt viscosity, a 4 mm long cylindrical section of loose quartz sand, of initially 200 μm mean grain diameter (d), was mounted at one end of the granite sample to act as a trap for melt squeezed out of the granite. Tests were carried out at 940 and 1000 °C (**Table 6.04**).

sample	WG23	WG24	WG25	WG27
T (°C)	1000	1000	940	950
$P_{confining}$ (MPa)	250	250	250	250
σ_{max} (MPa)	194.2	static	static	243.42
ε_{max} (%)	24.52	static	static	24.95
strain rate (s^{-1})	5E-05	static	static	1E-04
t before def (h)	2	static	static	4
t total (h)	3.75	3.3	3.5	7.6
ϕ in granite	0.089	0.088	0.06	0.076
ϕ granite + qtz	0.103	0.096	0.06	0.08
penetration (mm)	3.1	2.57	0	0.88

Table 6.04: Treatment histories and melt fractions for melt extraction experiments.

The melt extracted from the granite was squeezed into the pore spaces between the quartz grains (**Figure 3.10**), where a porosity (ϕ) of $\phi = 0.059$ was retained in the quartz layer after the experiments were completed. This porosity was determined by tracing pore space outlines from SEM collages and calculating the area fraction using the IGRAINS computer program (Evans 1995). A sharp boundary exists between quartz pore spaces entirely filled by melt and those filled by air (**Figure 3.10**). In no case was partial wetting of pore spaces observed. The boundary between melt filled and air filled porosity is slightly curved, with less penetration at the edges of the specimen. This was due to a higher degree of quartz grain hydrostatic crushing at the edges of the specimen and/or viscous boundary drag. There was no significant difference of penetration depth between deformed and hydrostatic tests. The hydrostatic pressure alone was sufficient in all cases to cause impingement crushing of the quartz grains and

to drive melt from the partially molten granite (at 250 MPa confining pressure) along a steep pressure gradient into the quartzite pores (effectively at zero pressure).

6.3.1 Viscosity calculation

The analysis is based on measuring the maximum distance that the melt has permeated in a known time (a few hours), driven by a melt pressure gradient from P_O (250 MPa) in the source region to effectively zero pressure in the pore spaces (1 MPa was used in calculations). The problem is analogous to the one-dimensional flow of heat into a half-space ($x > 0$) initially at a low temperature from an interface ($x = 0$) suddenly raised to a higher temperature at time $t = 0$ and maintained at that value for $t > 0$ (Carslaw & Jaeger 1959). For the analogous problem of permeation, the solution is:

$$\frac{P(x,t)}{P_O} = \mathrm{erfc}\,\frac{x}{2\sqrt{k\,t/\beta\,\eta}} \qquad \text{E6.02}$$

where $P(x, t)$ is the melt pressure in the zone of permeation, P_O is the source pressure, k is permeability, β is the fluid storage capacity of the solid, k is the permeability of the crushed quartz, η is the fluid viscosity, and *erfc* is the complementary error function (see Turcotte & Schubert (1982) p. 160, Table 4-5 for *erfc* calculation and values), that can be approximated by

$$\mathrm{erfc}\,(u) = 1 - (1 - \exp(-4\,u^2/\pi)^{1/2} \qquad \text{E6.03}$$

for the dummy constant u. The crushed quartzite porosity (ϕ) and grain size (z) were used to estimate the permeability (k) of the quartz grains using the relation **E6.04** (after McKenzie 1984), but with the denominator set at 400 to be consistent with the results of Bourbie & Zinszner (1985) on Fountainellen Sandstone of the same porosity.

$$k = \frac{z^2\,\phi^3}{400} \qquad \text{E6.04}$$

Using values of $\phi = 0.059$ and $z = 200 * 10^{-6}$ m (see above), the permeability is $k = 2 * 10^{-14}$ m^2.

The fluid storage capacity of the quartzite, β, is given by (Fischer 1992)

$$\beta = C_b + \phi\,C_f - (1 + \phi)\,C_r \qquad \text{E6.05}$$

where C_b is the compressibility of the pore-free quartzite, C_f is the compressibility of the melt and C_r is the quartzite compressibility. β can be approximated by $\phi\,C_f$, assuming

that C_b is proportional to C_f. Substituting values for $C_f = 8 * 10^{-11}$ Pa^{-1} as reported by Murase & McBirney (1973) for molten rocks at 1000 °C, and setting $P(x, t) / P_0 = 0.001$, with $P(x, t) \sim 0.1$ MPa at the maximum distance attained by the melt front after time t, where $x = 3.1$ mm and $t = 3.75$ hours (**Table 6.04**) the viscosity can be calculated as:

$$\eta = \frac{6.2\, k\, t\, \pi}{\beta\, x^2} \qquad \text{E6.06}$$

with $\eta = 0.99\ 10^8$ Pas (± 0.6) at 1000 °C for WG23. The factors of *6.2* and π give a simplifief solution to the complimentary error function. The viscosity estimate might be slightly high, as the model assumes for grains with constant diameter. Instead voids contain suspended fragments (**Figure 3.10**) that can restrict throat sizes between voids, decreasing the permeability.

6.3.2 Viscosity activation enthalpy calculation

The value of the activation enthalpy for viscous flow of melt (Q) does not depend on the values of ϕ, β and k, but only on the ratios of the transport distances and times, x_1, x_2, t_1 and t_2 respectively, at the two temperatures T_1 and T_2. Thus:

$$Q = R \frac{\ln\left(\left(\frac{x_1}{x_2}\right)^2 \cdot \left(\frac{t_2}{t_1}\right)\right)}{\left(\frac{1}{T_1} - \frac{1}{T_2}\right)} \qquad \text{E6.07}$$

Using values for x and t of WG23 and WG27 (**Table 6.05**) a value of $Q = 320 \pm 51.2$ kJ mol^{-1} can be calculated. The only known entity in **E6.05** is the C_f, the compressibility of the melt. However, as the melt is likely to be the most compressible entity the pore-free-solid and rock are assumed rigid with all compression taken up by the melt. This assumption leads to a large error margin on the viscosity value (correct within an order of magnitude), whereas the value for Q may be correct to 20% (error due to curved permeation front of melt and uncertainties of time estimates). From Shaw (1972) the value of Q for dry obsidian is 360 kJ mol^{-1}, and the viscosity at 1000 °C is $1.4 * 10^8$ Pas, close to the result obtained from the melt penetration experiment ($0.99 * 10^8$ Pas).

6.4 Viscosity variation with temperature and weight percent water

In order to compare melt viscosities to apparent sample viscosities, it is necessary to extrapolate the viscosity calculated from the permeation experiments at 1000 °C to

higher and lower temperatures. This together with the viscosity variation with water content is required for the modeling presented in **Chapter 8.**

At constant water content, the temperature dependency of viscosity is of the form (Shaw 1972):

$$\eta = \text{const} + \exp(Q/RT) \qquad \text{E6.08}$$

Where Q is the activation enthalpy for viscous flow of melt (determined to be 320 kJ/mol, see above), R is the universal gas constant and T is the temperature in Kelvin. Using equations **E6.06** and **E6.05** the equation **E6.07** can be re-written as:

$$\eta = 8.13 * 10^{-6} \exp(320000/RT) \qquad \text{E6.09}$$

6.5 Comparison of melt viscosity with apparent viscosity from deformation tests.

The deformation behaviour of partially molten experimental charges is controlled by both the melt and solid phases; therefore it is instructive to compare the maximum stress supported by deformed charges with the predicted behaviour of $\phi = 0.1$. In **Figure 6.04** the melt fraction is plotted against the maximum supported strength of experimental charges, deformed at a constant strain rate of $8*10^{-5}$ s^{-1}(**Table 5.01**). The x-axis can also be divided into a temperature scale, due to the melt fraction temperature dependence determined in **Chapter 3.3.** The theoretical maximum supported stress of the melt at a particular temperature can be calculated from the melt viscosity, the maximum supported stress, at constant strain rates, being proportional to the viscosity (**E6.01**). For **Figure 6.04** the melt viscosity calculated at 1000 °C from the WG23 permeation experiment was extrapolated to 800 and 1200 °C using **E6.09** (**Table 6.05**).

Temperature (°C)	viscosity (Pas)	σ_{max} (MPa)
800	$2.7 * 10^{10}$	6.7
900	$1.4 * 10^{9}$	$3.2 * 10^{-1}$
950	$3.4 * 10^{8}$	$8.2 * 10^{-2}$
1000	$1.0 * 10^{8}$	$2.4 * 10^{-2}$
1100	$1.2 * 10^{7}$	$2.7 * 10^{-3}$
1200	$1.7 * 10^{6}$	$4.0 * 10^{-3}$

Table 6.05: Melt viscosities and ultimate strengths at temperatures between 800 and 1200 °C, calculated using equation **E6.09.**

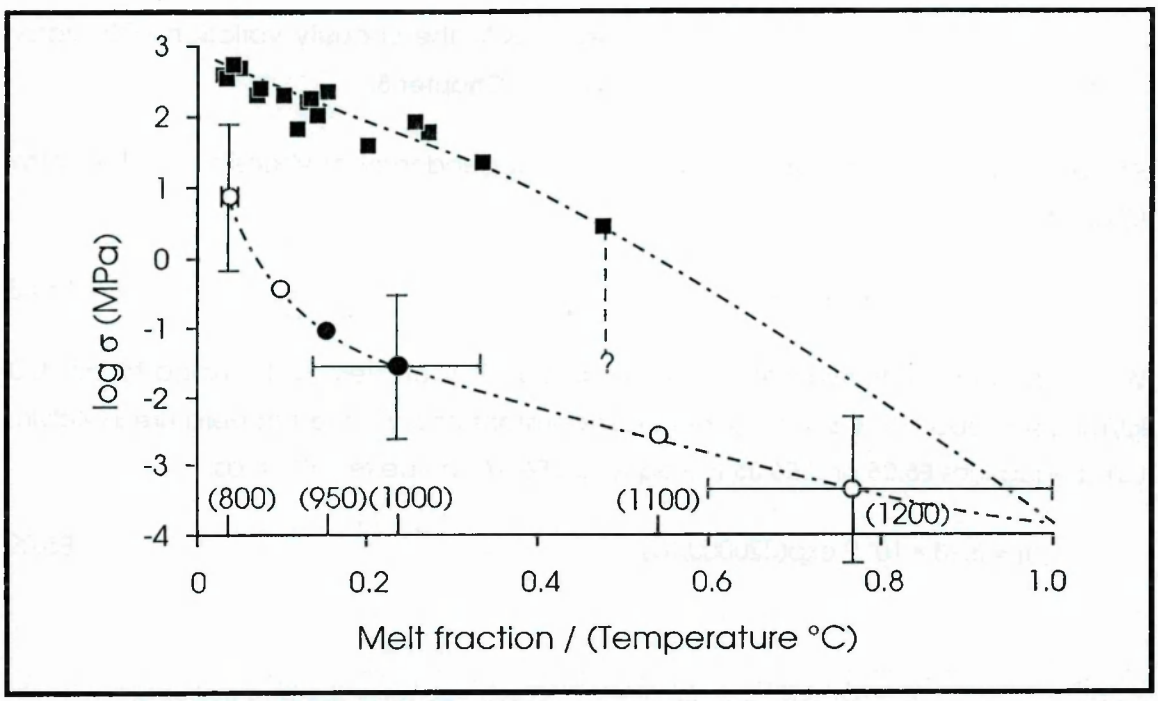

Figure 6.04: Plot of log maximum supported stress (equivalent to effective viscosity) against melt fraction and temperature at a constant strain rate of $5 * 10^{-5}$ s^{-1}. The maximum supported stress of all tests deformed at $5 * 10^{-5}$ s^{-1} is shown as filled squares. The filled circle is the calculated maximum supported stress of melt alone of $\eta = 0.99 * 10^{8}$ Pas at 1000 °C (as calculated in **Chapter 6.3.1**). Open circles represent maximum stress of melt between 800 and 1200°C extrapolated using **E6.08** (see **Table 6.05** for values). The temperature scale is derived from melt fraction by **E3.01** below 1050 °C; melt fraction of WG21 (neo-crystals plus glass fraction) was used to locate 1200 °C.

The results presented in **Figure 6.04** clearly indicate that, for the experiments on Westerly granite described here, the trend of decreasing effective viscosity with increasing melt fraction can be projected to intersect the 100 % melt viscosity trend with no step-like decreases in viscosity. This contrasts sharply with a step-like decrease in effective viscosity which van der Molen and Paterson (1979) suggested occurred at a *critical melt fraction*, where a transition from matrix to melt dominated sample behaviour occurs. Instead there is a smooth transition from effective viscosity dominated by matrix deformation behaviour to melt viscosity over the melting interval (**Figure 5.04**, **Figure 6.04**).

The results of van der Molen & Paterson (1979) apparently indicate that a critical melt fraction should have been observed in the Westerly granite tests between $\phi = 0.30$ and 0.40 melt fraction. Their experiments were all carried out at 800 °C, with increasing melt fraction achieved by adding from 0 - 2 % water to the samples (**Figure 6.05**); the highest melt fraction ($\phi = 0.24$) was achieved by first crushing the charge before adding 2 % water. It was also assumed that $\phi = 1.0$ granitic melt would have a viscosity of 10^{4} Pas. Problems with their approach are as follows:

1.) The addition of water to achieve higher melt fractions will significantly reduce the melt viscosity (Shaw 1965,).

2.) Crushing the final charge increased the sample porosity fraction to approximately 0.4 yet melt fraction was only $\phi = 0.24$, thus leaving a remnant porosity fraction of 0.16 in the partially molten sample. As shown by Rutter & Hadizadeh (1992), this would have dramatically reduced the mechanical strength of the sample.

3.) The viscosity assumed for $\phi = 1.0$ melt is considerably lower ($1 * 10^4$ Pas) than that predicted by Shaw (1965) for 800 °C and 2 % water ($\eta = 10^7$ Pas).

Up to $\phi = 0.20$, the data of van der Molen & Paterson (1979) define a trend very similar to that recorded in the present research (**Figure 5.04**). However, in their experiments the increase in melt fraction is directly linked to the increase in added water which would have reduced the melt viscosity in the same manner as temperature in the current experiments. The deviation of the powder sample from their log stress melt fraction trend, with a maximum supported stress below the detection limit of van der Molen & Paterson's (1979) apparatus (**Figure 6.05, a**), could be due to the increased initial porosity as suggested in **2.)** above. Finally, if more realistic higher granitic melt viscosities had been used by van der Molen & Paterson (1979) in their figure 14 (**Figure 6.05, b**) the necessity for a critical melt fraction would have been much less compelling.

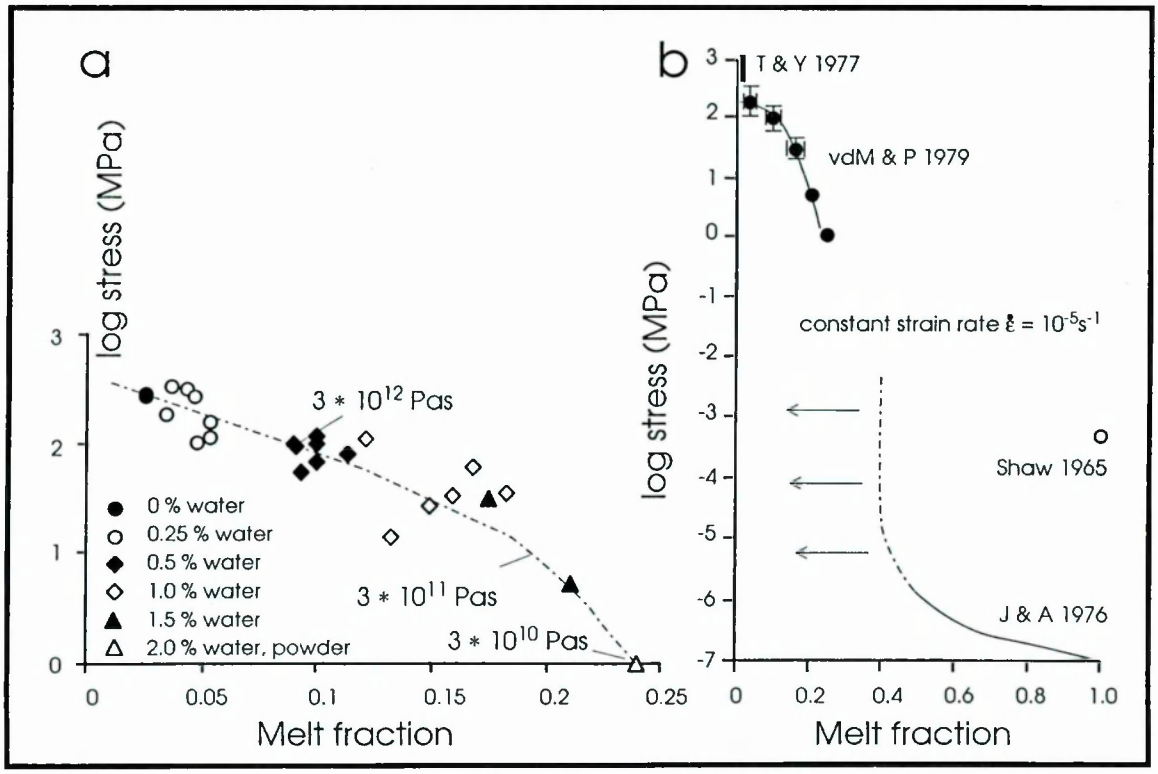

Figure 6.05: Effect of increasing melt fraction on ultimate strength and thus apparent viscosity of Delegate aplite (NSW Australia) with data from van der Molen & Paterson (1979). All samples were deformed at a common temperature of 800 °C and strain rate of $1 * 10^{-5}$ s^{-1}. The key indicates that different symbols are given to groups of samples to which varying weight fraction

of water have been added. In contrast to all others, the open triangle marks a test where the sample was crushed, prior to the addition of 2 wt % H_2O, in order to raise the produced melt fraction **a.)** log maximum supported stress versus melt fraction; **b.)** Plot of log differential stress versus melt fraction as published by van der Molen & Paterson (1979). Range bar (T&Y) shows range of plastic flow of Westerly granite between 700 and 900 °C, strain rates of 10^{-6} s^{-1} and high confining pressures (150 - 1500 MPa) after Tullis & Yund (1977), while the lower curve shows relative viscosity of suspension with a fluid viscosity of 10^4 Pas (after Jeffrey & Acrivos 1976). Filled circles are data from experimental deformation of Delegate aplite of van der Molen & Paterson (1979), while the open circle marks viscosity of granitic melt with 2 wt % water at 800 °C (after Shaw 1965).

6.6 Summary and Conclusions

It is felt that melt viscosities estimated using the temperature stepping methods (**Chapter 6.2**) are overestimates, due to large scale neo-crystallization of the melt phase during the deformation interval.

Melt viscosity estimated by the permeation experiment on WG23 (**Chapter 6.3**) is considerably lower than those estimated at similar strain rates and temperatures in samples using the temperature stepping method ($\eta = 10^8$ Pas ± 0.6 at 1000 °C), and agree with data of Shaw (1965). The activation enthalpy for viscous flow of melt was calculated to be $Q = 320 \pm 51.2$ kJ/mol.

With the aid of the activation enthalpy it was possible to approximate the melt viscosity of Westerly granite melt as $\eta = 8.13 * 10^{-6} \exp(320000/RT)$ (**Chapter 6.4**).

Comparing effective viscosity (max stress supported by matrix plus melt) with the viscosity of the melt a slow convergence of the two values with increasing melt fraction was observed (**Chapter 6.5**). No *critical melt fraction* was observed.

Chapter 7

Deformation microstructures

7.1 Introduction

In this chapter the microstructures of deformed Westerly granite charges are described. The variation of deformation style, as deformation temperature and stress-strain history are varied, is evaluated and the implications for melt extraction mechanisms are discussed. Finally the deformation mechanisms developed are placed in a geological context. All microstructural descriptions and conclusions are the work of the author; the discussion of geological context derives from the paper by Rutter and Neumann (1995).

7.2 Micro-cracks

The most prominent microstructures observed in all experimental charges heated at 250 MPa were grain transecting micro-cracks. These are developed in both hydrostatic and differential stress experiments. Crack maps were made (by tracing cracks from SEM collages (**Appendix 3**)) for a suite of both hydrostatic and differential stress samples.

In the hydrostatic experiments (WG 14 and WG15, **Figure 7.02, 7.03**), cracks develop without a strong preferred orientation. No shear displacement was seen across any of the cracks and they are not penetrated by melt. In differential stress tests (**Figures 7.04** to **Figure 7.02**) the cracks only rarely accommodate shear strain (e.g. the fault zone in WG2, **Figure 7.04**) but they commonly become dilatant and are penetrated by melt (e.g. WG 5 (**Figure 7.06**), WG12 (**Figure 7.07**) and WG13 **Figures 7.08**). The large areas of melt glass in WG13 (**Figure 7.08**) contain a low density of cracks that tend to be short.

Crack density and crack orientations were explored using scanned images of the crack maps using the IGRAINS and CRACKS software packages (**Appendix 3**). Apart from the marked increase in crack density over the starting material, no systematic variation of crack density with either temperature, maximum differential stress or strain rate could be defined (**Figure 7.1, Table 7.1**). Samples at temperatures below 0.2 melt fraction show a greater spread of crack densities than those heated to higher melt fractions.

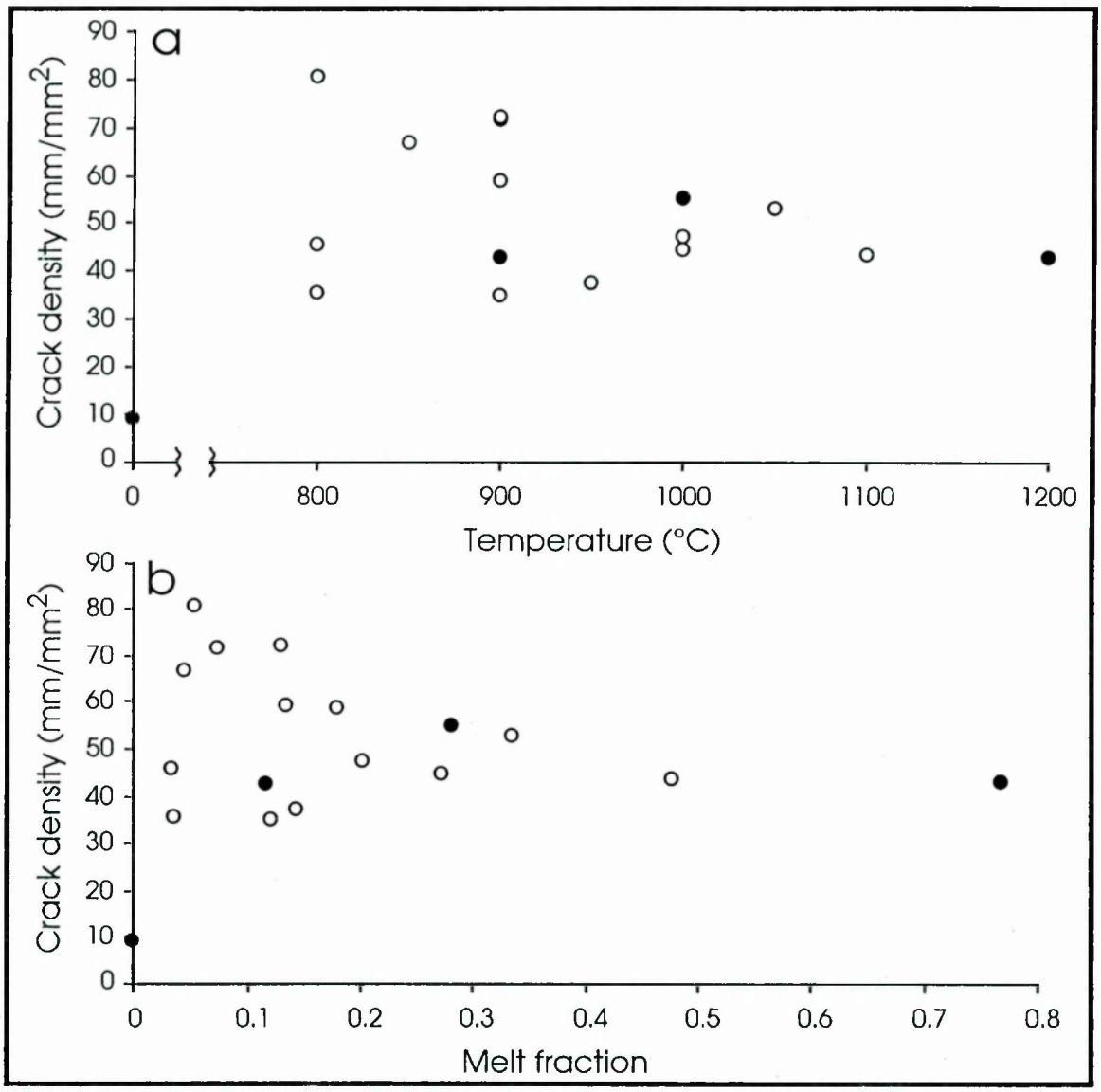

Figure 7.01: Crack densities of deformed (open circles) and static (filled circles) tests plotted against temperature and melt fraction. The starting material is plotted as a filled circle at 0 °C and 0 melt fraction.

Figure 7.03: SEM collage of the static sample WG15 with phase boundary and crack maps.

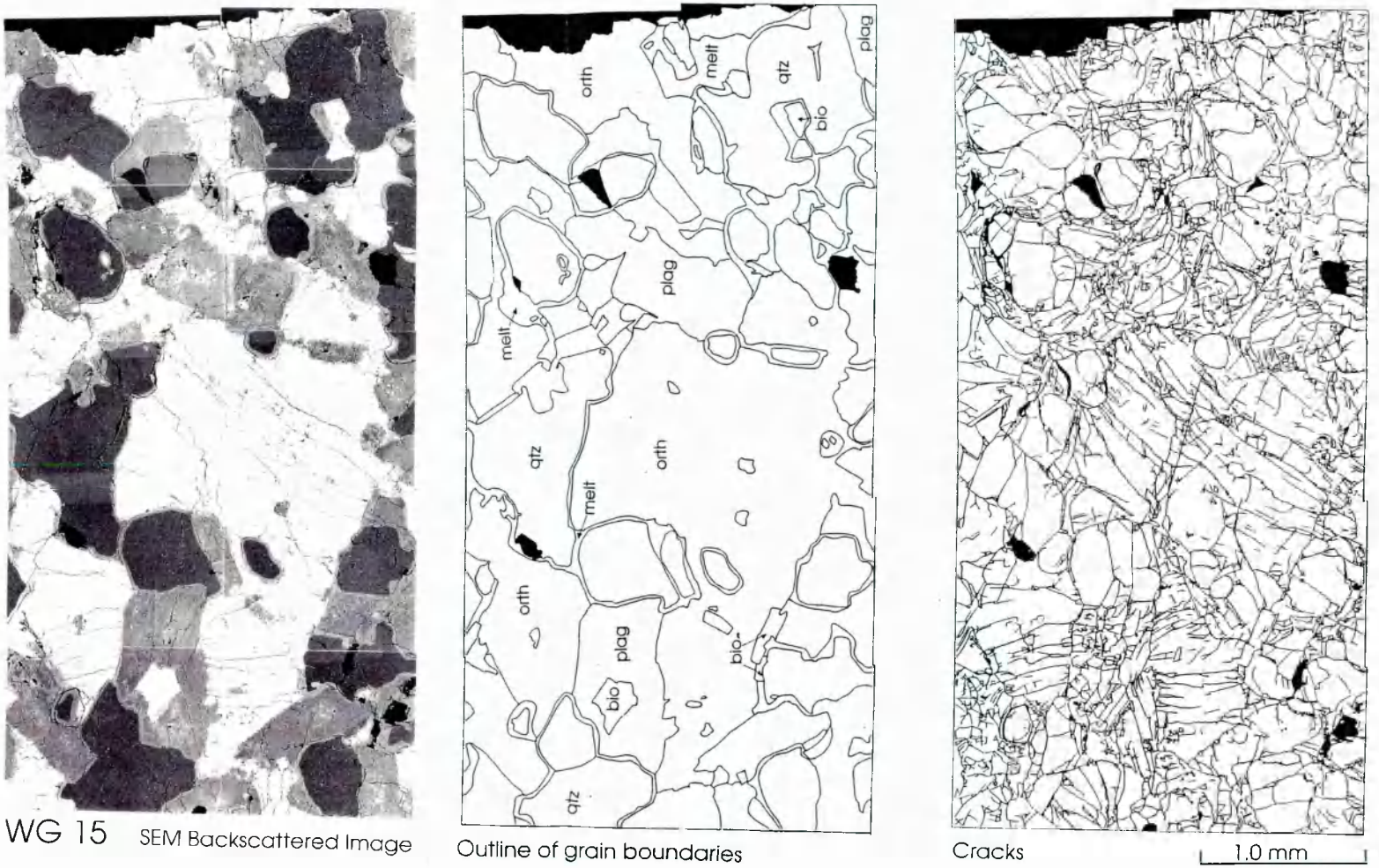

Figure 7.02: SEM collage of the static sample WG14 with phase boundary and crack maps. The insert shows the approximate location of the SEM collage on the sample. Letters on the phase boundary map identifies some of the phases. Porosity is shaded black in the crack map.

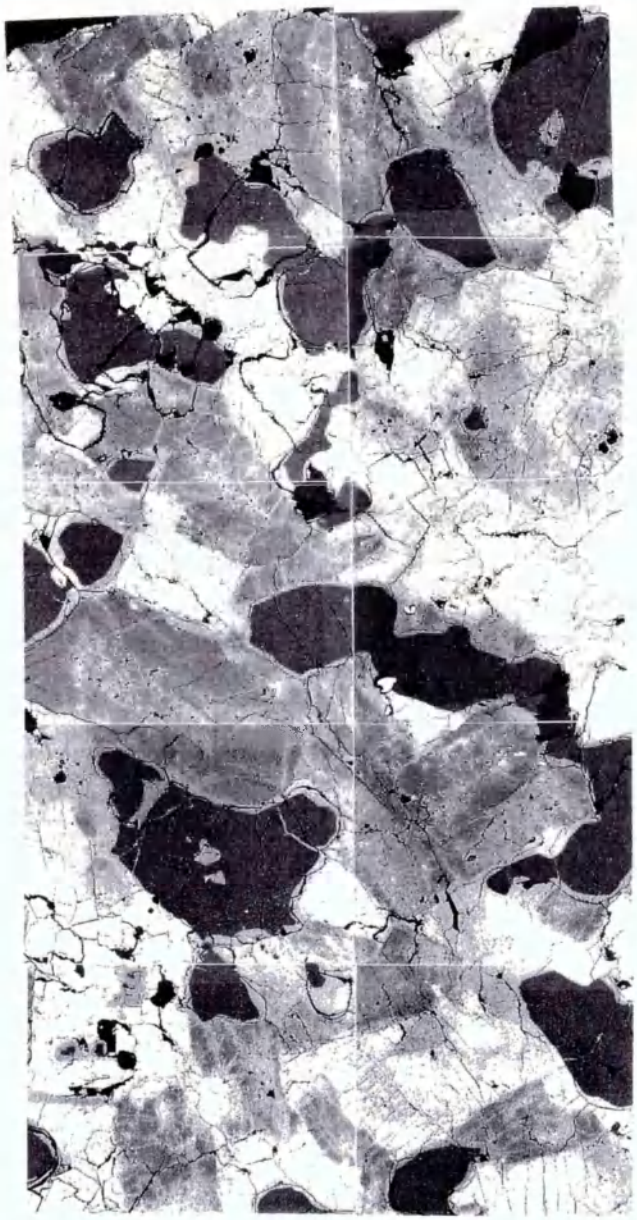

WG 14 SEM Backscattered Image

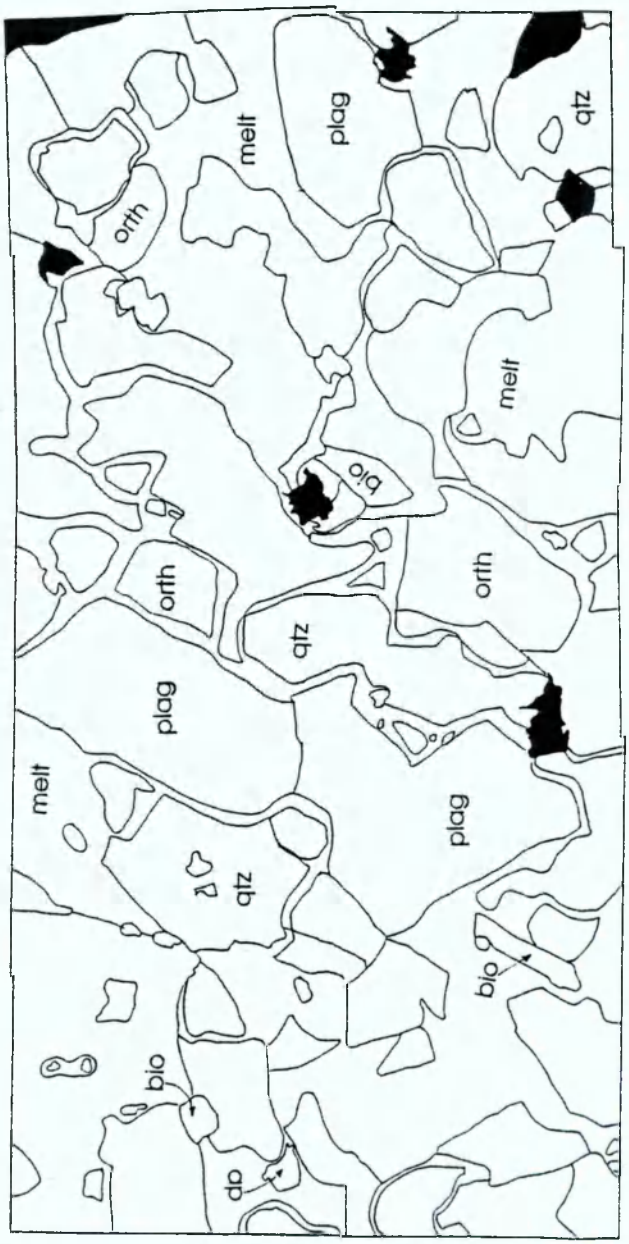

Outline of grain boundaries

Figure 7.06: SEM collage of WG5 with phase boundary and crack maps.

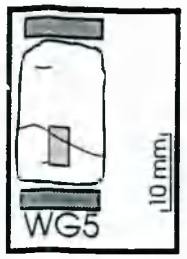

WG 5 SEM Backscattered Image

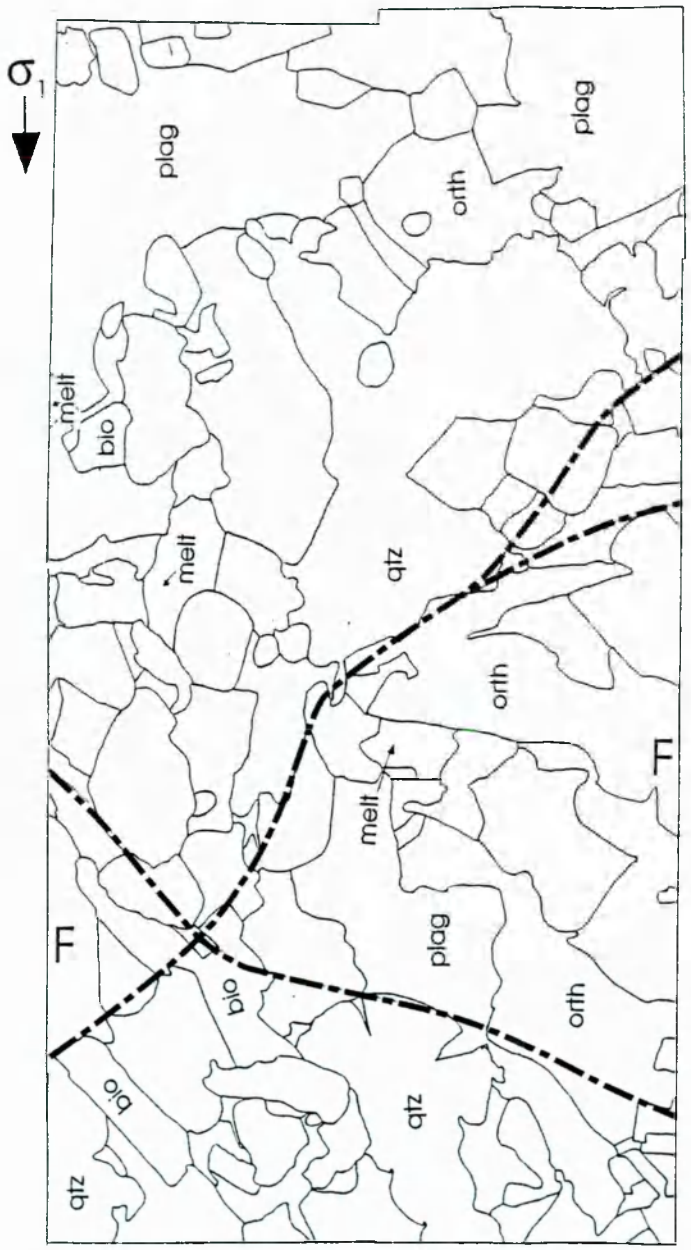

Outline of grain boundaries

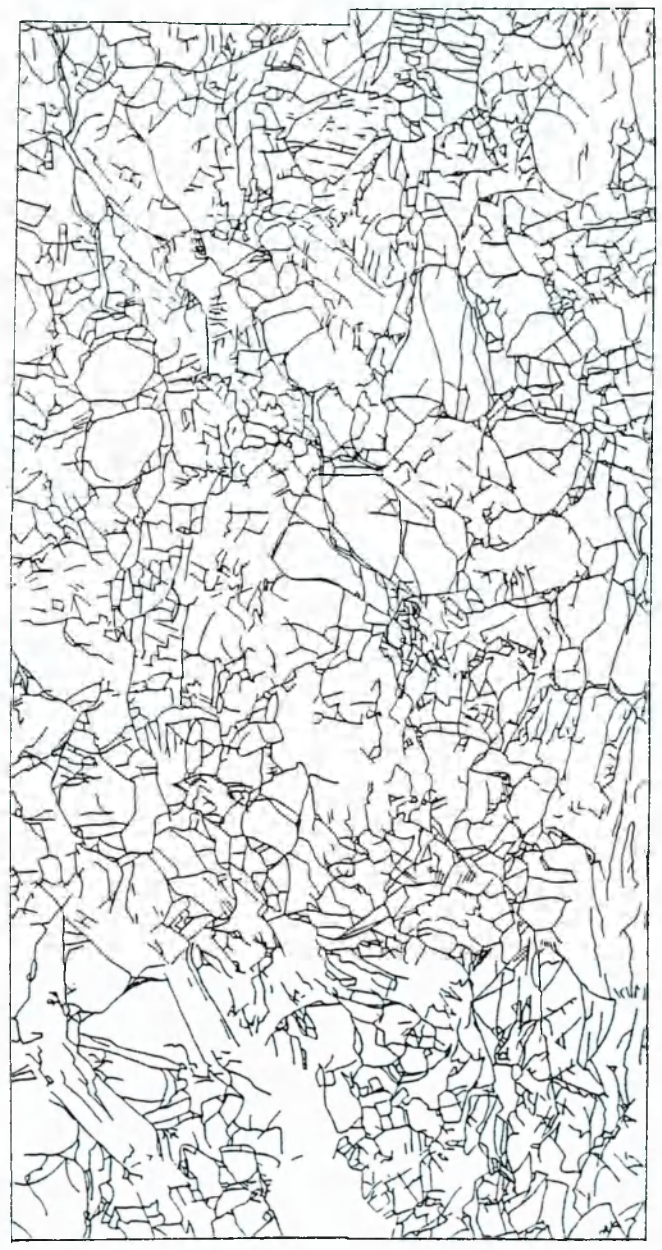

Cracks 1.0 mm

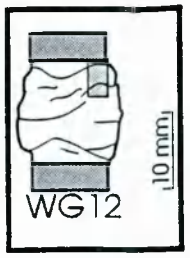

Figure 7.07: SEM collage of WG12 with phase boundary and crack maps.

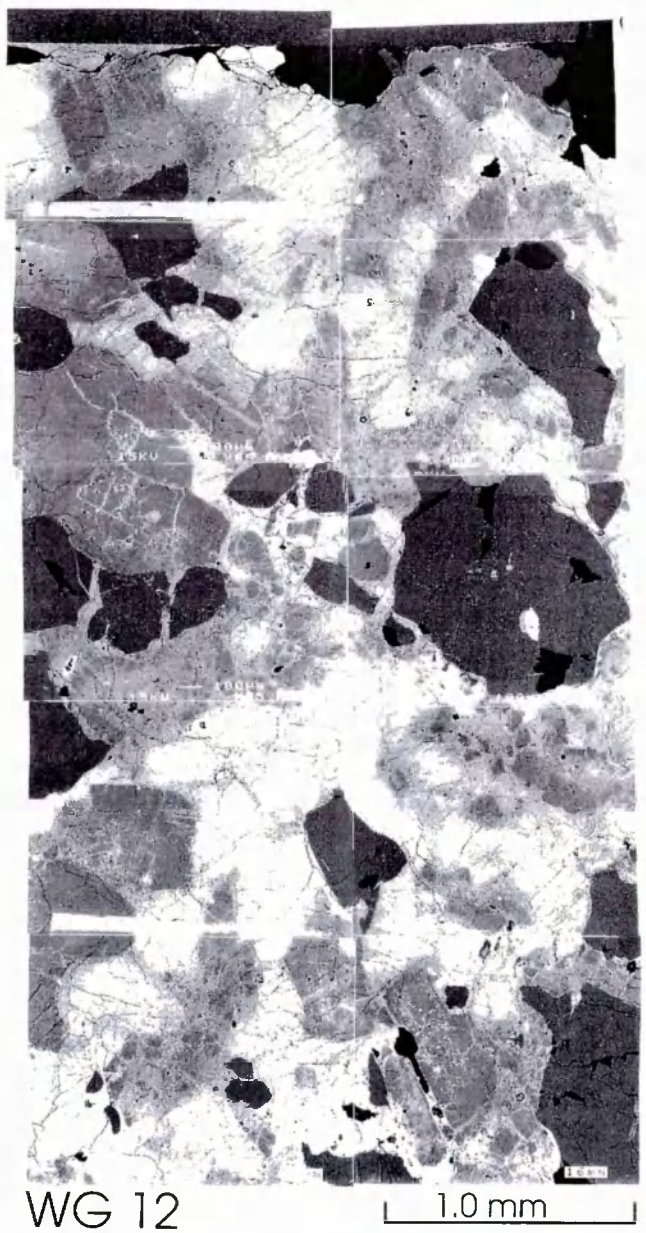

SEM Backscattered Image

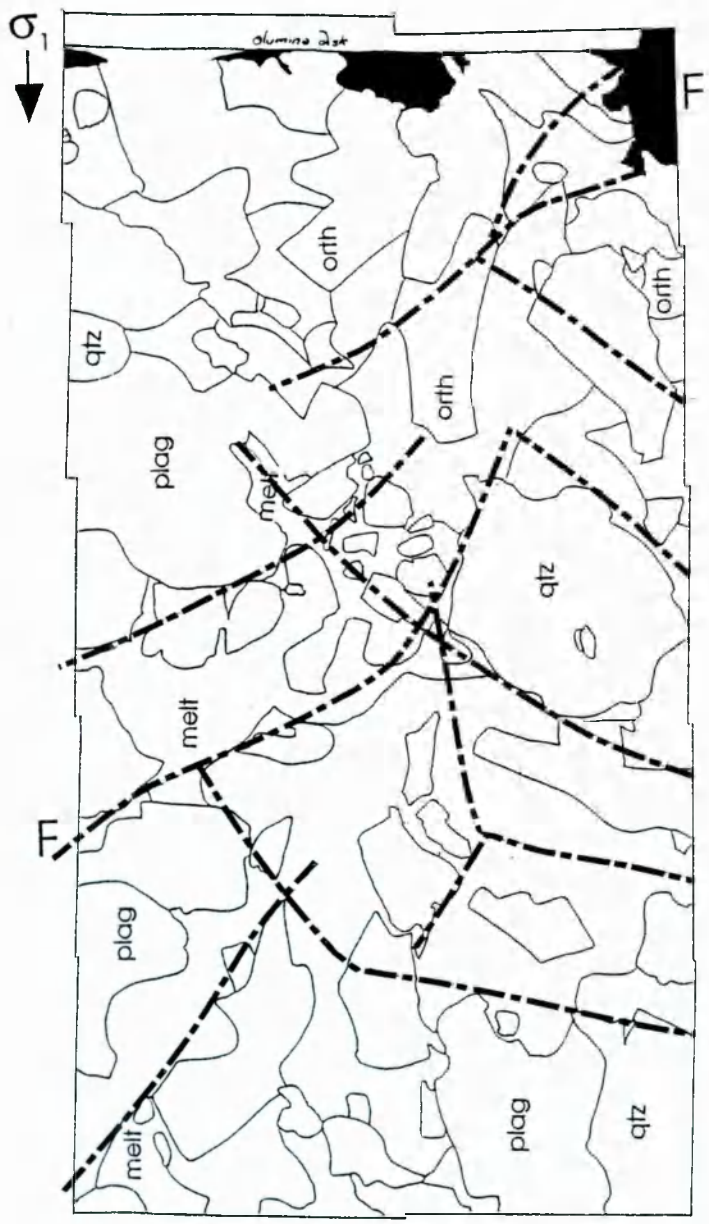

Outline of grain boundaries

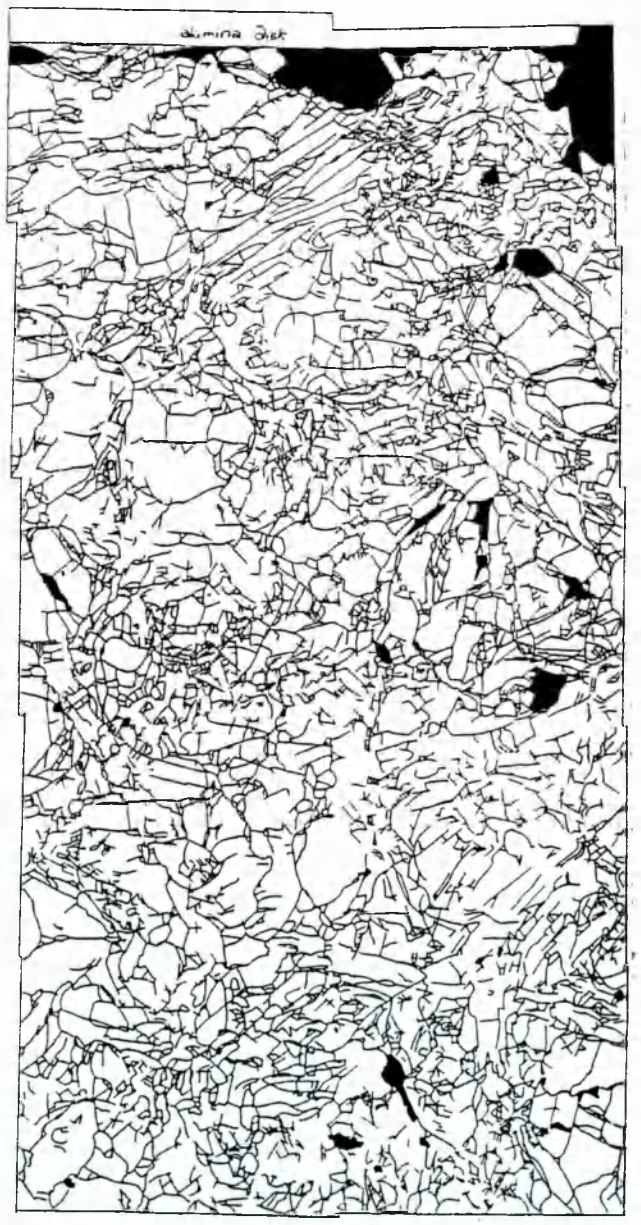

Cracks

Figure 7.04: SEM collage of WG2 with phase boundary and crack maps. Dot-dashed line mark the location of macroscopic fault lines, with terminations on the collage marked by the letter F. The uniaxial compression direction is parallel to the arrow.

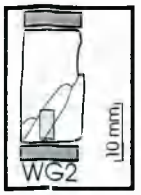

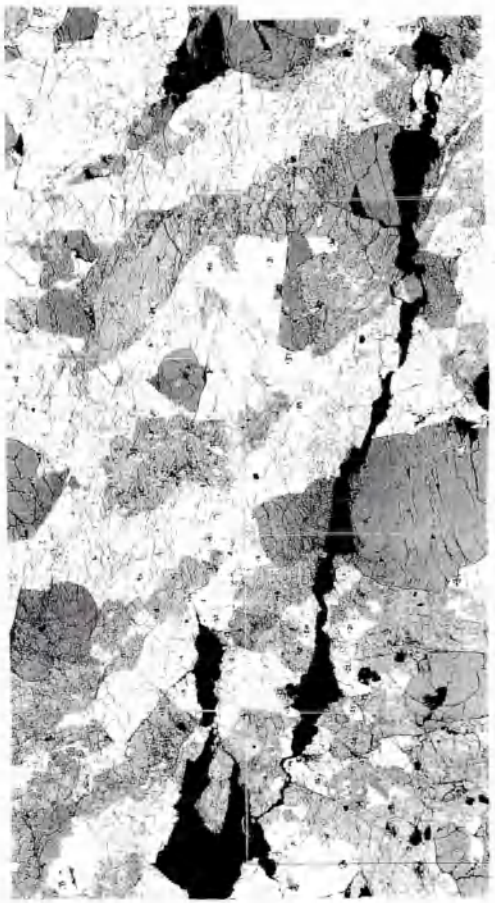

WG 2 SEM Backscattered Image

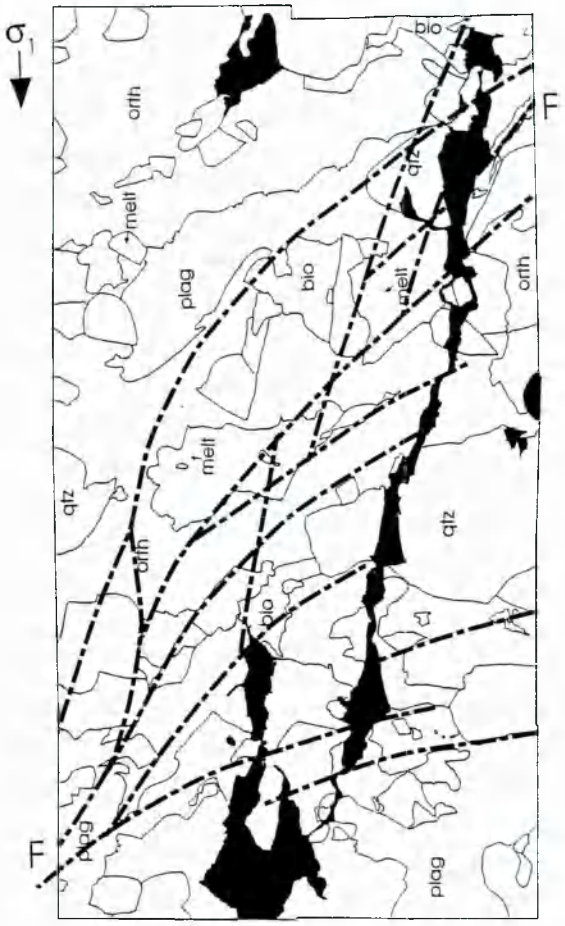

Outline of grain boundaries

Cracks 1.0 mm

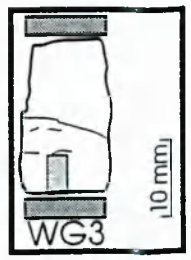

Figure 7.05: SEM collage of deformed sample WG3 with phase boundary and crack maps. Macroscopic fault traces are indicated by dot-dashed lines.

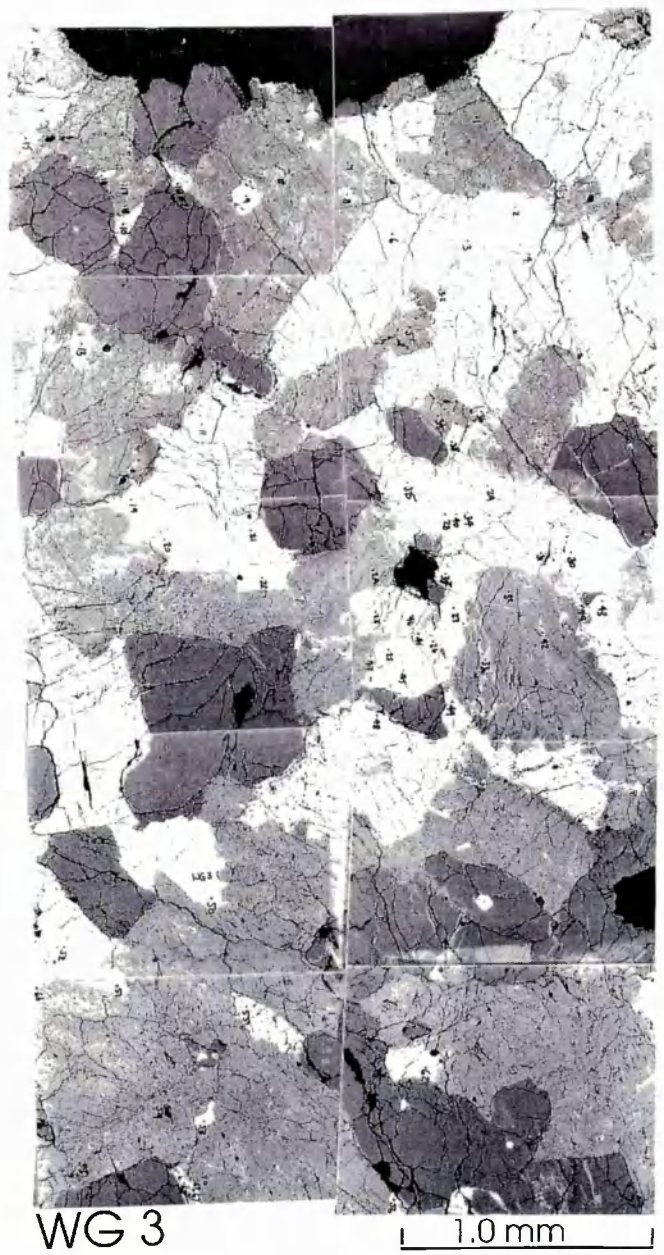

SEM Backscattered Image

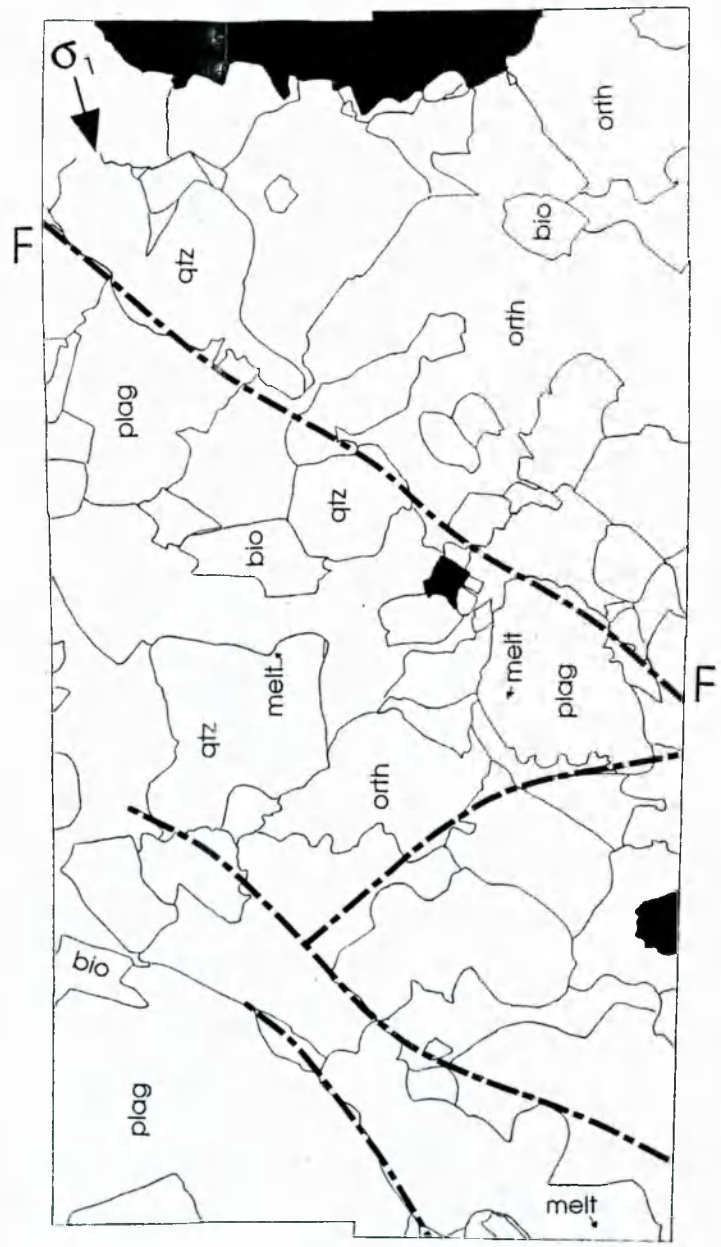

Outline of grain boundaries

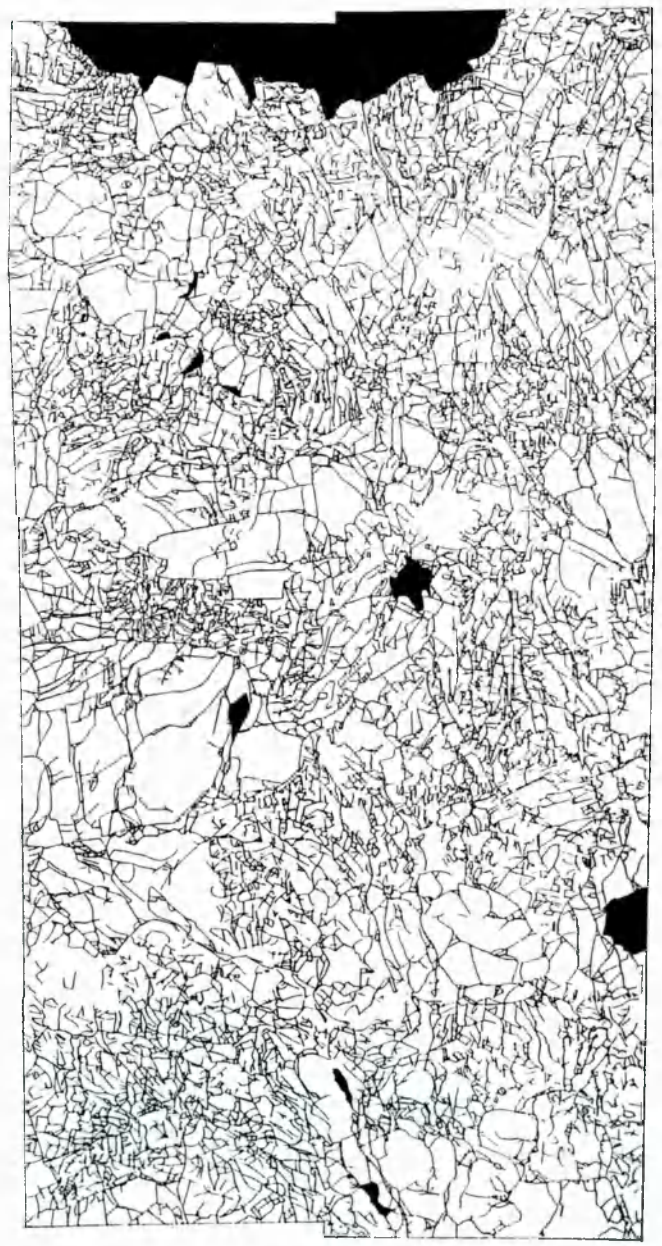

Cracks

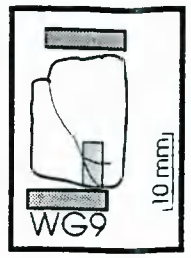

Figure 7.09: SEM collage of WG9 with phase boundary and crack maps.

WG 9 SEM Backscattered Image

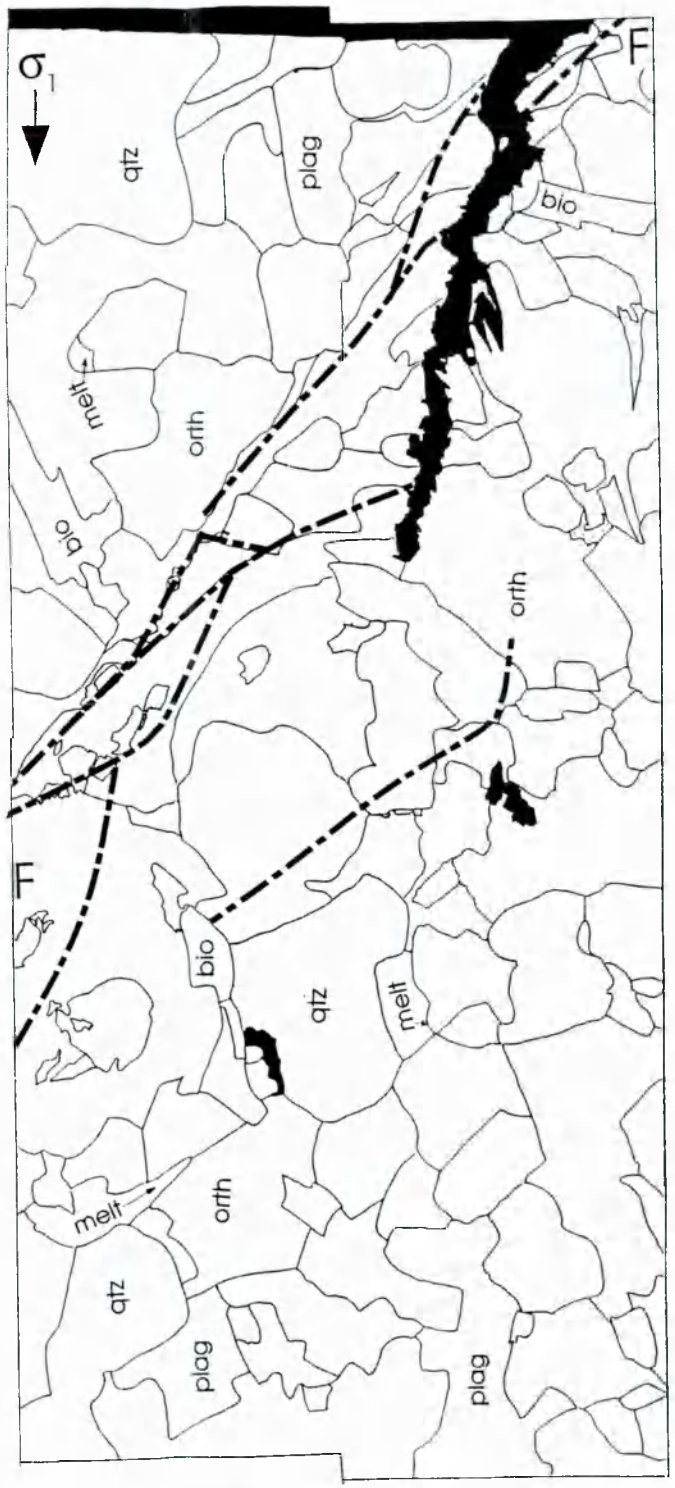

Outline of grain boundaries

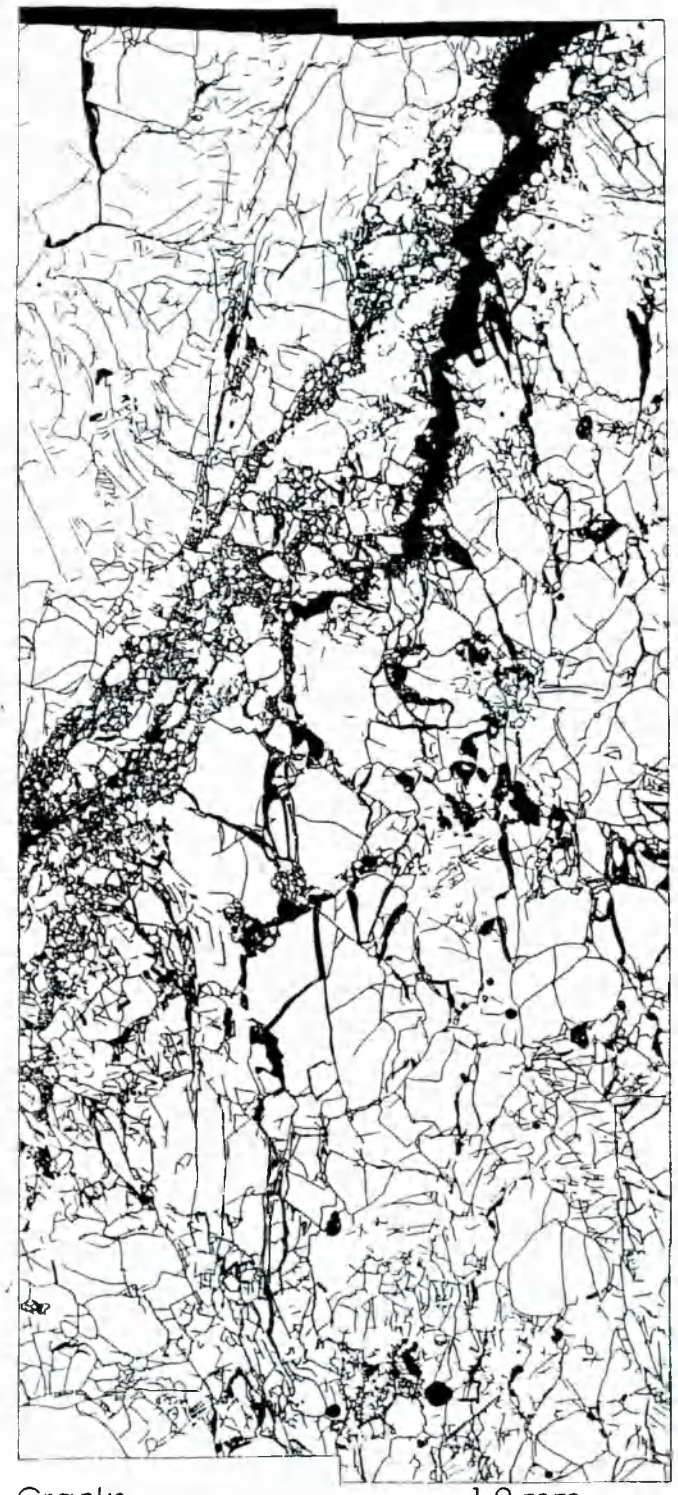

Cracks

1.0 mm

Figure 7.08: SEM collage of WG13 with phase boundary and crack maps.

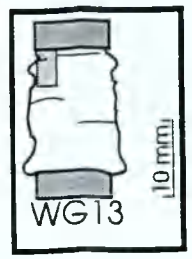

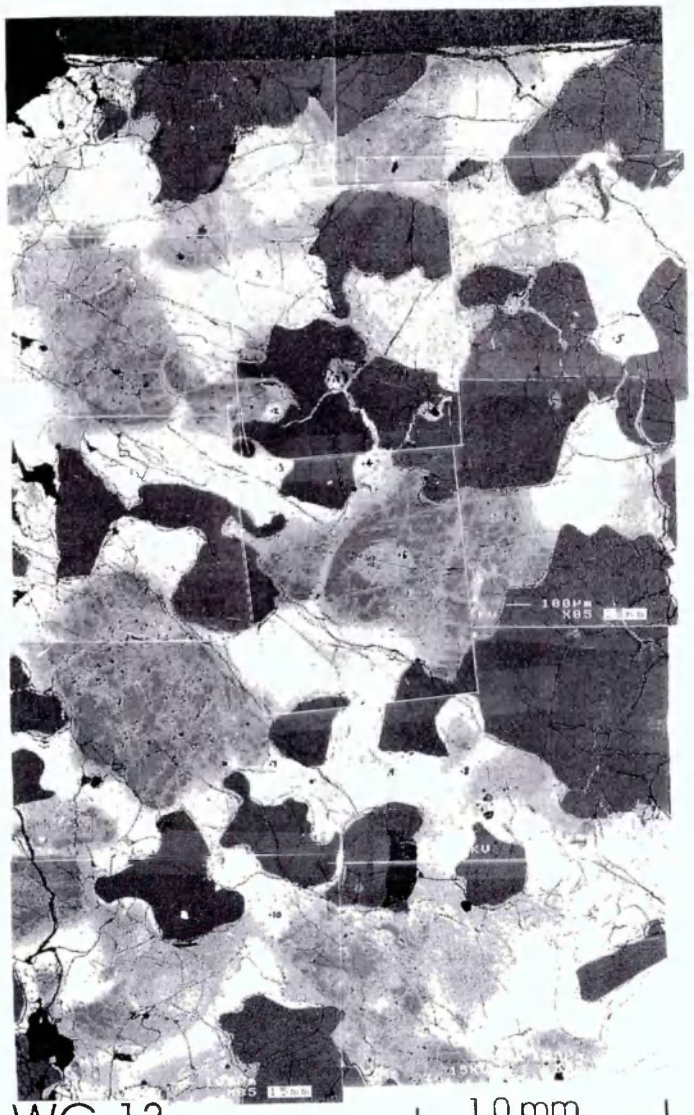

WG 13
SEM Backscattered Image

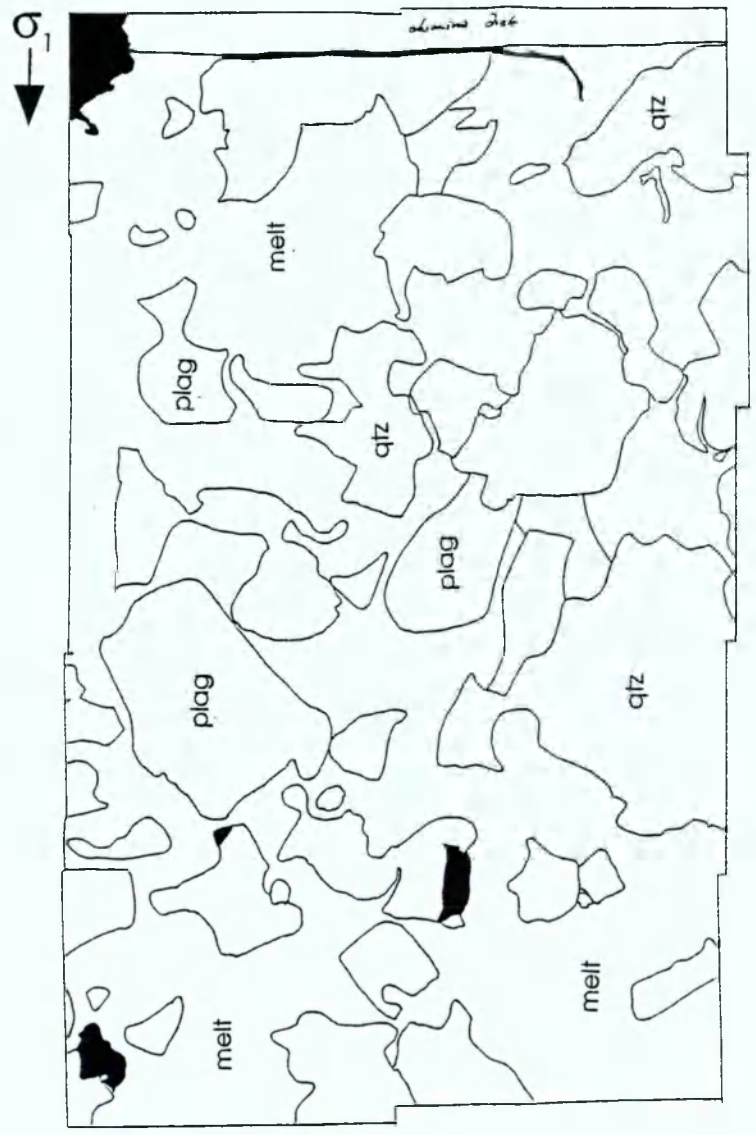

Outline of grain boundaries

Cracks

Sample	Strain rate	T(°C)	ϕ melt	cd (mm/mm^2)
Starting material				
WG0	0	20	0	8.80
Static samples				
WG15	0	900	0.117	42.68
WG14	0	1000	0.281	55.09
WG19	0	1200	0.768	42.85
Deformed samples				
WG2	8.00E-05	800	0.053	80.57
WG7	8.00E-05	800	0.033	45.68
WG8	8.00E-05	800	0.035	35.17
WG6	8.00E-05	850	0.044	66.88
WG3	8.00E-05	900	0.073	71.71
WG9	8.00E-05	900	0.12	34.85
WG10	8.00E-05	900	0.131	72.04
WG16	8.00E-05	900	0.135	59.00
WG17	8.00E-05	900	0.179	58.56
WG5	8.00E-05	950	0.144	37.28
WG4	8.00E-05	1000	0.203	47.11
WG11	8.00E-05	1000	0.271	44.56
WG12	8.00E-05	1050	0.335	52.88
WG13	8.00E-05	1100	0.477	43.49

Table 7.01: Crack density statistics of all samples on which crack density was measured.

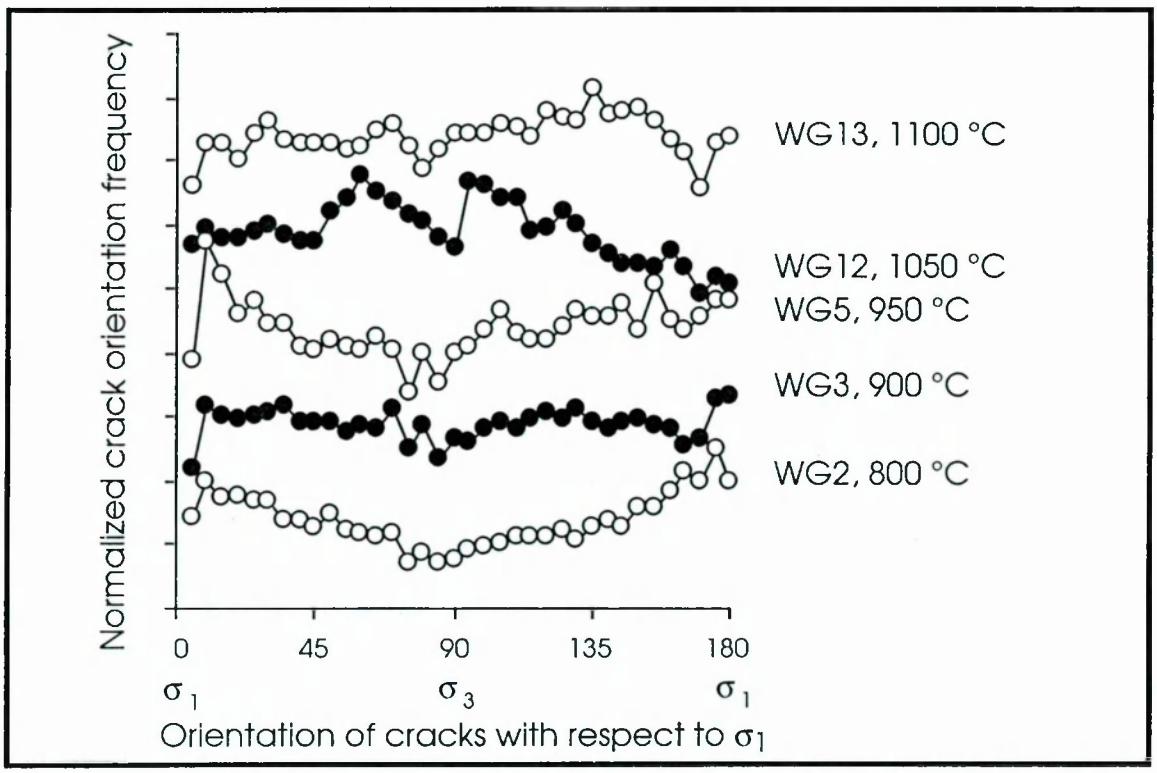

Figure 7.10: Crack orientation statistics of deformed samples WG2, WG3, WG5, WG12 and WG13 normalised to crack densities of WG0 (**Figure 2.04**) (**Appendix 4**). Relative crack orientation frequencies are plotted on the y-axis, instead of absolute crack orientation frequencies to allow easier comparison between samples.

A normalised plot of crack orientations (**Figure 7.10**) indicated that samples WG2 and WG5 have a marked preferred orientation sub-parallel to σ_1 but WG12 contains a conjugate set of fractures sub parallel to σ_3. In WG3 and WG13 no preferred crack orientation could be defined.

It is suggested that the micro-cracks developed as a response to compaction and heating at 250 MPa as a comparable crack density is seen in both static and differential stress samples. Either axial or shear cracks may be accentuated during the application of differential stress. Short cracks observed in glass, such as in WG13 (**Figure 7.08**), indicate that at least some of the cracks were formed during sample quenching. However, preferred orientation of cracks is too small, to allow crack orientation and densities to be used at deformation indicators.

7.3 Strain accommodation structures in samples with applied differential stress

To aid description, samples are divided into three groups using macroscopic characteristics (**Chapter 5.6**):

1. Localized faults: In these samples the strain is largely accommodated on a localized macroscopic fault.
2. Distributed grain size reduction: these samples also developed fault zones but significant strain is accommodated by more pervasive deformation.
3. Ductile flow: these appear to have deformed in a ductile manner on the scale of the whole sample.

7.3.1 Microstructures of samples with a localized brittle deformation

Samples belonging to this group show localized brittle deformation, manifest as a macroscopic fault with little deformation outside this zone. The deformation conditions and melt fractions for these samples are shown in **Table 7.02**.

Brittle faults cutting the specimen are not developed as a single continuous fracture on a microscopic scale, but consist of an array of sub-parallel anastamosing fractures in fault zones up to 80 μm wide. These form a relatively clean discrete fracture (**Figure 7.11**) or can be associated with intense cataclasis (**Figure 7.12, Figure 7.08**). Preferential alignment of fine grained material oblique to the fault zones in the fractures can be observed in WG7 (**Figure 3.06**). Deformation in these samples is concentrated along the

macroscopic fractures with sparse deformation apart from grain transecting micro-cracks away from the main fault.

Sample	strain rate (s^{-1})	max. strain (%)	T (°C)	time @ T (h)	ϕ
WG2	5E-05	9.41	800	2.4	0.053
WG3	8E-05	14.07	900	2.5	0.073
WG6	8E-05	8.44	850	2.5	0.044
WG7	8E-05	8.82	800	4.0	0.033
WG8	8E-05	14.3	800	96.0	0.035
WG9	8E-05	16.62	900	20.0	0.120
WG10	8E-05	15.26	940	94.0	0.131
WG23	8E-05	24.52	1000	3.2	0.103
WG27	8E-05, 1E-04	24.91	950	8.0	0.076

Table 7.02: Deformed samples that deformed by localized brittle behaviour, sample WG27 was deformed at two different strain rates. Samples WG 23 and 27 were run with a low pressure crushed quartz reservoir into which melt was extracted (**Chapter 3.4.4**).

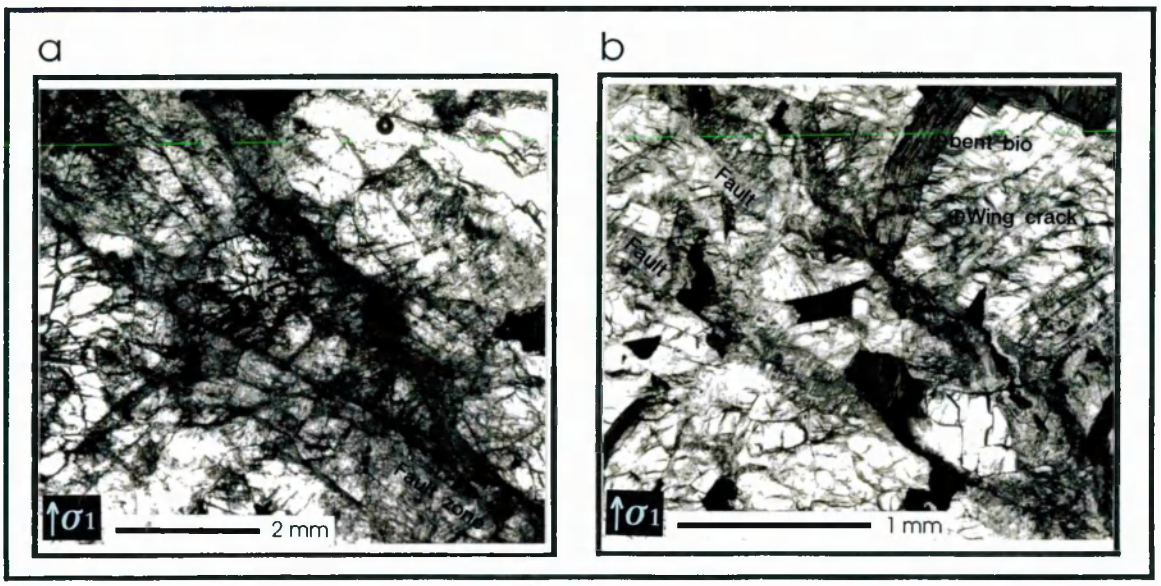

Figure 7.11: Optical thin section photographs of discrete, anastamosing fault zones in samples WG2 and WG7, both heated to 800 °C and deformed at 8E-05. **a.)** Fault zone splay in WG2, **b.)** Anastamosing fault zone in WG7.

The grain size reduction in the fault zone, resulting in (optically) unresolved crypto-crystalline grains, is best observed in specimen WG9 (**Figure 7.09**). Shear movement along the fault zone resulted in intense brecciation of all minerals, especially biotite (**Figure 7.11, b**). Biotite is bent into the fault zone and is then smeared out, often filling interstitial gaps between angular quartz and feldspar fragments. However, despite fragmentation and rotation, the biotite fragments retain optical continuity. Feldspars also suffer translation and brecciation. Quartz grains adjacent to the fault zone are

strained. Wing cracks are developed away from the fault zone, feeding into large, open, axial cracks (**Figure 7.09**). In the light of these observations it is suggested that the grain size reduction is entirely due to mechanical cataclasis, with crystalline plasticity limited to few quartz grains at the boundary between macroscopic fault zones and undeformed rock.

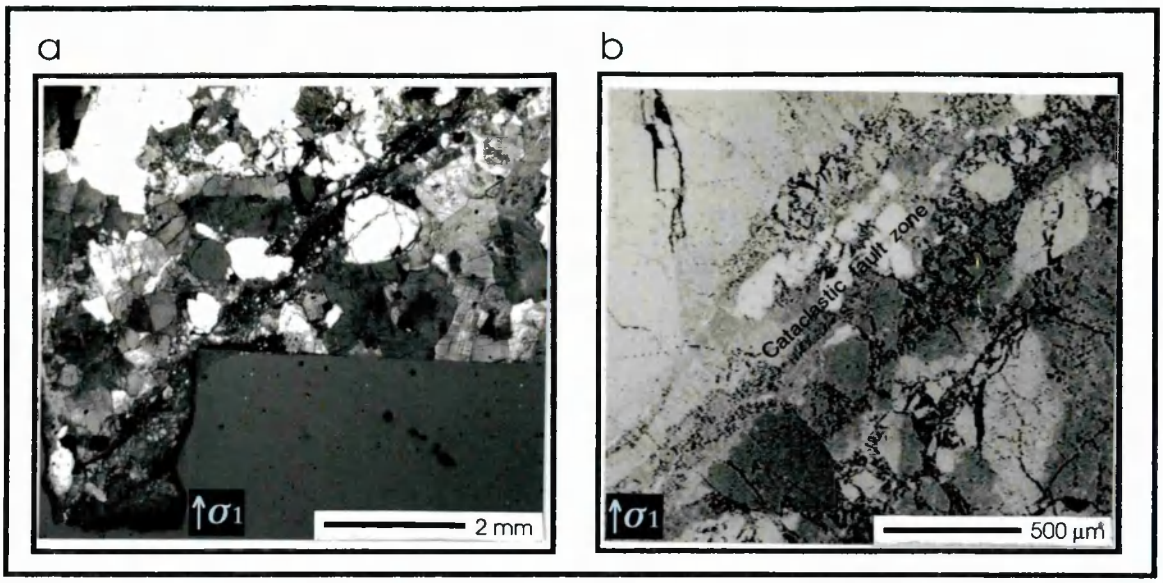

Figure 7.12: Samples WG23 and WG9 that deformed by forming a cataclastic fault zone. **a.)** optical thin section photo of WG23 (compare to SEM image of same image in figure 3.7) showing cataclastic fault. **b.)** SEM image of detail of cataclastic fault zone in sample WG9 (compare to **Figure 7.09**).

In most samples in this category, the open axial cracks and dilated fault zones are melt filled (**Figure 7.05**). This occurs because open pores within the sample will be at effectively zero pressure. The resulting steep pressure gradient between the open pores and the melt plus grain matrix (at a hydrostatic pressure of 250 MPa) will drive melt flow into the open pores. In contrast, the porosity in the dilatant fault zone and axial cracks of sample WG9 are open but not melt filled, despite the melt fraction of 0.13, coating quartz and feldspar grains, observed in this sample. It is thought that this is the result of a leak in the specimen jacket which would have allowed the penetration of high pressure argon into the pore space so inhibiting melt flow. This proposition is supported by the comparative weakness of the sample when compared to samples deformed under similar conditions (**Chapter 5.2.2**).

7.3.2 Samples with distributed grain size reduction

This category covers a range of microstructural styles. In some samples grain size reduction is only associated with macroscopic fault zones, but with cataclasis distributed over a broader, more diffuse, area than in the localized fault category (**Chapter 7.3.1**). At the other end of the spectrum grain size reduction is widely distributed throughout the specimen, except for the piston pressure shadows. All tests displaying pervasive brittle deformation also developed macroscopic faulting oblique to the main compression direction. Experimental conditions for samples in this category are summarised in **Table 7.03**.

Sample	strain rate (s^{-1})	max. strain (%)	T (°C)	time @ T (h)	ϕ melt
WG4	8E-05	12.25	1000	2.50	0.203
WG5	8E-05	13.77	940	3.00	0.144
WG11	8E-05	13.23	1000	20 00	0.271
WG12	8E-05	32.63	1050	4.50	0.335
WG16	8E-05	20.15	900	3.50	0.135
WG17	8E-06	1.620	900	33.00	0.179
WG20	8E-07, 5E-05	13.36	900	172.80	0.168
WG26	1E-03, 3E-02	14.77	1000	145.50	0.435
WG28	8E-05	42.14	900	51.00	0.155
WG29	8E-05	16.08	1000	44.75	0.257
WG30	2E-07,3E-04	28.33	1000	168.00	0.313

Table 7.03: Deformed samples showing pervasive brittle behaviour. Samples WG20 and WG26 were deformed at two strain rates.

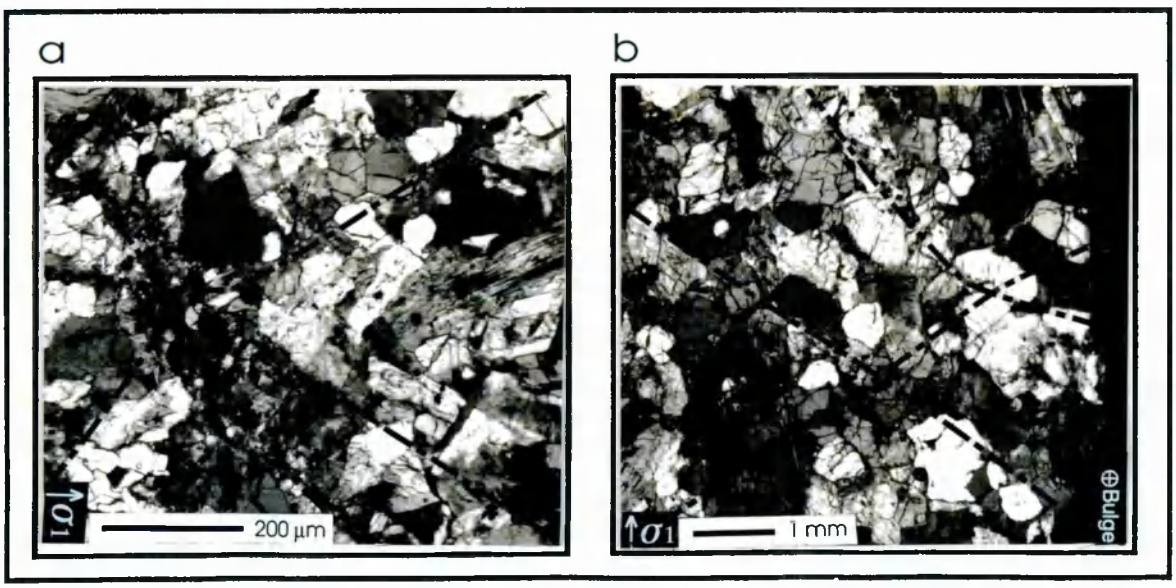

Figure 7.13: Conjugate fault zones defined by the alignment of isolated pockets of cataclastic material in **a.)** WG4 and **b.)** WG11.

At the more localised end of the spectrum, e.g. WG4 and WG11, conjugate fault zones are defined by the alignment of isolated pockets of grain size reduction (**Figure 7.13, a**). In WG11 the cataclastic material plus melt protrudes past the edge of the specimen on both sides of the thin section and the fault zone increases in width towards the centre of the specimen (**Figure 7.13, b**).

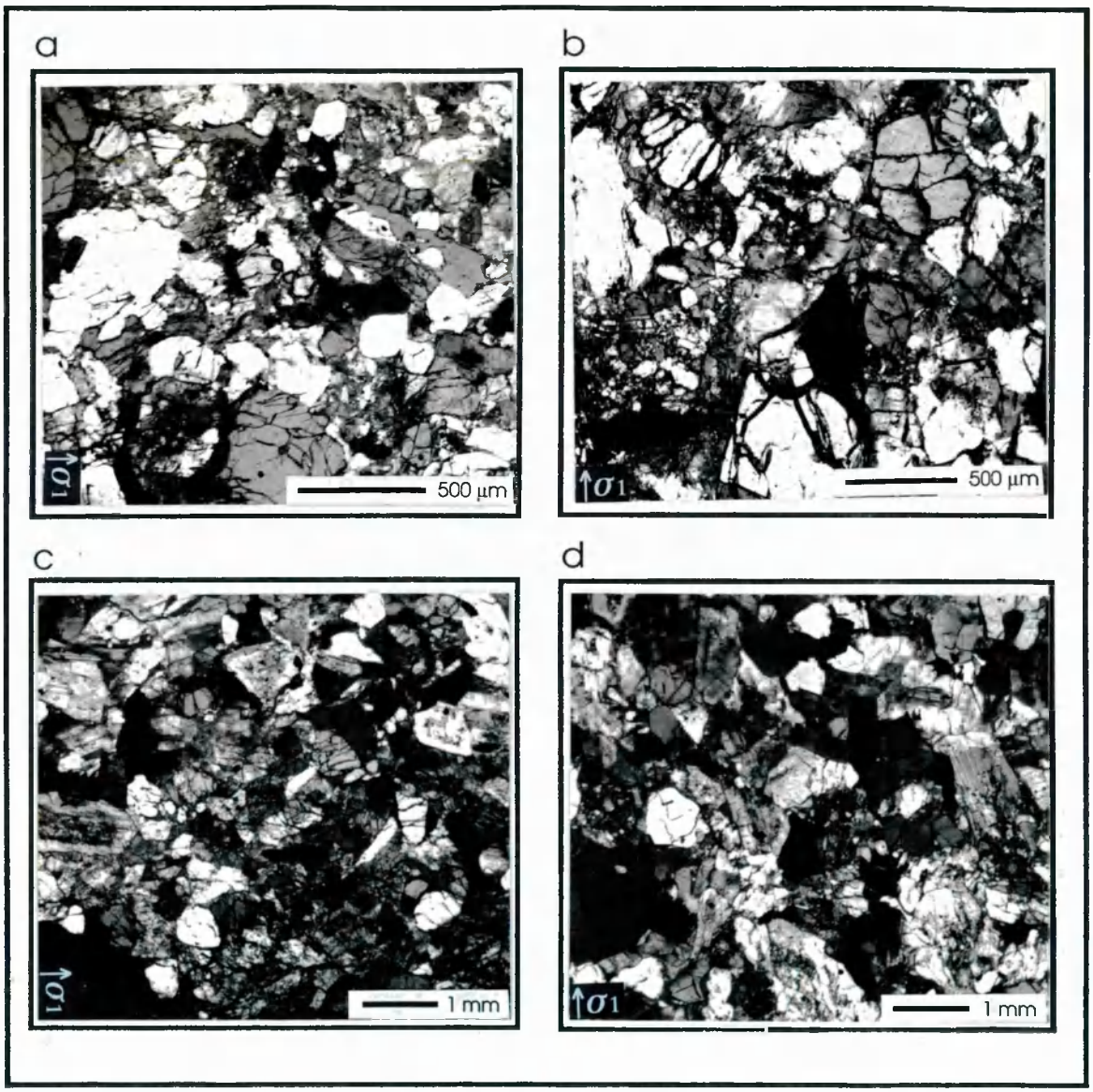

Figure 7.14: Grain size reduction in a central girdle parallel to σ_3 in samples WG16, WG5, WG20 and WG17, ordered according to increasing melt fraction. **a.)** WG16, 900 °C, 0.135 melt fraction; **b.)** WG5, 950 °C, 0.144 melt fraction; **c.)** WG17, 900 °C, 0.179 melt fraction **d.)** WG26, 1000 °C, 0.435 melt fraction.

In contrast, samples WG5, WG16, WG17 and WG26 are characterised by a girdle of grain size reduction at the centre of the specimen, parallel to σ_3, which is associated barreling of the sample (**Figure 7.14**). The width of the deformed zone is enlarged

towards the centre of the specimen in WG17 and WG26. The rock in the cataclastically deformed zone is structurally homogeneous, except for occasional short anastamosing shear zones at low angles to σ_3, containing cataclastic material. These shear zones provide channels for the extrusion of cataclastic material plus melt beyond the specimen periphery (**Figure 3.01**, **Figure 7.15**). Away from the short shear zones, grain size reduction is concentrated in isolated pockets (**Figure 7.14**). Material inside these pockets consist of crushed quartz and feldspars with the occasional biotite crystal, the interstitial spaces being infilled by melt. Evidence for crystal plastic deformation was not observed.

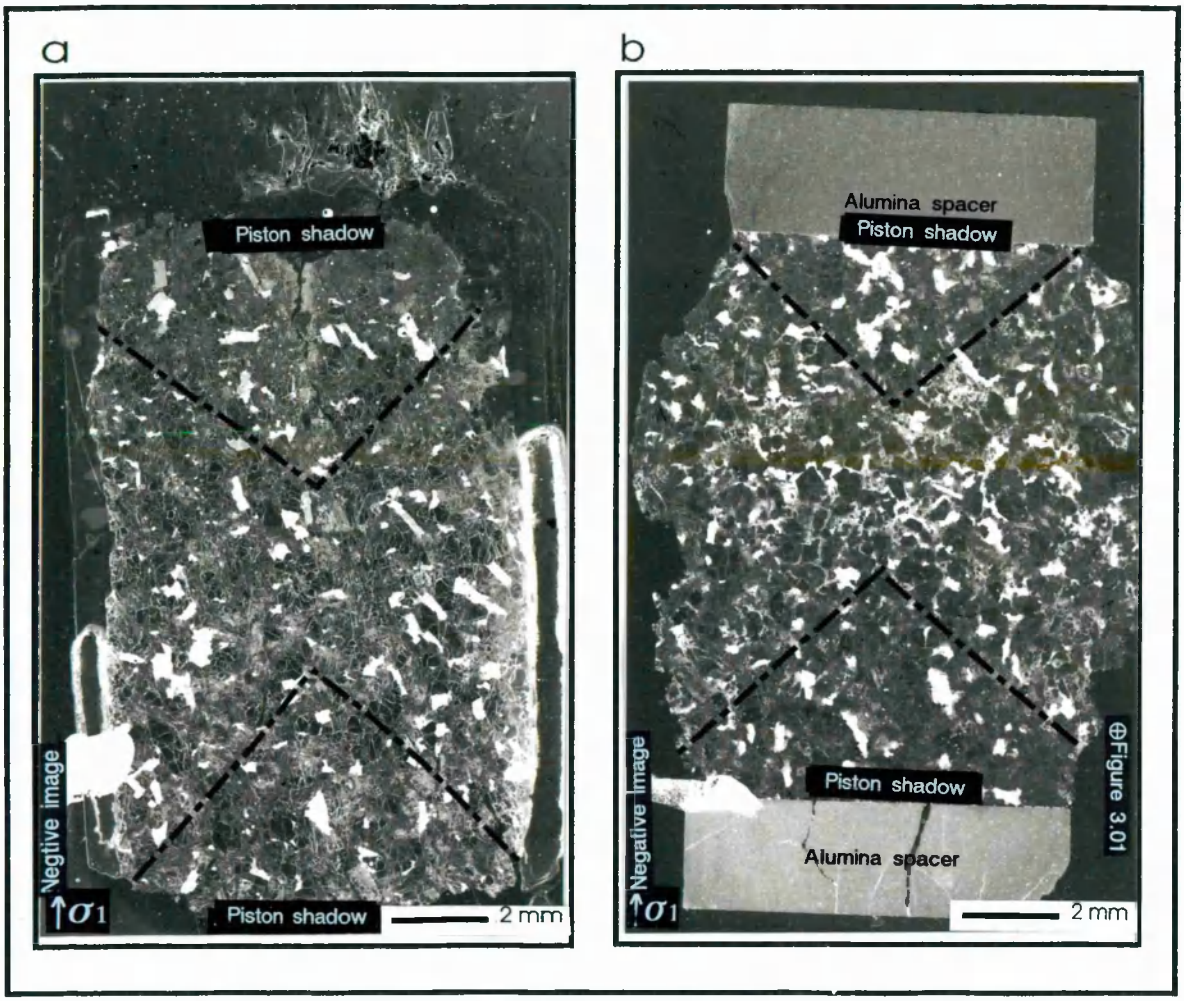

Figure 7.15: Whole thin section photos of **a.)** WG5 and **b.)** WG12, displaying pervasive cataclastic deformation behaviour.

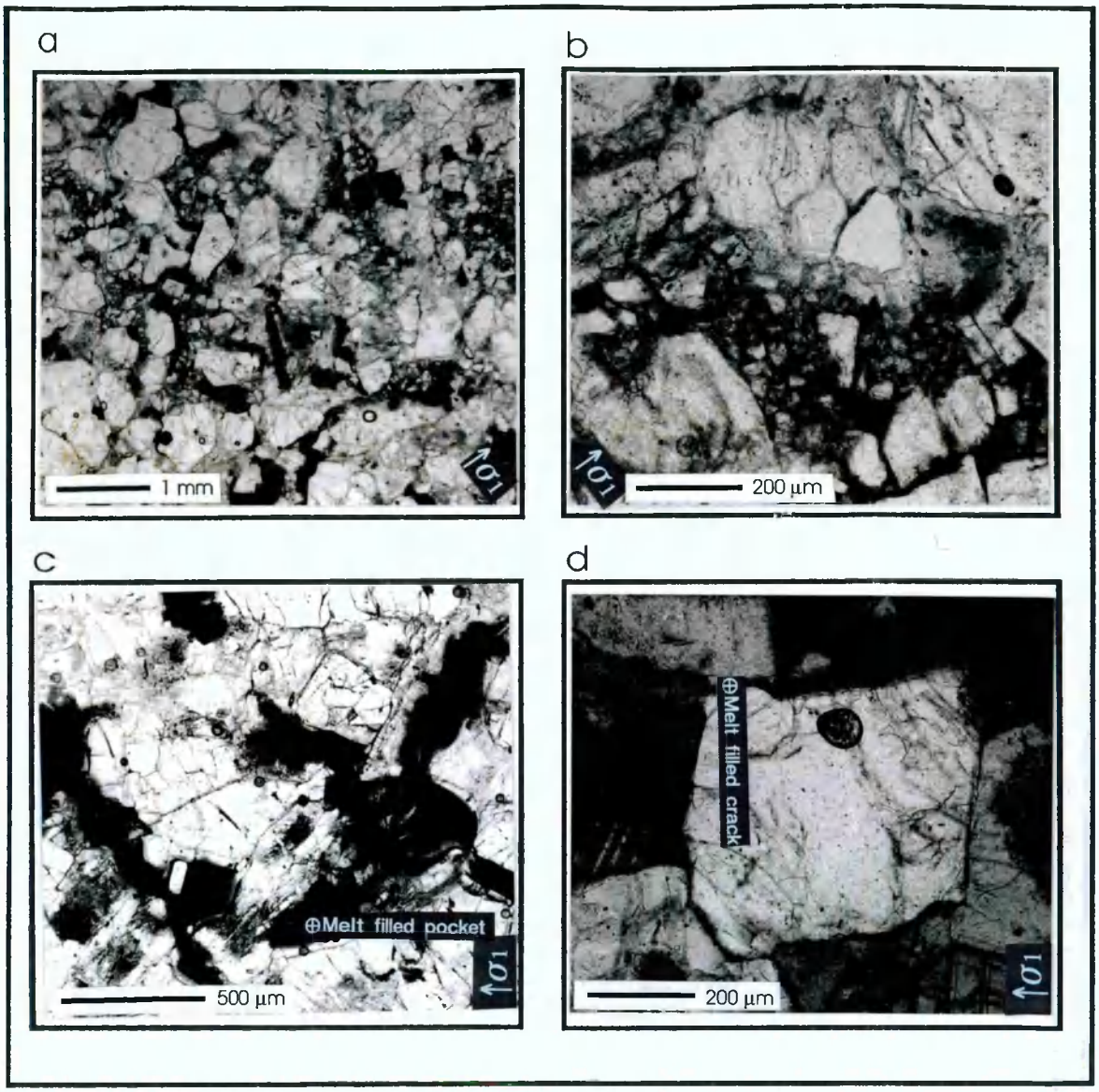

Figure 7.16: Pervasive cataclastic deformation in sample WG12. **a.)** & **b.)** Detail of pockets containing cataclastic fragments surrounded by melt in WG12. **c.)** Un-collapsed pocket in the piston shadow marking site of biotite that has almost completely melted. **d.)** Melt filled cracks in the piston shadow.

Pervasive grain size reduction is best developed in sample WG12, in which grain size reduction is common throughout the broad central zone of the specimen (**Figure 7.15** and **Figure 7.16, a, b**). On a macroscopic scale, the sample has assumed a distinct barrel shape, with a poorly developed fault zone at 33.5 ° to σ_1. In the pressure shadow zones, at either end of the specimen, the interlocking grain texture of the granite is still preserved. Here significant melt pools both at the sites of former biotites and in axial cracks can be found (**Figure 7.16, c, d**). However, the central zone appears to have been disaggregated; the maximum grain size is reduced, large grains are more rounded and no longer form an interlocking texture (**Figure 7.16, a, b**). The matrix of this zone consists of an intimate association of melt with small quartz and feldspar

fragments, located in discrete pockets and spread along the grain boundaries of the larger grains. No microstructural evidence for grain plasticity was observed. A weak preferred alignment of cataclastic pockets forming conjugate sets at 30 to 60 ° to σ_1 was observed. Deformation associated with the macroscopic fault was indistinguishable from the pervasive grain size reduction described above. Melt and cataclastic material have been squeezed from the confines of the specimen in the central zone (**Figure 7.16, a, b** and **Figure 3.01**).

It is thought that the distributed grain size reduction, described above, results largely from mechanical damage during dis-aggregation of the original interlocking mineral texture and subsequent melt lubricated grain boundary sliding which accommodated sample shortening. This could be described as deformation by pervasive cataclastic flow, as distinctly different from mylonitic grain size reduction, as no evidence for plastic deformation of both quartz and feldspar grains was observed.

7.3.3 Microstructures in ductile specimens

Microstructures in these specimens show little evidence for brittle deformation during the application of differential stress. All the shortening appears to have been accommodated by flow of the melt. Experimental conditions are summarised in **Table 7.04**.

Sample	T (°C)	strain rate (s^{-1})	max ε (%)	ϕ melt
WG13	1100	5E-05	30.13	0.477
WG18	1100 > 1027 - 896	1E-05, 8E-04	24.51	0.470/0.250
WG21	1200 > 850 - 953	1E-07, 1E-03	32.66	0.625/0.164

Table 7.04: Experimental conditions of samples with ductile deformation structures. Samples WG18 and 21 were cooled prior to being deformed between 850 and 1027 °C (for full experimental conditions see **Chapter 6.2, Table 6.01**). The second melt fraction in these two samples represents that of preserved glass after neo-crystallization.

In sample WG13 the melt displays irregular iron staining (crypto-crystalline iron oxide crystals) in optical microscopy (**Figure 7.17; Figure 7.08**). The swirly outline of iron oxide stained melt indicates that flow of the melt occurred, but was insufficient to homogenize the melt phase. This is consistent with chemical evidence (**Chapter 4**). Quartz grains are well rounded with thick melt films penetrating cracks. The only remaining feldspar, plagioclase, has ill-defined crystal shapes. Melt protrudes into the

crystals parallel and at right angle to cleavage, totally dis-aggregating original feldspar grains in places (**Figure 7.08**). Accessory phases such as pyroxenes form lath shaped crystals in bands around quartz grains but show no preferential orientation. Variation in the thickness of melt films between adjacent quartz crystals can be observed (**Figure 7.17, b**). There is occasional evidence of impingement damage to grains, though lacking evidence for grain plasticity.

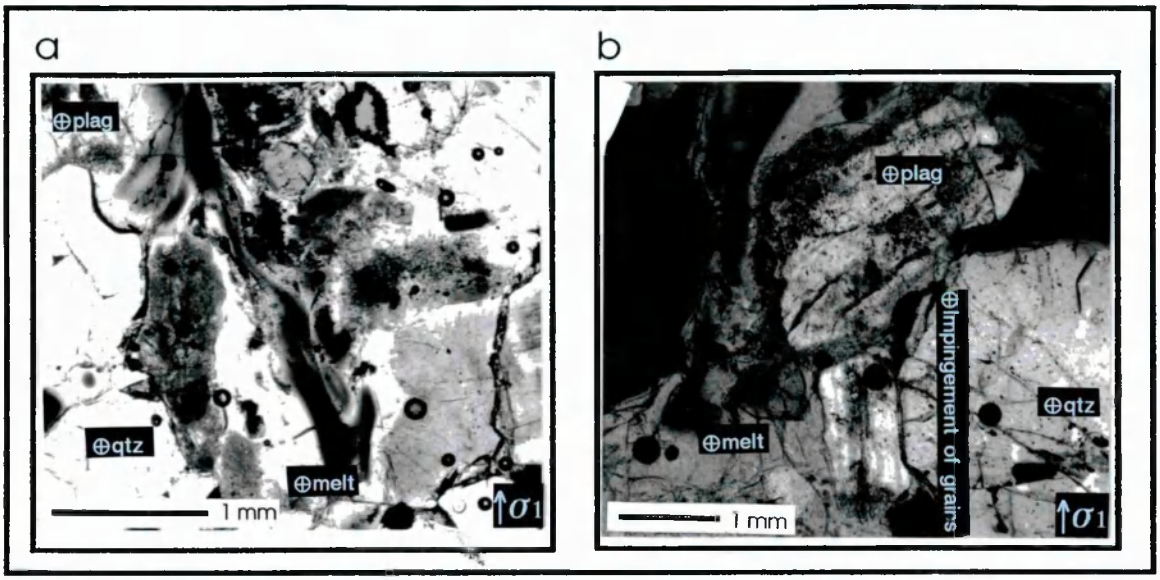

Figure 7.17: Microstructures of ductilely deformed sample WG13.

In both WG18 and WG21 neo-crystallization of the melt phase took place during deformation between 850 and 1027 °C (Compare with **Chapter 3.4.2** and **Chapter 5.2.4**). Despite extensive reduction in the melt fraction that this caused, little cataclasis took place with no deformation structures of the neo-crysts was observed (**Figure 3.09** for WG21 and **Figure 4.12** for WG18). The macroscopic faults visible on the exterior surfaces of both WG18 and WG21 are not apparent microstructurally.

7.4 Summary of microstructures

The most common microstructures are grain transecting micro-cracks. These appear to have developed during loading and heating. No systematic variation with temperature or stress history could be determined (**Figure 7.18**). On microstructural criteria samples can be split into three groups

1. Faulted samples with restricted cataclasite development. Grain plasticity in quartz was restricted to areas at the edge of the macroscopic fault zone. In

these samples strain was largely accommodated along single or conjugate cataclastic faults. Deformation was limited to grain transecting cracks away from fault zones. Melt commonly penetrated fault zones and open cracks.

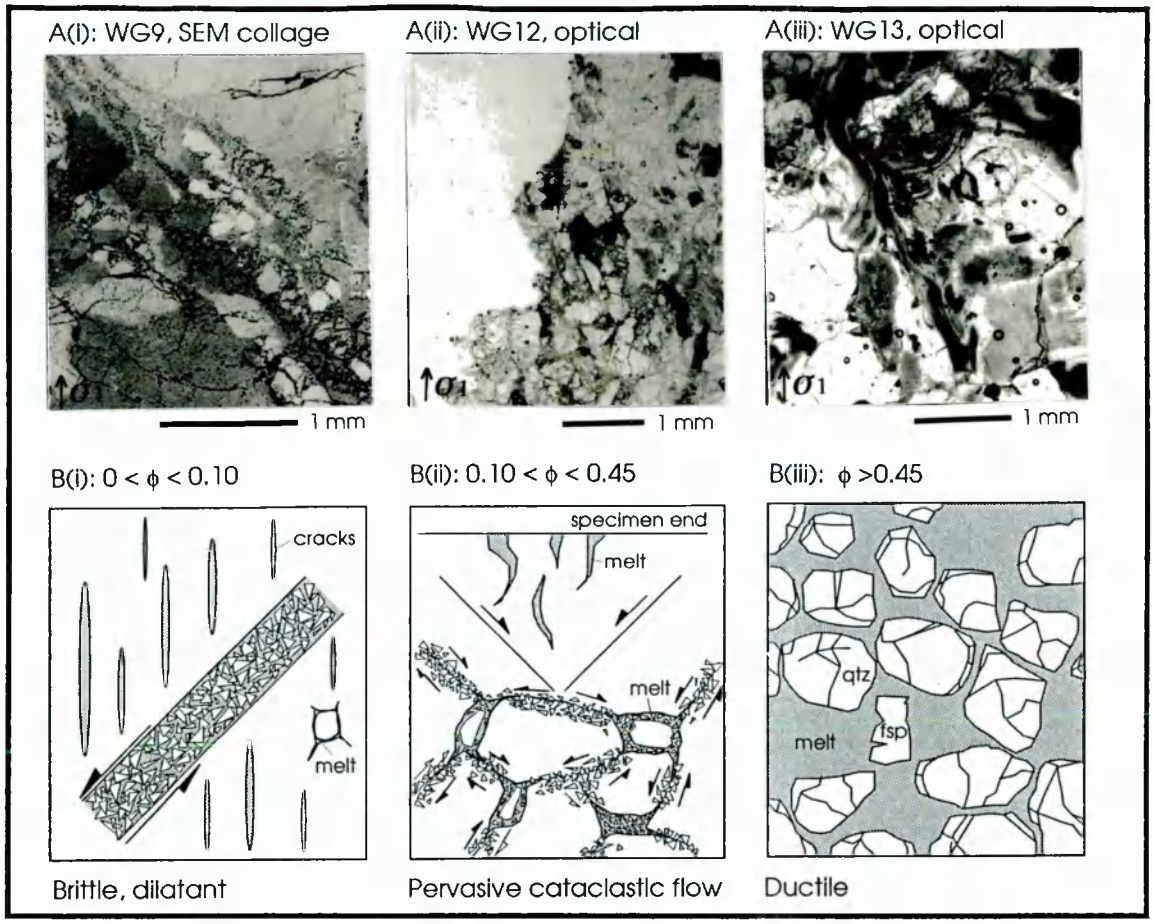

Figure 7.18: Summary of different microstructures observed in deformed samples of Westerly granite. Examples are taken form **i** WG9: brittle; **ii** WG12: pervasive cataclastic flow and **iii** WG13: ductile.

2. Faulted samples deformed by pervasive cataclastic flow. Deformation is characterized by textural dis-aggregation and cataclasis associated with melt assisted grain boundary sliding, without grains deforming plastically. Samples commonly developed barrel geometries. With increasing temperature and melt fraction, the zone of pervasive cataclastic flow expanded.

3. Samples deformed by ductile flow. At high melt fractions remnant crystals are suspended in the melt phase. Shortening is accommodated by flow in the melt phase.

7.5 Parameters influencing the style of microstructures developed in samples

There are several parameters that could influence the style of deformation of a sample. These include temperature, melt fraction, strain rate and maximum strain applied.

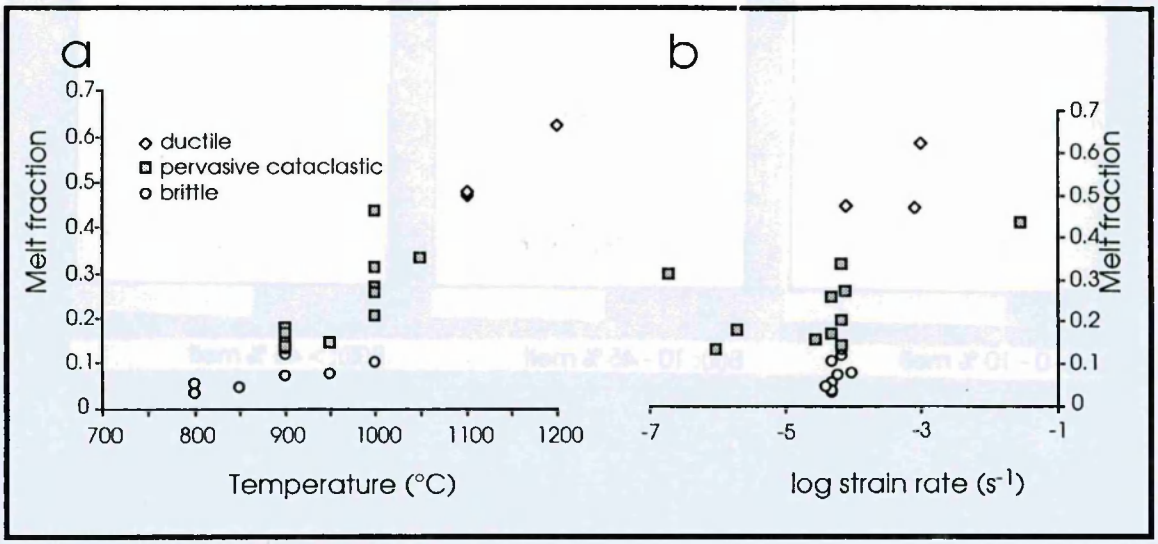

Figure 7.19: Plot of melt fraction versus temperature and log strain rate on which different deformation mechanisms are highlighted using different symbols. Open circles mark samples deforming by brittle deformation, filled squares samples that deformed by pervasive cataclastic flow, while the diamonds signify samples that deformed ductilely.

In **Figure 7.19** sample characteristics are plotted on melt fraction versus temperature and strain rate plots. Different symbols are given to the three different deformation style groups. There is little to no effect of temperature on deformation style (**Figure 7.19, a**), but deformation style is almost exclusively controlled by the melt fraction the sample contains. The observed dominant control of melt fraction on deformation behaviour is confirmed by WG23. In this test melt extraction resulted in localized brittle deformation, despite being deformed at temperatures usually associated with samples deforming by pervasive cataclasis (1000 °C).

The effect of maximum strain on the development of deformation style can not be evaluated as the peak stress was exceeded in all tests. Strain rate variation did not appear to effect the microstructures developed (**Figure 7.19, b**).

7.6 Interpretation of microstructures

In this section the change in observed deformation mechanisms as the melt fraction increases is explained as a consequence of the changing physical properties of the experimental charges.

7.6.1 Low melt fraction, brittle deformation

The localized brittle failure of low melt fraction specimens is typical of the microstructural development during low temperature brittle deformation in low porosity (i.e. crystalline) rocks (Paterson 1978). With increasing stress the specimen accumulate micro-crack accommodated strain (Paterson 1978). The increase in axial load results in micro-cracks opening predominantly parallel to the specimen axis (σ_1). This is associated with radial specimen dilatancy (Brace & Riley 1972), involving the formation of axial micro-cracks (**Figure 7.20, a**).

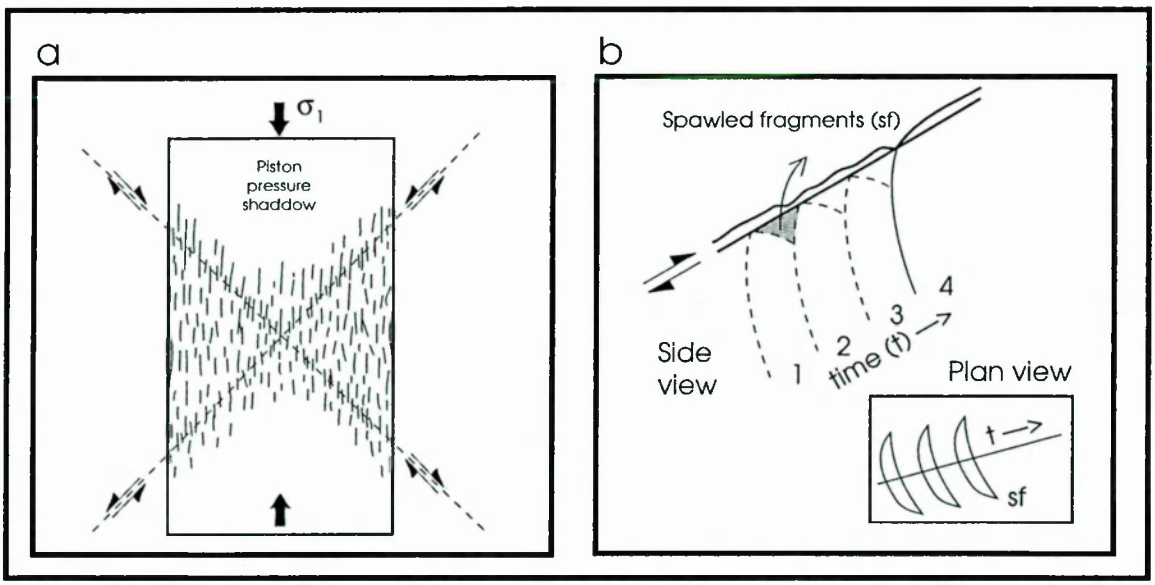

Figure 7.20: Development of single or conjugate sets of macroscopic faults associated with cataclasis. **a.)** En-echelon axial microcracks formed during radial specimen dilatancy link up to form single or conjugate sets of shear faults at the point of ultimate strength of the sample. **b.)** Fragment production on the fault surface due to shear movement on a rough fault surface. A moving indenter causes the generation of inclined cone cracks that link up to form angular fragments that themselves later act as indenters on the fault surface. Thus the amount of fragments in the fault zone increases exponentially.

Fault failure occurs at peak stress on the stress-strain curve (**Chapter 5.2.1**). Faulting develops parallel to a direction of high resolved shear stress in the specimen. The macroscopic fault develops by coalescing a series of en-echelon axial cracks (**Figure**

7.20, a). Friction along the rough fault surface results in spalding of fragments at grain edges, as a moving indenter causes the generation of inclined cone cracks that link up to produce angular fragments (**Figure 7.20, b**). These angular fragments act as indenters themselves, resulting in an exponential increase in fragments in the fault zone. This process of fragment generation culminates in the accumulation of cataclastic material in the fault zone.

7.6.2 Samples deforming by pervasive cataclastic flow

With increasing melt fraction (0.1 to 0.45) cataclastic deformation is no longer restricted to the macroscopic fault zone, but is distributed throughout the specimen (with the exception of the piston pressure shadows that contain melt filled, axial cracks). The boundaries to the fault zone are gradational and become associated with small pockets containing a mixture of melt and cataclastic material. Conjugate shear fractures connect pockets of cataclasite and melt. These microstructures can be compared to those generated by pore collapse in porous sands (Rutter & Hadizadeh 1991).

Compaction of porous sandstone

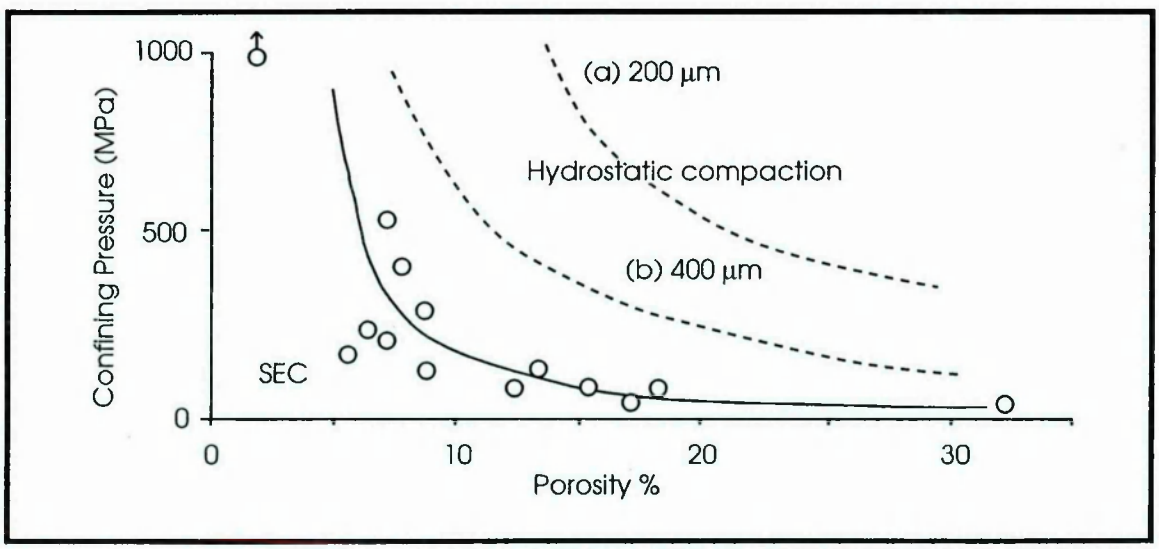

Figure 7.21: Reduction of hydrostatic pressure necessary to cause pore collapse (= pervasive cataclastic flow) by the application of a small deviatoric stress (after Rutter & Hadizadeh 1991). Solid line and filled circles represent samples of Ougthibridge Ganister (with 100 μm average diameter) deformed under a small deviatoric stress by Rutter and Hadizadeh (1991), while dotted lines show calculated transition lines for brittle-ductile transition of quartzite (with grain diameters of 200 (**a**) and 400 μm (**b**) respectively) using only hydrostatic stress after Zhang et al. (1990).

grain shape facilitates pore collapse through the sliding motion of the grains (**Figure 7.22, c, d**). Once sliding along a crack is induced, fragment production is self-perpetuating, pulverising the grain boundaries where sliding is taking place (**Figure 7.20**). This provides an explanation for the extreme width of cataclastic flow zones of up to half the grain size diameter. The large degree of grain damage induced by this process, *shear enhanced compaction* (SEC), would not be induced during purely hydrostatic compaction, accounting for the observed efficiency of a small differential stress in aiding pore collapse (**Figure 7.21**). Grain boundary sliding dominates over trans-granular axial cracking as confining pressure is increased provided that sufficient porosity is available to accommodate the mechanical fragments produced by the sliding (**Figure 7.23**). When all available pore space has been infilled the sample occupies the smallest volume. With continued increase of strain, dilatancy (in the form of axial cracking) supervenes and fault localization occurs.

Comparison of Shear enhanced compaction in porous sandstone with cataclastic flow in Westerly granite

Unlike Oughtibridge Ganister, the unmelted Westerly granite has a tight crystalline fabric with little to no porosity (0.9 % (Wong et al. 1989)). At first sight the microstructures developed by shear enhanced compaction of the sandstone are not directly analogous to those seen during the pervasive cataclastic flow deformation of Westerly granite. However, as the melt fraction in Westerly granite is increased, melt filled gaps between crystalline phases are generated. As demonstrated by the microstructures described, the melt phase is mobile in the presence of a pressure gradient (**Figure 3.01**); this was generated either by the application of a differential stress field or the existence of a low pressure reservoir (e.g. the crushed quartzite in samples WG23, WG24, WG25 and WG27 or open axial cracks). In this instance melt filled pockets can be reduced in size by grain boundary sliding, compacting the granite in a manner similar to Ougthibridge Ganister. No melt movement occurred in the static tests run without a low pressure reservoir (WG14 and WG15) and no melt pore collapse was observed (**Figure 3.04**).

During the shear enhanced compaction of Westerly granite, crystal fragments were collected in the centre of the collapsed pores and melt was displaced to lower pressure regions, including open axial cracks in the piston pressure shadows and the edge of the specimen (**Figure 7.16, d** and **Figure 3.01**). The high viscosity of the melt caused some of the fragments to be transported by the melt phase and to be

extruded at the specimen edge (**Figure 3.01**). It is suggested that fault failure of the samples occurred after all available melt pores had been collapsed.

The occurrence of shear enhanced compaction is also thought to be limited by the following two factors:

1.) The applied strain rate must be sufficiently low to allow flow of melt.

2.) The melt in the sample has to form an interconnected network, with sufficient contact remaining between remnant crystals to allow pressure to be applied to the solid framework. The melt wetting angles of 60 ° or less, expected for granitic systems, would allow the development of an interconnected melt network, even at low melt fractions (**Chapter 3.3**) (van Bargen & Waff 1979). The melt fraction must be low enough for the grain framework to support the applied stress field during deformation.

In summary, an analogy between the shear enhanced compaction of Ougthibridge Ganister and the pervasive cataclastic flow described from Westerly granite is drawn for two reasons:

1.) The pervasive cataclastic flow, seen best in WG12 (**Figure 7.15** and **Figure 7.16**), appears to cause the collapse of melt pools by grain boundary sliding associated with cataclasis;

2.) No compaction and collapse of melt pools were observed in samples with a similar melt fraction but subjected only to hydrostatic stress (**Figure 3.04**).

In order for shear enhanced compaction to be a viable deformation mechanism, the strain rate must be low enough to allow the melt phase to flow and the melt fraction low enough for there to be a grain fabric capable of supporting stress.

7.6.3 Ductile deformation structures

Iron oxide crystal staining that indicates movement within the sample was taken up by the melt phase (**Figure 7.17**). Variable thickness between remnant quartz and plagioclase crystals can be observed (**Figure 7.17**). This contrasts with the uniformly thick melt films observed in static test (**Figure 3.04**). Variable melt films confirm lateral movement of grains with respect to each other. This indicates that deformation took place by flow of the melt phase where remnant crystals of quartz and plagioclase suspended in the melt phase were carried about passively by the melt. The melt films

reduced impingement damage caused by collision of adjacent grains as no solid framework existed at these high melt fractions. The reduction of impingement damage resulted in a reduction of crack density compared to that found in both brittle and cataclastic flow tests.

Samples that developed neo-crystallization of the melt phase showed no evidence of deformation structures in the new phases (**Figure 3.09**, **Figure 4.15** and **Figure 4.16**). This indicates that crystallization was sufficiently small to allow deformation to be taken up by the melt phase. It is unlikely that the new crystals only formed after deformation was terminated, as quenching of the sample occurred within a very short time (0.5 hours max) of the termination of deformation. The crystallization of the melt phase during deformation was also confirmed by the marked increase in viscosity during deformation (**Chapter 6.2**). Macroscopic faulting evident as ridges on the jacket surrounding the sample (**Chapter 5.6**) must have taken place by localized shear in the melt phase in the direction of maximum resolved shear in the sample, rather than fracturing of crystalline material as suggested by the lack of brittle deformation structures.

7.7 Comparison of pervasive cataclastic flow in intermediate melt fraction samples of Westerly granite with the behaviour of saturated soils and porous sands.

In the following discussion, an extract from the paper by Rutter and Neumann (1995) explores the stress strain and yield surface shape of saturated soils and sandstones. This is necessary to develop a deeper understanding of the behaviour of partially molten rocks during shear enhanced compaction prior to the modeling presented in **Chapter 8**. This is followed by a discussion of the effect of melt fraction on the size of the yield surface and deformation behaviour of partially molten rock as explained using a yield surface shape used to describe the deformation behaviour of porous sands and saturated soils.

7.7.1 Deformation behaviour of saturated soils and porous sands

Cataclastic flow of saturated soils and porous sands has been previously been described and mathematically modeled by Muir & Wood (1990), Zhang et al. (1990 a) and Rutter & Hadizadeh (1991). If the pore fluid is immobile, the application of hydrostatic or deviatoric stress to the grain matrix causes a rise in pore pressure. If the pore fluid is not trapped, the resulting pore pressure gradient causes drainage, with concomitant collapse of the grain matrix and porosity reduction. Skempton (1954)

showed that the hydrostatic and deviatoric parts of the stress state can be identified with particular parts of the pore pressure increment *P*.

$$P = B\,(\sigma_3 + A(\sigma_1 - \sigma_3)) \qquad \text{E7.01}$$

where *B* is the pore fluid coefficient that is generated due to the change in σ_3 and *A* being the additional pressure due to the applied deviatoric stress. For a saturated soil *B* = 1, as a water filled, interconnected porosity will always have hydrostatic pressure equalling the pore pressure. For uniaxial compression *A* is expected to be about 1/3 if the pore pressure faithfully reflects the change in the mean stress through the collapse of the solid framework (*A* is below 1/3 for over-consolidated soils and positive for poorly consolidated soils such as quick sand). *A* also varies during the tests, as porosity is reduced. If the initial porosity is so small that deviatoric stress results in dilatancy during failure, pore pressure falls hence *A* can be negative.

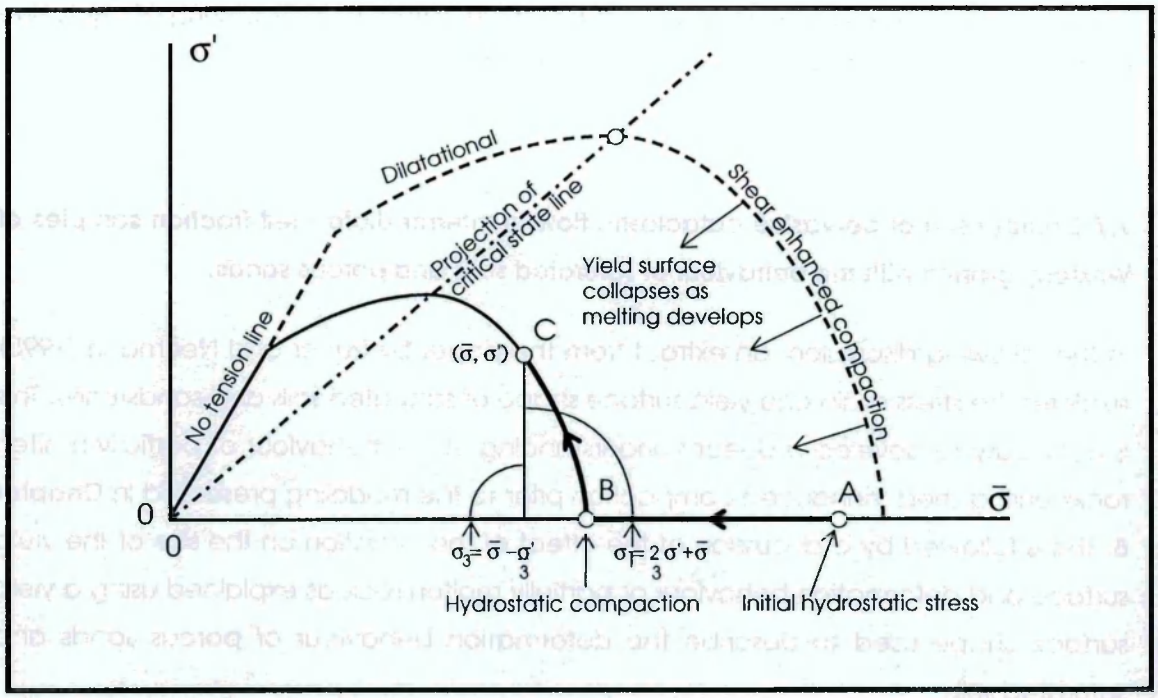

Figure 7.24: Plot of octahedral shear stress (σ) against effective hydrostatic stress ($\bar{\sigma}$) illustrating schematically the closed form of the yield surface for a porous solid. As porosity increases the size of the yield surface shrinks. To the left of the critical state line (constant volume deformation) the failure is dilatational (leading to fault localization); to the right it is compactive. Values of maximum and minimum principal stresses (σ_1 and σ_3) for axisymmetrical loading are indicated, corresponding to a given point on the failure surface (**C**). The change of the mechanical properties of a rock in which a partial melt (= porosity) is generated are described by the shrinkage of the yield envelope, reducing the effective stress state as melt pressure develops. Point (**A**) marks the strength of the unmolten protolith that decreases with increasing melt fraction (**B**). Strength is further reduced by the addition of a shear stress to (**C**).

Rocks with sufficient initial porosity can be made to collapse purely through the application of hydrostatic pressure (Schock 1973; Zhang et al. 1990 a) (**Figure 7.21**). Thus failure can occur without application of deviatoric stress. Initially lower porosities require dramatically higher pressures to cause pore collapse. At low pressures rocks fail by cataclastic fault formation with accompanying dilatancy that results in an increase of strength with decreasing mean pressure. However, the existence of hydrostatic compaction of porous rocks means that the failure surface must pass through a maximum and close back onto the hydrostatic stress axis. The failure surface becomes capped (**Figure 7.24**). The vector describing the distortional and volumetric components of strain is normal to this failure surface and directed outwards. Thus at the point of hydrostatic compaction the strain vector is parallel to the abscissa (no distortional strain). Where the slope of the failure surface is negative, the strain vector is the sum of a compactive and a distortional component. Where the slope is positive, at lower mean pressures, there is a dilative volumetric component plus a distortional component.

The maximum on the failure surface marks the transition from dilatant failure (resulting in fault formation) to compactive failure (accompanied by macroscopic ductility). In soil mechanics this is known as the *critical state*. The negative slope of the failure surface in the compactive region means that the combination of deviatoric stress with the mean stress leads to pore collapse at lower mean stress than would be required in the absence of deviatoric stress. For this reason the negative sloping failure surface is called the *region of shear enhanced compaction* (Curran & Carroll 1979; Zhang et al. 1990 a). With decreasing levels of initial porosity, the loop of the failure surface rapidly expands, defining a surface in porosity - deviatoric stress - means stress space. The crested line of this surface is the critical state line of soil mechanics. The intersection with the mean stress - porosity surface (at zero deviatoric stress) is called the *normal consolidation line*.

7.7.2 Comparison of porous sands with partially molten rock

The above characteristics of soils and porous rocks can aid the understanding of melt extraction from partially molten rocks. A rock under hydrostatic stress ($\overline{\sigma}$) (point *A* on **Figure 7.24**) just before the onset of melting has effectively zero porosity and lies well within the yield surface. As melting commences with the possibility of melt migration (if a local pore pressure gradient becomes established) the yield surface cap shrinks onto the point representing ($\overline{\sigma}$). Compaction commences and pore pressure rises above the hydrostatic pressure, if it has not already done so (if melting involves a specific volume increase). The effective mean stress now migrates along the hydrostat (pushed by the

shrinking yield surface) until a dynamic balance is attained between porosity loss by compaction and porosity creation by melting (point *B* on **Figure 7.24**). The point on the normal consolidation line provides sufficient effective pressure to drive the matrix compaction, as the pore fluid migrates down its pressure gradient.

If, in addition, a deviatoric stress, σ'(octahedral shear stress) is applied (point *C* on **Figure 7.24**), an additional component of pore pressure is generated, equal approximately to one third the deviatoric stress. Thus gradients of the deviatoric stress can additionally drive melt migration. These may be locally much steeper than the gravity-induced regional variation in mean stress. Under the high temperature conditions considered, the effective size of the yield surface loop will shrink with decreasing strain-rate. This is a factor that is not usually important in the behaviour of porous rocks at low temperatures.

It will be recalled that three characteristic microstructural types and failure modes were identified with progressively rising melt fraction. These were:

1. cataclastic faulting
2. distributed cataclasis of the grain matrix with pore collapse
3. flow of a viscous suspension without inter-granular cataclasis

The analogy with porous sandstone suggests that **1** and **2** correspond to Mohr-Coulomb dilatant faulting and shear-enhanced compaction respectively. The dramatic weakening of the rock over the melting range (**Figure 5.04**) testifies to the large scale collapse of the yield surface. The experiments using a porous quartzite sink (WG23, WG27) for extruded melt additionally demonstrated the strengthening and embrittlement that can result if porosity is reduced (**Figure 7.19, b**), and corresponds to the high pressure embrittlement reported for initially high porosity sands consequent upon hydrostatic pore collapse (Byerlee & Brace 1969; Zhang et al. 1990b).

7.8 Summary and Conclusion

1) With increasing melt fraction a change in deformation mechanism was documented from brittle failure at low (0 - 0.1) melt fractions, to distributed cataclastic flow at intermediate (0.1 - 0.45) melt fractions and viscous flow at high (>0.45) melt fractions (**Figure 7.18**). Little evidence was observed for crystal plastic flow of quartz and feldspar above 800 °C, which was described by Dell' Angelo & Tullis (1987 & 1988). This difference in observed microstructures relates to Dell' Angelo and Tullis's tests on

partially molten Westerly granite having been performed at higher confining pressures (1500 MPa) than those presented in this work (250 MPa).

2) It is proposed that the distributed cataclastic flow developed as a result of shear enhanced compaction. This process could contribute to the separation of melt from a partially molten region at melt fractions between 0.1 and 0.45 for a melt with similar characteristics to that produced under conditions similar to those in the experiments presented above.

Chapter 8

Mathematical modeling of melt extraction

8.1 Introduction

The mathematical modeling presented in this chapter is an attempt to quantify the possible rates of melt extraction from partially molten rocks in the mid crust (8 - 10 km depth = 250 MPa confining pressure). The kinetics of shear enhanced compaction are compared to those of other melt extraction mechanisms, and the time required to extract melt from systems with $\phi < 0.30$ is discussed. A mathematical model of melt extraction created by Prof. Rutter in the light of results reported in the previous chapters forms part of a paper submitted by Rutter and Neumann (1995). The discussion of the implications of this model as applied to partially molten granites and pelites (Chapter 8.2.4, 8.3) result from the numerical experiments of both Prof. Rutter and the author.

Firstly, using the equations of McKenzie (1984), it is demonstrated that it would take an infeasibly long time to separate significant quantities of granitic melt by gravitationally driven porous flow alone (**Chapter 8.2.1**). A two component partial melt extraction model is therefore erected. In the first component, it is envisaged that melt is separated from restite and flows into a network of veins by shear enhanced compaction (**Chapter 8.2.3**). In the second component, the melt in these veins is then collected into a dyke system and evacuated towards higher crustal levels, driven by the density contrast between the matrix and the melt, as proposed by Clemens & Mawer (1992) (**Chapter 8.2.2**).

In **Chapter 8.2.4** the model is established and extraction rates for a Westerly granite melt are calculated. This is followed by a discussion of the geological applications of this model (**Chapter 8.3**). The extraction rates for pelitic partial melts are calculated, the effects of changing melt water content (and hence viscosity) and the magnitude of the applied differential stress being explored.

8.2 The problem of the extraction of granitic magma from source regions.

In this section, melt extraction rates are calculated and compared using models of porous flow during compaction (McKenzie 1984), collapse of a vein network (Clemens & Mawer 1992), and shear enhanced compaction.

8.2.1 Gravity-driven extraction by porous flow

The problem of the extraction of melts from a compacting matrix, driven by the density contrast between melt and solid phases, has received a great deal of attention (**Figure 8.01**) (e.g. McKenzie 1984, 1985 and many subsequent developments).

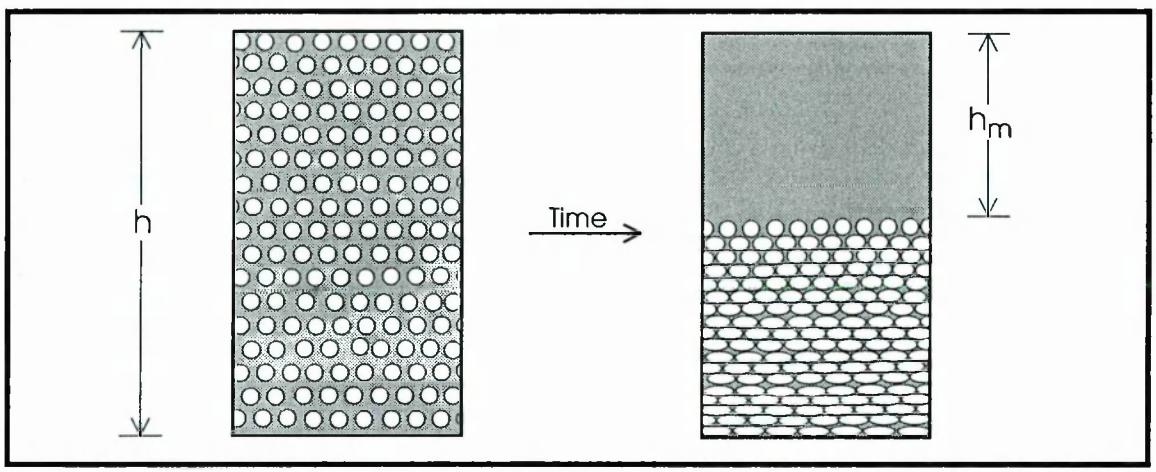

Figure 8.01: Dynamic model of melt extraction from a deformable matrix (after Richter & McKenzie 1984). White circles represent remnant grains with diameter (σ), while grey shaded areas are melt; h gives the initial thickness of the partially molten layer, h_m gives the thickness of the extracted layer of melt after time (t_h). **a.)** Initial state of uniform fluid content and distribution; **b.)** same system after time t_h has elapsed. Compaction of the matrix has caused segregation of the melt, associated with a growing fluid layer on the top of the system.

Wickham (1987) applied McKenzie's (1984) model to the origin of granitic magmas and concluded that the slow extraction rates resulting from the high viscosity of granitic liquids would preclude the origin of large plutons by this mechanism in reasonable periods of time. A simple assessment of the problem can be obtained by evaluating the following equations of McKenzie (1984):

The compaction length, δ_C, that measures a characteristic length scale, is

$$\delta_C = (\mu k / \eta)^{0.5} \qquad \text{E 8.01}$$

where μ is an effective viscosity for the solid matrix, k is the matrix permeability (defined by relation E 6.03) and η is the fluid viscosity.

The upward velocity of the fluid relative to the matrix (w_O) is

$$w_O = \frac{k\,(1-\phi)\,\Delta\rho\,g}{\eta\phi} \qquad \text{E 8.02}$$

where ϕ is the porosity (melt fraction), $\Delta\rho$ is the melt/matrix density difference and g is the gravitational acceleration.

The compaction time (τ_O) is

$$\tau_O = \frac{\delta_C}{w_O(1-\phi)} \qquad \text{E 8.03}$$

The time t_h to compact a layer of thickness h and the amount of melt h_m (**Figure 8.01**) produced after extracting a factor e (= 2.72) of the total melt, are given by:

$$t_h = \frac{\tau_O\, h}{\delta_C} \quad : \quad h_m = \frac{h\,\phi\,(e-1)}{e} \qquad \text{E 8.04}$$

Which can be rewritten as:

$$t_h = \frac{h}{w_O(1-\phi)} \qquad \text{E 8.05}$$

This demonstrates that the total compaction time is not dependent on the matrix viscosity if $\delta_C \ll h$.

In all previous studies, for lack of data, a figure of $3 * 10^{18}$ Pas has been used for the effective matrix viscosity, sometimes at arbitrarily chosen temperatures (e.g. Wickham 1987). This viscosity value is based on experimental data of Cooper & Kohlstedt (1984) for grain-size sensitive diffusive creep of peridotite saturated with 15% basaltic melt at 1300 °C. Based on experimental data presented in previous chapters, this viscosity is inappropriate and too high for partially molten granite. At face value the experimental data presented in **Chapters 5.5** and **6.2** suggest a value of $1.7 * 10^{17}$ Pas, which is the figure for Westerly granite at 900 °C, extrapolated to 1 MPa flow stress and 10% strain, when the melt fraction is about 10% by volume (using equations **E5.04** and **E6.01**). The matrix viscosity would increase slightly with decreasing strain rate as the stress falls owing to the non-linearity of the flow, unless diffusion creep becomes dominant. However, at the same temperature the matrix viscosity would be lower if time were allowed for a true equilibrium melt fraction to become established (**Chapter 3**). At 800 °C, at the same stress and strain but with ϕ only 0.04 , the viscosity would be about 100

times higher. At the *same melt fraction* the viscosity difference would be much less marked.

For *dry* granite at 900 °C, with a density contrast between melt and matrix of 500 kg m^{-3}, melt viscosity of $1.3 * 10^9$ Pas (**E6.06**), and a permeability of $2.5 * 10^{-12}$ m^2, based on a grain-size (d) of 1 mm and a melt fraction (porosity) of 10% and using $k = d^2 \phi^3/400$ (**Chapter 6.3.1, E6.04**), $\delta_C = 1.8 * 10^{-2}$ m. The separation velocity becomes $2.7 * 10^{-6}$ mm/a, and the compaction time is $7.4 * 10^6$ years. The time scale is better viewed by considering the compaction of a layer initially 1 km thick, whence t_h becomes $4 * 10^{11}$ years to extract 60 m of melt. This emphasizes the apparent impossibility of forming granitic plutons by gravity-induced porous flow alone.

8.2.2 Gravity-driven extraction of melt from a vein network

Clemens and Mawer (1992) demonstrated that by collecting magma into a dyke system (> 3 m wide and 1000 m long) from a system of melt filled veins (10's mm width) and propagating the dyke by 20 km in 8 months it is possible to inflate a batholith (of 2000 km^3 in 900 years, if the melt has a viscosity of 10^5 Pas). The magma velocity can be sufficient to achieve geologically realistic intrusion rates and avoid thermal 'death' of the system before reaching the upper crust. Sleep (1988) has also considered the role of tapping of melt by veins and dykes in connection with mafic magma emplacement. In this way, porous flow through intergranular pores may only have to transport melt a short distance, a few metres at most, to the nearest veins (**Figure 8.02**), in contrast to the McKenzie analysis above.

It is possible to examine approximately the kinetics of melt extraction from a vein network by analogy with McKenzie's gravitational compaction and porous flow model described above. In this analogy, an anastamosing network of melt veins may be considered as intergranular porosity; compaction proceeds by the deformation of matrix 'fish', bounded by these veins (**Figure 8.03**). This clearly results in a marked increase in the permeability of the rock mass when compared to the analysis in **Chapter 8.2.1**, but all other basic parameters remain the same.

The permeability of veins can be roughly estimated by considering laminar viscous flow through a parallel-sided channel of width b under pressure gradient dP/dx. In the system considered, a vertical pressure gradient will be caused by the density contrast between the melt and the surrounding rock.

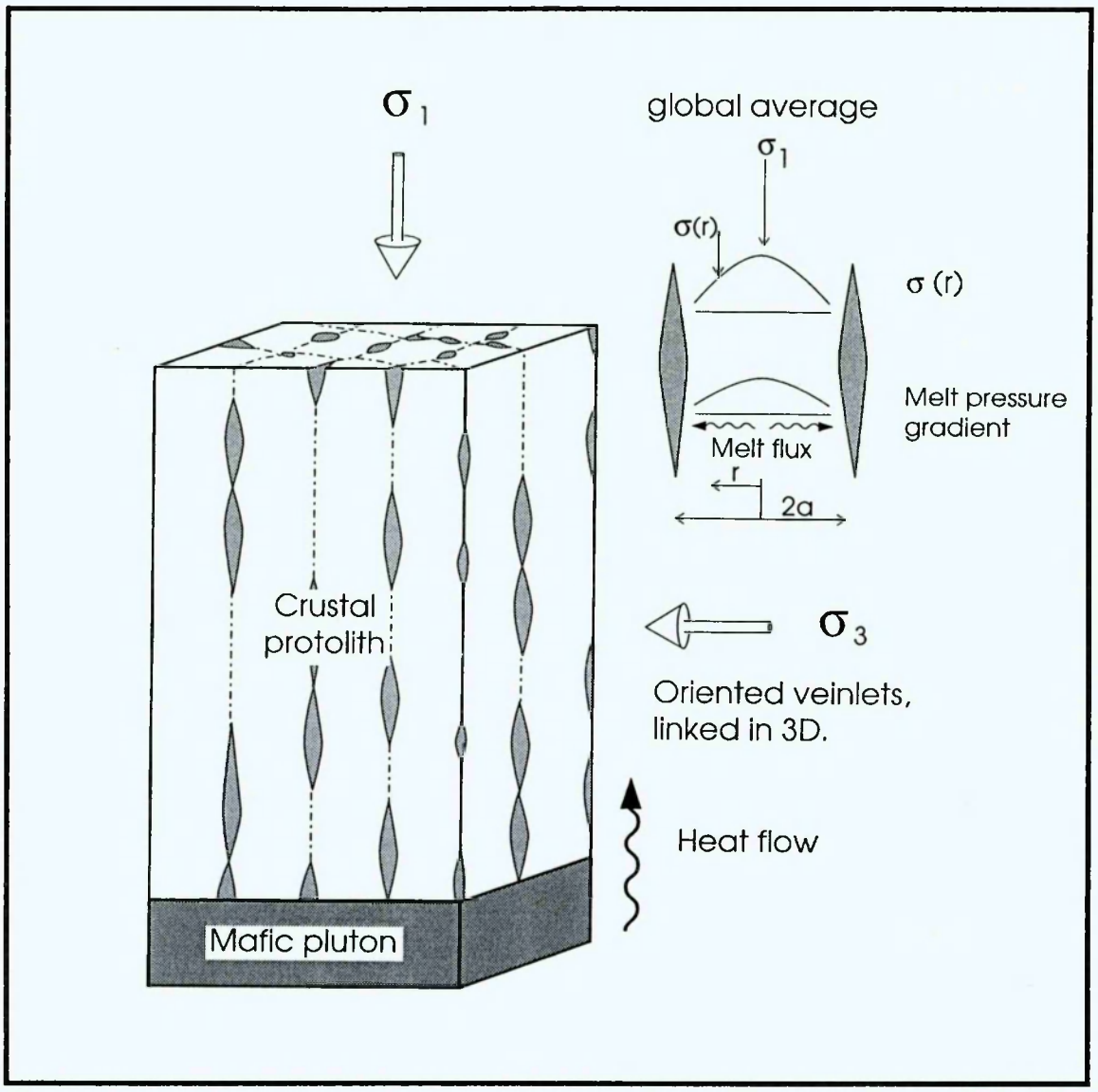

Figure 8.02: Illustration of the model for extraction of granitic melt from its protolith, which is heated from below. Melt is driven into orientated veins of average separation *2a*, as a result of shear enhanced compaction under axisymmetric loading. Even though veins are connected in three dimensions, the melt volume in the veins does not exceed 15 % of the volume of the whole rock, as it has to be possible to transmit shear stresses across the whole rock (impossible to transmit shear stresses across melt).

The mean velocity in the channel (U) is

$$U = -\left(\frac{b^2}{12\eta}\right) dP/dx \qquad \text{E 8.06}$$

For a network of N channels/m, this is analogous to Darcy's law with permeability given by

$$k = \frac{N b^3}{12} \qquad \text{E 8.07}$$

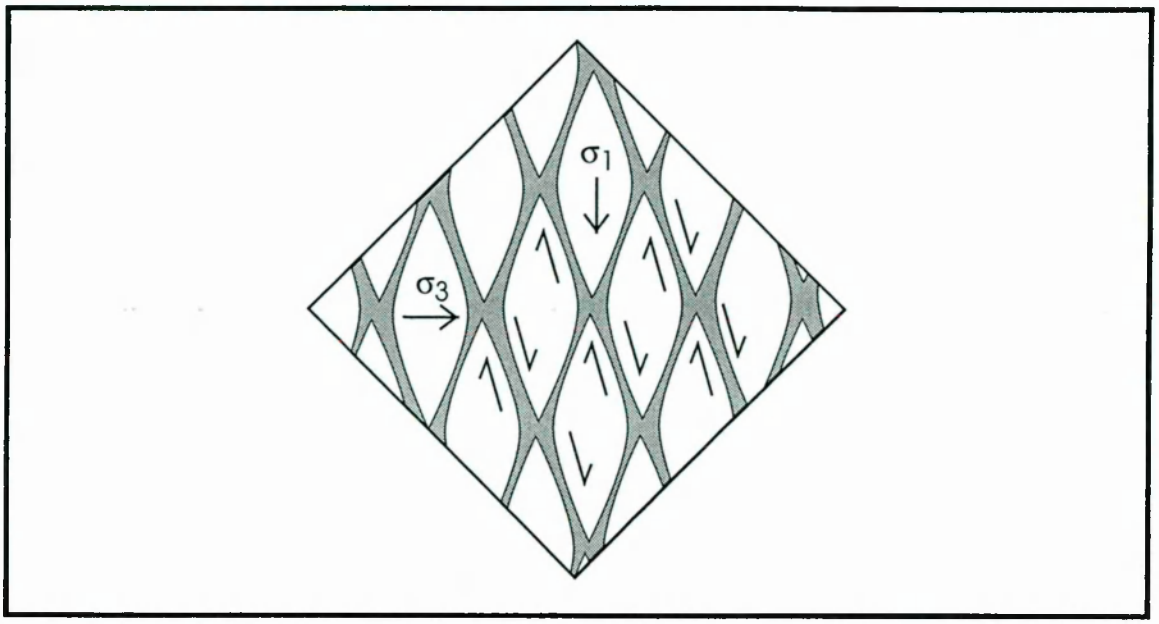

Figure 8.03: Sketch of gravitational compaction of melt filled veins, surrounding "fish" shaped parcels of rock. Compaction produces shear across the veins. However, as described in **Figure 8.02**, the melt fraction in the veins must remain below 0.15 for the combined melt extraction process of shear enhanced compaction and gravitational vein extraction to remain operational.

For 1 channel per metre, with b = 10 mm, ϕ = 0.01 and $k = 8.6 * 10^{-6}$ m^2. Thus δ_C is increased to 3.6 m, w_O is increased to 100 mm/a and τ_O is reduced to about 37 a. t_h is reduced to about 10^4 years to extract a 10 m layer of melt from an original layer 1 km thick. The formation of substantial masses of granitic magma from the drainage of vein networks is clearly a viable process within the time frame of a tectono-thermal event, largely owing to the high effective permeability of the vein network.

8.2.3 Shear-enhanced compaction to drive melt into vein networks

A two stage model is proposed, where shear enhanced compaction provides a viable process to drive melt into the vein system. The kinetics of this process must now be considered because the extrusion of melt into veins and the gravity-driven pooling of melt from the veins are sequential processes, the slower of which will control the overall rate of melt extraction. When the second process is faster, the overall rate is controlled by the vein filling process alone, and the width of the veins does not affect the overall rate. When the first process is faster, the veins will be kept filled to a level corresponding to the equilibrium melt fraction at that temperature. If this process operates at a slower rate than vein emptying, vein filling will control the ultimate kinetics of melt extraction. A kinetic model is now described and calculations are performed to see if shear enhanced compaction can provide a process that will fill the veins fast enough for

significant quantities of granitic melt to be extracted in a geologically reasonable time (below 10^6 a (Wickham 1987)).

A set of prismatic columns of partially molten rock is assumed that are bounded by variously oriented planar veins that intersect in a common direction, (v) which is the direction of σ_1 (**Figure 8.02**). The melt pressure in the veins is the local value of σ_3 (= σ_2), the minimum value of pore fluid pressure that will be able to keep parallel sided veins open. Melt fraction contained in the veins has to be sufficiently low to allow for shear stresses to be transmitted across the volume of the rock to allow shear enhanced compaction to occur in the rock surrounding the melt filled veins. If the vein walls are sufficiently irregular and discontinuous, melt pressure may sometimes be slightly less than σ_3 in the veins, as the vein may be kept open in places by the wall rock supporting the stress; this is a requirement for melt extraction into the veins to occur (Sleep 1988).

At the vein wall, σ_1 will also drop to σ_3 as the vein walls cannot support a shear stress. The local stress difference ($\sigma_1 - \sigma_3$) is inferred to generate a smaller difference in pore pressure ($\sigma_1 - \sigma_3$)/3 (from relation **E7.01**), the gradient of which drives melt radially into the veins (**Figure 8.02**). For convenience, it is assumed that this process is time-independent (steady-state), at least for the period that about 10 to 20% porosity collapse occurs. Steady-state requires that the overall rate of the process is controlled by the rate of melt production, which is in turn controlled by the heat flux into the zone of partial melting. Thus conditions are assumed isothermal, so that the heat input can just maintain the latent heat requirement for a constant rate of melt production. If the heat flux rises, then temperature and melt production rise, fluid and matrix viscosities fall, but the stress difference also falls, tending to counteract an increase in overall extraction rate, and *vice-versa* if heat flux is too low to maintain temperature. The heat budget is also influenced by the advective heat transfer from loss of melt.

The local fluid pressure $P(r)$ will be assumed to correspond to one-third the value of the mean stress with $\sigma(r)$ being the local stress (**Figure 8.02**)

$$P(r) = \frac{(\sigma(r) + 2\sigma_3)}{3} \qquad \text{E 8.08}$$

For steady-state radial permeation, Laplace's equation must be satisfied for the pore pressure

$$\nabla^2 P = \frac{-J\eta}{k} \qquad \text{E 8.09}$$

where J is the rate of production of melt (melt fraction per second), which is constant at all points in the (isothermal) material, and ∇^2 being Laplace's operator. The solution is

$$P(r) - P_V = \frac{J\,h\,(a^2 - r^2)}{4k} \qquad \text{E 8.10}$$

and substituting for $P(r)$ and assuming $P_V = \sigma_3$

$$\sigma(r) = \sigma_3 + \frac{3\,J\,\eta\,(a^2 - r^2)}{4\,k} \qquad \text{E 8.11}$$

where P_V is the fluid pressure in the veins and a is the effective radius of the column (**Figure 8.02**).

The condition of mechanical equilibrium for each column is

$$\sigma_a\,a^2 = 2\int_0^a \sigma(r)\,r\,dr \qquad \text{E 8.12}$$

where σ_a is the average value of the remotely applied maximum stress (σ_1). Substituting for $\sigma(r)$ and integrating gives

$$J = \frac{8\,k\,(\sigma_a - \sigma_3)}{3\,a^2\,\eta} \qquad \text{E 8.13}$$

which gives the rate at which melt is added to the veins.

The deviatoric stress must also be consistent with the resultant strain rate. The rate of vein filling, J, can be considered to be equivalent to the stress-induced strain rate as given by the flow law (**E5.04**), provided the strain is dominantly compactive rather than distortional. Thus

$$J \equiv \dot{\varepsilon} = D \exp\frac{-H}{RT}\,(\sigma_1 - \sigma_3)^n \qquad \text{E 8.14}$$

where D and n are empirical constants, R is the gas constant, T is the temperature in Kelvin and H is the activation enthalpy for flow of the partially molten rock (after **E5.03**). In this analysis values for D, n and H ($10^{-5.832}$ Pa^{-n} s^{-1}, 2.92 and 510061 J mol^{-1}) are taken from the empirical flow law derived from the deformation experiments on Westerly granite (**E5.04**). Simultaneous equations **E8.13** and **E8.14** can be solved for J and $(\sigma_1 - \sigma_3)$ in order to ensure that the extraction rate is consistent with both constraints.

Inserting values for Westerly granite at 900 °C, equivalent to those utilised in the vein compaction calculations in the preceding sections (i.e. $k = 2.5 * 10^{-12}$ m^2, $\eta = 1.3 * 10^9$ Pas, $a = 0.5$ m), the solution for $(\sigma_a - \sigma_3)$ is 0.04 MPa and the melt extraction rate, J, is $2.6 * 10^{-8}$ a^{-1}. Thus the time to extract a volume fraction of $\phi = 0.10$ of the available melt volume (i.e. sufficient melt to fill the vein system with 1% porosity) is $4 * 10^5$ a. This is one order of magnitude slower than the time required for gravity-driven compaction to

extract melt from the veins (see above), but still sufficient to supply an intrusion within a reasonable geological time scale (below 10^6 years). A decrease in viscosity, possible by either increasing the temperature or increasing the water content , will make the extraction rates more favourable (**Figure 8.04, a** and **Figure 8.05**).

8.2.4 Extraction rate sensitivity to temperature, vein spacing and grain size

An increase in temperature will increase the melt fraction, reduce the melt viscosity and decrease the strength of the matrix. These factors should both increase melt extraction rates from the vein system and speed up vein filling by shear enhanced compaction. The effects of vein spacing are less clear. On the one hand it is expected that as veins become more closely spaced, melt has less distance to flow through the rock matrix, speeding up the vein filling process. However, on the other hand, for a given melt fraction, the width the veins when fully charged is reduced; this will reduce the vein effective permeability, slowing down the evacuation of melt from the vein system. An increase in grain size should increase the speed of extraction. These three factors are investigated to quantify their influence on extraction rates and to determine under what conditions the vein filling (equal to the shear enhanced extraction rate) or vein emptying process controls the overall kinetics.

Figure 8.04, a graphically displays the time required to extract a fraction of melt ϕ, from a layer initially 1 km thick of Westerly granite under isothermal conditions for a range of temperatures from 700 °C to 1050 °C. The extraction rates for both vein extraction and shear enhanced compaction were calculated (**Appendix 9**), the time relevant to the slower rate being plotted. For comparison, the time to extract ϕ of melt from the same layer of Westerly granite, over the same range of temperatures, by McKenzie's gravity driven porous flow model is also shown.

To calculate melt fraction and melt viscosity at each temperature, the empirical relations reported earlier (**E3.03, E6.01**, and **E6.09**) were used. The matrix permeability was estimated from melt fraction and grain-size, using the two porosity relationships **E6.03** and **E8.07**. When overall kinetics are controlled by vein emptying, it is supposed that the vein thickness is controlled by the available melt fraction, thus:

$$b = \frac{\phi}{N} \text{ hence } k = \frac{\phi^3}{12\,N^2} \qquad \text{E 8.15}$$

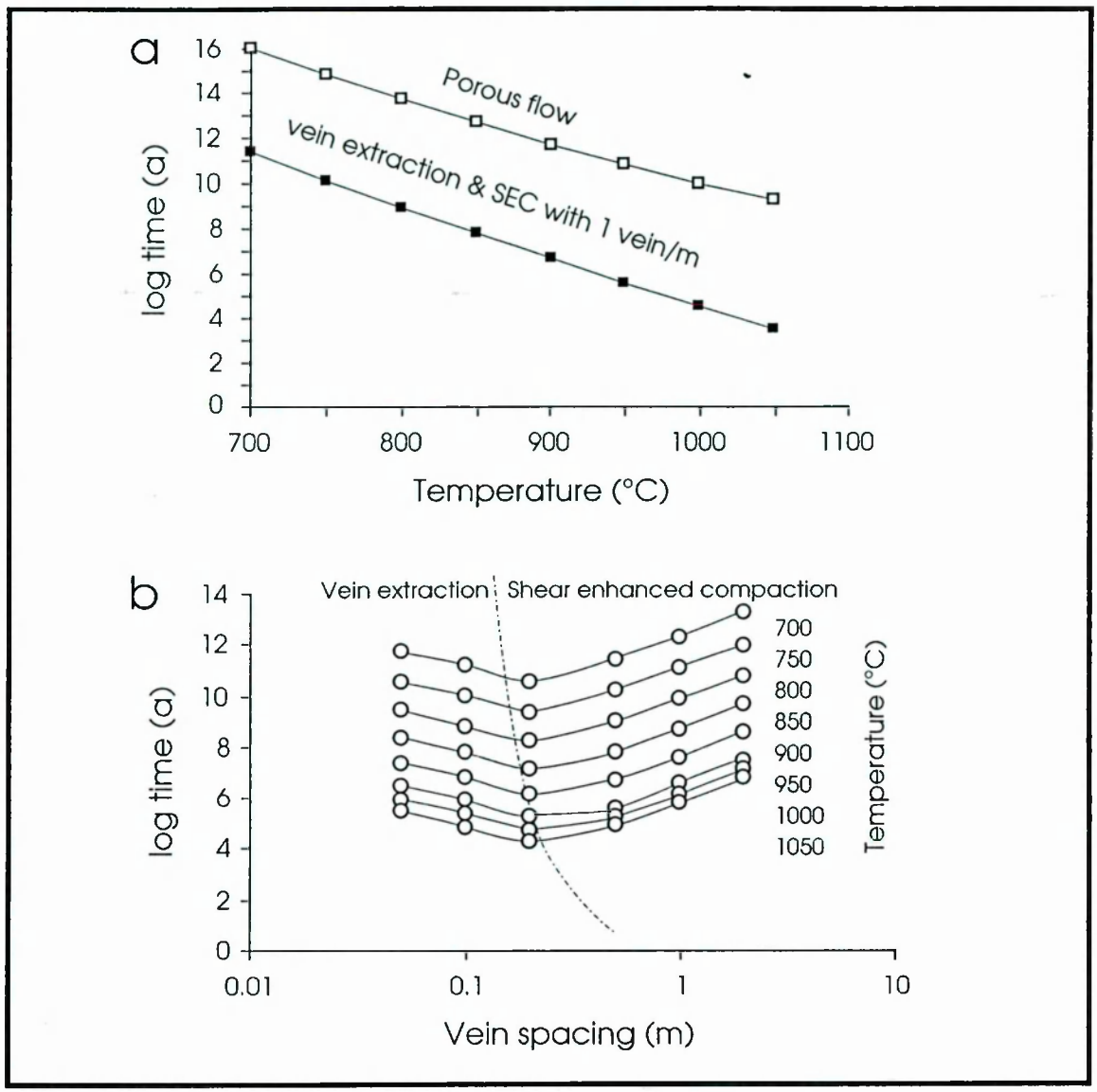

Figure 8.04: **a.)** Comparison of extraction times of $\phi = 0.10$ by porous flow model (McKenzie 1984) and a combination of vein extraction plus shear enhanced compaction with vein spacing $2\sigma = 1$ m. **b.)** change in extraction times of Westerly granite with varying vein spacing at different temperatures. The dot-dashed line marks the transition between vein extraction and shear enhanced compaction being the extraction rate limiting process.

for parallel veins in two dimensions. However, in three dimensional space an additional set of veins occurs at right angle to the set seen in the two dimenional version. Hence, the formula has to be changed to $k = \phi^3/(4 * N^2 * 12)$. This reduces the permeability of the veins, as veins become thinner as each vein is assigned a smaller fraction of melt.

However, melt fraction is subject to a maximum value of $\phi = 0.15$, set to allow shear stress to be supported across the rock. With higher melt fraction shear stress may not be successfully translated across the rock, as melt can not support shear stress. N, the number of veins per metre, may be determined from field observations. To construct

Figure 8.04, a a value of 1 vein per metre was used (as in **Chapter 8.2.2**), which results in a value of 0.5 m for the effective radius (a).

The results of these calculations indicate that (with veins spaced at 1 per metre) the time to extract a proportion ϕ of dry Westerly granite melt from a 1 km layer will always be controlled by shear enhanced compaction (**Figure 8.04**). If it is assumed that a thermal event responsible for granite magma generation might last for 10^6 - 10^7 years (e.g. Clemens & Mawer 1992), melt extraction is viable above 900 °C, corresponding to a melt fraction of 0.10. This is in stark contrast to the time scale for melt extraction by porous flow which never drops below 10^9 years for the temperature range considered.

In order to investigate the control of the vein spacing on the extraction rate, the calculation was re-run varying the vein spacing from 0.5 veins per m to 20 veins per metre. By plotting vein spacing against time for a series of isothermal conditions, it is clear that the extraction time falls to a minimum at between 2 and 5 veins per metre (i.e. a spacing of 0.5 - 0.2 metre) (**Figure 8.04 b**). The minimum also coincides with a change from vein compaction rate control at low vein spacing to shear enhanced compaction control at high vein spacing.

8.3 Extension of the model to general granitoid pelitic partial melts

Granitic melts with different water contents are characterized by different melt viscosities at a given temperature. There is also an increase in melt fraction with increasing water content. Therefore it was considered pertinent to extend the modelling described above to cover general granitoid pelitic partial melts with variable water content. For this purpose an empirical equation has to be found to calculate the melt fraction and viscosity for given water content and temperature.

8.3.1 Calculation of melt fraction and melt viscosity at varying temperature and water content

The melt fraction with varying water content of the source rock was approximated from the curves presented by Clemens and Vielzeuf (1987), adjusted to 250 MPa (**Figure 3.10**). By re-plotting the data presented in **Figure 3.10** as log melt % versus temperature (**Figure 8.05, a**) it is possible to fit a straight line to Clemens & Vielzeuf's (1987) data between 700 and 950 °C, giving:

$$\log \phi = \text{constant} + 0.9 \log \psi \qquad \text{E8.16}$$

with ϕ being the melt fraction and ψ the weight percentage of H_2O in the rock.

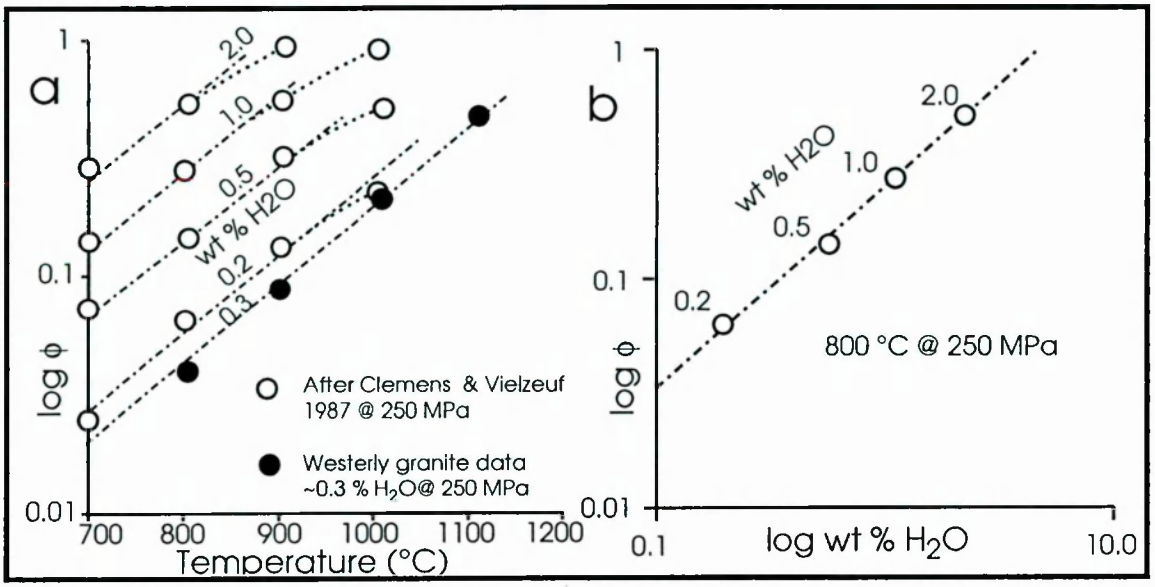

Figure 8.05: Dependence of melt fraction on temperature and water content of the source rock with data from Clemens & Vielzeuf (1987) adjusted to 250 MPa (compare to **Figure 3.10**). **a.)** Plot of log melt fraction versus temperature where open circles are data for partially molten pelite by Clemens & Vielzeuf (1987) and filled circles Westerly granite data from this study. **b.)** Plot of log melt fraction versus log water content of pelitic source rocks at 800 °C and 250 MPa. Note that the melt phase will have between 5 and 10 wt % H_2O from dehydration melting, depending on the amount of mica present.

Combining **E3.03** and **E8.16** the melt fraction equation can be re-written so that:

$$\log \phi = \log f + 0.9 \log \psi + \frac{0.00875}{2.303} T_C \qquad \text{E8.17}$$

where T_C is temperature in °C. By inserting values for T_C = 800 °C, ϕ = 0.10, and ψ = 0.4 it is possible to calculate the value of f, thus obtaining an equation for melt fraction with varying temperature and water content.

$$\phi = 10^{-3.68} \psi^{0.9} \exp(0.00875\, T_C) \qquad \text{E 8.18}$$

This relation is correct to within about 10 % of the value of ϕ up to about 950 °C and for water contents between about 0.2 and 3 wt %.

The empirical data published by Shaw (1965) (**Figure 8.06**) were used to infer the relation between water content and fluid viscosity. Applying a first order best fit representing log viscosity versus log water content over the range of 0.1 to 5 wt % water a relationship between viscosity and water content can be described as

$$\log \eta = \text{constant} - 3.3 \log \psi \qquad \text{E8.19}$$

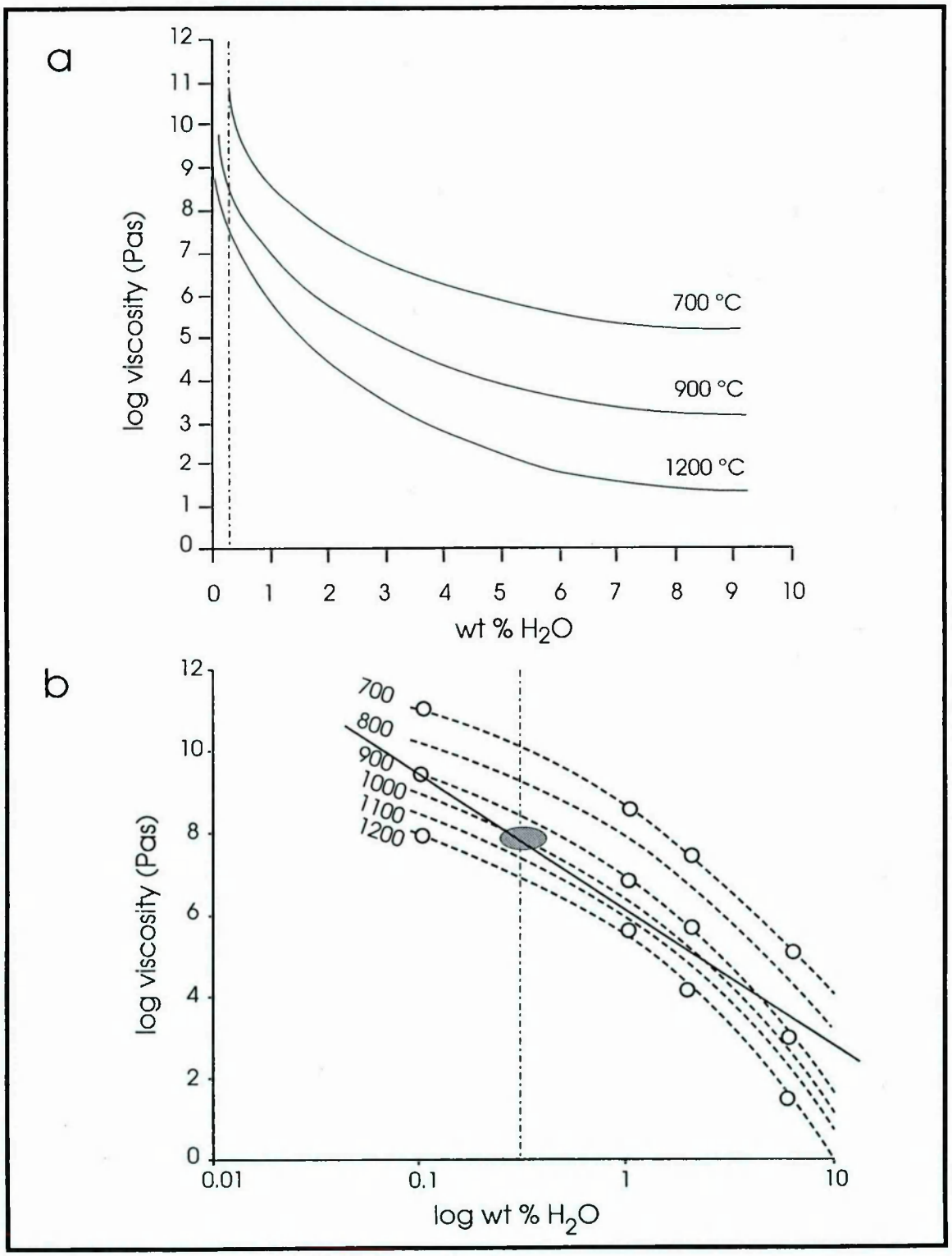

Figure 8.06: Relationship between viscosity and water content at temperatures between 700 and 1200 °C (after Shaw 1965 and Petford 1993). Vertical dot-dashed line indicates water content of Westerly granite. **a.)** log viscosity versus water content; **b.)** log viscosity versus log water content plot. Open circles show position of data as transferred from **a.)** with dashed lines linking data of the same temperature. The inclined solid line shows linear fit applied. The grey shaded ellipse gives the viscosity of Westerly granite at 1000 °C (Compare to **Chapter 6**).

Combining equation **E8.19** with the equation giving the change in viscosity of Westerly granite melt with temperature, **E6.08**, an equation for viscosity can be found

$$\log \eta = \log i + 3.3 \log \psi + \frac{Q}{RT} \qquad \text{E8.20}$$

Substituting the value of 320 kJ mol^{-1} for Q, the activation enthalpy for viscous flow of Westerly granite melt (**Chapter 6.4**), as determined in **E6.06** and inserting values for viscosity and temperature (10^8 Pas and 1000 °C respectively) the factor *i* can be calculated, thus giving an equation for melt viscosity with varying temperature and water content

$$\eta = 10^{-6.82} \exp \frac{Q}{RT} \; \psi^{-3.3} \qquad \text{E 8.21}$$

produces a maximum error of * 5 for water contents ranging between 0.2 and 5 wt % at 1000 °C.

8.3.2 Modeling of melt extraction of granitoid pelitic melts

The calculation **E8.14** was repeated for vein spacings of 1 vein per metre (**Figure 8.07, a**) and 10 veins per metre (**Figure 8.07, b**) for melts with 0.3, 0.5, 1 and 3 weight % water; the models are contoured for the differential stress responsible for shear enhanced compaction. At 1 vein per m, the rate of melt extraction tends to be governed by shear enhanced compaction, whereas at 10 veins per m, the rate of vein emptying is the controlling process. If a cut off of 10^7 years is applied for the length of a melt producing event, then for both models the lowest temperature at which all the available melt can be extracted is 850 °C for the dry melts, dropping to below 700 °C for the wetter melts.

For the wetter melts (above 0.5 wt % in the 10 veins per m model and 3% in the 1 vein per metre model) the calculations require progressively unrealistically high deviatoric stresses due to shear enhanced compaction having to balance the rate of vein filling. The rate of extraction is more than likely ultimately limited by stress-controlled boundary conditions, where the origin of the deviatoric stress can be due to local lateral density variations (due to different adjacent rock types) and tectonic deviatoric stresses. For this reason, an arbitrary upper limit of 10 MPa deviatoric stress was applied in this model. This limits the rate at which melt can enter the vein system, driven by shear enhanced compaction, at a particular temperature. This effect has been taken into account in the curves presented for melt with 1 and 3 wt % water in the 10 veins per m model and

the 3 wt % water curve in the 1 vein per m model. Overall, the effect of a limit on the maximum attainable deviatoric stress is to increase the time required to fill the vein system and, where shear enhanced compaction is the rate controlling process, the time to extract the melt.

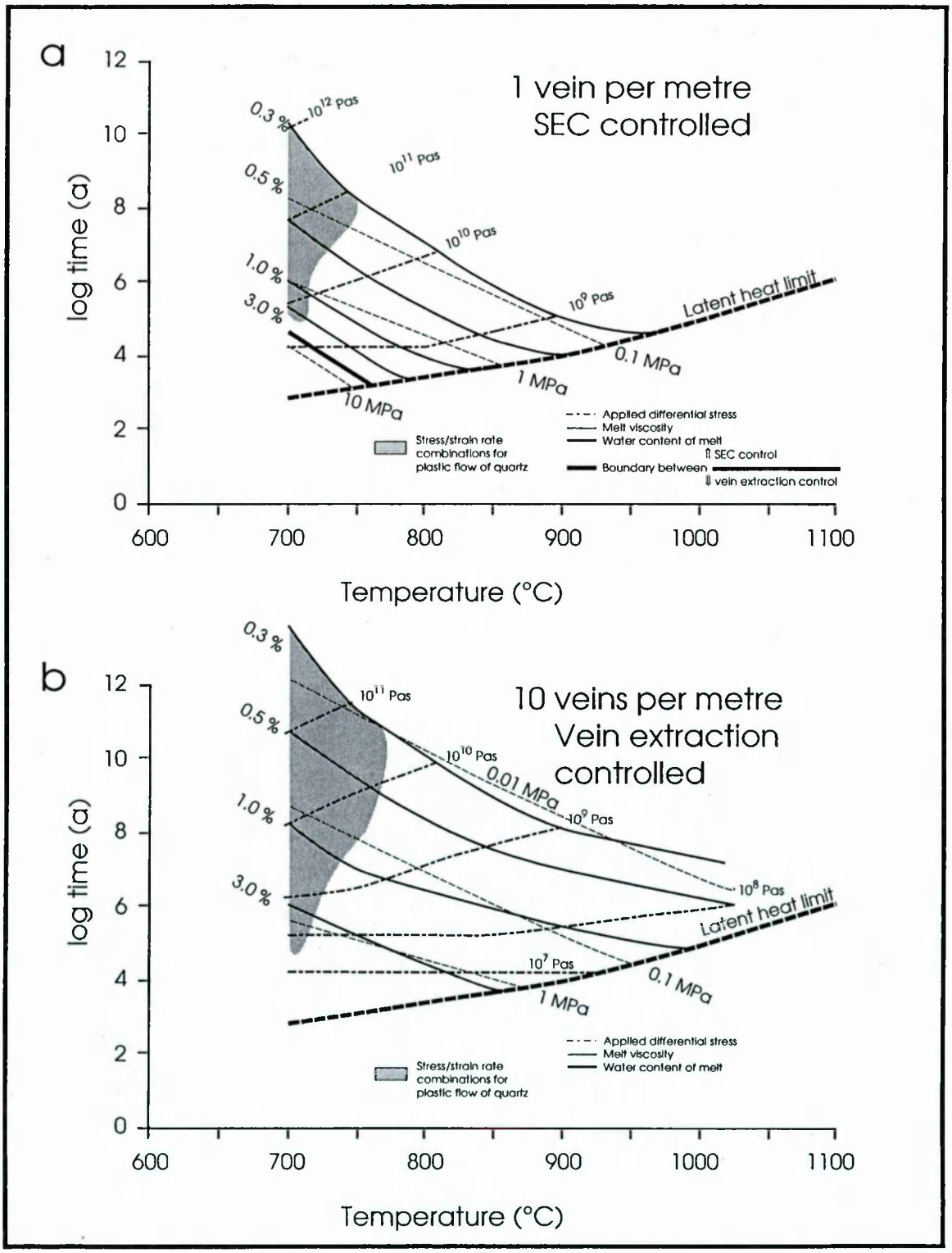

Figure 8.07: Vein extraction of partial melts with water contents between 0.3 and 3.0 wt %. The plots are contoured also for constant viscosity and differential stress, with a cutoff applied at 10 MPa. Grey shaded area gives zone where plastic deformation of quartz can take place (after Paterson & Luan 1990). **a.)** extraction times assuming vein spacing of 1 vein per metre, with the extraction controlled by shear enhanced compaction. **b.)** Extraction times of melt in a system with 10 veins per metre. Extraction is controlled by the speed of vein drainage. Latent heat limit after Bergantz (1989). In both models an average grain diameter of 1 mm was used.

A further limiting factor at high rates of melt extraction is the maximum attainable rate of melting, as determined by the heat flux (e.g. Bergantz 1989). Assuming that the zone that finally undergoes partial melting is heated by an igneous intrusion underlying this zone (**Figure 8.02**) the time at which partial melting of the country rock at a distance y from the boundary to the igneous contact reaches the temperature T_Δ which is between T_O, (the temperature of the intrusion) and T_b (the temperature of the country rock. The temperature T_Δ can be calculated (after Turcotte & Schubert 1982) as:

$$\frac{T_\Delta - T_b}{T_o - T_b} = \text{erfc}\,\frac{y}{2\sqrt{k\,t}} \qquad \text{E8.22}$$

with *erfc* being the complimentary error function (Turcotte & Schubert 1982, p. 160) and κ being the thermal diffusivity of the country rock with

$$\kappa = \frac{\gamma}{\rho c} \qquad \text{E8.23}$$

where γ is the coefficient of thermal conduction, ρ is the density and c is the specific heat. Substituting values for granite with γ = 3.2 W m^{-1} K^{-1} a density of 2650 kg m^{-3} and a specific heat of 1 kJ kg^{-1} K^{-1} the thermal diffusivity of granite can be calculated as 0.1 mm^2 s^{-1}. This value for γ completely ignores the latent heat of fusion needed to cause melting of the country rock protolith. The latent heat of fusion of granite is similar to that of basalt with 320 kJ kg^{-1} (Turcotte & Schubert 1982). However, if only a fraction of ϕ = 0.10 of the rock is molten, this value effectively drops to 32 kJ kg^{-1}. If this amount of melting takes place over a temperature interval of 50 °C the latent heat of fusion is 0.61 kJ kg^{-1} K^{-1}. As this value is on the same order of magnitude as the specific heat, and if the temperature of the country rock has to be raised by several hundred degrees Celsius before melting commences, it can be ignored in future calculations.

Assuming a hot body kept at 1100 °C intruded into country rock initially at 600 °C it is possible to calculate the time for a distance y = 500 m (half way through the layer that partially melts) from the contact to reach each temperature at which the extraction rate was estimated.

Using equations **E8.18** and **E8.21** in conjunction with **E8.22** it is possible to calculate extraction rates of melt from a partially molten protolith, contoured for constant viscosity, differential stress and water content (**Figure 8.09**).

The effect of changing grain diameter (z) on extraction rate is studied in **Figure 8.08**. While extraction rates in **Figure 8.07**, a were calculated for grain size diameter of 1 mm, in **Figure 8.08** grain size diameters of 2 and 5 mm were used respectively, with vein spacing at 1 vein per metre.

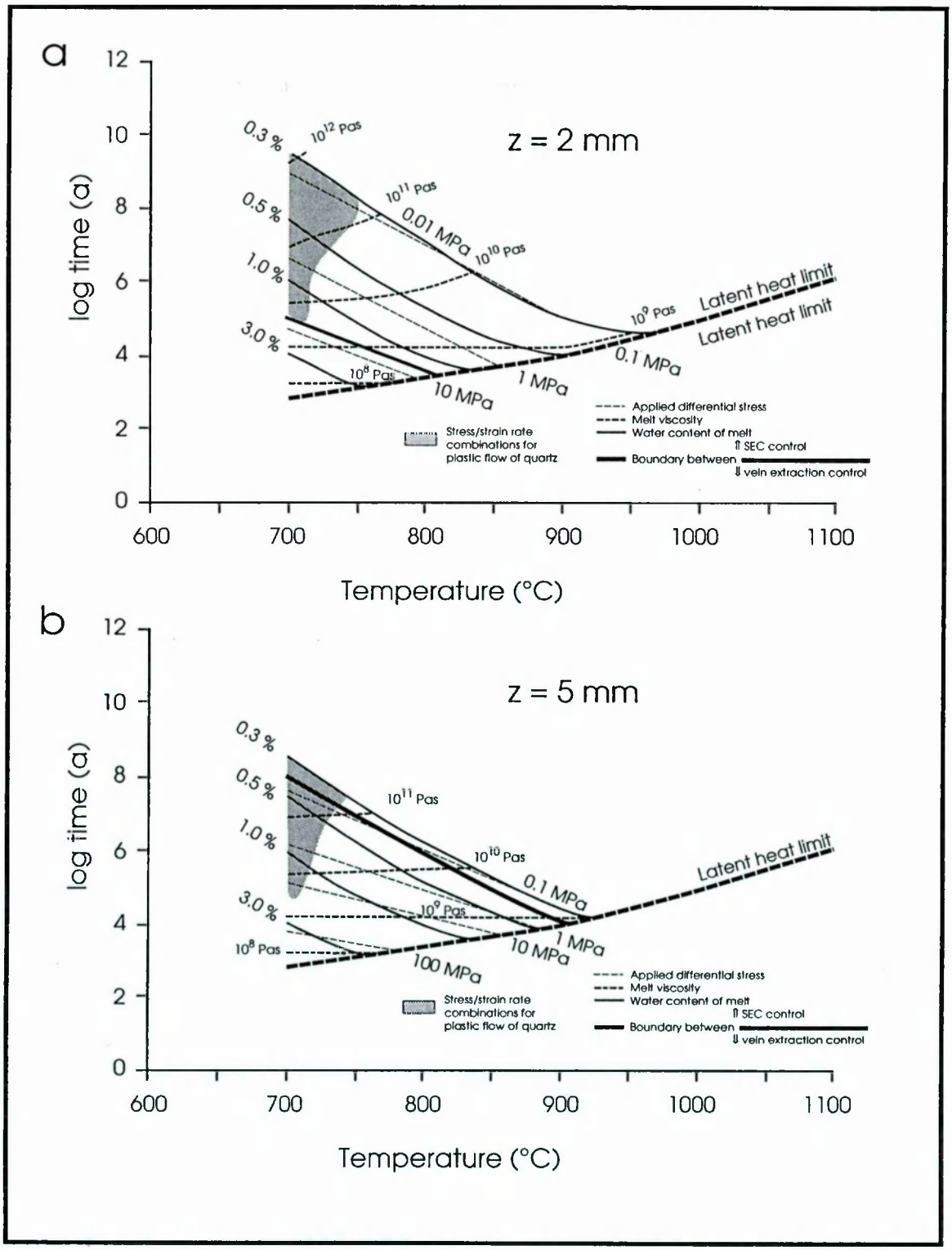

Figure 8.08: Vein extraction of partial melts with water contents between 0.3 and 3.0 wt % with constant vein spacing of 1 vein per metre. Gain diameters in permeability, stress and viscosity calculations were varied between **a.)** 2 mm and **b.)** 5 mm.

With increasing grain size the extraction time drops exponentionally. While melt extraction at 2 mm is dominantly controlled by shear enhanced compaction the rate of vein emptying is the dominant rate controlling step in a senario with an average grain size diameter of 5 mm. However, with increasing grain size the applied differential stress also rises exponentially, reaching unrealistic values (above 10 MPa) in melts from a source rock that contains above 1 wt % H_2O and has a temperature below 850 °C.

It is also possible to calculate extraction rates with increasing temperature (controlled by an increase in temperature) at a constant water content (**Figure 8.09**).

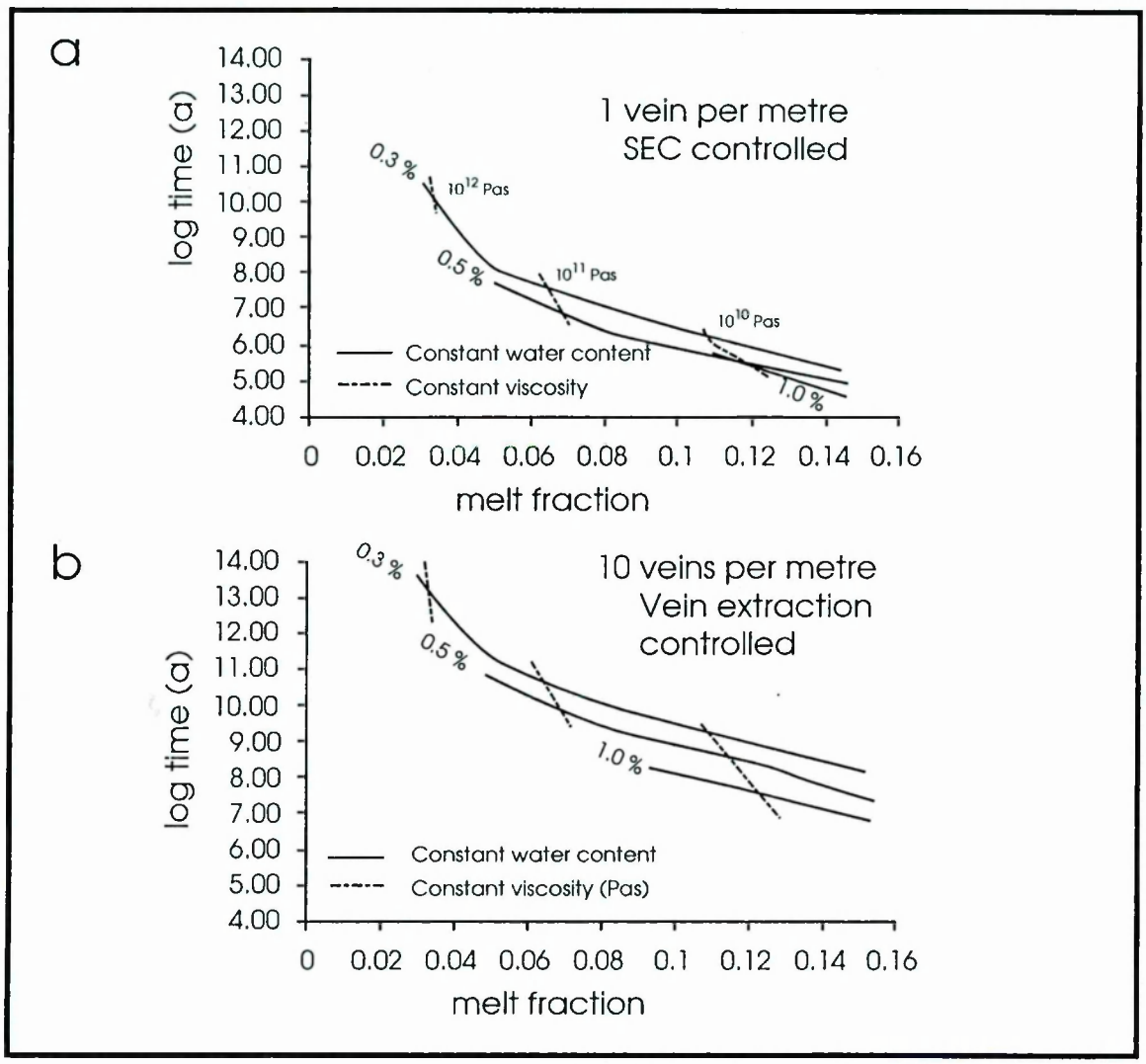

Figure 8.09: Illustration of the change in extraction time with changing water content assuming a vein spacing of **a.)** 1 vein per metre, and **b.)** 10 veins per metre. Plots are contoured for constant viscosity and water content.

This indicates that the 1 vein per metre model is more efficient at extracting melt and in this case it is even possible to extract a $\phi = 0.08$ within the 10^7 years time limit. As might

be expected, a wetter less viscous melts can be extracted more quickly than a drier more viscous melt at the same melt fraction.

8.4 Physical requirements of the two stage model

It is not immediately clear whether conditions for shear enhanced compaction (SEC) and vein formation can arise simultaneously. SEC requires the fluid pressure in the veins to be less than effective σ_3 (**Figure 8.02**), although the difference may be rather small. However, it is commonly held that fluid pressure must equal or exceeded σ_3 for extensional fractures to occur (Clemens & Mawer 1992). This situation could arise sporadically, for example as a result of the net specific volume increase associated with vapour absent melting (Clemens & Vielzeuf 1987, Davidson & Schmid 1993). Vein formation might also be favoured if there is a pre-existing planar fabric in the rock, or through the upward propagation of hydraulic fractures from beneath, where the melt pressure may be higher. As demonstrated in **Chapter 7**, brittle failure under differential stress can lead to axially orientated cracking even under high effective mean stress, although long cracks probably require a low effective mean stress (Davidson & Schmid 1993). Once a slightly irregular vein network had formed it would be unlikely that veins could be closed completely, thus conditions of melt pressure slightly lower than σ_3 should be able to exist for periods of time (Davidson & Schmid 1993).

No information regarding the form of the yield surface for a partially molten system, in particular whether it is tall and narrow or short and wide in $\sigma' - \bar{\sigma}$ space is available (**Figure 8.10**). If the former, it is possible for a single stress state to give rise to shear-enhanced compaction in the σ_1 direction associated with contemporaneous formation of extensional veins. If the latter, the two conditions cannot arise simultaneously, but vein or shear fault formation conditions would have to arise sporadically. This kind of shift due to sporadic increase in pore fluid pressure, due to an increase in melt volume has been previously described as *melt embrittlement* by Davidson and Schmid (1993).

The flow law assumed to describe the solid matrix (**E5.04**) is that obtained by extrapolation of the empirical law for Westerly granite. Insofar as the extrapolation is valid, it applies to the particular water content and melt fraction of Westerly granite. No attempt has been made to compensate for the larger melt fractions associated with truly equilibrium melting and the greater melt fractions for wetter rocks. Changing the flow law derived in equation **E5.04**, to include a steeper increase in melt fraction with temperature, then the activation enthalpy (H) and supported stress will decrease. This

will result in a lower strain rate needing to be applied to cause viscous flow of partially molten rock at constant temperature. This will lead to faster extraction rates with increasing temperature than modeled above.

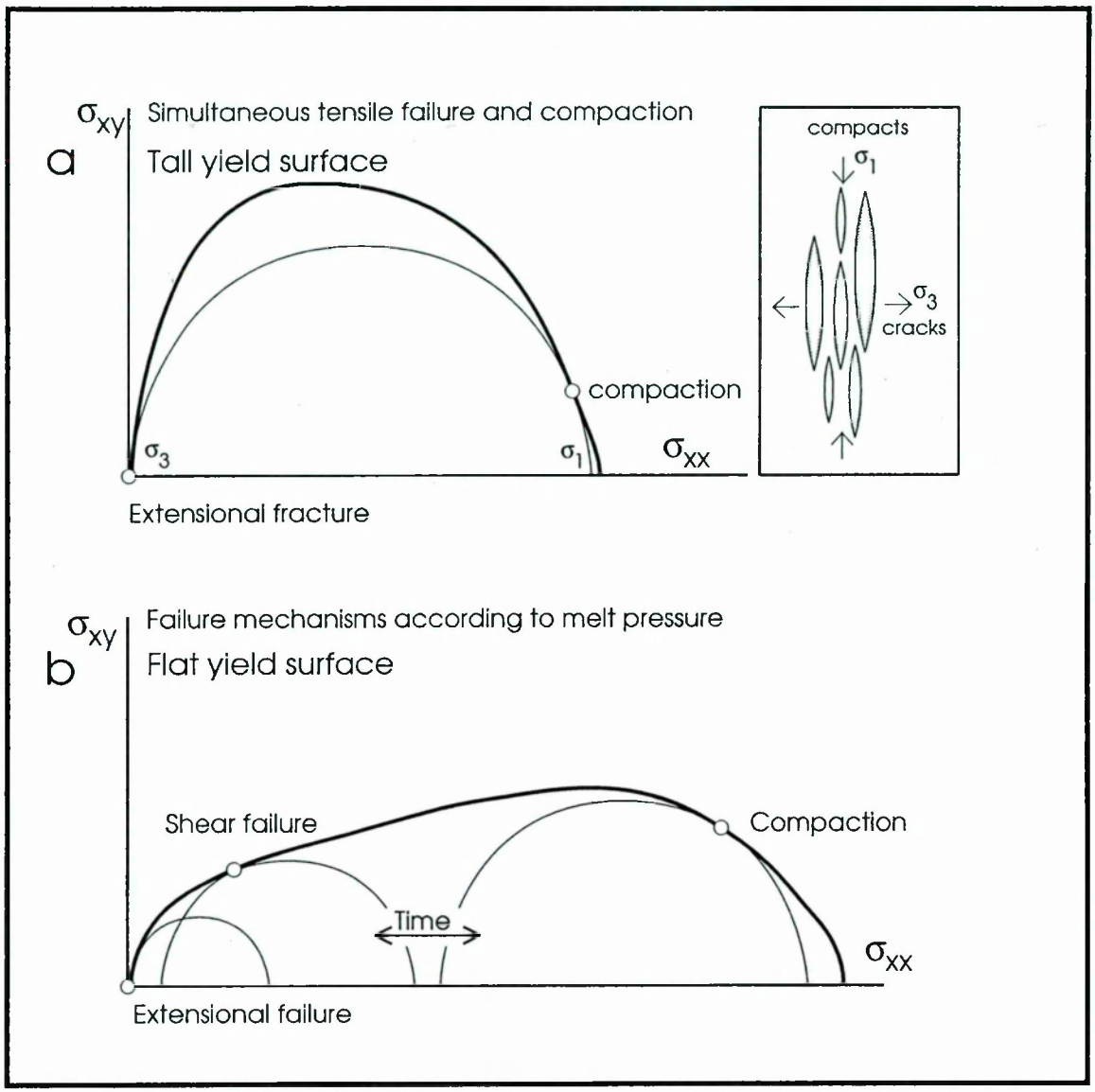

Figure 8.10: Possible shapes for the failure surface of a partially molten rock. **a.)** Steep failure surface in which extensional failure and shear enhanced compaction can occur contemporaneously. **b.)** An episodic shift in pore pressure results in consecutive formation of extensional cracks and shear enhanced compaction of the surrounding matrix.

Although cataclastic deformation of the matrix was clearly involved in all the experiments, it is not known how much more effective melt-assisted diffusion creep becomes with decreasing strain-rate (e.g. Dell' Angelo & Tullis 1987; Dell' Angelo et al. 1988; Tullis & Yund 1977), and how this will modify the flow law, but all these effects are expected to enhance the kinetics, as plastic deformation of grains will allow smaller melt volumes to be extracted at lower applied stresses and strain rates.

Limited indications of intra-crystalline flow were only seen in the experimental microstructures at 800 °C (**Chapter 6**). This is not surprising, for the differential stresses applied were too low to activate intra-crystalline plasticity in quartz or feldspars above this temperature. Indeed, using the preferred plastic flow laws for quartz plasticity of Paterson & Luan (1990) the stress/strain-rate combinations associated with granite magma extraction lie below those required for quartz plasticity over most of the temperature/time space considered. **Figures 8.07** shows the limited extent of the region (700 to 800 °C) wherein it is expected that quartz plasticity might be expected in partially molten granite (grey shaded area).

8.5. General Discussion and Conclusions

The above 2-stage model for melt extraction provides a method whereby a viscous granitic melt can be separated from a partially molten source area and transported a significant distance in a geologically realistic time scale. This process is qualitatively similar to that outlined by Clemens & Mawer (1992), in which the role of deformation synchronous with melt extraction was emphasized.

It has been common in discussions of this point in the literature to concentrate on the question of vein formation by hydraulic fracture and to neglect that of how melt becomes expelled into the veins.

The overall kinetics arising from the model proposed in **Chapter 8.2.3** are faster than gravity-driven porous flow model for two reasons. First, in the stage of extraction of melt by porous flow, transport distances to the veins are small and melt pressure gradients, although small, are hundreds to thousands of times higher than those arising in large-scale porous flow. Secondly, once the melt has accumulated in veins, the effective permeability due to channel flow in the fractures is several orders of magnitude higher than that for intergranular flow, although now the pressure gradient is reduced to the low, gravity-induced value. There is ample scope for adjusting the details of the model and the values of the parameters used, but it is seems clear that the combination of shear enhanced compaction together with local segregation into veins provides the basis of a viable mechanism for granite extraction.

Chapter 9

Summary and conclusion

9.1 Summary

This thesis set out to explore the process of melt extraction from a protolith containing a small melt fraction and to establish a flow law for partially molten granite. For these purposes a series of experiments was carried out on dry Westerly granite over the temperature range of 800 to 1200 °C at 250 MPa confining pressure. Most of the samples were uniaxially deformed at constant strain rates that varied between $4 * 10^{-4}$ to $2 * 10^{-7}$ s^{-1}, associated with stress relaxation tests to study the mechanical behaviour of a partially molten rock over a wide temperature and melt fraction (ϕ = 0.03 to 0.77) and strain rate range. Static tests were carried out to evaluate melt morphologies, while chemical analysis of phases in selected samples allowed evaluation of melting kinetics and crystalline phases generated as a melt by-product.

All experimental samples were cored from a single block of Westerly granite, a fine grained monzogranite with an average grain size of 300 µm, though the greatest part of the rock volume is made up of grains with an average diameter of 960 µm (**Chapter 2.3**). The rock is isotropically textured and the modal composition can be given as plagioclase ($An_{0\ to\ 15}$) = 38%, K-feldspar ($Or_{90\ to\ 98}$) = 26 %, quartz = 29%, biotite = 5 % with accessory quantities of muscovite, chlorite, apatite, ilmenite, hematite and sphene. There are variable degrees of sericitization of plagioclase crystals.

In static experiments melt was distributed as thin films along grain boundaries indicating a low melt wetting angle ($\phi < 5°$), thus allowing a high contiguity of melt, even at low melt fractions (**Chapter 3.3.1**). Melting takes place at low temperatures (800 °C) along quartz and biotite grain boundaries and at sites of plagioclase sericitization. Complete melting of chlorite and muscovite occurs even in the lowest temperature samples (at 800 °C), whereas biotite and K-feldspar were not observed in samples heated above 1050 °C. Plagioclase occurs in samples up to 1100 °C, while the highest temperature sample (1200 °C) only remnant quartz was observed.

With increasing temperature the melt fraction increased smoothly from ϕ = 0.03 at 800 °C to ϕ = 0.77 at 1200 °C. A small increase in melt fraction with time was observed, though this effect was secondary compared to the increase in melt fraction with

increasing temperature. The melt distribution was heterogeneous and in deformed samples was concentrated along macroscopic fault zones and in low pressure regions.

An equilibrium melt fraction was not attained in any sample, including the powder sample WG1, during times ranging between 2 and 170 h the sample remained at temperature (**Chapter 3.4.3**). The volume fraction of melt (ϕ) in samples heated for 2 hours at temperature T_C (in Celsius) over the temperature range of 700 to 1000 °C can be approximated by:

$$\phi = 3.77 * 10^{-5} \exp (0.00875 * T_C) \qquad \text{E 3.03}$$

The disequilibrium nature of partial melting was also expressed by the heterogeneity of melt compositions in all samples analyzed (**Chapter 4.3**). Melt compositions strongly reflected the compositions of adjacent crystals involved in the melting process, and formed as a melt by-product, with compositional equilibration only attained locally. The crystalline melt by-products varied widely in composition and included olivine, that can not exist in equilibrium with granitic melts, thus indicating the relative chemical isolation of melts, and the limited degree of mechanical and chemical homogenization (**Chapter 4.2.4**).

A smooth decrease of maximum supported strength with increasing melt fraction over the melt interval (800 to 1100 °C) occurred at the same strain rate (**Chapter 5.2.2**). A *rheological critical melt fraction* predicted by van der Molen and Paterson (1979) was not observed. Strain rate stepping tests in conjunction with stress relaxation tests confirmed that stress relaxation data can be used to predict deformation behaviour of partially molten samples at strain rates below those accessible in the experimental set-up (**Chapter 5.4**), as deformation behaviour is unaffected by the deformation history of the sample. Multiple regression of stress relaxation data defines a flow law for partially molten Westerly granite deformed under the present experimental conditions (**Chapter 5.5**):

$$\dot{\varepsilon} = 10^{-5.832} \exp \frac{-510061}{RT} \sigma^{2.92} \qquad \text{E5.04}$$

with temperature (T) in Kelvin and stress (σ) in Pascals and R being the gas constant (in J mol^{-1} K^{-1}) and $\dot{\varepsilon}$ being the strain rate (in s^{-1}).

The viscosity of melt alone (η), estimated by the permeation distance into porous sandstone under a known pressure gradient (**Chapter 6.3**), can be approximated to change with temperature by:

$$\eta = 8.13 * 10^{-6} \exp(320000/RT) \qquad \text{E6.08}$$

This agrees with viscosity estimates by Shaw (1965), and are equivalent to melt extracted from a pelitic source rock that contains 0.3 wt % H_2O (Clemens and Vielzeuf 1987),. This proportion of water is consistent with the proportion of hydrous phases present in the starting material (**Chapter 2.3**).

With increasing melt fraction deformation microstructures change. At low melt fractions ($0 < \phi < 0.10$) Westerly granite samples fail by brittle failure (**Chapter 7.3.1**), with the development of a macroscopic, cataclastic fault zone. Deformation is limited away from the fault zone. Melt fills voids between cataclastic fragments and axial cracks. At intermediate melt fractions ($0.10 < \phi < 0.45$ %) samples deformed by pervasive cataclastic flow (**Chapter 7.3.2**), whereas samples containing $\phi > 0.45$ melt deformed by viscous flow (**Chapter 7.3.3**). By analogy with uniaxial deformation of porous sands (e.g. Rutter & Hadizadeh 1992) the two lower melt fraction deformation mechanisms correspond to Mohr-Coulomb dilatant faulting and shear enhanced compaction respectively. The voids in the granite are the volume filled by melt. As these voids collapse melt is expelled into low pressure regions and outside the sample confines. The dramatic weakening of the rock with increasing melt fraction testifies to the large scale collapse of the yield surface (**Chapter 7.7**).

Using soil mechanics the extraction rate of granitic melt from a partially molten rock by *shear enhanced compaction* can be calculated. Combining this approach with a model of the gravity-driven extraction of melt from an interconnected network of veins (Clemens & Mawer 1992), steady-state extraction rates (J) for Westerly granite can be calculated by simultaneously solving the extraction of melt from the vein network (**E8.13**) and extraction rate of melt from the partially molten protolith by using the flow law derived above (**E5.04, E8.14**) :

$$J = \frac{8\, k\, (\sigma_a - \sigma_3)}{3\, a^2\, \eta} \qquad \text{E 8.13}$$

$$J \equiv \dot{\varepsilon} = 10^{-5.832} \exp\frac{-510061}{RT} (\sigma_1 - \sigma_3)^{2.92} \qquad \text{E 8.14}$$

with k being permeability, σ_a the average of the remotely applied deviatoric stress, and a being half the distance between veins into which the melt drains. The combined extraction rate (where the slower process is rate controlling) is orders of magnitude faster than the gravity-driven porous flow model (McKenzie 1984). This is due to:

a.) shorter transport distances in the porous flow of the model (*shear enhanced compaction*) at pressure gradients orders of magnitude higher than those arising during gravity-driven porous flow and

b.) higher effective permeability of rock once melt has accumulated in the vein network.

Factors that are found to limit the occurrence of *shear enhanced compaction plus vein extraction* were found to be the latent heat limit (rate at which heat can conduct to the rock where partial melting takes place) and the maximum deviatoric stress that can be applied in a natural setting (unlikely to exceed 10 MPa). The latter has to increase with decreasing melt viscosity and increasing melt fraction, indicating that it is much easier to extract a low volume of high viscosity melt from a host than a low viscosity melt at large volumes, though it will take longer.

9.2 Future work - application of melt extraction model to a natural setting

There is ample scope for adjusting the details of the model and the values of parameters used, and ultimately to extend the concepts to derive a non-steady state model of melt extraction by a combination of stress-assisted compaction together with local segregation into veins to provide the basis of a viable mechanism for granite extraction.

However, one of the most challenging aspects for future work will be to demonstrate that shear enhanced compaction can occur in a natural setting. To demonstrate that melt extraction, as proposed above, takes place geological evidence for shear enhanced compaction and vein extraction will need to be identified.

Microstructural investigations of the experimental charges deformed by *shear enhanced compaction* revealed cataclastic flow on a grain scale. In nature, however, cataclastic deformation is usually confined to flow of decimetre sized slithers (herring-shaped and -sized rock parcels) (Rutter et al. 1993). It seems pertinent, therefore, to devise experiments at an intermediate scale (with decimetre to metre sample size) to study the development of microstructures in analogue materials prior to examining natural equivalents. Zones of cataclastic flow need to be associated with melt filled veins, preferably extending beyond the zone of partial melting.

Cataclastic flow structures have been observed both in a contact aureole setting (e.g. Mount Stafford area, Australia (Vernon, Clark & Collins 1990), and Grenville Front,

Quebec, Canada (Sawyer 1991)) and in a regional partial melting setting (e.g. Taylor Valley, Antarctica (Allibone & Norris 1992), Ivrea-Verbano Zone, Alps, Italy (Rutter et al. 1993; Quick et al. 1992), Trois Seigneurs Massif, Pyrenees (Wickham 1987), Hercynian plutons, Pyrenees (Bouchez et al. 1992), and NW Ariondacks near Harrisville, New York, USA (Powers & Bohlen 1985)). Meso- and macroscopic evidence of syn-melting deformation is commonly preserved, though re-crystallization commonly overprinted microstructures associated with deformation during the partial melting interval. Melt filled veins are commonly observed (e.g. Clemens & Mawer 1992). However, the link between cataclastic flow and melt filled veins leading to melt extraction has not been made to date.

9.3 Conclusion

This thesis set out to solve the paradox of extracting low fraction granitic melt from its host. Deformation experiments on Westerly granite suggested that extraction of melt occupying a melt fraction below $\phi = 0.30$ (the *rheological critical melt fraction* envisaged by van der Molen and Paterson (1979)) is possible by *shear enhanced compaction*.

Shear enhanced compaction in association with gravity aided *vein extraction* (Clemens & Mawer 1992) is calculated to allow extraction of very low (below $\phi = 0.05$) melt volumes of high viscosity (10^{11} Pas) in geologically realistic time-scales (10^7 years), as long as a small deviatoric stress (0.001 to 10 MPa) is applied to the source rock during partial melting.

References

ALLIBONE, A.H., NORRIS, R.J., 1992, *Journal of Metamorphic Geology*, **10**, 589 - 600, Segregation of leucogranite microplutons during syn-anatectic deformation: An example from the Taylor Valley, Antarctica.

ARZI, A.A., 1978, *Tectonophysics*, **44**, 173 - 184, Critical phenomena in the rheology of partially melted rocks.

ASHWORTH, J.R. MCLELLAN, E.L., 1985, *In: Migmatites, Blackie & Sons Ltd, Glasgow, (Ashworth J.R. ed.)*, **1-35**, 180 - 203, Textures.

AUER, F., BERKHEMER, H., OEHLSCHLEGEL, G., 1981, *Journal of Geophysics*, **49**, 89 - 92, Steady-state creep of fine grain granite at partial melting.

BAILEY, E.B., MAUFE, M.A., 1960, *Memoirs of the Geological Survey, Scotland, Edinburgh: Her Majesty's stationary office*, 307 pp, The Geology of Ben Nevis and Glen Coe and the surrounding country (Explanation of sheet 53), second edition.

BERGANTZ, G.W., 1989, *Science*, **245**, 1093 - 1095, Underplating and partial melting: Implications for melt generation and extraction.

BOUCHEZ, J.L., DELAS, C., GLEIZES, G., NÉDÉLEC, A., 1992, *Geology*, **20**, 35 - 38, Submagmatic microfractures in granite.

BOURBIE, T., ZINSZER, B., 1985, *Journal of Geophysical Research*, **90**, 11524 - 11532, Hydraulic and acoustic properties as a function of porosity in Fountainbleu sandstone.

BRACE, W.F., RILEY, D.K., 1972, *Journal of Rock Mechanics and Mineral Sciences*, **9**, 271 - 288, Static uniaxial deformation of 15 rocks to 30 kb.

BRACE, W.F., WALSH, J.B., FRANGOS, W.T., 1968, *Journal of Geophysical Research*, **73**, 2225 - 2236, Permeability of granite under high pressures.

BULAU, J.R., WAFF, H.S., TYBURCZY, J.A., 1979, *Journal of Geophysical Research*, **84 (B11)**, 6102 - 6108, Mechanical and thermodynamic constraints on fluid distribution in partial melts.

BYERLEE, J.D., BRACE, W.F., 1969, *Science*, **164**, 713 - 715, High pressure mechanical instability in rocks.

CARSWELL, H.S., JAEGER, J.C., 1959, *Oxford University Press*, pp 497, Conduction of Heat in Solids (2nd edition).

CARTER, N.L., ANDERSON, D.A., HANSEN, F.D., KRANZ, R.L., 1981, *In: Mechanical behaviour of crustal rocks. Geophysical Monograph 24, American Geophysical Union*, 61 - 82, Creep and creep fracture of granitic rocks.

CLEMENS, J.D., MAWER, C.K., 1992, *Tectonophysics*, **204**, 339 - 360, Granitic transport by fracture propagation.

CLEMENS, J.D., VIELZEUF, D., 1987, *Earth and Planetary Science Letters*, **86**, 287 - 306, Constrains on melting and magma production in the crust.

COOPER, R.F., 1990, *Journal of Geophysical Research*, **95**, 6979 - 6992, Differential stress-induced melt migration: An experimental approach.

COOPER, R.F., KOHLSTEDT, D.L., 1984, *Tectonophysics*, **107**, 207 - 233, Solution-percipitation enhanced diffusional creep of partially molten olivine-basalt aggregates during hot-pressing.

COVEY-CRUMP, S.J., 1993, *Unpublished PhD thesis, Imperial College, London*, 292 pp, Application of a state variable description of inelastic deformation to geological materials.

COX, K.G., BELL, J.D., PANKHURST, R.J, 1979, 450 pp, The interpretation of igneous rocks, George, Allen & Unwin, London.

CURRAN, J.H., CARROLL, M.M., 1979, *Journal of Geophysical Research*, **84**, 1105 - 11112, Shear stress enhancement of void compaction.

DAVIDSON, C., HOLLISTER, L.S., SCHMID, S.M., 1992, *Tectonics*, **11**, 348 - 359, Role of melt in the formation of a deep-crustal compressive shear zone: The Maclaren Glacier Metamorphic Belt, South central Alaska.

DAVIDSON, C., SCHMID, S.M., 1993, *Terra Abstracts*, **5**, Suplement 1, C12.12, 303, Role of melt during deformation in the deep crust.

DEER, W.A., HOWIE, R.A., ZUSSMAN, J., 1966, *Longman Scientific & Technical*, 528 pp, An introduction to the rock-forming minerals (1st edition).

DEER, W.A., HOWIE, R.A., ZUSSMAN, J., 1992, *Longman Scientific & Technical*, 696 pp, An introduction to the rock-forming minerals (2nd edition).

DELL'ANGELO, L.N., TULLIS, J., 1988, *Journal of Metamorphic Geology*, **6**, 495 - 515, Experimental deformation of partially melted granitic aggregates.

DELL'ANGELO, L.N., TULLIS, J., YUND, R.A., 1987, *Tectonophysics*, **139**, 325 - 332, Transition from dislocation creep to melt-enhanced diffusion creep in fine-grained granitic aggregates.

DROOP, G.T.R., 1987, *Mineralogical Magazine*, **51**, 431 - 435, The general equation for estimating Fe (3+) concentrations in ferromagnesian silicates and oxides from microprobe analysis, using stoichiometric criteria.

EBADI, H., JOHANNES, W., 1991, *Contributions to Mineralogy and Petrology*, **106**, 286 - 295, Beginning of melting and composition of first melts in the system Qz-Ab-Or-H_2O-CO_2.

EVANS, P.J., 1995, *Unpublished. PhD thesis, Victoria University of Manchester*, Structural geometry of parts of the lower crustal section of the Ivrea-Verbano zone.

FOWLER, T.J., 1994, *Tectonophysics*, **234**, 197 - 215, Sheeted and bulbous pluton intrusion mechanisms of a small granitoid from southeastern Australia: Implications for dyke-to-pluton transformation during emplacement.

FROST, H.J., ASHBY, M.F., 1982, *In: Deformation mechanism maps, the plasticity and creep of metals and ceramics*, Pergamon, New York, 61 - 66, Chapter 8: Pure iron and ferrous alloys.

GRIGGS, D.T., 1936, *Journal of Geology*, **44**, 541 pp, Deformation of rocks under high confining pressures.

HADLEY, K., 1976, *Journal of Geophysical Research*, **81**, 3484 - 3495, Comparison of calculated and observed crack densities and seismic velocities in Westerly Granite.

HALL, D.L., BODNAR, R.J., 1989, *Tectonophysics*, **168**, 283 - 296, Comparison of fluid inclusion decrepidation and acoustic emission profiles of Westerly granite and Sioux quartzite.

HARTE, B., PATTISON, D.R.M., LINKLATER, C.M., 1992, *In: Equilibrium and Kinetics Metamorphism: The Ballachulish Igneous Complex and its aureole. (Voll, G.,*

Toelpel, J., Seifert, F. eds.), Springer Verlag, Berlin, Field relations and petrography of patially melted pelitic and semi-pelitic rocks.

HAWKES, I., MELLOR, M., 1970, *Engineering Geology*, **4**, 177 - 285, Uniaxial testing in rock mechanics laboratories.

HIPPERTT, J.F., 1994, *Tectonophysics*, **234**, 169 - 196, Structures indicative of helicoidal flow in a migmatite diapir (Bação Complex, southeastern Brazil).

HUTTON, D.H.W., DEMPSTER, T.J., BROWN, P.E., BECKER, S.D., 1990, *Nature*, **343**, 452 - 455, A new mechanism of granite emplacement: Intrusion in active extensional shear zones.

HUTTON, D.H.W., INGRAM, G.M., 1992, *Transactions of the Royal Society of Edinburgh: Earth Sciences.*, **83**, 383 - 386, The great tonalite sill of Southeastern Alaska and British Columbia: Emplacement into an active contractional high angle reverse shear zone (extended abstract).

JANACH, W., 1977, *Rock Mechanics, Mineral Sciences & Geomechanical Abstracts*, **14**, 209 - 215, Failure of granite under compression.

JEFFREY, D.J., ACRIVOS, A., 1976, *American Institute of Chemical Engineering Journal*, **22**, 417 - 432, The rheological properties of ridgid particles.

JUREWICZ, S.R., WATSON, E.B., 1984, *Contributions to Mineralogy and Petrology*, **85**, 25 - 29, Distribution of partial melt in a felsic system: The importance of surface energy.

JUREWICZ, S.R., WATSON, E.B., 1985, *Geochimica et Chosmochimica Acta*, **49**, 1109 - 1121, The distribution of partial melt in a granitic system: The application of liquid phase sintering theory.

KRANZ, R.L., HARRIS, W.J., CARTER, N.L., 1982, *Geophysical Research Letters*, **9**, 001 - 004, Static fatigue of granite at 200 °C.

LAPORTE, D., 1994, *Contributions to Mineralogy and Petrology*, **116**, 486 - 499, Working behaviour of partial melts during crustal anatexis: The distribution of hydrous silicic melts in polycrystalline aggregates of quartz.

LINKLATER, C.M., 1990, *Unpublished. PhD thesis, University of Edinburgh*, 311 pp, Partial melting in the Ballachulish aureole.

LLOYD, G.E., 1985, *In: Mineralogical Association of Canada. A short course in Applications of electron microscopy in the Earth Sciences (White, J.C. ed.)*, 151 - 188, Review of instrumentation, techniques and applications of SEM in mineralogy.

MACRAE, N.D., NESBITT, H.W., 1980, *Contributions to Mineralogy and Petrology*, **75**, 21 - 26, Partial melting of common metasedimentary rocks: A mass balance approach.

MCKENZIE, D., 1984, *Journal of Petrology*, **25**, 713 - 765, The generation and compaction of partially molten rock.

MCKENZIE, D., 1985, *Earth and Planetary Science Letters*, **74**, 81 - 91, The generation and extraction of magma from the crust and mantle.

MCLELLAN, E.L., 1984, *Geological Magazine*, **121**, 339 - 345, Deformation behaviour of migmatites and problems of structural analysis in migmatite terrains.

MOGI, K., 1966, *Felsmechanik in der Ingenieurgeologie*, **4**, 41 - 55, Dome precise measurements of fracture strength of rocks under uniform compressive stress.

MUIR, J.H, WOOD, D., 1990, 462 pp, Soil behaviour and critical state soil mechanics., Cambridge University press.

MURASE, T., MCBIRNEY, A.R., 1973, *Geological Society of America Bulletin*, **84**, 3563 - 3592, Properties of some common igneous rocks and their melts at high temperatures.

NADAI, A., 1938, *In: Timoshenko Anniversary Volume, New York, Macmillan*, 150 - 170, The influence of time upon creep, the hyperbolic since creep law.

NICOLAS, A., REUBER, I., BENN, K., 1988, *Tectonophysics*, **151**, 87 - 105, A new magma chamber model based on structural studies in the Oman ophiolite.

PAQUET, J., FRANCOIS, P., 1980, *Tectonophysics*, **68**, 131 - 146, Experimental deformation of partially melted granitic rocks at 600 - 900 °C and 250 MPa confining pressure.

PAQUET, J., FRANCOIS, P., NEDELEC, A., 1981, *Tectonophysics*, **78**, 545 - 565, Effect of partial melting on rock deformation: Experimental and natural evidences on rocks of granitic composition.

PATERSON, M.S., 1978, 245 pp, Experimental Rock deformation - the brittle field, Springer Verlag, Heidelberg.

PATERSON, M.S., LUAN, F.C., 1990, *In: Deformation Mechanisms, Rheology and Tectonics*, Geological Society of London special Publication **12**, 299 - 38, Quartzite rheology under geological conditions.

PATTISON, D.R.M., 1985, *Unpublished. PhD thesis, University of Edinburgh*, 590 pp, Petrogenesis of pelitic rocks in the Ballachulish Thermal Aureole.

PETFORD, N., 1993, *In: Flow and Creep in the Solar System: Observations, modeling and theory (Stone, D. B., Runcorn, S.K. eds.)*, Kluwer Academic Publishers, 261 - 283, Porous media flow in granitoid magmas: An assessment.

PIWINSKII, A.J., MARTIN, R.F., 1970, *Contributions to Mineralogy and Petrology*, **29**, 001 - 10, An experimental study of equilibrium with granitic rocks at 10 kb.

PLATTEN, I. M., 1990, unpublished, 44 pp, Partial melting of Leven Schist at Coire Chaorann, Ballachulish aureole.

POWERS, R.E., BOHLEN, S.R., 1985, *Contributions to Mineralogy and Petrology*, **90**, 401 - 409, The role of synmetamorphic igneous rocks in the metamorphism and partial melting of metasediments, Northwest Airondacks.

QUICK, J.E., SINIGOI, S., NEGRINI, L., DEMARCHI, G., MAYER, A., 1992, *Geology*, **20**, 613 - 616, Synmagmatic deformation in the underplated igneous complex of the Ivrea-Verbano zone.

RICHTER, F.M., MCKENZIE, D., 1984, *Journal of Geology*, **92**, 729 - 740, Dynamic models for melt segregation from a deformable matrix.

ROEDDER, E., 1984, *Reviews in Mineralogy 12, Mineralogical Society of America*, Fluid inclusions.

RUTTER, E.H., BRODIE, K.H, EVANS, P.J., 1993, *Journal of Structural Geology*, **15**, 647 - 662, Structural geometry, lower crustal magmatic underplating and lithospheric stretching in the Ivrea-Verbano zone, northern Italy.

RUTTER, E.H., HADIZADEH, J., 1991, *Journal of Structural Geology*, **13**, 609 - 614, On the influence of porosity on the low-temperature brittle - ductile transition in siliciclastic rocks.

RUTTER, E.H., NEUMANN, D.H.K., 1995, *Journal of Geophysical Research*, in press, Experimental deformation of partially molten Westerly granite under fluid-absent conditions, with implications for the extraction of granitic magmas.

SAWYER, E.W., 1991, *Journal of Petrology*, **32**, 701 - 738, Disequilibrium melting and the rate of melt-residuum separation during migmatization of mafic rocks from the Grenville Front, Quebec.

SCHOCK, R.N., HEARD, H.C., STEPHENS, D.R., 1973, *Journal of Geophysical Research*, **78**, 5922 - 5941, Stress-strain behaviour of a granodiorite and greywackes on compression to 20 kbar.

SCHOLZ, C.H., KRANZ, R., 1974, *Journal of Geophysical Research*, **79**, 2132 - 2135, Notes on dilatancy recovery.

SERMONT, B., 1993, *Unpublished. PhD thesis, University of Montpellier*, 231 pp, Déformation expérimentale à haute pression et haute température d'agrégats polycristallins de plagioclase et d'olivine.

SHAW, H.R., 1965, *American Journal of Science*, **265**, 120 - 152, Comments on viscosity, crystal settling and convection in granitic magmas.

SHAW, H.R., 1972, *American Journal of Science*, **272**, 870 - 893, Viscosities and magmatic silicate melts: An empirical method of prediction.

SKEMPTON, D.J., 1954, *Géotechnique*, **4**, 143 - 147, The pore pressure coefficients A and B.

SLEEP, N.H., 1988, *Journal of Geophysical Research*, **93** (B9), 10.255 - 10.272, Tapping of melt by veins and dykes.

TULLIS, J., YUND, R.A., 1977, *Journal of Geophysical Research*, **82**, 5705 - 5718, Experimental deformation of dry Westerly granite.

TURCOTTE, D.L., SCHUBERT, G., 1982, *John Wiley & Sons Inc.*, 450 pp, Geodynamics, application of continuum physics to geological problems.

UNDERWOOD, E.E., 1970, *Addison-Wesley Publishing Company, Reading, Massachusetts*, 274 pp, Quantitative Stereology.

VAN DER MOLEN, I., PATERSON M.S., 1979, *Contributions to Mineralogy and Petrology*, **70**, 229 - 318, Experimental deformation of partially-melted granite.

VERNON, R.H., CLARKE, G.L., COLLINS, W.J., 1990, *In: High-temperature metamorphism and crustal anatexis (Ashworth, J.R., Brown, M eds.)*, 272 - 319, Chapter 11: Local, mid-crustal granulite facies metamorphism and melting: An example in the Mount Stafford area, central Australia.

VON BARGEN, N., WAFF, H.S., 1986, *Journal of Geophysical Research*, **91**, 9261 - 9276, Permabilities, interfacial areas and curvature of partially molten systems: Results of numerical computations of equilibrium microstructures.

WALKER, A.N., 1991, *Unpublished PhD thesis, Imperial College, London*, 318 pp, An experimental study of grain size sensitive flow of hot-pressed, synthetic rocks.

WEISS, S., 1986, *Unpublished. PhD thesis, Ludwig-Maximilians- Universitaet, München*, 228 pp, Petrogenese des Intrusivcomplexes von Ballachulish, Westschottland: Krystallisationsverlauf in einem zonierten kaledonischen Pluton.

WHITE, A.J.R., CHAPPELL, B.W., 1977, *Tectonophysics*, **43**, 007 - 22, Ultrametamorphism and granitoid genesis.

WICKHAM, S.M., 1987, *Journal of the Geophysical Society, London*, **144**, 281 - 297, The segregation and emplacement of granitic magmas.

WONG, T-F., 1982, *International Journal of Rock Mechanics, Mineral Sciences & Geomechanical Abstracts*, **19**, 49 - 64, Micromechanics of faulting in Westerly granite.

WONG, T-F., FREDRICH, J.T., GWANMESIA, G.D., 1989, *Journal of Geophysical Research*, **94**, 10267 - 10278, Crack aperture statistics and pore space fractal geometry of Westerly granite and Rutland quartzite: Implications for an elastic contact model of rock compressibility.

WU, F.T., THOMSEN, L., 1975, *International Journal of Rock Mechanics, Mineral Sciences & Geomechanical Abstracts*, **12**, 167 - 173, Microfracturing and deformation of Westerly granite under creep condition.

ZHANG, J., WONG, T-F., DAVIS, D.M., 1990a, *Journal of Geophysical Research*, **95**, 341 - 352, Micromechanics of pressure-induced grain crushing in porous rocks.

ZHANG, S., WONG T.-F., DAVIS, D.M., 1990b, *In: Rock mechanics contributions and challenges (Hustrulid, W.A., Johnson, G.A. eds)*, Proceedings of the 31st United States Symposium on rock mechanics, Balkema, Rotterdam, 653 - 660, High pressure embrittlement and shear-enhanced compaction of Berea sandstone: Acoustic emission measurement and microstructural observations.

ZOBACK, M.D., BYERLEE, J.D., 1975, *Journal of Geophysical Research*, **80**, 752 - 755, The effect of microcrack dilatancy on the permeability of Westerly granite.

Appendices

Appendix 1

"Paterson" Gas Rig

A1. 1 Introduction

All experiments described in this thesis were carried out using a Paterson-ANUtech, internally heated, argon gas medium deformation apparatus located in the Experimental Rock Deformation Laboratory of the Geology Department at the Victoria University of Manchester (**Figure A1.01**). The specifications and functionality of the rig are described first (**Chapter A1.2**), followed by a description of sample preparation and procedures employed during the deformation tests run (**Chapter A1.3**).

A1.2 Apparatus description

A1.2.1 Hydrostatic Pressure

The pressure vessel (Figure A1.01), which has an internal volume 1.25 litres, contains the furnace windings, pistons and specimen assemblage (Figure 1.03). All pressure seals in the pressure vessel are fundamentally the same design. They seal by the combined action of a plastic O-ring and a mitre ring that consists of copper with a 2 % beryllium component that adds extra hardness and elasticity to the copper ring. These two components are inserted into a groove in the outer section of the two circular components that need sealing (Figure A1.02, top insert). The copper ring is very springy until it is inserted into the groove. The added O-ring tries to push the mitre ring out of the groove as it is compressed against the inner material wall. The mitre ring deforms to close against the walls of both components and forms the seal.

Elevated pressures are achieved using pure argon as a confining medium. As argon is inert, it is safe to use and a strictly hydrostatic testing environment is assured as there are no problems with polymerization or chemical breakdown with increasing pressure and temperature. Argon pressure is first raised from the bottle pressure using the gas booster in conjunction with an externally powered vacuum pump. The pressure is then raised further to the required test pressure by the 10 : 1 intensifier (**Figure A1.01, c**). The gas valves used to control flow of argon during rig pressurization are located on the gas flow scheme diagram on the front panel of the gas rig (**Figure A1.01, c**).

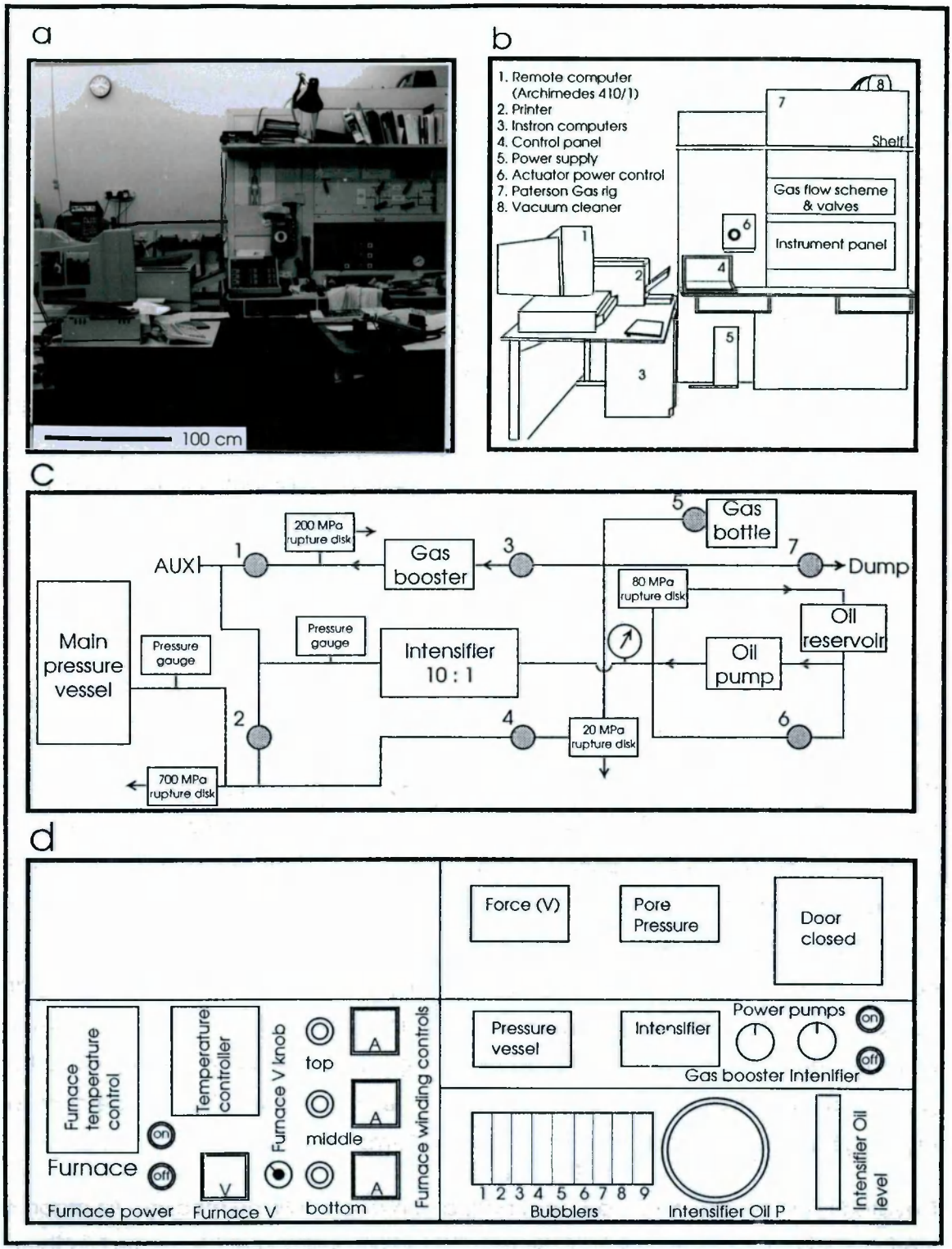

Figure A1.01: External view of the Paterson gas rig. **a.)** and **b.)** photo and sketch of external view of the Paterson gas rig at the Department of Geology, Victoria University of Manchester. **c.)** *Gas flow scheme* and valves situated as a panel on the front of the gas rig, showing the gas circuit for hydrostatic pressure application. Filled circles mark the position of valves. **d.)** *Instrument panel* located at the front panel of the gas rig. The left hand side controls temperature application, while the right side of the panel controls hydrostatic pressure application. *Bubblers* enable leak detection in the hydrostatic pressure system at various points around the Intensifier and pressure vessel, while the *intensifier oil level* displays the position of the piston in the intensifier.

If hydrostatic pressure can not be raised sufficiently high by the initial stroke of the intensifier, the pressure vessel can be isolated from the remainder of the gas circuit (by closing the valve 2 (**Figure A1.01, c**)), followed by restroking of the intensifier to allow a further increment of confining pressure. The pressure vessel can withstand pressures up to 700 MPa before blowing the safety rupture disk. Leak detection is by a series of *bubblers* (clear Perspex tubes divided into two chambers that are connected by thin connection tubes that are partially filled with oil), situated in the *instrument panel* at the front of the gas rig (**Figure A1.01, d**) that are connected to strategic sites around the gas circuit.

A1.2.2 High temperature facility

Specimens within the pressure chamber can be heated to temperatures of up to 1200 °C. These elevated temperatures are achieved by a furnace that has three molybdenum windings arranged to provide a uniform temperature zone of 50 mm length and 21 mm diameter. This furnace is inserted inside the pressure vessel with a bore just wide enough to insert the sample assemblage (**Figure A1.03**). The combination of three furnace windings give a high degree of control on the thermal profile across the specimen. Each winding is monitored by a platinum-rhodium thermocouple situated adjacent to the winding.

Power to the furnace is controlled by the left hand Eurotherm unit on the let hand part of the instrument panel (**Figure A1.01, d**), while the right hand Eurotherm unit adjacent to the first acts as a temperature control (measuring relative temperature, as part of the connection is made via the pressure vessel, thus distorting the readings). Separate thyristors (situated at the bottom right corner of the left hand instrument panel) control the allocation of total power available to individual windings. The thyristors are fitted with current limitators to avoid currents in excess of about 15 A during heating as otherwise very large currents would be drawn when applying full voltage to cold molybdenum windings. This is because cold windings have very low resistance and only on warming up do they acquire resistances in the order of Ohms. The control signal from the Eurotherm control unit is connected in parallel to all three thyristors but is attenuated individually with the rheostats situated to the left of the ammeters. The rheostats enable the relative power in the windings to be adjusted to achieve a desired temperature distribution. To maintain a uniform temperature across the sample, the temperature has to be constant over 50 mm in the central part of the furnace to within ± 2°C. The desired test temperature can be achieved by varying the control Eurotherm

that is linked to the control thermocouple and/or varying the current settings for individual windings using the rheostats.

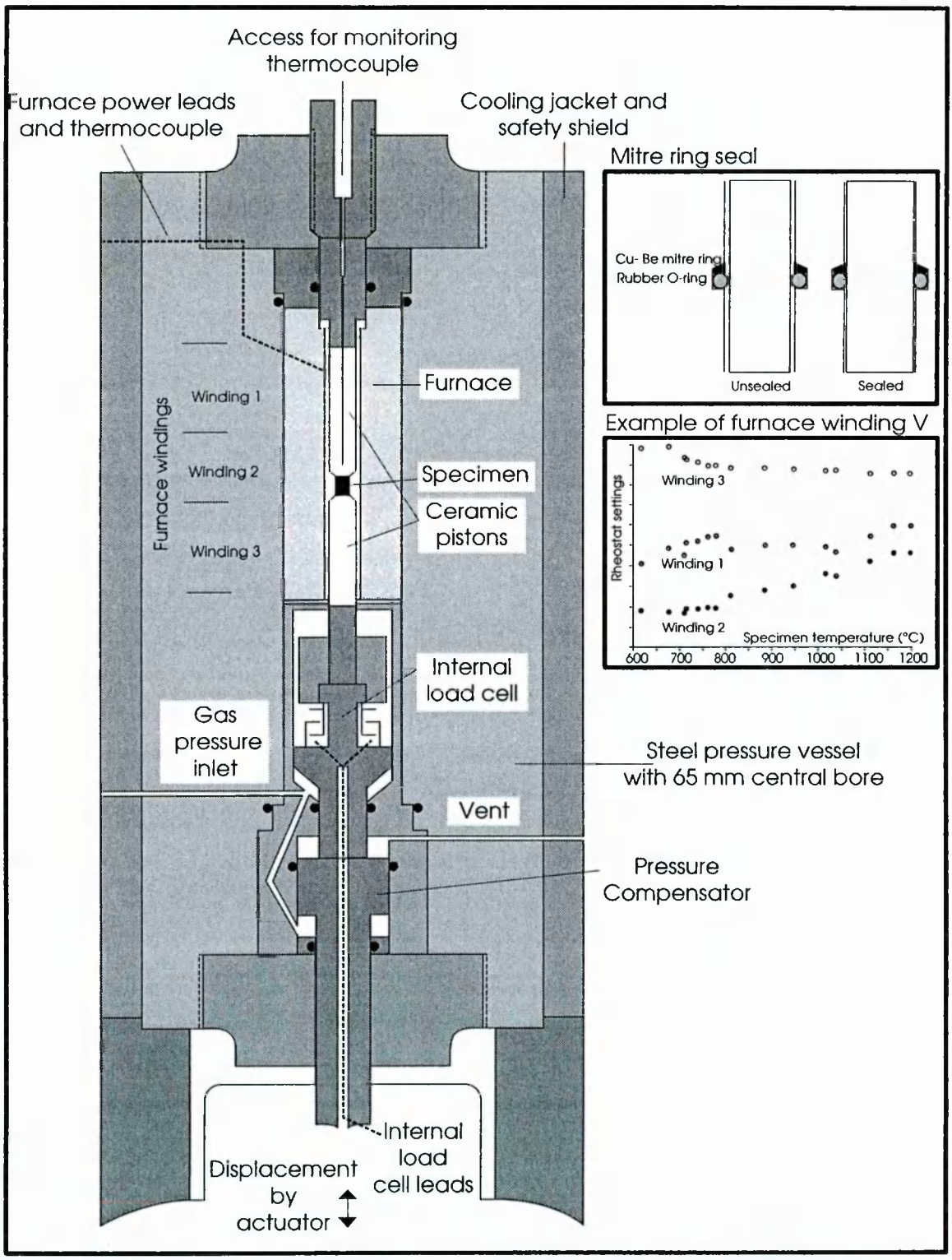

Figure A1.02: Schematic diagram of the pressure vessel of the Paterson gas rig (not to scale, illustrating the relative positions of sample, furnace and internal load cell. Inserts demonstrate the improved sealing mechanism, using a deformable mitre ring seal in conjunction with a rubber O-

ring, and an example of varying allocations of total voltage to the three furnace windings with temperature at a pressure of 250 MPa.

To maximize the lifetime of the furnace, a setting for all three rheostats is sought at each temperature that minimizes the current flowing through individual windings, especially the bottom winding that takes the bulk of the current (while the middle winding carries the smallest current). In order to avoid thermal shock damage to the furnace the current supplied to the furnace is kept low at the initial stages of heating by controlling the output increase from the temperature control at a steady rate. This rate control is called a ramp and is set on the left hand control Eurotherm on the left instrument panel.

A constant temperature across the specimen was ensured by calibration of the winding rheostat settings with a dummy sample containing a series of thermocouples (see **Figure A1.02** for example calibration). The test temperature is monitored by a thermocouple situated in the central bore of the top piston just above the specimen (**Figure A1.02**). These kinds of calibrations were used to set the control Eurotherm and winding rheostats to optimum conditions for the hydrostatic pressure and temperatures desired during the test run.

Rapid quenching is achieved by releasing the argon to atmosphere over a period of approximately half an hour. Adiabatic expansion of the gas causes the specimen temperature to fall by up to 100 °C/min.

A1.2.3 Deformation facility

The deformation is achieved by applying an axial load to the specimen via the bottom piston (**Figure A1.02**). Tests can be run using a constant piston displacement rate, effectively a constant strain rate, and a constant load, effectively constant stress creep. Deformation tests can be interrupted at any stage to observe the stress relaxation behaviour of the specimen. The bottom piston can exert a force of up to 100 kN on the specimen with a maximum piston displacement of 30 mm. The pressure-compensated loading piston is moved by the application of gas pressure to the reverse side of the annular boss on the main bottom piston, counterbalancing the load on the piston due to the applied hydrostatic pressure (**Figure A1.02**). Thus the force applied to cause movement of the bottom piston is solely due to the differential stress imposed by deformation of specimen and jacket plus friction in the piston. This differential load was applied by the Instron actuator (**Figure A1.02**) driven by an Instron 8500 controller coupled to a microcomputer (**Figure A1.01, b**). Using this apparatus the maximum compressive strain is limited to approximately 20% (over the whole sample). Above this

strain samples tend to buckle as there is no lateral restraint on the specimen as it passes through the furnace coils.

A1.2.4 Load cells

The axial load on the specimen is measured an external and internal load cell. The external load cell is located between the actuator and the bottom piston (**Figure A1.02**), while the internal load cell resides between the top of the lower piston assemblage and the base of the steel piston that is inserted as part of the specimen assemblage.

The Paterson capacitance internal load cell (Sermont 1993) is capable of a load resolution of ca 10 N and located at the base of the specimen assemblage. It measures the capacitance between three parallel disks, of which the top and bottom one are fixed closest to the sample assemblage, while the middle disk is attached to the bottom of the load cell. Elastic deformation of this part of the lower piston assemblage will cause a shift in capacitance reading between the capacitors, thus allowing the applied load to be calculated. The internal load cell also acts as the anvil through which the force is applied to the specimen assemblage itself. The internal load cell is calibrated against the external load cell.

The load applied by the actuator is monitored by the external load cell, located between the actuator and the bottom piston. It measures the length change of the lower piston assemblage due to elastic deformation caused by the applied differential force.

The loads recorded by the internal and external load cell will differ as a result of the frictional resistance of the piston assemblage influencing readings on the external load cell, but not on the capacitance load cell. Because the difference between the two load cell readings will change as the machine wears, regular calibration is required in order to compare the two readings. The internal load cell tends to better reflect the differential load carried by the sample it was used in the data reprocessing stages (**Appendix 2**).

A1.3 Experimental procedures.

A1.3.1 Sampling

Cylindrical specimens (9.4 ± 0.01 mm diameter, 20-21 mm length) were drilled from a single hand specimen of Westerly granite using a 10 mm diameter diamond corer. The cores were roughly cut to length using a small diamond saw and the ends planed flat, perpendicular to the length of the core, with sand paper. All specimens were dried in an oven at 110 °C for at least 12 hours. In order to allow calculation of applied stress and finite strains achieved during deformation, the dimensions of all samples were measured with a micrometer, to an accuracy of 0.001 mm, prior to assembly of the machine charge.

A1.3.2 Experimental charge assembly

First the cylindrical specimen, together with two ceramic alumina (Al_2O_3) spacers, 10 mm diameter and 3 mm long, were inserted into a 0.254 mm thick copper tubing (**Figure A1.03**) which was cut to the length of the specimen plus alumina spacers. For experiments run at temperatures below 900 °C, the copper tube was annealed.

For samples WG23, WG24, WG25 and WG27 sample lengths were reduced to between 14.7 and 16.4 mm (**Table 3.04**), and a 4 mm thick layer of loosely compacted quartz sand capped with a 1 mm thick disk of Ougthibridge Gannister sandstone (**Figure 3.10**) was inserted between the granite sample and the bottom spacer. The quartz sand was compacted by gently tapping the assemblage of Westerly granite sample and sand, encased in the copper jacket, on a hard surface. To complete the specimen assemblage, the sleeved specimen was placed between two tapered alumina pistons (15 mm diameter, and 50 mm long) which were in turn sandwiched between two PSZ steel pistons. This combination was enclosed in an iron jacket (**Figure A1.03**), that had been swaged over a steel mandrel to give a near perfect fit over the sample and angled pistons. Care was taken to cut the upper part of the iron jacket exactly to size, as it would buckle if too long and break the pressure seal if too short. The top two pistons had a continuous 1 mm central bore to insert the control thermocouple to measure the specimen temperature.

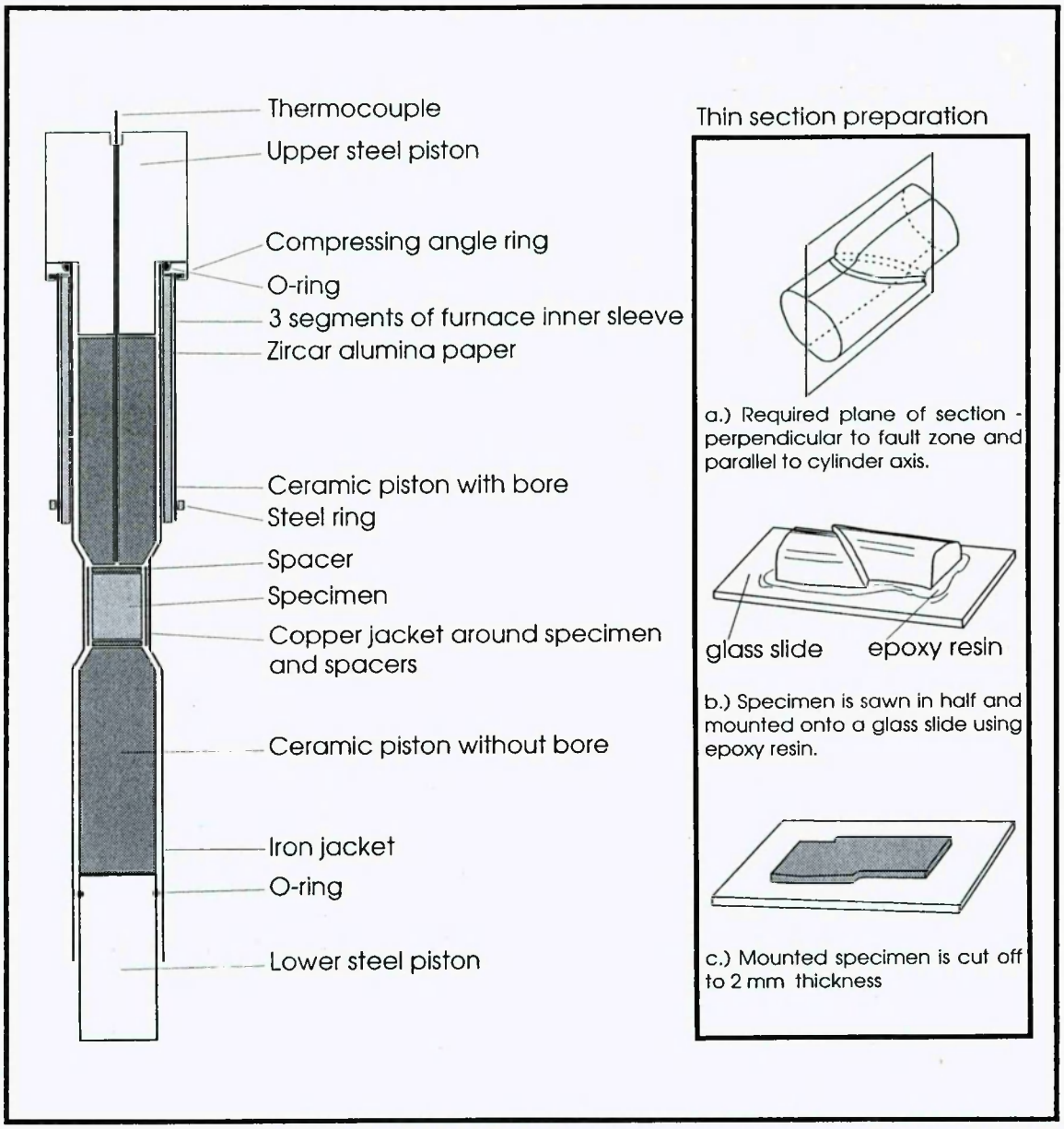

Figure A1.03: Specimen assemblage that was lowered into the pressure vessel of the Paterson gas rig. The insert shows thin section preparation of samples after the sample had been extracted from the Paterson gas rig after termination of the test and after the alumina pistons had been removed, yielding two thin sections.

Two to three layers of 100 mm wide, heat treated, Zircar alumina paper (APA2) were wrapped around the upper part of the iron jacket. This wadding-like material was compressed onto the jacket by the 3 segments of furnace inner sleeve. The lips on these segments were pushed under the retaining lip on the O-ring compression nut (**Figure 1.03, b**). Any excess Zircar alumina material protruding from the three steel segments was removed with a razor blade. A steel ring fixed the other end securing this assemblage. This ring was pushed up by the furnace core on insertion of the specimen

into the pressure vessel but slid down to more or less the same position on removing the specimen assemblage from the furnace again.

Using the threaded insertion tool, the specimen assemblage was inserted through the top plug using a small rotary motion, feeling it past various close fits and finally finding contact to the anvil seat on the internal load cell. Contact with the anvil was confirmed by differential readings on the internal load cell on the control panel (**Figure A1.01**). The small specimen access nut was screwed into place by the large plug-supporting nut until contact was made with the specimen assemblage and then backed off quarter of a turn. This allowed for thermal expansion of the specimen assemblage during heating and also provided a "run-in" period before applying a differential stress across the specimen.

Finally the top nut was sealed using a small roll of plasticine that was pressed around the joint and all previously disconnected leak detection tubes were fitted into the appropriate apertures. These connect the leak test sites to the *bubblers* on the right hand instrument panel (**Figure A1.01, d**).

A1.3.3 High pressure high temperature compressive deformation testing

After specimen assembly, the pressure in the apparatus was increased to 250 MPa for all tests and the furnace heated to the required test temperature, a range of 800-1200 °C being used in the present study.

Prior to the initiation of deformation, the hit point, the actuator position which places the compression piston assemblage in contact with the specimen assemblage, was established by manually driving the actuator until the first registration of load on the internal load cell was observed. The piston position, as indicated on the control panel (**Figure A1.01, b**) was recorded and the piston backed off for a sufficient distance to allow the establishment of a base line of supported stress (due to machine friction) prior to deviation of the load with time caused by resistance to deformation of the specimen. The specimen will support a small initial small load without damage. Establishment of the hit point was carried out at test conditions.

During the deformation, movement of the actuator was determined by either a displacement function (i.e. strain rate test) or applied stress (i.e. stress creep test) function, as measured by the internal load cell. Once the desired deformation had been achieved, stress relaxation tests were performed by cycling the piston position at the maximum extension position and recording the decay of supported stress as the

specimen continued to contract. Several cycles of loading and stress relaxation were carried out during some tests (**Table 5.01**).

On completion of the test, the motion of the bottom piston was reversed to remove the load, backing off a little from the specimen. The piston was then advanced again to establish a new base line measurement to establish whether frictional resistance of the pistons had changed during the test run. Also a new hit point was established, defining the finite extension achieved during the experiment. This will always be less than that recorded during deformation as a result of elastic strain accommodated by the machine and specimen.

On completion of the experiments, the pressure was released and the furnaces turned off. As described above, adiabatic expansion of the argon confining medium resulted in cooling rates of up to 100 °C/ min, quenching any melt to glass. The sample was left in the machine for a further 12 hours to reduce damage on sealing O-rings that swell on contact with high pressure argon.

A1.3.4 Sample treatment after experiment termination

Immediately after removal from the apparatus, the specimen was photographed together with scale bar and specimen number. The alumina pistons were carefully removed by sawing through the iron jacket at the position of the alumina spacers. Excess iron on the pistons was removed by peeling the iron gently away from the steel piston end. At the specimen end of the pistons, the iron jacket commonly annealed to the surface of the ceramic material and had to be removed using hot, 50 % proof, nitric acid.

Many of the low temperature test specimens were friable and had to be impregnated. This was done by first sawing through the iron and copper jackets parallel to the specimen cylinder, to allow glue penetration, before submerging the specimen in Araldite™ under vacuum. Particular care was taken with specimens topped by crushed quartzite reservoirs used in the viscosity determination experiments (WG23, WG24, WG25 and WG27). In experiments where porosity was to be observed in optical thin sections Keystone oil blue A (a blue anthraquinone compound) was added to the glue as a dye.

Finally the specimens were sawn in half lengthways, normal to any fault zone that may have developed (insert on **Figure A1.03**). Two polished thin sections were then carefully created from each half of the specimen, the best being carbon coated for SEM use.

Appendix 2

Data processing of gas rig output

A2.1 Introduction

In this appendix the manipulation of data from the deformation experiments is discussed and the errors in output due to measuring uncertainties and approximations are assessed. This is carried out as part of the software program !ROCKDEF (see **Appendix 7** and **Appendix 8**). The necessary steps of data reduction are described including machine calibrations and induced errors. Calculation of stress, strain and strain rate for stress-strain and stress relaxation experiments are described and assumptions made are discussed.

A2.2 Data acquisition

Data was acquired by the microcomputer running the program !ROCKDEF from the Instron and DVM via the serial and parallel ports. Real time data processing converted milliVolt readings into relevant SI units. The post testing data processing incorporated correction factors such as machine distortion, machine compliance and specimen shape change to obtain mechanical data solely relating to the test material, irrespective of machine inputs and shape of the specimen.

A2.3 Factors limiting data quality

The need to pressurise and heat an otherwise isolated specimen causes four problems that need to be compensated for in data reduction:

1. Deformation variables need to be determined remotely which result in uncertainty in hydrostatic pressure, temperature, differential stress and strain measurements.

2. The deformation environment can not be changed instantaneously leading to errors at switching points between compressional and stress relaxation deformational environments.

3. Iron and copper jackets used to isolate the sample from the hydrostatic compression medium support some of the differential load applied to the specimen.

4. Approximations need to be made about specimen deformation behaviour and the shape change of the sample with increasing strain.

A2.3.1 Calibration and data measurement errors

Confining Pressure

No calibration of either pressure gauge (situated in the Intensifier and pressure vessel high pressure lines) has been carried out to date on the gas rig. Prior to delivery the transducers were calibrated by the manufacturers to be accurate within 0.5 % at full scale of 700 MPa (Sermont 1993) giving an inaccuracy of ± 3.5 MPa. The pressure transducers were assumed to be accurate to within 0.5 %. MilliVolt outputs from the pressure transducers are recorded by respective digital panel meters located on the instrument panel at the front of the gas rig (**Figure A1.01, d**). Information from the digital panel meters were imported via the DVM and the 8-bit parallel port into the linked Archimedes micro-computer to be further processed by the IROCKDEF program. Errors in the confining pressure readings were thought to be the same as that stated for the transducers at 250 MPa, being ± 1.25 MPa.

Temperature

Throughout the gas rig temperature is measured by Ni Cr/Ni Al base metal thermocouples. These measure microVolt output across a nickel-chromium nickel-aluminium alloy wires interface. Standard output published by the manufacturers is 41.2 microVolts per °C. Thermocouples were produced by Radio Spares Components Ltd and are specified to have an accuracy of ±3 °C between 0 °C and + 400 °C and of ±0.75 % between 400 °C and 1100 °C. Accuracy of the thermocouple was not specified above 1100 °C but maximum spot reading is quoted as 1300 °C. This would mean an inaccuracy of temperature reading at the temperatures studied (800 to 1200 °C) of between 6 and 9 °C. However, inaccuracy of the thermocouple will increase with wear.

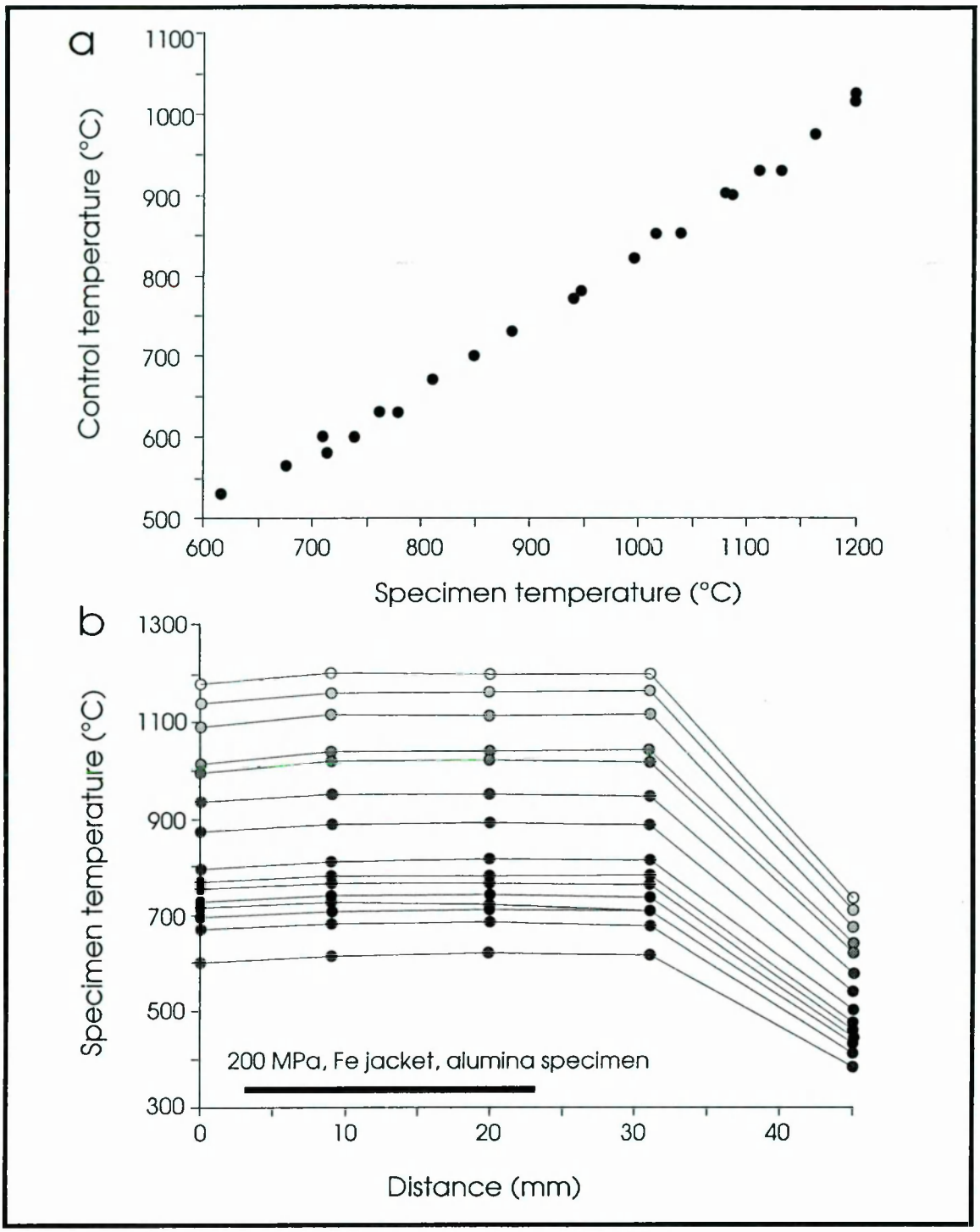

Figure A2.01: **a.)** Temperature of sample measured by the control thermocouple (lowered through the top piston (**Figure A1.03**)) versus specimen temperature measured as the average from furnace winding temperatures. **b.)** Temperature profiles over the sample location in the furnace (marked by the horizontal bar) using five thermocouples arranged in a dummy specimen during temperature calibration tests performed at 250 MPa confining pressure.

Three thermocouples were connected to respective furnace windings (**Appendix 1**) though the temperature reading used for temperature calculations as part of the IROCKDEF (**Appendix 8**) program was the control thermocouple that was lowered

through the pore fluid inlet in the upper piston (**Figure A1.02**) and sits adjacent to the top alumina spacer inside the central core of the aluminium oxide piston. Average readings from the furnace winding thermocouples are compared to readings obtained from the control thermocouple. These show good agreement in **Figure A3.01, a.**

The temperature profiles across the specimen location in the furnace were performed using five stationary thermocouples instead of the one mobile. Thermocouples were fixed to cover two positions inside the aluminium oxide cylinder with further thermocouples placed both in the top and bottom pistons (**Figure A2.01, b**). Thermocouples were read sequentially and temperature plotted against distance in the pressure vessel column. This allowed the adjustment of winding controls to achieve a flat thermal profile across the specimen at various temperatures with minimum current through the three windings, limiting furnace fatigue.

Differential load

The external load cell was supplied by Instron Ltd (High Wycombe) and was calibrated to have an accuracy above 0.1 % of cell-rated output or 0.5 % of indicated load, whichever the greater. At full scale of 100 kN this would mean an inaccuracy of 0.5 kN.

The internal load cell was calibrated against the external load cell (**Figure A2.02, a**). A linear relationship was found between internal and external load cell measurements. This suggests that there was a ± 0.5 % degree of inaccuracy of the internal load cell at full scale of (10 tons). This is the uncertainty for change in load rather than absolute load and zero load is measured at the beginning of each test and taken as the baseline prior to engagement of pistons and specimen. Inaccuracy arises from friction on the sealing rings. Additional friction, increasing load readings on both internal and external load cell, occurs when the sample dog-legs at higher strains. This resulted in a sloping baseline that had to be corrected for in the data reduction procedure in both stress-strain and stress relaxation experiments.

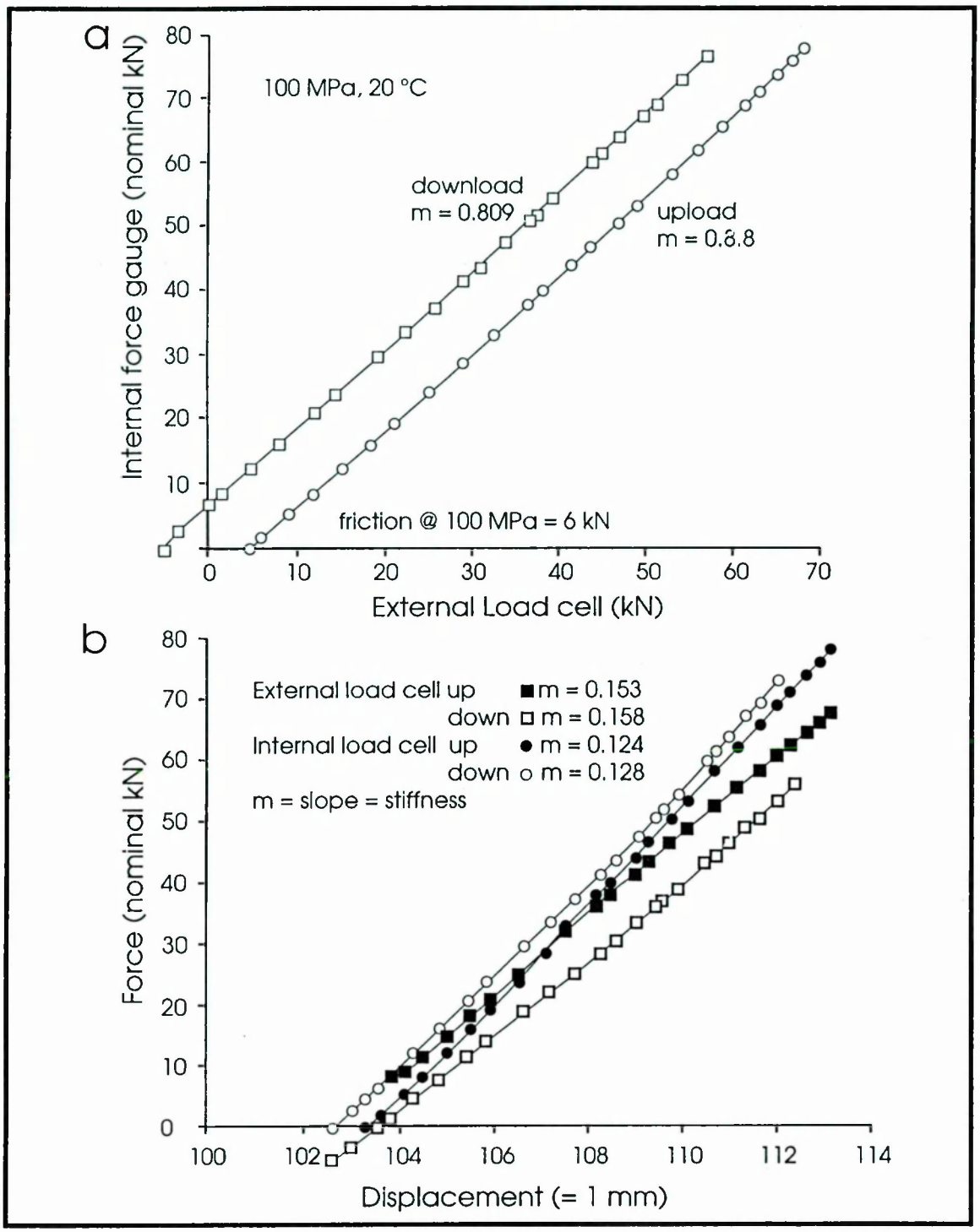

Figure A2.02: Calibration of load cells **a.)** External load cell versus internal load cell measurement with external load cell = m * internal load cell measurement + δ. **b.)** Machine complience where displacement = m * force + δ, with δ marking the intersect with the x-axis and *m* being proportional to the machine complience.

Crosshead displacement

Crosshead displacement needs to be known to enable apparatus deformation and specimen displacement determination. Crosshead displacement was measured by a LBDT displacement transducer fitted to the actuator supplied by Instron Ltd (High Wycombe). It was installed to measure travel lengths of up to 20 mm with a precision of 0.02 % or 0.08 mm over the whole distance. Relative displacement between two distance points placed at 5 mm spacing (= 25 % strain) were measured rather than the actual position of the displacement of the transducer. Uncertainty resulted from linearity of the processor. At small strains and especially slow strain rates the precision of crosshead displacement was ± 0.01 mm.

Apparatus compliance

During deformation of the specimen part of the applied axial force was accommodated by elastic distortion of the apparatus. The axial distortion (stiffness) of the machine was defined by the axial load divided by the axial displacement. The stiffness of the machine was defined as the applied load on the pistons divided by the change in the total length of the pistons.

Stiffness calibration was carried out by inserting a solid alumina specimen between the upper and lower pistons. Several loading tests are performed. Using the Young's modulus (E) it is possible to calculate the compliance (= 1/stiffness) of the alumina specimen (s_a):

$$\frac{1}{s_a} = \frac{E*\Theta}{L_o} \qquad \text{EA2.01}$$

where Θ is the cross section area of alumina specimen and L_o is the specimen length. The specimen compliance was subtracted from the crosshead displacement giving the displacement (deformation) experienced by the axial column of the apparatus. The slope of the linear relationship between load versus apparatus displacement was taken as apparatus complience. For data reduction apparatus compliance is subtracted from crosshead displacement to obtain specimen strain. Two parallel slopes are obtained for internal and external load readings (**Figure A2.02, b**). As the actuator pushed the piston into the specimen the lower part of the piston underwent more deformation than the upper part, while during extension the upper part of the assembly was preferentially deformed. Internal force gauge readings were more accurate than external force gauge readings due to the absence of friction readings of the lower

piston that were recorded by the external force gauge. However, the slope of the curves are the same. Machine compliance can thus be calculated as:

$$s_m = s_t - s_a \qquad \text{EA2.02}$$

where s_m is the machine compliance and s_t is the total compliance. Compliance is non-linear and the data from load/displacement output are better fitted with a quadratic curve than a straight line (**Figure A2.02, b**). Apparatus compliance is assumed as linear and pressure independent in data reduction for convenience. It was calculated to be $s_m = 0.0153$ mm kN^{-1}.

Summary

Data measurement problems add various degrees of errors to deformation variables. These are:

Confining pressure: ± 0.5 % = 1.25 MPa at 250 MPa
Temperature: ± 6 to 9 °C between 800 to 1100 °C
Differential load: ± 0.5 % at 10 ton full scale
Crosshead displacement: ± 0.01 mm
Apparatus compliance = 0.0153 mm kN^{-1}, pressure independent.

A2.3.2 Inertia of machine deformation

Apparatus design was such that a certain amount of inertia exists when changing from one differential deformation state to another. Changing from stress-strain to stress relaxation deformation tests involved the termination of the actuator to allow the specimen to relax while at maximum strain. However, load differential in the piston/specimen assemblage resulted in re-equilibration during relaxation, introducing anelastic effects into the relaxation curve. To reduce the anelastic effect of piston relaxation a servo control on the actuator cycled the lower piston through extensional and compressional movements to effectively reduce the length of the anelastically relaxing piston column. However, in practice this cycling did not overcome the friction of the seals and therefore did not affect stress relaxation readings.

Re-pressurisation of the pressure vessel during long term stress relaxation tests could lead to unloading of the specimen. The specimen was either reloaded or was allowed to relax further if the off-loading event was small enough. The off-loading by

pressurisation had no effect on microstructural and mechanical states of the relaxing specimen. Effects caused by machine inertia were ignored during data processing.

A2.3.3 Jacket corrections

The specimen was isolated from the pressure medium during test conditions by either a single iron jacket or a combined iron and copper jacket (see **Appendix 1**). Part of the load in the deformation experiments was supported by the jackets and this amount needed to be subtracted from the load supported by the specimen assembly to obtain a true reading for the stress solely supported by the rock sample. For this purpose the σ/ε curves for the two materials constituting the jackets were determined.

Copper jacket strength

A detailed discussion of the problems of copper jacket strength and testing of two different copper jacket materials have been described by Covey-Crump (1993). The temperatures at which deformation tests were performed in this study are very close to the melting temperature of copper. The iron jacket also supported a much larger proportion of stress than the copper jacket so that in practice no correction for the copper jacket was applied to the data.

Iron jacket strength

A correction for the force supported by the iron jacket was applied to the data after data reduction as iron jackets were much stronger than copper jackets at elevated temperatures. There are several different ways in which the stress supported by the jacket can be measured. The first involves deformation of a dummy specimen made out of jacket material over the temperature range, while a second method involves deformation of a specimen with well constrained deformation behaviour that has been surrounded by the jacket to be investigated. Rather than using either of these two methods the strength supported by the iron jacket was calculated using the flow strength of iron, as described by Frost and Ashby (1982) and multiplying the flow stress indicated on **Figure A2.03** by the area of the iron jacket (0.165 mm^2). However, the stress supported by the jacket will fall as the jacket buckles, leading to over-estimation of jacket supported stress.

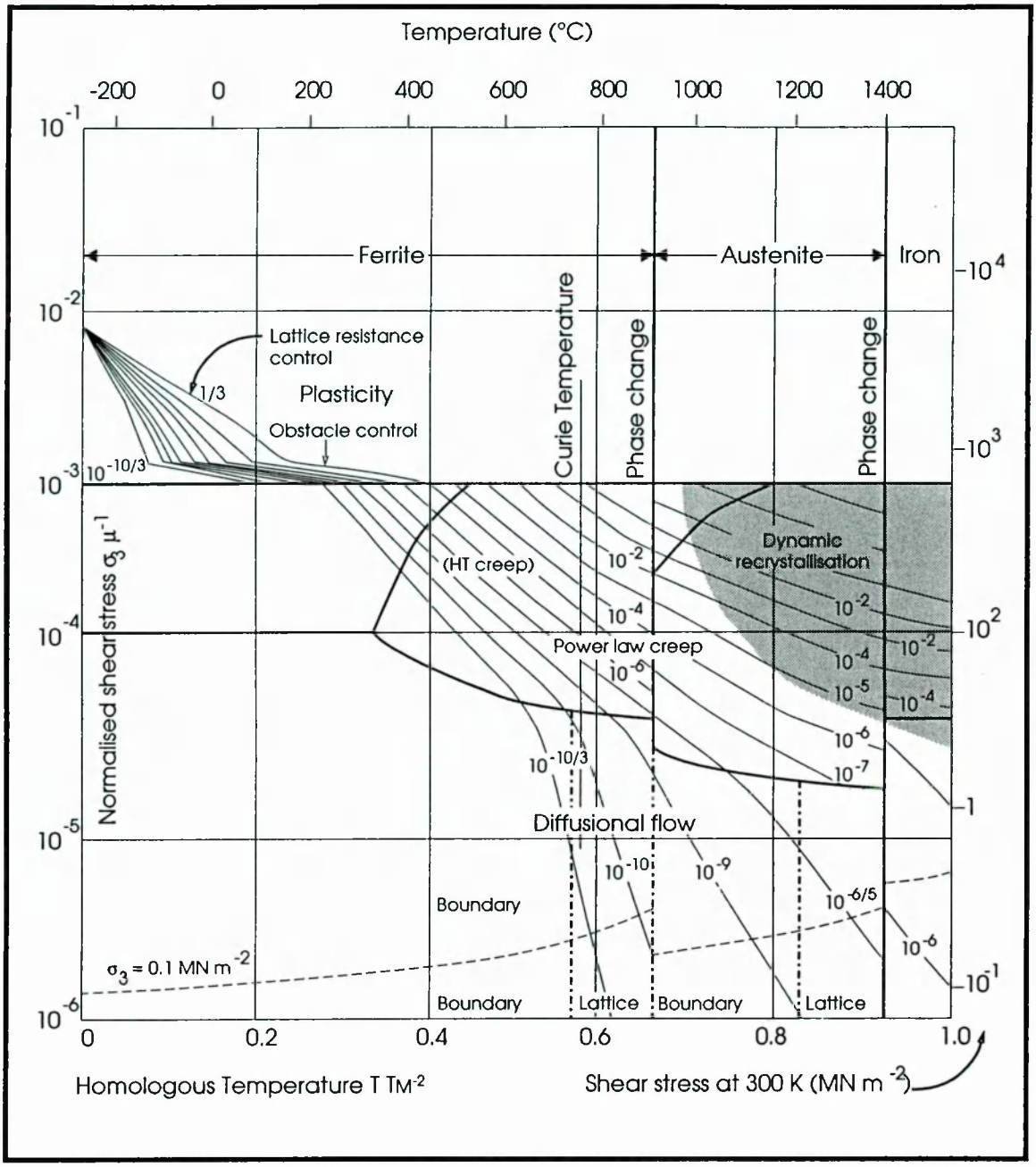

Figure A3.03: Flow stress of pure iron at temperatures between -200 and 1500 °C (after Frost & Ashby 1982).

The force supported by the iron jacket was almost constant over the temperature interval studied. There is an exponential increase in strength with increasing strain rate from 3 MPa at $5 * 10^{-5}$ s^{-1} to 12 MPa at $8 * 10^{-3}$ s^{-1} at 1000 °C as shown in **Figure A3.03**, resulting in very high stresses being supported even at high temperatures at fast strain rates. Deformation tests used for viscosity determination (**Chapter 6.2**) were not performed at temperatures in excess of 1100 °C as the jacket correction uncertainty induces large errors in the determination of the force supported by the specimen.

A2.3.4 Diameter change of sample during deformation.

The stress experienced by the specimen is the force supported over a given cross sectional area. Hence, to determine the stress supported by the specimen at any given instant during deformation it was necessary to know the cross-sectional area of the specimen at that time. As the specimen is deformed it changed its aspect ratio. The strain experienced by a particular section of the specimen is defined as its diameter after deformation divided by the overall diameter prior to deformation. Assuming constant volume deformation the specimen shortened and increased in diameter with increasing strain. Engineering strain is calculated which divides the change in length of the specimen (L_f being the current length) by the original length (L_O):

$$\text{engineering strain} = \frac{(L_f - L_O)}{L_O} \qquad \text{EA2.03}$$

rather than

$$\text{natural strain} = \ln \frac{L_f}{L_O} \qquad \text{EA2.04}$$

The assumption of homogeneous deformation of the specimen is an approximation as the increase in cross-section area of the piston did not proceed at the same rate as the specimen. Lateral constraints of the specimen immediately adjacent to the piston lead to a cone-shaped low pressure region adjacent to the piston with a geometrically forced high shear zone separating it from the volume of more homogeneously strained material in the centre of the specimen (**Figure A2.04, d**). With the onset of deformation the specimen quickly assumes a barrel shape with low pressure zones where the piston ends shield material and maximum deformation towards the mid point along the length of the specimen cylinder (**Figure A2.04, a** and **b**). When comparing the homogeneous deformation model with the more realistic barrel shape (**Figure A2.04, b**) only at two discrete cross sections of the cylinder (close to the specimen ends) was the real deformation the same as the assumed homogeneous deformation. This end effect becomes much more significant at length : diameter ratios of less than 2:1. Further derivations from the perfect cylindrical shape arose when the axis of deformation did not coincide with the axis of the specimen. This resulted in a kinked specimen. If the offset was significant this offset did affect stress-strain behaviour (**Appendix A2.3.1**).

Microstructure such as axial cracking (**Chapter 7.20**) were very sensitive to platen or end conditions, as end effects such as frictional differences between the piston and specimen materials could modify stress conditions sufficiently to suppress longitudinal

splitting. Small friction coefficients promoted axial splitting by inducing transverse tensile stresses (Paterson 1978).

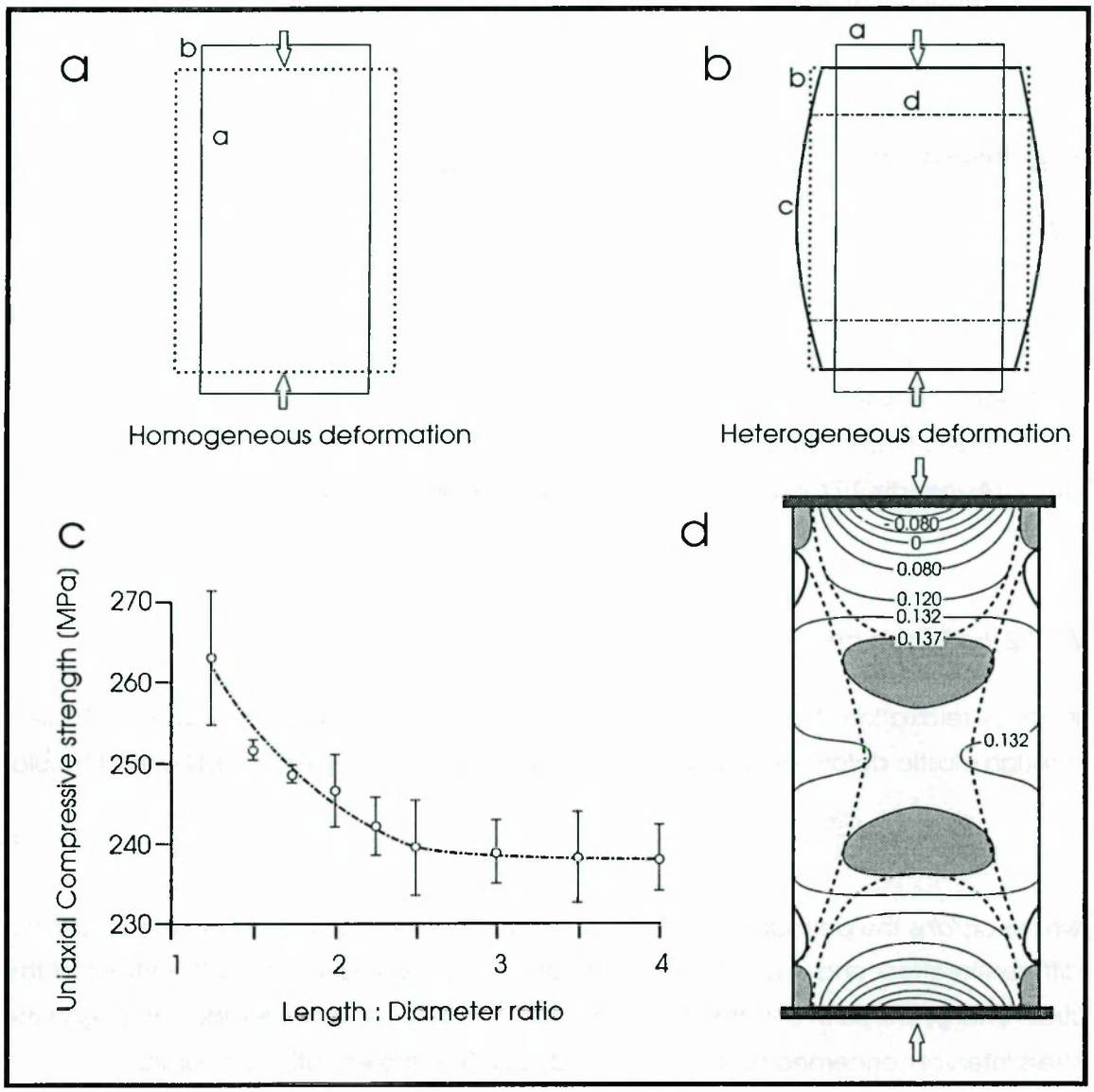

Figure A2.04: Shape change of specimen during compressive deformation, arrows indicating the direction of σ_1. **a.)** Homogeneous deformation, *a* = original, *b* = deformed cross-section. **b.)** heterogeneous deformation, *c* = barrel shaped cross-section, *b* = homogeneous deformation as in **a.)** and *d* marking where homogeneous = heterogeneous cross-section. **c.)** Dependence of uniaxial compressive strength on sample length : diameter ratio for Westerly granite at room temperature and confining pressure (after Mogi 1966). **d.)** Elastic distribution in uniaxially compressed samples with complete radial constraint at the ends; the contours represent relative intensity of stress on the modified Griffith criterion of failure with closed cracks, the shaded areas being most severely stressed (after Hawkes & Mellor 1970).

However, compared to the reproducibility of experimental results at the same experimental conditions and the natural specimen variability the effect of heterogeneous deformation was negligible, especially as maximum strains did not exceed 35 % in uniformly deformed samples. However, this effect on samples WG28,

WG29 and WG30 is uncertain, as only the lower half of the samples were deformed (**Chapter 5.2.6**). For this reason the stress-strain measurements on these three samples was qualitative, rather than quantitative.

A2.4 Data Processing

A2.4.1 Processing necessary for stress strain tests

For any given time interval engineering strain and force on the specimen were calculated. Specimen stress is a function of force supported at a given cross-section that increases with increasing strain. A component of force supported by the jacket also needed to be subtracted. Data was displayed by plotting differential stress against strain. (**Appendix 10** for mechanical data of deformed samples WG2 to WG30).

A2.4.2 Processing necessary for stress relaxation tests

In stress relaxation the elastic strain energy stored in the assembly was dissipated through plastic deformation within the specimen. This can be expressed by the formula:

$$\frac{d\varepsilon}{dt} = - s_S * \frac{d\sigma}{dt} \qquad \text{EA2.05}$$

where $d\varepsilon/dt$ is the permanent strain rate, $(d\sigma/dt)$ the true rate of change of the applied differential stress and s_S is the specimen compliance. In order to take the effect of the strain energy stored in the machine into account the stiffness of the machine (s_m) in the stress interval concerned had to be added to s_S. Thus the equation becomes:

$$(s_S + s_m) = \frac{\Theta}{L_O * S} + \frac{1}{E} \qquad \text{EA2.06}$$

where Θ is the specimen cross-section area, L_O is the specimen length, S is the machine stiffness and E is the Young's modulus of the specimen. Two closely spaced points on the stress trace were chosen and the different amounts of machine distortion corresponding to these two points was calculated (**Figure A3.05**). The strain rate (i.e. gradient on the stress versus time plot) could then be calculated using successive points on the stress trace. The average of these two points was taken to be the strain rate at an intermediate point. Thus a plot of strain-rate versus stress can be plotted.

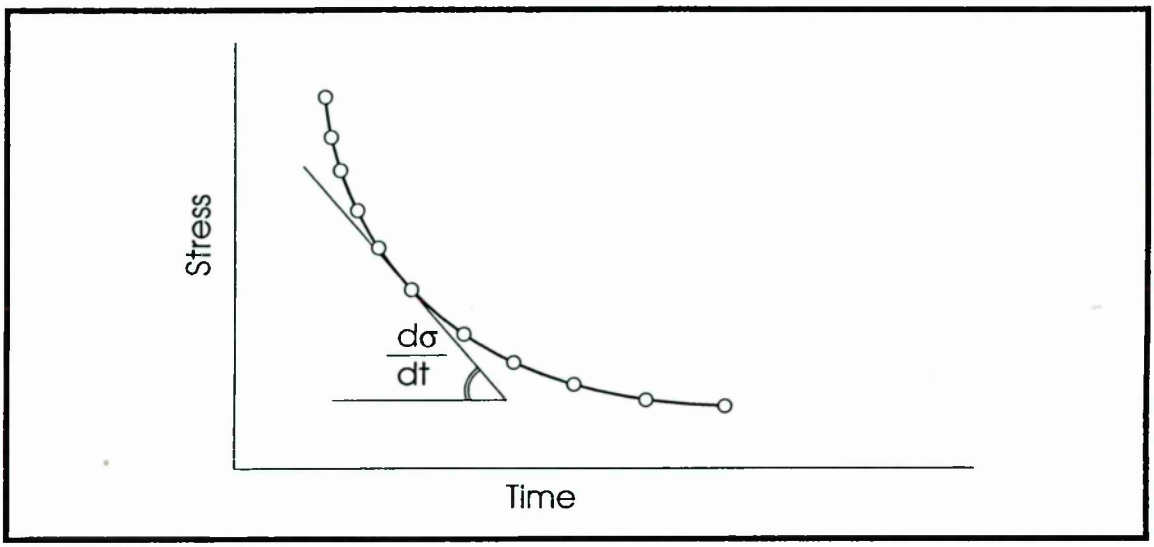

Figure A2.05: Data reduction for stress relaxation experiments. The tangent to the curve allows strain rates to be calculated (after Walker 1991).

Appendix 3

Scanning electron microscope (SEM)

A3.1. Introduction

Electron microscopy was carried out on the Manchester Geology Department's scanning electron microscope JSM-6400 (SEM) which includes a wavelength, electron dispersion micro probe with optional cathodo-luminescence digital image processing facility. This facility was used to carry out detailed microstructural and geochemical analysis of experimental charges of Westerly granite. Back-scattered electron microscope images were used to determine mineral distribution and crack characteristics.

A3.2 Specimen preparation

Carbon coated thin sections were inserted into the SEM on a thin section holder. Electric contact between the specimen holder and the thin section was established by silver lacquer bridging the gap between the holder and the top surface of the thin section with a trail leading to the rock material itself. Adjacent to the specimen was a small bar containing the standard cobalt and several minerals of known composition to allow calibration of the micro-probe facility.

A3.3 SEM data output and treatment

The electron microscope provides a grey scale image of an enlarged surface area of between 10 and 300.000 times. Secondary and back-scattered electron images were studied. X-ray radiation allowed the chemical composition of minerals and melt.

A3.3.1 Secondary electron images

Surface topography was revealed by secondary electrons (Lloyd 1985). As samples were polished thin sections the only topographic information obtainable from

secondary elements were the location of cracks. However, as these were also easily distinguished on back-scattered images, this type of image was only used to check on the quality of polish on the thin section as a bad polish results in a deterioration of x-ray analysis, and to study microstructures due to shear enhanced compaction in Ougthibridge Gannister (**Figure 7.22**)

A3.3.2 Back-scattered electron images

Back-scattered electrons resulted in different grey values for elements with different atomic numbers and therefore display compositional and crystallographic contrasts in minerals (Lloyd 1985). Locations of x-ray spot analysis were chosen on frozen back-scattered images and their locations marked on thermal prints for future reference (**Figure 4.11**). Six to eight adjoining images per thin section at the same magnification were taken from each sample. These were assembled to form a collage to enable the tracing of cracks and minerals, using tracing film overlays. The resulting crack maps were used to determine crack density and preferred orientation (see **Appendix 4**). Phase boundary maps gave information on phase distribution in the specimen. The collages and single back-scattered images were also used for the determination of melt morphology and distribution.

Grey scale images at a magnification of * 110 were imported into an image processing package that is part of the eXL link computer. The image was transformed into an 8 colour image, where different colours represented eight different bands of the continuous grey scale from black to white. The width and position of the bands were altered so that one prominent colour matched the grey scale of the melt phase in the image. The computer then calculated the areal fraction of this colour band. 49 to 78 different images were thus analysed per thin section. The average of areal melt fractions per thin section was taken to equal the volumetric melt fraction (Underwood 1965). Limitations to the accuracy of areal melt fractions were set by the difficulty in determining the exact dimensions of the melt phase in each image, as the melt grey-scale was located between those for plagioclase and K-feldspar, with often gradational contacts between minerals and melt. This error increases with decreasing melt fraction (see discussion in **Chapter 3.2**).

Melt fractions estimated using the SEM imagery package were compared and contrasted to optical transmission photo collages of the same thin sections. Here melt areas were traced and the line drawing imported into the !GRAINS image processing package (Evans 1995).

A3.3.3 X-ray radiation

X-ray radiation emitted from the target area provides quantitative micro-analytical analysis in association with other signals (Lloyd 1985) and was used to determine the composition of minerals and melt. A 1 μm diameter area for geochemical analysis was chosen on a frozen back-scattered image by adjusting two orthogonal lines to overlap above the point of analysis. On bombardment with radiation the emitting x-rays were analysed by the computer and compared to stored x-ray emissions for elements previously selected. The element fraction was recalculated in terms of oxide percentage (**Appendix 6**).

Appendix 4

Measurement of micro-crack density and orientation

A4.1 Introduction

As part of the microstructural investigation of Westerly granite samples the density and population characteristics of cracks were explored. To this effect adjoining back-scattered electron imaged were taken at a constant magnification of * 85. Cracks and holes, showing up black, were then traced onto tracing film (**Appendix 3**). Another tracing was carried out, tracing boundaries between different phases. The tracings were then scanned and read into an Archimedes or personal computer. Crack density statistics were analysed using the program !GRAINS (EVANS 1995). Crack orientation statistics were carried out using the PC program CRACKS (Neumann per com 1994).

In the first section the methods used to produce crack maps are described in detail. The errors introduced during this stage are discussed. In the second part of this appendix the theories behind the crack analysis used in the computer programs are discussed. Finally the remaining crack maps, that are not displayed in Chapters 2, 3 and 7 are displayed, from which grain density data was collected.

A4.2 Errors in data acquisition in crack densities and orientation measurements induced during the assembly of crack maps

Errors arising from the tracing process can be grouped into several categories:

1. Errors arising from difficulty in crack identification
2. Errors in drawing location and shape of individual cracks
3. Subjective crack selection by observer.

1. Cracks were traced from instant thermal prints of BSEM images. These were generated by a printer laying strips of grey values onto thermal paper. These horizontal strips split the image into parallel horizontal lines, making small scale cracks (close to the resolution of the printer strips) difficult to identify. This set a lower limit on crack length that could be detected to about 0.001 mm.

Further difficulty in recognizing small cracks was due to the apparently fractal character of cracks. This means that with increasing magnification the number of cracks and length of already identified cracks will increase. This effect was particularly pronounced in an area of high crack density such as feldspars affected by sericitization. A magnification of * 85 was chosen as a relatively large proportion of grains could be studied on a limited number of images while still supplying a reasonable crack density. Also, as all images for all samples were taken at the same magnification this effect was negligible, as only relative crack densities were compared.

2. Slight distortion at the edge of the instant thermal prints used for the BSEM collages lead to occasional misfit of photos. Also, due to complexity of crack shapes (curvilinear and interlinked) errors in the exact determination of crack shapes were likely to occur. However, location of cracks are thought to be accurate to within 0.001 mm. Crack shape accuracy is more difficult to evaluate. However, as cracks were not studied in isolation from each other but as a whole at the scale of the collage, small errors in crack orientation are thought to alter orientation histograms by less than 1 %. Both photocopiers and scanners did distort images on reproduction. The photocopier showed a slight vertical distortion (longer side of A4 sheet). However, this distortion is only on the order of 0.28 %. Loss of resolution and preferential orientations towards vertical and horizontal direction are the direct result from importing the tracings into the computer software by scanning. Pixel size depends on the resolution set on the scanner. The larger the resolution the smaller the pixel size, but also the larger the data file generated. All images were scanned at 300 dots per inch.

3. Each observer will introduce a certain bias when collecting orientation data, as it was very tempting to emphasise an identified preferred orientation. In order to evaluate this bias Dr P.T.S. Rose volunteered to create a crack map from one of the collages already traced by the author. The collage of WG6 was chosen (**Figure A4.01**, **Figure A4.03**). Significant differences in crack density and degree of preferred orientation were observed between the authors tracing and that produced by Dr. P.T.S. Rose. In the latter tracing a lower crack density was recorded and a preferred orientation of long cracks was emphasised compared to the tracing carried out by the author.

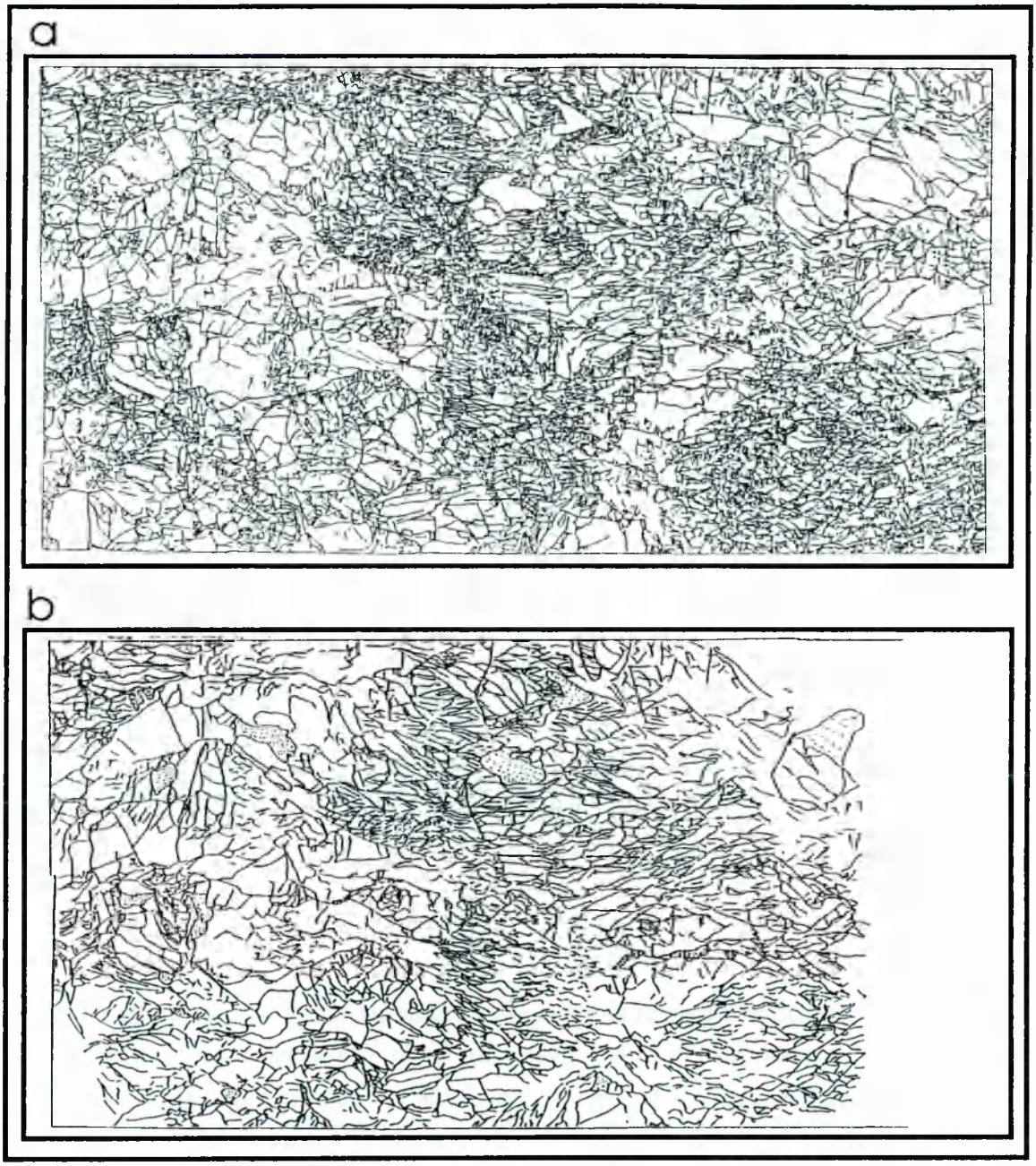

Figure A4.01: Comparison between crack tracings (crack map) from the BSEM collage of WG6 (**Figure A4.03**). **a.)** Crack map produced by the author and **b.)** by Dr P.T.S Rose. Crack densities are $\varphi = 66.87$ mm mm^{-2} for **a.)** and $\varphi = 30.25$ mm mm^{-2} for **b.)**.

A4.3 Crack density and average width of cracks

The crack tracings were scanned as a black and white line tracing and stored in pixel form. This means that cracks are black against a white background. These sprite files were imported into the Quick Basic program !GRAINS (Evans 1994) for crack density analysis.

The sub-routine LINE INTERCEPT was used to determine the average width of cracks in OS units. The number of black and white pixels were counted in a previously selected square of known original dimensions. The number of black pixels was then divided by the sum of black and white pixels to get an average crack density. This black/white coefficient was then divided by the average crack width previously determined and re-scaled to get a value for crack density in mm mm^{-2}.

A4.4 Crack orientation

Crack orientations were measured using the CRACKS Turbo-Pascal program written by J.L. Neumann (1994) for PC computers. The shape of cracks, especially the interconnectivity of cracks posed problems in identifying and isolating individual cracks, introducing errors to the orientation measurements. Cracks have a finite pixel width. A curved crack will have different orientation measurements depending on whether the inner or outer arc of the crack is measured. Ideally an infinitely thin line running down the axis of the crack should be measured. Infinitely thin lines would pose problems when a branching crack is encountered, as one of the branches would have to be chosen as the dominant branch, thus making it necessary to somehow disconnect the "minor" branch from the "dominant" crack. An additional problem arose when a dense network of cracks was present (e.g. **Figure 7.03**).

The method to determine crack orientation in the program CRACKS does not attempt to follow individual cracks. Instead it looks at the shapes of the spaces between the cracks. For this purpose the scanned image was divided into a pre-selected number of tiles. Each tile was studied in turn. Square tiles were further trimmed to a circle with diameter equalling half the tile length, in order to reduce the the probability of measuring horizontal and vertical lines preferentially. Thus, for each point in the circle:

$$(I\text{-}O)^2 < j^2 \qquad \text{EA4.01}$$

with *O* marking the mid point of the square and *I* being an arbitrary point in the circle or radius *j*. For each tile a single straight line was determined that best described the distribution of black pixels in the tile. Tiles were discarded if either they contained numbers of black pixels below and above the previously set limits, or the average spacing between black pixels (α_{av}) exceeds the set α_{max}. Once the orientation of a line had been determined (φ) (between 0 and 180 °) with the above conditions fulfilled, it was included in the data file for statistical analysis. However, vertical and horizontal orientation frequencies are spurious, as a strong preferred vertical and horizontal orientation was recorded on all crack maps (**Figure 2.07**). In practice all

crack orientations were normalized to WG0, the starting material, that was assumed to have an isotropic crack distribution.

A4.5 Crack maps not previously displayed, but used in crack density analysis

On the following pages the crack maps of WG4, WG6, WG7, WG8, WG10, WG11, WG16 and WG17 are displayed that were used in crack density analysis. Deformation conditions and melt percentages are listed in **Table A4.01**

	T (°C)	σ_{max} (MPa)	ε_{max} (%)	$\dot{\varepsilon}$ (%)	ss/sr Nº	t to def (h)	t total (h)	ϕ melt (fract)	fault (°)
WG4	1000	36.79	12.25	5E-05	1	2	2.5	0.203	78, 81
WG6	850	518.86	8.44	5E-05	1	2	2.5	0.044	45, 47
WG7	800	372.63	8.82	5E-05	1	2	4	0.033	37, 41
WG8	800	343.4	14.3	5E-05	1	90	96	0.035	37, 40, 44
WG10	900	153.58	15.26	5E-05	1	94	96	0.131	52
WG11	1000	58.13	13.23	5E-05	1	69.5	71	0.271	53
WG16	900	181.68	22.6	5E-05	3	3.5	17.5	0.135	42, 63
WG17	900	119.94	17.36	2E-6	1	0	52.4	0.179	90, 90, 90

Table A4.01: Test conditions of deformed samples whole SEM collages (plus associated phase boundary and crack maps) are displayed in the following fan-folds.

The insert specimen drawing on each crack map shows the location of the SEM collages on a drawing of the specimen outlines (after **Figure 5.16**) drawn to their true scale. The trace of macroscopic fault lines are indicated on the phase boundary maps by dot-dashed lines.

This page has intentionally been left blank

Figure A4.02: SEM collage, phase boundary and crack map of sample WG4.

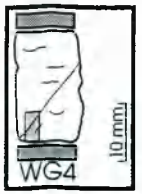

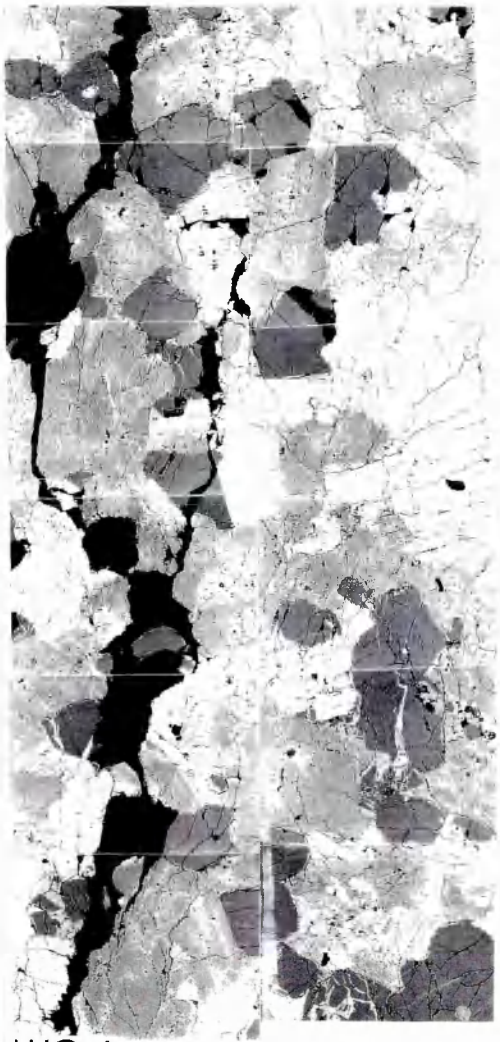

WG 4 SEM Backscattered Image

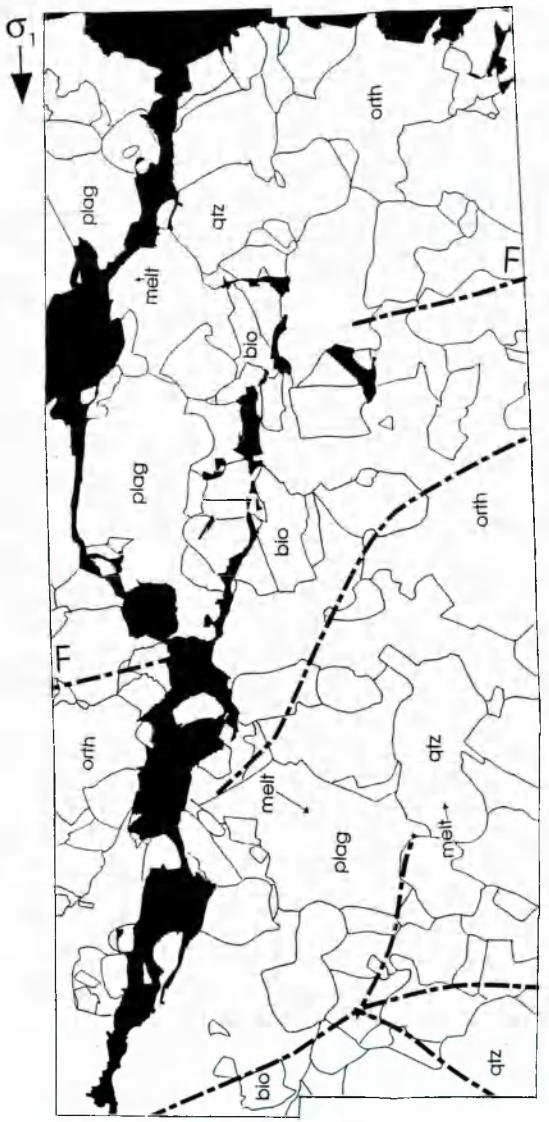

Outline of grain boundaries

Cracks 1.0 mm

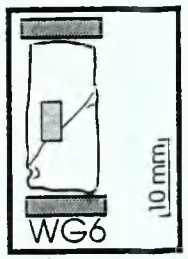

Figure A4.03: SEM collage, phase boundary and crack map of sample WG6.

WG 6 SEM Backscattered Image

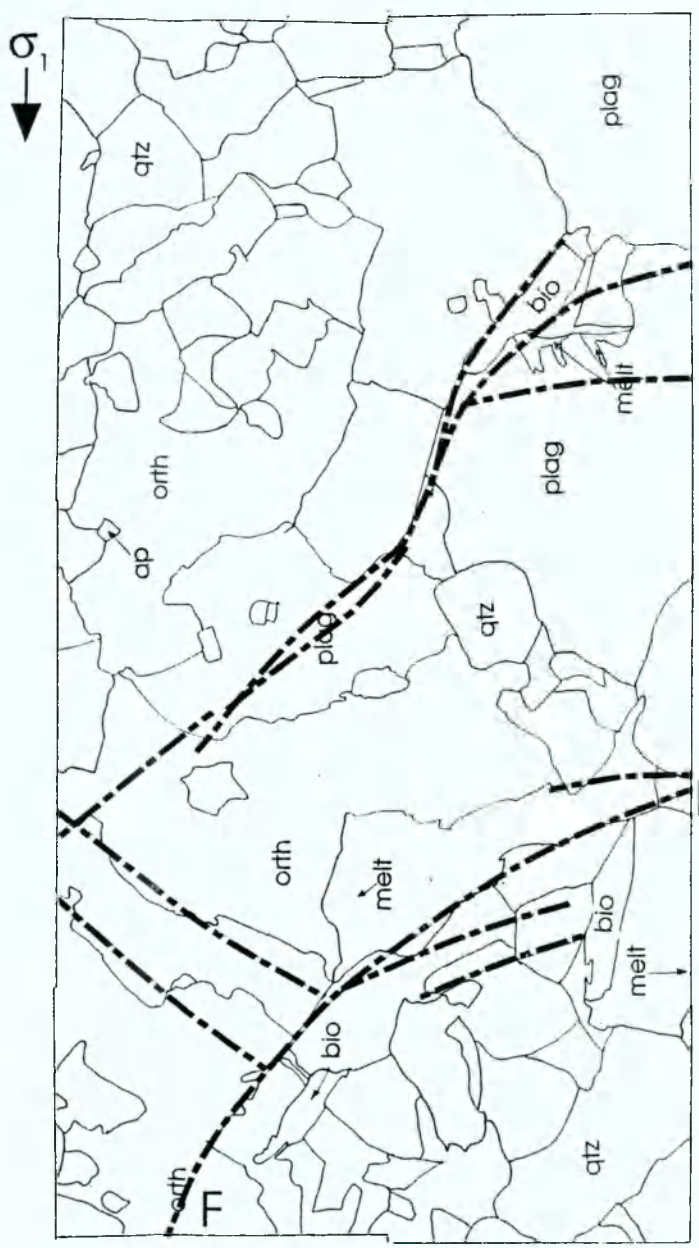

Outline of grain boundaries

Cracks 1.0 mm

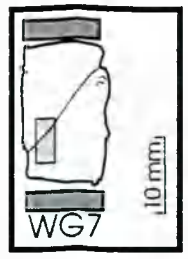

Figure A4.04: SEM collage, phase boundary and crack map of sample WG7.

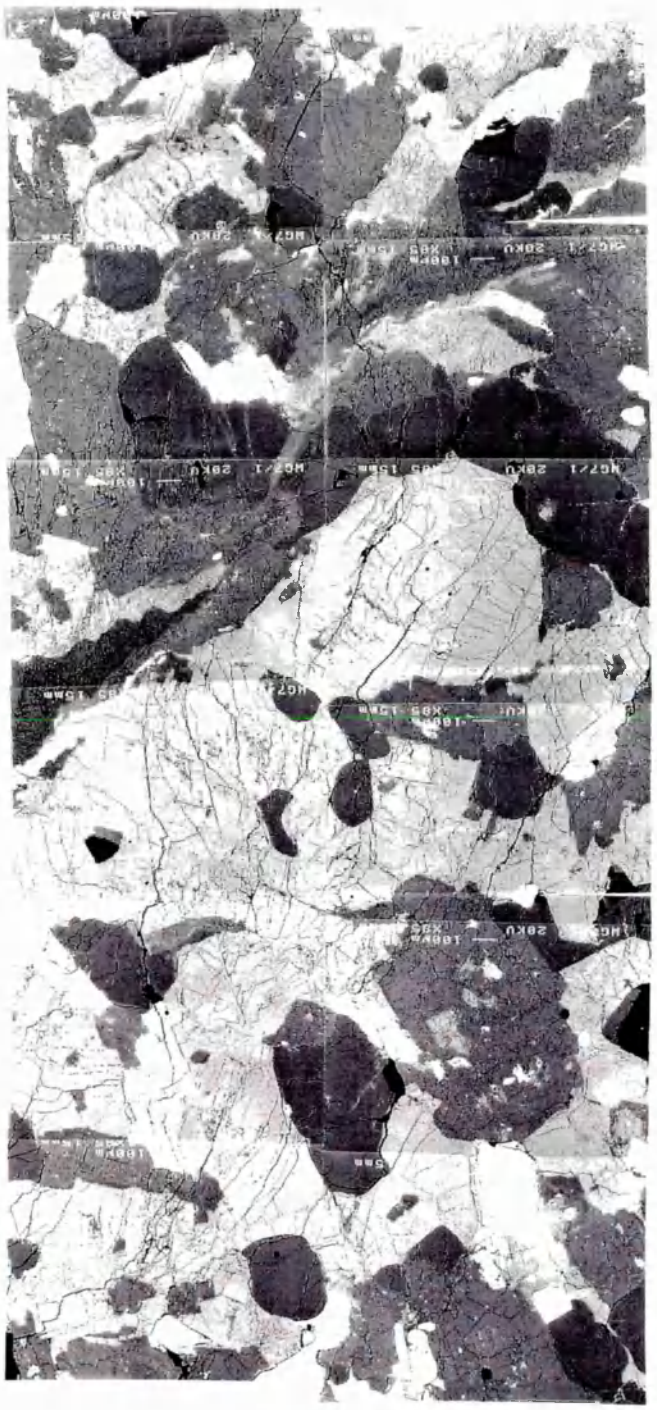

WG 7 SEM Backscattered Image

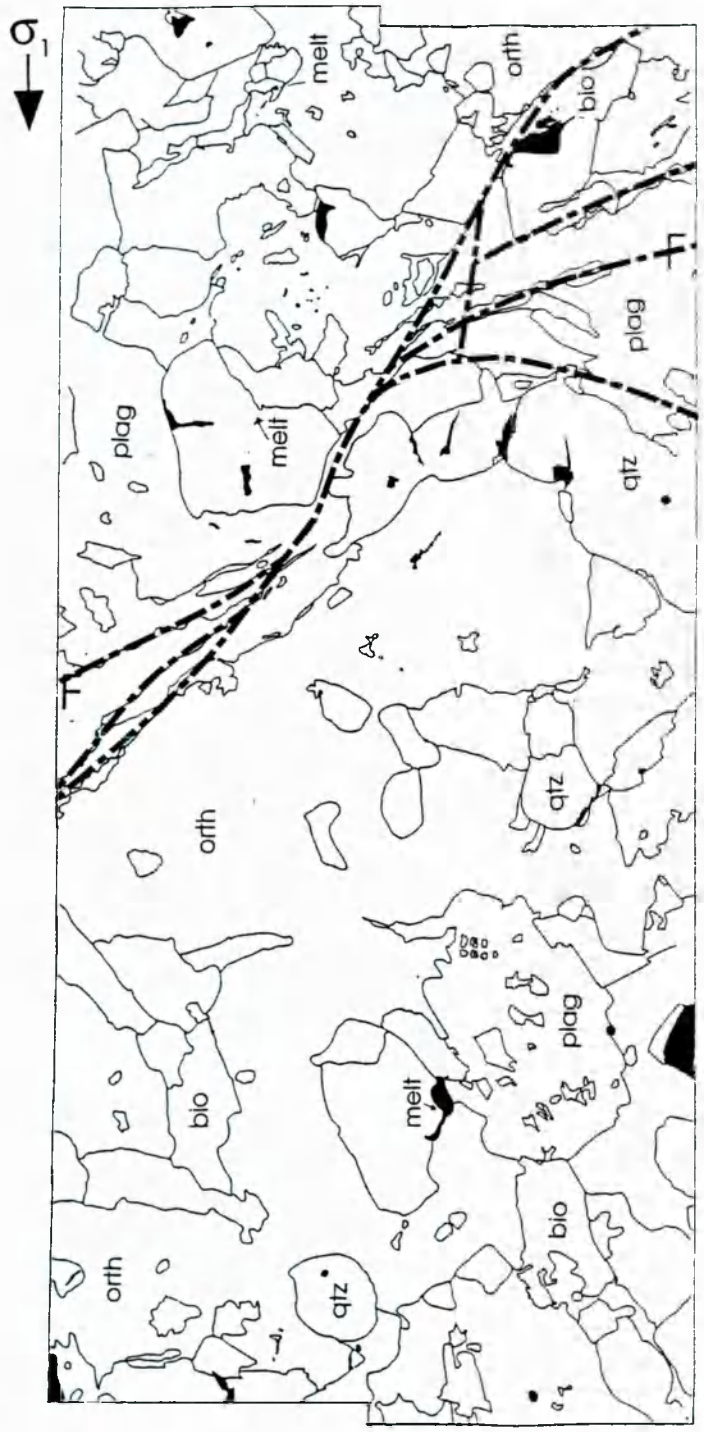

Outline of grain boundaries

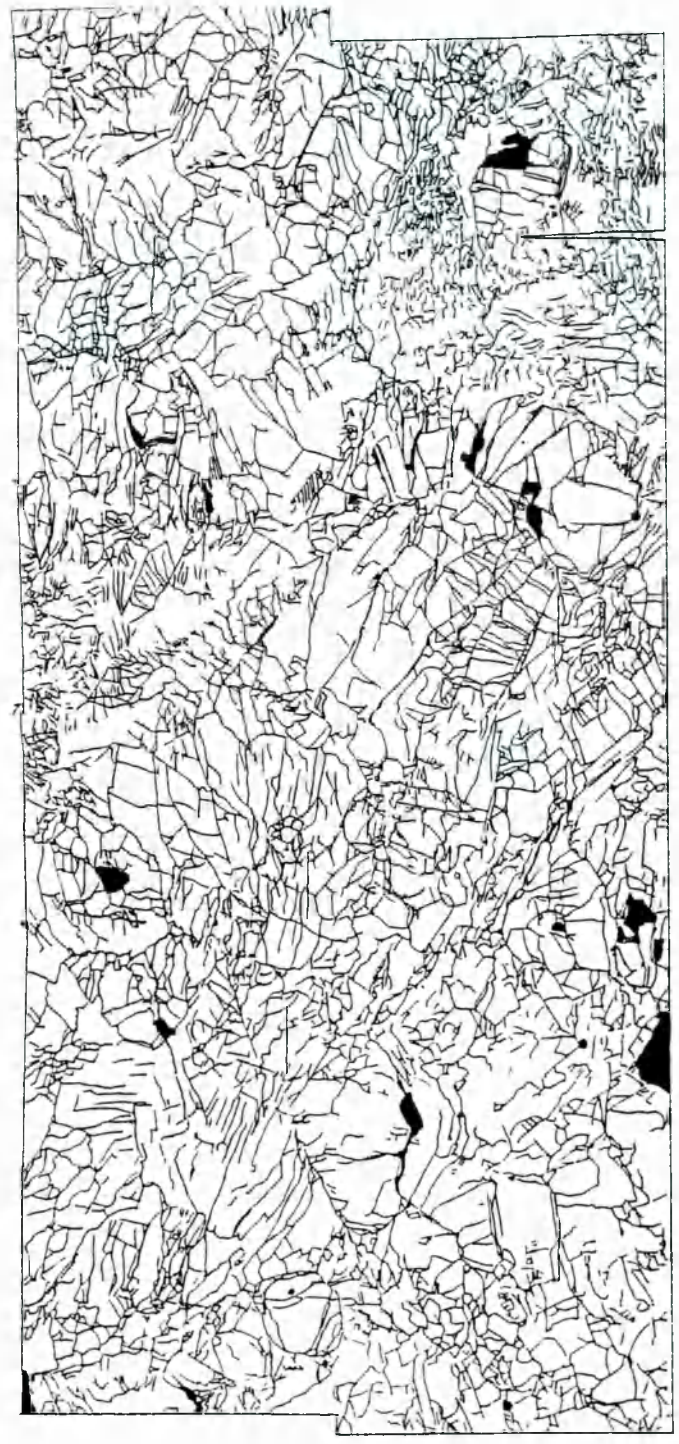

Cracks 1.0 mm

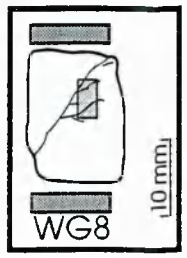

Figure A4.05: SEM collage, phase boundary and crack map of sample WG8.

WG 8 SEM Backscattered Image

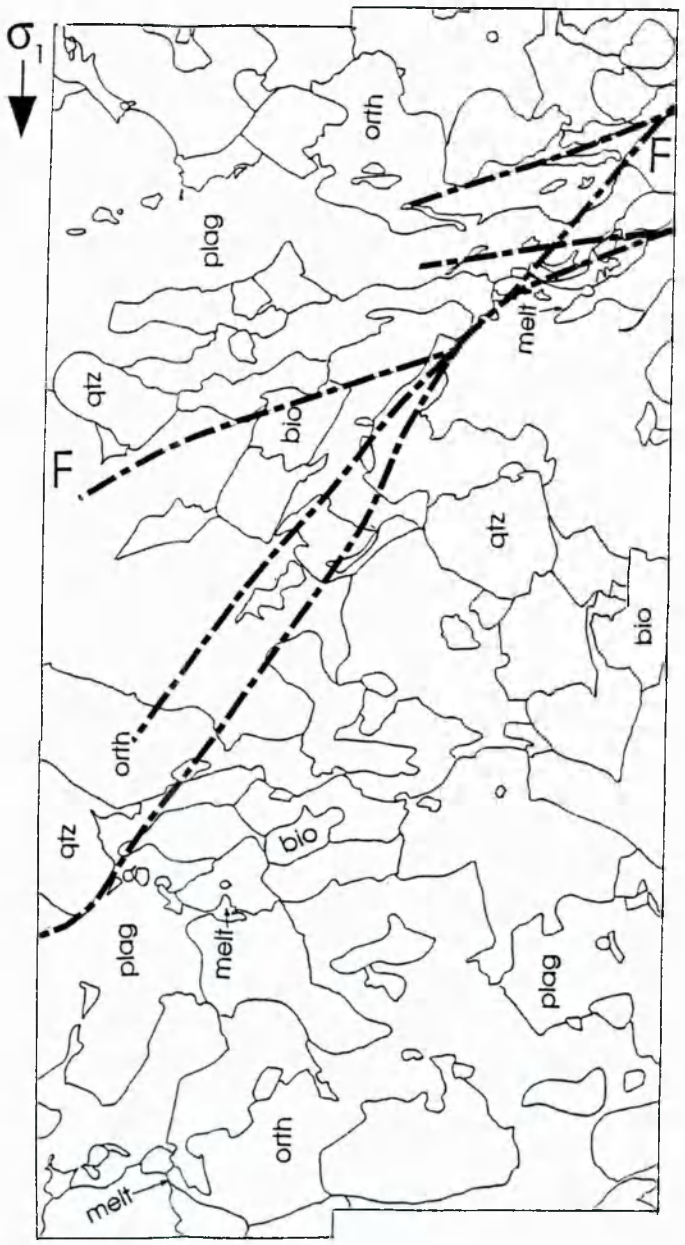

Outline of grain boundaries

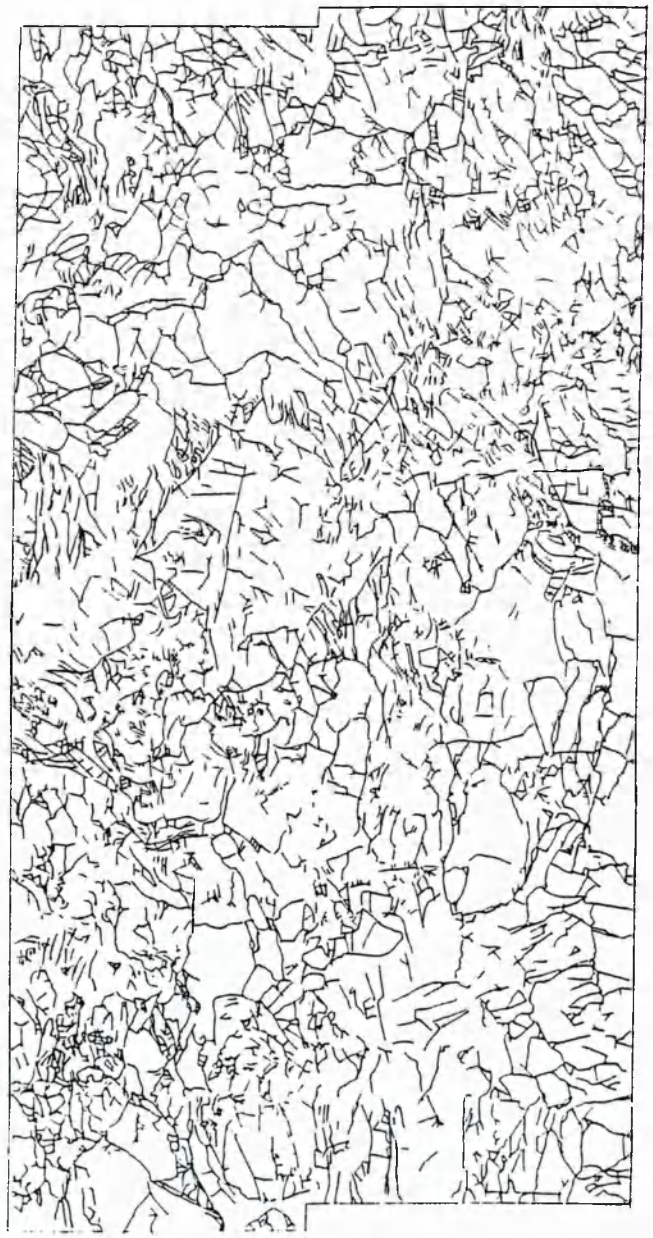

Cracks 1.0 mm

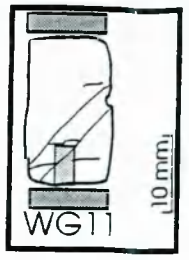

Figure A4.07: SEM collage, phase boundary and crack map of sample WG11.

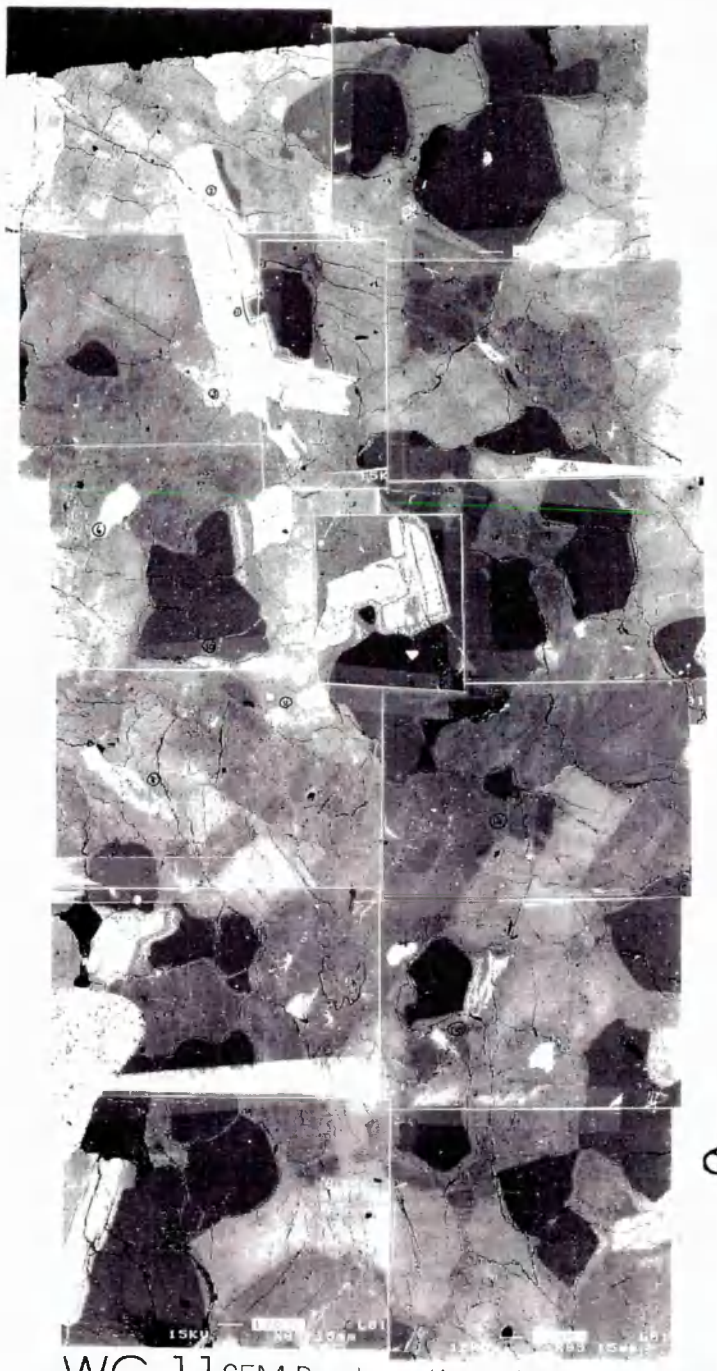

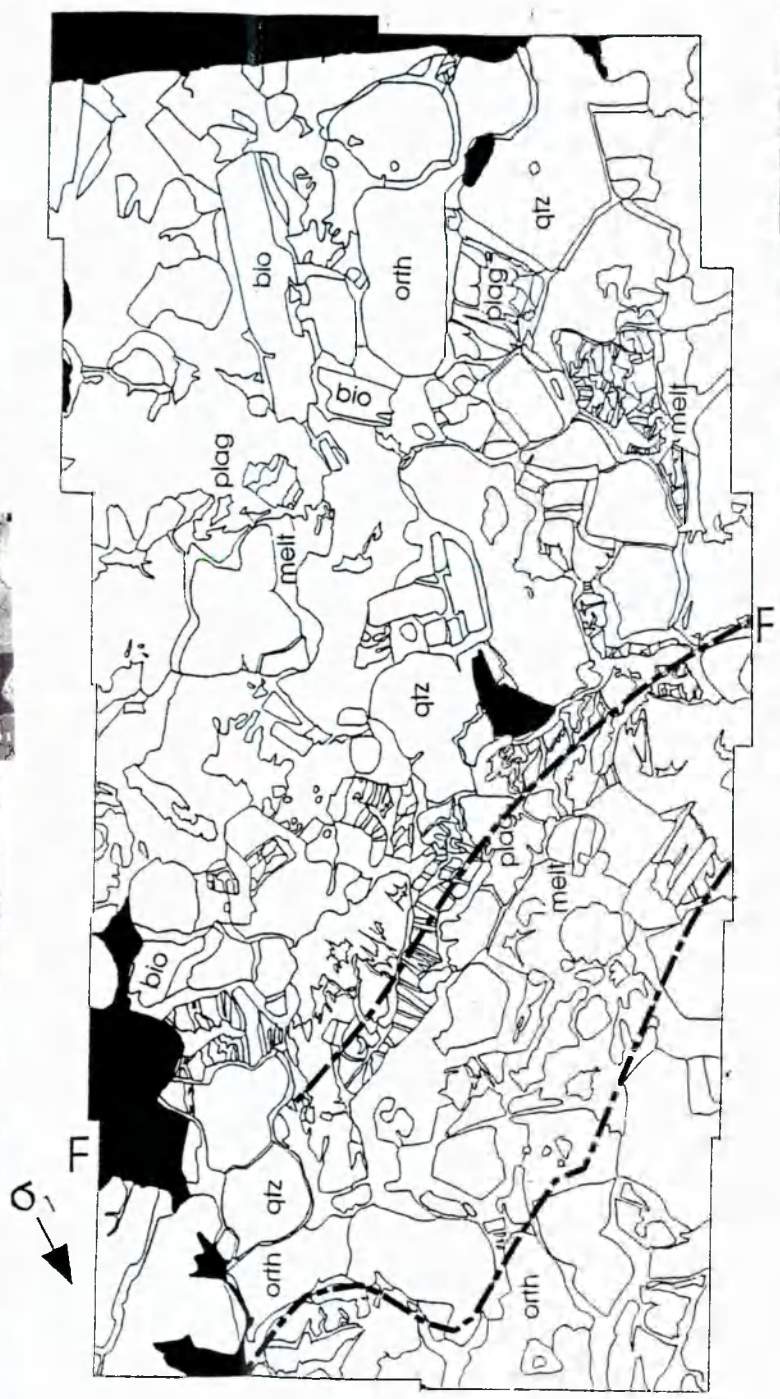

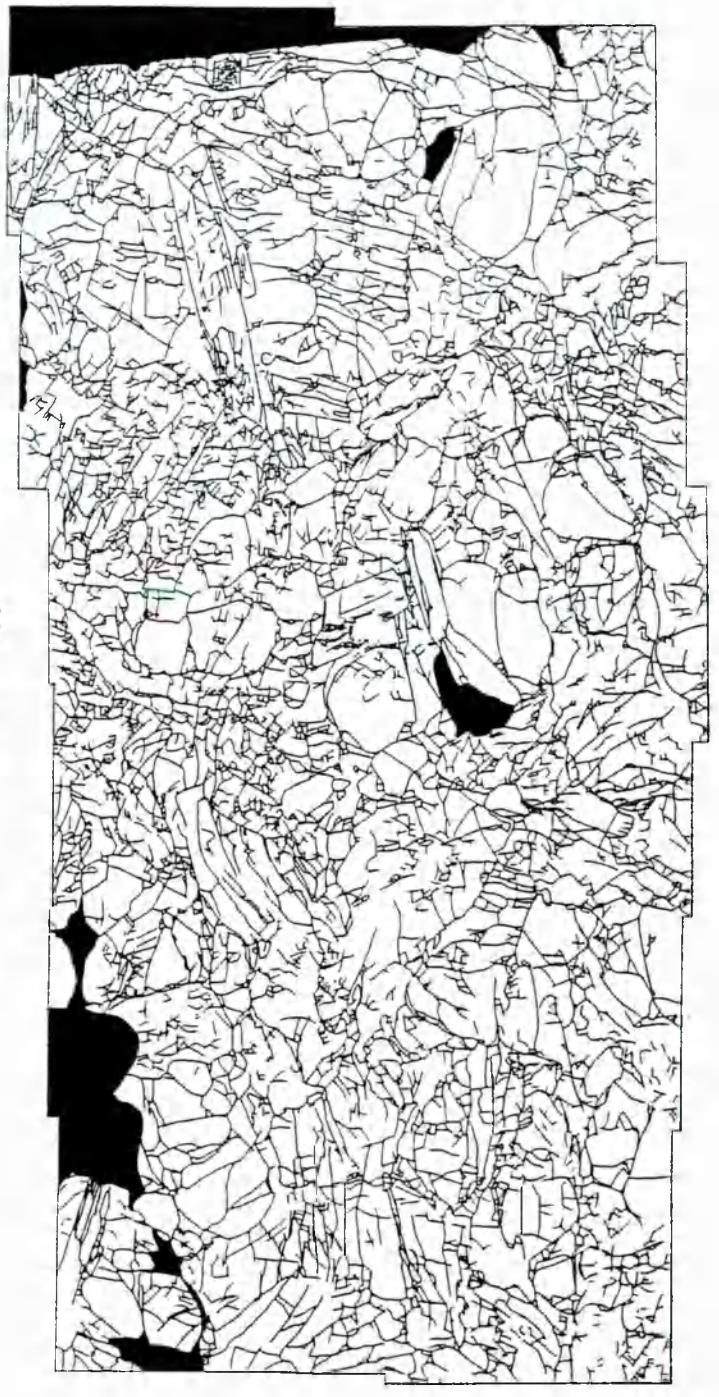

Figure A4.06: SEM collage, phase boundary and crack map of sample WG10.

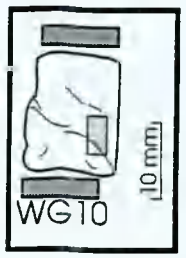

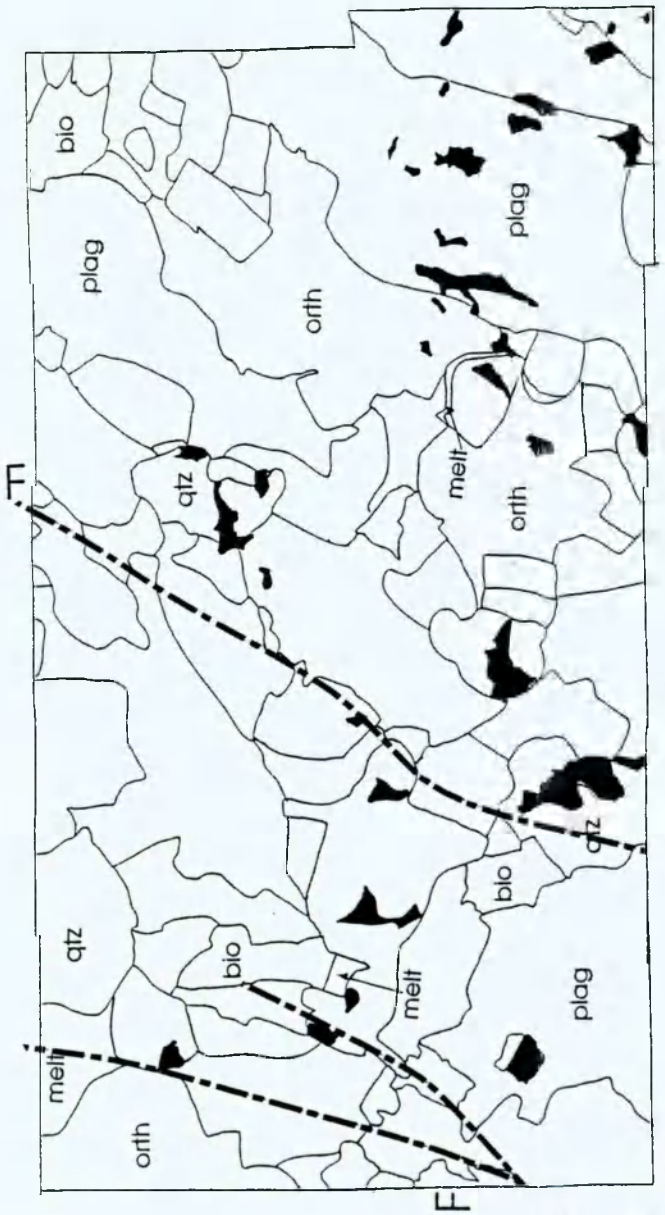

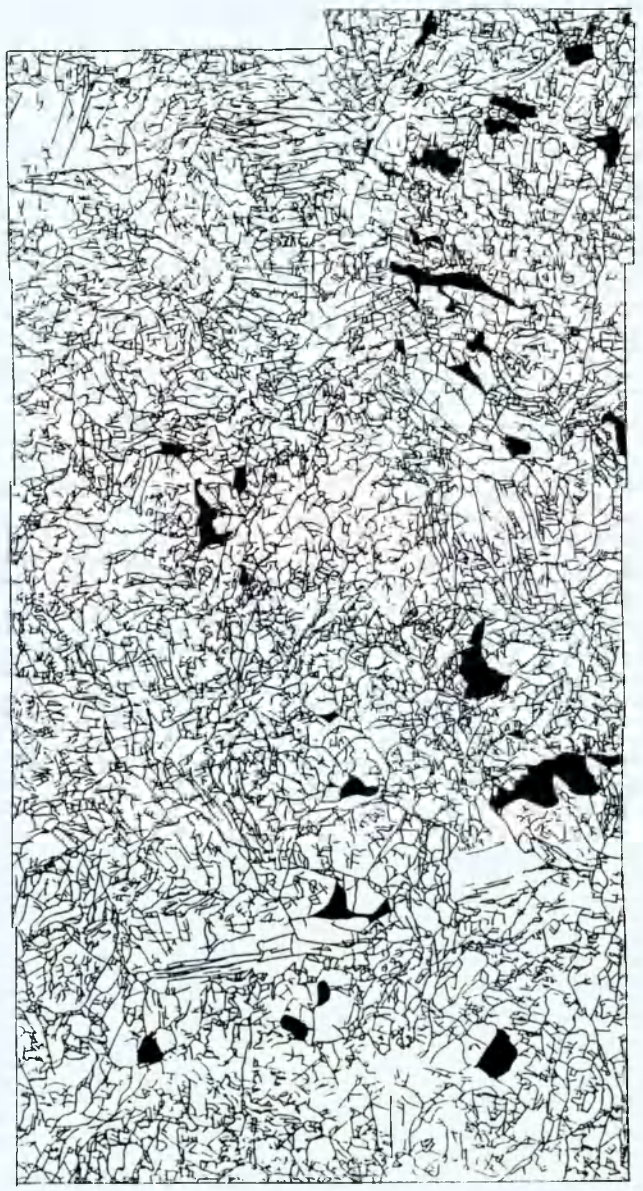
Cracks

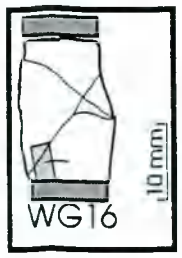

Figure A4.08: SEM collage, phase boundary and crack map of sample WG16.

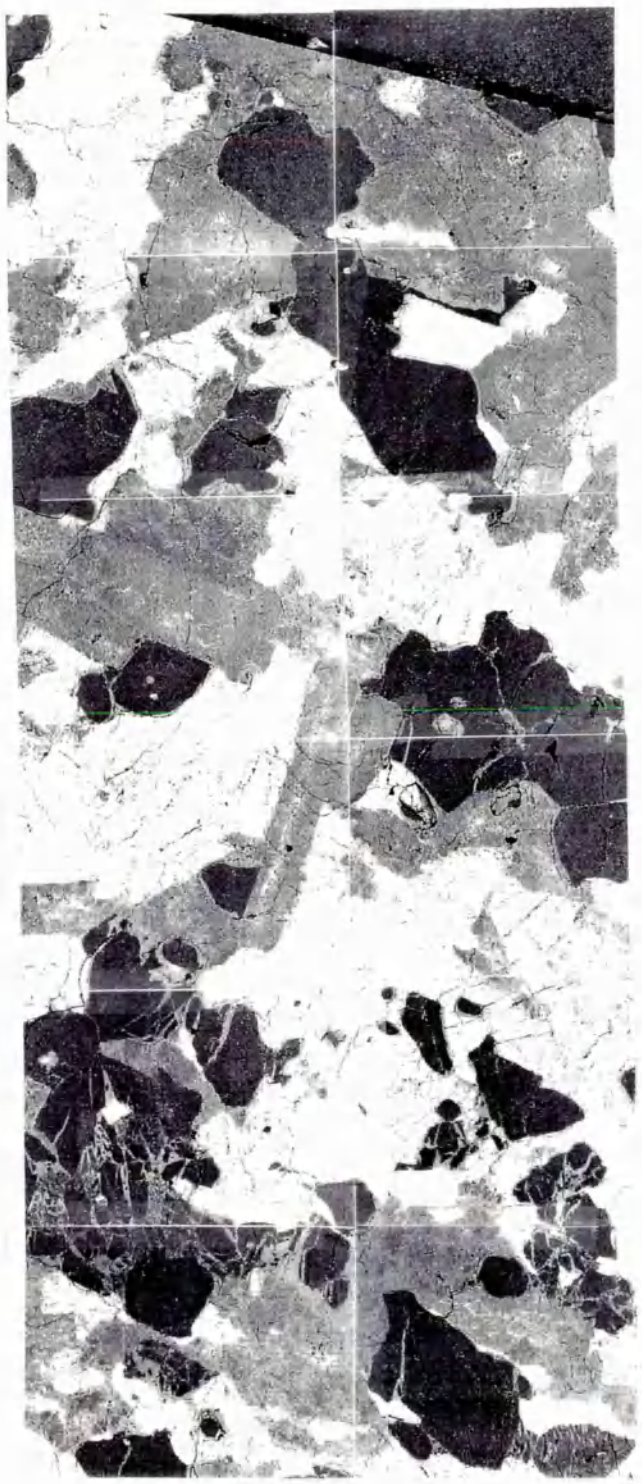

WG 16 SEM Backscattered Image

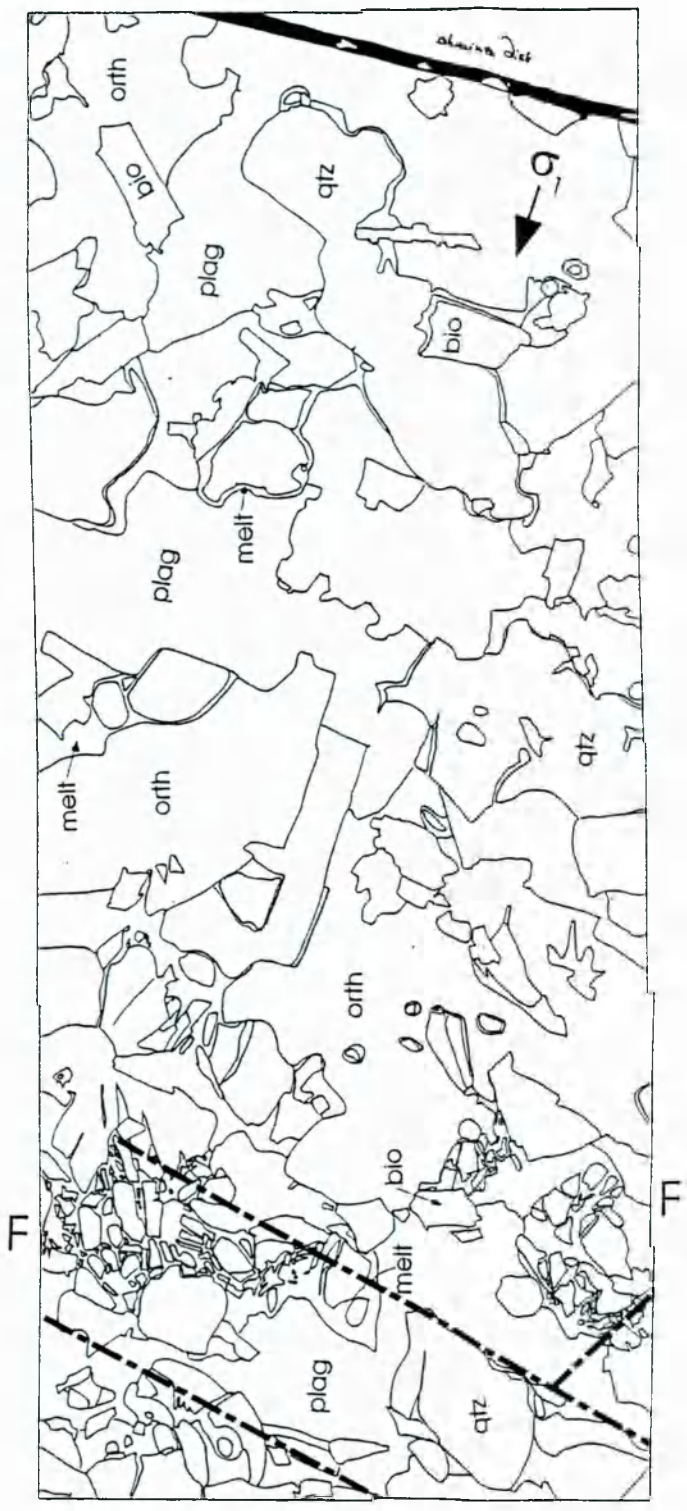

Outline of grain boundaries

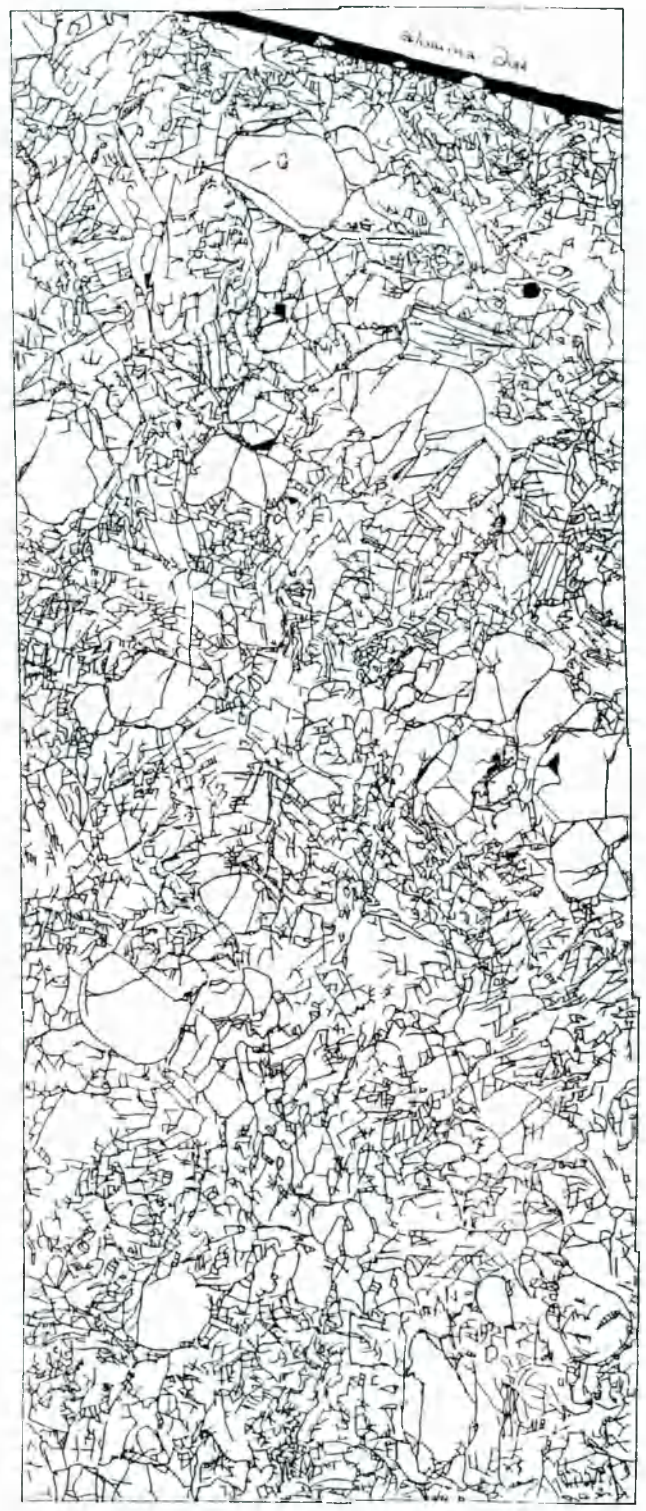

Cracks 1.0 mm

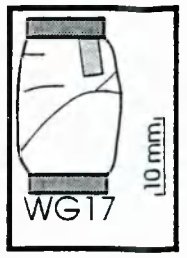

Figure A4.09: SEM collage, phase boundary and crack map of sample WG17.

WG 17 SEM Backscattered Image

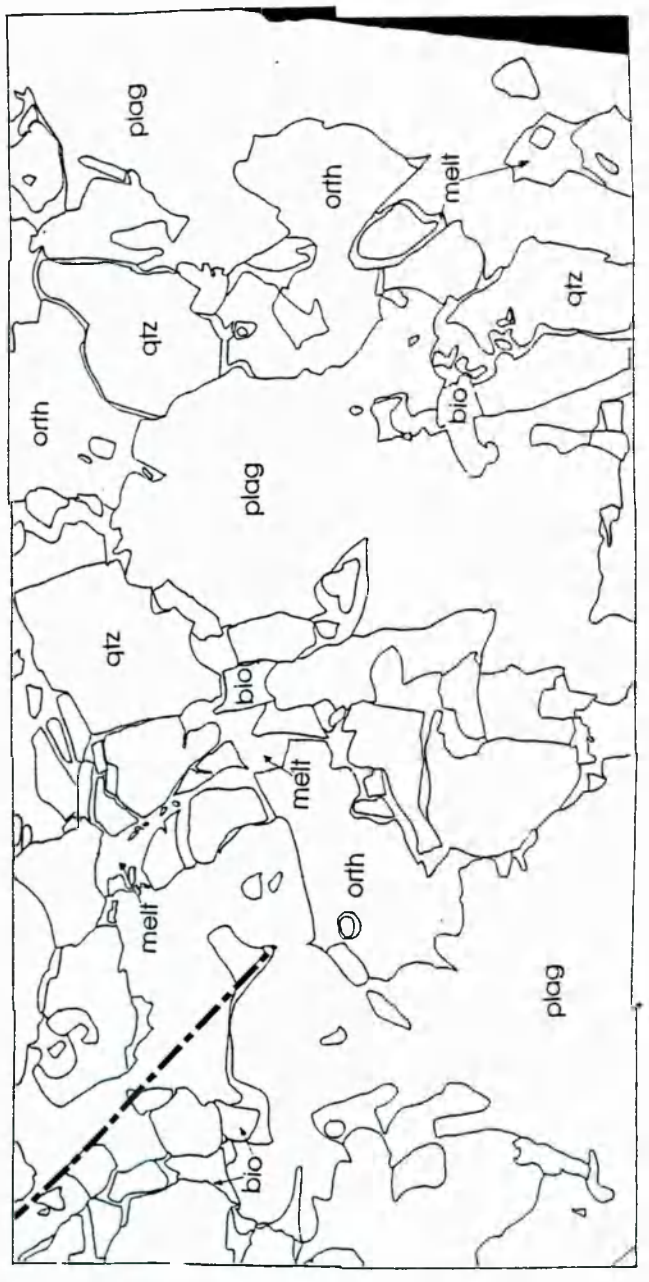

Outline of grain boundaries

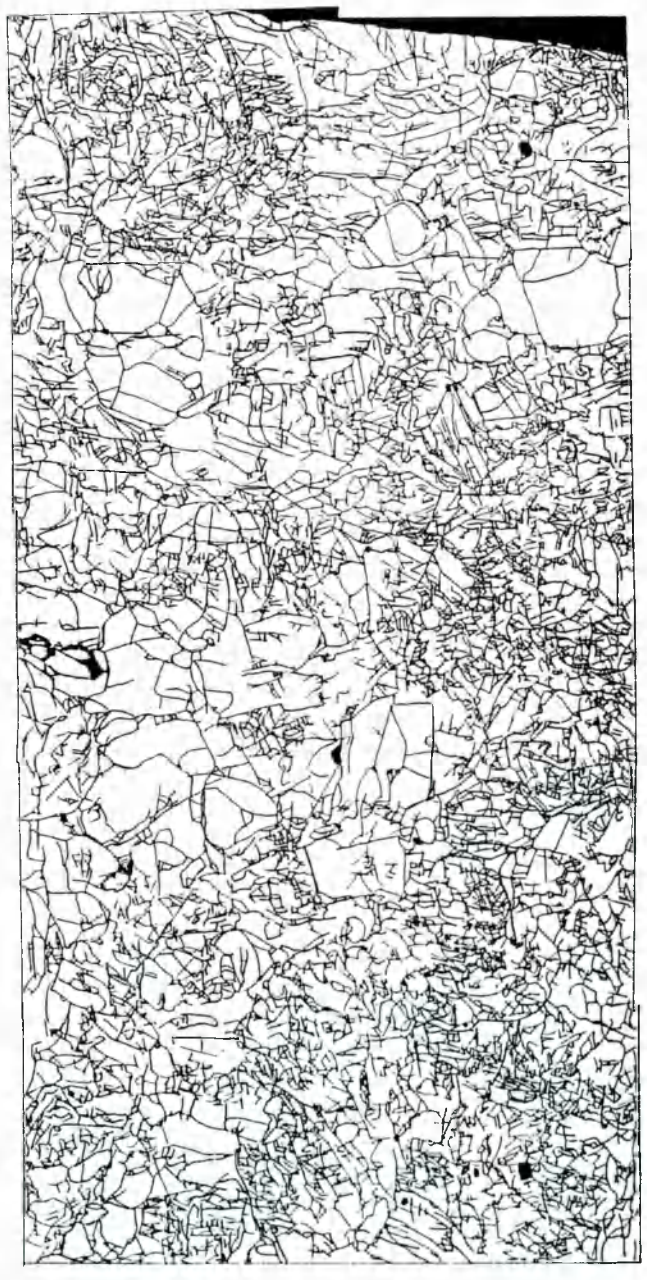

Cracks 1.0 mm

Appendix 5

Thermogravimetry

A5.1 Introduction

The water content of Westerly granite was determined using thermogravimetry by Cathy Davies at the Victoria University of Manchester. Tests were performed on a PL - STA 1500 H instrument built by PL - Sciences (Surrey, U.K.).

A5.2 Sample preparation

A block of Westerly granite was crushed using a jaw crusher and agate ball mill to achieve a grain size below 20 µm. The powder was thoroughly mixed in order to obtain a homogeneous sample. Approximately 20 mg were transferred into a rhodium-platinum crucible. Prior to insertion into the instrument the sample plus crucible was weighed.

A5.3 Apparatus setup

The thermogravimetry machine used measures weight loss and heat flow of the sample material over a given temperature interval. Weight is measured by comparing the weight of the sample with that of a reference dummy while the heat flow is measured by comparing the temperature of the furnace with that of the sample using a reference thermocouple and one attached to the sample. To prohibit volatile contamination and precipitation the sample assemblage is suspended in a continuously flowing stream of argon gas of high purity.

The machine is calibrated by analyzing blanks under the same conditions as the test run (**Figure A5.01, a**). The blanks and samples were heated in a continuous argon gas flow with 30 ml/min through-put to extract any volatiles produced by dehydration and melting reactions. The applied gas pressure raised the pressure inside the furnace only marginally above room pressure. Temperature was raised from 20 ° to 120 °C at a rate of 20.0 °C/min. The assemblage was allowed to equilibrate at 120 °C for 10 minutes. This was followed by a further temperature rise from 120 ° to 1100 °C at a rate of 20.0 °C/

min. Thermal equilibration of the assemblage was achieved by keeping the assemblage at 1100 °C for 40 minutes prior to cooling. Both weight and heat flow of the blanks were measured every 10.00 seconds and the data stored.

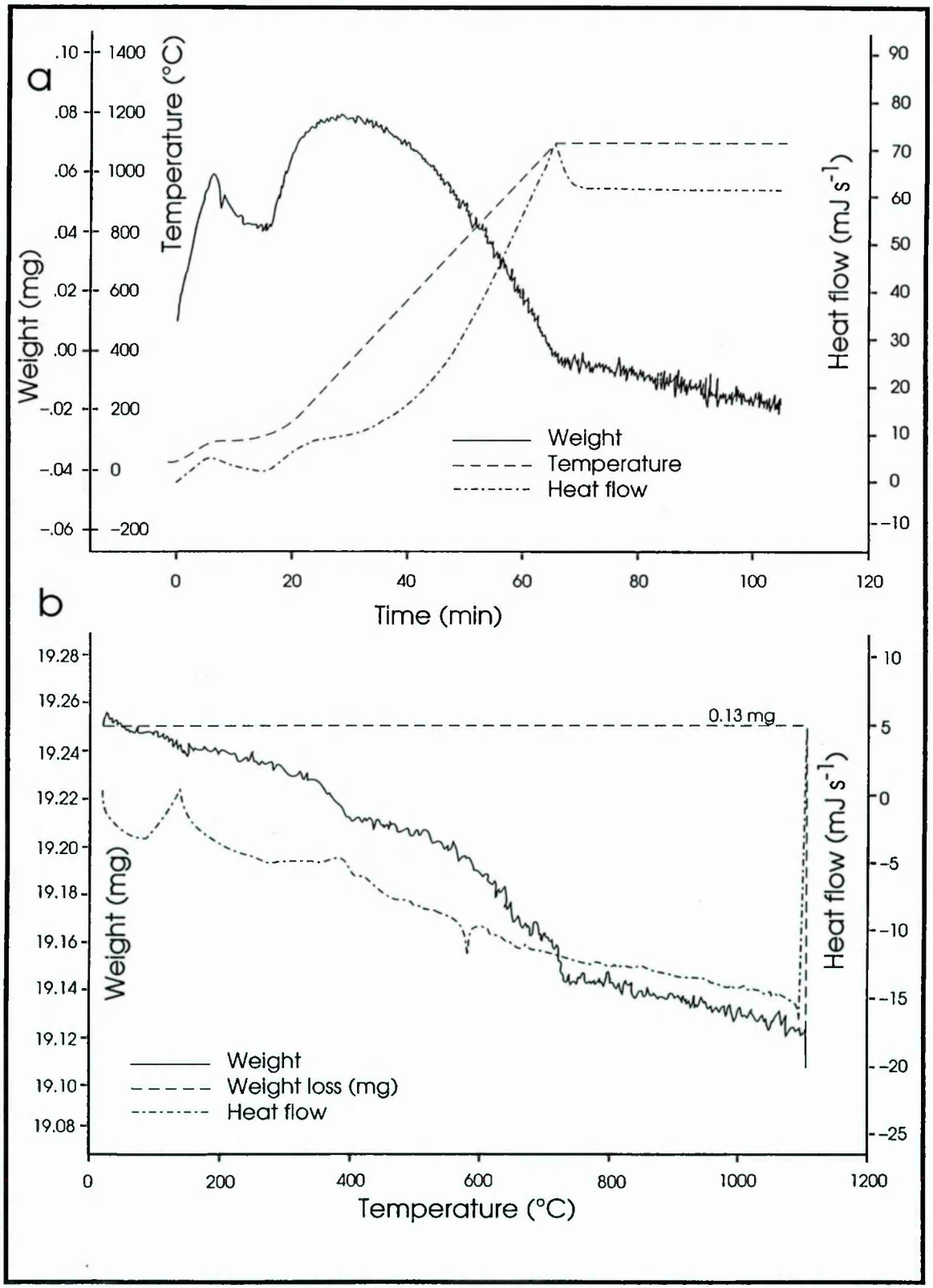

Figure A5.01: Thermogravimetric investigation of volatile content of Westerly granite. **a.)** Baseline measurements of heat flow and weight loss of blanks. **b.)** Heat flow and weight loss of Westerly granite that has been normalized to the base line above.

While thermal stability, weight measurements and heat flow had quite large error margins at temperatures below 150 °C, however error in temperature measurement improved significantly with temperature.

After running the test with blanks the exercise was repeated with crushed Westerly granite. The baseline results (Figure A5.01, a) were subtracted from the results obtained in the sample run to give true variations in heat flow and weight (Figure A5.01, b). The corrected weight loss of the Westerly granite sample was taken to equal the loss of volatiles. Heat flux was measured, as this gives a measurement of the accuracy of the temperature measurement, as a sharp decrease in flux is generally associated with polymorph phase transitions.

A5.4 Results

A total of four thermogravimetric runs were performed. The weight of the crushed Westerly granite and associated weight loss over the temperature range (21 to 1100 °C) are recorded in **Table A5.01** together with the calculated volatile content.

sample wt (mg)	wt loss over ΔT (mg)	calculated volatile content (%)
19.430	0.10	0.514
19.250	0.13	0.675
19.300	0.12	0.623
19.100	0.14	0.733

Table A5.01: Calculated volatile content of Westerly granite using thermogravimetry.

Averaging these results thermogravimetry suggests a volatile content of 0.636 %. This value reflect the weight loss of all volatiles, mostly H_2O and CO_2.

Appendix 6

Chemical analyses of minerals and melt

A6.1 Introduction

In this appendix chemical analysis of minerals and melt are listed. The first number in each analysis name is the analysis number, which is a combination of sample number (e.g. 2 for sample WG2) followed by a number that identifies the actual spot analysed, as marked on a series of SEM thermal printouts, of which three are displayed in **Figure 4.11**. Samples analyzed are listed in **Table 4.01**, which is repeated below:

Sample	T_{max}(°C)	P (MPa)	t (h) @ T	ϕ melt
WG2	800	250	2.4	0.053
WG8	800	250	96.0	0.035
WG3	900	250	2.5	0.073
WG11	1000	250	71.0	0.271
WG12	1050	250	4.0	0.335
WG13	1100	250	4.0	0.477

Table 4.01: Experimental test temperatures , confining pressures, duration of heating and melt fractions of samples used in chemical evaluation.

In the following sections analyses are ordered by mineral type plus melt with analyses relating to different samples ordered with increasing temperature.

However, analyses of the power sample WG1 is listed in a separate section, where analyses are listed chronologically.

Analyses showing totals of 100 ± 4 % were included in the tables, with the exception of analysis of hydrous minerals (i.e. biotite, chlorite and muscovite) and minerals forming very small volume fractions and small diameters that proved difficult to analyse (e.g. haematie, pyroxene, sphene, zircon, epidote), where totals inclused were lowered to between 80 and 100 %. However, even lower totals analyses were included for Amphibole (65%), as otherwise no amphibole would be recorded in the starting material (WG0). Also Calcite totals of 50 % were permitted, as the carbon coating on the sample prevented carbon oxide in this sample to be determined. Also, in WG3 apatite analysis failed to record phosphorus oxide, hence the low totals for this group. In sample WG1, due to samll number of total analyses, a cut-off of 93 % was applied generally. Fe^{+2} and Fe^{+3} reallocation was carried out after Droop (1987), as part of the MINTAB program, that also allocated feldspar, olivine and pyroxene data.

A6.2 Amphibole

	SiO_2	TiO_2	Al_2O_3	FeO	MnO	MgO	CaO	Na_2O	K_2O	Total
0.67	29.605	12.419	0	12.226	0	1.04	10.601	0	0	65.891
0.67	32.34	13.74	1.133	10.64	0	1.006	10.15	0	0.47	69.479
2.56.2	37.36	9.09	11.48	24.45	0.35	7.96	5.83	1.1	2.21	99.83
12.26	48.71	1.827	11.67	28.58	0.807	7.036	1.367	2.318	2.505	104.8
12.27	47.245	1.311	12.77	28.573	0.674	4.763	1.748	3.606	3.146	103.84
12.12	45.642	4.533	7.669	24.21	0.341	8.96	2.18	3.156	2.173	98.864
12.141	55.065	1.341	10.598	11.816	0.443	2.879	13.53	3.182	2.142	101

A6.3 Apatite

	SiO_2	TiO_2	Al_2O_3	FeO	MnO	MgO	CaO	Na_2O	K_2O	P_2O_5	Total
0.12	0.296	0	0	0.634	0	0	54.467	0.324	0	41.405	97.126
0.15	0	0	0	0	0	0	55.333	0	0	42.714	98.047
0.16	0	0	0	0.566	0	0	54.974	0.183	0	41.625	97.348
0.18	0	0	0	0.6	0	0	54.503	0.158	0	41.127	96.388
0.38	0.336	0	0.228	0.686	0	0	55.164	0.267	0.41	42.958	100.049
0.66	0	0	0	0.517	0	0	54.443	0	0	41.285	96.245
0.72	0	0	0	0	0	0	55.537	0	0	42.801	98.338
0.76	0	0	0	0.7	0	0	56.546	0	0	43.628	100.874
0.78	0.463	0	0.196	0	0	0	55.735	0	0	42.603	98.997
0.84	0.802	0	0.24	0	0	0.217	54.848	0	0.339	42.031	98.477
0.89	0	0	0	0	0	0	55.062	0	0	41.992	97.054
8.13	0	0	0	0	0	0	54.77	0	0	43.74	98.51
8.82	0.47	0.28	0	0.65	0	0	55.13	0	0	42.67	99.2
8.96	0	0	0	0	0	0	55.73	0	0	43.63	99.36
3.27.1	0.23	0.28	0.21	0	0	0	55.03	0.34	0		56.09
3.28	0.37	0	0.31	0.9	0	0	53.89	0	0.32		55.79
11.2	43.55	0	35.54	0.58	0	0	19.36	0	0.21	0	99.24
11.84	0.26	0	0	0.81	0	0	55.35	0	0.2	42.24	98.86
11.114	0.72	0	0	0.39	0	0	54.44	0	0.21	42.09	97.85
11.138	0	0	0	0	0	0	54.88	0	0	42.76	97.64

A6.4 Biotite

	SiO_2	TiO_2	Al_2O_3	FeO	MnO	MgO	CaO	Na_2O	K_2O	Total
0.25	38.39	2.33	15.13	20.1	0	11.1	0	0.39	9.57	97.01
0.26	37.17	2.49	14.76	20.7	0	10.1	0	0	9.78	95
0.4	37.95	2.68	14.57	20.3	0.33	10.1	0.19	0.42	9.71	96.26
0.41	37.24	2.83	14.51	20.7	0.36	10.3	0	0.51	9.84	96.28
0.45	37.24	2.98	14.91	20.1	0.3	10	0	0.38	9.67	95.58
0.46	37.04	2.94	14.41	20.9	0.23	9.89	0	0.7	9.82	95.92
0.5	37.78	3.2	15.24	19.6	0	10.3	0.13	0.39	9.48	96.13
0.72	37.31	2.27	14.65	20.4	0.33	10.2	0	0	9.86	95.03
2.1	35.97	2.78	14.41	20.77	0	9.51	0	0.35	9.66	93.45
2.7	38.23	2.52	15.56	20.8	0.36	10.3	0.18	0.32	9.6	97.88
2.29.5	36.92	0.41	19.99	27.36	0	1.63	0.69	1.96	5.99	94.94
2.31.4	36.33	2.96	14.83	19.84	0.3	10.08	0.25	0.59	9.27	94.44
2.33.2	45.55	1.74	28.29	5.59	0	2.32	0.46	0.47	9.94	94.36
2.33.5	36.74	2.96	15.16	19.07	0.34	11.14	0.33	0.74	9.35	95.83
2.33.6	47.43	2.94	20.84	9.63	0	4.75	1.99	2.34	5.99	95.92
2.33.8	44.06	7.31	15.08	11.44	0	8.04	0.79	1.71	6.08	94.51
2.34.2	36.47	3.12	15.72	19.97	0.33	10.98	0.26	0.66	9.13	96.65
2.35.1	37.01	3.31	15.09	20.24	0.35	10.17	0.23	0.58	9.53	96.53
2.36.1	36.89	2.61	14.79	18.95	0.52	10.7	0.22	0.63	9.62	94.93

2.37.1	38.19	2.98	15.74	19.91	0.3	10.94	0.25	0.71	9.62	98.64
2.37.2	35.83	3.02	15.19	19.54	0.26	10.34	0.16	0.63	9.16	94.12
2.37.5	36.12	2.23	15.31	19.13	0.27	11.09	0.25	0.52	9.22	94.14
2.39	37.35	2.65	15.33	19.68	0.34	10.75	0.26	0.95	9.24	96.56
2.40.1	36.45	2.71	15.11	20.49	0.28	10.73	0.25	0.7	9	95.72
2.41.1	36.2	2.65	14.9	20.65	0	9.59	0.23	0.94	8.86	94.03
2.41.3	38.8	3.09	15.61	20.17	0	9.44	0.28	1	8.65	97.02
2.41.4	34.7	1.82	17.14	24.22	0.29	10.52	0.37	0.72	7.05	96.81
2.44	36.95	3.22	14.77	19.98	0.41	10.23	0.25	1.12	8.39	95.32
2.45	37.08	2.71	14.72	21.05	0.39	10.47	0	0.68	9.35	96.47
2.36	37.82	3.08	15.69	19.01	0.37	9.63	0.3	0.93	8.82	95.64
2.47	36.93	2.43	14.97	19.71	0.28	10.07	0.33	0.62	9.32	94.64
2.55.1	36.9	2.64	15.29	19.91	0.31	10.48	0.31	0.71	9.42	95.97
2.54	36.78	2.6	15.44	19.61	0.22	9.87	0.19	0.63	9.37	94.73
2.53.1	36.97	2.23	15.63	19.38	0.24	10.58	0.32	0.6	9.3	95.25
2.52	36.75	2.99	15.16	20.07	0.44	10.1	0.29	0.29	9.1	95.19
2.5	37.32	2.72	15.38	20.51	0.4	10.56	0.28	0.95	9.54	97.66
2.51	36.83	2.52	14.87	20.68	0	10.45	0.26	0.67	9.45	95.73
8.14	38.98	2.8	15.48	20	0	11.65	0	0.89	9.27	99.07
8.34	37.53	3.11	15.3	21.7	0.39	9.42	0	0.55	9.81	97.81
8.41	38.23	2.22	15.64	20.42	0.31	11.06	0	0.63	9.73	98.24
8.46	37.01	2.6	14.66	20.07	0.34	10.48	0	0	9.53	94.69
8.56	35.74	0.91	26.2	17.61	0.28	7.41	0.18	0.78	9.63	98.74
8.72	42.52	4.47	18.99	19.21	0	6.44	1.36	2.23	7.14	102.4
8.81	38.14	3.29	15.35	20.34	0	10.66	0	0	9.68	97.46
8.91	36.92	3.04	15.53	20.73	0.37	10.42	0	0.48	9.13	96.62
8.97	38	2.92	14.79	21.04	0.32	10.69	0.2	0.58	9.47	98.01
8.99	38.42	2.64	15.6	20.08	0	11.41	0	0.47	9.65	98.27
8.101	37.3	3.19	14.44	19.63	0	11.56	0	0	9.85	95.97
3.2.1	36.56	3.09	14.68	21.38	0	10.01	0	0.42	9.2	95.34
3.2.6	34.27	1.34	23.18	14.52	0	11.52	0	1.4	8.83	95.06
3.2.11	37.66	2.38	15.67	21.13	0.33	11.06	0	0.64	9.19	98.06
3.14	36.97	2.31	15.09	20.37	0	11.44	0.18	0.81	9.43	96.59
3.2	36.85	3.03	14.55	21.1	0	10.18	0	0.52	9.51	95.73
3.19.9	37.65	2.37	15.41	20.68	0.36	10.79	0	0.52	9.3	97.08
3.25.3	36.65	1	16.82	15.33	0	15.64	0	1.41	8.09	94.95
3.25.6	37.36	2.7	15.44	20.77	0	10.49	0.18	0.77	9.49	97.2
3.34	37.19	3.29	15.04	20.58	0.33	8.97	0.18	1.12	8.88	95.57
11.21	38.72	2.43	15.78	19.49	0	11.47	0	0.82	8.93	97.64
11.83	37.85	3.51	15.42	21.88	0.32	10.3	0	0	9.68	98.96
11.12	37.01	5.72	13.02	13.8	0	14.26	0	1.08	8.69	93.58
11.14	36.43	2.63	14.46	20.19	0.34	10.96	0.18	0.52	9.51	95.22
12.17	46.1	0	16.02	19.93	0	3.27	0.85	4.26	5.35	95.78
12.28	56.89	0.8	19.65	8.73	0	1.66	1.69	4.86	6.08	100.4
12.34	44.31	0.3	13.85	19.83	0	7.74	0.49	2.35	6.9	95.77
12.47	52.62	1.14	15.31	14.23	0.29	3.32	0.41	3.39	6.51	97.22
12.83	36.59	3.19	14.81	19.98	0	10.51	0	0.71	9.44	95.23
12.12	36.67	3.38	14.99	20.82	0.35	10.73	0	0.49	9.4	96.83

A6.5 Calcite

	SiO_2	Al_2O_3	TiO_2	FeO	MnO	MgO	CaO	K_2O	Na_2O	SO_4	P_2O_5	Cl	Total
0.13	0.564	0.277	0	0.919	0	0	73.55	0.454	0	0	0	0	75.764
0.65	0.27	0	0	0.34	0	0	76.91	0	0.347	0	0	0	77.867
0.92	0	0.243	0	0	0	0.243	52.73	0	0	0	0	0	53.216
0.93	0.342	0.22	0	0.475	0.555	0	52.128		0	0	0	0	0 53.72

A6.6 Chlorite

	SiO_2	Al_2O_3	TiO_2	FeO	MnO	MgO	CaO	K_2O	Na_2O	Total
0.44	26.04	18.33	0	27.62	0.526	14.25	0	0	0.678	87.44
0.45	25.44	18.66	0	27.32	0.494	13.45	0	0	0	85.35
0.5	23.79	17.71	0	26.78	0.467	12.38	0	0	0	81.12
0.51	25.73	18.41	0	27.84	0.386	13.39	0	0	0	85.75
0.52	25.46	16.9	0	26.62	0.505	12.93	0	0	0	82.42
0.57	25.86	17.63	0	25.74	0.373	13.19	0	0.32	0.398	83.51
0.58	24.84	17.94	0.312	26.27	0.581	13.07	0	0.328	0	83.34
0.62	34.74	13.8	2.186	18.86	0	9.715	0	9.134	0.373	88.8
0.63	35.86	14.4	2.642	19.92	0.263	10.03	0	9.568	0.391	93.24

A6.7 Epidote

	SiO_2	Al_2O_3	TiO_2	FeO	MnO	MgO	CaO	K_2O	Na_2O	P_2O_5	SO_4	Total
0.79	57.02	18.57	3.391	0	0.257	0	0.215	12.498	0.633	0	0	92.58
0.82	45.43	34.89	0	0.468	0	0	0.173	11.194	0	0	0	92.15
0.83	58.16	18.55	3.35	0	0	0	0	14.014	0.339	0	0	94.413

A6.8 Feldspars

	SiO_2	TiO_2	Al_2O_3	FeO	MnO	MgO	CaO	Na_2O	K_2O	Total	Albite	Anorth.	Orth
0.1	61.38	0.35	17.36	0	0	0	0	0.59	15.11	94.8	5.618	0	94.382
0.2	62.34	0.37	17.68	0	0	0	0	0.98	14.53	95.9	9.26	0	90.74
0.7	61.21	0	21.27	0	0	0	3.1	9.26	0.16	95	83.567	15.465	0.968
0.11	62.68	0	19.78	0	0	0	1.71	9.85	0.15	94.17	90.4	8.676	0.924
0.13	64.94	0	18.92	0	0	0	0.35	10.53	0.11	94.85	97.527	1.791	0.682
0.16	61.74	0	21.74	0	0	0	3.68	8.75	0.12	96.03	80.536	18.719	0.745
0.17	62.59	0	22.26	0	0	0	3.56	8.87	0.2	97.48	80.837	17.939	1.224
0.2	61.21	0	21.59	0	0	0	3.69	8.65	0.17	95.31	80.091	18.885	1.024
0.21	65.09	0	21.4	0	0	0	2.86	9.56	0.18	99.09	84.936	14.036	1.028
0.22	60.41	1.63	18.39	0	0	0	0	0.75	14.13	95.31	7.472	0	92.528
0.29	64.91	0.26	18.57	0.45	0	0	0	0.87	15.45	100.51	7.858	0	92.142
0.32	64.3	0.32	18.41	0	0	0	0	0.65	15.47	99.15	6.022	0	93.978
0.33	66.16	0	21.72	0	0	0	2.48	10.14	0	100.5	88.092	11.908	0
0.34	67.05	0	21.14	0.22	0	0	1.82	10.38	0.14	100.74	90.452	8.762	0.785
0.35	64.32	0	18.19	0	0	0	0	1.04	15.28	98.83	9.407	0	90.593
0.36	66.76	0	21.01	0	0	0	0.2	11.18	0	99.14	99.021	0.979	0
0.37	65.89	0	21.07	0	0	0	2.18	10.23	0.11	99.48	88.92	10.468	0.612
0.38	64.45	0	22.22	0.32	0	0	3.24	9.48	0.22	99.94	83.04	15.675	1.285
0.39	63.67	0.28	18.24	0	0	0	0.15	0.78	15.33	98.45	7.124	0.757	92.119
0.47	64.12	0.3	18.23	0.26	0	0	0	0.69	15.19	98.79	6.476	0	93.524
0.48	65.85	0.31	18.92	0	0	0	0	1.18	15.38	101.63	10.421	0	89.579
0.51	64.06	0	21.4	0.44	0	0	2.83	9.33	0	98.06	85.644	14.356	0
0.52	64.76	0.25	18.81	0	0	0	0	0.97	15.45	100.24	8.729	0	91.271
0.53	67.44	0	20.46	0	0	0	1.15	10.83	0.13	100.01	93.78	5.502	0.718
0.54	64.28	0	21.15	0	0	0	3.18	9.35	0.09	98.05	83.736	15.739	0.525
0.55	63	0	22.54	0.3	0	0	4.09	8.81	0.25	98.99	78.393	20.114	1.493
0.56	68.89	0	19.61	0	0	0	0.42	11.41	0.16	100.5	97.107	1.975	0.918
0.57	64.09	0.29	18.27	0	0	0	0	0.46	15.82	98.93	4.233	0	95.767
0.59	65.18	0	21.48	0	0	0	2.69	9.51	0.13	98.99	85.794	13.41	0.795
0.61	57.99	2.82	19.02	0	0	0	0.16	0.86	13.35	94.19	8.789	0.909	90.302
0.62	64.17	0.19	18.19	0	0	0	0	0.68	15.8	99.03	6.132	0	93.868
0.63	65.15	0.3	18.52	0	0	0	0	1	15.46	100.43	8.966	0	91.034

0.65	69.19	0	20.74	0	0	0	0.7	11.37	0.14	102.14	95.969	3.264	0.766
0.66	64.37	0	17.99	0	0	0	0	0.98	15.24	98.58	8.887	0	91.113
0.67	63.35	0.5	18.48	0	0	0	0	0.97	14.98	98.27	8.926	0	91.074
0.68	65.59	0	22.07	0	0	0	3.06	9.74	0.14	100.61	84.522	14.678	0.8
0.69	59.7	0	27.8	0	0	0	3.64	8.77	0.19	100.1	80.407	18.453	1.141
0.71	65.2	0.17	18.54	0	0	0	0	0.35	16.23	100.49	3.138	0	96.862
2.2	65.48	0.25	18.91	0	0	0	0	0.88	15.57	101.1	7.925	0	92.075
2.3	65.46	0	23.23	0	0	0	3.95	8.75	0.23	101.62	78.94	19.683	1.377
2.3	66.48	0	22.55	0	0	0	2.69	10.13	0.31	102.16	85.697	12.571	1.732
2.5	65.59	0.21	19.07	0	0	0	0.14	1.41	15.02	101.44	12.396	0.676	86.928
2.6	64.07	0	22.73	0	0	0	3.98	9.48	0.23	100.5	80.112	18.582	1.306
2.9	64.99	0.4	19.25	0	0	0	0	0.87	15.65	101.15	7.759	0	92.241
2.10	64.48	0	22.81	0	0	0	3.85	9.44	0.17	100.75	80.85	18.214	0.936
2.11	65.22	0.3	18.75	0	0	0	0	0.61	15.71	100.59	5.608	0	94.392
2.15	65.98	0	20.5	0	0	0	1.33	9.09	1.81	98.71	82.501	6.673	10.826
2.16	66.06	0.36	19.08	0	0	0	0	0.98	15.63	102.1	8.658	0	91.342
2.17	69.07	0	20.17	0	0	0	0.33	11.67	0.2	101.44	97.395	1.512	1.093
2.18	67.61	0	21.91	0	0	0	2.07	11.07	0.12	102.79	90.05	9.297	0.653
2.22	64.38	0.42	19.32	0	0	0.32	0.34	1.02	14.93	100.73	9.253	1.723	89.025
2.24	63.56	0	22.8	0	0	0	3.52	9.39	0.24	99.5	81.718	16.92	1.363
2.26	64.67	0.33	19.15	0	0	0.34	0.43	0.91	15.16	100.98	8.167	2.112	89.721
2.27	64.85	0	22.49	0	0	0	3.02	10.13	0	100.5	85.853	14.147	0
2.34.3	65.89	0.43	18.4	0.36	0	0.28	0.32	1.28	13.58	100.55	12.296	1.723	85.982
2.43.3	64.33	0	21.8	0.21	0	0	2.37	9.36	0.23	98.31	86.473	12.117	1.41
2.49	64.16	0.48	19.01	0	0	0.27	0.4	1.76	13.1	99.17	16.611	2.06	81.329
8.3	66.09	0	22.02	0	0	0	2.95	10.13	0.15	101.34	85.414	13.749	0.838
8.2	66.56	0.42	19.03	0	0	0	0	2.71	12.67	101.38	24.533	0	75.467
8.4	68.18	0	19.86	0	0	0	0.39	11.22	0	99.64	98.134	1.866	0
8.5	66.02	0	19.47	0	0	0	0.55	3.84	10.28	100.16	35.209	2.806	61.985
8.7	63.93	0	18.73	0	0	0	0.92	5.04	8.18	96.8	46.118	4.65	49.231
8.9	64.05	0.29	18.04	0	0	0	0	0.56	15.54	98.49	5.201	0	94.799
8.11	68.38	0	19.51	0	0	0	0.27	11.18	0.38	99.71	96.562	1.284	2.154
8.20.	67.01	0	20.87	0	0	0	1.53	10.73	0	100.15	92.703	7.297	0
8.21	64.17	0.48	17.65	0	0	0	0.51	3.2	10.7	96.7	30.434	2.659	66.907
8.22	66.32	0.29	19.14	0	0	0	0	2.53	13.54	101.82	22.09	0	77.91
8.23	67.67	0	21.48	0	0	0	1.69	10.51	0	101.35	91.863	8.137	0
8.24.5	63.31	0	21.05	0.32	0	0	0.46	4.28	10.33	99.73	37.746	2.23	60.025
8.24.8	64.72	0.43	20.03	0	0	0	0.73	5.18	8.85	99.94	45.384	3.552	51.064
8.24.9	67.2	0	21.47	0	0	0	2.05	9.75	1.54	102.01	81.952	9.541	8.507
8.26	64.33	0.43	18.51	0	0	0	0	1.02	15.52	99.81	9.051	0	90.949
8.27	64.33	0.4	18.07	0.4	0	0	0	1.2	14.78	99.18	10.962	0	89.038
8.29	66.82	0	22.77	0	0	0	3.02	9.83	0.39	102.83	83.609	14.192	2.199
8.38.6	64.57	0.49	18.84	0.41	0	0	0	1.61	13.92	99.85	14.983	0	85.017
8.39	65.28	0.32	19.08	0	0	0	0	1.94	13.54	100.17	17.908	0	82.092
8.47	64.96	0	18.04	0	0	0	0	0.9	15.56	99.46	8.098	0	91.902
8.49	65.56	0	18.66	0.4	0	0	0	2.18	13.72	100.52	19.462	0	80.538
8.5	65.52	0.33	19.19	0	0	0	0	1.77	14.52	101.33	15.633	0	84.367
8.54	65.77	0.32	18.71	0	0	0	0	1.46	14.9	101.15	12.942	0	87.058
8.58	65.2	0	18.94	0	0	0	0	1.62	14.85	100.61	14.189	0	85.811
8.59	69.16	0	21.11	0	0	0	1.23	10.1	1.3	102.9	86.799	5.863	7.338
8.60.	67.2	0	20.63	0	0	0	1.63	5.81	6.98	102.25	51.421	7.971	40.608
8.61	65.39	0	18.85	0	0	0	0.22	0.56	15.86	100.89	5.072	1.108	93.82
8.62	65.39	0.25	18.7	0.76	0	0	0.2	2.54	13.28	101.13	22.293	0.975	76.732
8.63	64.92	0	23.17	0.36	0	0	3.83	9.2	0.32	101.8	79.821	18.336	1.843
8.64	64.1	0	22.87	0	0	0	4.19	8.41	0.63	100.19	75.474	20.774	3.751
8.80.	64.81	0.26	18.58	0	0	0	0	0.64	15.58	99.87	5.91	0	94.09
8.88	66.36	0.39	19.35	0	0	0	0	0.94	16.09	103.13	8.177	0	91.823
8.92	63.69	0	22.34	0.44	0	0	3.71	8.95	0.24	99.35	80.231	18.365	1.404
8.93	65.34	0	23.44	0	0	0	3.71	9.36	0.3	102.15	80.619	17.68	1.701
8.94	63.75	0	22.87	0.61	0	0	5.24	7.3	1.47	101.23	65.385	25.969	8.646
8.95	64.64	0.54	18.46	0	0	0	0	0.86	15.44	99.94	7.764	0	92.236
8.103	64.55	0	17.87	0	0	0	0.21	2.19	13.29	98.11	19.857	1.03	79.113
8.104	65.16	0	22.11	0	0	0	2.94	9.57	0.27	100.06	84.137	14.306	1.556
8.105	64.79	0	18.07	0	0	0	0	1.01	15.03	98.91	9.258	0	90.742
3.1	67.05	0	20.66	0	0	0	0.81	9.45	2.85	100.82	80.249	3.821	15.93
3.2.7	62.47	0	23.16	0	0	0	3.69	7.18	3.4	99.9	62.666	17.8	19.534
3.3.1	63.69	0.41	18.7	0	0	0	0.2	0.75	15.15	98.89	6.927	1.016	92.057
3.3.2	64.59	0	21.49	0	0	0	3	8.99	0.64	98.71	81.219	14.957	3.824
3.5.1	63.56	0	22.61	0	0	0	4.02	9.08	0.16	99.44	79.567	19.482	0.951
3.5.3	55.76	0.35	25.51	0	0	0	0.43	3.59	8.59	94.22	37.879	2.479	59.642
3.5.4	63.8	0.37	18.1	0	0	0	0	1.45	14.78	98.51	12.987	0	87.013
3.5.5	64.25	0	22.24	0	0	0	3.02	8.46	1.86	99.83	74.513	14.713	10.774
3.39	63.6	0	23.45	0	0	0	3.85	9.25	0.23	100.39	80.216	18.455	1.33
3.38.3	63.25	0.42	18.22	0	0	0	0	0.97	15.09	97.95	8.876	0	91.124
3.38.4	65.31	0.32	18.98	0	0	0	0	1.12	15.41	101.14	9.964	0	90.036
3.38.5	62.48	0	23.5	0	0	0	3.95	6.98	3.35	100.27	61.393	19.207	19.4

3.6	64.36	0	18.59	0.31	0	0	0	0.75	15.52	99.52	6.809	0	93.191
3.7.1	64.8	0	21.75	0	0	0	2.3	9.44	0.77	99.05	84.185	11.315	4.501
3.7.4	60.89	0	23.62	0	0	0	3.93	7.6	2.29	98.34	67.375	19.253	13.372
3.7.6	62.03	0	21.33	0	0	0	2.04	7.9	3.17	96.48	71.07	10.163	18.767
3.10.	62.9	0.27	17.85	0	0	0	0.2	0.48	15.49	97.19	4.458	1.05	94.491
3.10.2	64.45	0.33	18.54	0	0	0	0	1.44	14.4	99.16	13.2	0	86.8
3.16.4	66.69	0	20.58	0	0	0	1.16	10.13	0.51	99.06	91.19	5.758	3.052
3.15	61.44	0.37	18.95	0	0	0	0	0.53	14.85	96.14	5.108	0	94.892
3.13.1	63.05	0.34	18.78	0	0	0	0	1.26	15.19	98.61	11.226	0	88.774
3.13.2		59.5	1.76	18.31	0	0	0	0	1.27	13.32	94.17	12.69	0 87.31
3.13.3	62.38	0	23.38	0	0	0	4.32	8.99	0	99.07	79.01	20.99	0
3.11	63.9	0.55	18.01	0	0	0	0	1.1	15.05	98.61	10.006	0	89.994
3.19.7	62.92	0	22.96	0	0	0	4.02	9.08	0.18	99.16	79.5	19.463	1.037
3.19.8	64.46	0	23.28	0	0	0	3.78	9.72	0.23	101.48	81.247	17.466	1.287
3.23	63.24	0.7	18.55	0	0	0	0	0.87	14.69	98.04	8.232	0	91.768
3.46	63.85	0.39	18.46	0	0	0	0	1.01	15.24	98.94	9.127	0	90.873
3.24	62.8	0	22.17	0	0	0	3.76	8.93	0.21	97.88	80.118	18.655	1.227
3.24	63.54	0	23.06	0	0	0	4.03	9.37	0.2	100.21	79.899	18.99	1.111
3.41	61.56	0	23.05	0.88	0	0	5.14	5.98	2.14	98.76	58.472	27.758	13.77
3.23.2	62.79	0.29	17.69	0	0	0	0	1.11	14.88	96.76	10.185	0	89.815
3.49.1	64.03	0	18.28	0	0	0	0	0.6	15.44	98.36	5.61	0	94.39
3.49.2	64.89	0.29	17.72	0	0	0	0.22	3.84	10.54	97.5	35.235	1.101	63.664
3.49.3	67.06	0.25	18.49	0.39	0	0	0	3.31	11.65	101.16	30.125	0	69.875
3.49.5	73.66	0.27	13.42	2.18	0	0.36	0.86	2.69	4.64	98.08	43.237	7.65	49.112
3.49.6	50.84	0	8.53	2.22	0	0	4.75	1.61	2.86	70.81	26.282	42.92	30.798
3.37.4	65.1	0.44	18.64	0	0	0	0	2.57	13.05	99.81	23.056	0	76.944
3.35.1	63.53	0.24	18.41	0.32	0	0	0	1.16	14.63	98.3	10.79	0	89.21
3.35.8	63.84	0.25	17.95	0	0	0	0	0.81	15.26	98.12	7.507	0	92.493
11.1	62.86	0.52	17.95	0	0	0	0.24	0.95	14.48	96.99	8.972	1.24	89.788
11.21	66.22	0	21.84	0	0	0	3.09	9.8	0.26	101.21	83.891	14.644	1.465
11.63	66.44	0.49	20.05	0	0	0	0.19	2.17	14.51	103.85	18.379	0.897	80.723
11.64	64.99	0.7	19.67	0	0	0	0.9	3.9	9.4	99.56	36.834	4.694	58.471
11.67	67.51	0	19.28	0	0	0	0.26	4.24	10.99	102.28	36.516	1.236	62.248
11.67	66.57	0.36	19.2	0	0	0	0	3.08	11.96	101.18	28.149	0	71.851
11.77	67.05	0	23.75	0	0	0	3.93	9.43	0.48	104.64	79.098	18.24	2.662
11.78	66.59	0	23.06	0	0	0	3.59	9.5	0.54	103.27	80.261	16.753	2.986
11.80.	63.96	0	22.6	0	0	0	3.91	7.49	2.05	100.01	68.095	19.641	12.264
11.82	66.94	0	18.92	0	0	0	0	3.01	12.35	101.22	27.028	0	72.972
11.87	66.12	0	23.42	0.29	0	0	4.01	9.26	0.22	103.33	79.709	19.073	1.217
11.1	65.2	0.34	18.49	0	0	0	0	2.58	12.55	99.16	23.8	0	76.2
11.11	65.35	0.42	18.92	0	0	0	0	1.26	15.12	101.07	11.231	0	88.769
11.110	64.38	0.55	18.86	0	0	0	0	1.08	14.45	99.32	10.185	0	89.815
11.120	65.32	0	18.64	0	0	0	0.19	3.57	11.2	98.92	32.348	0.926	66.726
11.13	66.05	0.28	19.16	0	0	0	0.27	3.45	11.58	100.79	30.753	1.32	67.926
11.13	65.95	0.42	18.85	0	0	0	0	2.69	12.59	100.5	24.514	0	75.486
11.13	65.81	0	18.92	0	0	0	0.43	4.51	9.79	99.46	40.315	2.099	57.587
11.13	63.84	0.44	18.19	0	0	0	0	1.7	13.86	98.03	15.675	0	84.325
11.14	65.8	0.29	18.93	0	0	0	0	3.37	11.79	100.18	30.286	0	69.714
11.14	67.73	0	19.2	0	0	0	0	3.12	12.35	102.41	27.74	0	72.26
12.1	65.65	0.41	19.25	0	0	0	0.42	5.19	9.04	99.97	45.655	2.055	52.29
12.2	65.02	0.31	18.71	0	0	0	0	1.7	14.15	99.88	15.407	0	84.593
12.3	62.85	0	23.69	0	0	0	4.58	9.31	0.15	100.59	77.986	21.21	0.804
12.6	64.44	0	22.41	0	0	0	3.73	9.36	0.37	100.31	80.255	17.674	2.07
12.8	65.84	0	21.63	0	0	0	2.34	10.34	0.25	100.4	87.622	10.961	1.417
12.10.	62.26	0	22.9	0	0	0	4.59	8.86	0.17	98.78	76.984	22.027	0.989
12.11	65.18	0.51	18.63	0	0	0	0.32	4.7	9.35	98.68	42.66	1.583	55.757
12.13	65.63	0.39	19.06	0	0	0	0.28	4.75	9.56	99.67	42.44	1.358	56.202
12.14	63.1	0	23.07	0	0	0	4.57	8.98	0.22	99.93	77.073	21.684	1.243
12.19	62.83	0	23.75	0	0	0	4.97	8.96	0.26	100.77	75.412	23.12	1.468
12.20.	48.48	0	32.31	0	0	0	15.38	1.96	1.2	99.34	17.448	75.525	7.026
12.21	46.68	0	34.58	0	0	0	17.21	1.5	0.72	100.69	13.021	82.824	4.155
12.22	64.1	0	22.82	0	0	0	3.86	9.23	0.19	100.21	80.314	18.576	1.11
12.23	62.4	0.39	20.03	0.4	0	0	2.02	5.17	6.99	97.4	47.528	10.246	42.227
12.32	65.21	0	22.83	0	0	0	4.02	8.71	0.78	101.55	76.095	19.419	4.485
12.38	65.69	0	23.48	0	0	0	3.79	9.95	0.26	103.16	81.461	17.143	1.396
12.55	67.28	0.32	19.61	0	0	0	0	2.88	12.79	102.89	25.495	0	74.505
12.57	64.46	0	22.63	0	0	0	3.79	9.4	0.31	100.58	80.373	17.906	1.721
12.66	65.04	0.41	18.66	0	0	0	0	3.04	12.45	99.6	27.082	0	72.918
12.67	65.59	0	18.71	0	0	0	0	2.59	13.13	100.02	23.085	0	76.915
12.69	64.83	0.58	19.13	0	0	0	0	1.3	14.97	100.82	11.668	0	88.332
12.70.	63.94	0.43	18.33	0	0	0	0.29	4.09	10.27	97.35	37.152	1.461	61.386
12.72	63.31	0	22.9	0	0	0	4.15	9.01	0.14	99.53	79.044	20.12	0.837
12.73	66.6	0.48	19.58	0	0	0	0	2.43	13.4	102.49	21.568	0	78.432
12.75	64.27	0	22.94	0	0	0	3.71	9.22	0.24	100.37	80.702	17.927	1.371
12.78	64.85	0	23.27	0	0	0	3.84	9.52	0.19	101.67	80.942	18.017	1.04
12.80.	61.71	0	23.82	0	0	0	5.6	8.31	0.31	99.74	71.591	26.651	1.758
12.99	63.37	0	22.21	0.36	0	0	3.68	9.13	0.15	98.9	81.082	18.054	0.865

12.100	61.73	0	23.51	0	0	0	4.92	8.28	0.17	98.61	74.529	24.482	0.989
12.1	64.31	0	22.22	0	0	0	3.77	9.13	0.19	99.62	80.493	18.393	1.114
12.11	56.31	0	27.62	0.64	0	0	9.8	5.67	0.6	100.64	49.384	47.161	3.455
12.11	60.8	0	23.51	0	0	0	5.93	7.33	0.63	98.2	66.504	29.746	3.749
12.13	62.45	0	21.44	0	0	0	3.62	8.85	0.33	96.69	79.978	18.084	1.938
12.13	65.41	0.29	18.89	0	0	0	0	2.52	12.82	99.93	23.002	0	76.998
12.13	65.28	0.25	18.71	0	0	0	0	1.17	15.23	100.65	10.479	0	89.521
12.13	59.86	0.8	19.71	4.83	0	1.1	2.33	4.08	5.52	98.25	45.351	14.314	40.335
12.13	64.51	0	23.04	0	0	0	4.02	9.44	0.28	101.28	79.712	18.738	1.55
12.14	64.89	0.34	18.53	0	0	0	0	1.51	14.81	100.08	13.426	0	86.574
12.140	65.88	0	23.88	0	0	0	4.07	9.69	0.14	103.67	80.536	18.682	0.782
13.1	65.42	0	23.44	0	0	0	3.83	9.38	0.15	102.22	80.887	18.24	0.874
13.2.8	61.64	0	22.99	0	0	0	5.15	7.33	1	98.12	67.655	26.249	6.097
13.4.10.	63.07	0	22.52	0	0	0	3.86	8.46	0.7	98.61	76.528	19.288	4.185
13.6.2	64.77	0	22.74	0.33	0	0	4.08	7.82	2.54	102.28	66.582	19.199	14.219
13.6.3	64.45	0	22.55	0	0	0	3.71	9.73	0.2	100.64	81.68	17.199	1.121
13.6.4	61.6	0	22.7	0	0	0	4.97	7.4	1.48	98.15	66.54	24.706	8.754
13.6.5	64.21	0	23.08	0	0	0	3.77	9.41	0.25	100.72	80.74	17.844	1.416
13.6.7	65.65	0	23.69	0	0	0	3.97	9.78	0.3	103.38	80.377	18.012	1.611
13.6.8	60.68	0	22.88	0	0	0	4.9	5.14	4.7	98.3	46.99	24.75	28.26
13.7.6	65.18	0	23.03	0	0	0	4.43	8.94	0.92	102.49	74.535	20.417	5.049
13.8.8	63.7	0	22.32	0	0	0	4.19	9.28	0.21	99.71	79.071	19.729	1.2
13.10.9	62.92	0	24.3	0	0	0	5.83	8.25	0.68	101.97	69.207	27.048	3.744
13.10.11	64.87	0	23.01	0	0	0	3.94	9.1	0.3	101.21	79.308	18.978	1.714
13.10.13	65.73	0.53	18.92	0	0	0	0.39	4.16	10.13	99.86	37.691	1.947	60.362

A6.9 Garnet

	SiO_2	TiO_2	Al_2O_3	FeO	MnO	MgO	CaO	Na_2O	K_2O	Total
2.30.2	30.77	31.03	6.36	1.23	0	0	28.05	0	0	97.44
3.17.2	42.75	0	35.79	0	0	19.25	0	0	0	97.79
3.17.3	45.82	0	26.86	0	0	24.88	0.62	0	0	98.18
3.25.7	25.8	0	18.85	39.3	0.62	17.34	0.17	0.67	0	102.8

A6.10 Haematite

	SiO_2	Al_2O_3	TiO_2	FeO	MnO	MgO	CaO	K_2O	Na_2O	Total
0.31	0	0	0	91.12	0	0	0	0	0	91.12
0.71	0	0.218	0	94.42	0	0	0	0	0	94.64
0.o.24	0.447	0	0	93.84	0	0	0	0	0	94.29
0.o.31	0	0	0	91.12	0	0	0	0	0	91.12
0.o.71	0	0	0.218	94.42	0	0	0	0	0	94.64
3.4	0	0	0	92.41	0	0	0	0	0.164	92.57
3.26.1	0	0	0	93.8	0	0	0	0	0	93.8
3.38.1	0	0		91.38	0	0	0.197	0	0	91.57

A6.11 Ilmenite

	SiO_2	TiO_2	Al_2O_3	FeO	MnO	MgO	CaO	Na_2O	K_2O	Total	Fe_2O_3	FeO
0.49	0.36	44.75	0	51.6	0.56	0	0	0	0	97.27	•	•
2.14	0.22	47.6	0	50.79	2.8	0	0	0	0	101.4	11.73	40.23
2.21.3	0.15	18.58	0.58	75.9	0	0	0	0	0	95.21	65.58	16.89
2.21.4	0	37	0	58.77	0	0	0.14	0	0	95.91	28.54	33.09
2.28.2	0.18	46.38	0	50.27	1.8	0	0	0	0	98.63	11.31	40.09
2.28.4	0.28	47.43	0	47.01	1.79	0	0	0.29	0	96.79	8.005	39.81
2.29.4	0.32	49.07	0.19	39.2	9.81	0	1.85	0	0.09	100.5	8.087	31.93

2.29.7	0.23	49.35	0	41.11	6.45	0.54	0.12	0.33	0	98.13	6.266	35.47
2.42	0.2	25.37	0	67.64	0.29	0.21	0	0.43	0	94.15	52.53	20.38
2.43	0.16	45.4	0	49.82	1.74	0	0	0	0	97.12	11.74	39.26
8.38.10	0.82	58.19	0.26	39.8	1.05	1.79	0	0.6	0	102.5	•	•
8.74	1.48	49.04	0.72	45.79	1.44	2.58	0.18	0.47	0.31	102	•	•
3.37.1	0	47.69	0	49.43	3.2	0.29	0	0	0	100.6	11.46	39.12
11.13	2.67	45.85	0.78	44.32	0	3.09	0	0.76	0.19	97.66	10.55	34.83
11.85	0	51.49	0.42	45.38	1.62	2.92	0	0	0	101.8	6.578	39.47
11.93	0	50.71	0	48.95	2.53	0.8	0	0	0	103	8.17	41.6
11.111	0.47	49.52	0.26	46.04	0.48	3.26	0	0	0.14	100.2	8.534	38.36
11.132	0.26	50.75	0.43	45.84	1.56	2.62	0	0	0	101.5	6.833	39.69
13.6.12	0	50.32	0.55	42.81	1.26	3.91	0	0	0	98.85	6.452	37

A6.12 Melt

	SiO_2	TiO_2	Al_2O_3	FeO	MnO	MgO	CaO	Na_2O	K_2O	Total
2.20.	63.47	0.33	18.8	0	0	0.26	0.28	0.83	15.11	99.07
2.23	64.05	0	22.39	0	0	0.61	2.71	9.73	0.4	99.89
2.25	64	0.22	18.95	0	0	0.27	0.24	0.97	14.77	99.43
2.31.5	65.04	0	22.33	0.57	0	0	2.65	10	0.12	100.72
2.33.7	41.07	0.71	33.85	4.66	0	1.79	13.28	1.08	0.88	97.32
2.33.10.	39.29	0.41	21.04	14.3	0.22	5.7	16.41	1.07	0.26	98.7
2.33.11	50.23	2.81	24.85	6.1	0	2.41	5.11	3.76	4.23	99.5
2.33.12	56.99	0.97	23.66	2.61	0	1.53	5.49	4.66	3.05	98.96
2.33.14	52.1	2.99	21.58	7.47	0	3.46	2.89	3.19	4.55	98.22
2.33.15	52.52	0.87	27	8.22	0.24	3.38	1.89	3.27	3.85	101.24
2.33.16	30.5	0.23	25.26	26.12	0.55	15.22	0.52	0.77	0.15	99.32
2.34.6	39.06	0.25	17.8	21.77	0.6	15.84	0	0.75	0.33	96.39
2.34.8	21.11	2.12	22.68	30.05	0.69	20.84	0	0.64	0	98.13
2.36.10.	62.71	0.57	25.11	1.58	0	1.82	1.22	2.07	3.86	98.94
2.36.20.	33.03	12.8	11.01	16.81	0.19	8.42	10.75	1.62	1.3	95.93
2.40.3	26.83	0	18.06	37.56	0.48	16.29	0.14	0.85	1	101.21
2.46.2	48.81	0.16	34.1	5.15	0	1.1	0.28	0.87	10.53	100.99
2.48	36.12	0	19.02	26.33	0.25	14.88	0.14	1	0.2	97.94
2.53.3	36.97	0	16.91	20.41	0.2	12.56	0.39	1.83	7.38	96.66
2.53.3	50.02	0.23	0.72	7.26	1.37	0.36	38.53	0	0	98.49
2.53.6	43.67	0.74	28.55	5.6	0	3.71	12.79	1.92	2.3	99.28
2.53.7	46.55	0	19.91	1.68	0.39	0.46	29.09	0.69	0	98.77
8.10.	65.53	0	20.69	0	0	0	3.1	6.29	3.93	99.53
8.18	48.73	0.47	28.76	3.93	0	2.15	11.43	3.06	1.74	100.28
8.24.3	55.37	0	21.89	0.96	0	0.42	0.62	4.29	8.64	92.19
8.24.4	25.77	0.91	65.02	1.19	0	0	0.21	2.37	3.02	98.49
8.24.7	43.3	0.49	36.73	5.62	0	2.63	0.47	3.89	5.97	99.11
8.30.	75.31	0	12.4	0.36	0	0	0.59	2.11	4.51	95.27
8.30.	76.82	0	12.23	0	0	0	0.41	2.1	4.78	96.36
8.38.2	49.06	1.86	11.24	12.7	0	18.29	0	0.43	6.52	100.09
8.38.5	64.33	1.59	19.79	0.77	0	0.92	0.19	3.24	11.29	102.14
8.43	68.62	0	20.9	0.34	0	0	1.71	9.64	0.69	101.89
8.44	65.02	0	20.42	0.36	0	0	3.83	5.04	3.21	97.87
8.51	62.69	0	24.22	0.3	0	0	5.53	7.26	1.59	101.58
8.52	79.06	0	13.45	1.28	0	0	0.64	2.21	4.65	101.29
8.53	65.25	0.31	20.38	0.31	0	0	0.54	3.28	11.4	101.47
8.67	71.06	0	16.18	0.48	0	0	2.5	4.41	3.14	97.78
8.71	59.59	0.76	19.58	2.45	0	1.29	2.09	4.84	7.36	97.94
8.77	69.29	0	14.65	1.54	0	0.83	2.95	3.4	3.76	96.41
8.78	65.6	0	21.11	0.44	0	0	3.15	8.02	2.07	100.4
8.82	78.42	0	11.21	0.75	0	0	0.36	1.83	4.13	96.69
8.83	77.98	0	11.89	0.75	0	0	0.42	2.02	4.51	97.57
8.84	77.26	0	12.37	0.6	0	0	0.58	2.12	5.13	98.05
8.85	67.24	0	7.59	9.41	0.4	4.19	8.57	1.25	2.4	101.04
8.89	64.04	0	21.29	0.52	0	0	4.36	6.76	2.38	99.35
8.100.	61.96	0	23.95	0	0	0	4.96	7.65	1.6	100.13
8.102	62.96	0	23.85	0	0	0	4.55	7.03	2.55	100.93
3.2.9	62.05	1.41	19.67	0.62	0	0	0.42	2.93	10.9	98.01
3.38	66.2	0.35	19.56	0	0	0.31	0.86	15.94	15.94	119.16
3.38.2	63.64	0.29	18.62	0	0.29	0.26	0	0.8	15.17	99.08
3.7.2	65.47	0.5	19.34	0	0	0.35	0.23	1.16	15.03	102.09
3.19.5	43.72	0	32.53	1.74	0	1.17	15.69	1.45	0.7	97.01
3.21.2	72.86	0.34	12.46	2.22	0	0	0.69	1.96	4.7	95.23

3.25.3	31.84	0.27	8.74	43.64	0.81	17.31	0.18	0.57	0.28	103.65
3.49.4	66.82	0	19.94	0	0	0	2.61	6.09	4.15	99.61
3.26.2	37.54	2.49	15.25	20.43	0.34	10.8	0	0.62	9.66	97.13
3.26.3	37.92	2.4	14.86	20.18	0	10.49	0	0.46	9.67	95.99
3.26.5	64.01	0.33	9.8	8.74	0.34	5.5	1.03	1.4	3.7	94.85
3.26.6	57.11	0	25.87	1.93	0	0	6.81	5.52	2.07	99.31
3.26.9	63	0	22.43	0.43	0	0	4.23	8.05	1.08	99.22
3.37.6	61.12	1.85	19.77	0	0	0	0.71	3.34	9.77	96.55
3.37.8	64.72	0.46	18.81	0	0	0	0.33	3.57	10.93	98.82
3.37.9	60.58	0	25.22	0	0	0	6.34	6.56	1.68	100.38
3.35.4	59.22	0.55	26.15	0.5	0	0	2.39	5.16	6.6	100.57
3.35.6	61.5	0.9	23.47	0	0	0.28	0.3	2.93	10.7	100.07
11.7	68	0.45	15.85	2.96	0	0.41	0.76	3.98	5.88	98.29
11.8	70.13	0.44	12.32	2.37	0	0.29	0.32	2.65	5.35	93.86
11.11.4	80.56	0.4	7.57	2.4	0	0.24	0	1.86	4.07	97.1
11.11.5	94.41	0	2.16	0.46	0	0	0	0.75	0.81	98.58
11.11.7	84.72	0.32	4.3	1.76	0	0	0.18	1.15	2.25	94.67
11.22	68.47	0.58	15.23	3.07	0	0.31	0.77	3.57	5.75	97.74
11.23	72.09	0.32	11.77	2.44	0	0.26	0.5	2.71	5.6	95.67
11.16	70.59	0	15.09	1.06	0	0	0.58	3.04	6.3	96.66
11.17	65.02	0	22.04	0	0	0	2.95	9.44	0.3	99.75
11.18	63.07	0	20.78	0	0	0	2.48	6.45	5.54	98.31
11.19	63.79	0	21.52	0	0	0	3.46	6.24	4.67	99.68
11.26	64.77	0.64	15.71	3.56	0.27	0.43	1.65	3.58	5.58	96.18
11.27	65.74	0.41	15.9	3.85	0	0.4	1.61	3.17	5.57	96.65
11.28	56.12	0	27.15	0.68	0	0	9.88	5.36	0.8	100
11.30.	56.88	0	27.14	0.75	0	0	9.58	5.36	1.09	100.8
11.31	62.95	0	22.73	0.31	0	0	4	6.6	3.79	100.36
11.32	65.58	0	21.78	0	0	0	2.84	8.78	1.23	100.2
11.40.	46.58	0	33.81	1.71	0	0	17.72	1.35	0.19	101.36
11.41	63.29	0	17.4	3.12	0	0.43	1.46	3.74	8.91	98.36
11.47	64.48	0.45	16.48	3.72	0	0.46	2.06	3.73	6.08	97.47
11.43	62.72	0	18.82	2.21	0	0.31	2.49	3.91	6.61	97.07
11.48	60.6	0	19.8	1.56	0	0	3.98	5.08	4.85	95.86
11.49	61.93	0.45	16.95	6.27	0.41	0.56	2.17	4.24	6.64	99.62
11.50.	58.67	0.28	23.91	1.52	0	0.29	6.75	5.6	2.89	99.89
11.53	56.94	0	24.52	0.8	0.25	0	8.2	5.23	1.5	97.44
11.57	79.38	0	9.42	1.24	0	0	0.17	2.06	4.64	96.92
11.58	74.12	0	12.69	0.99	0	0	0.48	2.72	5.42	96.41
11.59	75.04	0	12.7	1.09	0	0	0.52	2.42	5.47	97.24
11.6	74.82	0	13.96	1.04	0	0.28	0.42	2.69	5.32	98.52
11.61	73.69	0	15.17	1.3	0	0	0.69	3.46	5.89	100.19
11.62	72.4	0	16.41	1.61	0	0	0.98	3.47	5.97	100.85
11.62	65.94	0.66	18.99	0	0	0	0.77	3.99	9.43	99.78
11.65	80.03	0	12.1	0.38	0	0	0.26	1.89	5.2	99.85
11.66	77.72	0	12.63	0	0.25	0	0.48	2.33	5.36	98.78
11.68	74.38	0	14.81	0.34	0	0	0.69	3.16	5.94	99.32
11.71	72.59	0	15.27	0.81	0	0	0.73	3.22	6.24	98.85
11.72	71.61	0	15.72	1.75	0	0	0.84	2.74	5.56	98.21
11.73	77.48	0	11.23	1.9	0	0	0.47	1.93	5.26	98.27
11.74	75.16	0	13.33	2.1	0	0	0.6	2.53	5.64	99.37
11.75	71.64	0	13.9	1.93	0	0	0.74	2.55	5.63	96.39
11.76	70.58	0	15.79	2.01	0	0.31	0.77	2.95	5.93	98.34
11.79	63.03	0	22.28	0	0	0	4.22	6.43	3.36	99.32
11.81	67.35	0	22.69	0	0	0	3.25	9.48	1.22	103.99
11.86	72.44	0	14.7	2.92	0	0.47	0.61	3.21	5.17	99.52
11.88	77.11	0	13.98	1.18	0	0	0.45	2.6	5.74	101.07
11.89	64.16	0.57	19.61	1.8	0	0	3.17	4.63	5.69	99.62
11.90.	63.8	0.59	21.06	0.94	0	0	3.97	6	4.42	100.79
11.94	66.1	1.69	19.48	0	0	0	0	3.53	10.52	101.81
11.97.2	76.58	0	12.69	0.99	0	0	0.39	2.83	5.54	99.03
11.102	75.56	0	13.03	1.17	0	0	0.22	2.69	5.44	98.12
11.103	64.74	0.5	19.86	0	0	0	1.05	4.16	9.25	99.55
11.104	66.41	0.35	17.36	2.99	0	0.44	0.81	3.73	9.51	101.6
11.105	69.71	0	15.39	2.28	0	0.35	0.54	2.71	5.91	96.9
11.107	66.27	0.42	19.51	0	0	0	0.77	4.42	9.63	101.03
11.108	64.13	0.27	18.31	0	0	0	0	2.4	13.23	98.35
11.113	68.51	0.4	16.06	3.65	0	0.84	0.84	3.16	5.52	98.97
11.116	65.94	0.44	18.99	0	0	0	0.28	4.11	10.72	100.46
11.117	65.33	0.32	18.52	1.15	0	0	0.63	4.05	9.01	99.01
11.119	73.74	0	14.29	0	0	0	0.43	3.12	6.19	97.77
11.124	64.3	0	21.76	0	0	0	3.08	7.77	2.54	99.45
11.125	70.93	0	17.35	0.56	0	0.29	0.86	3.95	6.98	100.93
11.137	64.14	0	22.84	0	0	0	3.84	7.91	1.95	100.69
11.141	66.32	0	18.64	0.92	0	0	0.53	5.2	8.81	100.4
12.4	76.67	0	12.9	0.35	0	0	0.37	2.65	5.7	98.63
12.5	65.22	0.31	18.83	0	0	0	1.08	5.22	7.78	98.43

12.7	69.74	0	17.5	0	0	0	1	4.01	6.44	98.68
12.15	64.24	0	20.92	0	0	0	1.14	5.91	7.04	99.26
12.18	59.11	0	25.62	0.77	0	0.61	6.68	5.66	3.76	102.23
12.24	64.02	0.42	21.68	0.35	0	0	2.48	5.83	6.63	101.4
12.25	59.96	0.58	18.37	5.3	0	1.05	1.4	4.23	5.24	96.13
12.33	63.91	0	20.45	0.86	0	0.34	1.87	5.38	7.25	100.05
12.35	56.99	0.38	17.87	9.56	0	2.05	1.68	4.99	5.56	99.09
12.31	57.78	0	26.38	0.4	0	0	8.29	5.8	1.42	100.07
12.39	63.77	0	22.88	0	0	0	3.89	8.73	1.34	100.61
12.40.	57.53	0.83	15.86	11.93	0	4.62	1.69	3.84	5.67	101.97
12.44	62.5	0.51	19.12	3.27	0	0.83	1.24	4.26	5.46	97.19
12.45	63.49	0	22.78	0.4	0	0	4.18	6.91	3.37	101.13
12.48	60.45	0.43	18.59	4.29	0	1.16	2.14	5.3	6.07	98.43
12.49	69.23	0.46	15.36	3.22	0	0.82	1.02	3.52	5.11	98.72
12.60.	65.28	0	18.93	0.36	0	0	0.67	4.44	6.37	96.05
12.63	65.26	0	19.19	0.5	0	0	0.51	4.58	6.46	96.5
12.64	53.2	0	30.8	0.44	0	0.56	8.52	4.73	1.94	100.18
12.65	64.95	0	20.61	0	0	0	1.7	5.61	7.07	99.94
12.74	65.94	0	18.24	0.38	0	0	0.43	4.82	8.03	97.83
12.79	62.49	0	21.52	0	0	0	3.59	7.21	2.49	97.31
12.82	53.29	1.33	17.4	9.02	0	5.11	0.98	3.61	6.78	97.52
12.84	62.1	0.54	20.49	0.37	0	0	2.56	5.73	6.07	97.86
12.85	56.21	0.69	17.95	9.5	0	2.86	0.81	3.73	5.99	97.74
12.86	52.37	1.09	15.5	11.81	0	5.68	0.42	2.89	7.01	96.76
12.87	56.91	0.63	18.1	7.69	0	1.61	0.7	4.8	5.81	96.25
12.88	61.3	0.27	22.97	0.35	0	0	4.69	6.27	3.82	99.66
12.89	64.15	0.32	20.93	0	0	0	1.71	5.44	7.67	100.22
12.90.	54.82	0	27.19	0.72	0	0.34	9.93	4.88	1.65	99.54
12.91	65.3	0	21.31	0	0	0	3.53	6.11	4.35	100.6
12.92	64.17	0	21.58	0	0	0	3.14	7.37	3.46	99.72
12.93	67.73	0.67	15.2	2.94	0	0.98	1.1	3.1	5.54	97.55
12.95	61.07	0.47	18.62	3.06	0	1.1	1.45	3.79	5.65	95.21
12.101	62.43	1.04	17.46	4.95	0	1.68	2.02	4.05	4.82	98.44
12.105	68.32	0	16.27	2.06	0.26	0.55	1	3.63	5.62	97.72
12.106	63.77	0.54	16.96	3.33	0	1.11	1.73	3.54	5.25	96.23
12.109	47.19	4.1	8.72	23.63	0.45	9.01	2.32	2.88	2.47	101.07
12.110.	63.45	0.56	19	1.54	0	0.38	2.08	5.9	5.91	98.81
12.111	56.72	2.45	13.55	12.22	0	4.69	1.5	4.33	4.52	99.97
12.113	59.79	0	24.58	0	0	0	6.73	6.01	2.54	99.65
12.116	60.99	0.51	17.59	7.25	0	2.13	1.61	4.34	5.9	100.31
12.117	54.44	2.06	14.23	13.15	0	4.32	1.21	3.05	4.84	97.3
12.118	58.45	0.83	16.45	8.88	0	3.4	1.64	2.99	4.75	97.39
12.119	64.21	0.28	18.25	1.29	0	0	1.5	5.44	6.08	97.05
12.121	63.37	0.43	18.56	1.09	0	0	1.76	5.81	6.54	97.56
12.124	59.52	0.62	19.42	3.51	0	1.07	1.6	4.18	5.45	95.36
12.130.	61.63	0.53	22.1	1.15	0	0.63	3.59	5.59	5.62	100.84
12.138	64.43	0.47	16.6	3.33	0	0.72	1.42	4.11	5.3	96.39
12.139	64.26	0.43	16.68	3.41	0	1.01	2.28	4.28	5.21	97.55
12.141	55.07	1.34	10.6	11.82	0.44	2.88	13.53	3.18	2.14	101
12.143	63.1	0.51	17.24	3.53	0	0.67	4.78	5.84	5.04	100.7
13.2.1	73.19	6.12	11.75	2.44	0	0.31	0.69	2.38	6.12	96.88
13.2.2	66.25	6.51	15.98	2.48	0	0.75	1.52	3.39	6.51	97.17
13.2.3	63.3	6.45	17.44	3.17	0	1.02	1.88	3.6	6.45	97.5
13.2.1	62.59	6.3	17.97	3.51	0	1.12	2.08	3.58	6.3	97.9
13.2.6	60.78	6.17	18.02	3.05	0	1	2.36	3.82	6.17	95.76
13.2.7	62.23	7.67	19.3	0.9	0	0.39	2.04	4.29	7.67	97.32
13.2.9	70.49	6	12.34	2.34	0	0.75	1.15	2.44	6	95.97
13.2.10	59.72	4.61	22.89	0	0	0	5.6	5.17	4.61	97.99
13.3.1	73.68	4.9	7.51	4.29	0	0.96	0.95	2.15	4.9	95.35
13.3.2	74.64	5.07	8.37	4.5	0	1.04	1.02	2.2	5.07	97.75
13.3.7	71.24	5.38	9.66	4.42	0	1.08	1.27	2.22	5.38	96.11
13.3.15	62.11	5.51	14.37	5.87	0	1.96	2.19	3.02	5.51	96.29
13.3.16	63.03	5.65	13.17	5.47	0	1.7	2.09	3.08	5.65	95.53
13.3.17	73.11	4.88	8.61	4.55	0	1.11	1.02	1.93	4.88	96.1
13.4.6	66.65	6.27	16.23	2.61	0	1.01	1.28	3.45	6.27	97.5
13.4.8	64.52	6.45	18.01	1.78	0	0.74	1.5	3.57	6.45	96.57
13.4.9	58.52	3.17	23.4	0.39	0	0	6.28	5.08	3.17	96.84
13.4.11	63.37	4.44	22.05	0	0	0.49	4.1	5.73	4.44	100.2
13.4.12	60.94	4.05	21.15	0	0	0	4.09	5.86	4.05	96.08
13.4.17	76.23	4.42	8.27	3.38	0	1.21	0.8	1.51	4.42	96.36
13.5.3	68.04	4.7	9.82	6.51	0	2.52	0.72	2.55	4.7	96.07
13.5.15	57.32	5.68	19.34	6.78	0	1.35	2.95	4.17	5.68	98.83
13.5.16	57.05	5.41	18.3	8.09	0	2.87	2.09	4.01	5.41	99.79
13.5.17	39.56	9.19	15.52	11.28	0	17.87	0.24	1.05	9.19	99.14
13.5.18	37.81	7.89	15.56	10.73	0	15.14	0	1.15	7.89	95.68
13.5.20	56.89	5.41	19.49	7.63	0	1.83	3.03	3.57	5.41	99.32
13.5.21	51.51	6.85	17.38	8.88	0	7.55	1.73	2.51	6.85	98.24

13.5.11	77.72	5.06	6.72	6.28	0	1.24	0.94	2.22	5.06	101.1
13.6.1	63.94	5.07	22.4	0	0	0	4.7	4.91	5.07	101
13.6.5	62.45	6.68	22.31	0.71	0	0	3.73	4.9	6.68	100.8
13.6.6	63.43	8.31	19.41	1.29	0	0.36	1.75	4.34	8.31	99.2
13.6.9	61.6	2.29	24.18	0	0	0	5.82	6.72	2.29	100.6
13.6.10	58.48	6.41	21.69	2.95	0	0.97	3.57	4.52	6.41	98.58
13.6.13	59.76	5.99	20.61	3.72	0.32	0.42	1.1	4.33	5.99	97.8
13.7.2	63.24	5.78	15.9	6.98	0.27	2.19	1.92	3.38	5.78	100.6
13.7.3	61.82	6.6	20.12	4.91	0	1.29	1.64	4.26	6.6	100.9
13.7.4	62.05	6.83	19.91	2.66	0	0.97	1.56	4.21	6.83	98.47
13.7.5	64.21	6.58	19.6	2.12	0	0.78	1.13	4.06	6.58	98.47
13.7.8	62.51	5.61	16.05	7.62	0	2.32	1.83	3.67	5.61	100.8
13.7.9	59.69	5.68	14.58	6.81	0	1.77	1.65	3.52	5.68	95.15
13.7.10	61.87	5.92	15.59	6.18	0	1.65	1.66	3.47	5.92	97.55
13.7.12	60.45	6.48	18.86	3.65	0	1.13	1.19	3.53	6.48	96.02
13.7.13	72.59	6.45	13.21	2.95	0	1	0.57	3.03	6.45	99.8
13.7.14	65.1	6.24	14.12	5.8	0	0.88	1.04	3.16	6.24	97.19
13.8.1	75.89	4.95	7.54	4.39	0	1.4	0.8	1.77	4.95	97.85
13.8.3	67.7	6.11	13.15	4.73	0	1.37	1.32	3.08	6.11	98.62
13.8.5	64.09	6.6	17.65	2.85	0	1.01	1.27	3.6	6.6	97.54
13.8.6	65.75	7.31	19.23	1.24	0	0.37	0.91	3.96	7.31	98.77
13.8.7	60.6	7.47	20.14	1.97	0	0.46	0.96	5.31	7.47	96.92
13.8.9	61.42	6.48	19.71	3.14	0	0.77	1.6	4.01	6.48	97.13
13.8.11	60.26	8.98	19.7	2.15	0	0.74	1.07	4.18	8.98	97.09
13.9.3	59.15	6	19.61	4.52	0	0.68	2.83	3.69	6	97.37
13.9.7	58.93	7.05	18.54	5.02	0	1.72	1.87	3.68	7.05	98.24
13.9.8	66	7.33	19.16	1.07	0	0.51	0.63	3.83	7.33	98.54
13.9.9	58.87	6.27	19.51	4.89	0	1.62	1.71	3.99	6.27	98
13.9.10	63.27	6.16	16.92	4.71	0	1.71	1.32	3.57	6.16	98.43
13.9.12	61.79	6.68	19.74	4.49	0	1.44	1.66	4.17	6.68	100.4
13.9.13	65.31	10.52	18.94	0.5	0	0	0.3	3.81	10.52	99.89
13.9.14	59.01	6.42	18.13	5.76	0	1.92	1.93	3.41	6.42	97.93
13.9.15	76.89	5.16	8.28	4.31	0	0.96	0.44	2.18	5.16	98.97
13.10.2	64.11	6.72	19.16	3.72	0	1.23	1.2	4.35	6.72	100.5
13.10.3	60.86	6.41	20.59	4.55	0	1.5	1.43	4.53	6.41	99.87
13.10.4	59.98	6.31	19.98	3.84	0	1.21	1.46	4.38	6.31	97.63
13.10.5	65.25	7.49	20.19	1.7	0	0.42	1.17	4.7	7.49	100.9
13.10.6	61.67	6.56	18.73	3.54	0	1.14	1.51	4.28	6.56	97.9
13.10.7	62.26	6.31	16.84	4.46	0	1.44	1.62	3.81	6.31	97.58
13.10.8	58.44	8.09	19.04	7.66	0	1.8	0.5	4.18	8.09	100.3
13.10.10	55.77	6.37	19.17	10.14	0	2.04	2.33	4.16	6.37	99.97
13.10.12	61.21	6.21	18.4	4.57	0	1.38	1.35	4.99	6.21	99.04
13.10.14	67.79	6.15	13.79	3.33	0	1.12	0.98	2.94	6.15	96.67
13.10.16	74	5.75	9.97	3.88	0	0.95	0.76	2.54	5.75	98.47

A6.13 Muscovite

	SiO_2	Al_2O_3	TiO_2	FeO	MnO	MgO	CaO	K_2O	Na_2O	SO_4	Total	
0.39	43.115	23.725		1.139	3.808	0	1.579	0	9.752	0	0	83.118
0.47	46.661	26.362		0.865	4.85	0	2.702	0	10.567	0	0	92.007
0.73	47.292	28.643		0.23	4.61	0	2.198	0.199	11.408	0.335	0	94.915
0.85	46.029	27.709		1.178	4.885	0	1.593	0	10.958	0	0	92.352

A6.14 Olivine

	SiO_2	TiO_2	Al_2O_3	FeO	MnO	MgO	CaO	Na_2O	K_2O	Total	Fayalite	Forst	Tephroite
11.112	35.1	0	0	42.11	0.98	22.27	0.23	0.5	0	101.19	50.865	47.936	1.1989
12.131	35.89	0.24	0	36.19	0.93	27.13	0	0	0	100.38	42.339	56.559	1.102
12.132	35.91	0	0	35.49	0.79	27.16	0	0.55	0	99.9	41.906	57.149	0.9448
13.5.12	37.92	0	0.42	30.57	0.55	32.48	0.16	0	0	102.1	34.346	65.028	0.6259
13.8.12	38.51	0	0	28.13	0.4	35.81	0	0	0	102.9	30.46	69.1	0.439

13.9.5	37.89	0	0	26.64	0.66	34.79	0	0	0	99.99	29.831	69.421	0.7485
13.9.6	38.35	0	0	27.74	0.38	33.99	0.19	0.56	0	101.21	31.276	68.29	0.4339
13.9.11	37.41	0	0	27.6	0.43	35.15	0	0.67	0	101.26	30.439	69.081	0.4803

A6.15 Pyroxene

	SiO_2	TiO_2	Al_2O_3	FeO	MnO	MgO	CaO	Na_2O	K_2O	Total	Enstatite	Ferrosilite	Wollaston.
8.38.3	50.41	0.51	1.75	18.07	0.52	9.54	16.22	0.58	0.76	98.38	30.45	32.35	37.2
8.38.9	58.1	0.3	0.56	19.43	0.81	9.36	13.79	0	0.21	102.6	31.02	36.13	32.85
8.75	23.46	0	20.25	40.32	1.16	16.18	0.19	1.13	1.15	103.9	41.55	58.09	0.36
3.25.8	61.53	0	10.42	14.52	0	6.32	1.29	1.44	2.6	98.12	41.06	52.91	6.032
3.26.3	32.16	0.26	16.41	32.84	0.34	15.9	0	0.71	4.25	102.9	100	0	0
3.26.4	35.89	1.15	17.89	17.75	0	13.56	0	1.34	8.07	95.64	100	0	0
11.4	51.83	0.29	0.46	29.44	0.85	16.23	0.59	0.58	0.15	100.4	49.69	49.01	1.299
11.34	50.17	0.53	2.15	16.05	1.72	10.43	18.43	0.85	0	100.3	33.93	22.97	43.1
12.137	55.51	0.4	1.6	15.63	0.29	17.93	9.88	0.73	0.29	102.3	53.04	25.95	21.01
13.3.3	58.42	0.27	2.38	16.38	0.31	17.54	2.42	0.72	0.97	99.4	61.63	32.27	6.102
13.3.4	54.81	0	0.66	18.66	0.5	23.35	1.87	0	0	99.85	66.41	29.78	3.82
13.3.5	53.4	0.34	0.52	19.53	0.47	22.46	1.06	0	0.15	97.93	65.71	32.06	2.225
13.3.6	54.62	0.34	0.61	20.05	0.62	22.95	1.38	0	0	100.6	65.22	31.96	2.814
13.3.17	54.29	0	0.73	19.31	0.46	23.57	1.27	0	0	99.63	66.74	30.68	2.579
13.4.16	54.65	0	1.34	17.64	0.42	21.81	1.06	0.5	0.46	97.86	67.18	30.48	2.34
13.5.8	51.45	0	0	22.49	0.38	21.25	0.35	0	0	95.91	62.28	36.98	0.737
13.7.7	53.44	0	0	20.5	0	22.57	1.17	0	0	97.69	64.65	32.94	2.412
13.9.2	38.64	3.54	15.01	11.81	0	17.58	0	1.05	9.07	96.71	100	0	0

A6.16 Quartz

	SiO_2	TiO_2	Al_2O_3	FeO	MnO	MgO	CaO	Na_2O	K_2O	Total
0.3	97.37	0	0.181	0	0	0	0	0	0	97.55
0.4	96.03	0	0	0	0	0	0	0	0	96.03
0.8	95.44	0	0.215	0	0	0	0	0	0	95.66
0.64	100.9	0	0.418	0	0	0	0	0	0	101.4
0.6	95.57	0	0.399	0	0	0	0	0	0	95.97
0.9	97.43	0	1.409	1.521	0	0.948	0	0	0	101.3
0.33	98.84	0	0.386	0	0	0	0	0	0	99.23
2.4	101.3	0	0.242	0.234	0	0	0	0	0	101.8
2.33.4	99.77	0	0.737	0.258	0	0	0	0	0	100.8
2.34.4	98.62	0	0.667	0.326	0	0	0	0	0	99.61
8.33	100.9	0	0.551	0	0	0	0	0	0	101.4
8.4	99.77	0	0	0.318	0	0	0	0	0	100.1
3.35.5	100.7	0	0	0	0	0	0	0	0	100.7
11.24	97.18	0	0	0	0	0	0	0	0	97.18
13.4.18	95.51	0	1.714	0.451	0	0	0	0	0.509	98.18

A6.17 Rutile

	SiO_2	TiO_2	Al_2O_3	FeO	MnO	MgO	CaO	Na_2O	K_2O	Total
0.E.46	1.604	95.38	0.616	1.693	0	0	0.781	0	0	100.1
0.E.54	0.376	96.6	0	0.457	0	0	0	0.267	0	97.7
0.E.55	6.827	76.92	1.329	1.988	0	0.248	5.81	0	0	93.12
2.21.1	0	98.69	0	1.91	0	0	0	0	0	100.6
2.33.3	3.49	88.51	1.91	4.05	0	0.38	0	0.4	0.44	99.19
3.45	0.47	98.45	0.37	1.53	0	0	0.14	0	0	101

A6.18 Sphene

	SiO_2	TiO_2	Al_2O_3	FeO	MnO	MgO	CaO	Na_2O	K_2O	Total
0.59	29.174	6.063	29.09	1.429	0	0	27.515	0	0	93.271
8.68	30.45	2.53	35.79	2.42	0	0	27.66	0	0	98.84

A6.19 Spinel

	SiO_2	TiO_2	Al_2O_3	FeO	MnO	MgO	CaO	Na_2O	K_2O	Total	Fe_2O_3	FeO
0.4	0	0	47.62	44.28	6.367	0	0	0	0	98.27	•	•
8.55	1.04	0	58.16	35.8	0.37	4.97	0	0.58	0.3	101.2	•	•
3.2.4	2.18	0	59.89	30.29	0	7.93	0	0.73	0.19	101.2	1.472	28.97
3.35.9	1.14	0	58.27	31.66	0	6.57	0	0	0.29	97.93	0.502	31.21
11.98	3.71	0.57	52.1	35.66	0.67	8.43	0.2	1.26	0.19	102.8	9.66	26.97
11.99	5.63	1.06	45.35	40.3	1.02	5.83	0.62	1.06	0.15	101	8.833	32.36
12.133	4.43	6.08	12.57	69.84	0.42	4.64	0	1	0.46	99.45	41.3	32.7
13.5.13	1.37	10.63	19.08	61.46	0.49	6.34	0	0.65	0.25	100.3	31.21	33.37
13.5.19	0.39	12.63	14.49	63.08	0	6.12	0	0.75	0	97.46	32.95	33.43
13.5.22	2.08	2.17	46.48	36.79	0	11	0	0.74	0.21	99.47	14.72	23.55
13.9.1	0.32	11.33	14.93	63.35	0.49	7.3	0	0.49	0	98.21	35.58	31.33

A6.20 Wollastonite

	SiO_2	TiO_2	Al_2O_3	FeO	MnO	MgO	CaO	Na_2O	K_2O	Total	Enstati.	Ferrosili.	Wollaston.
8.19	52.07	0.28	0.5	0.81	0.82	0	48.56	0	0	103.04		0	0 100
3.16.2	51.53	0	0.55	0.71	0.48	0	46.26	0	0	99.53	0	1.19	98.81
3.16.3	51.21	0	0.4	0.67	0.42	0.29	45.94	0	0	98.93	0.858	1.123	98.019
12.14	51.36	0	0.53	0.39	0	0.4	46.96	0	0	99.64	1.158	0.641	98.201

A6.21 Zircon

	SiO_2	Al_2O_3	TiO_2	FeO	MnO	MgO	CaO	K_2O	Na_2O	SO	P_2O_5	Total
0.e.60	35.558	0	0	0.429	0	0	0	0	0	0	34.95	70.937
0.e.90	37.986	0	0	0	0	0	0.177	0	0	0	37.45	75.611
0.o.22	37.487	0.456	0	1.452	0	0	0	0	0	0	37.1	76.495
0.o.23	35.537	0.291	0	0.553	0	0.2	0	0	0	0	34.15	70.757
0.o.24	37.374	0	0	0.707	0	0	0	0	0.36	0	37.79	76.232
0.o.60	35.558	0	0	0.429	0	0	0	0	0	0	34.95	70.937
0.o.90	37.986	0	0	0	0	0	0.177	0	0	0	37.45	75.611

A6.22 Analysis of the powder sample WG1

Analysie are listed chronologically with the second column indicating the mineral or melt analyzed. Letters stand for following phases:

AP Apatite
BI Biotite
FP Feldspar, both orthoclase and plagioclase
IL Ilmenite
Q Quartz
XX Melt

	Min	SiO2	TiO2	Al2O3	FeO	MnO	MgO	CaO	Na2O	K2O	SO_4	P2O5	total
1.2	FP	62.702		21.787				4.072	7.736	0.324	0	0	96.62
1.5.1	BI	53.855	0.246	2.287	30.214	0.879	12.67	1.406	0.636	0.658	0	0	102.852
1.8	FP	62.82		21.637				3.956	7.921	0.221	0	0	96.556
1.9	FP	63.763	0.195	17.326	0.208				2.192	13.185	0	0	96.868
1.11	FP	59.804		22.871	0.3			6.363	6.413	0.629	0	0	96.381
1.12	FP	65.003	0.362	18.129				0.166	2.926	12.25	0	0	98.836
1.13	FP	62.946		21.249				4.359	7.206	1.05	0	0	96.081
1.14.1	BI	39.435	3.81	13.782	15.209	13.708		0.221	0.939	9.121	0.142	0	96.362
1.14.3	FP	64.752	0.201	17.918					2.579	12.434	0	0	97.885
1.14.4	FP	64.782		19.194	0.252			1.668	6.751	3.753	0	0	96.401
1.15	FP	61.482		21.377				4.937	6.244	2.185	0	0	96.224
1.17	XX	71.799	0.227	13.721	1.261			0.469	1.668	4.938	0	0	94.103
1.18	XX	73.377	0.245	11.864	1.46		0	0.472	1.582	5.103	0	0	94.103
1.20.	FP	64.993	0.314	17.929	0.263			0.333	3.122	11.369	0	0	98.324
1.21	FP	61.725		21.828				4.484	7.719	0.343	0	0	96.099
1.22	FP	63.816	0.329	17.388	0.247			0.187	3.192	10.888	0	0	96.047
1.23	AP			0.198	0.248			56.5	0.135	0	0	42.115	99.197
1.24	FP	63.495	0.456	17.508					2.05	13.339	0	0	96.848
1.25	FP	61.798		21.217	0.27			4.274	5.881	2.649	0	0	96.088
1.26	FP	61.538		22.211	0.232			5.208	6.911	0.836	0	0	96.936
1.27	FP	61.972		21.413				4.397	6.142	2.678	0	0	96.602
1.30.	IL	0.395	47.658	0.262	51.744	0.561		1.592	0.138		0	0	102.35
1	XX	72.159	0.274	11.514	1.336			0.475	1.989	5.518	0.124	0	93.389
2	FP	63.344	0.319	17.53				0.296	2.909	11.49	0	0	95.888
3	FP	60.914		20.77				4.606	5.953	2.598	0	0	94.841
4	FP	64.097		17.275				0.281	2.824	11.653	0	0	96.13
6	XX	81.043		7.527	0.93			0.364	1.585	3.809	0	0	95.258
7	XX	73.857	0.311	11.857	1.457			0.472	1.57	5.548	0.162	0	95.251
9	XX	75.359	0.216	12.575	0.892			0.393	1.427	3.642	0	0	94.504
10	BI	49.013	0.249	7.536	1.82		0.3	17.448	1.307	3.44	0	0	95.414
12	XX	72.061		11.258	1.26			0.445	1.811	5.47	0.126	0	92.431
13	XX	72.755	0.253	11.333	1.268			0.429	1.555	5.348	0	0	92.942
14	XX	84.394		7.547	0.563			0.229	0.96	2.231	0	0	95.879
15	FP	61.164	1.056	17.029				0.314	2.659	10.648	0	0	92.871

Appendix 7

!ROCKDEF

A7.1 Introduction

In this appendix parts of the program !ROCKDEF (written by Prof Rutter) are discussed. This program is cooperatively multitasking and run from the desktop of an Archimedes that is linked to the gas rig. It was written in Acorn Quick Basic 5.

The Screen setup and data displays visible when the program is operational are first discussed. This is followed by a description of program loops responsible for data acquisition, real time processing and post-test data processing. Factors such as apparatus calibration, jacket corrections and diameter change of sample that are incorporated as functions in the !ROCKDEF program are discussed in **Appendix 2.** A full copy of the program !ROCKDEF is included in **Appendix 8.**

A7.2 Screen setup and data display

The first part of the program defines the setup of the screen (**Figure A5.01**). The program is fully mouse operated. On opening the program an icon appears on the bottom command bar of the screen. A menu can be popped up by depressing the central mouse button while the indicator rests on top of this Rock Def icon. A data panel contains in the top bar a clock and six coloured boxes that relate to the different channels of input data. The second row displays on-line data processed values for the different channels. Function buttons occupy the bottom half of the data panel. The largest panel displays unprocessed milliVolt versus record number graphical displays of selected channels.

Rockdef icon and Menu: The Rock Def icon is located on the command bar at the bottom of the screen and contains a pull-down menu. Functions and sub-functions accessible via the !Rockdef icon are as follows:

- Info gives very general information on the use and origin of the !Rockdef program.

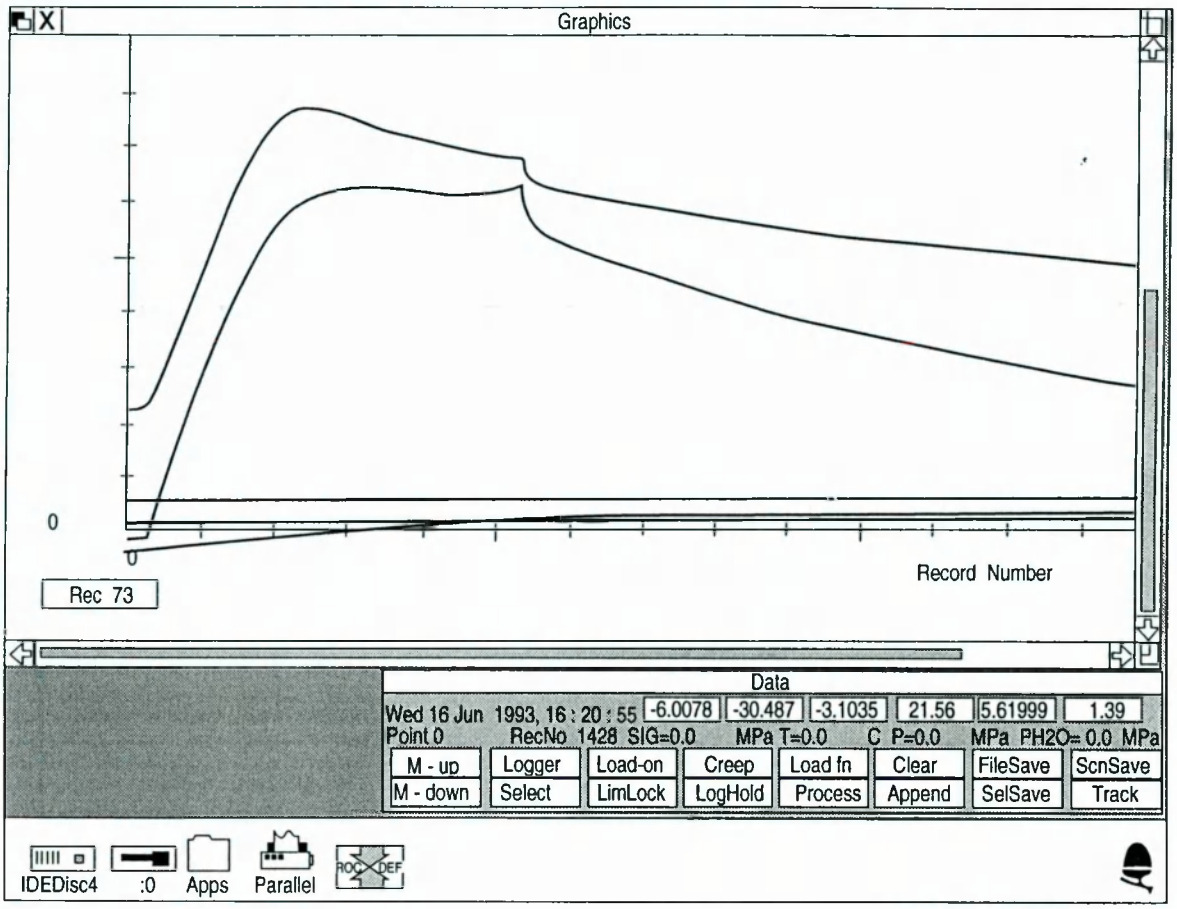

Figure A7.01: Graphics display of the Acorn Basic 5 program !ROCKDEF. The !ROCKDEF icon is on the command bar at the bottom of the screen and is the one furthest right of the left hand group. The *Data* window is always visible when the program is running. The *Graphics* window is optional.

Graph set	This allows the adjustment of maximum and minimum values on the plot of milliVolt reading (y-axis) versus record number (x-axis), displayed in the *Graphics* window.
Set param	The following parameters controlling gas rig deformation behaviour can be set using this option:
constant d	sets constant deformation rate in mm min^{-1}.
constant e	sets constant strain rate in sec^{-1}.
constant s	constant stress in MPa.
length	enters specimen length, default 20 mm.
diam	enters specimen diameter, default 10 mm.
filename	an appropriate filename is entered to signify the number of the test to be run or to reload a previous test. Letters are used to identify the sample material (e.g. WG20 is the twentieth test performed on Westerly granite).
set log	The logging interval is set in seconds.

limits — This allows the setting of limits of minimum and maximum force in kN and displacement in mm. In practice these limits are set on the control console of the Instron (See **A2.7.2**).

Quit — This terminates the !ROCKDEF program.

Data window: In the top row of the *Data* window numerical outputs of the different channels in milliVolts are recorded in a series of coloured boxes together with the current date and time. From left to right the boxes display displacement, external force gauge, internal force gauge, temperature, confining pressure and pore pressure channels. The second row shows real-time re-calculations of channel outputs in terms of their relevant SI units, rather than mV.

The third and fourth row contain 16 function buttons that enable control of the gas rig via the IEEE bus interface. Functions on the *Data* window are selected by clicking the left hand button on the mouse while the mouse arrow is perched on top of the relevant box. Activities are terminated by re-clicking the relevant box. The box will change colour to indicate that it has been selected on the data panel. The various buttons have the following functions:

M-up: This activates the actuator resulting in compressive movement of the piston (compare with **Appendix 1**).

M-down: Causes the lower piston to be lowered, resulting in extensional movement.

Logger — When this function is activated incoming data is stored in the buffer. On deactivation the data is only displayed on the *Graphic* window but is irrevocably lost when the screen is reset. Usually, the logger is only activated during the actual stress-strain and stress-relaxation part of the experiment, not in the period of heating to test temperature and equilibration time. Logging rates are determined by inserting the relevant time interval in seconds in the log time section of the menu.

Select — This function is used in data processing after termination of the test. It enables selection of points on the mV versus record number chart to be selected. By selecting **REC** in the *Graphics* window points on the internal force gauge trace can be selected, with data corresponding to the chosen record number of all channels transferred to a DAT file. The left hand mouse button creates a red point on the trace and identifies stress-

strain data while the left hand button creates cyan spots that identify stress relaxation data. By de-selecting the **REC** and **Select** buttons a marker is inserted that terminates the processing function. Both buttons have to be de-selected immediately after the termination of data selection.

Load-on This function is used to initiate real-time data processing. By selecting a point on the internal force gauge curve to signify conditions prior to specimen deformation, this point is taken as a starting point for on-line data processing.

LimLock This button was written into the program to allow the settings of force and displacement limits. Once these limits are breached they will override actuator movements and in effect terminates the program. In practice, it proved easier to set the limits on the control console of the Instron (**Figure A1.01**).

Creep If a constant stress deformation is set to be below 1000 MPa on the menu and the **Creep** button is activated the chosen stress is induced, until the creep function is deactivated.

LogHold If there is any need to stop the logging process in the middle of a test run, without resetting the record number back to zero **LogHold** can be activated. In practice this function was not used, as it was more convenient to increase the logging time to a sufficiently high value, hence enabling a very limited but sufficient control on the test during a duration of relative inactivity.

Load fn After termination of a test, the DAT file containing all milliVolt outputs from all channels can be imported back into the !ROCKDEF program. The appropriate filename is entered into the parameter section of the menu and the information is loaded when the **Load fn** button is activated.

Process Following the selection of suitable data from a stored DAT file and after de-selecting the **Select** and **Rec** buttons the data is processed by clicking on the **Process** button.

Clear This clears an array containing DAT values.

Append Occasionally it becomes necessary to join two data files belonging to the same test, for example if the gas rig and associated Instron computer

crashed during the test run. The first part of the test is loaded in the usual way using **Load fn** facilities, clicking the **Append** button will allow other data to be added.

FileSave This facility saves accumulated data as a DAT file. If constantly activated, the function will automatically save accumulated data approximately every 5 minutes.

Selsave On commencing data processing, the selected data is stored in a DATs file that contains both milliVolt outputs of selected channels and corrected results in SI units.

ScrnSave This creates a screen dump, saved as a *Sprite* file (**Figure A7.01**).

Track During stress relaxation, this function makes the external force track the internal force trace using a cycling motion on the actuator, causing an effective shortening of the relaxing axial column length and increasing the stiffness of the machine. This results in a more effective stress relaxation of the specimen. This function was not available during research for the present thesis.

Graphics window: The data is displayed in terms of milliVolt output versus record number. Only channels previously selected on the data panel are displayed once the screen is reset by activating the **Graph set**. Data points for post run data processing are selected on the trace by clicking **Select** on the data window and **REC** in the bottom left corner of the *Graphic* window.

A7.3 Data acquisition

This section considers the procedures in the !Rockdef program responsible for the data acquisition. The procedures necessary to accumulate data and save it are described. Numbers after the procedure headings relate to the relevant line numbers from the program listing (**Appendix 8**).

PROC adr (10 - 1120): This is the first routine in the program and starts to initialise the following 6 proceedings, setting up communication with the Gas Rig via Instron and

DVM (see section **A2.7.2** for connections). It also includes the screen setup and the poling loop. Default values for the graph setup and log rates are set.

PROC initialise IEEE (6340 - 6410): Contact to the IEEE bus interface is established in this loop that links the Archimedes computer to the Instron.

PROC take control (6430 - 6570): This procedure transfers control from the Instron control console (**A2.7.2**) to the computer. It is necessary to activate the remote control button on the Instron control panel to enable implementation of this procedure and other gas rig control functions. The Instron watchdog and bus interrupt requests are disabled. The emergency stop is reset and the actuator is switched on. To reverse this procedure the sequence PROC return_control is activated at the end of the program.

PROC setup (6790 - 7002): This procedure collects the buffer of the three Instron channels that get filled every second and store the output in binary code in the memory. Thus it forms the link between the Instron Computer Housing and the "remote" computer.

PROC createinfobox (490 - 895): In this section of PROC adr (**A4.3.11**) the menu functions and boxes displayed in the data panel are set. The size and lettering in the boxes are defined. Procedures that relate to functions enabled by activating these buttons are listed in program lines between 7810 and 11960.

PROC poll (1000 - 1120): This procedure acquires data after a set time interval has passed. The poling loop, line 920 to 940 addresses each task in turn with a serial adjustment. The graphics and numerical displays are updated by redrawing them, using PROC redraw and PROC buttons. The timer is reset and the Instron is instructed to start its data collection sequence. This poling sequence is repeated once the logging time has elapsed. Also the screen is redrawn if buttons in the display are pressed by responding to line 1070 command (or when a menu is pulled down line 1090 takes effect, activating PROC menuselect). If no functions are activated during the time span of the loop the background task of data acquisition is carried out via the WHEN 0: statement in line 1030.

PROC getdata (11975 - 12090): This procedure acquires data from all channels of the IEEE bus interchange and the DVM (**A2.7.1**). Data from Instron and DVM output are assigned to different channels, which are saved to a DAT file as in the PROC filesave procedure.

PROC update_displays (12110 - 12270): In this procedure the acquired data is allocated and displayed in different coloured boxes on the menu-bar of the screen.

PROC grafupdate (12280 - 12550): PROC grafupdate produces real-time milliVolt versus time plots of any channel outputs selected in the top row of buttons in the *Data* window.

PROC filesave (12860 - 12980): All data acquired in PROC getdata (**A4.3.7**) are saved as a single sequential data file (DAT file). The data are formatted in eight columns with up to 5000 rows. The columns record following data:

1. Displacement
2. Internal load cell
3. External load cell
4. Temperature
5. Pressure
6. Time
7. Marker
8. Pore pressure

The marker column signifies the beginning and end of the logging cycle. It has an allocated value of zero when the logger is deactivated, that changes to the value one as logging commences. The logging is terminated when the marker changes its value to two. This DAT file is then stored automatically under the filename entered previously, and can be recalled for data processing at a later date.

PROC loader (13100 - 13210): I this procedure, data previously stored in the DAT file are imported into the !Rockdef program to allow real time processing, as well as data manipulation after the termination of the test run.

PROC convert_time (13230 - 13320): Beside storing the data output from the 8 channels in the DAT sheet, an indication of time is included. This is achieved by converting the output from the computer clock into an 8 digit number, where the two digits furthest to the left mark the month, the next day, followed by hour, minute and second relating to the time the data were recorded. The process is reversed during data processing by the procedure PROC seconds (**A7.4.2**).

A7.4 Real time data processing

Real-time data processing has no data storage facility but converts mV inputs from the different channels into relevant SI units. (see **Appendix 10**). It further uses a sub-program called PROC seconds to convert record numbers into time. All procedures described

below are repeated during each poling loop. As in the data acquisition section (**A3.3.1**), bracketed numbers following procedure names relate to the line numbers in the program.

PROC realtimeprocess (17300 - 17450): PROC realtimeprocess sets the force gauge zero as the value set by the **Load-on** button in the *Data* window. Length and diameter of the sample are imported from values set in the sub-proceedure **Set param** in the !ROCKDEF icon menu. A default of 20 mm length and 10 mm diameter is set. Consequent force gauge readings are subtracted from the force gauge zero and the resultant milliVolt reading is recalculated to express the force in kN by applying a second order polynomial conversion fit to force / mV conversion data (**Appendix 2**).

Displacement of the pistons at the record number selected by the **Load-on** is set as zero. Subsequent specimen displacement values are calculated by subtracting the machine displacement from the total recorded displacement. Strain on the sample is calculated by dividing displacement by the initial specimen length and multiplying the result by 100 to give percentage. No jacket correction was carried out in this procedure. Finally stress is calculated by the following formula:

$$\text{stress} = \frac{\text{strain}}{100} * \text{initial sample diameter} \qquad \text{EA7.01}$$

This denominator corrects the initial area for the change resulting from the axial specimen strain, assuming that the deformation is homogeneous and at constant volume.

PROC seconds (15060 - 15270): This procedure converts record numbers into elapsed time in seconds. Time is stored as a 8 digit number where the first two digits correspond to the month, the second two digits to day, the third pair to hour, the fourth pair to minutes and the last two digits to seconds. This number is split into its component pairs which are then recalculated to give a value of seconds by multiplying minutes by 60, hours by 3600, days by 86400. A value for the month is added in seconds. If - then statements allocate a number of seconds to corresponding months, depending on the number of days it contains. No allowance is made for leap years.

A7.5 Post test data processing

After completing a test run on the gas rig, it is possible to use !ROCKDEF to calculate stress,strain and strain rate.The data stored during the test, as a serial.DAT file, is recalled via the PROC loader (**A4.3.11**) procedure. The data is displayed on the graphics panel

and data points are selected by mouse. The following procedures are necessary for the data processing:

PROC find rec (14335 - 14500): This procedure converts coordinates selected on the screen to corresponding record numbers and places them into a text file, called DATS, where they are processed. The data is transferred from the DAT file into the DATS file without retaining a copy of the chosen record number channel data in the original file. It is the DATS which is operated on by the procedures PROC process_data (**A4.5.2**), PROC stresstrainloop (**A4.5.3**) and PROC relax (**A4.5.4**) which are described below.

PROC process_data (15300 - 15480): Once the process button is activated on the data panel on the screen (**A4.2.2**) this procedure comes into action. It takes the first point selected on the mV / record number trace to be the value of force gauge zero prior to the onset of deformation. It uses the length information entered and converts diameter measurements into cross section area for the specimen. Using the procedure PROC seconds (**A4.4.2**) it calculates the start time in seconds and sets this as zero. The counter is set to repeat the stress-strain loop until the marker indicates that the next point relates to stress relaxation. The relaxation loop now takes over until either the marker indicates another loading event, in which case the stress-strain loop is repeated, or the marker indicates the end of the processable data. In this case the data is saved as a text file. this file is stored under the same name as the original DAT file and can consequently be imported into spreadsheets and drawing packages.

PROC stresstrainloop (15500 - 15770): This procedure calculates the force exerted on the specimen by subtracting the value at any record number from force gauge zero. It converts a temperature reading from mV into °C and applies a scaling factor to the hydrostatic and pore pressure readings to convert them from mV to MPa. Force gauge readings are converted by using the calibration data. This is done by applying a suitable second order polynomial that is the best fit to the calibration data. These include the following:

1. Machine stiffness by applying a quadratic equation that is temperature and force dependent (**Appendix 2**).

2. Elapsed time is calculated by using PROC seconds (**A4.4.2**).

3. Displacement rate by subtracting machine position from the starting displacement.

4. Strain in the sample is taken to equal elapsed time multiplied by the displacement rate. The strain rate therefore equals the elapsed displacement.

A jacket correction is carried out at a later date in the spreadsheet as the calibration data has not been incorporated into the data to date. As strain and force are now known it is possible to calculate stress by adjusting the cross-section of the specimen to take account of the shape change with increasing strain. Assuming that strain took place homogeneously, the stress can be calculated by:

$$\text{stress} = \frac{\text{force (N)}}{\text{cross section area}} - \text{jacket correction} \qquad \text{EA7.02}$$

PROC relax (15800 - 16100): All parameters are calculated in the same way as in the stress-strain loop with output data again assigned to the DATs file. Stress and strain are calculated for adjacent points and the stress drop between those two points is evaluated. By knowing the specimen stiffness it is possible to recalculate the stress drop in the time interval between the two recordings of data as strain suffered by the sample. A strain rate can thus be calculated.

PROCsavetextfile (14910 - 15040): This final procedure saves the processed data as a text file called DATS that can be displayed as a spreadsheet with 16 columns and rows relating to chosen record numbers. A maximum of 500 sets of data can be processed for each test run. Columns are from left to right:

First row:
- filename
- length of sample
- diameter of sample
- Displacement rate

Second row:
- Displacement
- External force gauge
- Internal force gauge
- Temperature in mV
- Hydrostatic pressure in mV
- Time in seconds
- Pore pressure in mV
- Marker
- T in °C
- Pressure in MPa
- Pore pressure in MPa
- Strain %
- Stress MPa
- Strain rate
- Strain rate per second

Stress in MPa.

In **Appendix 10** the DATS columns for deviatorically deformed samples WG2 to WG30 are displayed. However, milliVolt outputs have been removed for convenience of display.

Appendix 8

!Rockdef program

A8.1 Introduction

In this appendix the program !Rockdef is listed. The functions of this program and sub-routines are discussed in **Appendix 7**.

A8.2 Listing of program

```
5 REM LAST MODIFIED 8 FEB 1993 (REVISION OF MF TO 1/1.106, INSTRON RAMP LIMITS TO 35%, PH2O
      CALIB)
6 REM MODIFIED 22 MAY 1993 TO ALLOW FOR TWEAKING OF CREEP CONTROL PARAMETERS
7REM MODIFIED 11 OCT 1993 FOR ENTIRELY IEEE LOGGING
10 GOTO20
15PROCIOSET("01234567"):REM SET ALL USER PORT BITS TO OUTPUT
16PROCON(0):PROCON(1):PROCON(2):PROCON(3):PROCON(4):PROCON(5):PROCON(6):PROC
      ON(7)
20DIM nr% 4
30DIM BITSET(8)
40DIM buffer(20,3)
45DIM pointer% 250
50KN=0
52selector%=0:append%=0
53INPUT"data logging (any key) or processing only (1)";SS$
55IF SS$="1" selector%=1:GOTO 90
60PROCinitialise_IEEE
70PROCtake_control
75PROCsetup
77PROCadrandoutput(0,15,"C900,100"):REMset update time interval to 0.1 s
84REM enable all channels for control
 85PROCadrandoutput(0,15,"C312,1,1")
86PROCadrandoutput(0,15,"C312,2,1")
87PROCadrandoutput(0,15,"C312,3,1")
90TIME=0
95PROCpremaset
110DIM block% &200, menu% &100, menu2% &100, menu3% &100, menu4% &100
120DIM DAT(5000,8),Y(8),DATs(500,15)   125FOR I%=0 TO 5000:DAT(I%,7)=0:NEXT
130FOR I%=1 TO 8:Y(I%)=99.99:NEXT I%
140FOR I%=1 TO 500:DATs(I%,8)=0:NEXT
150KNT%=0
155CLOSE#0
160DTA=0:G=0:`CONVX=0:`X=0:motorUP%=0:motorDN%=0:relax%=0:selstart%=0:serdat=0:TM=0:pro
      cess%=0:printer%=0:Nrecs%=0:sKNT%=0:Prec%=0:zerorec%=0:xpos%=0:ypos%=0:hitpoint%=0:l
      oaded%=0:rtprocess%=0
170REM Enter default values of variables
180DIM text1% &20:$text1%="0"
190DIM text2% &20:$text2%="500"
200DIM text3% &20:$text3%="0"
210DIM text4% &20:$text4%="100"
220DIM text5% &20:$text5%=".01"
230DIM text6% &20:$text6%="-4"
240DIM text7% &20:$text7%="1000"
```

```
250DIM text8% &20:$text8%="20"
260DIM text9% &20:$text9%="10"
270DIM text10% &20:$text10%="Noname"
280DIM text11% &20:$text11%="6"
290DIM text12% &20:$text12%=LEFT$(STR$(Y(1)),7)
300DIM text13% &20:$text13%=LEFT$(STR$(Y(2)),7)
310DIM text14% &20:$text14%=LEFT$(STR$(Y(3)),7)
320DIM text15% &20:$text15%=LEFT$(STR$(Y(4)),7)
330DIM text16% &20:$text16%=LEFT$(STR$(Y(5)),7)
340DIM text17% &20:$text17%=LEFT$(STR$(Y(6)),7)
342DIM text18% &20:$text18%=".01"
343DIM text19% &20:$text19%=".1"
344DIM text20% &20:$text20%=".15"
345DIM text21% &20:$text21%="1"
346DIM text22% &20:$text22%="Rec"
348initsp$=$text18%:dead1=VAL($text18%):dead2=VAL($text20%):multip=VAL($text21%)
350ONERROR PROCerror:END
360SS$="":txt$="":Buffer%=0:RecNo%=0:SIG=0:TM=0:P=0:PH2O=0:cfg%=0:Filename$="Noname":inter
      val=600:time2%=TIME+interval:GJK%=0:STRMPA=0:TSTRAIN=0:EDOT=0
370REM  set all lconstate flags to zero
380motor%=0:logger%=0:loadon%=0:zeroset%=0:loadfn%=0:clear%=0:filesave%=0:scrnsave%=0:y1
      %=0:y2%=0:y3%=0:y4%=0:y5%=0:y6%=0:choice%=0:choice2%=0:clg%=0:constd%=1:constE%
      =0:constS%=0
390reason%=-1:chan%=0:Zflag%=0:BUFSIZ=128:BUFCNT=0
392maxf=50:minf=-10:maxd=-44:maxd=-25
393MF=1/1.106:fgofset=0:REM internal fg zero error
394track%=0:trakflag%=0:creep%=0:creepflag%=0:strcon=1000:SIG=0:lok%=0
395IF selector%=1 GOTO 400 ELSE PROCinstr_start
400quit%=FALSE
410 x0%=0:y0%=0:`SX=VAL($text1%):`SY=VAL($text3%): `LX= VAL ($text2%): `LY=VAL($text4%)
      420time%=TIME+300:time3%=TIME:time4%=TIME  430REM INITIALISE WIMP
440$block%="TASK"
450KNT%=0
460SYS "Wimp_Initialise",200,!block%,"TEST" TO version%,task%
470REM CREATE WINDOW
480i4handle%=FNicon(-2,0,0,68,68,&3002,"!rocdef",0,0,0)
490 PROCcreateinfobox
500PROCcreatedialogbox1("min X RecNo")
510PROCcreatedialogbox2("max X RecNo")
520PROCcreatedialogbox3("min Y mV")
530PROCcreatedialogbox4("max Y mV")
540PROCcreatedialogbox5("enter mm/min")
550PROCcreatedialogbox6("enter n/sec")
560PROCcreatedialogbox7("enter MPa")
570PROCcreatedialogbox8("Length in mm")
 580PROCcreatedialogbox9("Dia in mm")
590PROCcreatedialogbox10("Filename")
600PROCcreatedialogbox11("LogRate (sec)")
 602PROCcreatedialogbox18("Initial d-rate")
603PROCcreatedialogbox19("deadband1(kN)")
 604PROCcreatedialogbox20("deadband2(kN)")
605PROCcreatedialogbox21("Multiplier")
610PROCdrawmenu(menu%,"Menu,Info,SetGraph,SetParam,SetLog,CrpSet,Quit")
620PROCdrawmenu(menu2%,"SetGraph,minX,maxX,minY,maxY")
630PROCdrawmenu(menu3%,"SetParam,constD,constE,constS,Length,Diam,Filename")
632PROCdrawmenu(menu4%,"Crpset,Ini-rate,deadbnd1,deadbnd2,multip")
640 menu%!32=ibhandle%
650menu%!(32+24)=menu2%
660menu2%!(32)=dialogbox1%:menu2%!(32+24)=dialogbox2%
670menu2%!(32+48)=dialogbox3%:menu2%!(32+72)=dialogbox4%
680menu%!(32+48)=menu3%
690menu3%!(32)=dialogbox5%:menu3%!(32+24)=dialogbox6%
700menu3%!(32+48)=dialogbox7%:menu3%!(32+72)=dialogbox8%
710menu3%!(32+96)=dialogbox9%:menu3%!(32+120)=dialogbox10%
715menu%!(32+96)=menu4%
716menu4%!(32)=dialogbox18%:menu4%!(32+24)=dialogbox19%
717menu4%!(32+48)=dialogbox20%:menu4%!(32+72)=dialogbox21%
720menu%!(32+72)=dialogbox11%
730whandle%=FNcreate(20,450,2000,1600,0,0,&FF00000F,"Graphics")
```

```
734@%=&20105
735dahandle%=FNcreate(10,110,1200,180,0,0,&84000002,"Data")
740i1handle%=FNicon(dahandle%,10,-130,140,48,&800B43D,"M-up",0,0,0)
745i1ahandle%=FNicon(dahandle%,10,-180,140,48,&800B43D,"M-down",0,0,0)
750i2handle%=FNicon(dahandle%,160,-130,140,48,&800B43D,"Logger",0,0,0)
755i2ahandle%=FNicon(dahandle%,160,-180,140,48,&800B43D,"Select",0,0,0)
760i3handle%=FNicon(dahandle%,310,-130,140,48,&800B43D,"Load-on",0,0,0)
765i3ahandle%=FNicon(dahandle%,310,-180,140,48,&800B43D,"LimLock",0,0,0)
770i4handle%=FNicon(dahandle%,460,-130,140,48,&800B43D,"Creep",0,0,0)
775i4ahandle%=FNicon(dahandle%,460,-
        180,140,48,&800B43D,"LogHold",0,0,0)780i5handle%=FNicon(dahandle%,610,-
        130,140,48,&800B43D,"Load fn",0,0,0)
785i5ahandle%=FNicon(dahandle%,610,-180,140,48,&800B43D,"Process",0,0,0)
790i6handle%=FNicon(dahandle%,760,-130,140,48,&800B43D,"Clear",0,0,0)
795i6ahandle%=FNicon(dahandle%,760,-180,140,48,&800B43D,"Append",0,0,0)
800i7handle%=FNicon(dahandle%,910,-130,140,48,&800B43D,"FileSave",0,0,0)
805i7ahandle%=FNicon(dahandle%,910,-180,140,48,&800B43D,"SelSave",0,0,0)
810i8handle%=FNicon(dahandle%,1060,-130,140,48,&800B43D,"ScrnSave",0,0,0)
820i8ahandle%=FNicon(dahandle%,1060,-180,140,48,&800B43D,"Track",0,0,0)
840Y1handle%=FNicon(dahandle%,400,-42,120,42,&B00B53D,"",text12%,-1,&20)
850Y2handle%=FNicon(dahandle%,530,-42,120,42,&A00B53D,"",text13%,-1,&20)
860Y3handle%=FNicon(dahandle%,660,-42,120,42,&800B53D,"",text14%,-1,&20)
870Y4handle%=FNicon(dahandle%,790,-42,120,42,&900B53D,"",text15%,-1,&20)
880Y5handle%=FNicon(dahandle%,920,-42,120,42,&F00B53D,"",text16%,-1,&20)
890Y6handle%=FNicon(dahandle%,1050,-42,120,42,&E00B53D,"",text17%,-1,&20)
895Y7handle%=FNicon(whandle%,50,-1550,180,48,&B00B53D,"",text22%,-1,&20)
900REM WIMP POLL
910ONERROR IF FNwimperror THEN END
920REPEAT
930PROCpoll
940UNTIL quit%
950$block%="TASK"
960SYS "Wimp_CloseDown",task%,!block%
970END
980REM
990:
1000DEFPROCpoll
1010SYS "Wimp_Poll",,block% TO reason%
1020CASE reason% OF
1030WHEN 0:IF TIME>=time%THEN PROCgetdata:SYS"Wimp_ForceRedraw",dahandle%,0,-
        42,400,0:PROCupdate_displays:time%=TIME+100:PROCinstr_start
1040WHEN 1 :PROCredraw
1050WHEN 2 :SYS "Wimp_OpenWindow",,block%
1060WHEN 3 :SYS "Wimp_CloseWindow",,block%
1070WHEN 6:PROCbuttons
1080WHEN 8:SYS "Wimp_ProcessKey",block%!24
1090WHEN 9:PROCmenuselect
1100WHEN 17,18:PROCreceive
1110ENDCASE
1120ENDPROC
1130:
1140DEFFNcreate(vwx%,vwy%,vww%,vwh%,extx%,exty%,flags%,title$)
1150$block%=STRING$(88,CHR$0):REM CLR VISIBLE WORKAREA
1160block%!0=vwx%
1170block%!4=vwy%
1180block%!8=vwx%+vww%
1190block%!12=vwy%+vwh%
1200block%!24=-1
1210block%!28=flags%
1220REM WINDOW COLORS
1230block%?32=7
1240block%?33=2
1250block%?34=7
1260block%?35=1:REM work area background color
1270block%?36=3
1280block%?37=1
1290block%?38=12
1300REM WORK AREA EXTENT
1310block%!40=0
```

```
1320block%!44=-vwh%-exty%
1330block%!48=vww%+extx%
1340block%!52=0
1350block%!56=&3D:REM TITLE ICON FLAGS
1360block%!60=3<<12
1370$(block%+72)=title$
1380SYS "Wimp_CreateWindow",,block% TO handle%
1390=handle%
1400:
1410DEFPROCredraw
1420handle%=block%!0
1430SYS "Wimp_RedrawWindow",,block% TO more%
1440PROCgetorigin(block%,x0%,y0%)
1450WHILE more%
1460 IF handle%=whandle% AND process%=0 THEN PROCdraw(x0%,y0%)
1465REM IF handle%=whandle% AND process%=1 THEN PROClistout:process%=0
1470IF handle%=ibhandle% THEN PROCdraw2(x0%,y0%)
1480IF handle%=dahandle% THEN PROCdraw3(x0%,y0%)
1490SYS "Wimp_GetRectangle",,block% TO more%
1500ENDWHILE
1510ENDPROC
1520DEFPROCgetorigin(block%,RETURN x0%, RETURN y0%)
1530x0%=block%!4-block%!20
1540y0%=block%!16-block%!24
1550ENDPROC
1560:
1570DEFPROCdraw(x0%,y0%)
1580CLS:MOVE x0%+100,y0%-50
1590PROCplotit
1600SYS "Wimp_SetColour",10
1610ENDPROC
1620:
1630DEFPROCclose
1640$block%="TASK"
1650SYS "Wimp_CloseDown",task%,!block%
1652PROCadrandoutput(0,15,"C316,1"):REM STOP DATA COLLECTION
1653PROCadrandoutput(0,15,"C316,0"):REM DATA COLLECTION OFF
1655PROCreturn_control
1660ENDPROC
1670:
1680DEFPROCerror
1690ON ERROR OFF
1700$block%="TASK"
1710SYS "Wimp_CloseDown",task%,!block%
1720PRINT REPORT$;" at line ";ERL
1725PROCFIN
1730ENDPROC
1740:
1750DEFFNwimperror
1760!block%=ERR
1770$(block%+4)=REPORT$+" at line "+STR$ERL+CHR$0
1780SYS "Wimp_ReportError",block%,3,"TEST WINDOW" TO ,response%
1790IF response%=2 THEN PROCclose:=TRUE ELSE =FALSE
1800:
1810:
1820DEFFNicon(whandle%,ix%,iy%,iw%,ih%,flag%,text$,d1%,d2%,d3%)
1830block%!0=whandle%
1840block%!4=ix%:block%!8=iy%
1850block%!12=ix%+iw%
1860block%!16=iy%+ih%
1870block%!20=flag%
1880IF d1%=0 THEN
1890$(block%+24)=text$
1900ELSE
1910block%!24=d1%:block%!28=d2%
1920block%!32=d3%
1930ENDIF
1940SYS "Wimp_CreateIcon",,block% TO ihandle%
1950=ihandle%
```

```
1960DEFPROCPath_GetDetails(p%)
1970LOCAL ends%
1980Path_fcol%=!p%
1990Path_lcol%=p%!4
2000Path_thick%=(p%!8)*ObjMod_fac
2010ends%=(o%!12)
2020?ObjMod_cj%=ends% AND 3
2030ObjMod_cj%?1=(ends%>>2 AND 3)
2040ObjMod_cj%?2=(ends%>>4 AND 3)
2050ObjMod_cj%?3=0
2060ObjMod_cj%!4=&30000
2070ObjMod_cj%!8=(ends%>>16)<<4
2080ObjMod_cj%!10=(ends%>>24)<<4
2090ObjMod_cj%!12=ObjMod_cj%!8  2100Path_strst%=p%+16
2110IF ends%>>7 AND 1 THEN
2120Path_pat%=Path_strst%
2130Path_strst%=Path_strst%+(Path_pat%!4+2)*$
2140ELSE
2150Path_pat%=0
2160ENDIF
2170IF (ends%>>6)AND 1 THEN Path_wind%=&32 ELSE Path_wind%=&30
2180ENDPROC
2190:
2200DEFPROCopenwindow(handle%)
2210block%!0=handle%
2220SYS "Wimp_GetWindowState",,block%
2230SYS "Wimp_OpenWindow",,block%
2240ENDPROC
2250:
2260DEFPROCbuttons
2270x%=block%!0:y%=block%!4
2272 IF block%!12=whandle% AND block%!16=Y7handle% SOUND 1,-
        15,70,4:PROCupdate(whandle%,Y7handle%):selstart%=Iconstate%:relax%=0:GOTO 2278
2273SYS"Wimp_GetPointerInfo",,block%:IF block%!8=1 relax%=1:SOUND 1,-15,150,4
2275IF selector%=1 AND block%!12=whandle% AND RecNo%>2 AND selstart%=1 PROCfind_rec
2276IFblock%!12=whandle% AND RecNo%>2 AND selstart%=0 PROCshowrec
2277GOTO 2280
2278IF selstart%=0 DATs(sKNT%,8)=4
2279Nrecs%=sKNT%:sKNT%=2  2280CASE TRUE OF
2290WHEN block%!12=-2
2300IFblock%!8 AND 2 THEN
2310 PROCshowmenu(menu%,x%,y%,TRUE,3)  2330ELSE IF block%!8 AND 5 THEN
        PROCopenwindow(whandle%):PROCopenwindow(dahandle%)
2340ENDIF
2345REM  IF ARGUMENT OF motor-on() IS +VE MOTOR GOES UP, IF -VE GOES DOWN
2350 WHEN block%!12=dahandle% AND block%!16=i1handle% :SOUND 1,-
        15,70,4:PROCupdate(dahandle%,i1handle%):motorUP%=Iconstate%:IF motorUP%=1 AND
        motorDN%=0 PROCmotor_on(1) ELSE PROCmotor_off:ENDCASE
2355 WHEN block%!12=dahandle% AND block%!16=i1ahandle% :SOUND 1,-
        15,70,4:PROCupdate(dahandle%,i1ahandle%):motorDN%=Iconstate%:IF motorDN%=1 AND
        motorUP%=0 PROCmotor_on(-1) ELSE PROCmotor_off:ENDCASE
2360 WHEN block%!12=dahandle% AND block%!16=i2handle% :SOUND 1,-
        15,70,4:PROCupdate(dahandle%,i2handle%):logger%=Iconstate%:IF logger%=1
        RecNo%=1:ENDCASE
2365 WHEN block%!12=dahandle% AND block%!16=i2ahandle% :SOUND 1,-
        15,70,4:PROCupdate(dahandle%,i2ahandle%):selector%=Iconstate%:ENDCASE
2370 WHEN block%!12=dahandle% AND block%!16=i3handle% :SOUND 1,-
        15,70,4:PROCupdate(dahandle%,i3handle%):loadon%=Iconstate%:IF loadon%=1AND
        Prec%>0 PROCmarkzero:ENDCASE
2375 WHEN block%!12=dahandle% AND block%!16=i3ahandle% :SOUND 1,-
        15,70,4:PROCupdate(dahandle%,i3ahandle%):limits%=Iconstate%:IF limits%=1
        PROCset_limits ELSE PROCunset_limits:ENDCASE
2380 WHEN block%!12=dahandle% AND block%!16=i4handle% :SOUND 1,-
        15,70,4:PROCupdate(dahandle%,i4handle%):creep%=Iconstate%:strcon=VAL($text7%)
2385 WHEN block%!12=dahandle% AND block%!16=i4ahandle% :SOUND 1,-
        15,70,4:PROCupdate(dahandle%,i4ahandle%):loghold%=Iconstate%:IF loghold%=1
        logger%=0 ELSE logger%=1:ENDCASE
```

```
2390 WHEN block%!12=dahandle% AND block%!16=i5handle% :SOUND 1,-
     15,70,4:PROCupdate(dahandle%,i5handle%):loadfn%=lconstate%:IF loadfn%=1
     PROCloader:ENDCASE
2395 WHEN block%!12=dahandle% AND block%!16=i5ahandle% :SOUND 1,-
     15,70,4:PROCupdate(dahandle%,i5ahandle%):process%=lconstate%:IF process%=1
     PROCprocess_data:ENDCASE
2400 WHEN block%!12=dahandle% AND block%!16=i6handle% :SOUND 1,-
     15,70,4:PROCupdate(dahandle%,i6handle%):clear%=lconstate%:IF clear%=1
     PROCresetarray:ENDCASE
2405 WHEN block%!12=dahandle% AND block%!16=i6ahandle% :SOUND 1,-
     15,70,4:PROCupdate(dahandle%,i6ahandle%):append%=lconstate%:ENDCASE
2410 WHEN block%!12=dahandle% AND block%!16=i7handle% :SOUND 1,-
     15,70,4:PROCupdate(dahandle%,i7handle%):filesave%=lconstate%:IF filesave%=1
     PROCfilesave:ENDCASE
2415 WHEN block%!12=dahandle% AND block%!16=i7ahandle% :SOUND 1,-
     15,70,4:PROCupdate(dahandle%,i7ahandle%):selsave%=lconstate%:IF selsave%=1 AND
     selector%=1 PROCsavetextfile:ENDCASE
2420 WHEN block%!12=dahandle% AND block%!16=i8handle% :SOUND 1,-
     15,70,4:PROCupdate(dahandle%,i8handle%):scrnsave%=lconstate%:IF scrnsave%=1
     PROCscrnsave:ENDCASE
2425 WHEN block%!12=dahandle% AND block%!16=i8ahandle% :SOUND 1,-
     15,70,4:PROCupdate(dahandle%,i8ahandle%):track%=lconstate%:ENDCASE  2430 WHEN
     block%!12=dahandle% AND block%!16=Y1handle% :SOUND 1,-15,70,4:IF y1%=0 THEN y1%=1
     ELSE IF y1%=1 THEN y1%=0:ENDCASE
2440 WHEN block%!12=dahandle% AND block%!16=Y2handle% :SOUND 1,-15,70,4:IF y2%=0 THEN
     y2%=1 ELSE IF y2%=1 THEN y2%=0:ENDCASE
2450 WHEN block%!12=dahandle% AND block%!16=Y3handle% :SOUND 1,-15,70,4:IF y3%=0 THEN
     y3%=1 ELSE IF y3%=1 THEN y3%=0:ENDCASE
2460 WHEN block%!12=dahandle% AND block%!16=Y4handle% :SOUND 1,-15,70,4:IF y4%=0 THEN
     y4%=1 ELSE IF y4%=1 THEN y4%=0:ENDCASE
2470 WHEN block%!12=dahandle% AND block%!16=Y5handle% :SOUND 1,-15,70,4:IF y5%=0 THEN
     y5%=1 ELSE IF y5%=1 THEN y5%=0:ENDCASE
2480 WHEN block%!12=dahandle% AND block%!16=Y6handle% :SOUND 1,-15,70,4:IF y6%=0 THEN
     y6%=1 ELSE IF y6%=1 THEN y6%=0:ENDCASE
2500ENDCASE
2510ENDPROC
2520:
2530REM DEFPROCdrawmenu(m%,menu$,x%,y%,oniconbar%)
2540 DEFPROCdrawmenu(menu%,menu$)
2550menu%?12=7:menu%?13=2
2560menu%?14=7:menu%?15=0
2570menu%!16=140:menu%!20=44
2580menu%!24=0:ptr%=menu%+28
2590$menu%=LEFT$(menu$,INSTR(menu$,",")-1)  2600menu$+=","
2610entries%=0
2620WHILE menu$<>""
2630menu$=MID$(menu$,INSTR(menu$,",")+1)  2640IF menu$<>"" THEN
2650SM$=LEFT$(menu$,INSTR(menu$,",")-1)
2660!ptr%=0
2670PROCpointer
2680ptr%!4=-1
 2690ptr%!8=&7000021
2700$(ptr%+12)=SM$
2710ptr%+=24
2720entries%+=1
2730ENDIF
2740ENDWHILE
2750ptr%!-24=ptr%!-24 OR &80:REM mark item as last
2760ENDPROC
2770:
2780DEFPROCshowmenu(menu%,x%,y%,oniconbar%,entries%)
2790IF oniconbar% THEN ypos%=96+entries%*44 ELSE ypos%=y%+20
2800SYS "Wimp_CreateMenu",,menu%,x%-64,ypos%
2810ENDPROC
2820:
2830DEFPROCmenuselect
2840choice%=!block%
2850choice2%=block%!4
```

```
2860IF choice%=2 AND choice2%=0
      THEN:constd%=1:constE%=0:constS%=0:PROCdrawmenu(menu3%,"SetParam,constD,constE
      ,constS,Length,Diam,Filename"):ENDIF
2870IF choice%=2 AND choice2%=1
      THEN:constE%=1:constd%=0:constS%=0:PROCdrawmenu(menu3%,"SetParam,constD,constE
      ,constS,Length,Diam,Filename"):ENDIF
2880IF choice%=2 AND choice2%=2
      THEN:constS%=1:constd%=0:constE%=0:strcon=VAL($text7%):incfrac=0:lok%=0:PROCdrawm
      enu(menu3%,"SetParam,constD,constE,constS,Length,Diam,Filename"):ENDIF
2890IF choice%=2 PROCmenu3boxes
2900 IF choice%=1 THEN `SX=VAL($text1%):`SY=VAL($text3%):`LX=VAL($text2%):`LY=VAL($text4%)
2910IF choice%=1 THEN SYS"Wimp_ForceRedraw",whandle%,0,-1600,2000,0:choice%=-1
2920IF choice%=2 THEN
      disrate%=VAL($text5%):edot=VAL($text6%):constress=VAL($text7%):len=VAL($text8%):dia=V
      AL($text9%):Filename$=$text10%:choice%=0
2930IF choice%=3 THEN lograte%=VAL($text11%):choice%=0:interval=lograte%*100
2935IF choice%=4 THEN
      initsp$=$text18%:dead1=VAL($text18%):dead2=VAL($text20%):multip=VAL($text21%)
2940IF choice%=5 THEN quit%=TRUE
2950IF NOT quit% THEN
2960SYS "Wimp_GetPointerInfo",,block%
2970cfg%=1
2980IF block%!8=1 THEN PROCshowmenu(menu%,x%,y%,TRUE,3)
2990ENDIF
3000ENDPROC
3010:
 3020:
3030:
3040DEFPROCcreateinfobox
3050DIM ibicon%(4),iconindirect% &80
3060ibhandle%=FNcreate(0,0,636,216,0,0,&84000002,"Prog Info")
3070FOR i%=0 TO 3
3080READ text$
3090$(iconindirect%+i%*&20)=text$
3100ibicon%(i%)=FNicon(ibhandle%,154,-(i%+1)*52,476,48,&70001BD,"",iconindirect%+i%*&20,-
      1,&20)
3110NEXT
3120ENDPROC
 3130:
 3140DATA !rocdef,Machine Data Logging,E.H.Rutter ,22 May.1993
3150:
3160DEFPROCdraw2(x0%,y0%)
3170MOVE x0%,y0%-16
 3180PRINT"   Name: "
3190MOVE x0%,y0%-68
3200PRINT" Purpose:"
3210MOVE x0%,y0%-120
3220PRINT" Author:"
3230MOVE x0%,y0%-172
3240PRINT" Version:"
3250ENDPROC
3260:
3270DEFPROCreceive
3280CASE block%!16 OF
3290WHEN 0:quit%=TRUE
3300WHEN 3:VDU4:SOUND 1,-15,200,1
3310PRINT TAB(0,0)"DataLoad Message"
3320T%=INKEY(100)
3330PRINT TAB(0,0)SPC17:VDU5
3340ENDCASE
3350ENDPROC
3360:
3480:
3490DEFPROCplotit
3505PROCgraf("Record Number")
3507IF clear%=1 clear%=0:ENDPROC
3508block%!0=whandle%
3509SYS"Wimp_GetWindowState",,block%
3510PROCorderrecs
```

```
3512grad=(FN`CVX(`LX)-FN`CVX(`SX))/(`LX-`SX)
3515maxrec%=((block%!12-FN`CVX(`SX))/grad)+`SX
3516minrec%=((block%!4-FN`CVX(`SX))/grad)+`SX
3518IF minrec%<1 minrec%=1
3520DTA=0
3530IF KNT%<maxrec% THEN maxrec%=KNT%
3544FOR KT%=minrec% TO maxrec%
3548SYS "Wimp_SetColour",11
3550IF y1%=1 PROCpoint(KT%,DAT(KT%,1))
3560SYS "Wimp_SetColour",10
3570IF y2%=1 PROCpoint(KT%,DAT(KT%,2))
3580SYS "Wimp_SetColour",8
3590IF y3%=1 PROCpoint(KT%,DAT(KT%,3))
3600SYS "Wimp_SetColour",9
3610IF y4%=1 PROCpoint(KT%,DAT(KT%,4))
3620SYS "Wimp_SetColour",15
3630IF y5%=1 PROCpoint(KT%,DAT(KT%,5))
3640SYS "Wimp_SetColour",14
3650IF y6%=1 PROCpoint(KT%,DAT(KT%,8))
3660NEXT KT%
3670ENDPROC
3671:
3672DEFPROCorderrecs
3673RC%=0
3674FOR KT%=1 TO KNT%
3675IF DAT(KT%,7)=1 RC%=RC%+1:FOR NJ%=1 TO 8:DAT(RC%,NJ%)=DAT(KT%,NJ%):NEXT NJ%
3676NEXT KT%
3677KNT%=RC%
3678ENDPROC
3690:
3700DEFPROCgraf(B$)
3710TST%=0
3720PROCSCALE
3730PROCAXES
3740PROCGRADUATE
3750PROCNUMBER
3760PROCNAMEX(B$)
3770PROCNAMEY("MILLIVOLTS")
3780ENDPROC
3790:
3800:
3810DEFPROCGRAPH
3820PROCSCALE
3830PROCAXES
3840PROCGRADUATE
3850PROCNUMBER
3860FOR`J=1TOX(0)
3870DTA=8:PROCPOINT(X(`J),Y(`J))
3880IF`J=1THENGOTO3920
3890MOVEFN`CVX(X(`J-1)),FN`CVY(Y(`J-1)):DRAWFN`CVX(X(`J)),FN`CVY(Y(`J))
3900IF`J<X(0)GOTO3920
3910VDU5:PRINTTAB(FN`CVX(X(`J))+2,FN`CVY(Y(`J))+2);A$(NJ):VDU4
3920NEXT`J
3930ENDPROC
3940:
3950DEFPROCSCALE
3960PROCSCALE2(`SY,`LY):`SY=`S:`LY=`L
3970`STY=`ST:`CBY%=`CBN%
3980PROCSCALE2(`SX,`LX):`SX=`S:`LX=`L
3990`STX=`ST:`CBX%=`CBN%
4000`X=1700/(`LX-`SX):`Y=1300/(`LY-`SY)
4010`CONVX=200-`SX*`X :`CONVY=270-`SY*`Y
4020ENDPROC
4030:
4040:
4050DEFFN`CVX(G)=`X*G+`CONVX-15+x0%
4060DEFFN`CVY(G)=(`Y*G+y0%+`CONVY-1700)
4070:
4080DEFPROCSCALE2(L,H):@%=&0101090A
```

```
4090`LL=VAL(LEFT$(STR$(L),INSTR(STR$(L),"E")-1))
4100`LH=VAL(LEFT$(STR$(H),INSTR(STR$(H),"E")-1))
4110`PL=VAL(MID$(STR$(L),INSTR(STR$(L),"E")+1))
4120`LH=`LH*10^(VAL(MID$(STR$(H),INSTR(STR$(H),"E")+1))-`PL)
4130`D=`LH-`LL  4140IF`D<=3THENREPEAT`D=`D*10 :`PL=`PL-1 :`LL=`LL*10 :`LH=`LH*10 :UNTIL `D>3
4150IF`D>30THENREPEAT`D=`D/10:`PL=`PL+1:`LL=`LL/10:`LH=`LH/10:UNTIL`D<30
4160`LL=INT(`LL+.1):`LH=INT(`LH+.5)
4170@%=&10:`CBN%=SGN(`LL)*(VAL(RIGHT$(STR$(`LL),1))+.1)
4180`S=VAL(STR$(`LL)+"E"+STR$(`PL))
4190`L=VAL(STR$(`LH)+"E"+STR$(`PL)):`ST=ABS(`L-`S)/(`LH-`LL)
4200ENDPROC
4210:
4220DEFPROCAXES
4230`X0=0:`Y0=0
4240IF`SX>0THEN`X0=`SXELSEIF`LX<0THEN`X0=`LX
4250IF`SY>0THEN`Y0=`SYELSEIF`LY<0THEN`Y0=`LY
4260 REM PRINT SOLTEMP
4270MOVEFN`CVX(`SX),FN`CVY(`Y0):DRAWFN`CVX(`LX),FN`CVY(`Y0)
4280MOVEFN`CVX(`X0),FN`CVY(`SY):DRAWFN`CVX(`X0),FN`CVY(`LY)
4290ENDPROC
4300:
4310DEFPROCGRADUATE
4320FORX=`SXTO`LX+.1*`STX STEP `STX
4330IF`CBX%MOD5=0THENDTA=16ELSEDTA=8
4340`CBX%=`CBX%+1:PROCpoint(X,`Y0):NEXTX
4350FORY=`SYTO`LY+.1*`STY STEP `STY
4360IF`CBY%MOD5=0THENDTA=16ELSEDTA=8
4370`CBY%=`CBY%+1:PROCpoint(`X0,Y):NEXTY  4380ENDPROC
4390:
4400DEFPROCNUMBER:VDU5
4410MOVEFN`CVX(`LX)-4*LEN(STR$(`LX)),FN`CVY(`Y0)-20 :PRINT;`LX
4420MOVEFN`CVX(`X0)-150,FN`CVY(`LY):PRINT;`LY
4430IF`LX>0AND`SX<0AND`LY>0AND`SY<0THENENDPROC
4440MOVEFN`CVX(`SX),FN`CVY(`Y0)-20:PRINT;`SX
4450MOVEFN`CVX(`X0)-150,FN`CVY(`SY)+30:PRINT;`SY:VDU4
4460ENDPROC
4470:
4480DEFPROCPOINT(A,B)
4490VDU5
4500MOVEFN`CVX(A),FN`CVY(B):DRAWFN`CVX(A)+DTA,FN`CVY(B)
 4510IF TST%=CN% THEN GOTO 4540
4520IF X(1)>`SX+(`LX-`SX)DIV5 THEN GOTO 4530 ELSE GOTO 4540
4530TST%=TST%+1:MOVEFN`CVX(A),FN`CVY(B):VDU8,8,8,8,8,8,8,8:PRINT NC%(TT%):GOTO4540
4540VDU4
4550ENDPROC
4560DEF PROCpoint(A,B)
4570MOVEFN`CVX(A)-DTA,FN`CVY(B):DRAWFN`CVX(A)+DTA,FN`CVY(B)
4580MOVEFN`CVX(A),FN`CVY(B)-DTA:DRAWFN`CVX(A),FN`CVY(B)+DTA
4590ENDPROC
4600:
4610DEFPROCNAMEY(`VNAME$):VDU5
4620FOR`A=1TOLEN(`VNAME$)
4630MOVEFN`CVX(`X0)-60,FN`CVY(`LY)-`A*32-32 :PRINTMID$(`VNAME$,`A,1)
4640NEXT`A:VDU4
4650ENDPROC
4660:
 4670DEFPROCNAMEX(`HNAME$)
4680MOVEFN`CVX(`LX)-32*LEN(`HNAME$)-64,FN`CVY(`Y0)-52 :VDU5:PRINT`HNAME$:VDU4
4690ENDPROC
4700:
4710:
4720DEF PROCparam
4730VDU7
4740CLS:CLG
4750PRINT "***** TEST PARAMETER ENTRY *****":PRINT
4760PRINT"** EXISTING VALUES ** ":PRINT
4770PRINT"SPECIMEN LENGTH, L1,L2 ";L1,L2
4780PRINT"SPECIMEN DIAMETER, D1 THRU D6 ";D1,D2,D3,D4,D5,D6
4790PRINT"STARTING DISPLACEMENT, mm "; STARTT
```

```
4800PRINT"DISPLACEMENT RATE, mm/min ";GRAD
4810PRINT"FORCE GAUGE ZERO, mV ";FGZO
4820PRINT"PH2OO, PO, TO ";PH2OO,PO,T0 :PRINT
4830PRINT"FILENAME = ";T$
4840INPUT"TO MODIFY, Y/N OR LOAD-ON TIME, L ";TRY$
4850IF TRY$="L" THEN GOTO 4860 ELSE GOTO 4910
4860INPUT"ENTER LOAD-ON TIME";LONTIM%
4870INPUT"ENTER LOAD-ON PRESSURE, mV ";PO
4880INPUT"ENTER LOAD-ON TEMPERATURE, mV "T0
4890INPUT"ENTER LOAD-ON DISPLACEMENT, mV (CREEP TESTS ONLY) ";LVDTO  4900GOTO 5000
4910IF TRY$=("Y") THEN GOTO 4920 ELSE GOTO 5000
4920INPUT"SPECIMEN LENGTH, L1,L2 ";L1,L2
4930INPUT"SPECIMEN DIAMETER, D1 THRU D6 ";D1,D2,D3,D4,D5,D6
4940DIA=((D1+D2+D3+D4+D5+D6)/6):AVL=(L1+L2)/2:AREA=((DIA/2)^2)*PI
4950INPUT"STARTING DISPLACEMENT, mm "; STARTT
4960INPUT"DISPLACEMENT RATE, mm/min ";GRAD
4970FOR KTT%=1 TO 14
4980INPUT"PH2OO, PO, TO ";PH2OO,PO,T0
4990INPUT"DATAFILE NAME  = ";T$
5000DATIME=1:DBTIME=0:DADIST=0:DBDIST=0:DB=0:DA=GRAD/25.4
5010 PROCsave_param
5020ENDPROC
5030:
5040:
5050:
5060DEFPROCshowdata
5070REM TO DISPLAY REDUCED DATA  5080VDU28,58,11,79,5
5090@%=&20207
5100PRINT"FORCE(ton)=";FG
5110PRINT"DISPL(thou)=";DISPL
5120PRINT" T deg C   =";TM
5130PRINT" P (Kbar)  =";PRESS
5140IF CON%=1 THEN PRINT"control ON ";STRCON;" b" ELSE PRINT"Stress control OFF"
5150IF TCON=1 THEN PRINT"Tcontrol ON ";TEMPDEG;" C" ELSE PRINT" T control OFF"
5160MOVE900,640:DRAW900,900
5170MOVE900,640:DRAW1278,640
5180MOVE1278,900:DRAW900,900
5190MOVE1276,900:DRAW1276,640
5200MOVE1278,900:DRAW1278,640
5210GCOL1
5220MOVE902,642:DRAW902,898
5230MOVE904,642:DRAW904,896
5240MOVE902,898:DRAW1278,898
5250MOVE904,896:DRAW1278,896
5260MOVE906,642:DRAW906,894
5270MOVE906,894:DRAW1276,894
5280GCOL7
5290@%=10
5300ENDPROC
5310:
5320 DEFPROCprocess(Y(1),Y(2),Y(3),Y(4))
5330 P=Y(2):FG=Y(3):LVDT=Y(4)
5340 ELTIM%=VAL(time$)
5350 PROCCONV(ELTIM%)
5360 ELTIM%=ATIME%
5370 PROCCONV(LONTIM%)
5380 LONTIM%=ATIME%
5390 ETIME%=ELTIM%-LONTIM%
5400 PROCtempconv
5410 MP=795.6:intp=-53.79
5420 PRESS=(P*MP+intp)*.001388
5430 REM PRESS IS MULTIPLIED BY FACTOR .001388TO CONVERT PSI INTO KILOBARS ON SPECIMEN
5440 FG=FG+.25
5450 FG=-.1727+.5188*FG+.2699*(FG^2)-.01718*(FG^3)+.00051*(FG^4)
5460DISPL=ETIME%*GRAD/60
5470 SL$=INKEY$(1)
5480 IF SL$="L" LVDTO=Y(4):VDU7:PROCsave_param
5490 IF SL$="P" PO=Y(2):VDU7:PROCsave_param
5500 IF SL$="F" FGO=Y(3):VDU7:PROCsave_param
```

```
5510 IF SL$="H" T0=SOLTEMP:VDU7:PROCsave_param
5520DISPL=(LVDT-LVDTO)*7.78
5530:
5540 ENDPROC
5550DEFPROCJACKT
5560ACU=-3.054E-2*T+25:BCU=-3.41132E-4*T+0.5:CCU=-.253875*T+200
5570IF(CDISPL+STARTT)<.025 THEN CJACK=CCU*(CDISPL+STARTT) ELSE
        CJACK=ACU*(CDISPL+STARTT)^BCU
5580IF T>590 AND (CDISPL+STARTT)>.25 THEN CJACK=5.28
5590STRMPA=STRMPA-CJACK
5600ENDPROC
5610:
5620:
5630DEFPROCtest_data
5640RECno%=10
5650PROCreader
5660LVDTO=VAL(F$(1))
5670STARTT=VAL(F$(2))
5680AVL=VAL(F$(3))
5690DIA=VAL(F$(4))
5700GRAD=VAL(F$(5))
5710T$=F$(6)
5720RECno%=11
5730PROCreader
5740FGZO=VAL(F$(1))
5750PH2OO=VAL(F$(2))
5760PO=VAL(F$(3))
5770T0=VAL(F$(4))
5780STRCON=VAL(F$(5))
5790CON%=VAL(F$(6))
5800RECno%=12
5810PROCreader
5820REcno%=VAL(F$(1))
5830LONTIM%=VAL(F$(2))
5840MOFFSIG=VAL(F$(3))
5850L1=AVL:L2=AVL
5860D1=DIA:D2=DIA:D3=DIA:D4=DIA:D5=DIA:D6=DIA
5870ENDPROC
5880:
5890DEFPROCreader
5900PTR#file=RECno%*72
5910FOR F%=1TO6
5920INPUT#file,F$(F%)
5930NEXTF%
5940ENDPROC
5950:
5960DEFPROCTHURLBY
5970SOL$=MID$(SOL$,2,7)
5980SOLTEMP=VAL(SOL$)
5990ENDPROC
6000:
6010DEF PROCON(N%)
6020IF N%<0 OR N%>7 THEN ENDPROC
6030N%=2^N%
6040PROCsys(150,96,C%)
6050N%=C% OR N%
6060PROCsys(151,96,N%)
6070ENDPROC
6080:
6090DEF PROCoff(N%)
6100IF N%<0 OR N%>7 THEN ENDPROC
 6110N%=2^N%
6120PROCsys(150,96,C%)
6130N%=C% AND (NOT N%)
6140PROCsys(151,96,N%)
6150ENDPROC
6160:
6170DEF PROCIOSET(S$)
6180LOCAL I,S%
```

```
6190S%=0
6200FOR I=1 TO LEN(S$)
6210S%=S%+2^EVAL(MID$(S$,I,1))
6220NEXT I
6230PROCsys(151,98,S%)
6240ENDPROC
6250:
6260DEFPROCsys(writebyte%,offset%,n%)
6270 osbyte%=6
6280 IF writebyte%=150 GOTO 6290 ELSE GOTO 6310
6290SYS osbyte%,writebyte%,offset% TO A,B,C%
6300 GOTO6320
6310SYS osbyte%,writebyte%,offset%,n%
6320 ENDPROC
6330 REM ** PROCEDURES LIBRARY INSTPROCS **
6340DEFPROCinitialise_IEEE
6350REM PROCeos_in_1chr(10)
6360PROCeos_out_1chr(10)
6368 PROCtimeout_period(10)
6370 PROCtimeout_on
6380 PROCinit
6390PROCadr_to_listen(15)
6391PROCadr_to_listen(7)
6392PROCadr_to_listen(1)
6400convert=(100/(2^30))
6410ENDPROC
6420:
6430DEFPROCtake_control
6440PROCadrandoutput(0,15,"C909,1"):REM REQUEST CONTROL
6450CLS
6460PRINT"Press REMOTE on console to take control"
6470REPEAT
6480PROCadrandoutput(0,15,"Q909")
6490data$=FNadrandinput(1,15,255)
6500incontrol=VAL(data$)
6510UNTIL incontrol = 1
6520PROCadrandoutput(0,15,"C904,0"):REM DISABLE WATCHDOG
6530PROCadrandoutput(0,15,"C23,1"):REM ACTUATOR ON
6540PROCadrandoutput(0,15,"C314,0"):REM RESET EMERGENCY STOP
6550PROCadrandoutput(0,15,"C913,0"):REM DISABLE BUS SRQ'S
6560PRINT" COMPUTER NOW HAS CONTROL"
6570ENDPROC
6580:
6590DEFPROCreturn_control
6600PROCadrandoutput(0,15,"C909,0"):REM return control to 8500
6610CLS:PRINT "  Control returned to 8500 "
6620ENDPROC
6630:
6640DEFPROCcycles
6650PROCadrandoutput(0,15,"C201,1,0"):REM SETUP SINEWAVE TYPE
6660PROCadrandoutput(0,15,"C202,1,.005"):REM 0.01 HERTZ
6670PROCadrandoutput(0,15,"C203,1,.5"):REM 5% AMPLITUDE
6680PROCadrandoutput(0,15,"C300,1"):REM SET STROKE CONTROL
6690PRINT "PRESS 'S' TO STOP WAVEFORM"
6700PROCadrandoutput(0,15,"C200,1"):REM START WAVEFORM
6710ENDPROC
6720PROCgetbuf
6730REPEAT
6740 S$=INKEY$(10)
6750UNTIL S$="S"
6760PROCadrandoutput(0,15,"C200,2"):REM HOLD WAVEFORM
6770ENDPROC
6780:
6790DEFPROCsetup
6800convert=100/(2^30)
6820REM COLLECT BUFFER OF 10 POINTS BY 3 CHANNELS, BINARY DATA DIRECTLY TO    6830REM
      MEMORY.
6830REM MEMORY.
6840REM DIM pointer% 100
```

```
6850REM  DIM nr% 4
6860REM  DIM BITSET(8)
6870REM  DIM buffer(20,3)
6880REM 20POINTS*4 BYTES PER DATAPOINT+8
6890REM SETUP COLLECTION PARAMETERS
6900PROCadrandoutput(0,15,"C316,0"):REM DATACOLLECTION OFF
6910PROCadrandoutput(0,15,"C137,1,0"):REM SET STROKE FEEDBACK
6920PROCadrandoutput(0,15,"C137,2,0"):REM SET LOAD FEEDBACK
6930PROCadrandoutput(0,15,"C137,3,0"):REM SET STRAIN FEEDBACK
6940REM ASSIGN STROKE, LOAD & STRAIN TO BUFFER OFFSETS 1, 2 & 3
6950PROCadrandoutput(0,15,"C316,1"):REM DATA COLLECTION IDLE
6960PROCadrandoutput(0,15,"C318,0,1,1"):REM STROKE AT OFFSET 0
6970PROCadrandoutput(0,15,"C318,1,1,2"):REM LOAD AT OFFSET 1
6980PROCadrandoutput(0,15,"C318,2,1,3"):REM STRAIN AT OFFSET 2
6990PROCadrandoutput(0,15,"C317,0,70,1"):REM MODE, RATE, NR BUFFERS
7000PROCadrandoutput(0,15,"C319,10,0"):REM BUFFER SIZE, LAST SIZE
7002ENDPROC
7005:
7010DEFPROCinstr_start
7015IF selector%=1 ENDPROC
7020BUFSIZ=128:BUFCNT=0
7025PROCadrandoutput(0,15,"C316,1"):REM DATA COLLECTION IDLE
7030PROCadrandoutput(0,15,"C316,3"):REM START DATA COLLECTION
7032ENDPROC
7033:
7035DEFPROCget_instron
7038crt%=0
7040REPEAT
7045crt%=crt%+1
7050devicestatus%=FNserial_poll(15)
7060PROCbinpoll
7070IF BITSET(8)=1 THEN PROClogdata
7075IF crt%>300 BUFCNT=1
7080UNTIL BUFCNT=1
7090ENDPROC
7140:
7150DEFPROClogdata
7160nvec=10:nchn=3
7170PROCadrandoutput(0,15,"Q327"):REM REQUEST NR OF BUFFERS
7180rpt$=FNadrandinput(1,15,255)  7190NUMBUF=VAL(rpt$)
7200FORindex=1 TO NUMBUF
7210PROCadrandoutput(0,15,"Q320"):REM REQUEST BINARY BUFFER
7220PROCadrandinputmem(2,15,pointer%,128)
7230PROCconvert_buffer
7250BUFCNT=BUFCNT+1
7260NEXT index
7270ENDPROC
7280:
7290DEFPROCbinpoll
7300binary$=""
7310REPEAT
7320binary$=STR$(devicestatus% MOD 2)+binary$
7330devicestatus%=devicestatus% DIV 2
7340UNTIL devicestatus%=0
7350FOR CNTR%=1 TO 8
7360BITSET(CNTR%)=VAL(RIGHT$(binary$,1))
7370binary$=LEFT$(binary$)
7380NEXT CNTR%
7390ENDPROC
7400:
7410:
7490:
7500DEFPROCdenbin
7510denary=0:b=LENtemp$
7520FOR digit=1 TO b
7530denary=denary+VAL(MID$(temp$,digit,1))*2^(b-digit)
7540NEXT
7550temp=denary
7560ENDPROC
```

```
7570:
7580DEFPROCconvert_buffer
7640offset=8
7650FOR index1=1 TO nvec
7660FOR index2=1 TO nchn
7670temp1%=?(pointer%+offset)
7680temp2%=?(pointer%+offset+1)
7690temp3%=?(pointer%+offset+2)
7700temp4%=?(pointer%+offset+3)
7710?(nr%)=temp4%:?(nr%+1)=temp3%:?(nr%+2)=temp2%:?(nr%+3)=temp1%
7720temp%=!nr%
7740temp=temp%*convert
7750buffer(index1,index2)=temp
7760offset=offset+4
7770NEXT index2
7780NEXT index1
7790ENDPROC
7800:
7810REM INTELLIGENT INTERFACES LTD IEEE488 PROCEDURES AND FUNCTIONS LIBRARY V1.02
7820REM abort on error
7830REM Copyright Intelligent Interfaces Ltd
7840REM 18 January 1988
7850
7860DEF PROCeos_out_1chr(eos1%)
7870SYS &40340,&00,&03,&01,eos1%
7880ENDPROC
7890
7900DEF PROCeos_out_2chr(eos1%,eos2%)
7910SYS &40340,&00,&03,&02,eos1%,eos2%
7920ENDPROC
7930
7940DEF PROCeos_in_1chr(eos1%)
7950SYS &40340,&00,&04,&01,eos1%
7960ENDPROC
7970
7980DEF PROCeos_in_2chr(eos1%,eos2%)
7990SYS &40340,&00,&04,&02,eos1%,eos2%
8000ENDPROC
8010
8020DEF PROCtimeout_period(period)
8030SYS &40340,&00,&05,INT(&00200000*(period/8))
8040ENDPROC
8050
8060DEF PROCtimeout_on
8070SYS &40340,&00,&06
8080ENDPROC
8090
8100DEF PROCtimeout_off
8110SYS &40340,&00,&07
8120ENDPROC
8130
8140DEF PROCinit
8150LOCAL d0%,d1%,ma%
8160SYS &40340,&00,&02 TO d0%,d1%,ma%
8170IF (ma% AND &80) THEN SYS &40340,&00,&11,ma% ELSE SYS &40340,&00,&10,ma%
8180ENDPROC
8190
8200DEF PROCifc
8210SYS &40340,&00,&0D
8220ENDPROC
8230
8240DEF PROCren_true
8250SYS &40340,&00,&0E
8260ENDPROC
8270
8280DEF PROCren_false
8290SYS &40340,&00,&0F
8300ENDPROC
8310
```

```
8320DEF PROCdevice(archadr%)
8330SYS &40340,&00,&10,archadr%
8340ENDPROC
8350
8360DEF PROCcontroller(archadr%)
8370SYS &40340,&00,&11,archadr%
8380ENDPROC
8390
8400DEF PROCatn_true
8410SYS &40340,&00,&12
8420ENDPROC
8430
8440DEF PROCatn_true_sync
8450SYS &40340,&00,&13
8460ENDPROC
8470
8480DEF PROCcmd(cmd%)
8490SYS &40340,&00,&14,&00,&00,&00,CHR$(cmd%),&01
8500ENDPROC
8510
8520DEF PROClisten(lad%)
8530SYS &40340,&00,&15,&00,lad%
8540ENDPROC
8550
8560DEF PROClistenext(lad%,sad%)
8570SYS &40340,&00,&16,&00,lad%,sad%
8580ENDPROC
8590
8600DEF PROCtalk(tad%)
8610SYS &40340,&00,&17,&00,tad%
 8620ENDPROC
8630
8640DEF PROCtalkext(tad%,sad%)
8650SYS &40340,&00,&18,&00,tad%,sad%
8660ENDPROC
8670
8680DEF PROCsecondary(sad%)
8690SYS &40340,&00,&19,&00,&00,sad%
8700ENDPROC
8710
8720DEF PROCunlisten
8730SYS &40340,&00,&1A
8740ENDPROC
8750
8760DEF PROCuntalk
8770SYS &40340,&00,&1B
8780ENDPROC
8790
8800DEF PROCadr_to_listen(lad%)
8810SYS &40340,&00,&1C,&00,lad%
8820ENDPROC
8830
)8840DEF PROCadr_to_listenext(lad%,sad%)
8850SYS &40340,&00,&1D,&00,lad%,sad%
8860ENDPROC
8870
8880DEF PROCadr_to_talk(tad%)
8890SYS &40340,&00,&1E,&00,tad%
8900ENDPROC
8910
8920DEF PROCadr_to_talkext(tad%,sad%)
8930SYS &40340,&00,&1F,&00,tad%,sad%
8940ENDPROC
8950
8960DEF PROCgo_to_local(lad%)
8970SYS &40340,&00,&20,&00,&00,&00,CHR$(lad%),&01
8980ENDPROC
8990
9000DEF PROCselected_device_clear(lad%)
```

```
9010SYS &40340,&00,&21,&00,&00,&00,CHR$(lad%),&01
9020ENDPROC
9030
9040DEF PROCgroup_execute_trigger(lad%)
9050SYS &40340,&00,&22,&00,&00,&00,CHR$(lad%),&01
9060ENDPROC
9070
9080DEF PROClocal_lockout
9090SYS &40340,&00,&23
9100ENDPROC
9110
9120DEF PROCdevice_clear
9130SYS &40340,&00,&24
9140ENDPROC
9150
9160DEF PROCparallel_poll_unconfigure
9170SYS &40340,&00,&25
9180ENDPROC
9190
9200DEF PROCatn_false
9210SYS &40340,&00,&26
9220ENDPROC
9230
9240DEF PROCrequest_service(stb%)
9250SYS &40340,&00,&29,stb%
9260ENDPROC
9270
9280DEF FNserial_poll(tad%)
9290LOCAL d0%,d1%,stb%
9300SYS &40340,&00,&2B,&00,tad% TO d0%,d1%,stb%
9310=stb%
9320
9330DEF PROCparallel_poll_enable(lad%,sp3p2p1%)
9340SYS &40340,&00,&2E,sp3p2p1%,lad%
9350ENDPROC
9360
9370DEF PROCparallel_poll_disable(lad%)
9380SYS &40340,&00,&2F,&00,lad%
9390ENDPROC
9400
9410DEF FNparallel_poll
9420LOCAL d0%,d1%,ppr%
9430SYS &40340,&00,&30 TO d0%,d1%,ppr%
9440=ppr%
9450
9460DEF PROCpasscontrol(tad%)
9470SYS &40340,&00,&31,&00,tad%
9480ENDPROC
9490
9500DEF PROCoutput(mode%,data$)
9510SYS &40340,&00,&08,mode%
9520SYS &40340,&00,&36,&00,&00,&00,data$,LEN(data$)
9530ENDPROC
9540
9550DEF PROCadrandoutput(mode%,lad%,data$)
9560SYS &40340,&00,&08,mode%
9570SYS &40340,&00,&3C,&00,lad%,&00,data$,LEN(data$)
9580ENDPROC
9590
9600DEF PROCadrextandoutput(mode%,lad%,sad%,data$)
9610SYS &40340,&00,&08,mode%
9620SYS &40340,&00,&3E,&00,lad%,sad%,data$,LEN(data$)
9630ENDPROC
9640
9650DEF PROCoutputmem(mode%,memadr%,bytecnt%)
9660SYS &40340,&00,&08,mode%
9670SYS &40340,&00,&36,&00,&00,&00,memadr%,bytecnt%
9680ENDPROC
9690
```

```
9700DEF PROCadrandoutputmem(mode%,lad%,memadr%,bytecnt%)
9710SYS &40340,&00,&08,mode%
9720SYS &40340,&00,&3C,&00,lad%,&00,memadr%,bytecnt%
9730ENDPROC
9740
9750DEF PROCadrextandoutputmem(mode%,lad%,sad%,memadr%,bytecnt%)
9760SYS &40340,&00,&08,mode%
9770SYS &40340,&00,&3E,&00,lad%,sad%,memadr%,bytecnt%
9780ENDPROC
9790
9800DEF FNinput(mode%,bytecnt%)
9810LOCALd0%,d1%,d2%,d3%,d4%,databuf$,d6%,xcnt%
9820IFbytecnt%>254THEN bytecnt% = 254
9830databuf$ = STRING$(bytecnt%," ")
9840SYS &40340,&00,&09,mode%
9850SYS &40340,&00,&37,&00,&00,&00,databuf$,bytecnt% TO
        d0%,d1%,d2%,d3%,d4%,databuf$,d6%,xcnt%
9860=LEFT$(databuf$,xcnt%)
9870
9880DEF FNadrandinput(mode%,tad%,bytecnt%)
9890LOCALd0%,d1%,d2%,d3%,d4%,databuf$,d6%,xcnt%
9900IFbytecnt%>254THEN bytecnt% = 254
9910databuf$ = STRING$(bytecnt%," ")
9920SYS &40340,&00,&09,mode%
9930SYS &40340,&00,&3D,&00,tad%,&00,databuf$,bytecnt% TO
        d0%,d1%,d2%,d3%,d4%,databuf$,d6%,xcnt%
9940=LEFT$(databuf$,xcnt%)
9950
9960DEF FNadrextandinput(mode%,tad%,sad%,bytecnt%)
9970LOCALd0%,d1%,d2%,d3%,d4%,databuf$,d6%,xcnt%
9980IFbytecnt%>254THEN bytecnt% = 254
9990databuf$ = STRING$(bytecnt%," ")
10000SYS &40340,&00,&09,mode%
10010SYS &40340,&00,&3F,&00,tad%,sad%,databuf$,bytecnt% TO
        d0%,d1%,d2%,d3%,d4%,databuf$,d6%,xcnt%
10020=LEFT$(databuf$,xcnt%)
10030
10040DEF PROCinputmem(mode%,memadr%,bytecnt%)
10050SYS &40340,&00,&09,mode%
10060SYS &40340,&00,&37,&00,&00,&00,memadr%,bytecnt%
10070ENDPROC
10080
10090DEF PROCadrandinputmem(mode%,tad%,memadr%,bytecnt%)
10100SYS &40340,&00,&09,mode%
10110SYS &40340,&00,&3D,&00,tad%,&00,memadr%,bytecnt%
10120ENDPROC
10130
10140DEF PROCadrextandinputmem(mode%,tad%,sad%,memadr%,bytecnt%)
10150SYS &40340,&00,&09,mode%
10160SYS &40340,&00,&3F,&00,tad%,sad%,memadr%,bytecnt%
10170ENDPROC
10180
10190DEF FNservice_requested
10200LOCAL d0%,d1%,d2%,d3%,bussts%,status%
10210SYS &40340,&00,&00 TO d0%,d1%,d2%,d3%,bussts%
10220IF (bussts% AND &04) = 0 THEN status%=FALSE ELSE status% = TRUE
10230=status%
10240
10250DEF FNtalker
10260LOCAL d0%,d1%,d2%,d3%,d4%,addsts%,status%
10270SYS &40340,&00,&00 TO d0%,d1%,d2%,d3%,d4%,addsts%
10280IF (addsts% AND &0A) = 0 THEN status%=FALSE ELSE status% = TRUE
10290=status%
10300
10310DEF FNlistener
10320LOCAL d0%,d1%,d2%,d3%,d4%,addsts%,status%
10330SYS &40340,&00,&00 TO d0%,d1%,d2%,d3%,d4%,addsts%
10340IF (addsts% AND &14) = 0 THEN status%=FALSE ELSE status% = TRUE
10350=status%
```

```
10360
10370DEF FNattention
10380LOCAL d0%,d1%,d2%,d3%,bussts%,status%
10390SYS &40340,&00,&00 TO d0%,d1%,d2%,d3%,bussts%
10400IF (bussts% AND &80) = 0 THEN status%=FALSE ELSE status% = TRUE
10410=status%
10420
10430DEF FNlocked_out
10440LOCAL d0%,d1%,d2%,d3%,d4%,addsts%,status%
10450SYS &40340,&00,&00 TO d0%,d1%,d2%,d3%,d4%,addsts%
10460IF (addsts% AND &40) = 0 THEN status%=FALSE ELSE status% = TRUE
10470=status%
10480
10490DEF FNremote
10500LOCAL d0%,d1%,d2%,d3%,d4%,addsts%,status%
10510SYS &40340,&00,&00 TO d0%,d1%,d2%,d3%,d4%,addsts%
10520IF (addsts% AND &80) = 0 THEN status%=FALSE ELSE status% = TRUE
10530=status%
10540
10550DEF FNdevice_cleared
10560LOCAL d0%,d1%,d2%,d3%,d4%,d5%,devsts%,status%
10570SYS &40340,&00,&00 TO d0%,d1%,d2%,d3%,d4%,d5%,devsts%
10580IF (devsts% AND &08) = 0 THEN status%=FALSE ELSE status% = TRUE
10590=status%
10600
10610DEF FNtriggered
10620LOCAL d0%,d1%,d2%,d3%,d4%,d5%,devsts%,status%
10630SYS &40340,&00,&00 TO d0%,d1%,d2%,d3%,d4%,d5%,devsts%
10640IF (devsts% AND &80) = 0 THEN status%=FALSE ELSE status% = TRUE
10650=status%
10660
10670DEF FNinterface_cleared
10680LOCAL d0%,d1%,d2%,d3%,d4%,d5%,devsts%,status%
10690SYS &40340,&00,&00 TO d0%,d1%,d2%,d3%,d4%,d5%,devsts%
10700IF (devsts% AND &0100) = 0 THEN status%=FALSE ELSE status% = TRUE
10710=status%
10720
10730DEF FNsh_error
10740LOCAL d0%,d1%,d2%,d3%,d4%,d5%,devsts%,status%
10750SYS &40340,&00,&00 TO d0%,d1%,d2%,d3%,d4%,d5%,devsts%
10760IF (devsts% AND &4000) = 0 THEN status%=FALSE ELSE status% = TRUE
10770=status%
10780
10790DEF FNcontroller_in_charge
10800LOCAL d0%,d1%,d2%,d3%,d4%,d5%,d6%,ctrlinchg%,status%
10810SYS &40340,&00,&00 TO d0%,d1%,d2%,d3%,d4%,d5%,d6%,ctrlinchg%
10820IF (ctrlinchg% AND &FF) = 0 THEN status%=FALSE ELSE status% = TRUE
10830=status%
10840
10850DEF FNsystem_controller
10860LOCAL d0%,d1%,ma%
10870SYS &40340,&00,&02 TO d0%,d1%,ma%
10880IF (ma% AND &80) = 0 THEN status%=FALSE ELSE status% = TRUE
10890=status%
10900
10910DEF FNinitialised
10920=TRUE
10930
10940DEF FNaddress
10950LOCAL d0%,d1%,ma%
10960SYS &40340,&00,&02 TO d0%,d1%,ma%
10970=(ma% AND &1F)
10980
10990DEFPROCmake_array
11000FOR IK%=1 TO 50 11010DAT(IK%,1)=50*SIN(2*PI*IK%/100)
11020DAT(IK%,2)=50*SIN((2*PI*IK%/100)+0.5)
11030DAT(IK%,3)=50*SIN((2*PI*IK%/100)+1)
11040DAT(IK%,4)=50*SIN((2*PI*IK%/100)+1.5)
11050DAT(IK%,5)=50*SIN((2*PI*IK%/100)+2)
```

```
11060DAT(IK%,6)=50*SIN((2*PI*IK%/100)+2.5)
11070NEXT IK%
11080ENDPROC
11090DEFPROCcreatedialogbox1(txt$)
11100dialogbox1%=FNcreate(0,0,500,100,0,0,&84000002,"Dialog")
11110db11icon%=FNicon(dialogbox1%,20,-52,476,48,&800B43D,txt$,0,0,0)
11120db12icon%=FNicon(dialogbox1%,20,-2*52,476,48,&800F53D,"",text1%,-1,&20)
11130ENDPROC
11140:
11150DEFPROCcreatedialogbox2(txt$)
11160dialogbox2%=FNcreate(0,0,500,100,0,0,&84000002,"Dialog")
11170db21icon%=FNicon(dialogbox2%,20,-52,476,48,&800B43D,txt$,0,0,0)
11180db22icon%=FNicon(dialogbox2%,20,-2*52,476,48,&800F53D,"",text2%,-1,&20)
11190ENDPROC
11200:
11210DEFPROCcreatedialogbox3(txt$)
11220dialogbox3%=FNcreate(0,0,500,100,0,0,&84000002,"Dialog")
11230db31icon%=FNicon(dialogbox3%,20,-52,476,48,&800B43D,txt$,0,0,0)
11240db32icon%=FNicon(dialogbox3%,20,-2*52,476,48,&800F53D,"",text3%,-1,&20)
11250ENDPROC
11260:
11270DEFPROCcreatedialogbox4(txt$)
11280dialogbox4%=FNcreate(0,0,500,100,0,0,&84000002,"Dialog")
11290db41icon%=FNicon(dialogbox4%,20,-52,476,48,&800B43D,txt$,0,0,0)
11300db42icon%=FNicon(dialogbox4%,20,-2*52,476,48,&800F53D,"",text4%,-1,&20)
11310ENDPROC
11320:
11330DEFPROCcreatedialogbox5(txt$)
11340dialogbox5%=FNcreate(0,0,500,100,0,0,&84000002,"Dialog")
11350db51icon%=FNicon(dialogbox5%,20,-52,476,48,&800B43D,txt$,0,0,0)
11360db52icon%=FNicon(dialogbox5%,20,-2*52,476,48,&800F53D,"",text5%,-1,&20)
11370ENDPROC
11380:
11390DEFPROCcreatedialogbox6(txt$)
11400dialogbox6%=FNcreate(0,0,500,100,0,0,&84000002,"Dialog")
11410db61icon%=FNicon(dialogbox6%,20,-52,476,48,&800B43D,txt$,0,0,0)
11420db62icon%=FNicon(dialogbox6%,20,-2*52,476,48,&800F53D,"",text6%,-1,&20)
11430ENDPROC 11440:
11450DEFPROCcreatedialogbox7(txt$)
11460dialogbox7%=FNcreate(0,0,500,100,0,0,&84000002,"Dialog")
11470db71icon%=FNicon(dialogbox7%,20,-52,476,48,&800B43D,txt$,0,0,0)
11480db72icon%=FNicon(dialogbox7%,20,-2*52,476,48,&800F53D,"",text7%,-1,&20)
11490ENDPROC
11500:
11510DEFPROCcreatedialogbox8(txt$)
11520dialogbox8%=FNcreate(0,0,500,100,0,0,&84000002,"Dialog")
11530db81icon%=FNicon(dialogbox8%,20,-52,476,48,&800B43D,txt$,0,0,0)
11540db82icon%=FNicon(dialogbox8%,20,-2*52,476,48,&800F53D,"",text8%,-1,&20)
11550ENDPROC
11560:
11570DEFPROCcreatedialogbox9(txt$)
11580dialogbox9%=FNcreate(0,0,500,100,0,0,&84000002,"Dialog")
11590db91icon%=FNicon(dialogbox9%,20,-52,476,48,&800B43D,txt$,0,0,0)
11600db92icon%=FNicon(dialogbox9%,20,-2*52,476,48,&800F53D,"",text9%,-1,&20)
11610ENDPROC
11620:
11630DEFPROCcreatedialogbox10(txt$)
11640dialogbox10%=FNcreate(0,0,500,100,0,0,&84000002,"Dialog")
11650db101icon%=FNicon(dialogbox10%,20,-52,476,48,&800B43D,txt$,0,0,0)
11660db102icon%=FNicon(dialogbox10%,20,-2*52,476,48,&800F53D,"",text10%,-1,&20)
11670ENDPROC
11680:
11690DEFPROCcreatedialogbox11(txt$)
11700dialogbox11%=FNcreate(0,0,500,100,0,0,&84000002,"Dialog")
11710db111icon%=FNicon(dialogbox11%,20,-52,476,48,&800B43D,txt$,0,0,0)
11720db112icon%=FNicon(dialogbox11%,20,-2*52,476,48,&800F53D,"",text11%,-1,&20)
11730ENDPROC
11732DEFPROCcreatedialogbox18(txt$)
11733dialogbox18%=FNcreate(0,0,500,100,0,0,&84000002,"Dialog")
```

```
11734db181icon%=FNicon(dialogbox18%,20,-52,476,48,&800B43D,txt$,0,0,0)
11735db182icon%=FNicon(dialogbox18%,20,-2*52,476,48,&800F53D,"",text18%,-1,&20)
11736ENDPROC
11737:
11738DEFPROCcreatedialogbox19(txt$)
11739dialogbox19%=FNcreate(0,0,500,100,0,0,&84000002,"Dialog")
11740db191icon%=FNicon(dialogbox19%,20,-52,476,48,&800B43D,txt$,0,0,0)
11741db192icon%=FNicon(dialogbox19%,20,-2*52,476,48,&800F53D,"",text19%,-1,&20)
11742ENDPROC
11743:
11744DEFPROCcreatedialogbox20(txt$)
11745dialogbox20%=FNcreate(0,0,500,100,0,0,&84000002,"Dialog")
11746db201icon%=FNicon(dialogbox20%,20,-52,476,48,&800B43D,txt$,0,0,0)
11747db202icon%=FNicon(dialogbox20%,20,-2*52,476,48,&800F53D,"",text20%,-1,&20)
11748ENDPROC
11749:
11750DEFPROCcreatedialogbox21(txt$)
11751dialogbox21%=FNcreate(0,0,500,100,0,0,&84000002,"Dialog")
11752db211icon%=FNicon(dialogbox21%,20,-52,476,48,&800B43D,txt$,0,0,0)
11753db212icon%=FNicon(dialogbox21%,20,-2*52,476,48,&800F53D,"",text21%,-1,&20)
11754ENDPROC
11755:
11758DEFPROCdraw3(x0%,y0%)
11760@%=&20206
11770MOVE x0%,y0%-18
11780PRINT TIME$
11790@%=&00004:PRINT "Point ";Buffer%;
11800@%=&00004:PRINT TAB(12);"RecNo ";RecNo%;
11810@%=&20105:PRINT TAB(23);"SIG=";SIG;TAB(34);"MPa T=";TM;TAB(46);" C P=";P;TAB(57);"MPa
      PH2O=";PH2O;TAB(72);"MPa"
11820:
11830@%=&10
11840ENDPROC
11850:
11860DEFPROCupdate(handle%,ihandle%)
11870block%!0=handle%:block%!4=ihandle%
11880SYS "Wimp_GetIconState",,block%
11890Iconstate%=(block%!24)DIV(2^21)MOD&4
11910ENDPROC
11920:DEFPROCreset_accept
11930block%!0=whandle%:block%!4=i5handle%
11940SYS "Wimp_GetIconState",,block%
11950!block%24=block%!0-2^21
11960ENDPROC
11962:
11963DEFPROCpremaset
11964PROCadrandoutput(0,7,"A0")
11965PROCadrandoutput(0,7,"R1")
11967PROCadrandoutput(0,7,"T1")
11968PROCadrandoutput(0,7,"L0")
11969PROCadrandoutput(0,7,"S0")
11970ENDPROC
11971:
11978DEFPROCgetdata
11980IF time3%>100000 AND filesave%=1 AND logger%=1 PROCfilesave
11981IF time3%>100000 time4%=TIME
11982time3%=TIME-time4%
11985IF selector%=1 ENDPROC
11986IFlogger%=1 KNT%=RecNo%:GOTO 11989
11987KNT%=KNT%+1
11988IF KNT%>4999 KNT%=KNT%-4999
11989PROCget_instron
11991DAT(KNT%,7)=0
11993IF logger%=1 AND TIME>=time2% DAT(KNT%,7)=1
      :RecNo%=RecNo%+1:time2%=TIME+interval:PROCtrack
12000DAT(KNT%,1)=(-buffer(10,1))*5-220
12010DAT(KNT%,2)=-buffer(10,2)
12012DAT(KNT%,3)=-buffer(10,3)*MF:GOTO 12020
12020 PROCconvert_time:DAT(KNT%,6)=Ctime%
```

```
12025prem$=FNadrandinput(1,7,255)
12026serdat=VAL(prem$)*1000
12030 IFchan%=1 DAT(KNT%,4)=serdat:DAT(KNT%,5)=DAT(KNT%-1,5):DAT(KNT%,8)=DAT(KNT%-1,8)
12032IFchan%=2 DAT(KNT%,5)=serdat:DAT(KNT%,4)=DAT(KNT%-1,4):DAT(KNT%,8)=DAT(KNT%-1,8)
12033IFchan%=3 DAT(KNT%,8)=serdat:DAT(KNT%,4)=DAT(KNT%-1,4):DAT(KNT%,5)=DAT(KNT%-1,5)
12034IFchan%=4 DAT(KNT%,4)=DAT(KNT%-1,4):DAT(KNT%,5)=DAT(KNT%-
    1,5):DAT(KNT%,8)=DAT(KNT%-1,8)
12036IF chan%=4 chan%=0
12038chan%=chan%+1
12042PROCadrandoutput(0,1,STR$(chan%+8))
12055Buffer%=KNT%
12060IF zeroset%=1 PROCfind_zero
12065TM=20+DAT(KNT%,4)/.0413:REM this line for base metal thermocouples
12066GOTO12080
12070IF DAT(KNT%,4)<2 TM=20+125*DAT(KNT%,4) ELSE TM=50.79+117.63*DAT(KNT%,4)-
    3.13*(DAT(KNT%,4))^2+0.07*(DAT(KNT%,4))^3:REM TM IS TEMP DEG C, ROOM TEMP ASSUMED
    20 C
12080P=(DAT(KNT%,5)-1.737)/0.0155:REM P IN MPa
12085PH2O=(DAT(KNT%,8)-.06)*36.97:REM in MPa
12090ENDPROC
12100:
12110DEFPROCupdate_displays
12120PROCgrafupdate
12130REM SYS "Wimp_ForceRedraw",whandle%,FN`CVX(KNT%-(`LX/40)),-800,FN`CVX(KNT%),0
12134SYS "Wimp_ForceRedraw",dahandle%,0,-80,1200,-40
12140block%!0=dahandle%:block%!4=Y1handle%:block%!8=0:block%!12=0
12150$text12%=LEFT$(STR$(DAT(KNT%,1)),7)
12160SYS "Wimp_SetIconState",,block%
12170block%!0=dahandle%:block%!4=Y2handle%:block%!8=0:block%!12=0:$text13%=LEFT$(STR$(D
    AT(KNT%,2)),7)
12180SYS "Wimp_SetIconState",,block%
12190block%!0=dahandle%:block%!4=Y3handle%:block%!8=0:block%!12=0:$text14%=LEFT$(STR$(D
    AT(KNT%,3)),7)
12200SYS "Wimp_SetIconState",,block%
12210block%!0=dahandle%:block%!4=Y4handle%:block%!8=0:block%!12=0:$text15%=LEFT$(STR$(D
    AT(KNT%,4)),7)
12220SYS "Wimp_SetIconState",,block%
12230block%!0=dahandle%:block%!4=Y5handle%:block%!8=0:block%!12=0:$text16%=LEFT$(STR$(D
    AT(KNT%,5)),7)
12240SYS "Wimp_SetIconState",,block%
12250block%!0=dahandle%:block%!4=Y6handle%:block%!8=0:block%!12=0:$text17%=LEFT$(STR$(D
    AT(KNT%,8)),7)
12260SYS "Wimp_SetIconState",,block%
12270ENDPROC
12280DEFPROCgrafupdate
12285IF logger%=1 AND zerorec%>0 AND selector%=0 PROCrealtimeprocess
12287IF strcon<1000 AND logger%=1 AND zerorec%>0 AND selector%=0 PROCstresscontrol
12290block%!0=whandle%
12295PROCgetorigin(block%,x0%,y0%)
12300block%!4=0:REM FN`CVX(KNT%-(`LX/40))
12310block%!8=-1600
12320block%!12=2000:REM FN`CVX(KNT%+(`LX/40))
12330block%!16=0
12340SYS "Wimp_UpdateWindow",,block% TO more%
12350WHILE more%
12355PROCgetorigin(block%,x0%,y0%)
12400xp%=FN`CVX(KNT%)
12410yp1%=FN`CVY(DAT(KNT%,1))
12420yp2%=FN`CVY(DAT(KNT%,2))
12430yp3%=FN`CVY(DAT(KNT%,3))
12440yp4%=FN`CVY(DAT(KNT%,4))
12450yp5%=FN`CVY(DAT(KNT%,5))
12460yp6%=FN`CVY(DAT(KNT%,8))
12470IF y1%=1 THEN SYS "Wimp_SetColour",11:PROCplot(xp%,yp1%)
12480IF y2%=1 THEN SYS "Wimp_SetColour",10:PROCplot(xp%,yp2%)
12490IF y3%=1 THEN SYS "Wimp_SetColour",8:PROCplot(xp%,yp3%)
12500IF y4%=1 THEN SYS "Wimp_SetColour",9:PROCplot(xp%,yp4%)
12510IF y5%=1 THEN SYS "Wimp_SetColour",15:PROCplot(xp%,yp5%)
12520IF y6%=1 THEN SYS "Wimp_SetColour",14:PROCplot(xp%,yp6%)
```

```
12530SYS "Wimp_GetRectangle",,block% TO more%
12540ENDWHILE
12550ENDPROC
12560DEFPROCplot(A,B)
12565 DTA=0
12570MOVEA-DTA,B:DRAWA+DTA,B
12580MOVEA,B-DTA:DRAWA,B+DTA
12590ENDPROC
12600:
12610DEFPROCresetarray
12630FOR KT%=0 TO KNT%
12640FOR IJ%=1 TO 8
12650DAT(KT%,IJ%)=0
12660NEXT IJ%
12670NEXT KT%
12680KNT%=0
12700SYS "Wimp_ForceRedraw",whandle%,0,-1600,2000,0
12705RecNo%=0
12710ENDPROC
12720:
12730DEFPROCpointer
12740REM constd%=0:constE%=1:constS%=0
12750IF constd%=1 AND SM$="constD" THEN !ptr%=1:ENDPROC
12760IF constE%=1 AND SM$="constE" THEN !ptr%=1:ENDPROC
12770IF constS%=1 AND SM$="constS" THEN !ptr%=1:ENDPROC
12780ENDPROC
12790:
12800DEFPROCmenu3boxes
12810menu3%!(32)=dialogbox5%:menu3%!(32+24)=dialogbox6%
12820menu3%!(32+48)=dialogbox7%:menu3%!(32+72)=dialogbox8%
12830menu3%!(32+96)=dialogbox9%:menu3%!(32+120)=dialogbox10%
12840ENDPROC
12850:
12860DEFPROCfilesave
12880CLOSE#0
12890file=OPENOUT($text10%)
12900REM send header data
12910FOR LM%=1 TO KNT%
12920FOR JK%=1 TO 8
12930PRINT#file,DAT(LM%,JK%)
12940NEXT JK%
12950NEXT LM%
12960CLOSE#file
12970VDU7
12980ENDPROC
12990:
13030
13100DEFPROCloader
13110infile%=OPENIN($text10%)
13111 IF append%=1 GOTO 13130
13120KNT%=0
13130REPEAT
13140KNT%=KNT%+1
13150FOR JK%=1 TO 8
13160INPUT#infile%,DAT(KNT%,JK%)
13170NEXT JK%
13180DAT(KNT%,7)=1
13190UNTIL EOF#infile%
13195RecNo%=KNT%
13200CLOSE#infile%
13205PROCorderrecs
13210ENDPROC
13220:
13230DEFPROCconvert_time
13232Ctime$=TIME$
13234T1$=RIGHT$(Ctime$,2)
13236T2$=MID$(Ctime$,20,2)
13238T3$=MID$(Ctime$,17,2)
13240T4$=MID$(Ctime$,5,2)
```

```
13242T5$=MID$(Ctime$,8,3)
13244IF T5$="Jan" T5$="01"
13246IF T5$="Feb" T5$="02"
13248IF T5$="Mar" T5$="03"
13250IF T5$="Apr" T5$="04"
13252IF T5$="May" T5$="05"
13254IF T5$="Jun" T5$="06"
13256IF T5$="Jul" T5$="07"
13258IF T5$="Aug" T5$="08"
13260IF T5$="Sep" T5$="09"
13262IF T5$="Oct" T5$="10"
13264IF T5$="Nov" T5$="11"
13266IF T5$="Dec" T5$="12"
13270Ctime$=T5$+T4$+T3$+T2$+T1$
13280Ctime%=VAL(Ctime$)
13320ENDPROC
13330:
13350:
13360:
13370:
13380:
13400:
13410DEFPROCscrnsave
13420OSCLI "SCREENSAVE S"+$text10%
13425VDU7
13430ENDPROC
13440:
13450DEFPROCfind_zero
13460REM FINDS MOUSE COORDINATES CORRESPONDING TO PRESSING SELECT BUTTON
13470REPEAT
13475block%!0=whandle%
13480SYS "Wimp_GetPointerInfo",,block%
13490but%=block%!8
13494mX%=block%!0:mY%=block%!4 :REM MOUSE COORDINATES
13500UNTIL but%<>0 :REM UNTIL ANY BUTTON IS PRESSED
13505VDU4:PRINT mX%;"  ";mY%:VDU5
13510IF block%!16<>-1 Zflag%=0 ELSE Zflag%=1:REM INVALID IF PRESSED OUTSIDE WORK AREA
13540ENDPROC
13550:
13560DEFPROCmarkzero
13565zerorec%=Prec%
13570SYS"Wimp_SetColour",11
13580DTA=4:MOVExpos%-DTA,ypos%:DRAWxpos%+DTA,ypos%:MOVExpos%,ypos%-
      DTA:DRAWxpos%,ypos%+DTA
13600ENDPROC
13610:
13700DEFPROCmotor_on(sense%)
13705PROCadrandoutput(0,15,"C300,1")
13710PROCadrandoutput(0,15,"C1,0")
13720PROCadrandoutput(0,15,"C2,1,0")
13730IF sense%=1 PROCadrandoutput(0,15,"C4,1,-.35"):REM SET RAMP AMPLITUDE TO BE .35 OF
      FULL SCALE, I.E. 17mm
13733IF sense%=-1 PROCadrandoutput(0,15,"C4,1,.35")
13735tt=VAL($text5%):rate=ABS(tt)/3000:rate$=STR$(rate)
13740PROCadrandoutput(0,15,"C6,1,"+rate$):REM SET RAMP RATE AS FRACTION OF FULL SCALE
      PER SECOND
13750PROCadrandoutput(0,15,"C300,1")
13760PROCadrandoutput(0,15,"C1,1")
13770ENDPROC
13780:
13790DEFPROCmotor_off
13795PROCadrandoutput(0,15,"C300,1")
13800PROCadrandoutput(0,15,"C1,0")
13810ENDPROC
13820:
13840DEFPROCset_limits
13850 ENDPROC
13851mind=VAL($text21%):mind=mind/50:mind$=STR$(mind)
13852maxd=VAL($text19%):maxd=maxd/50:maxd$=STR$(maxd)
```

```
13853minf=VAL($text18%):minf=minf/50:minf$=STR$(minf)
13854maxf=VAL($text20%):maxf=maxf/50:maxf$=STR$(maxf)
13860PROCadrandoutput(0,15,"C326,0"):REM UNLOCK ALL LIMITS
13880PROCadrandoutput(0,15,"C122,1,0,"+mind$):REM SET MIN LIMIT THRESHOLD
13882PROCadrandoutput(0,15,"C122,2,0,"+minf$):REM SET MIN LIMIT THRESHOLD
13890PROCadrandoutput(0,15,"C123,1,0,1"):REM SET MIN LIMIT ACTION (d) TO ACTUATOR OFF
13892PROCadrandoutput(0,15,"C123,2,0,1"):REM SET MIN LIMIT ACTION (f) TO ACTUATOR OFF
13900PROCadrandoutput(0,15,"C121,1,0,1"):REM ARM MIN LIMIT (displ)
13901PROCadrandoutput(0,15,"C121,2,0,1"):REM ARM MIN LIMIT (force)
13920PROCadrandoutput(0,15,"C122,1,1,"+maxd$):REM SET MAX LIMIT THRESHOLD
13921PROCadrandoutput(0,15,"C122,2,1,"+maxf$):REM SET MAX LIMIT THRESHOLD
13922PROCadrandoutput(0,15,"C123,2,1,1"):REM SET MAX LIMIT ACTION TO ACTUATOR OFF
13930PROCadrandoutput(0,15,"C123,1,1,1"):REM SET MAX LIMIT ACTION TO ACTUATOR OFF
13940PROCadrandoutput(0,15,"C121,1,1,1"):REM ARM MAX LIMIT (displ)
13942PROCadrandoutput(0,15,"C121,2,1,1"):REM ARM MAX LIMIT (force)
13950PROCadrandoutput(0,15,"C326,1"):REM LOCK ALL LIMITS
13960ENDPROC
13970:
14000DEFPROCunset_limits
14005ENDPROC
14010PROCadrandoutput(0,15,"C326,0"):REM UNLOCK ALL LIMITS
14020REM disarm all limits
14030PROCadrandoutput(0,15,"C121,1,0,0")
14040PROCadrandoutput(0,15,"C121,1,1,0")
14050PROCadrandoutput(0,15,"C121,2,0,0")
14060PROCadrandoutput(0,15,"C121,2,1,0")
14070ENDPROC
14080:
14100 DEFPROCread_serial
14110LOCAL X$,XY$
14120*FX7,7
14130*FX8,7
14140*FX2,1
14150*FX21,1
14160*FX3,6
14170INPUT XY$
14180*FX3
14190X$=MID$(XY$,4,5)
14200serdat=VAL(X$)
14205IF MID$(XY$,2,1)="-" serdat=-serdat
14210*FX3,0
14220*FX21,1
14230*FX2
14240ENDPROC
14250:
14260DEFPROCFIN
14270VDU26
14280*FX3,0
14290*FX21,1
14300*FX2
14310CLOSE#0
14320ENDPROC
14330:
14335DEFPROCfind_rec
14338sKNT%=sKNT%+1
14339block%!0=whandle%
14340SYS"Wimp_GetWindowInfo",,block%
14344PROCgetorigin(block%,x0%,y0%)
14350grad=(FN`CVX(`LX)-FN`CVX(`SX))/(`LX-`SX)
14365 Prec%=((x%-FN`CVX(`SX))/grad)+`SX
14370block%!0=whandle%:block%!4=Y7handle%:block%!8=0:block%!12=0
14380$text22%="Rec "+STR$(Prec%)
14390SYS"Wimp_SetIconState",,block%
14392IF Prec%<0 Prec%=0
14395yp%=FN`CVY(DAT(Prec%,3))
14397SYS"Wimp_SetColour",11
14398DAT(Prec%,7)=2:REM marks selected point for processing
14399IF relax%=1 DAT(Prec%,7)=3:SYS"Wimp_SetColour",15:relax%=0
14400DTA=4:MOVEx%-DTA,yp%:DRAWx%+DTA,yp%:MOVEx%,yp%-DTA:DRAWx%,yp%+DTA
```

```
14405REM Augment DATs() array
14407DATs(sKNT%,1)=DAT(Prec%,1)
14409DATs(sKNT%,2)=DAT(Prec%,2)
14411DATs(sKNT%,3)=DAT(Prec%,3)
14413DATs(sKNT%,4)=DAT(Prec%,4)
14415DATs(sKNT%,5)=DAT(Prec%,5)
14417DATs(sKNT%,6)=DAT(Prec%,6)
14419DATs(sKNT%,8)=DAT(Prec%,7)
14421DATs(sKNT%,7)=DAT(Prec%,8)
14500ENDPROC
14510:
14550DEFPROCprint_data
14560:
14570ENDPROC
14580:
14600DEFPROClistout
14605CLS
14610REM prepares processed data for listing and printing
14620IF printer%=1 VDU2 ELSE VDU3
14630*FX6
14640FOR II%=1 TO 100:PRINT II%; "  HELLO WORLD":NEXT II%
14700ENDPROC
14790VDU3:printer%=0
14800ENDPROC
14900:
14910DEFPROCsavetextfile
14915ATIME%=DATs(3,6)
14917PROCseconds
14918ATIMO%=ATIME%
14920Tfile=OPENOUT($text10%+"t")
14930BPUT#Tfile,"File "+$text10%
14940BPUT#Tfile,"Length "+CHR$(9)+$text8%+CHR$(9);
14950BPUT#Tfile,"Diameter "+CHR$(9)+$text9%+CHR$(9);
14951BPUT#Tfile,"Disp.rate "+CHR$(9)+$text5%
14952BPUT#Tfile," Displ."+CHR$(9)+" Ext.Force"+CHR$(9)+" Int.Force"+CHR$(9)+" Temp
      mV"+CHR$(9)+" Press mV"+CHR$(9)+" time s"+CHR$(9)+" Pore P.mV"+CHR$(9)+"
      marker"+CHR$(9)+" T. deg C"+CHR$(9)+" P(MPa)"+CHR$(9)+" PH2O(MPa)"+CHR$(9);
14953BPUT#Tfile," Strain%"+CHR$(9)+" Stress MPa"+CHR$(9)+" Str.Rate/s"
14960FOR KTR%=3 TO Nrecs%
14962ATIME%=DATs(KTR%,6)
14964PROCseconds
14966DATs(KTR%,6)=ATIME%-ATIMO%:REM now is elapsed time
14970FOR KTT%=1 TO 14
14980AS$=STR$(DATs(KTR%,KTT%))
14990BPUT#Tfile,AS$+CHR$(9);
15000NEXT KTT%
15010BPUT#Tfile,CHR$(10);
15020NEXT KTR%
15030CLOSE#Tfile
15035VDU7
15040ENDPROC
15050:
15060DEFPROCseconds
15070REM to convert time to elapsed seconds
15080MON%=ATIME%DIV100000000
15090DAY%=(ATIME%MOD100000000)DIV1000000
15100HR%=(ATIME%MOD1000000)DIV10000
15110MIN%=(ATIME%MOD10000)DIV100
15120SEC%=ATIME%MOD100
15130IF MON%=01 THEN MON%=0
15140IF MON%=02 THEN MON%=2678400
15150IF MON%=03 THEN MON%=5097600
15160IF MON%=04 THEN MON%=8568000
15170IF MON%=05 THEN MON%=10368000
15180IF MON%=06 THEN MON%=13046400
15190IF MON%=07 THEN MON%=15638400
15200IF MON%=08 THEN MON%=18316800
15210IF MON%=09 THEN MON%=20995200
15220IF MON%=10 THEN MON%=23587200
```

```
15230IF MON%=11 THEN MON%=26265600
15240IF MON%=12 THEN MON%=28857600
15250REM total elapsed seconds are :
15260ATIME%=SEC%+MIN%*60+HR%*3600+DAY%*86400+MON%
15270ENDPROC
15280:
15300DEFPROCprocess_data
15310REM initial values
15320FGZ=DATs(3,3):DZ=DATs(3,1)
15330len=VAL($text8%):dia=VAL($text9%):DRATE=VAL($text5%)
15340area0=(PI*(dia/2)^2)/1000000: REM in square metres
15350REM convert time for t0
15360ATIME%=DATs(3,6)
15370PROCseconds
15380t0%=ATIME%
15390REM ctr% is counter for times round stress/strain loop
15400ctr%=0
15410REM dct% is counter for array of selected datapoints
15420dct%=2
15430REPEAT
15435 IF DATs(dct%+1,8) <2 OR DATs(dct%,8) >4 GOTO 15475
15440IF DATs(dct%+1,8)=2 PROCstressstrainloop
15445IF DATs(dct%,8)=4 VDU7: ENDPROC
15450IF DATs(dct%,8)=3 PROCrelax
15470UNTIL DATs(dct%,8)=4
15475VDU7
15477process%=0
15480ENDPROC
15490:
15500DEFPROCstressstrainloop
15510ctr%=ctr%+1
15520REPEAT
15530dct%=dct%+1
15540FG=(DATs(dct%,3)-FGZ)
15550TM=(DATs(dct%,4)/.0413)+20
15560P=(DATs(dct%,5)-1.737)/.0155
15570PH20=(3504*DATs(dct%,7)-7394)/145
15580FKN=(.9479-.0000196*TM)*(FG)-.001148*(FG)^2
15590MDISPL=(.0166-.0000001*TM)*(FKN)-.00001*(5.34-.00165*TM)*(FKN)^2-
        FKN*(.000725*(1+.000006*TM))
15600ATIME%=DATs(dct%,6)
15610PROCseconds
15620ELTIME%=ATIME%-t0%
15623IFdct%=3 GOTO 15630:REM because DRATE yet indeterminate from next line
15625DRATE=60*(DATs(dct%,1)-DZ)/(10*ELTIME%):REM +ve for compression
15630STRAIN=100*((ELTIME%*DRATE/60)-(MDISPL))/len
15635 Cjack=0:REM is expressed as MPa on specimen
15640STRESS=((FKN/1000)/((1+(STRAIN/100))*area0))-Cjack
15650IF dct%=3 EDOT=0:GOTO 15670
15655 IF ELTIME%=PELTIME% EDOT=0:GOTO 15670
15660EDOT=(STRAIN-PSTRAIN)/(100*(ELTIME%-PELTIME%))
15670:
15680REM Assign output values
15690DATs(dct%,9)=TM
15700DATs(dct%,10)=P
15710DATs(dct%,11)=PH20
15720DATs(dct%,12)=STRAIN
15730DATs(dct%,13)=STRESS
15740DATs(dct%,14)=EDOT
15750PSTRAIN=STRAIN:PELTIME%=ELTIME%:PFKN=FKN 15760UNTIL DATs(dct%,8)<>2
15763 sts=INKEY(100)
15765VDU7
15770ENDPROC
15780:
15800DEFPROCrelax
15810REPEAT
15820dct%=dct%+1
15850FG=(DATs(dct%,3)-FGZ)
15860TM=(DATs(dct%,4)/.0413)+20
```

```
15870P=(DATs(dct%,5)-1.737)/.0155
15880PH20=(3504*DATs(dct%,7)-7394)/145
15890FKN=(.9479-.0000196*TM)*(FG)-.001148*(FG)^2
15900MDISPL=(.0166-.0000001*TM)*(FKN)-.00001*(5.34-.00165*TM)*(FKN)^2-
        FKN*(.000725*(1+.000006*TM))
15905IF track%=1 MDISPL=MDISPL-FKN*.0026
15910PMDISPL=(.0166-.0000001*TM)*(PFKN)-.00001*(5.34-.00165*TM)*(PFKN)^2-
        PFKN*(.000725*(1+.000006*TM))
15915IF track%=1 PMDISPL=PMDISPL-FKN*.0026
15920ATIME%=DATs(dct%,6)
15930PROCseconds
15940ELTIME%=ATIME%-t0%
15950DTIME%=ELTIME%-PELTIME%
15960DDISPLM=ABS(MDISPL-PMDISPL)
15970DDISPLS=(FKN-PFKN)*len*(1-
        PSTRAIN/100)/(30000000*area0*(1+PSTRAIN/100)) 15980STRAIN=100*(len-((1-
        PSTRAIN/100)*len-ABS(DDISPLM)-ABS(DDISPLS)))/len
15985STRESS=((FKN/1000)/((1+(STRAIN/100))*area0))-Cjack
15990EDOT=(ABS(DDISPLM)+ABS(DDISPLS))/(len*(DTIME%+1))
16000:
16010REM assign output values
16020DATs(dct%,9)=TM
16030DATs(dct%,10)=P
16040DATs(dct%,11)=PH20
16050DATs(dct%,12)=STRAIN
16060DATs(dct%,13)=STRESS
16070DATs(dct%,14)=EDOT
16080PSTRAIN=STRAIN:PELTIME%=ELTIME%:PFKN=FKN
16090UNTIL DATs(dct%,8)<>3
16095SOUND 1,-15,150,4
16100ENDPROC
16110:
16140:
16150DEFPROConlinereport
16152ENDPROC: REM proc not finished yet
16155REM to read the 3 instron channels as live, one shot reports
16160REPEAT
16170data$="nodata"
16180REPEAT
16190PROCadrandoutput(0,15,"C901,0,2,0,1")
16200PROCadrandoutput(0,15,"C901,1,2,0,2")
16210PROCadrandoutput(0,15,"C901,2,2,0,3")
16220devicestatus%=FNserial_poll(15)
16230PROCbinpoll
16240UNTIL BITSET(4)=1
16250PROCadrandoutput(0,15,"Q902")
16260data$=FNadrandinput(1,15,248)
16270R2%=0:R3%=0
16280REM Decompose string into 3 values
16290R1=VAL(LEFT$(data$,11))
16300FOR RT%=1 TO LEN(data$)
16310IF R2%>1 GOTO
16320IF MID$(data$,RT%,1)=","AND R2%=0 THEN R2%=RT%+1:GOTO
16330IF MID$(data$,RT%,1)=","AND R3%=0 THEN R3%=RT%+1
16340NEXT RT%
16350R2=VAL(MID$(data$,R2%,11))
16360R3=VAL(MID$(data$,R3%,11))
16370REM R1, R2, AND R3 ARE THE VALUES OF THE 3 INSTRON CHANNELS
16380IF ABS(R3-zeroload)>=1 hit%=1 ELSE hit%=0
16390IF hit%=1 PROCmotor_off
16400DAT(KNT%1)=R1
16410startdispl=R1
16420:
16430:
17000DEFPROCshowrec
17010block%!0=whandle%
17020SYS"Wimp_GetWindowInfo",,block%
17030PROCgetorigin(block%,x0%,y0%)
17040grad=(FN`CVX(`LX)-FN`CVX(`SX))/(`LX-`SX)
```

```
17050 Prec%=((x%-FN`CVX(`SX))/grad)+`SX
17060block%!0=whandle%:block%!4=Y7handle%:block%!8=0:block%!12=0
17070$text22%="Rec "+STR$(Prec%)
17080SYS"Wimp_SetIconState",,block%
17090IF Prec%<0 Prec%=0
17095xpos%=x%
17096ypos%=FN`CVY(DAT(Prec%,3))
17100ENDPROC
17110:
17120:
17300DEFPROCrealtimeprocess 17310FGZ=DAT(zerorec%,3)
17320len=VAL($text8%):dia=VAL($text9%):DRATE=VAL($text5%)
17330area0=(PI*(dia/2)^2)/1000000: REM in square metres
17340ATIME%=DAT(zerorec%,6)
17350PROCseconds
17360t0%=ATIME%
17370FG=(DAT(KNT%,3)-FGZ)
17380FKN=(.9479-.0000196*TM)*(FG)-.001148*(FG)^2
17390MDISPL=(.0166-.0000001*TM)*(FKN)-.00001*(5.34-.00165*TM)*(FKN)^2-
    FKN*(.000725*(1+.000006*TM))
17400DISPL=(DAT(KNT%,1)-DAT(zerorec%,1))/10:REM DISPL in mm
17410CDISPL=DISPL-MDISPL
17420STRAIN=(CDISPL/len)*100
17430Cjack=0
17440SIG=((FKN/1000)/((1+(STRAIN/100))*area0))-Cjack
17445rtprocess%=1
17450ENDPROC
17460:17470DEFPROCstresscontrol
17500 IF dead1>=dead2 dead2=dead1+.001
17501ATIME%=DAT(KNT%,6):PROCseconds:t0%=ATIME%
17503 IF rtprocess%=0 ENDPROC:REM prevents access to stress control unless rtprocess has been
    accesed first
17505IF creep%<>1 AND creepflag%=1
    PROCadrandoutput(0,15,"C300,1"):creepflag%=0:ENDPROC
17510IF track%=1 OR creep%<>1 ENDPROC
17520REMcalculate desired internal load from realtime
    stress17530DKN=strcon*1000*(1+(STRAIN/100))*area0
17531 IF DKN<FKN AND loaded%=1 creepflag%=1:ENDPROC
17532 IF DKN<FKN AND loaded%=0
    PROCmotor_off:PDISPL=CDISPL:ATIME%=DAT(KNT%,6):PROCseconds:PTIME%=ATIME%:creep
    flag%=1:loaded%=1:ENDPROC
17533 IF FKN<(DKN-dead2) AND loaded%=0 AND $text5%<>initsp$ THEN $text5%=initsp$: GOTO
    17550: REM if load drops too low because motor cant keep up, revert to initial loading
    configuration
17534IF FKN<(DKN-dead2) AND loaded%=1 $text5%=initsp$: loaded%=0: GOTO 17550: REM if load
    drops too low, revert to initial loading configuration
17535 IF DKN>=FKN AND DKN<=(FKN+dead1) creepflag%=1:ENDPROC
17536 IF FKN<(DKN-dead1) AND loaded%=0:creepflag%=1:ENDPROC: REM prevents interruption
    of motor during initial loading
17537 rlxrate=ABS(ABS(CDISPL)-ABS(PDISPL))/ABS(1+t0%-PTIME%):REM in mm/sec
17545 $text5%=STR$(rlxrate*60*multip):REM  sets new motor rate in mm/min ATTHE RELAXATION
    RATE * MULTIPLIER
17550 PROCmotor_on(1):loaded%=0
17575creepflag%=1
17580ENDPROC
17590:
17600:
17610DEFPROCtrack
17620IF track%<>1 AND trakflag%=1 PROCadrandoutput(0,15,"C300,1"):trakflag%=0
17630IF track%<>1 OR creep%=1 ENDPROC
17640REM IF track%=1 AND trakflag%<>1 PROCmotor_off
17650IF strcon<1000 ENDPROC
17660frac=-ABS((DAT(KNT%,3)-fgofset)*MF)/100
17670IF ABS(frac)>0.9 VDU7:trakflag%=0:ENDPROC
17680PROCadrandoutput(0,15,"C323,2,"+STR$(frac))
17690trakflag%=1
17700ENDPROC
17710:
```

Appendix 9

Modeling of melt extraction rates

A9.1 Introduction

In this appendix the spreadsheets used to calculate the extraction rates of granitic melt from partially molten Westerly Granite and from a protoliths containing a higher water content are presented, as presented in **Chapter 8**. These spreadsheets were used to construct **Figure 8.04** and **Figure 8.08**. Initially, the formulas used in the spreadsheets are presented, with columns labelled from **A** to **X**. Reference to **A1** refers to an unchanging cell, containing a constant. This is followed by the spreadsheets.

A9.2 Westerly granite and granitic melt.

In this spreadsheet the extraction rates of Westerly granite and granitic melt with vein spacing of 1 vein per meter are modeled (**Table A9.01**). Porous flow is modeled after McKenzie(1984) with the denominator in the permeability equation chosen after Bourbie and Zinszer (1985). The limits of plastic deformation of quartz were modeled after Paterson and Luan (1990), assuming Q = 135 kJ mol^{-1} and n = 2.5. In the first columns of the formula tables the name of the column is listed that is later used in the formulas lower down. The next column lists the name of the variable that is being calculated. This is followed by a listing of the actual formula used to calculate the numbers in the spreadsheet. The right hand column indicated which equation was used in the formula column.

Westerly granite

C	Variables	Formula	Equation
A1	Temp	Constant temperature in °C	
B1	vein phi	(EXP(0.00875*A1))/265	E3.01
C1	melt %	(EXP(0.00875*A1))/265	E3.01
D1	vein phi/e	B1/2.71828	
E1	k	((0.001)^2)*((B1/100)^3)/400	E6.03
F1	viscosity	0.00000813*EXP(320000/(8.31441*(A1+273)))	E6.08
G1	stress (Pa)	(8*E1/(3*0.25*F1*10^(-5.832)*EXP(-510061/(8.31441*(A1+273)))))^(1/1.92)	E8.13

H1	J (comp)	8*E1*G1/(3*0.25*F1)	E8.13
I1	J (flolaw)	(10^(-5.832))*(G1^(2.92))*(EXP(-510061/(8.31441*(A1+273))))	E8.14
J1	t (a)	((B1/100)/I1)/31536000	E8.14
K1	Temp	A1	
L1	log time (a)	LOG(J1)	
M1	Wo,(m/s)	O1*(1-(B1/100))*500*10/(F1*(B1/100))	E8.02
N1	log th(a,1km)	LOG(1000/(M1*(1-(B1/100))*31536000))	E8.03
O1	k(cracks)	(B1/100)^3/((4*12))	E8.07
P1	Temp	A1	
Q1	log (tot.time)	IF(L1>N1,L1,N1)	

McKenzie (1984)

C	Variables	Formula	Equation
S1	Wo,(m/s)	(T1*(1-(B1/100))*500*9.81/(F1*(B1/100)))	E8.02
T1	k(pores)	((0.001^2))*((B1/100)^3)/400	E6.03
U1	Temp	A1	
V1	log(tot.time)	LOG(1000/(S1*(1-(B1/100))*31536000))	E8.05
W1	COMPL(m)	(T1*(170000000000000000)/F1)^0.5	E8.01
X1	COMPtime(a)	W1/(31536000*S1*(1-B1/100))	E8.03

General granite

C	Variables	Formula	Equation
	water content	H2O% content = A1= 0.3	
A1	Temperature	Constant temperature in °C	
B1	porosity	100*(10^(-3.682))*((A1)^0.9)*(EXP(0.00875*A1))	E8.18
C1	melt %	100*(10^(-3.682))*((A1)^0.9)*(EXP(0.00875*A1))	E8.18
D1	vein phi/e	B1/2.71828	
E1	k	((0.001)^2)*((B1/100)^3)/400	E6.03
F1	viscosity	(10^(-6.82))*EXP(320000/(8.31441*(A1+273))*(A1^(-3.3)))	E8.21
G1	stress (Pa)	(8*E1/(3*0.25*F1*10^(-5.832)*EXP(-510061/(8.31441*(A1+273)))))^(1/1.92)	E8.13
H1	J (comp)	8*E1*G1/(3*0.25*F1)	E8.13
I1	J (flolaw)	(10^(-5.832))*(G1^(2.92))*(EXP(-510061/(8.31441*(A1+273))))	E8.14
J1	t (a)	((B1/100)/I1)/31536000	E8.14
K1	Temp	A1	
L1	log time (a)	LOG(J1)	
M1	Wo, (m/s)	O1*(1-(B1/100))*500*9.81/(F1*(B1/100))	E8.02
N1	log th (a,1km)	LOG(1000/(M1*(1-(B1/100))*31536000))	E8.03

O1	k (cracks)	(**B1**/100)^3/((4*12))	E8.07
P1	Temp	**A1**	
Q1	log (tot.time)	IF(**L1**>**N1**,**L1**,**N1**)	

Paterson and Luan (1990) quartz flowlaw

C	Variables	Formula	Equation
S1	flowstress MPa	(**I1***EXP(135000/(8.31441*(**P1**+273)))/0.000000065)^(1/2.5)	
T1	diff (MPa)	**S1**-(**G1**/1000000)	
U1	flowstress MPa	((**I1***EXP(135000/(8.31441*(P1+273)))))/0.0000000004)^(1/4)	
V1	diff (MPa)	**U1**-(**G1**/1000000)	

A9.3 Calculation of melt extraction rates of Westerly granite with variable vein spacing

In this spreadsheet the effect of variable vein spacing on melt extraction between 20 and 0.5 veins per metre was calculated, that was used to construct **Figure 8.04, b** (**Table A9.02**). This was carried out by extracting melt from partially molten Westerly granite and altering the vein spacing in successive blocks of data at temperatures between 700 and 1050 °C.

C	Variables	Formula	Equation
A1	Temp	Constant temperature in °C	
B1	vein phi	(EXP(0.00875***A1**))/265	E3.01
C1	melt %	(EXP(0.00875***A1**))/265	E3.01
D1	vein phi/e	**B1**/2.71828	
E1	k	((0.001)^2)*((**B1**/100)^3)/400	E6.03
F1	viscosity	0.00000813*EXP(320000/(8.31441*(**A1**+273)))	E6.08
G1	stress(Pa)	(8***E1**/(3*((1/(**A1**)^**2**)^2)***F1***10^(-5.832)*EXP	
		(-510061/(8.31441*(**A1**+273)))))^(1/1.92)	E8.13
H1	J (comp)	8***E1****G1**/(3*((1/**A1**)^2)***F1**)	E8.13
I1	J (flolaw)	(10^(-5.832))*(**G1**^(2.92))*(EXP(-510061/(8.31441*(**A1**+273))))	E8.14
J1	t(a)	((**B1**/100)/I1)/31536000	E8.14
K1	Temp	**A1**	
L1	log time (a)	LOG(**J1**)	
M1	Wo,(m/s)	**O1***(1-(**B1**/100))*500*9.81/(**F1***(**B1**/100))	E8.02
N1	log th (a,1km)	LOG(1000/(**M1***(1-(**B1**/100))*31536000))	E8.03

O1	k(cracks)	(**B1**/100)^3/(4*(**A1**^2)*12)	E8.07
P1	Temp	**A1**	
Q1	log (tot.time)	IF(**L1**>**N1**,**L1**,**N1**)	

Table A9.01: Modeling of melt extraction rate of granitoid melt with z = 1mm and N = 1 vein per metre.

| Westerly granite data | | |

Table A9.02: Modeling of the effect of variable vein spacing on melt extarction rate of Westerly granite.

Westerly granite data 20 veins per met				20												
Temp	vein phi	melt %	vein phi/e	k	viscosity	stress(Pa)	J(comp)	J(flolaw)	f(a)	Temp	log time(a)	Wo,(m/s)	logTh(a,1km)	k(cracks)	Temp	log(tot.time)
700	1.73	1.73	0.63	1.28E-14	1.23E+12	2.21E+05	2.47E-18	2.47E-18	2.22E+08	700	8.35	6.09E-17	11.72	2.67E-10	700	11.72
750	2.67	2.67	0.98	4.77E-14	1.77E+11	2.41E+05	6.90E-17	6.90E-17	1.23E+07	750	7.09	1.00E-15	10.51	9.93E-10	750	10.51
800	4.14	4.14	1.52	1.77E-13	3.07E+10	2.77E+05	1.70E-15	1.70E-15	7.70E+05	800	5.89	1.36E-14	9.38	3.69E-09	800	9.38
850	6.41	6.41	2.36	6.58E-13	6.23E+09	3.35E+05	3.78E-14	3.78E-14	5.38E+04	850	4.73	1.58E-13	8.33	1.37E-08	850	8.33
900	9.93	9.93	3.65	2.45E-12	1.44E+09	4.23E+05	7.63E-13	7.63E-13	4.12E+03	900	3.62	1.57E-12	7.35	5.10E-08	900	7.35
950	15.00	15.38	5.52	8.44E-12	3.78E+08	5.32E+05	1.27E-11	1.27E-11	3.75E+02	950	2.57	1.29E-11	6.46	1.76E-07	950	6.46
1000	15.00	23.81	5.52	8.44E-12	1.10E+08	3.63E+05	2.98E-11	2.98E-11	1.60E+02	1000	2.20	4.45E-11	5.92	1.76E-07	1000	5.92
1050	15.00	36.88	5.52	8.44E-12	3.50E+07	2.55E+05	6.55E-11	6.55E-11	7.26E+01	1050	1.86	1.40E-10	5.43	1.76E-07	1050	5.43
Westerly granite data 10 veins per me				10												
Temp	vein phi	melt %	vein phi/e	k	viscosity	stress(Pa)	J(comp)	J(flolaw)	f(a)	Temp	log time(a)	Wo,(m/s)	logTh(a,1km)	k(cracks)	Temp	log(tot.time)
700	1.73	1.73	0.63	1.28E-14	1.23E+12	1.07E+05	3.00E-19	3.00E-19	1.83E+09	700	9.26	2.44E-16	11.12	1.07E-09	700	11.12
750	2.67	2.67	0.98	4.77E-14	1.77E+11	1.17E+05	8.38E-18	8.38E-18	1.01E+08	750	8.00	4.00E-15	9.91	3.97E-09	750	9.91
800	4.14	4.14	1.52	1.77E-13	3.07E+10	1.35E+05	2.07E-16	2.07E-16	6.34E+06	800	6.80	5.46E-14	8.78	1.48E-08	800	8.78
850	6.41	6.41	2.36	6.58E-13	6.23E+09	1.63E+05	4.59E-15	4.59E-15	4.43E+05	850	5.65	6.31E-13	7.73	5.49E-08	850	7.73
900	9.93	9.93	3.65	2.45E-12	1.44E+09	2.05E+05	9.27E-14	9.27E-14	3.40E+04	900	4.53	6.28E-12	6.75	2.04E-07	900	6.75
950	15.00	15.38	5.52	8.44E-12	3.78E+08	2.58E+05	1.54E-12	1.54E-12	3.09E+03	950	3.49	5.17E-11	5.86	7.03E-07	950	5.86
1000	15.00	23.81	5.52	8.44E-12	1.10E+08	1.76E+05	3.61E-12	3.61E-12	1.32E+03	1000	3.12	1.78E-10	5.32	7.03E-07	1000	5.32
1050	15.00	36.88	5.52	8.44E-12	3.50E+07	1.24E+05	7.96E-12	7.96E-12	5.98E+02	1050	2.78	5.58E-10	4.82	7.03E-07	1050	4.82
Westerly granite data 5 veins per m				5.00E+00												
Temp	vein phi	melt %	vein phi/e	k	viscosity	stress(Pa)	J(comp)	J(flolaw)	f(a)	Temp	log time(a)	Wo,(m/s)	logTh(a,1km)	k(cracks)	Temp	log(tot.time)
700	1.73	1.73	0.63	1.28E-14	1.23E+12	5.22E+04	3.64E-20	3.64E-20	1.50E+10	700	10.18	9.74E-16	10.52	4.28E-09	700	10.52
750	2.67	2.67	0.98	4.77E-14	1.77E+11	5.68E+04	1.02E-18	1.02E-18	8.32E+08	750	8.92	1.60E-14	9.31	1.59E-08	750	9.31
800	4.14	4.14	1.52	1.77E-13	3.07E+10	6.54E+04	2.51E-17	2.51E-17	5.22E+07	800	7.72	2.18E-13	8.18	5.91E-08	800	8.18
850	6.41	6.41	2.36	6.58E-13	6.23E+09	7.91E+04	5.58E-16	5.58E-16	3.65E+06	850	6.56	2.52E-12	7.13	2.19E-07	850	7.13
900	9.93	9.93	3.65	2.45E-12	1.44E+09	9.97E+04	1.13E-14	1.13E-14	2.80E+05	900	5.45	2.51E-11	6.15	8.15E-07	900	6.15
950	15.00	15.38	5.52	8.44E-12	3.78E+08	1.26E+05	1.87E-13	1.87E-13	2.54E+04	950	4.41	2.07E-10	5.26	2.81E-06	950	5.26
1000	15.00	23.81	5.52	8.44E-12	1.10E+08	8.56E+04	4.39E-13	4.39E-13	1.08E+04	1000	4.03	7.12E-10	4.72	2.81E-06	1000	4.72
1050	15.00	36.88	5.52	8.44E-12	3.50E+07	6.01E+04	9.66E-13	9.66E-13	4.92E+03	1050	3.69	2.23E-09	4.22	2.81E-06	1050	4.22
Westerly granite data 2 veins per mete				2												
Temp	vein phi	melt %	vein phi/e	k	viscosity	stress(Pa)	J(comp)	J(flolaw)	f(a)	Temp	log time(a)	Wo,(m/s)	logTh(a,1km)	k(cracks)	Temp	log(tot.time)
700	1.73	1.73	0.63	1.28E-14	1.23E+12	2.01E+04	2.24E-21	2.24E-21	2.44E+11	700	11.39	6.09E-15	9.72	2.67E-08	700	11.39
750	2.67	2.67	0.98	4.77E-14	1.77E+11	2.19E+04	6.27E-20	6.27E-20	1.35E+10	750	10.13	1.00E-13	8.51	9.93E-08	750	10.13
800	4.14	4.14	1.52	1.77E-13	3.07E+10	2.52E+04	1.55E-18	1.55E-18	8.47E+08	800	8.93	1.36E-12	7.38	3.69E-07	800	8.93
850	6.41	6.41	2.36	6.58E-13	6.23E+09	3.05E+04	3.43E-17	3.43E-17	5.92E+07	850	7.77	1.58E-11	6.33	1.37E-06	850	7.77
900	9.93	9.93	3.65	2.45E-12	1.44E+09	3.84E+04	6.93E-16	6.93E-16	4.54E+06	900	6.66	1.57E-10	5.35	5.10E-06	900	6.66
950	15.00	15.38	5.52	8.44E-12	3.78E+08	4.83E+04	1.15E-14	1.15E-14	4.13E+05	950	5.62	1.29E-09	4.46	1.76E-05	950	5.62
1000	15.00	23.81	5.52	8.44E-12	1.10E+08	3.30E+04	2.70E-14	2.70E-14	1.76E+05	1000	5.25	4.45E-09	3.92	1.76E-05	1000	5.25
1050	15.00	36.88	5.52	8.44E-12	3.50E+07	2.32E+04	5.95E-14	5.95E-14	7.99E+04	1050	4.90	1.40E-08	3.43	1.76E-05	1050	4.90
Westerly granite data 1 vein per mete				1												
Temp	vein phi	melt %	vein phi/e	k	viscosity	stress(Pa)	J(comp)	J(flolaw)	f(a)	Temp	log time(a)	Wo,(m/s)	logTh(a,1km)	k(cracks)	Temp	log(tot.time)
700	1.73	1.73	0.63	1.28E-14	1.23E+12	9.76E+03	2.72E-22	2.72E-22	2.01E+12	700	12.30	2.44E-14	9.12	1.07E-07	700	12.30
750	2.67	2.67	0.98	4.77E-14	1.77E+11	1.06E+04	7.61E-21	7.61E-21	1.11E+11	750	11.05	4.00E-13	7.91	3.97E-07	750	11.05
800	4.14	4.14	1.52	1.77E-13	3.07E+10	1.22E+04	1.88E-19	1.88E-19	6.98E+09	800	9.84	5.46E-12	6.78	1.48E-06	800	9.84
850	6.41	6.41	2.36	6.58E-13	6.23E+09	1.48E+04	4.17E-18	4.17E-18	4.87E+08	850	8.69	6.31E-11	5.73	5.49E-06	850	8.69
900	9.93	9.93	3.65	2.45E-12	1.44E+09	1.87E+04	8.42E-17	8.42E-17	3.74E+07	900	7.57	6.28E-10	4.75	2.04E-05	900	7.57
950	15.00	15.38	5.52	8.44E-12	3.78E+08	2.35E+04	1.40E-15	1.40E-15	3.40E+06	950	6.53	5.17E-09	3.86	7.03E-05	950	6.53
1000	15.00	23.81	5.52	8.44E-12	1.10E+08	1.60E+04	3.28E-15	3.28E-15	1.45E+06	1000	6.16	1.78E-08	3.32	7.03E-05	1000	6.16
1050	15.00	36.88	5.52	8.44E-12	3.50E+07	1.12E+04	7.23E-15	7.23E-15	6.58E+05	1050	5.82	5.58E-08	2.82	7.03E-05	1050	5.82
Westerly granite data 0.5 vein per met				0.5												
Temp	vein phi	melt %	vein phi/e	k	viscosity	stress(Pa)	J(comp)	J(flolaw)	f(a)	Temp	log time(a)	Wo,(m/s)	logTh(a,1km)	k(cracks)	Temp	log(tot.time)
700	1.73	1.73	0.63	1.28E-14	1.23E+12	4.74E+03	3.30E-23	3.30E-23	1.66E+13	700	13.22	9.74E-14	8.52	4.28E-07	700	13.22
750	2.67	2.67	0.98	4.77E-14	1.77E+11	5.16E+03	9.25E-22	9.25E-22	9.16E+11	750	11.96	1.60E-12	7.31	1.59E-06	750	11.96
800	4.14	4.14	1.52	1.77E-13	3.07E+10	5.95E+03	2.28E-20	2.28E-20	5.75E+10	800	10.76	2.18E-11	6.18	5.91E-06	800	10.76
850	6.41	6.41	2.36	6.58E-13	6.23E+09	7.19E+03	5.07E-19	5.07E-19	4.01E+09	850	9.60	2.52E-10	5.13	2.19E-05	850	9.60
900	9.93	9.93	3.65	2.45E-12	1.44E+09	9.06E+03	1.02E-17	1.02E-17	3.08E+08	900	8.49	2.51E-09	4.15	8.15E-05	900	8.49
950	15.00	15.38	5.52	8.44E-12	3.78E+08	1.14E+04	1.70E-16	1.70E-16	2.80E+07	950	7.45	2.07E-08	3.26	2.81E-04	950	7.45
1000	15.00	23.81	5.52	8.44E-12	1.10E+08	7.78E+03	3.99E-16	3.99E-16	1.19E+07	1000	7.08	7.12E-08	2.72	2.81E-04	1000	7.08
1050	15.00	36.88	5.52	8.44E-12	3.50E+07	5.46E+03	8.78E-16	8.78E-16	5.42E+06	1050	6.73	2.23E-07	2.22	2.81E-04	1050	6.73

Time vs vein spacing																
700 data																
0.05	11.72413	750 data														
0.1	11.12207	0.05	10.512912	800 data												
0.2	10.52001	0.1	9.9108516	0.05	9.384717	850 data										
0.5	11.38756	0.2	9.3087916	0.1	8.782657	0.05	8.331961	900 data								
1	12.3032	0.5	10.130785	0.2	8.180597	0.1	7.729901	0.05	7.3507828	950 data						
2	13.21883	1	11.046418	0.5	8.928049	0.2	7.127841	0.1	6.7487228	0.05	6.4600265	1000 data				
		2	11.96205	1	9.843682	0.5	7.7721389	0.2	6.1466628	0.1	5.8579665	0.05	5.92321975	1050 data		
				2	10.75931	1	8.6877718	0.5	6.6570659	0.2	5.2559066	0.1	5.32115976	0.05	5.427	
						2	9.6034047	1	7.5726988	0.5	5.6160676	0.2	4.71909977	0.1	4.8249	
								2	8.4883317	1	6.5317005	0.5	5.24531886	0.2	4.2229	
										2	7.4473335	1	6.16095176	0.5	4.9026	
												2	7.07658467	1	5.8182	
														2	6.7339	

Appendix 10

Stress-strain and stress relaxation mechanical data

A10.1 Introduction

This appendix contains a list of the processed data from stress-strain and stress relaxation experiemnts that was used to construct the various plots in chapter 5 and others.

The marker column (*M*) at the left hand side of each set of data signifies the state of events in the deformation experiment

2. Stress-strain experiement - undergoing active deformation

3. Stress relaxation - the sample is allowed to relax under max σ

4. Termination of test

Temperature is recorded in °C, while confining pressure is always constant at 250 MPain all tests, hence it was not listed. *Corstress* is the corrected stress, while *stress in MPa* is the *corstress* minus the jacket correction, listed in *corjack*. *Strain rate* is recorded as strain per second. *logedot* is the log to the base of 10 of the strain rate, with *logstress* the equivalent for stress.

Due to the large volume of data it is printed out at fontsize 6.

A10.2 Mechanical data

WG2

M	T (°C)	Strain%	corstress	Stress MPa	Str.Rate (s-1)	log edot	log stress	corjacket
2	800.15	0	0.00	0	3.50E-05			0.00
2	800.15	0.15	38.63	37.15	3.56E-05	-4.45	1.59	3.41
2	800.15	0.27	83.76	76.92	2.79E-05	-4.55	1.92	3.30
2	800	0.43	138.65	125.41	2.73E-05	-4.56	2.14	3.28
2	800.15	0.68	198.66	178.57	3.71E-05	-4.43	2.30	3.43
2	800.15	0.86	245.36	219.82	3.61E-05	-4.44	2.39	3.42
2	800	1.07	289.71	259.1	4.39E-05	-4.36	2.46	3.52
2	799.9	1.26	324.98	290.21	3.88E-05	-4.41	2.51	3.46
2	799.9	1.46	361.91	322.86	4.09E-05	-4.39	2.56	3.48
2	800.15	1.65	390.70	348.37	4.78E-05	-4.32	2.59	3.57
2	800	1.89	427.55	381.01	5.64E-05	-4.25	2.63	3.65

2	799.9	2.09	445.90	397.16	4.90E-05	-4.31	2.65	3.58
2	800.15	2.3	466.55	415.48	5.71E-05	-4.24	2.67	3.67
2	800.15	2.59	487.08	433.67	6.26E-05	-4.20	2.69	3.72
2	800.29	2.84	498.91	444.18	7.02E-05	-4.15	2.70	3.78
2	800.39	3.29	496.51	442.15	8.45E-05	-4.07	2.70	3.89
2	800.39	3.62	488.25	434.84	8.33E-05	-4.08	2.69	3.87
2	800.39	3.98	476.31	424.24	7.51E-05	-4.12	2.68	3.82
2	800.63	4.73	440.02	392.43	1.23E-04	-3.91	2.64	4.11
2	800.87	5.16	428.80	382.36	9.16E-05	-4.04	2.63	3.93
2	800.98	5.74	422.53	376.79	8.69E-05	-4.06	2.63	3.90
2	801.11	6.34	417.42	372.28	8.66E-05	-4.06	2.62	3.90
2	801.36	6.89	413.15	368.47	8.21E-05	-4.09	2.62	3.86
2	801.6	7.57	409.19	365.01	8.65E-05	-4.06	2.61	3.90
2	801.6	8.16	403.55	360.01	8.43E-05	-4.07	2.61	3.89
2	801.84	8.8	399.55	356.44	7.95E-05	-4.10	2.60	3.85
3	801.84	9	385.14	343.66	7.21E-05	-4.14	2.59	3.79
3	801.84	9.09	372.77	332.25	2.57E-05	-4.59	2.57	3.25
3	801.84	9.2	359.70	320.57	1.86E-05	-4.73	2.56	3.10
3	801.84	9.24	354.66	315.78	7.81E-06	-5.11	2.55	2.72
3	801.84	9.27	350.41	311.86	4.77E-06	-5.32	2.54	2.53
3	802.08	9.3	346.81	308.57	3.44E-06	-5.46	2.54	2.41
3	802.08	9.32	343.73	305.79	2.87E-06	-5.54	2.54	2.34
3	802.32	9.35	340.95	303.25	2.21E-06	-5.66	2.53	2.25
3	802.32	9.37	337.77	300.41	1.96E-06	-5.71	2.53	2.21
3	802.32	9.39	335.28	298.17	1.68E-06	-5.77	2.53	2.17
4	802.81	9.41	332.01	295.28	1.69E-06	-5.77	2.52	2.17

WG3

M	T (°C)	Strain%	corstress	Stress MPa	Str.Rate (s-1)	log edot	log stress	corjacket
2	898.93	0	0.00	0	6.50E-05			15.74
2	898.93	0.45	7.89	12.15	6.85E-05	-4.16	0.90	5.86
2	898.93	0.78	28.47	30.23	6.22E-05	-4.21	1.45	5.74
2	898.93	1.2	54.74	53.46	6.34E-05	-4.20	1.74	5.76
2	898.69	1.54	76.93	73.07	6.36E-05	-4.20	1.89	5.77
2	898.69	1.92	103.90	96.79	5.74E-05	-4.24	2.02	5.64
2	899.18	2.45	132.60	122.31	6.62E-05	-4.18	2.12	5.82
2	898.93	3.15	161.51	147.85	6.62E-05	-4.18	2.21	5.82
2	899.18	3.87	179.22	163.65	7.59E-05	-4.12	2.25	5.99
2	899.18	4.55	188.67	171.99	7.50E-05	-4.12	2.28	5.98
2	898.93	5.29	194.02	176.77	7.84E-05	-4.11	2.29	6.04
2	898.69	6.36	196.94	179.37	7.96E-05	-4.10	2.29	6.06
2	898.45	7.37	198.69	180.96	8.29E-05	-4.08	2.30	6.11
2	898.69	8.46	195.62	178.25	8.31E-05	-4.08	2.29	6.11
2	898.93	9.94	189.80	173.12	8.43E-05	-4.07	2.28	6.13
2	899.18	11.22	185.26	169.08	8.18E-05	-4.09	2.27	6.09
2	899.42	12.13	180.75	165.14	8.53E-05	-4.07	2.26	6.15
2	899.66	12.74	177.09	161.91	8.58E-05	-4.07	2.25	6.15
2	899.9	13.17	176.07	160.94	8.10E-05	-4.09	2.25	6.08
3	899.9	13.34	162.70	148.75	5.74E-05	-4.24	2.21	5.64
3	899.9	13.46	149.75	136.58	2.78E-05	-4.56	2.18	4.82
3	899.9	13.55	139.43	127.17	2.01E-05	-4.70	2.14	4.49
3	900.15	13.65	127.29	116	1.17E-05	-4.93	2.10	3.99
3	900.15	13.71	120.89	110.16	9.09E-06	-5.04	2.08	3.78
3	900.39	13.75	116.27	105.93	7.44E-06	-5.13	2.07	3.62
3	900.39	13.79	111.70	101.83	6.85E-06	-5.16	2.05	3.55
3	901.11	13.83	106.68	97.31	5.92E-06	-5.23	2.03	3.44
3	901.36	13.87	101.88	92.95	4.96E-06	-5.30	2.01	3.31
3	901.6	13.92	95.99	87.63	4.14E-06	-5.38	1.98	3.18
3	902.32	13.99	88.67	80.98	3.01E-06	-5.52	1.95	2.97
3	901.84	14.04	82.58	75.38	2.03E-06	-5.69	1.92	2.73
4	901.84	14.07	79.62	72.68	1.72E-06	-5.76	1.90	2.63

WG4

M	T (°C)	Strain%	corstress	Stress MPa	Str.Rate (s-1)	log edot	log stress	corjacket
2	999.66	0	0.00	0	7.70E-05			
2	999.66	0.32	2.60	6.04	7.70E-05	-4.11	0.42	4.22
2	999.66	0.59	9.64	12.28	7.80E-05	-4.11	0.98	4.23
2	999.66	0.79	13.87	15.93	7.00E-05	-4.16	1.14	4.13
2	999.66	0.99	17.02	18.75	7.20E-05	-4.14	1.23	4.15
2	999.9	1.32	21.83	23.11	8.20E-05	-4.09	1.34	4.27
2	999.66	1.74	26.81	27.45	7.50E-05	-4.12	1.43	4.19
2	999.66	2.27	30.44	30.78	8.60E-05	-4.07	1.48	4.31
2	999.9	2.68	32.63	32.58	7.40E-05	-4.13	1.51	4.17
2	999.9	3.34	34.84	34.62	8.10E-05	-4.09	1.54	4.26
2	999.66	4.27	35.57	35.3	8.40E-05	-4.08	1.55	4.29
2	999.66	4.93	36.52	36.1	8.10E-05	-4.09	1.56	4.26
2	999.66	5.62	36.37	36.01	8.40E-05	-4.08	1.56	4.29
2	999.42	6.35	36.79	36.36	8.10E-05	-4.09	1.57	4.27
2	999.66	7.04	36.74	36.33	8.30E-05	-4.08	1.57	4.28
2	999.66	7.8	36.67	36.28	8.40E-05	-4.07	1.56	4.30
2	999.66	8.62	37.17	36.72	8.40E-05	-4.07	1.57	4.30
2	999.42	9.51	37.17	36.69	8.10E-05	-4.09	1.57	4.26
2	999.42	10.17	37.21	36.72	8.10E-05	-4.09	1.57	4.26
2	999.42	10.96	36.83	36.39	8.20E-05	-4.09	1.57	4.27
2	999.42	11.85	36.74	36.36	8.60E-05	-4.07	1.57	4.32
3	999.42	12.02	37.02	36.57	8.20E-05	-4.08	1.57	4.28
3	999.42	12.08	30.68	30.2	3.00E-05	-4.53	1.49	3.42
3	999.42	12.13	26.02	25.58	1.30E-05	-4.88	1.42	2.88
3	999.42	12.16	23.06	22.65	7.00E-06	-5.14	1.36	2.52
3	999.42	12.18	20.13	19.94	6.00E-06	-5.25	1.30	2.39
3	999.42	12.2	18.38	18.12	3.00E-06	-5.52	1.26	2.08
3	999.42	12.22	16.23	16.26	3.00E-06	-5.48	1.21	2.13
3	999.42	12.22	15.71	15.73	3.00E-06	-5.54	1.20	2.06
3	999.42	12.22	16.01	15.6	1.00E-06	-6.04	1.20	1.61
3	999.42	12.23	14.81	14.88	2.00E-06	-5.61	1.17	1.99
3	999.42	12.24	14.43	14.4	2.00E-06	-5.79	1.16	1.82
3	999.18	12.24	13.54	13.67	2.00E-06	-5.71	1.13	1.90
4	999.18	12.25	13.72	13.49	1.00E-06	-6.17	1.14	1.51

WG5

M	T (°C)	Strain%	corstress	Stress MPa	Str.Rate (s-1)	log edot	log stress	corjacket
2	955.84	0	0.00	0	6.26E-05			
2	955.84	0.29	11.79	14.7	6.26E-05	-4.20	1.07	4.78
2	955.59	0.63	22.83	24.63	7.26E-05	-4.14	1.36	4.93
2	955.59	1.1	39.45	39.37	7.13E-05	-4.15	1.60	4.91
2	955.59	1.6	55.83	53.85	6.80E-05	-4.17	1.75	4.86
2	955.59	2.02	66.58	63.42	6.98E-05	-4.16	1.82	4.89
2	955.35	2.61	75.35	71.32	7.90E-05	-4.10	1.88	5.02
2	955.35	3.12	80.83	76.16	7.76E-05	-4.11	1.91	5.00
2	955.35	4.08	84.78	79.7	8.01E-05	-4.10	1.93	5.04
2	955.35	4.87	87.85	82.47	8.42E-05	-4.07	1.94	5.09
2	955.11	5.82	90.44	84.71	7.85E-05	-4.11	1.96	5.02
2	955.35	6.85	91.65	85.84	8.30E-05	-4.08	1.96	5.08
2	955.59	7.92	93.73	87.65	8.03E-05	-4.10	1.97	5.04
2	955.59	8.77	96.61	90.25	8.43E-05	-4.07	1.99	5.10
2	956.08	9.68	97.05	90.6	8.12E-05	-4.09	1.99	5.05
2	956.32	10.62	99.64	92.91	8.23E-05	-4.08	2.00	5.07
2	956.56	11.36	102.43	95.35	7.87E-05	-4.10	2.01	5.02
2	956.8	12.16	102.90	95.78	7.97E-05	-4.10	2.01	5.03
2	957.05	12.98	105.17	97.82	8.15E-05	-4.09	2.02	5.06
3	957.29	13.26	101.47	94.58	8.50E-05	-4.07	2.01	5.11
3	957.29	13.34	92.30	85.76	4.02E-05	-4.40	1.97	4.34
3	957.53	13.43	82.21	76.33	2.21E-05	-4.66	1.91	3.81
3	957.29	13.5	74.44	69	1.18E-05	-4.93	1.87	3.32
3	957.53	13.56	67.75	62.84	8.06E-06	-5.09	1.83	3.06
3	957.77	13.6	63.73	59.05	5.47E-06	-5.26	1.80	2.81
3	958.01	13.64	59.15	54.9	4.68E-06	-5.33	1.77	2.72

3	958.26	13.68	54.54	50.7	3.81E-06	-5.42	1.74	2.60
3	958.01	13.7	51.93	48.34	3.44E-06	-5.46	1.72	2.54
3	958.26	13.73	49.37	45.95	2.68E-06	-5.57	1.69	2.41
3	958.26	13.75	46.78	43.66	2.78E-06	-5.56	1.67	2.43
4	958.26	13.77	44.60	41.62	2.17E-06	-5.66	1.65	2.30

WG6

M	T (°C)	Strain%	corstress	Stress MPa	Str.Rate (s-1)	log edot	log stress	corjacket
2	854.38	0	0.00	0	4.00E-05			
2	854.38	0.2	38.15	39.9	3.88E-05	-4.41	1.58	2.57
2	854.38	0.29	79.29	80.01	2.09E-05	-4.68	1.90	2.34
2	854.38	0.5	136.57	136.3	3.25E-05	-4.49	2.14	2.50
2	854.38	0.69	189.21	187.9	3.34E-05	-4.48	2.28	2.51
2	854.14	0.84	233.46	231.25	3.20E-05	-4.50	2.37	2.49
2	854.14	1.06	280.75	277.66	3.74E-05	-4.43	2.45	2.55
2	854.14	1.23	324.73	320.71	3.13E-05	-4.51	2.51	2.48
2	854.14	1.44	364.51	359.83	4.58E-05	-4.34	2.56	2.63
2	854.14	1.62	403.91	398.36	3.59E-05	-4.44	2.61	2.54
2	853.9	1.85	441.61	435.39	4.48E-05	-4.35	2.65	2.62
2	853.66	2.03	461.15	454.62	5.37E-05	-4.27	2.66	2.69
2	853.9	2.2	482.73	475.7	4.56E-05	-4.34	2.68	2.63
2	853.9	2.45	501.20	493.94	6.37E-05	-4.20	2.70	2.76
2	853.66	2.63	511.76	504.26	5.95E-05	-4.23	2.71	2.74
2	853.66	3.01	519.01	511.46	7.47E-05	-4.13	2.72	2.83
2	853.66	3.39	509.75	502.45	8.84E-05	-4.05	2.71	2.90
2	853.41	3.67	497.57	490.6	1.09E-04	-3.96	2.70	2.99
2	853.41	3.97	481.67	474.99	1.01E-04	-4.00	2.68	2.96
2	853.41	4.4	459.95	453.76	1.18E-04	-3.93	2.66	3.03
2	853.41	4.97	433.61	427.91	1.06E-04	-3.97	2.64	2.98
2	853.41	5.49	413.18	407.85	9.89E-05	-4.00	2.62	2.95
2	853.41	6.08	392.68	387.76	9.92E-05	-4.00	2.59	2.95
2	853.17	6.72	377.43	372.78	9.21E-05	-4.04	2.58	2.92
2	853.17	7.31	366.15	361.71	8.98E-05	-4.05	2.56	2.91
2	853.41	7.83	360.51	356.18	8.84E-05	-4.05	2.56	2.90
3	853.41	7.96	346.34	342.05	4.83E-05	-4.32	2.54	2.65
3	853.41	8.05	335.42	331	1.90E-05	-4.72	2.53	2.31
3	853.17	8.11	329.21	324.61	7.15E-06	-5.15	2.52	1.99
3	853.17	8.17	321.69	317.06	3.79E-06	-5.42	2.51	1.81
3	852.93	8.22	316.64	311.98	2.28E-06	-5.64	2.50	1.68
3	852.93	8.26	311.63	306.99	1.57E-06	-5.80	2.49	1.59
3	852.45	8.3	306.70	302.06	1.03E-06	-5.99	2.49	1.49
3	852.69	8.39	296.71	292.16	6.20E-07	-6.21	2.47	1.39
4	853.41	8.44	291.28	286.76	4.10E-07	-6.39	2.46	1.30

WG7

M	T (°C)	Strain%	corstress	Stress MPa	Str.Rate (s-1)	log edot	log stress	corjacket
2	798.69	0	0.00	0	4.00E-05			
2	798.69	0.18	36.50	39.08	3.32E-05	-4.48	1.56	3.38
2	798.69	0.38	77.98	79.84	4.08E-05	-4.39	1.89	3.48
2	798.69	0.61	123.75	124.65	3.66E-05	-4.44	2.09	3.43
2	798.45	0.79	157.99	158.25	4.04E-05	-4.39	2.20	3.48
2	798.21	0.98	187.57	187.27	4.27E-05	-4.37	2.27	3.51
2	798.21	1.23	224.05	223.07	4.62E-05	-4.34	2.35	3.55
2	798.45	1.49	261.84	260.1	4.50E-05	-4.35	2.42	3.53
2	798.45	1.76	292.59	290.28	4.90E-05	-4.31	2.47	3.58
2	798.69	2.01	315.65	312.95	5.56E-05	-4.26	2.50	3.65
2	798.69	2.32	339.38	336.22	5.74E-05	-4.24	2.53	3.66
2	798.69	2.85	363.06	359.51	6.71E-05	-4.17	2.56	3.75
2	798.93	3.23	370.68	367.03	7.34E-05	-4.13	2.57	3.80
2	798.93	3.67	372.63	368.98	7.84E-05	-4.11	2.57	3.84
2	798.69	4.23	366.87	363.37	8.35E-05	-4.08	2.56	3.88
2	798.93	4.81	351.61	348.5	9.69E-05	-4.01	2.55	3.96
2	798.93	5.38	334.67	331.9	9.69E-05	-4.01	2.52	3.96
2	798.93	5.87	324.13	321.52	9.03E-05	-4.04	2.51	3.92
2	799.18	6.59	312.33	309.98	9.48E-05	-4.02	2.49	3.95
2	799.18	7.12	304.59	302.34	8.50E-05	-4.07	2.48	3.89

2	799.42	7.75	298.83	296.69	8.47E-05	-4.07	2.48	3.88
2	799.18	8.3	295.94	293.86	8.58E-05	-4.07	2.47	3.89
3	799.18	8.38	282.87	280.55	3.35E-05	-4.47	2.45	3.38
3	799.18	8.47	272.47	270.05	1.71E-05	-4.77	2.44	3.06
3	799.18	8.51	267.32	264.71	8.70E-06	-5.06	2.43	2.76
3	798.93	8.55	263.77	261.13	6.73E-06	-5.17	2.42	2.66
3	798.69	8.58	259.95	257.28	5.07E-06	-5.29	2.41	2.55
3	798.93	8.61	256.20	253.51	4.01E-06	-5.40	2.41	2.46
3	798.69	8.65	252.56	249.92	3.79E-06	-5.42	2.40	2.44
3	798.45	8.67	249.54	246.84	2.58E-06	-5.59	2.40	2.31
3	798.45	8.69	247.32	244.63	2.34E-06	-5.63	2.39	2.27
3	798.45	8.73	243.58	240.9	1.96E-06	-5.71	2.39	2.21
3	798.45	8.76	239.75	237.13	1.88E-06	-5.73	2.38	2.20
3	798.69	8.79	236.01	233.42	1.65E-06	-5.78	2.37	2.16
4	798.93	8.82	233.26	230.7	1.50E-06	-5.82	2.37	2.13

WG8

M	T (°C)	Strain%	corstress	Stress MPa	Str.Rate (s-1)	log edot	log stress	corjacket
2	793.37	0	0.00	0	5.00E-05			
2	793.12	0.36	20.45	23.68	5.68E-05	-4.25	1.31	3.66
2	793.12	0.51	41.36	44.11	4.66E-05	-4.33	1.62	3.55
2	793.37	0.74	77.29	79.34	4.24E-05	-4.37	1.89	3.50
2	793.37	1.02	116.32	117.71	4.56E-05	-4.34	2.07	3.54
2	793.37	1.22	142.53	143.45	4.54E-05	-4.34	2.15	3.54
2	793.37	1.47	175.52	175.87	4.72E-05	-4.33	2.24	3.56
2	793.37	1.89	220.05	219.67	5.30E-05	-4.28	2.34	3.62
2	793.37	2.31	255.63	254.63	5.59E-05	-4.25	2.41	3.65
2	793.37	2.81	291.45	289.82	5.64E-05	-4.25	2.46	3.65
2	793.37	3.52	320.67	318.61	6.75E-05	-4.17	2.51	3.75
2	793.12	4.29	336.27	333.97	7.25E-05	-4.14	2.53	3.79
2	793.12	5.17	342.20	339.85	7.99E-05	-4.10	2.53	3.85
2	793.37	6.22	343.40	341.03	8.00E-05	-4.10	2.54	3.85
2	793.12	7.26	341.90	339.59	8.54E-05	-4.07	2.53	3.89
2	793.37	8.62	334.19	331.99	8.11E-05	-4.09	2.52	3.86
2	793.37	10.05	326.06	324.03	8.60E-05	-4.07	2.51	3.89
2	793.85	10.97	325.57	323.52	8.02E-05	-4.10	2.51	3.85
2	794.33	12.52	326.09	324.04	8.09E-05	-4.09	2.51	3.86
3	794.58	12.78	312.19	310.36	7.79E-05	-4.11	2.49	3.84
3	794.58	12.94	293.91	292.05	4.00E-05	-4.40	2.47	3.47
3	794.58	13.05	281.66	279.55	1.49E-05	-4.83	2.45	3.00
3	794.58	13.12	273.76	271.56	8.51E-06	-5.07	2.44	2.76
3	794.58	13.19	266.40	264.25	6.90E-06	-5.16	2.43	2.67
3	794.58	13.25	260.12	257.9	4.25E-06	-5.37	2.42	2.48
3	798.45	13.35	248.67	246.6	3.71E-06	-5.43	2.40	2.43
3	798.93	13.45	237.12	235.04	1.95E-06	-5.71	2.37	2.21
3	799.18	13.53	227.99	226.07	1.91E-06	-5.72	2.36	2.21
3	799.18	13.58	222.59	220.63	1.23E-06	-5.91	2.35	2.07
3	799.42	13.63	216.67	214.82	1.25E-06	-5.90	2.34	2.07
3	799.18	13.72	206.82	205.09	1.05E-06	-5.98	2.32	2.02
3	798.69	13.8	198.60	196.98	9.00E-07	-6.04	2.30	1.97
3	798.69	13.86	191.95	190.37	6.90E-07	-6.16	2.28	1.90
3	797.97	13.93	184.37	182.92	6.70E-07	-6.17	2.27	1.89
3	797.72	14	176.42	175.08	6.00E-07	-6.22	2.25	1.86
3	797.48	14.05	170.35	169.07	5.00E-07	-6.30	2.23	1.81
3	797.72	14.13	162.27	161.13	5.00E-07	-6.30	2.21	1.80
3	797.72	14.19	155.09	154.04	4.20E-07	-6.37	2.19	1.76
3	796.03	14.25	148.86	147.89	3.90E-07	-6.41	2.17	1.74
4	796.03	14.3	143.52	142.61	3.20E-07	-6.50	2.16	1.69

WG9

M	T (°C)	Strain%	corstress	Stress MPa	Str.Rate (s-1)	log edot	log stress	corjacket
2	895.79	0	0.00	0	5.00E-05			
2	895.79	0.19	2.01	7.56	6.02E-05	-4.22	0.30	5.70
2	896.03	0.31	14.92	20.09	5.47E-05	-4.26	1.17	5.58
2	896.03	0.48	33.71	38.27	4.45E-05	-4.35	1.53	5.34
2	896.03	0.78	46.75	51.53	6.66E-05	-4.18	1.67	5.82

2	896.03	1.15	54.44	59.27	7.88E-05	-4.10	1.74	6.04
2	895.54	1.53	60.70	65.34	7.41E-05	-4.13	1.78	5.96
2	895.3	1.78	64.34	68.96	7.74E-05	-4.11	1.81	6.02
2	895.54	2.29	64.11	68.73	7.72E-05	-4.11	1.81	6.02
2	895.3	2.74	68.36	72.98	8.20E-05	-4.09	1.83	6.09
2	895.3	3.29	64.74	69.53	8.88E-05	-4.05	1.81	6.20
2	895.3	3.71	63.63	68.4	8.61E-05	-4.06	1.80	6.16
2	895.3	4.24	59.44	64.25	8.32E-05	-4.08	1.77	6.11
2	895.3	4.69	55.53	60.42	8.33E-05	-4.08	1.74	6.11
2	895.54	5.38	50.66	55.72	8.79E-05	-4.06	1.70	6.19
2	896.03	6.11	45.83	50.99	8.85E-05	-4.05	1.66	6.20
2	896.27	6.9	43.14	48.23	8.05E-05	-4.09	1.63	6.07
2	896.76	7.79	41.54	46.79	8.92E-05	-4.05	1.62	6.21
2	897.48	8.65	40.54	45.7	8.18E-05	-4.09	1.61	6.09
2	897.48	9.57	40.29	45.45	8.18E-05	-4.09	1.61	6.09
2	897.97	10.49	39.75	44.94	8.27E-05	-4.08	1.60	6.10
2	898.21	11.17	40.03	45.19	8.14E-05	-4.09	1.60	6.08
2	898.45	12.16	40.19	45.39	8.35E-05	-4.08	1.60	6.12
2	898.93	12.97	40.84	45.99	8.09E-05	-4.09	1.61	6.08
2	898.93	14.11	41.23	46.43	8.51E-05	-4.07	1.62	6.14
2	899.42	15.06	41.05	46.17	7.96E-05	-4.10	1.61	6.05
2	899.66	16.44	40.95	46.13	8.33E-05	-4.08	1.61	6.11
3	899.9	16.58	39.73	44.86	7.86E-05	-4.10	1.60	6.04
4	899.9	16.62	37.04	40.76	2.12E-05	-4.67	1.57	4.54

WG10

M	T (°C)	Strain%	corstress	Stress MPa	Str.Rate (s-1)	log edot	log stress	corjacket
2	900.87	0	0.00	0	0.00E+00			
2	900.87	0.26	13.98	19.17	5.45E-05	-4.26	1.15	5.58
2	900.63	0.44	37.52	42.11	4.91E-05	-4.31	1.57	5.45
2	900.63	0.63	56.03	60.28	5.01E-05	-4.30	1.75	5.48
2	900.63	1.03	77.67	81.77	6.33E-05	-4.20	1.89	5.76
2	900.63	1.63	94.42	98.32	7.03E-05	-4.15	1.98	5.89
2	900.39	2.33	110.66	114.27	7.23E-05	-4.14	2.04	5.93
2	891.67	2.82	122.03	125.41	7.23E-05	-4.14	2.09	5.93
2	900	3.47	135.83	138.97	7.43E-05	-4.13	2.13	5.96
2	900.15	4.02	140.89	143.97	7.67E-05	-4.12	2.15	6.01
2	900.15	4.73	147.68	150.63	7.68E-05	-4.11	2.17	6.01
2	899.9	5.81	151.93	154.88	8.24E-05	-4.08	2.18	6.10
2	899.9	6.69	153.48	156.35	7.92E-05	-4.10	2.19	6.05
2	899.9	7.82	151.63	154.62	8.42E-05	-4.07	2.18	6.13
2	843.24	8.92	146.29	149.37	8.31E-05	-4.08	2.17	6.11
2	900.15	9.89	140.23	143.47	8.55E-05	-4.07	2.15	6.15
2	900.15	10.85	134.49	137.88	8.81E-05	-4.06	2.13	6.19
2	899.9	11.86	122.57	126.2	8.79E-05	-4.06	2.09	6.19
2	899.9	12.71	113.70	117.5	8.80E-05	-4.06	2.06	6.19
2	899.9	13.43	105.70	109.7	9.05E-05	-4.04	2.02	6.23
2	900.15	14.38	93.26	97.5	8.96E-05	-4.05	1.97	6.21
3	900.15	14.61	83.68	87.87	7.45E-05	-4.13	1.92	5.97
3	900.15	14.72	72.58	75.97	3.10E-05	-4.51	1.86	4.93
3	900.15	14.79	66.61	69.33	1.37E-05	-4.86	1.82	4.13
3	900.15	14.86	59.46	61.91	8.28E-06	-5.08	1.77	3.70
3	900.15	14.9	55.13	57.33	5.30E-06	-5.28	1.74	3.36
3	900.15	14.94	50.91	53.01	4.09E-06	-5.39	1.71	3.18
3	900.15	14.98	47.37	49.36	3.14E-06	-5.50	1.68	3.00
3	900.15	15	45.75	47.6	2.33E-06	-5.63	1.66	2.81
3	900.15	15.03	42.02	43.89	2.15E-06	-5.67	1.62	2.76
3	900.15	15.08	37.09	38.81	1.40E-06	-5.85	1.57	2.52
3	899.42	15.13	32.69	34.34	1.01E-06	-6.00	1.51	2.34
3	898.93	15.16	29.46	31.01	7.30E-07	-6.14	1.47	2.18
3	898.21	15.21	24.52	26.06	5.70E-07	-6.25	1.39	2.07
3	898.21	15.23	22.30	23.73	4.00E-07	-6.40	1.35	1.91
4	898.21	15.26	19.30	20.7	3.20E-07	-6.50	1.29	1.82

WG11

M	T (°C)	Strain%	corstress	Stress MPa	Str.Rate (s-1)	log edot	log stress	corjacket
2	999.42	0	0.00	0	5.00E-05			
2	999.42	0.1	2.24	2.19	6.73E-05	-4.17	0.35	4.09
2	999.66	0.17	5.48	9.19	5.48E-05	-4.26	0.74	3.91
2	999.66	0.29	14.61	18.17	5.79E-05	-4.24	1.16	3.96
2	999.9	0.45	23.29	26.75	6.47E-05	-4.19	1.37	4.06
2	1000.15	0.6	30.10	33.36	6.11E-05	-4.21	1.48	4.01
2	1000.39	0.95	36.15	39.49	7.77E-05	-4.11	1.56	4.22
2	1000.63	1.3	39.66	42.92	7.79E-05	-4.11	1.60	4.22
2	1000.87	1.74	44.01	47.19	7.88E-05	-4.10	1.64	4.24
2	1000.87	2.16	47.96	50.98	7.30E-05	-4.14	1.68	4.17
2	1001.11	2.51	50.78	53.83	8.04E-05	-4.09	1.71	4.25
2	1001.11	2.96	52.93	55.98	8.41E-05	-4.08	1.72	4.30
2	1001.36	3.37	54.83	57.75	7.68E-05	-4.11	1.74	4.21
2	1001.6	3.86	56.22	59.17	8.16E-05	-4.09	1.75	4.27
2	1001.59	4.4	58.13	61.04	8.27E-05	-4.08	1.76	4.28
2	1001.84	4.94	56.50	59.44	8.18E-05	-4.09	1.75	4.27
2	1002.08	5.63	56.19	59.14	8.28E-05	-4.08	1.75	4.28
2	1002.32	6.55	54.30	57.31	8.34E-05	-4.08	1.73	4.29
2	1002.32	7.44	52.21	55.25	8.27E-05	-4.08	1.72	4.28
2	1002.57	8.26	49.90	53.03	8.59E-05	-4.07	1.70	4.32
2	1002.57	9.14	47.37	50.53	8.37E-05	-4.08	1.68	4.29
2	1003.05	9.84	45.03	48.26	8.54E-05	-4.07	1.65	4.31
2	1003.05	10.55	42.38	45.68	8.59E-05	-4.07	1.63	4.32
2	1003.05	11.15	40.48	43.76	8.15E-05	-4.09	1.61	4.27
2	1003.29	11.88	37.30	40.69	8.46E-05	-4.07	1.57	4.30
2	1003.05	12.43	35.53	38.99	8.76E-05	-4.06	1.55	4.33
2	1003.04	12.92	34.56	38	8.38E-05	-4.08	1.54	4.29
3	1003.2	12.99	30.78	33.91	5.36E-05	-4.27	1.49	3.89
3	1003.23	13.02	28.36	30.86	2.14E-05	-4.67	1.45	3.19
3	1003.05	13.05	26.10	28.35	1.36E-05	-4.87	1.42	2.89
3	1003.2	13.08	23.34	25.39	8.57E-06	-5.07	1.37	2.61
3	1003.25	13.1	21.30	23.15	5.36E-06	-5.27	1.33	2.36
3	1003.56	13.12	19.25	21.02	4.18E-06	-5.38	1.28	2.24
3	1003.54	13.14	16.72	18.42	3.24E-06	-5.49	1.22	2.12
3	1003.54	13.16	14.96	16.49	1.98E-06	-5.70	1.17	1.90
3	1003.54	13.18	13.63	15.06	1.38E-06	-5.86	1.13	1.76
3	1003.78	13.2	11.76	13.14	1.12E-06	-5.95	1.07	1.68
3	1003.78	13.21	10.43	11.73	8.00E-07	-6.10	1.02	1.56
3	1003.78	13.22	9.30	10.58	7.00E-07	-6.15	0.97	1.52
4	1004.02	13.23	8.63	9.78	4.30E-07	-6.37	0.94	1.36

WG12

M	T (°C)	Strain%	corstress	Stress MPa	Str.Rate (s-1)	log edot	log stress	corjacket
2	1047.12	0	0.00	0	8.00E-05			
2	1046.88	0.14	1.44	1.56	7.57E-05	-4.12	0.16	3.59
2	1046.88	0.25	2.54	4.74	8.26E-05	-4.08	0.40	3.66
2	1046.88	0.43	3.23	7.24	6.51E-05	-4.19	0.51	3.47
2	1047.12	0.67	4.90	9.4	9.85E-05	-4.01	0.69	3.80
2	1047.12	0.81	6.68	11.04	7.13E-05	-4.15	0.82	3.54
2	1047.36	1.05	9.94	14.57	7.11E-05	-4.15	1.00	3.54
2	1047.36	1.32	13.00	17.93	7.65E-05	-4.12	1.11	3.59
2	1047.6	1.51	15.22	20.38	8.03E-05	-4.10	1.18	3.63
2	1047.36	1.71	16.98	22.26	7.95E-05	-4.10	1.23	3.63
2	1047.36	1.99	18.99	24.4	7.51E-05	-4.12	1.28	3.58
2	1061.16	2.32	20.21	25.78	8.10E-05	-4.09	1.31	3.64
2	1047.6	2.72	20.75	26.33	7.89E-05	-4.10	1.32	3.62
2	1061.16	3.2	20.24	25.9	9.08E-05	-4.04	1.31	3.73
2	1047.6	3.48	19.72	25.27	8.38E-05	-4.08	1.29	3.67
2	1047.85	4.15	18.55	23.96	7.90E-05	-4.10	1.27	3.62
2	1047.6	5.22	16.75	22.08	8.52E-05	-4.07	1.22	3.68
2	1047.85	6.34	15.18	20.35	8.25E-05	-4.08	1.18	3.65
2	1048.09	7.65	13.45	18.51	8.52E-05	-4.07	1.13	3.68
2	1047.85	8.81	12.33	17.28	8.25E-05	-4.08	1.09	3.65

2	1048.09	9.82	11.59	16.49	8.44E-05	-4.07	1.06	3.67
2	1048.33	11.11	10.54	15.34	8.22E-05	-4.09	1.02	3.65
2	1048.57	12.78	10.06	14.83	8.34E-05	-4.08	1.00	3.66
2	1048.81	14.4	9.36	14.07	8.30E-05	-4.08	0.97	3.66
2	1049.06	16.47	8.81	13.48	8.33E-05	-4.08	0.94	3.66
2	1048.57	18.03	9.07	13.76	8.34E-05	-4.08	0.96	3.66
2	1049.06	20.04	8.48	13.11	8.19E-05	-4.09	0.93	3.65
2	1049.06	21.79	8.61	13.27	8.40E-05	-4.08	0.93	3.67
2	1049.06	22.91	8.18	12.78	8.11E-05	-4.09	0.91	3.64
2	1048.81	24.25	7.96	12.56	8.29E-05	-4.08	0.90	3.66
2	1049.06	25.36	7.73	12.32	8.45E-05	-4.07	0.89	3.67
2	1048.81	26.72	7.14	11.68	8.38E-05	-4.08	0.85	3.67
2	1048.81	28.02	6.76	11.25	8.24E-05	-4.08	0.83	3.65
2	1049.3	29.55	6.28	10.74	8.29E-05	-4.08	0.80	3.66
2	1049.3	30.84	5.83	10.25	8.30E-05	-4.08	0.77	3.66
2	1049.3	31.76	5.86	10.3	8.48E-05	-4.07	0.77	3.68
2	1048.81	32.47	5.38	9.74	8.01E-05	-4.10	0.73	3.63
3	1048.81	32.55	4.55	8.48	5.19E-05	-4.28	0.66	3.30
3	1048.81	32.57	3.45	6.28	1.09E-05	-4.96	0.54	2.36
3	1048.81	32.58	2.83	5.15	4.40E-06	-5.36	0.45	1.93
3	1048.81	32.59	2.03	4.16	3.30E-06	-5.48	0.31	1.82
3	1048.81	32.6	1.28	3.18	2.20E-06	-5.66	0.11	1.66
3	1048.81	32.61	0.66	2.19	9.00E-07	-6.04	-0.18	1.37
3	1048.81	32.62	0.14	1.5	6.00E-07	-6.23	-0.84	1.25
3	1048.81	32.62	0.28	1.29	1.00E-07	-6.87	-0.55	0.91
3	1048.81	32.62	0.03	1.07	2.00E-07	-6.76	-1.47	0.96
4	1049.54	32.63	0.03	0.87	1.00E-07	-7.18	-1.56	0.78

WG13

M	T (°C)	Strain%	corstress	Stress MPa	Str.Rate (s-1)	log edot	log stress	corjacket
2	1093.59	0	0.00	0	8.00E-05			
2	1093.61	0.13	1.73	1.87	7.90E-05	-4.10	0.24	3.13
2	1093.61	0.24	2.44	2.63	7.84E-05	-4.11	0.39	3.12
2	1093.37	0.7	2.55	2.76	8.47E-05	-4.07	0.41	3.18
2	1092.88	1.33	2.70	2.92	8.32E-05	-4.08	0.43	3.16
2	1093.61	1.82	2.65	2.86	8.45E-05	-4.07	0.42	3.17
2	1093.37	2.33	2.81	3.04	7.87E-05	-4.10	0.45	3.13
2	1093.37	3.13	2.69	2.91	8.43E-05	-4.07	0.43	3.17
2	1093.61	3.89	2.59	2.8	8.46E-05	-4.07	0.41	3.17
2	1093.61	4.74	2.55	2.76	8.29E-05	-4.08	0.41	3.16
2	1093.37	5.4	2.49	2.7	8.11E-05	-4.09	0.40	3.15
2	1093.37	6.23	1.98	2.14	8.35E-05	-4.08	0.30	3.17
2	1093.37	7.41	1.78	1.92	8.26E-05	-4.08	0.25	3.16
2	1093.61	8.16	1.72	1.86	8.53E-05	-4.07	0.24	3.18
2	1093.37	9.3	1.95	2.11	8.27E-05	-4.08	0.29	3.16
2	1093.61	10.56	1.69	1.83	8.14E-05	-4.09	0.23	3.15
2	1093.85	11.88	1.75	1.89	8.42E-05	-4.07	0.24	3.17
2	1093.85	13.26	1.59	1.72	8.19E-05	-4.09	0.20	3.15
2	1093.85	14.44	1.51	1.64	8.35E-05	-4.08	0.18	3.17
2	1094.09	15.89	1.66	1.79	8.33E-05	-4.08	0.22	3.16
2	1094.09	17.67	1.53	1.65	8.24E-05	-4.08	0.18	3.16
2	1094.09	19.38	1.60	1.73	8.34E-05	-4.08	0.21	3.17
2	1093.61	21.09	1.60	1.72	8.33E-05	-4.08	0.20	3.16
2	1093.85	22.28	1.62	1.75	8.19E-05	-4.09	0.21	3.15
2	1093.37	23.61	1.52	1.64	8.29E-05	-4.08	0.18	3.16
2	1094.09	24.98	1.43	1.54	8.32E-05	-4.08	0.15	3.16
2	1093.85	26.44	1.45	1.57	8.43E-05	-4.07	0.16	3.17
2	1093.85	27.49	1.33	1.44	7.98E-05	-4.10	0.12	3.14
2	1093.85	28.72	1.32	1.42	8.36E-05	-4.08	0.12	3.17
2	1093.61	30.07	1.30	1.41	8.21E-05	-4.09	0.12	3.15
3	1093.61	30.13	0.97	1.05	3.93E-05	-4.41	-0.01	2.69
3	1093.61	30.13	0.73	0.79	9.00E-07	-6.05	-0.14	1.18
3	1093.61	30.13	0.55	0.6	5.00E-07	-6.28	-0.26	1.05
3	1093.61	30.13	0.40	0.44	3.00E-07	-6.55	-0.40	0.92
3	1093.61	30.13	0.39	0.42	0.00E+00	-7.48	-0.41	0.58
4	1093.61	30.13	0.34	0.36	2.00E-07	-6.79	-0.47	0.82

WG16

M	T (°C)	Strain%	corstress	Stress MPa	Str.Rate (s-1)	log edot	log stress	corjacket
2	899.42	0	0.00	0	6.00E-05			
2	899.42	0.27	5.22	11.88	6.43E-05	-4.19	0.72	5.78
2	899.18	0.54	30.54	38.97	5.20E-05	-4.28	1.48	5.52
2	899.18	0.86	59.17	69.88	5.09E-05	-4.29	1.77	5.49
2	899.18	1.04	76.25	88.35	5.12E-05	-4.29	1.88	5.50
2	898.93	1.29	95.42	109.02	4.97E-05	-4.30	1.98	5.47
2	898.93	1.7	119.21	135.02	6.18E-05	-4.21	2.08	5.73
2	898.99	2.22	145.08	162.99	6.25E-05	-4.20	2.16	5.75
2	898.93	2.91	159.23	178.51	7.41E-05	-4.13	2.20	5.96
2	899.42	3.97	172.07	192.42	7.59E-05	-4.12	2.24	5.99
2	899.66	5.14	177.66	198.56	8.12E-05	-4.09	2.25	6.08
2	899.66	6.42	181.68	202.87	7.95E-05	-4.10	2.26	6.05
2	899.9	8.25	181.43	202.66	8.26E-05	-4.08	2.26	6.10
2	899.9	9.41	181.31	202.46	7.87E-05	-4.10	2.26	6.04
2	899.9	10.77	180.38	201.54	8.36E-05	-4.08	2.26	6.12
2	900.15	11.97	180.77	201.9	7.97E-05	-4.10	2.26	6.06
2	900.39	13.38	182.29	203.6	8.35E-05	-4.08	2.26	6.12
2	900.63	14.49	184.81	206.3	8.19E-05	-4.09	2.27	6.09
2	900.87	15.88	187.07	208.73	8.11E-05	-4.09	2.27	6.08
2	901.11	17.04	188.91	210.7	8.06E-05	-4.09	2.28	6.07
2	901.36	18.21	190.80	212.72	7.91E-05	-4.10	2.28	6.05
3	901.36	18.39	173.99	194.42	7.16E-05	-4.14	2.24	5.92
3	901.36	18.52	161.15	180.19	5.51E-05	-4.26	2.21	5.59
3	901.6	18.67	146.57	163.74	3.14E-05	-4.50	2.17	4.95
3	901.6	18.79	135.26	151.19	2.36E-05	-4.63	2.13	4.65
3	901.84	18.94	120.71	135.02	1.53E-05	-4.81	2.08	4.23
3	901.84	19.09	107.15	119.98	1.03E-05	-4.99	2.03	3.88
3	901.84	19.21	95.53	107.11	7.10E-06	-5.15	1.98	3.59
3	901.84	19.33	84.66	95.18	5.80E-06	-5.24	1.93	3.42
3	901.84	19.44	74.41	83.85	4.10E-06	-5.38	1.87	3.18
3	902.08	19.51	67.26	75.96	3.30E-06	-5.48	1.83	3.03
3	902.08	19.59	60.00	67.95	2.60E-06	-5.58	1.78	2.88
3	902.08	19.67	52.86	60.04	1.90E-06	-5.72	1.72	2.69
3	902.08	19.74	46.78	53.38	1.70E-06	-5.78	1.67	2.62
3	898.69	19.82	38.84	44.84	1.80E-06	-5.75	1.59	2.66
3	897.97	19.85	36.90	42.28	8.00E-07	-6.11	1.57	2.22
3	897.72	19.88	33.49	38.63	9.00E-07	-6.07	1.52	2.26
3	899.9	19.9	32.80	37.3	2.00E-07	-6.61	1.52	1.72
3	902.08	19.94	28.17	32.8	7.00E-07	-6.14	1.45	2.18
3	902.57	19.99	23.52	27.68	6.00E-07	-6.22	1.37	2.09
3	902.32	20.04	19.43	23.15	5.00E-07	-6.32	1.29	1.99
3	902.08	20.07	16.46	19.82	4.00E-07	-6.44	1.22	1.88
3	902.32	20.11	12.74	15.66	3.00E-07	-6.58	1.11	1.75
3	902.57	20.15	9.27	11.71	2.00E-07	-6.80	0.97	1.57
2	899.65	20.15	0.00	0	4.00E-07	-6.39	-0.04	1.35
2	899.66	20.16	0.67	3.32	4.00E-07	-6.40	-0.17	1.88
2	899.42	20.19	3.12	7.12	1.10E-06	-5.96	0.49	2.37
2	899.18	20.22	5.99	10.89	1.10E-06	-5.96	0.78	2.41
2	898.93	20.23	10.56	16.03	3.00E-07	-6.52	1.02	1.80
2	898.69	20.27	13.93	21.24	1.20E-06	-5.92	1.14	2.44
2	898.93	20.27	18.04	26.44	1.00E-06	-6.00	1.26	2.34
2	898.93	20.32	22.21	31.91	1.10E-06	-5.96	1.35	2.38
2	898.93	20.35	25.65	36.21	9.00E-07	-6.05	1.41	2.26
2	898.69	20.44	28.87	41.05	2.10E-06	-5.68	1.46	2.76
2	898.69	20.47	32.80	45.41	7.00E-07	-6.15	1.52	2.19
2	898.45	20.51	36.10	49.67	7.00E-07	-6.15	1.56	2.18
2	898.56	20.57	39.12	53.9	1.20E-06	-5.92	1.59	2.43
2	899.18	20.67	43.80	59.95	1.10E-06	-5.96	1.64	2.40
2	899.18	20.76	46.20	63.26	1.50E-06	-5.82	1.66	2.55
2	899.42	20.85	49.21	67.09	1.40E-06	-5.85	1.69	2.50
2	899.42	20.9	51.85	70.28	1.00E-06	-6.00	1.71	2.31
2	899.42	20.98	54.59	73.99	1.20E-06	-5.92	1.74	2.44
2	899.42	21.04	56.81	76.8	1.10E-06	-5.96	1.75	2.38
2	899.66	21.14	57.98	78.84	2.20E-06	-5.66	1.76	2.78
2	899.9	21.23	60.26	81.42	1.40E-06	-5.85	1.78	2.50
2	900.39	21.32	62.00	83.7	1.40E-06	-5.85	1.79	2.51
2	899.9	21.38	63.31	85.36	1.30E-06	-5.89	1.80	2.48
2	900.15	21.45	65.13	87.73	1.30E-06	-5.89	1.81	2.48

WG18

M	T (°C)	Strain%	corstress	Stress MPa	Str.Rate (s-1)	log edot	log stress	corjacket
2	1094.09	0	0.00	0	7.80E-04			
2	1093.66	0.31	0.21	5.33	7.64E-04	-3.12	-0.68	5.12
2	1093.85	1.3	0.31	5.35	9.03E-04	-3.04	-1.43	5.31
2	1093.61	1.92	0.46	5.61	7.82E-04	-3.11	-0.33	5.15
2	1093.61	2.24	0.57	5.74	7.96E-04	-3.10	-0.24	5.17
2	1093.61	2.58	0.48	5.73	8.49E-04	-3.07	-0.31	5.24
3	1093.37	2.76	0.06	4.07	2.48E-04	-3.61	-1.21	4.01
3	1093.37	2.77	1.08	2.71	4.00E-06	-5.40	0.03	1.63
3	1094.58	2.77	0.90	2.09	9.00E-07	-6.04	-0.04	1.19
3	1093.37	2.78	0.38	1.35	4.00E-07	-6.45	-0.42	0.97
3	1026.54	2.78	0.01	0.8	1.00E-07	-7.29	-1.94	0.79
3	1026.05	2.79	0.01	1.33	5.00E-07	-6.26	-2.15	1.32
2	1026.05	2.79	0.01	1	1.00E-07	-6.85	-1.85	0.99
2	1026.05	3.39	1.03	7.08	5.97E-04	-3.22	0.01	6.05
2	1025.81	3.49	1.67	5.77	9.96E-05	-4.00	0.22	4.10
2	1029.69	3.78	3.22	5.99	1.64E-05	-4.78	0.51	2.77
2	1028.23	3.89	3.49	6.37	1.98E-05	-4.70	0.54	2.88
2	1028.23	3.94	4.42	7.05	1.29E-05	-4.89	0.65	2.63
2	1029.2	3.98	4.61	6.79	5.50E-06	-5.26	0.66	2.18
3	1029.2	4	2.58	4.65	4.30E-06	-5.37	0.41	2.07
3	1029.2	4	2.59	3.87	5.00E-07	-6.32	0.41	1.29
3	1029.2	4.01	1.37	2.8	8.00E-07	-6.11	0.14	1.43
3	1028.47	4.02	1.85	2.65	1.00E-07	-7.28	0.27	0.80
2	1028.23	4.04	1.46	3.06	1.30E-06	-5.89	0.17	1.59
2	1028.47	4	1.92	8.23	8.32E-04	-3.08	0.28	6.31
2	1028.47	4.17	2.57	9.06	8.26E-04	-3.08	0.41	6.49
2	1028.47	4.5	7.32	13.53	6.70E-04	-3.17	0.86	6.20
2	1028.47	4.97	9.08	15.48	7.70E-04	-3.11	0.96	6.40
2	1028.72	5.61	9.26	15.91	9.22E-04	-3.04	0.97	6.65
2	1028.72	6.31	9.69	16.1	7.76E-04	-3.11	0.99	6.41
2	1028.72	6.85	9.00	15.61	8.96E-04	-3.05	0.95	6.61
3	1028.47	7.18	6.55	12.52	5.61E-04	-3.25	0.82	5.97
3	1028.47	7.21	6.57	9.9	3.86E-05	-4.41	0.82	3.34
3	1028.23	7.23	4.78	7.47	1.44E-05	-4.84	0.68	2.69
3	1027.75	7.24	3.59	5.83	6.10E-06	-5.22	0.56	2.23
3	1026.78	7.25	3.65	4.9	4.00E-07	-6.36	0.56	1.26
2	945.18	7.29	1.57	2.89	2.00E-07	-6.81	0.20	1.32
2	944.94	7.87	4.36	5.67	1.00E-07	-6.82	0.64	1.31
2	944.94	7.92	5.17	8.41	9.70E-06	-5.01	0.71	3.24
2	945.18	7.91	5.07	11.55	2.35E-04	-3.63	0.70	6.48
2	945.42	7.96	10.12	14.34	3.28E-05	-4.48	1.01	4.23
2	945.42	7.96	11.38	17.98	2.56E-04	-3.59	1.06	6.60
2	945.42	7.96	12.30	18.93	2.60E-04	-3.59	1.09	6.63
2	944.94	7.79	13.97	20.05	1.75E-04	-3.76	1.15	6.08
2	944.94	8.06	18.40	25.06	2.66E-04	-3.57	1.26	6.66
2	944.94	8.23	38.70	45.46	2.83E-04	-3.55	1.59	6.75
2	944.94	8.41	59.23	65.66	2.27E-04	-3.64	1.77	6.44
2	944.94	8.52	66.43	73.15	2.78E-04	-3.56	1.82	6.72
2	944.94	8.58	69.39	76.32	3.20E-04	-3.50	1.84	6.93
2	944.94	8.85	80.31	87.29	3.32E-04	-3.48	1.90	6.99
2	944.94	8.99	83.44	90.56	3.63E-04	-3.44	1.92	7.13
2	945	10.46	87.45	94.67	3.85E-04	-3.41	1.94	7.22
2	945.18	11.17	82.83	90.18	4.19E-04	-3.38	1.92	7.35
2	945	11.8	81.99	89.46	4.50E-04	-3.35	1.91	7.46
2	945.18	12.64	78.47	85.75	4.00E-04	-3.40	1.89	7.28
3	945.18	12.81	71.93	78.72	2.91E-04	-3.54	1.86	6.79
3	945.18	12.89	64.36	69.87	1.11E-04	-3.95	1.81	5.51
3	945.18	12.94	59.37	63.69	3.63E-05	-4.44	1.77	4.32
3	945.42	12.99	54.76	58.81	2.69E-05	-4.57	1.74	4.05
3	945.42	13.03	50.79	54.22	1.27E-05	-4.90	1.71	3.44
3	945.91	13.07	46.65	49.77	8.20E-06	-5.09	1.67	3.13
3	946.39	13.1	43.63	46.49	5.40E-06	-5.27	1.64	2.85
3	946.39	13.12	40.73	43.58	5.40E-06	-5.27	1.61	2.85
3	946.15	13.14	38.71	41.3	3.50E-06	-5.46	1.59	2.60
3	946.39	13.18	35.33	37.62	1.90E-06	-5.71	1.55	2.28
3	946.63	13.22	30.71	32.9	1.60E-06	-5.80	1.49	2.19
3	946.39	13.26	26.04	28.09	1.20E-06	-5.92	1.42	2.06
2	894.33	13.51	25.73	28.59	2.30E-06	-5.65	1.41	2.86

2	900.39	21.54	65.37	88.43	2.20E-06	-5.66	1.82	2.79
3	900.39	21.56	64.16	86.33	1.10E-06	-5.96	1.81	2.38
3	900.15	21.59	61.62	83.39	1.80E-06	-5.74	1.79	2.66
3	900.15	21.62	59.36	80.26	1.40E-06	-5.85	1.77	2.50
3	900.15	21.64	57.55	77.95	1.40E-06	-5.85	1.76	2.53
3	900.15	21.67	55.61	75.34	1.30E-06	-5.89	1.75	2.46
3	900.39	21.7	52.95	71.84	1.20E-06	-5.92	1.72	2.42
3	900.39	21.72	51.48	69.82	1.00E-06	-6.00	1.71	2.33
3	900.39	21.74	50.06	67.92	9.00E-07	-6.05	1.70	2.29
3	900.63	21.76	47.83	65.06	1.00E-06	-6.00	1.68	2.32
2	900.63	21.77	46.67	63.94	1.60E-06	-5.80	1.67	2.61
2	900.45	20.97	9.69	15.68	1.60E-06	-5.80	0.99	2.40
2	900.39	20.95	10.95	17.24	1.00E-06	-6.00	1.04	2.34
2	900.39	20.93	13.14	20.08	1.00E-06	-6.00	1.12	2.34
2	900.15	20.94	14.28	20.56	2.00E-07	-6.70	1.15	1.57
3	899.9	20.94	14.01	19.99	1.00E-07	-7.00	1.15	1.39
3	899.66	20.95	13.86	19.69	1.00E-07	-7.00	1.14	1.31
4	899.66	20.95	14.25	19.76	1.00E-07	-7.00	1.15	0.98

WG17

M	T (°C)	Strain%	corstress	Stress MPa	Str.Rate (s-1)	log edot	log stress	corjacket
2	896.51	0	0.00	0	8.00E-07			
2	895.79	0.17	5.62	8.48	8.00E-07	-6.09	0.75	2.23
2	895.2	0.45	19.95	23.99	8.00E-07	-6.08	1.30	2.24
2	895.06	0.66	28.74	33.5	9.00E-07	-6.06	1.46	2.27
2	894.09	0.8	36.47	41.76	7.00E-07	-6.14	1.56	2.18
2	896.03	1.02	46.47	52.64	8.00E-07	-6.08	1.67	2.24
2	896.03	1.43	58.68	65.9	9.00E-07	-6.04	1.77	2.29
2	895.3	1.88	71.60	79.86	9.00E-07	-6.03	1.85	2.30
2	895.06	2.35	82.21	91.32	9.00E-07	-6.03	1.91	2.30
2	895.3	2.67	89.00	98.63	9.00E-07	-6.06	1.95	2.27
2	894.82	3.11	94.92	105.09	1.00E-06	-6.01	1.98	2.33
2	895.79	3.62	99.56	110.11	1.00E-06	-6.00	2.00	2.34
2	897.48	4.36	104.23	115.19	1.10E-06	-5.97	2.02	2.37
2	899.18	5.12	106.02	117.13	1.10E-06	-5.97	2.03	2.37
2	899.66	5.83	106.42	117.56	1.10E-06	-5.98	2.03	2.37
2	899.66	6.33	107.17	118.36	1.00E-06	-5.98	2.03	2.36
2	899.9	7.14	108.93	120.28	1.10E-06	-5.97	2.04	2.38
2	893.61	7.82	110.86	122.36	1.00E-06	-5.98	2.04	2.36
2	895.06	8.7	115.61	127.43	1.00E-06	-6.02	2.06	2.31
2	894.58	9.04	119.94	132.14	1.00E-06	-5.99	2.08	2.35
2	894.82	9.55	119.37	131.59	1.10E-06	-5.95	2.08	2.40
2	891.91	10.65	123.42	135.93	1.00E-06	-5.98	2.09	2.36
2	892.4	11.7	120.75	133.07	1.10E-06	-5.96	2.08	2.38
2	892.4	12.63	118.04	130.12	1.10E-06	-5.97	2.07	2.38
2	893.61	13.3	113.60	125.37	1.20E-06	-5.93	2.06	2.42
2	894.82	14.16	108.22	119.54	1.10E-06	-5.95	2.03	2.39
2	895.54	14.75	103.12	114.04	1.10E-06	-5.94	2.01	2.40
2	895.3	15.38	98.67	109.21	1.10E-06	-5.96	1.99	2.39
2	897	16.13	92.99	103.12	1.20E-06	-5.92	1.97	2.43
2	896.51	16.55	88.71	98.48	1.20E-06	-5.93	1.95	2.42
2	888.28	16.89	72.20	80.63	1.16E-06	-5.94	1.86	2.41
2	888.88	16.91	70.45	77.51	6.00E-08	-7.21	1.85	1.27
2	892.88	17.04	62.55	69.51	2.80E-07	-6.55	1.80	1.78
2	892.88	17.1	57.66	64.1	2.10E-07	-6.69	1.76	1.66
2	891.43	17.18	52.44	58.36	1.60E-07	-6.81	1.72	1.56
2	892.4	17.21	50.23	55.78	9.00E-08	-7.04	1.70	1.39
2	892.4	17.31	47.48	53.07	1.90E-07	-6.72	1.68	1.63
3	893.12	17.32	45.48	50.59	8.00E-08	-7.12	1.66	1.34
3	892.64	17.34	43.53	48.62	1.10E-07	-6.94	1.64	1.46
4	892.64	17.36	41.97	46.86	9.00E-08	-7.04	1.62	1.39

2	894.09	13.37	27.00	29.75	1.90E-06	-5.72	1.43	2.75
2	893.85	13.53	54.53	61.87	1.73E-04	-3.76	1.74	7.34
2	893.85	13.66	75.01	82.74	2.20E-04	-3.66	1.88	7.73
2	893.85	13.89	115.35	122.89	1.96E-04	-3.71	2.06	7.54
2	893.85	14.13	143.93	151.74	2.31E-04	-3.64	2.16	7.81
2	893.85	14.31	157.45	165.77	3.08E-04	-3.51	2.20	8.32
2	894.09	14.57	173.46	181.69	2.93E-04	-3.53	2.24	8.23
2	894.09	14.88	176.04	184.72	3.76E-04	-3.42	2.25	8.68
2	894.33	15.37	175.82	184.86	4.53E-04	-3.34	2.25	9.05
2	894.58	15.81	172.95	181.74	3.96E-04	-3.40	2.24	8.79
3	894.58	15.91	166.28	174.3	2.60E-04	-3.58	2.22	8.02
3	894.82	16.06	149.64	156.91	1.66E-04	-3.78	2.18	7.27
3	895.3	16.2	135.89	141.56	5.29E-05	-4.28	2.13	5.67
3	895.54	16.28	126.99	131.95	2.87E-05	-4.54	2.10	4.96
3	894.82	16.35	119.28	123.73	1.74E-05	-4.76	2.08	4.45
3	893.85	16.42	111.95	116.11	1.28E-05	-4.89	2.05	4.16
3	894.58	16.49	104.46	107.82	4.70E-06	-5.32	2.02	3.36
3	893.85	16.58	94.41	97.55	3.50E-06	-5.45	1.98	3.15
3	892.64	16.65	86.39	89.2	2.10E-06	-5.68	1.94	2.81
3	892.88	16.69	82.29	84.82	1.30E-06	-5.89	1.92	2.53
3	892.88	16.74	76.54	79	1.10E-06	-5.95	1.88	2.45
3	892.88	16.79	71.72	74.08	9.00E-07	-6.03	1.86	2.36
3	892.64	16.81	68.60	70.78	6.00E-07	-6.19	1.84	2.18
3	892.64	16.85	65.36	67.37	4.00E-07	-6.35	1.82	2.01
3	892.64	16.88	61.67	63.74	5.00E-07	-6.28	1.79	2.08
3	892.64	16.9	59.32	61.28	4.00E-07	-6.40	1.77	1.96
3	892.64	16.92	56.55	58.49	4.00E-07	-6.42	1.75	1.94
3	892.64	16.95	54.14	56.1	4.00E-07	-6.40	1.73	1.95
3	892.88	16.96	52.88	54.66	3.00E-07	-6.59	1.72	1.78
3	892.88	16.97	51.31	53.1	3.00E-07	-6.58	1.71	1.79
3	892.88	16.99	49.99	51.6	2.00E-07	-6.79	1.70	1.61
3	893.37	17.04	43.99	45.76	2.00E-07	-6.61	1.64	1.77
3	893.61	17.08	39.33	40.98	2.00E-07	-6.75	1.59	1.65
3	894.58	17.12	35.07	36.56	1.00E-07	-6.94	1.54	1.49
3	895.06	17.15	31.33	32.72	1.00E-07	-7.09	1.50	1.39
3	897.01	17.19	27.64	28.94	1.00E-07	-7.23	1.44	1.29
3	896.03	17.21	25.44	26.65	0.00E+00	-7.36	1.41	1.21
3	896.27	17.22	24.96	25.94	0.00E+00	-7.78	1.40	0.98
3	89.157	17.23	22.80	23.88	0.00E+00	-7.59	1.36	1.08
3	898.21	17.24	22.28	23.08	0.00E+00	-8.19	1.35	0.80
3	897.48	17.27	19.37	20.41	0.00E+00	-7.67	1.29	1.04
2	947.12	17.47	30.61	32.32	5.00E-07	-6.28	1.49	1.72
2	946.63	16.7	44.22	45.93	5.00E-07	-6.29	1.65	1.70
2	946.39	17.48	75.59	83.63	6.44E-04	-3.19	1.88	8.04
2	946.39	18.13	91.43	99.49	6.51E-04	-3.19	1.96	8.06
2	946.15	18.96	99.78	108.3	8.37E-04	-3.08	2.00	8.51
2	946.15	19.72	103.18	111.51	7.58E-04	-3.12	2.01	8.33
2	945.91	20.84	104.09	112.52	8.00E-04	-3.10	2.02	8.43
2	945.91	22.42	103.13	111.64	8.32E-04	-3.08	2.01	8.50
2	946.15	23.45	100.08	108.65	8.60E-04	-3.07	2.00	8.56
3	946.15	23.6	100.32	107.91	4.93E-04	-3.31	2.00	7.59
3	946.39	23.79	79.77	86.44	2.73E-04	-3.56	1.90	6.67
3	946.88	23.9	69.89	74.67	5.86E-05	-4.23	1.84	4.78
3	947.85	23.98	61.33	65.4	2.78E-05	-4.56	1.79	4.06
3	949.3	24.06	53.32	56.95	1.66E-05	-4.78	1.73	3.63
3	949.3	24.12	46.18	49.64	1.32E-05	-4.88	1.66	3.46
3	948.57	24.18	40.75	43.89	8.40E-06	-5.07	1.61	3.13
3	950.02	24.24	34.13	36.75	3.70E-06	-5.43	1.53	2.62
3	948.09	24.3	28.24	30.52	2.00E-06	-5.71	1.45	2.28
3	946.88	24.36	22.26	24.29	1.10E-06	-5.94	1.35	2.03
3	946.88	24.41	16.93	18.63	5.00E-07	-6.29	1.23	1.70
3	947.12	24.44	13.24	14.65	2.00E-07	-6.66	1.12	1.42
3	947.12	24.48	9.95	11.19	1.00E-07	-6.92	1.00	1.24
3	947.12	24.49	8.42	9.4	0.00E+00	-7.41	0.93	0.97
3	947.12	24.5	7.17	8.15	0.00E+00	-7.39	0.86	0.98
4	947.12	24.51	7.25	7.92	0.00E+00	-8.17	0.86	0.66

WG20

M	T (°C)	Strain%	corstress	Stress MPa	Str.Rate (s-1)	log edot	log stress	corjacket
2	899.66	0	0.00	0	2.00E-07			
2	897.24	0.15	2.68	4.31	2.00E-07	-6.73	0.43	1.62
2	894.33	0.31	11.61	13.17	2.00E-07	-6.81	1.06	1.56
2	895.25	0.48	19.52	21.07	2.00E-07	-6.82	1.29	1.55
2	894.09	0.7	28.97	30.57	2.00E-07	-6.76	1.46	1.60
2	893.61	0.91	37.69	39.26	2.00E-07	-6.80	1.58	1.57
2	893.12	1.14	44.75	46.35	2.00E-07	-6.76	1.65	1.60
2	895.06	1.46	51.73	53.35	2.00E-07	-6.73	1.71	1.62
2	895.55	1.75	58.34	59.94	2.00E-07	-6.76	1.77	1.60
2	897.48	2.07	62.25	63.88	2.00E-07	-6.72	1.79	1.63
2	898.45	2.43	66.59	68.22	2.00E-07	-6.73	1.82	1.62
2	898.45	2.72	69.75	71.4	2.00E-07	-6.70	1.84	1.64
2	897.24	3.04	72.33	73.95	2.00E-07	-6.73	1.86	1.62
2	895.79	3.35	76.91	78.52	2.00E-07	-6.75	1.89	1.61
2	894.58	3.6	80.49	82.1	2.00E-07	-6.74	1.91	1.61
2	895.79	4	85.42	87.04	2.00E-07	-6.73	1.93	1.62
2	896.03	4.59	89.76	91.4	2.00E-07	-6.70	1.95	1.65
2	894.58	5.08	91.96	93.59	2.00E-07	-6.71	1.96	1.63
2	896.51	5.65	96.24	97.87	2.00E-07	-6.72	1.98	1.63
2	896.76	6.4	99.36	101	2.00E-07	-6.71	2.00	1.64
2	897.78	7.03	100.20	101.87	2.00E-07	-6.68	2.00	1.67
2	897.72	7.75	102.78	104.41	2.00E-07	-6.73	2.01	1.63
2	896.27	8.53	100.28	101.95	2.00E-07	-6.68	2.00	1.67
3	892.15	8.71	105.84	107.66	3.00E-07	-6.50	2.02	1.82
3	893.12	8.82	93.51	95.05	1.00E-07	-6.83	1.97	1.54
3	895.06	8.91	83.64	85.06	1.00E-07	-7.00	1.92	1.42
3	894.58	8.97	76.34	77.67	1.00E-07	-7.12	1.88	1.33
3	895.06	9.04	68.67	69.97	1.00E-07	-7.18	1.84	1.29
3	896.27	9.1	61.77	63	1.00E-07	-7.27	1.79	1.24
3	894.82	9.16	54.89	56.09	0.00E+00	-7.33	1.74	1.20
3	894.09	9.21	48.56	49.67	0.00E+00	-7.48	1.69	1.11
3	893.61	9.25	44.51	45.52	0.00E+00	-7.68	1.65	1.01
3	897.24	9.26	42.87	43.7	0.00E+00	-8.07	1.63	0.83
3	896.51	9.3	38.38	39.49	0.00E+00	-7.49	1.58	1.11
3	896.76	9.32	36.02	36.99	0.00E+00	-7.77	1.56	0.96
2	896.76	9.81	17.45	20.45	3.20E-06	-5.50	1.24	3.00
2	896.76	8.86	7.23	10.56	5.10E-06	-5.29	0.86	3.33
2	894.58	8.94	2.31	5.43	3.80E-06	-5.42	0.36	3.12
2	892.88	9.02	14.78	18.1	5.00E-06	-5.30	1.17	3.32
2	892.88	9.14	37.39	40.64	4.50E-06	-5.34	1.57	3.25
2	892.88	9.28	54.11	57.62	6.50E-06	-5.19	1.73	3.51
2	892.88	9.34	66.71	69.86	4.00E-06	-5.40	1.82	3.15
2	892.88	9.48	88.31	91.67	5.30E-06	-5.28	1.95	3.36
2	891.91	9.65	113.20	116.58	5.40E-06	-5.26	2.05	3.38
2	891.43	9.75	126.29	129.57	4.70E-06	-5.32	2.10	3.28
2	891.43	9.9	132.23	136.08	9.80E-06	-5.01	2.12	3.84
2	891.43	10	138.58	142.07	6.30E-06	-5.20	2.14	3.49
2	891.43	10.21	139.19	142.87	8.00E-06	-5.09	2.14	3.68
2	890.7	11.18	132.67	136.1	5.80E-06	-5.24	2.12	3.42
2	890.7	11.68	130.30	134.2	1.05E-05	-4.98	2.11	3.90
2	890.7	12.15	124.66	128.52	1.00E-05	-5.00	2.10	3.86
2	890.94	12.67	119.99	123.86	1.00E-05	-5.00	2.08	3.86
3	890.94	12.82	107.57	111.06	6.30E-06	-5.20	2.03	3.49
3	890.94	12.9	99.12	101.95	2.40E-06	-5.62	2.00	2.83
3	890.94	12.96	92.93	95.32	1.10E-06	-5.96	1.97	2.39
3	890.94	13.01	87.30	89.58	9.00E-07	-6.06	1.94	2.27
3	891.43	13.07	79.70	81.8	6.00E-07	-6.22	1.90	2.10
3	891.91	13.15	71.37	73.26	4.00E-07	-6.43	1.85	1.89
3	891.43	13.2	65.63	67.41	3.00E-07	-6.55	1.82	1.78
3	891.43	13.24	60.93	62.53	2.00E-07	-6.75	1.78	1.61
3	890.94	13.28	56.61	58.17	2.00E-07	-6.81	1.75	1.56
3	890.94	13.31	53.23	54.69	1.00E-07	-6.94	1.73	1.46
4	890.94	13.36	47.68	49.16	1.00E-07	-6.91	1.68	1.48

WG21

M	T (°C)	Strain%	corstress	Stress MPa	Str.Rate (s-1)	log edot	log stress	corjacket
2	900.12	0	0.00	0	5.00E-06			3.32
2	900.12	0.08	0.01	5.15	3.72E-05	-4.43	-2.00	5.13
2	901.23	0.11	7.86	11.45	7.14E-06	-5.15	0.90	3.58
2	901.11	0.12	11.37	14.31	2.90E-06	-5.54	1.06	2.95
2	901.11	0.17	13.71	17.09	5.48E-06	-5.26	1.14	3.38
2	900.15	0.23	17.35	20.77	5.77E-06	-5.24	1.24	3.42
2	900.87	0.28	20.65	24.2	6.86E-06	-5.16	1.31	3.55
2	900.87	0.34	23.32	26.88	6.92E-06	-5.16	1.37	3.56
2	900.87	0.38	26.01	29.41	5.63E-06	-5.25	1.42	3.40
2	900.87	0.41	28.25	30.84	1.59E-06	-5.80	1.45	2.58
2	900.87	0.46	28.11	30.81	1.94E-06	-5.71	1.45	2.70
2	900.63	0.5	28.71	30.9	7.40E-07	-6.13	1.46	2.19
2	900.15	0.53	27.89	29.97	5.76E-07	-6.24	1.45	2.07
2	899.9	0.63	28.91	31.16	8.34E-07	-6.08	1.46	2.25
2	900.15	0.63	29.68	30.77	3.00E-08	-7.52	1.47	1.09
2	900.63	0.67	29.67	31.74	5.65E-07	-6.25	1.47	2.07
2	899.9	0.68	28.78	30.64	3.52E-07	-6.45	1.46	1.86
2	900.87	0.69	29.23	30.99	2.74E-07	-6.56	1.47	1.76
2	841.31	1.03	31.49	35.43	3.98E-06	-5.40	1.50	3.94
2	845.42	1.03	35.62	38.24	6.02E-07	-6.22	1.55	2.62
2	847.36	1.05	32.49	35.2	7.13E-07	-6.15	1.51	2.71
2	846.88	1.05	32.64	35.36	7.13E-07	-6.15	1.51	2.71
2	847.12	1.03	33.35	36	6.38E-07	-6.20	1.52	2.65
2	846.88	1.05	33.41	35.87	4.53E-07	-6.34	1.52	2.46
2	847.12	1.05	34.01	35.55	5.20E-08	-7.28	1.53	1.54
2	846.88	1.06	31.76	33.55	1.06E-07	-6.97	1.50	1.79
2	846.63	1.06	29.83	32.52	6.84E-07	-6.16	1.47	2.69
2	846.88	1.06	31.08	32.98	1.40E-07	-6.85	1.49	1.90
2	846.88	1.04	30.23	32.9	6.64E-07	-6.18	1.48	2.67
2	846.88	1.04	31.45	33.4	1.55E-07	-6.81	1.50	1.95
2	846.63	1.07	29.50	31.99	4.83E-07	-6.32	1.47	2.49
2	846.63	1.06	29.29	31.56	3.16E-07	-6.50	1.47	2.27
2	846.63	1.06	29.37	31.59	2.83E-07	-6.55	1.47	2.22
2	846.39	1.07	29.46	31.57	2.26E-07	-6.65	1.47	2.11
2	846.15	1.1	31.04	33.35	3.43E-07	-6.46	1.49	2.31
2	846.39	1.09	30.61	32.96	3.63E-07	-6.44	1.49	2.34
2	846.39	1.09	31.74	34	3.02E-07	-6.52	1.50	2.25
2	846.63	1.1	30.47	32.28	1.14E-07	-6.94	1.48	1.82
2	846.39	1.11	29.54	31.62	2.13E-07	-6.67	1.47	2.09
2	846.39	1.11	29.96	32.22	3.06E-07	-6.51	1.48	2.26
2	846.88	1.1	30.36	32.54	2.65E-07	-6.58	1.48	2.19
2	894.09	0.84	27.53	31.03	2.29E-06	-5.64	1.44	3.50
2	901.6	0.81	30.64	32.49	3.33E-07	-6.48	1.49	1.84
2	901.6	0.84	28.27	30.61	1.01E-06	-5.99	1.45	2.35
2	900	0.85	26.68	28.39	2.37E-07	-6.63	1.43	1.71
2	899.42	0.91	28.09	30.91	2.38E-06	-5.62	1.45	2.82
2	899.42	0.91	27.40	29.13	2.53E-07	-6.60	1.44	1.73
2	900.39	0.92	28.76	30.53	2.76E-07	-6.56	1.46	1.77
2	900.15	0.99	25.99	28.68	1.90E-06	-5.72	1.41	2.69
2	900.39	0.99	28.34	29.73	9.20E-08	-7.04	1.45	1.39
2	899.66	1.11	29.88	32.1	7.90E-07	-6.10	1.48	2.22
2	899.9	1.1	29.05	30.84	2.95E-07	-6.53	1.46	1.79
2	899.66	1.14	30.67	32.55	3.63E-07	-6.44	1.49	1.88
2	899.66	1.14	29.96	31.44	1.22E-07	-6.91	1.48	1.48
2	899.66	1.21	30.61	32.91	9.31E-07	-6.03	1.49	2.30
2	899.42	1.23	29.57	31.47	3.83E-07	-6.42	1.47	1.90
2	899.18	1.23	30.03	31.15	3.30E-08	-7.48	1.48	1.12
2	899.18	1.29	28.72	30.88	6.91E-07	-6.16	1.46	2.16
2	899.66	1.29	29.63	31.44	3.06E-07	-6.51	1.47	1.81
2	898.93	1.37	30.19	32.19	4.93E-07	-6.31	1.48	2.00
2	899.66	1.41	31.84	33.51	2.18E-07	-6.66	1.50	1.68
2	899.42	1.43	30.23	31.9	2.13E-07	-6.67	1.48	1.67
2	899.42	1.46	29.78	31.51	2.47E-07	-6.61	1.47	1.72
2	900.15	1.46	30.12	31.08	1.70E-08	-7.77	1.48	0.97
2	900.63	1.5	29.06	30.9	3.31E-07	-6.48	1.46	1.84
2	900.15	1.6	30.01	31.95	4.24E-07	-6.37	1.48	1.94
2	901.11	1.63	29.58	31.08	1.29E-07	-6.89	1.47	1.50
2	901.84	1.66	29.19	30.79	1.76E-07	-6.75	1.47	1.60

2	901.84	1.74	28.26	30.24	4.63E-07	-6.33	1.45	1.98
2	901.6	1.74	30.67	31.7	2.30E-08	-7.64	1.49	1.03
2	901.6	1.81	28.89	30.75	3.52E-07	-6.45	1.46	1.86
2	902.08	1.83	29.56	31.05	1.24E-07	-6.91	1.47	1.49
2	902.81	1.9	31.05	32.91	3.52E-07	-6.45	1.49	1.86
2	902.08	1.96	28.83	30.64	3.14E-07	-6.50	1.46	1.82
2	902.32	1.94	28.79	30.64	3.41E-07	-6.47	1.46	1.85
2	903.29	2.01	29.94	31.82	3.75E-07	-6.43	1.48	1.89
2	902.57	2.07	28.90	30.68	2.84E-07	-6.55	1.46	1.78
2	903.29	2.1	30.06	31.65	1.71E-07	-6.77	1.48	1.59
2	904.02	2.18	30.04	31.88	3.27E-07	-6.49	1.48	1.83
2	904.26	2.19	30.11	31.41	6.70E-08	-7.17	1.48	1.30
2	904.26	2.29	30.02	32.01	4.76E-07	-6.32	1.48	1.99
2	904.02	2.3	29.81	31.12	7.00E-08	-7.15	1.47	1.31
2	904.5	2.32	30.72	32.27	1.49E-07	-6.83	1.49	1.55
2	904.75	2.38	30.18	32.05	3.54E-07	-6.45	1.48	1.87
2	904.26	2.41	29.22	30.7	1.23E-07	-6.91	1.47	1.48
2	905.23	2.57	31.84	33.67	3.28E-07	-6.48	1.50	1.83
2	905.71	2.58	29.41	30.67	5.70E-08	-7.24	1.47	1.26
2	905.47	2.61	29.79	31.67	3.73E-07	-6.43	1.47	1.89
2	905.23	2.63	29.67	31.13	1.15E-07	-6.94	1.47	1.46
2	905.47	2.69	29.60	31.79	7.37E-07	-6.13	1.47	2.19
2	905.71	2.68	28.45	30.3	3.39E-07	-6.47	1.45	1.85
2	946.15	2.93	23.15	25.49	2.31E-06	-5.64	1.36	2.33
2	953.66	2.96	26.68	28.62	1.00E-06	-6.00	1.43	1.94
2	951.48	3.14	25.40	28.17	5.11E-06	-5.29	1.40	2.77
2	951.96	3.27	26.83	29.52	4.48E-06	-5.35	1.43	2.69
2	952.93	3.41	26.96	29.57	3.84E-06	-5.42	1.43	2.60
2	952.2	3.62	26.33	29.04	4.59E-06	-5.34	1.42	2.71
2	953.17	3.76	27.02	29.62	3.82E-06	-5.42	1.43	2.60
2	953.17	3.96	27.47	30.25	5.17E-06	-5.29	1.44	2.78
2	953.41	4.16	27.19	29.89	4.49E-06	-5.35	1.43	2.69
2	953.9	4.42	26.56	29.33	5.13E-06	-5.29	1.42	2.77
2	953.66	4.62	24.00	26.79	5.25E-06	-5.28	1.38	2.79
2	953.41	4.72	24.37	27.08	4.62E-06	-5.34	1.39	2.71
2	953.41	4.87	26.20	28.96	5.05E-06	-5.30	1.42	2.76
2	953.66	5.07	27.35	30.22	6.03E-06	-5.22	1.44	2.87
2	953.41	5.31	25.94	28.73	5.27E-06	-5.28	1.41	2.79
2	953.17	5.52	27.14	29.93	5.29E-06	-5.28	1.43	2.79
2	954.14	5.83	26.94	29.89	6.86E-06	-5.16	1.43	2.95
2	954.12	6.05	27.83	30.62	5.32E-06	-5.27	1.44	2.79
2	953.9	6.4	24.72	27.64	6.49E-06	-5.19	1.39	2.92
2	953.17	6.59	24.73	27.64	6.37E-06	-5.20	1.39	2.91
2	953.17	6.84	27.01	29.99	7.18E-06	-5.14	1.43	2.98
2	953.17	7.1	24.74	27.56	5.50E-06	-5.26	1.39	2.82
2	958.04	12.08	18.05	22.98	7.25E-05	-4.14	1.26	4.93
2	958.5	15.75	16.64	21.87	9.52E-05	-4.02	1.22	5.23
2	954.87	16.31	18.26	22.57	3.89E-05	-4.41	1.26	4.31
2	953.17	16.56	22.18	26.21	2.88E-05	-4.54	1.35	4.04
2	958.74	16.83	19.92	24.29	4.16E-05	-4.38	1.30	4.37
2	955.35	17.24	19.17	23.47	3.85E-05	-4.41	1.28	4.30
2	958.01	16.76	20.72	25.06	4.02E-05	-4.40	1.32	4.34
2	954.38	17.26	20.13	24.42	3.83E-05	-4.42	1.30	4.29
2	953.66	19.12	22.69	27.08	4.22E-05	-4.37	1.36	4.39
2	954.87	19.38	22.22	-14.2	4.51E-06	-5.35	1.35	2.70
2	954.62	19.52	22.22	-11.52	4.72E-05	-4.33	1.35	4.49
2	954.62	19.52	22.22	-11.52	4.00E-05	-4.40	1.35	4.33
2	954.62	19.65	22.22	-3.32	5.77E-05	-4.24	1.35	4.69
2	954.38	19.78	22.22	3.93	4.29E-05	-4.37	1.35	4.40
2	954.14	19.89	22.22	8.88	4.90E-05	-4.31	1.35	4.53
2	954.14	20.01	22.22	14.38	4.28E-05	-4.37	1.35	4.40
2	954.14	20.19	22.22	19.85	6.80E-05	-4.17	1.35	4.86
2	954.14	20.64	22.22	25.62	6.06E-05	-4.22	1.35	4.74
2	954.14	21.18	22.22	26.93	5.82E-05	-4.23	1.35	4.70
2	954.14	21.53	20.60	25.45	6.70E-05	-4.17	1.31	4.85
2	954.14	21.85	19.37	24.13	6.17E-05	-4.21	1.29	4.76
2	954.14	22.46	19.80	24.6	6.42E-05	-4.19	1.30	4.80
2	954.14	23.11	19.57	24.36	6.35E-05	-4.20	1.29	4.79
2	954.14	23.68	18.11	22.91	6.40E-05	-4.19	1.26	4.80
2	953.41	24.31	16.54	21.36	6.53E-05	-4.19	1.22	4.82
2	953.17	24.8	15.66	20.48	6.54E-05	-4.18	1.19	4.82
2	952.93	25.37	15.11	19.91	6.38E-05	-4.20	1.18	4.80
2	952.93	25.46	14.24	18.86	5.32E-05	-4.27	1.15	4.61
2	952.93	25.63	23.51	29.57	1.87E-04	-3.73	1.37	6.06
2	952.93	25.78	25.12	32.18	3.78E-04	-3.42	1.40	7.06

2	952.93	26.32	27.40	34.49	3.85E-04	-3.41	1.44	7.09
2	953.12	27.11	26.78	33.89	3.92E-04	-3.41	1.43	7.12
2	952.98	27.52	24.63	32.02	4.64E-04	-3.33	1.39	7.38
3	952.87	27.52	25.56	32.02	2.50E-04	-3.60	1.41	6.45
3	953.41	27.63	14.81	20.56	1.47E-04	-3.83	1.17	5.75
3	953.41	27.7	7.15	12.35	9.26E-05	-4.03	0.85	5.20
3	953.41	27.73	4.57	8.98	4.34E-05	-4.36	0.66	4.41
3	953.41	27.79	4.37	2.03	3.70E-05	-4.43	0.64	4.26
3	953.66	27.81	3.65	0.12	1.57E-05	-4.80	0.56	3.54
3	953.9	27.85	3.32	-4.63	1.80E-05	-4.75	0.52	3.64
3	953.9	27.89	3.12	-9.01	1.05E-05	-4.98	0.49	3.24
3	953.66	27.92	3.05	-11.36	8.91E-06	-5.05	0.48	3.13
3	953.41	27.94	2.88	-13.85	6.13E-06	-5.21	0.46	2.88
3	953.17	27.96	2.63	-15.8	4.36E-06	-5.36	0.42	2.68
3	953.41	27.96	2.33	-16.81	2.31E-06	-5.64	0.37	2.33
3	953.66	27.98	2.48	-17.96	3.08E-06	-5.51	0.39	2.48
3	953.9	27.98	4.56	-18.61	1.86E-06	-5.73	0.66	2.22
2	953.9	28.27	6.08	12.72	2.85E-04	-3.55	0.78	6.64
2	954	28.28	23.94	28.6	5.60E-05	-4.25	1.38	4.66
2	954.1	29.07	32.22	41.49	1.32E-03	-2.88	1.51	9.27
2	954.14	31.12	28.00	37.63	1.58E-03	-2.80	1.45	9.64
2	954.14	31.71	25.47	35.56	1.96E-03	-2.71	1.41	10.10
3	954.14	32.18	5.48	14.52	1.17E-03	-2.93	0.74	9.03
3	954.14	32.25	0.43	6.8	2.35E-04	-3.63	-0.37	6.37
3	954.14	32.36	0.33	-4.86	1.33E-04	-3.87	-0.48	5.63
3	954.14	32.4	0.32	-9.23	6.69E-05	-4.17	-0.49	4.85
3	954.14	32.43	0.30	-12.79	4.68E-05	-4.33	-0.52	4.49
3	954.14	32.47	0.28	-17.09	3.60E-05	-4.44	-0.55	4.24
3	954.14	32.49	0.26	-19.58	3.28E-05	-4.48	-0.59	4.15
3	953.9	32.52	0.24	-22.27	1.91E-05	-4.72	-0.62	3.69
3	953.9	32.53	0.22	-23.87	1.35E-05	-4.87	-0.66	3.42
3	953.9	32.55	0.20	-25.58	1.76E-05	-4.75	-0.70	3.63
3	954.14	32.59	0.18	-29.69	8.47E-06	-5.07	-0.74	3.09
3	954.62	32.6	0.16	-31.63	6.41E-06	-5.19	-0.80	2.91
3	954.87	32.62	0.14	-33.15	4.86E-06	-5.31	-0.85	2.74
3	955.59	32.63	0.12	-34.46	4.04E-06	-5.39	-0.92	2.63
3	956.08	32.64	0.10	-35.97	3.91E-06	-5.41	-1.00	2.61
4	956.56	32.66	0.08	-37.71	2.57E-06	-5.59	-1.10	2.39

WG23

M	T (°C)	Strain%	corstress	Stress MPa	Str.Rate (s-1)	log edot	log stress	corjacket
2	995.54	0	0.00	0	5.16E-05			
2	995.79	0.25	26.15	30.01	5.16E-05	-4.29	1.42	3.86
2	995.79	0.43	61.42	65.08	4.02E-05	-4.40	1.79	3.66
2	995.54	0.62	93.45	97.11	4.00E-05	-4.40	1.97	3.66
2	995.3	0.87	120.81	124.74	5.61E-05	-4.25	2.08	3.93
2	995.54	1.08	141.14	144.96	4.89E-05	-4.31	2.15	3.82
2	995.54	1.27	155.42	159.37	5.74E-05	-4.24	2.19	3.95
2	995.54	1.51	168.64	172.68	6.30E-05	-4.20	2.23	4.03
2	995.54	1.83	180.36	184.49	6.98E-05	-4.16	2.26	4.12
2	995	2.32	192.01	196.17	7.27E-05	-4.14	2.28	4.16
2	995.56	3.03	192.15	196.43	8.25E-05	-4.08	2.28	4.28
2	995.12	3.64	194.22	198.45	7.83E-05	-4.11	2.29	4.23
2	995.3	4.42	189.63	193.88	8.06E-05	-4.09	2.28	4.26
2	995.3	5.56	183.89	188.18	8.33E-05	-4.08	2.26	4.29
2	995.3	6.66	179.71	183.96	8.05E-05	-4.09	2.25	4.26
2	995.06	7.84	175.22	179.51	8.34E-05	-4.08	2.24	4.29
2	994.82	8.88	169.23	173.49	8.15E-05	-4.09	2.23	4.27
2	995.3	10.03	163.07	167.36	8.36E-05	-4.08	2.21	4.29
2	995.06	10.86	157.90	162.2	8.38E-05	-4.08	2.20	4.29
2	995.54	12.1	151.46	155.75	8.38E-05	-4.08	2.18	4.29
2	995.3	12.87	147.25	151.52	8.20E-05	-4.09	2.17	4.27
2	995.79	14.07	141.35	145.63	8.27E-05	-4.08	2.15	4.28
2	995.79	15.28	137.55	141.84	8.32E-05	-4.08	2.14	4.29
2	996.27	16.72	131.64	135.92	8.24E-05	-4.08	2.12	4.28
2	996.27	17.86	126.76	131.04	8.27E-05	-4.08	2.10	4.28
2	996.51	18.8	123.43	127.68	8.05E-05	-4.09	2.09	4.26
2	996.76	19.6	119.83	124.14	8.53E-05	-4.07	2.08	4.31
2	996.76	20.72	116.83	121.09	8.08E-05	-4.09	2.07	4.26
2	997	21.64	113.04	117.31	8.25E-05	-4.08	2.05	4.28
2	997	22.87	108.49	112.77	8.23E-05	-4.08	2.04	4.28

2	997.24	23.76	104.97	109.25	8.34E-05	-4.08	2.02	4.29
2	997.48	24.38	102.95	107.23	8.28E-05	-4.08	2.01	4.28
3	997.48	24.42	96.99	100.55	3.53E-05	-4.45	1.99	3.56
3	997.48	24.47	90.86	94.31	3.07E-05	-4.51	1.96	3.45
4	997.48	24.52	85.68	88.95	2.38E-05	-4.62	1.93	3.27

WG26

M	T (°C)	Strain%	corstress	Stress MPa	Str.Rate (s-1)	log edot	log stress	corjacket
2	999.25	0	0.00	0	1.15E-07	-6.94	0.00	0.00
2	996.85	0.12	2.28	3.39	1.15E-07	-6.94	0.36	1.11
2	996.1	0.26	2.87	3.98	1.14E-07	-6.94	0.60	1.11
2	996.37	0.38	4.29	5.48	1.31E-07	-6.88	0.74	1.19
2	995.71	0.52	4.37	5.5	1.18E-07	-6.93	0.74	1.13
2	994.96	0.66	5.70	6.87	1.27E-07	-6.90	0.84	1.17
2	994.92	0.82	5.65	6.84	1.31E-07	-6.88	0.84	1.19
2	994.46	0.97	6.39	7.53	1.21E-07	-6.92	0.88	1.14
2	994.02	1.09	7.74	8.86	1.17E-07	-6.93	0.95	1.12
2	997.34	1.24	6.65	7.84	1.31E-07	-6.88	0.89	1.19
2	996.32	2.17	9.77	10.93	1.24E-07	-6.91	1.04	1.16
2	996.2	2.63	11.18	12.32	1.21E-07	-6.92	1.09	1.14
2	997.19	3	10.60	11.76	1.23E-07	-6.91	1.07	1.16
2	997.41	3.36	11.58	12.74	1.24E-07	-6.91	1.11	1.16
2	998.62	3.78	12.05	13.22	1.26E-07	-6.90	1.12	1.17
2	999.54	4.25	13.79	14.94	1.23E-07	-6.91	1.17	1.15
2	999.06	4.79	13.46	14.61	1.22E-07	-6.91	1.16	1.15
2	998.33	5.39	13.69	14.86	1.26E-07	-6.90	1.17	1.17
2	998.5	6.09	14.04	15.2	1.23E-07	-6.91	1.18	1.16
2	998.45	6.6	14.00	15.15	1.22E-07	-6.91	1.18	1.15
2	998.55	7.17	14.08	15.24	1.24E-07	-6.91	1.18	1.16
2	998.81	7.65	13.18	14.36	1.28E-07	-6.89	1.16	1.18
2	998.6	8.11	13.04	14.19	1.22E-07	-6.91	1.15	1.15
3	997.87	8.19	12.62	13.76	1.19E-07	-6.92	1.14	1.14
3	997.89	8.22	9.22	10.12	7.54E-08	-7.12	1.01	0.90
3	997.92	8.25	6.65	7.52	7.03E-08	-7.15	0.88	0.87
3	997.46	8.26	5.47	6.1	3.71E-08	-7.43	0.79	0.63
3	998.26	8.27	4.54	5.11	3.01E-08	-7.52	0.71	0.57
3	998.57	8.27	3.75	4.28	2.64E-08	-7.58	0.63	0.53
3	998.86	8.28	3.20	3.67	2.03E-08	-7.69	0.57	0.47
3	999.23	8.29	2.22	2.73	2.39E-08	-7.62	0.44	0.51
2	998.06	8.31	-0.06	0.62	4.35E-08	-7.36	-0.21	0.68
2	998.06	8.16	3.64	4.33	4.35E-08	-7.36	0.64	0.69
2	998.06	8.28	8.06	10.51	5.52E-06	-5.26	1.02	2.45
2	997.77	8.39	10.71	13.42	6.74E-06	-5.17	1.13	2.71
2	997.77	8.59	18.55	21.05	5.74E-06	-5.24	1.32	2.50
2	997.92	8.76	21.87	24.53	6.54E-06	-5.18	1.39	2.66
2	997.92	8.82	23.59	26.01	5.41E-06	-5.27	1.42	2.42
2	997.92	9.04	25.88	28.43	5.98E-06	-5.22	1.45	2.55
2	997.7	9.5	26.28	28.93	6.47E-06	-5.19	1.46	2.65
2	997.77	9.55	26.01	28.46	5.52E-06	-5.26	1.45	2.45
2	997.77	9.83	24.77	27.46	6.67E-06	-5.18	1.44	2.69
3	997.75	10	19.51	21.87	5.09E-07	-6.29	1.34	2.36
3	997.58	10.03	16.27	17.97	2.66E-07	-6.58	1.25	1.70
3	997.53	10.06	13.64	15.07	1.89E-07	-6.72	1.18	1.43
3	997.85	10.08	11.38	12.59	1.35E-07	-6.87	1.10	1.21
3	997.8	10.1	9.64	10.75	1.14E-07	-6.94	1.03	1.11
3	998.04	10.11	8.00	9.02	9.59E-08	-7.02	0.96	1.02
3	997.51	10.13	5.47	6.52	1.02E-07	-6.99	0.81	1.05
3	997.6	10.14	5.25	6.01	5.31E-08	-7.27	0.78	0.76
3	997.51	10.15	3.74	4.66	7.77E-08	-7.11	0.67	0.92
3	997.55	10.16	2.73	3.61	7.10E-08	-7.15	0.56	0.88
3	997.68	10.17	2.06	2.86	5.99E-08	-7.22	0.46	0.80
3	997.72	10.17	2.50	3.1	3.35E-08	-7.47	0.49	0.60
2	997.68	10.2	3.51	5.12	2.41E-07	-6.62	0.71	1.61
2	997.7	9.87	8.70	10.3	2.36E-06	-5.63	1.01	1.60
2	997.7	10.11	13.39	14.99	2.36E-06	-5.63	1.18	1.60
2	997.7	10.11	13.39	14.99	2.36E-05	-4.63	1.18	1.60
2	997.63	11.61	38.32	44.11	3.08E-05	-4.51	1.64	5.79
2	997.6	12.55	38.14	44.05	3.21E-04	-3.49	1.64	5.91
2	997.6	13.5	35.00	40.95	3.27E-04	-3.49	1.61	5.95
2	997.7	14.46	29.47	35.35	3.17E-04	-3.50	1.55	5.88
3	997.68	14.5	23.25	27.18	1.43E-05	-4.85	1.43	3.93

3	997.55	14.54	18.60	22.09	1.12E-06	-5.95	1.34	3.49
3	997.63	14.59	14.15	16.9	6.94E-07	-6.16	1.23	2.75
3	998.11	14.61	11.99	14.14	4.30E-07	-6.37	1.15	2.15
3	998.45	14.64	8.62	10.78	4.30E-07	-6.37	1.03	2.16
3	998.23	14.66	7.26	9.11	3.18E-07	-6.50	0.96	1.85
3	998.4	14.67	6.17	7.8	2.45E-07	-6.61	0.89	1.63
3	998.16	14.68	4.60	6.36	2.85E-07	-6.54	0.80	1.76
3	997.87	14.69	4.21	5.64	1.89E-07	-6.72	0.75	1.43
3	997.89	14.71	2.59	4.05	1.97E-07	-6.71	0.61	1.46
3	997.87	14.72	1.05	2.32	1.50E-07	-6.82	0.37	1.27
3	998.11	14.74	-0.75	0.45	1.33E-07	-6.88	-0.35	1.20
3	997.97	14.76	-0.82	0.33	1.23E-07	-6.91	-0.48	1.15
3	998.01	14.77	-0.84	0.23	1.06E-07	-6.97	-0.64	1.07
4	998.04	14.77	-0.79	0.12	7.69E-08	-7.11	-0.92	0.91

WG27

M	T (°C)	Strain%	corstress	Stress MPa	Str.Rate (s-1)	log edot	log stress	corjacket
2	945.04	0	0.00	0	5.60E-05			
2	945.04	0.29	29.00	33.69	5.79E-05	-4.24	1.46	4.70
2	945.04	0.49	53.94	58.64	5.81E-05	-4.24	1.73	4.70
2	945.04	0.77	82.48	87.24	6.21E-05	-4.21	1.92	4.77
2	945.04	1.12	115.80	120.56	6.13E-05	-4.21	2.06	4.76
2	945.04	1.54	147.78	152.67	6.98E-05	-4.16	2.17	4.89
2	945.04	2.08	175.12	180.11	7.69E-05	-4.11	2.24	5.00
2	945.04	2.74	197.55	202.7	8.86E-05	-4.05	2.30	5.15
2	945.04	3.54	215.01	220.2	9.21E-05	-4.04	2.33	5.19
2	945.04	4.49	230.27	235.52	9.72E-05	-4.01	2.36	5.26
2	945.04	5.31	238.64	243.9	9.70E-05	-4.01	2.38	5.25
2	945.04	6.31	243.42	248.78	1.06E-04	-3.98	2.39	5.35
2	945.04	7.19	242.99	248.33	1.05E-04	-3.98	2.39	5.35
2	945.04	8.88	238.17	243.58	1.10E-04	-3.96	2.38	5.40
2	945.04	10.05	231.54	236.96	1.12E-04	-3.95	2.36	5.42
2	945.04	11.13	228.02	233.46	1.14E-04	-3.94	2.36	5.44
2	944.79	12.3	217.30	222.7	1.10E-04	-3.96	2.34	5.40
2	944.48	14.13	203.09	208.54	1.15E-04	-3.94	2.31	5.45
2	945.08	15.53	193.61	199.03	1.13E-04	-3.95	2.29	5.43
2	945.01	17.04	182.41	187.9	1.19E-04	-3.93	2.26	5.49
2	945.04	17.97	176.62	182.03	1.11E-04	-3.96	2.25	5.41
2	945.38	19.21	164.53	169.98	1.15E-04	-3.94	2.22	5.45
2	945.11	20.35	155.64	161.11	1.17E-04	-3.93	2.19	5.47
2	945.16	21.44	145.30	150.75	1.15E-04	-3.94	2.16	5.45
2	945.23	22.81	132.03	137.51	1.17E-04	-3.93	2.12	5.47
2	945.23	23.79	122.85	128.31	1.16E-04	-3.93	2.09	5.46
3	945.25	23.95	111.84	117.36	1.22E-04	-3.91	2.05	5.52
3	945.35	24.12	96.97	101.62	5.52E-05	-4.26	1.99	4.65
3	945.42	24.25	84.94	89.03	3.06E-05	-4.51	1.93	4.09
3	945.42	24.34	77.29	80.95	1.85E-05	-4.73	1.89	3.66
3	945.35	24.44	68.82	72.22	1.30E-05	-4.89	1.84	3.40
3	945.04	24.51	62.67	65.77	8.50E-06	-5.07	1.80	3.10
3	945.25	24.57	57.63	60.44	5.50E-06	-5.26	1.76	2.81
3	944.96	24.64	51.56	54.3	4.90E-06	-5.31	1.71	2.74
3	945.28	24.72	44.78	47.31	3.30E-06	-5.48	1.65	2.52
3	944.89	24.79	38.25	40.55	2.20E-06	-5.66	1.58	2.30
3	945.01	24.84	33.76	35.85	1.40E-06	-5.86	1.53	2.09
3	944.92	24.89	29.87	31.87	1.10E-06	-5.95	1.48	2.00
3	944.75	24.91	27.82	29.66	8.00E-07	-6.11	1.44	1.84
4	944.62	24.95	25.04	26.92	9.00E-07	-6.06	1.40	1.88

WG28

M	T (°C)	Strain%	corstress	Stress MPa	Str.Rate (s-1)	log edot	log stress	corjacket
2	899.49	0	0	0	0.00E+00			0
2	899.35	0.33	27.1	1.72E-02	2.09E+01	-4.06	1.32	6.18
2	899.23	0.62	56.56	1.66E-02	5.05E+01	-4.10	1.70	6.06
2	899.39	0.98	91.13	1.66E-02	8.51E+01	-4.10	1.93	6.05
2	899.39	1.32	116.53	1.74E-02	1.10E+02	-4.05	2.04	6.23
2	899.39	1.72	144.91	1.76E-02	1.39E+02	-4.04	2.14	6.25

2	899.39	2.07	166.66	1.83E-02	1.60E+02	-4.00	2.20	6.38
2	899.39	2.41	183.93	1.87E-02	1.77E+02	-3.98	2.25	6.45
2	899.39	2.69	198.69	1.91E-02	1.92E+02	-3.96	2.28	6.49
2	899.39	2.9	207.62	1.89E-02	2.01E+02	-3.97	2.30	6.46
2	899.39	3.04	212.53	1.96E-02	2.06E+02	-3.93	2.31	6.61
2	899.39	3.23	218.93	2.00E-02	2.12E+02	-3.91	2.33	6.68
2	899.39	3.6	228.45	2.02E-02	2.22E+02	-3.90	2.35	6.72
3	899.39	3.63	220.84	8.74E-03	2.16E+02	-4.74	2.34	4.41
3	899.39	3.89	202.33	1.12E-02	1.97E+02	-4.49	2.30	4.98
3	899.39	4.12	185.24	7.30E-03	1.81E+02	-4.92	2.26	4.03
3	899.39	4.33	170.37	5.80E-03	1.67E+02	-5.15	2.22	3.58
3	899.39	4.53	155.83	4.65E-03	1.53E+02	-5.37	2.18	3.21
3	899.39	4.66	146.52	4.05E-03	1.44E+02	-5.51	2.16	2.99
3	897.24	4.83	135.05	3.62E-03	1.32E+02	-5.62	2.12	2.86
3	896.22	5.05	119.71	3.09E-03	1.17E+02	-5.78	2.07	2.64
3	898.6	5.35	98.79	2.58E-03	9.64E+01	-5.96	1.98	2.4
3	898.14	5.46	91.12	2.09E-03	8.90E+01	-6.17	1.95	2.17
3	897.36	5.58	82.42	1.97E-03	8.03E+01	-6.23	1.90	2.11
2	896.9	6.32	132.02	9.10E-03	1.27E+02	-4.70	2.11	4.53
2	896.9	5.74	161.96	5.41E-03	1.58E+02	-5.22	2.20	3.49
2	896.9	5.88	170.65	1.89E-02	1.64E+02	-3.97	2.22	6.54
2	896.9	6.1	187.38	1.72E-02	1.81E+02	-4.06	2.26	6.24
2	896.9	6.42	204.47	1.81E-02	1.98E+02	-4.01	2.30	6.41
2	896.9	6.58	213.15	1.83E-02	2.07E+02	-4.00	2.32	6.44
2	896.9	6.93	223.12	1.98E-02	2.16E+02	-3.92	2.34	6.71
2	896.9	7.2	229.25	2.09E-02	2.22E+02	-3.87	2.35	6.87
2	896.9	7.59	235.53	2.09E-02	2.29E+02	-3.87	2.36	6.87
2	896.9	8.24	242.46	2.15E-02	2.35E+02	-3.84	2.37	6.99
2	896.9	9.13	244.96	2.19E-02	2.38E+02	-3.82	2.38	7.06
3	896.71	9.4	226.4	1.56E-02	2.20E+02	-4.16	2.34	5.94
3	896.66	9.86	194.2	9.00E-03	1.90E+02	-4.71	2.28	4.52
3	896.56	10.09	177.64	5.86E-03	1.74E+02	-5.14	2.24	3.65
3	896.42	10.39	157.26	4.99E-03	1.54E+02	-5.30	2.19	3.37
3	896.08	10.65	138.86	3.93E-03	1.36E+02	-5.54	2.13	2.99
3	896.13	10.89	122.76	3.12E-03	1.20E+02	-5.77	2.08	2.66
3	896.05	11.1	108.78	2.74E-03	1.06E+02	-5.90	2.03	2.5
3	895.57	11.26	97.51	2.38E-03	9.52E+01	-6.04	1.98	2.34
3	894.82	11.43	86.09	2.20E-03	8.38E+01	-6.12	1.92	2.25
3	894.38	11.59	75.71	1.73E-03	7.37E+01	-6.36	1.87	1.99
3	894.02	11.64	72.21	1.39E-03	7.04E+01	-6.58	1.85	1.79
3	892.95	11.72	66.9	1.29E-03	6.52E+01	-6.65	1.81	1.74
3	893.22	11.83	59.98	1.32E-03	5.82E+01	-6.63	1.77	1.75
3	892.98	11.92	53.81	1.21E-03	5.21E+01	-6.72	1.72	1.67
3	892.98	11.98	49.96	9.03E-04	4.85E+01	-7.01	1.69	1.45
3	893.2	12.04	46.07	9.98E-04	4.46E+01	-6.91	1.65	1.52
3	892.71	12.12	41.09	9.40E-04	3.96E+01	-6.97	1.60	1.48
2	892.59	12.63	74.19	7.99E-03	6.99E+01	-4.83	1.84	4.33
2	892.59	11.85	100.27	9.10E-03	9.57E+01	-4.70	1.98	4.62
2	892.59	12.09	127.52	1.55E-02	1.21E+02	-4.17	2.08	6.03
2	892.59	12.35	148	1.74E-02	1.42E+02	-4.05	2.15	6.39
2	892.59	12.71	170.18	1.80E-02	1.64E+02	-4.02	2.21	6.48
2	892.59	13.09	185.97	1.94E-02	1.79E+02	-3.94	2.25	6.74
2	892.59	13.46	196.35	2.07E-02	1.89E+02	-3.88	2.28	6.95
2	892.59	13.79	204.97	1.93E-02	1.98E+02	-3.95	2.30	6.73
2	892.59	14.45	212.86	2.17E-02	2.06E+02	-3.83	2.31	7.12
2	892.59	15.27	219.51	2.17E-02	2.12E+02	-3.83	2.33	7.11
2	892.59	15.8	221.95	2.40E-02	2.14E+02	-3.73	2.33	7.5
2	892.59	16.13	224.57	2.09E-02	2.18E+02	-3.87	2.34	6.98
3	892.59	16.46	204.97	1.62E-02	1.99E+02	-4.12	2.30	6.16
3	892.49	16.82	180.72	8.83E-03	1.76E+02	-4.73	2.25	4.55
3	892.59	16.97	170.57	6.10E-03	1.67E+02	-5.10	2.22	3.78
3	892.54	17.11	161.27	5.30E-03	1.58E+02	-5.24	2.20	3.53
3	892.91	17.25	151.36	4.75E-03	1.48E+02	-5.35	2.17	3.33
3	893.27	17.46	137.82	3.89E-03	1.35E+02	-5.55	2.13	3.01
3	893.27	17.61	127.76	3.09E-03	1.25E+02	-5.78	2.10	2.68
3	893.58	17.84	112.49	2.63E-03	1.10E+02	-5.94	2.04	2.48
3	893.54	18.03	100	2.22E-03	9.77E+01	-6.11	1.99	2.26
3	893.37	18.15	92.25	2.01E-03	9.01E+01	-6.21	1.95	2.16
3	901.07	18.29	83.5	1.65E-03	8.16E+01	-6.41	1.91	1.9
2	896.88	18.84	48.4	5.52E-03	4.49E+01	-5.20	1.65	3.53
2	898.09	18.68	95.42	5.41E-03	9.20E+01	-5.22	1.96	3.48
2	899.15	18.86	128.17	1.33E-02	1.23E+02	-4.32	2.09	5.43
2	899.95	19.1	154.92	1.53E-02	1.49E+02	-4.18	2.17	5.83
2	900.51	19.57	182.47	1.81E-02	1.76E+02	-4.01	2.25	6.32
2	900.65	19.92	192.28	1.96E-02	1.86E+02	-3.93	2.27	6.56

2	900.73	20.4	203.19	2.02E-02	1.97E+02	-3.90	2.29	6.67
2	901.07	21.16	209.76	2.11E-02	2.03E+02	-3.86	2.31	6.79
2	901.94	22.2	207.84	2.33E-02	2.01E+02	-3.76	2.30	7.12
2	902.06	23.71	205.03	2.24E-02	1.98E+02	-3.80	2.30	6.99
2	902.64	25.59	203.17	2.26E-02	1.96E+02	-3.79	2.29	7
2	902.88	27.24	201.12	2.26E-02	1.94E+02	-3.79	2.29	6.99
3	902.86	27.57	180.78	1.55E-02	1.75E+02	-4.17	2.24	5.78
3	902.57	27.89	160.11	1.01E-02	1.55E+02	-4.60	2.19	4.67
3	901.48	28.11	145.86	6.04E-03	1.42E+02	-5.11	2.15	3.62
3	901.94	28.32	132.55	4.89E-03	1.29E+02	-5.32	2.11	3.26
3	901.26	28.61	114.62	4.09E-03	1.12E+02	-5.50	2.05	2.98
3	901.48	28.84	100.03	3.21E-03	9.74E+01	-5.74	1.99	2.65
3	901.26	29.11	83.51	2.74E-03	8.11E+01	-5.90	1.91	2.44
3	901.07	29.29	72.65	1.91E-03	7.06E+01	-6.26	1.85	2.05
3	900.92	29.49	60.41	1.87E-03	5.84E+01	-6.28	1.77	2.03
3	900.7	29.67	49.34	1.56E-03	4.75E+01	-6.46	1.68	1.85
3	900.34	29.79	42.38	1.28E-03	4.07E+01	-6.66	1.61	1.68
2	899.95	30.17	64.78	1.04E-02	6.00E+01	-4.57	1.78	4.79
2	900.1	29.61	99.41	1.09E-02	9.45E+01	-4.52	1.98	4.9
2	900.24	29.82	128.77	1.43E-02	1.23E+02	-4.25	2.09	5.6
2	900.29	30.1	153.89	1.64E-02	1.48E+02	-4.11	2.17	6.03
2	900.22	30.53	173.6	1.87E-02	1.67E+02	-3.98	2.22	6.43
2	900.24	30.93	186.07	1.87E-02	1.80E+02	-3.98	2.25	6.41
2	900.36	31.56	194.48	2.13E-02	1.88E+02	-3.85	2.27	6.85
2	900.41	32.99	200.71	2.21E-02	1.94E+02	-3.81	2.29	6.97
2	900.41	34.24	201.5	2.26E-02	1.94E+02	-3.79	2.29	7.06
2	900.44	35.67	203.05	2.28E-02	1.96E+02	-3.78	2.29	7.07
2	900.68	36.84	202.52	2.24E-02	1.96E+02	-3.80	2.29	7.01
2	900.8	38.03	203.33	2.26E-02	1.96E+02	-3.79	2.29	7.04
2	901.02	39.08	204.15	2.28E-02	1.97E+02	-3.78	2.29	7.08
3	901.02	39.29	187.53	1.66E-02	1.82E+02	-4.10	2.26	6.02
3	900.92	39.53	173.01	1.27E-02	1.68E+02	-4.37	2.22	5.27
3	901.26	39.75	159.49	8.74E-03	1.55E+02	-4.74	2.19	4.38
3	901.38	39.97	145.76	6.67E-03	1.42E+02	-5.01	2.15	3.83
3	901.99	40.13	135.96	5.63E-03	1.32E+02	-5.18	2.12	3.5
3	901.4	40.52	112.75	4.56E-03	1.10E+02	-5.39	2.04	3.15
3	900.65	40.76	98.76	3.31E-03	9.61E+01	-5.71	1.98	2.7
3	900.9	41	84.42	2.63E-03	8.20E+01	-5.94	1.91	2.4
3	901.14	41.22	71.63	2.09E-03	6.95E+01	-6.17	1.84	2.14
3	901.11	41.49	55.99	1.78E-03	5.40E+01	-6.33	1.73	1.97
3	900.75	41.68	45.45	1.27E-03	4.38E+01	-6.67	1.64	1.67
3	900.61	41.84	36.36	1.21E-03	3.47E+01	-6.72	1.54	1.63
3	900.65	41.94	30.42	8.59E-04	2.91E+01	-7.06	1.46	1.37
3	899.98	42.01	26.92	7.32E-04	2.57E+01	-7.22	1.41	1.27
3	898.79	42.07	23.17	7.10E-04	2.19E+01	-7.25	1.34	1.26
4	898.35	42.14	19.4	6.36E-04	1.82E+01	-7.36	1.26	1.19

WG29

M	T (°C)	Strain%	corstress	Stress MPa	Str.Rate (s-1)	log edot	log stress	corjacket
2	1000	0	0	1.83E-02	0.00E+00	-4.00	-2.85	4.46
2	1000	0.47	10.08	2.02E-02	5.38E+00	-3.90	0.73	4.7
2	1000	0.9	23.44	2.09E-02	1.87E+01	-3.87	1.27	4.76
2	1000	1.48	35.3	2.04E-02	3.06E+01	-3.89	1.49	4.72
2	1000	2.2	48.77	2.09E-02	4.40E+01	-3.87	1.64	4.77
2	1000	2.73	58.19	2.11E-02	5.34E+01	-3.86	1.73	4.78
2	1000	3.41	67.89	2.15E-02	6.31E+01	-3.84	1.80	4.83
2	1000	3.92	73.86	2.11E-02	6.91E+01	-3.86	1.84	4.79
2	1000	4.53	78.86	2.26E-02	7.39E+01	-3.79	1.87	4.96
2	1000	5.19	82.68	2.19E-02	7.78E+01	-3.82	1.89	4.87
2	1000	5.93	84.7	2.21E-02	7.98E+01	-3.81	1.90	4.9
3	1000	6.19	76.46	1.85E-02	7.20E+01	-3.99	1.86	4.49
3	1000	6.35	65.45	1.05E-02	6.21E+01	-4.56	1.79	3.37
3	1000	6.48	56.23	8.07E-03	5.33E+01	-4.82	1.73	2.97
3	1002.42	6.6	48.54	5.98E-03	4.60E+01	-5.12	1.66	2.53
3	1001.45	6.74	38.79	4.65E-03	3.66E+01	-5.37	1.56	2.23
3	1000.41	6.84	32	3.77E-03	3.00E+01	-5.58	1.48	2.02
3	999.88	6.95	24.79	3.38E-03	2.29E+01	-5.69	1.36	1.92
3	1001.04	7.04	18.52	2.33E-03	1.69E+01	-6.06	1.23	1.59
3	1000.22	7.11	13.69	1.75E-03	1.23E+01	-6.35	1.09	1.37
3	999.81	7.15	11.13	1.44E-03	9.87E+00	-6.54	0.99	1.25
3	999.15	7.17	9.99	9.21E-04	8.98E+00	-6.99	0.95	1

3	998.81	7.21	6.96	1.22E-03	5.81E+00	-6.71	0.76	1.15
2	998.38	7.4	19.16	6.35E-03	1.65E+01	-5.06	1.22	2.63
2	998.38	7.28	30.52	6.74E-03	2.78E+01	-5.00	1.44	2.72
2	998.38	7.76	46.25	2.04E-02	4.15E+01	-3.89	1.62	4.74
2	998.38	8.18	58.47	1.93E-02	5.39E+01	-3.95	1.73	4.6
2	998.38	8.58	66.26	2.15E-02	6.14E+01	-3.84	1.79	4.86
2	998.38	8.99	71.9	2.13E-02	6.71E+01	-3.85	1.83	4.83
2	998.38	9.29	76.54	1.96E-02	7.19E+01	-3.93	1.86	4.65
2	998.38	9.6	78.24	2.26E-02	7.33E+01	-3.79	1.86	4.99
2	998.38	9.91	79.38	2.28E-02	7.44E+01	-3.78	1.87	5.01
3	998.38	10.23	73.24	1.74E-02	6.89E+01	-4.05	1.84	4.37
3	998.38	10.37	64.18	9.47E-03	6.10E+01	-4.66	1.79	3.23
3	998.38	10.47	57.13	7.99E-03	5.42E+01	-4.83	1.73	2.95
3	998.43	10.61	48.28	5.41E-03	4.58E+01	-5.22	1.66	2.44
3	998.38	10.78	37	4.17E-03	3.49E+01	-5.48	1.54	2.13
3	998.47	10.94	26.04	3.03E-03	2.42E+01	-5.80	1.38	1.82
3	997.51	11.09	16.58	2.24E-03	1.50E+01	-6.10	1.18	1.57
3	997.68	11.17	10.91	1.40E-03	9.67E+00	-6.57	0.99	1.24
3	996.97	11.24	6.4	1.03E-03	5.33E+00	-6.88	0.73	1.07
3	996.78	11.29	3.58	6.76E-04	2.72E+00	-7.30	0.43	0.86
3	996.88	11.31	2.16	4.62E-04	1.45E+00	-7.68	0.16	0.71
3	996.73	11.32	1.57	3.07E-04	9.80E-01	-8.09	-0.01	0.58
2	996.76	11.5	13.31	1.41E-02	9.35E+00	-4.26	0.97	3.96
2	996.76	11.43	23.78	1.83E-02	1.93E+01	-4.00	1.28	4.51
2	996.76	11.59	27.83	2.33E-02	2.27E+01	-3.76	1.36	5.09
2	996.76	12	40.21	1.93E-02	3.56E+01	-3.95	1.55	4.63
2	996.76	12.43	47.57	2.13E-02	4.27E+01	-3.85	1.63	4.87
2	996.76	12.94	56.13	2.07E-02	5.13E+01	-3.88	1.71	4.79
2	996.76	13.49	60.63	2.24E-02	5.56E+01	-3.80	1.75	5
2	996.76	13.84	64.33	1.98E-02	5.96E+01	-3.92	1.78	4.69
2	996.76	14.13	66.12	2.38E-02	6.10E+01	-3.74	1.79	5.12
3	996.76	14.41	61.55	1.69E-02	5.72E+01	-4.08	1.76	4.34
3	996.76	14.48	57.1	9.10E-03	5.39E+01	-4.70	1.73	3.18
3	996.76	14.58	50.26	7.30E-03	4.74E+01	-4.92	1.68	2.84
3	996.76	14.7	42.66	5.92E-03	4.01E+01	-5.13	1.60	2.56
3	996.76	14.8	36.2	4.13E-03	3.41E+01	-5.49	1.53	2.14
3	996.03	14.89	29.97	3.12E-03	2.81E+01	-5.77	1.45	1.86
3	996.2	15.04	20.65	2.88E-03	1.89E+01	-5.85	1.28	1.79
3	996.13	15.11	16.24	2.07E-03	1.47E+01	-6.18	1.17	1.52
3	995.62	15.16	12.82	1.46E-03	1.16E+01	-6.53	1.06	1.27
3	995.64	15.2	10.16	1.18E-03	9.01E+00	-6.74	0.95	1.15
3	998.52	15.25	6.86	1.11E-03	5.75E+00	-6.80	0.76	1.11
2	998.11	15.43	17.98	1.48E-02	1.39E+01	-4.21	1.14	4.05
2	998.16	15.39	29.66	1.47E-02	2.57E+01	-4.22	1.41	4.02
2	998.33	15.76	44.75	1.93E-02	4.02E+01	-3.95	1.60	4.59
2	998.52	16.08	52.48	2.07E-02	4.77E+01	-3.88	1.68	4.76
2	998.74	16.57	62.27	2.09E-02	5.75E+01	-3.87	1.76	4.78
2	998.67	16.91	66.79	1.98E-02	6.21E+01	-3.92	1.79	4.66
2	998.43	17.51	70.3	2.24E-02	6.54E+01	-3.80	1.82	4.95
2	998.14	18.1	73.95	2.21E-02	6.90E+01	-3.81	1.84	4.95
2	998.01	19.12	75.23	2.26E-02	7.03E+01	-3.79	1.85	4.98
2	998.23	20.03	74.69	2.31E-02	6.97E+01	-3.77	1.84	5.03
3	998.43	20.23	65.77	1.58E-02	6.16E+01	-4.15	1.79	4.16
3	998.6	20.38	56.51	1.03E-02	5.32E+01	-4.58	1.73	3.35
3	998.57	20.5	48.7	6.47E-03	4.60E+01	-5.04	1.66	2.66
3	998.57	20.64	39.78	5.20E-03	3.74E+01	-5.26	1.57	2.39
3	998.38	20.79	30.38	3.97E-03	2.83E+01	-5.53	1.45	2.08
3	998.06	20.92	22.23	2.79E-03	2.05E+01	-5.88	1.31	1.75
3	998.77	21.03	15.63	2.07E-03	1.41E+01	-6.18	1.15	1.5
3	998.72	21.11	10.21	1.56E-03	8.90E+00	-6.46	0.95	1.31
3	998.67	21.17	6.62	1.28E-03	5.44E+00	-6.66	0.74	1.18
3	998.23	21.2	4.85	9.59E-04	3.83E+00	-6.95	0.58	1.02
2	997.34	21.24	2.33	9.68E-04	1.29E+00	-6.94	0.11	1.04
2	997.38	21.47	21.92	4.56E-03	1.97E+01	-5.39	1.29	2.25
2	997.41	21.65	33.98	1.55E-02	2.98E+01	-4.17	1.47	4.14
2	997.48	21.89	41.73	2.07E-02	3.70E+01	-3.88	1.57	4.77
2	997.6	22.28	51.87	1.98E-02	4.72E+01	-3.92	1.67	4.67
2	997.75	22.74	59.12	2.04E-02	5.44E+01	-3.89	1.74	4.75
2	997.8	23.32	64.16	2.19E-02	5.93E+01	-3.82	1.77	4.91
2	997.72	24.02	67.08	2.26E-02	6.21E+01	-3.79	1.79	4.98
2	997.41	24.85	70.03	2.15E-02	6.52E+01	-3.84	1.81	4.88
2	997.51	26.07	70.2	2.28E-02	6.52E+01	-3.78	1.81	5.03
2	997.82	27.26	69.33	2.21E-02	6.44E+01	-3.81	1.81	4.94
2	997.82	28.58	68.26	2.31E-02	6.32E+01	-3.77	1.80	5.03
2	997.82	29.34	68.28	2.24E-02	6.33E+01	-3.80	1.80	4.97

2	997.82	30.42	66.74	2.31E-02	6.17E+01	-3.77	1.79	5.05
3	997.82	30.74	60.23	1.94E-02	5.56E+01	-3.94	1.75	4.62
3	997.82	30.88	51.37	1.08E-02	4.79E+01	-4.53	1.68	3.45
3	997.82	31.02	43.26	6.67E-03	4.05E+01	-5.01	1.61	2.71
3	997.82	31.15	35.35	5.30E-03	3.29E+01	-5.24	1.52	2.41
3	997.82	31.27	28.3	4.30E-03	2.61E+01	-5.45	1.42	2.17
3	997.75	31.34	24.02	3.09E-03	2.22E+01	-5.78	1.35	1.84
3	998.06	31.43	18.26	2.91E-03	1.65E+01	-5.84	1.22	1.79
3	997.92	31.5	14.29	2.29E-03	1.27E+01	-6.08	1.10	1.59
3	997.48	31.56	10.57	1.76E-03	9.17E+00	-6.34	0.96	1.39
3	997.58	31.62	7.17	1.84E-03	5.75E+00	-6.30	0.76	1.42
3	996.92	31.66	4.62	1.29E-03	3.42E+00	-6.65	0.53	1.19
2	996.92	31.95	21.3	1.81E-02	1.68E+01	-4.01	1.23	4.48
2	996.92	32.03	35.03	1.06E-02	3.16E+01	-4.55	1.50	3.42
2	996.92	32.25	42.51	1.96E-02	3.78E+01	-3.93	1.58	4.67
2	996.92	32.68	51.59	1.98E-02	4.69E+01	-3.92	1.67	4.68
2	996.92	33.47	57.14	2.21E-02	5.22E+01	-3.81	1.72	4.96
2	996.92	34.15	60.61	2.21E-02	5.57E+01	-3.81	1.75	4.94
2	996.92	35	62.87	2.21E-02	5.79E+01	-3.81	1.76	4.96
2	996.92	36.16	62.8	2.17E-02	5.79E+01	-3.83	1.76	4.91
2	999.47	37.48	59.08	2.40E-02	5.40E+01	-3.73	1.73	5.11
2	999.06	38.39	57.87	2.31E-02	5.28E+01	-3.77	1.72	5.03
2	998.45	39.28	59.05	2.28E-02	5.40E+01	-3.78	1.73	5
3	998.31	39.57	52.26	1.66E-02	4.80E+01	-4.10	1.68	4.28
3	998.67	39.66	46.8	9.56E-03	4.36E+01	-4.65	1.64	3.23
3	999.78	39.79	39.74	8.15E-03	3.68E+01	-4.81	1.57	2.98
3	998.64	39.9	33.13	5.74E-03	3.06E+01	-5.16	1.49	2.5
3	998.89	40	27.53	4.43E-03	2.53E+01	-5.42	1.40	2.2
3	998.81	40.11	20.93	3.35E-03	1.90E+01	-5.70	1.28	1.92
3	999.06	40.22	14.63	2.82E-03	1.29E+01	-5.87	1.11	1.75
3	999.37	40.27	11.96	1.99E-03	1.05E+01	-6.22	1.02	1.47
3	999.66	40.31	9.74	1.47E-03	8.48E+00	-6.52	0.93	1.26
3	999.69	40.36	6.73	1.80E-03	5.33E+00	-6.32	0.73	1.4
3	999.64	40.4	4.38	1.35E-03	3.17E+00	-6.61	0.50	1.21
2	999.35	40.53	11.74	7.45E-03	8.89E+00	-4.90	0.95	2.84
2	999.44	40.77	25.65	1.67E-02	2.14E+01	-4.09	1.33	4.26
2	999.44	41.03	34.34	1.87E-02	2.98E+01	-3.98	1.47	4.51
2	999.44	41.33	40.07	2.26E-02	3.51E+01	-3.79	1.55	4.96
2	999.44	41.68	48.52	1.78E-02	4.41E+01	-4.03	1.64	4.41
2	999.44	42.4	51.6	2.42E-02	4.65E+01	-3.72	1.67	5.13
2	999.49	42.86	52.62	2.09E-02	4.79E+01	-3.87	1.68	4.77
2	999.59	43.84	53.68	2.33E-02	4.86E+01	-3.76	1.69	5.04
2	999.69	44.45	52.65	2.26E-02	4.77E+01	-3.79	1.68	4.96
3	999.71	44.64	47.17	1.59E-02	4.30E+01	-4.14	1.63	4.17
3	999.85	44.75	40.92	1.01E-02	3.76E+01	-4.60	1.58	3.3
3	999.81	44.83	36.31	7.60E-03	3.34E+01	-4.88	1.52	2.87
3	999.88	44.93	30.82	5.35E-03	2.84E+01	-5.23	1.45	2.41
3	999.88	45.01	26.61	4.34E-03	2.44E+01	-5.44	1.39	2.17
3	999.85	45.08	22.62	3.52E-03	2.07E+01	-5.65	1.32	1.96
3	999.54	45.19	16.53	2.94E-03	1.48E+01	-5.83	1.17	1.79
3	999.52	45.29	10.45	2.03E-03	8.96E+00	-6.20	0.95	1.48
3	999.47	45.37	6.1	1.71E-03	4.73E+00	-6.37	0.67	1.37
3	999.32	45.41	3.82	1.32E-03	2.62E+00	-6.63	0.42	1.2
4	999.08	45.46	1.05	9.59E-04	3.00E-02	-6.95	-1.51	1.02

WG30

M	T (°C)	Strain%	corstress	Stress MPa	Str.Rate (s-1)	log edot	log stress	corjacket
2	1000	0	0	0	1.00E+00	0.00	0.00	1.26
2	997.8	0.99	6.3	4.86	1.87E-03	-6.28	0.69	1.44
2	998.16	2.04	10.9	9.52	1.75E-03	-6.35	0.98	1.38
2	996.3	3.2	14.92	13.5	1.82E-03	-6.31	1.13	1.42
2	995.59	4.44	17.43	16.02	1.80E-03	-6.32	1.20	1.42
2	995.84	5.74	18.65	17.22	1.84E-03	-6.30	1.24	1.43
2	994.55	7.06	22.72	21.31	1.78E-03	-6.33	1.33	1.41
2	993.95	8.51	23.61	22.18	1.82E-03	-6.31	1.35	1.43
2	995.18	9.82	25.25	23.82	1.84E-03	-6.30	1.38	1.43
2	996.61	11.53	25.92	24.49	1.84E-03	-6.30	1.39	1.42
2	995.06	13.07	27.61	26.18	1.82E-03	-6.31	1.42	1.43
2	999.1	14.82	23.88	22.42	1.93E-03	-6.25	1.35	1.45
2	998.74	16.32	23.41	21.99	1.82E-03	-6.31	1.34	1.41
2	997.75	17.64	24.47	23.05	1.84E-03	-6.30	1.36	1.42

2	998.98	18.94	25.34	23.93	1.84E-03	-6.30	1.38	1.41
2	999.42	19.85	25.51	24.11	1.80E-03	-6.32	1.38	1.4
2	997.46	21.39	25.51	24.09	1.85E-03	-6.29	1.38	1.43
2	997.46	22.57	26.69	25.29	1.80E-03	-6.32	1.40	1.41
2	997.77	24.87	26.22	24.8	1.84E-03	-6.30	1.39	1.42
2	997.19	25.77	25.35	23.89	1.93E-03	-6.25	1.38	1.46
2	997.36	27.07	26.38	24.97	1.80E-03	-6.32	1.40	1.41
2	998.6	28.38	26.26	24.83	1.87E-03	-6.28	1.39	1.43
2	998.14	29.27	26.24	24.84	1.80E-03	-6.32	1.40	1.4
2	997.43	28.17	1.43	0.01	1.84E-03	-6.30	-2.08	1.42
2	997.41	29.05	21.49	14.89	3.96E-02	-3.23	1.17	6.6
2	997.46	29.57	43.01	36.56	3.76E-02	-3.28	1.56	6.45
2	997.43	30.04	60.88	54.43	3.76E-02	-3.28	1.74	6.45
2	997.43	30.73	72.06	65.35	4.08E-02	-3.20	1.82	6.71
2	997.48	32.99	73.48	66.35	4.60E-02	-3.08	1.82	7.13
2	997.55	35.43	70.76	63.67	4.55E-02	-3.09	1.80	7.09
2	997.7	38.32	65.12	58.01	4.60E-02	-3.08	1.76	7.11
2	997.85	40.95	60.67	53.56	4.60E-02	-3.08	1.73	7.1
2	997.94	43.24	57.61	50.46	4.64E-02	-3.07	1.70	7.14
2	998.04	45.83	54.66	47.53	4.60E-02	-3.08	1.68	7.12
2	998.18	48.63	52	44.9	4.60E-02	-3.08	1.65	7.09
3	998.21	48.87	45.75	39.41	3.65E-02	-3.31	1.60	6.34
3	998.52	49.12	32.19	27.84	1.72E-02	-4.06	1.44	4.35
3	999.37	49.29	22.86	19.73	9.00E-03	-4.71	1.30	3.13
3	999.78	49.4	16.68	14.16	5.80E-03	-5.15	1.15	2.52
3	999.78	49.47	12.85	10.78	3.93E-03	-5.54	1.03	2.07
3	999.71	49.51	10.34	8.47	3.18E-03	-5.75	0.93	1.86
3	999.66	49.56	7.58	5.94	2.48E-03	-6.00	0.77	1.64
3	999.66	49.64	3.22	1.72	2.07E-03	-6.18	0.24	1.5
3	999.71	49.67	1.79	0.52	1.49E-03	-6.51	-0.29	1.27
3	999.66	49.71	1.28	0.01	1.49E-03	-6.51	-2.01	1.27
3	998.84	49.73	1.18	0.01	1.26E-03	-6.68	-1.99	1.17
2	998.67	50.16	21.73	18.15	1.17E-02	-4.45	1.26	3.58
2	998.74	50.03	28.34	24.89	1.09E-02	-4.52	1.40	3.45
2	998.74	50.49	36.62	30.05	3.96E-02	-3.23	1.48	6.57
2	998.74	51.25	41.18	34.23	4.42E-02	-3.12	1.53	6.95
2	998.79	52.43	43.58	36.57	4.50E-02	-3.10	1.56	7.02
2	998.79	53.74	43.59	36.42	4.69E-02	-3.06	1.56	7.17
2	998.79	54.89	42.85	35.87	4.46E-02	-3.11	1.55	6.98
2	998.86	56.27	43.35	36.29	4.55E-02	-3.09	1.56	7.06
3	998.86	56.52	43.71	36.65	4.55E-02	-3.09	1.56	7.05
3	998.91	56.7	33.87	28.36	2.79E-02	-3.58	1.45	5.51
3	998.86	56.82	27.49	23.02	1.83E-02	-4.00	1.36	4.47
3	998.89	56.89	23.62	20.07	1.16E-02	-4.46	1.30	3.55
3	998.98	56.96	19.68	16.51	9.19E-03	-4.69	1.22	3.17
3	999.37	57.01	16.92	14.23	6.60E-03	-5.02	1.15	2.69
3	999.78	57.06	14.57	11.93	6.41E-03	-5.05	1.08	2.64
3	999.81	57.11	11.72	9.29	5.46E-03	-5.21	0.97	2.44
3	999.81	57.18	8.19	6.12	3.93E-03	-5.54	0.79	2.07
3	999.9	57.23	5.37	3.46	3.35E-03	-5.70	0.54	1.91
3	1000	57.26	3.81	2.27	2.20E-03	-6.12	0.36	1.54
4	1000.17	57.3	1.85	0.32	2.15E-03	-6.14	-0.49	1.53